

Design and commissioning of a mono-energetic photoelectron source and active background reduction by magnetic pulse at the KATRIN experiment

Jan David Behrens, Dissertation 2016

Experimentelle Physik

Dissertationsthema

Design and commissioning of a mono-energetic photoelectron source and active background reduction by magnetic pulse at the KATRIN experiment

**Inaugural-Dissertation
zur Erlangung des Doktorgrades der Naturwissenschaften
im Fachbereich Physik
der Mathematisch-Naturwissenschaftlichen Fakultät
der Westfälischen Wilhelms-Universität Münster**

**vorgelegt von
Jan David Behrens
aus Crailsheim**

— 2016 —

(überarbeitete Version, Juli 2017)



Dekan: Prof. Dr. Michael Klasen
Erster Gutachter: Prof. Dr. Christian Weinheimer
Zweiter Gutachter: Prof. Dr. Dieter Frekers
Tag der mündlichen Prüfung: _____.____._____
Tag der Promotion: _____.____._____

Das Wesentliche ist für die Augen unsichtbar.

— Antoine de Saint-Exupéry, *Der kleine Prinz*

Abstract

The neutrino mass is an important parameter in particle physics, astrophysics and cosmology. Neutrino oscillation experiments that have been carried out over the last decades show unambiguously that the neutrino has a non-zero rest mass, which is in conflict with the established standard model of particle physics. Different experimental techniques have been established to access the absolute neutrino mass scale, such as kinematic measurements of the tritium β -spectrum that will be performed at the KATRIN experiment in the near future.

The KATRIN experiment is designed to achieve a neutrino mass sensitivity of $200 \text{ meV}/c^2$ at 90% C. L., which will reduce the established upper limit for kinematic measurements by roughly a factor of 10. A core part of the experiment is the main spectrometer, where the energy analysis of the β -decay electrons is performed with an energy resolution of 0.93 eV at the tritium endpoint of 18.6 keV. The spectrometer is designed after the MAC-E filter principle, which combines an electrostatic retarding potential with a spatially inhomogeneous magnetic field to achieve this energy resolution while providing having a large acceptance angle for signal electrons.

To determine the neutrino mass from the integral β -spectrum that is measured at KATRIN, one must consider systematic uncertainties like the stability of the β -electron source or the retarding potential, but also inhomogeneities in the electromagnetic fields at the MAC-E filter that define its transmission properties. These properties can be investigated with a dedicated electron source that produces electrons with well-defined properties, such as the emission of mono-energetic electrons under a specific angle to the magnetic field lines. The electrons act as a probe to determine the transmission function of the MAC-E filter over the complete magnetic flux tube of 191 T cm^2 . Such an electron source was developed at WWU Münster over the recent years and used in two commissioning phases of the KATRIN main spectrometer. The design of the source was improved for the second commissioning phase, and the device was successfully commissioned at the KATRIN main spectrometer after a series of test measurements at the monitor spectrometer. The commissioning measurements allowed to determine many important source parameters and verified that the pulsed, angular-selective, mono-energetic UV photoelectron source meets all its requirements. The electron source was then utilized for the main spectrometer commissioning with great success, allowing to precisely determine inhomogeneities of the electromagnetic fields that are relevant for the upcoming neutrino mass measurements at KATRIN. Particle-tracking simulations with the *Kassiopeia* software were conducted to gain further insights into the working principles of the electron source. The simulations utilize many of *Kassiopeia*'s features, especially regarding the simulation geometry and the 3D field computation, and provided crucial information that help to further characterize the electron source.

Another topic that is discussed in this thesis is the active removal of electrons that are stored in the KATRIN main spectrometer. Although the MAC-E filter combines excellent energy resolution with a large acceptance angle, it also serves as an ideal "magnetic bottle" for electrons that are created inside the spectrometer volume. A high storage probability combined with typically long storage times results in a large amount of background that can be created from single nuclear decays inside the spectrometer, like those from radon. This type of background cannot be discriminated easily as it energetically overlaps with the signal electrons due to the MAC-E filter design, and thus can severely limit the experiment's neutrino mass sensitivity. Passive background reduction methods have been implemented at the main spectrometer, such as LN_2 -cooled baffles that reduce the amount of radon nuclei entering the spectrometer volume. Active background reduction methods, using an electric dipole field or a magnetic pulse, have been developed in addition to passive methods in order to further reduce the overall background level. These complementary methods aim to actively remove stored electrons from the spectrometer, and can be operate dynamically if an increased background level is observed. The magnetic pulse method was developed and commissioned at the main spectrometer. It was shown that the reduction of the magnetic field over a short time frame can remove stored electrons from the spectrometer and thus reduces the radon-induced background.

Zusammenfassung

Die Neutrinomasse ist ein wichtiger Parameter in der Teilchenphysik, der Astrophysik und der Kosmologie. Bisherige Experimente zur Neutrinooszillation haben übereinstimmend gezeigt, dass Neutrinos im Widerspruch zum etablierten Standardmodell der Teilchenphysik keine masselosen Teilchen sind. Verschiedene experimentelle Methoden zur Untersuchung der absoluten Massenskala der Neutrinos wurden entwickelt, so etwa kinematische Messungen des Tritium- β -Spektrums, wie sie in naher Zukunft am KATRIN-Experiment durchgeführt werden.

Das KATRIN-Experiment wird eine Sensitivität auf die Neutrinomasse von $200 \text{ meV}/c^2$ bei 90% C. L. erreichen und so die etablierten Obergrenzen aus kinematischen Messungen um etwa einen Faktor 10 verbessern. Ein Kernaspekt des Experiments ist das Hauptspektrometer, in dem die Energieanalyse der β -Elektronen mit einer Auflösung von 0.93 eV am Tritium-Endpunkt bei 18.6 keV durchgeführt wird. Das Spektrometer ist dabei ein MAC-E-Filter, wo ein elektrisches Retardierungspotential mit einem räumlich inhomogenen Magnetfeld kombiniert wird, um die hohe Energieauflösung bei einem großen Öffnungswinkel für Signalelektronen zu erreichen.

Zur Bestimmung der Neutrinomasse aus dem integralen β -Spektrum, welches bei KATRIN vermessen wird, müssen systematische Unsicherheiten wie die Stabilität der β -Elektronenquelle oder des Retardierungspotentials berücksichtigt werden, aber auch Inhomogenitäten in den elektromagnetischen Feldern des MAC-E-Filters, welche dessen Transmissionseigenschaften beeinflussen. Dies kann mit einer speziellen Elektronenquelle untersucht werden, die Elektronen mit genau bestimmten Eigenschaften, wie Emission der Elektronen unter einem bestimmten Winkel zu den Magnetfeldlinien, produziert. Diese Elektronen dienen dabei als Sonde, um die Transmissionsfunktion des MAC-E-Filters innerhalb des gesamten magnetischen Flusschlauchs von 191 T cm^2 zu bestimmen. Eine solche Elektronenquelle wurde über die vergangenen Jahre an der WWU Münster entwickelt und in zwei Kommissionierungsphasen am KATRIN-Hauptspektrometer eingesetzt. Ihr Design wurde für die zweite Messphase überarbeitet, so dass die Elektronenquelle nach einigen Testmessungen am Monitorspektrometer schließlich erfolgreich am Hauptspektrometer in Betrieb genommen werden konnte. Durch die Messungen konnten eine Vielzahl wichtiger Quellparameter bestimmt werden und es wurde gezeigt, dass die gepulste, winkelselektive, mono-energetische UV-Photoelektronenquelle alle benötigten Voraussetzungen erfüllt. Die Quelle wurde daraufhin für die Inbetriebnahme des Hauptspektrometers eingesetzt, um die Inhomogenitäten der elektromagnetischen Felder zu bestimmen. Um weitere Einblicke in die Wirkungsprinzipien der Quelle zu bekommen, wurden außerdem Teilchensimulationen mit Hilfe der Software *Kassiopeia* durchgeführt. Die Simulationen nutzen eine Vielzahl von *Kassiopeia*'s Fähigkeiten, vor allem für die Simulationsgeometrie und die 3D-Feldberechnung, und liefern so wichtige Informationen für die weitere Charakterisierung der Quelle.

Ein weiteres Thema dieser Arbeit ist die aktive Entfernung von gespeicherten Elektronen aus dem KATRIN-Hauptspektrometer. Der MAC-E-Filter verbindet eine exzellente Energieauflösung mit einem großen Öffnungswinkel verbindet, wirkt allerdings auch als ideale „magnetische Flasche“ für Elektronen, die im Inneren des Spektrometers erzeugt werden. Eine hohe Speicherwahrscheinlichkeit und typischerweise lange Speicherzeiten für solche Elektronen können dazu führen, dass einzelne nukleare Zerfälle im Spektrometer, wie solche von Radon, die Untergrundrate erhöhen. Durch das Design des MAC-E-Filters überlappt dieser Untergrund energetisch mit Signalelektronen und ist so nur schwer zu unterbinden, wodurch die Sensitivität auf die Neutrinomasse eingeschränkt wird. Am Hauptspektrometer werden daher passive Methoden zur Untergrundreduktion eingesetzt, wie etwa LN_2 -gekühlte „Baffles“, die verhindern sollen dass Radon das Innere des Spektrometers erreicht. Zusätzlich wurden aktive Methoden entwickelt, die ein elektrisches Dipolfeld oder einen magnetischen Puls nutzen, um den Untergrund weiter zu reduzieren. Diese komplementären Methoden zielen darauf ab, bei erhöhtem Untergrund gespeicherte Elektronen aus dem Spektrometer zu entfernen. Die Methode des magnetischen Pulses wurde im Rahmen dieser Arbeit entwickelt und am Hauptspektrometer implementiert. Es konnte gezeigt werden, dass eine kurzzeitige Reduktion des Magnetfelds gespeicherte Elektronen aus dem Spektrometer entfernen kann und so den Radon-induzierten Untergrund reduziert.

Contents

1. Introduction	1
1.1. A brief history of neutrino physics	1
1.2. The neutrino in the standard model and beyond	3
1.2.1. The oscillation of neutrino flavors	4
1.2.2. Neutrino oscillation experiments	6
1.2.3. Neutrinos in the standard model	8
1.3. Determination of absolute neutrino masses	9
1.3.1. Cosmological studies	10
1.3.2. Neutrinoless double-beta decay	10
1.3.3. Supernovae	11
1.3.4. Kinematic measurements	12
1.4. Thesis outline	16
2. The KATRIN experiment	17
2.1. Experimental setup	18
2.1.1. Source and Transport section	18
2.1.2. Spectrometer and Detector section	20
2.1.3. Electromagnetic design	23
2.1.4. Background reduction	26
2.2. The MAC-E filter	29
2.2.1. Adiabatic collimation	29
2.2.2. Energy resolution	31
2.2.3. Transmission properties	33
2.2.4. Realistic MAC-E filters	35
2.3. Sensitivity to the neutrino mass	38
2.3.1. Theoretical model of the tritium beta spectrum	38
2.3.2. Systematic uncertainties	39
2.3.3. Statistical uncertainties	42
3. Simulation and analysis tools	47
3.1. Introduction	47
3.2. KASPER – The KATRIN simulation and analysis framework	48

3.3.	The particle-tracking software Kassiopeia	50
3.3.1.	Software design	50
3.3.2.	Kassiopeia configuration	51
3.3.3.	Particle generation	53
3.3.4.	Propagation through electromagnetic fields	55
3.3.5.	Navigation inside the simulation geometry	60
3.3.6.	Continuous and discrete interactions	61
3.3.7.	Termination of simulated tracks	63
3.3.8.	Simulation output	65
3.3.9.	Visualization methods	66
3.4.	The geometry toolkit KGeoBag	68
3.4.1.	Definition of geometric shapes	68
3.4.2.	Placement and nesting of geometric parts	69
3.4.3.	Extensions of the geometry system	70
3.5.	The electromagnetic field solver KEMField	70
3.5.1.	Evaluation of magnetic fields	71
3.5.2.	Evaluation of electric fields	74
3.5.3.	Computation of charge densities	76
3.6.	Accessing the KATRIN database with KaLi	79
3.6.1.	Run data from the detector systems	79
3.6.2.	Sensor data from the slow-control systems	81
3.7.	Analyzing measurement results with Beans	82
3.7.1.	Analysis with BEANS	83
3.7.2.	Extensions of the analysis framework	89
3.8.	The post-analysis framework Peaberry	90
3.8.1.	Software design	91
3.8.2.	Analysis procedure	95
3.8.3.	Fit methods	96
4.	A calibration source for the commissioning of the KATRIN main spectrometer	105
4.1.	Spectrometer transmission properties for a calibration source	105
4.1.1.	Transmission function with an angular-selective electron source	106
4.1.2.	Requirements for a calibration source	114
4.2.	Principle of the photo-electron source	118
4.2.1.	Electron creation by UV light	118
4.2.2.	The photoemission process	119
4.2.3.	Electron yield and the Fowler model	121
4.2.4.	Work function of realistic surfaces	123
4.2.5.	Description of the energy spectrum	125
4.2.6.	Imprinting of a well-defined pitch angle	127
4.2.7.	Adiabatic electron transport towards the spectrometer	129
4.3.	Design of the electron source	130
4.3.1.	Technical implementation	133
4.3.2.	Integration with other systems	137
4.4.	Measurement principles and analysis strategies	141
4.4.1.	Electron rate	141
4.4.2.	Dipole efficiency	145

4.4.3.	Time-of-flight	146
4.4.4.	Zero angle	147
4.4.5.	Magnetic reflection	148
4.4.6.	Energy spread	148
4.4.7.	Angular spread	150
4.4.8.	Work function	150
4.5.	Measurements at the monitor spectrometer	153
4.5.1.	Experimental setup	154
4.5.2.	Rate stability	156
4.5.3.	Dipole voltage	158
4.5.4.	Zero angle	160
4.5.5.	Magnetic reflection	163
4.5.6.	Energy and angular distributions	172
4.5.7.	Azimuthal transmission scans	184
4.5.8.	Photocathode work function	188
4.5.9.	Maximal electron rate	192
4.5.10.	Summary	196
4.6.	Measurements at the main spectrometer	197
4.6.1.	Experimental setup	197
4.6.2.	Rate stability	199
4.6.3.	Zero angle	203
4.6.4.	Magnetic reflection	205
4.6.5.	Energy and angular distributions	210
4.6.6.	Photocathode work function	225
4.6.7.	Stability issues	230
4.6.8.	Summary	234
4.7.	Particle-tracking simulations	235
4.7.1.	Implementation into Kassiopeia	235
4.8.	Simulations of the MoS and SDS-2 setups	241
4.8.1.	Alignment with the experimental setup	242
4.8.2.	Electromagnetic conditions in the electron source	249
4.8.3.	Electron transport between source and spectrometer magnet	256
4.8.4.	Produced pitch angles in the spectrometer magnet	259
4.8.5.	Energy and angular distributions	265
4.8.6.	Correlation between kinetic energy and pitch angle	271
4.8.7.	Zero-angle dependency on the dipole voltage	275
4.8.8.	Influence of the acceleration voltage	278
4.8.9.	Influence of the starting voltage	280
4.8.10.	Influence of photocathode misalignments	283
4.8.11.	Influence of zero angle offsets	287
4.8.12.	Comparison with SDS-1 design	288
4.8.13.	Summary	291
4.9.	Investigation of systematic uncertainties	293
4.9.1.	Energy distribution and transmission edge	297
4.9.2.	Energy distribution	300
4.9.3.	Angular distribution	303
4.10.	Chapter summary	306

5. Active background reduction by magnetic pulse	309
5.1. Background from nuclear decays	310
5.1.1. Background from stored particles	310
5.1.2. Countermeasures against radon-induced background	314
5.2. The magnetic pulse system	322
5.2.1. Using the air coil system to apply a magnetic pulse	322
5.2.2. Working principle of the FlipBox units	324
5.2.3. FlipBox integration and performance tests	327
5.3. Measurements at the main spectrometer	329
5.3.1. Experimental setup	329
5.3.2. Magnetic fields at the spectrometer	333
5.3.3. Measurements with an electron beam	335
5.3.4. Measurements with a radioactive $^{83\text{m}}\text{Kr}$ source	337
5.3.5. Measurements with a radioactive ^{220}Rn source	341
5.3.6. Measurements at nominal background	344
5.3.7. Summary	347
5.4. Particle-tracking simulations	348
5.4.1. Simulation setup	348
5.4.2. Magnetic field reduction	352
5.4.3. Removal efficiency	353
5.4.4. Trapping probability	356
5.4.5. Pulse timing	357
5.4.6. Storage conditions	359
5.4.7. Summary	364
5.5. Chapter summary	366
6. Conclusions and outlook	369
List of Figures	375
List of Tables	379
List of Acronyms	383
References	385
A. Technical design drawings	A1

Introduction

The Nobel Prize in Physics 2015 was awarded to T. KAJITA and A.B. McDONALD for the discovery of neutrino oscillations [Nob15]. The measurements at Super-Kamiokande [F⁺98] and the Sudbury Neutrino Observatory [A⁺02] revealed that atmospheric and solar neutrinos change their identity while they propagate to an observer, which, as stated by the Nobel Prize committee, “proves that neutrinos have mass”. This clearly is an important milestone in physics, as neutrinos do not possess a rest mass in the original standard model. An extension of the model is therefore necessary to take these effects into account. However, the story of the neutrino begins much earlier, in the 1930s when the new particle was first proposed to explain a discrepancy between theoretical and observed energy spectra of the beta-decay. In the following years, many efforts were made to expand our knowledge of the neutrino and its role in particle physics. Neutrinos have become an important factor in cosmology and astrophysics decades ago, and recently the first astronomical observations with neutrinos have been published by the IceCube collaboration [Col13]. Although it has been proven that neutrinos are not massless particles their exact mass is still unknown, as the oscillation measurements can only access the squared mass difference between the neutrino mass eigenstates, but not their absolute scale. Other dedicated experiments are required to probe the neutrino mass directly, which will further expand our knowledge of the physical particles and help us to understand the role that neutrinos play in the development of the universe.

The KARlsruhe Tritium Neutrino experiment, **KATRIN**, aims to measure the ‘effective mass of the electron-antineutrino’ by kinematic measurements with a sensitivity down to $0.2 \text{ eV}/c^2$ and thus further decreases the existing kinematic limits on the neutrino mass from its predecessor experiments in Mainz and Troitsk [A⁺05b]. This chapter will provide a brief overview of neutrino physics, beginning with the postulation and subsequent discovery of neutrinos as a new elementary particle and moving on to recent results in neutrino physics and current measurements in this field.

1.1 A brief history of neutrino physics

In the early years of the 20th century, radioactive decays had just been discovered by H. BECQUEREL and further investigated by M.&P. CURIE and E. RUTHERFORD. The β -decay at this time was thought

to be a two-body process where the full energy of the decay would be transferred to the emitted electron¹. The energy spectrum of the decay should thus show a single monochromatic line at the decay energy. Further investigations by L. MEITNER and O. HAHN showed first hints that the energy spectrum could instead be continuous as they observed multiple lines. This was confirmed in 1914 by J. CHADWICK, who for the first time measured a continuous β -spectrum [Cha14]. The question now was if the β -decay is indeed a two-body process, implying a violation of energy and momentum conservation to observe a continuous spectrum, or if instead a third unknown particle was involved in the process. In the following years, the continuous spectrum was closer investigated and confirmed in other experiments, but the puzzle of the β -decay could not be solved yet.

W. PAULI then offered a proposal to solve the contradiction and align the observations with the fundamental laws of physics, where energy and momentum are always conserved. In 1930 he postulated a new particle – he called this particle “neutron” at that time – which was supposed to be involved in β -decay, making it a three-body process [Pau30]. This electrically neutral particle with spin 1/2 had not been observed before; additionally it must only interact with other particles on a much weaker scale than any of the then-known particles. Pauli further postulated that the new particle must have a rest mass close to the electron. This solution was a major turnaround in the physical discussion, and Pauli himself called it a “desperate remedy” to save the fundamental laws of physics.

A theoretical description of the energy spectrum was proposed by E. FERMI in 1934 [Fer34]. In his model he considered the mass of the neutrino and could derive the transition probability for the β -decay at a given electron energy. He found that close to the maximal electron energy (the endpoint), the neutrino mass influences the shape of the energy spectrum (figure 1.1) and it would thus be possible to determine the neutrino mass from a precise measurement of the spectrum. From the data available at the time, he deduced that “the rest mass of the neutrino is either zero or at least very small in relation to the mass of the electron” [Fer34].

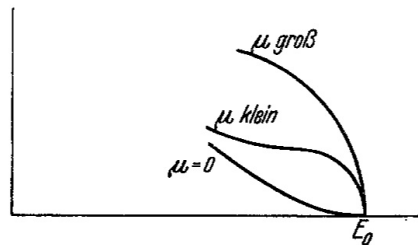


Figure 1.1.: Theoretical energy spectrum of the β -decay. The shape of the energy spectrum close to the endpoint energy E_0 depends on the neutrino mass $\mu = m_\nu$. Figure from [Fer34].

Looking back from today, it is clear that Pauli’s assumption of a third particle was indeed correct, although we know it under the name “neutrino” (which means “small neutron”). Fermi’s description of the β -spectrum and his suggestion of a small neutrino mass proved to be correct as well, and later experiments put an upper limit to the neutrino mass on the order of a few eV. The exact mass of the neutrino, however, is still unknown – even more than 80 years after its postulation.

With the help of this particle, the puzzle of the β -decay was solved from the theoretical point of view, but it took some decades until the existence of the neutrino was actually confirmed in experiments. The first discovery of the neutrino was achieved by C. COWAN and F. REINES in 1956 with the

1. The positron was only discovered later after it was postulated by DIRAC in 1928 [Dir28].

Poltergeist experiment [C⁺56]. It was constructed after measurements of the predecessor experiment **Herr Auge** lead to inconclusive results. The new experiment was dedicated to the direct detection of neutrinos, and was placed at the *Savannah River* nuclear power plant where a high flux of neutrinos from the reactor core was available. The detection principle of this experiment was the inverse β -decay,

$$p + \bar{\nu}_e \rightarrow n + e^+ . \quad (1.1)$$

Two tanks of water mixed with cadmium chloride were placed between three scintillation detectors in a sandwich-like setup. Protons in the water provided a target for the neutrino beam, so that an interaction results in a neutron and a positron being created. In this process the positron quickly annihilates with an electron from the surrounding liquid, emitting a characteristic signal of two 511 keV photons under an angle of 180° . The neutron takes a few microseconds to become thermalized and is then captured by Cadmium, which was dissolved in the water beforehand. Cadmium was chosen specifically in this setup due to its large cross-section for capturing thermal neutrons. The neutron capture process results in a photon being emitted from the daughter nucleus, which was observed in a delayed coincidence to the double-photon emission. This measurement technique resulted in a low background which is crucial to observe the small number of neutrino interactions, and allowed the first direct detection of the neutrino signal. In 1995, Reines received the Nobel Prize in physics [Nob95].

Numerous experiments have been conducted since the neutrino discovery, which expanded our knowledge of neutrinos and further developed our understanding of particle physics in general. The *standard model of particle physics* is today's universal theory of elementary particles and their interactions. It achieves a tremendous accuracy on different energy scales and has been confirmed by many experiments. Today, however, it is clear that this theory is still incomplete for a number of reasons, including the missing neutrino masses which are not predicted by the standard model.

1.2 The neutrino in the standard model and beyond

This section discusses the role of neutrinos in the current standard model of particle physics, and the neutrino masses which can be observed in neutrino mixing and oscillations.

Table 1.1.: Weak isospin doublets in the standard model.

	I. generation		II. generation		III. generation	
quarks	u	\bar{u}	c	\bar{c}	t	\bar{t}
	d'	\bar{d}'	s'	\bar{s}'	b'	\bar{b}'
leptons	e^-	e^+	μ^-	μ^+	τ^-	τ^+
	ν_e	$\bar{\nu}_e$	ν_μ	$\bar{\nu}_\mu$	ν_τ	$\bar{\nu}_\tau$

The standard model consists of 6 quarks and 6 fermions as elementary particles (table 1.1). Each particle has a corresponding anti-particle with opposed charge, but same mass and spin as its partner. The electron, muon and tauon and the three associated neutrino flavors form the lepton sector, which can be divided into three generations as shown in the table. For each generation of the massive leptons

and the associated neutrinos form three weak isospin doublets that participate in the weak interaction. Similarly, the quark sector consists of weak isospin doublets that are grouped in three generations as well.

For both sectors, the isospin doublets are eigenstates of the weak interaction that are different from the mass eigenstates. The relations in the quark sector can be written as a mixing matrix, which connects the weak eigenstates (d' , s' , b') with the eigenstates (d , s , b) of the strong interaction. It is known as *CKM matrix* named after N. CABBIBO, M. KOBAYASHI and T. MASKAWA who received a Nobel Prize in 2008 for their work [Nob08]:

$$\begin{pmatrix} d' \\ s' \\ b' \end{pmatrix} = U_{CKM} \cdot \begin{pmatrix} d \\ s \\ b \end{pmatrix}. \quad (1.2)$$

For the case of leptons, one can follow a similar approach to connect the neutrino mass eigenstates $\nu_{1,2,3}$ to their *flavors*, which correspond to eigenstates $\nu_{e,\mu,\tau}$ of the weak interaction. Again, the mixing can be written as a matrix equation using the *PMNS matrix*, which is named after B. PONTECORVO, Z. MAKI, M. NAKAGAWA and S. SAKATA [M⁺62]:

$$\begin{pmatrix} \nu_e \\ \nu_\mu \\ \nu_\tau \end{pmatrix} = U_{PMNS} \cdot \begin{pmatrix} \nu_1 \\ \nu_2 \\ \nu_3 \end{pmatrix}. \quad (1.3)$$

The contents of the PMNS matrix can be split up into three matrices, which correspond to the three mixing angles θ_{ij} and include a CP-violating phase δ ,

$$U_{PMNS} = \begin{pmatrix} 1 & 0 & 0 \\ 0 & c_{23} & s_{23} \\ 0 & -s_{23} & c_{23} \end{pmatrix} \begin{pmatrix} c_{13} & 0 & s_{13}e^{i\delta} \\ 0 & 1 & 0 \\ -s_{13}e^{i\delta} & 0 & c_{13} \end{pmatrix} \begin{pmatrix} c_{12} & s_{12} & 0 \\ -s_{12} & c_{12} & 0 \\ 0 & 0 & 1 \end{pmatrix}, \quad (1.4)$$

with $s_{ij} = \sin \theta_{ij}$ and $c_{ij} = \cos \theta_{ij}$. A non-zero phase δ indicates a CP-violation similar to the quark sector. This phase could be determined in future oscillation experiments, but is not known so far.

Two additional phases are added in case neutrinos turn out to be Majorana particle, i. e. they are their own anti-particles. The mixing matrix can be expanded by an additional term to account for the Majorana phases α_1 and α_2 :

$$U_{Majorana} = \begin{pmatrix} 1 & 1 & 1 \\ 1 & e^{i\alpha_1/2} & 1 \\ 1 & 1 & e^{i\alpha_2/2} \end{pmatrix}. \quad (1.5)$$

It should be noted that Majorana neutrinos are again an extension of the standard model, but the Majorana nature of the neutrino has not been observed yet.

1.2.1 The oscillation of neutrino flavors

The mixing of mass and flavor eigenstates allows neutrinos to change their flavor during propagation, an effect which is known as *neutrino oscillation*. In a weak interaction process, a neutrino is created as

a flavor eigenstate – e. g. a $\bar{\nu}_e$ created from beta-decay – which is a mixture of three mass eigenstates. The propagation itself takes place in the system of mass eigenstates and can be written as

$$|v_i(t)\rangle = e^{-iE_i t} |v_i\rangle, \quad (1.6)$$

with $\hbar = c = 1$ and $E = \sqrt{p^2 + m^2}$. Since E_i depends on the mass, the phase velocity of the propagation is different for the individual mass eigenstates. The flavor eigenstate is again relevant when a neutrino participates in a weak interaction, i. e. when it is observed in a detector. Since the mixture of mass eigenstates has changed during propagation, the observed flavor can turn out to be different from the original one.

To better understand this process, one can write the probability to observe a neutrino with flavor β some time after it was created as flavor eigenstate α as

$$P(\alpha \rightarrow \beta, t) = \left| \sum_i U_{\beta i} e^{iE_i t} U_{\alpha i}^* \right|^2. \quad (1.7)$$

Figure 1.2 shows the flavor composition for a typical reactor neutrino beam. It shows a typical pattern with a “fast” oscillation that occurs on the order of a few km, and a “slow” oscillation that occurs on the order of tens of km. At certain points along the beam axis, it is possible to observe neutrino flavors that are different from the originally emitted one.

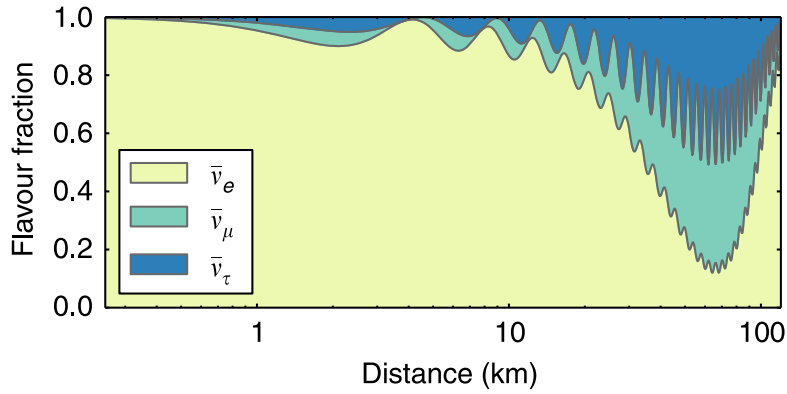


Figure 1.2.: Changing flavor composition of neutrinos due to neutrino oscillations. The flavor composition of the emitted $\bar{\nu}_e$ beam (here: reactor neutrinos with 4 MeV energy) changes with the distance from the source. At certain distances, the probability to observe a $\bar{\nu}_\mu$ or $\bar{\nu}_\tau$ is increased. The oscillations can be investigated by measuring the neutrino flux at different distances. Figure from [V⁺15].

For demonstrative purposes, this formalism is reduced to consider only two neutrino flavors (α, β) and mass eigenstates (1, 2). The mixing can now be described with only one mixing angle θ and the squared mass-difference $\Delta m^2 = m_2^2 - m_1^2$. Rewriting the oscillation probability from above gives

$$P(\alpha \rightarrow \beta) = \sin^2(2\theta) \cdot \sin^2\left(\frac{\Delta m^2 L}{4 E}\right). \quad (1.8)$$

Here the formula was adapted to consider the neutrino energy E and the oscillation length L . It can be shown that for a fixed neutrino energy, the probability oscillates between zero and a maximum value, depending on the oscillation length. The maximum value is defined by the mixing angle,

while the oscillation frequency is defined by the squared mass difference. Measuring the ratio of flavor eigenstates at different oscillation lengths and energies allow to determine both parameters. The absolute neutrino mass, however, can not be determined by oscillation experiments.

1.2.2 Neutrino oscillation experiments

The method described above is used in *neutrino oscillation experiments*, where all three neutrino flavors and mass eigenstates have to be considered. By constructing experiments that operate in different regions of the parameter space and comparing the mixing ratio at different oscillation lengths, the three mixing angles and squared mass-differences can be determined experimentally. A first observation of neutrino oscillation was performed in the 1960s by R. DAVIS, who in 2002 shared the Nobel Prize for his discoveries along with M. KOSHIBA and R. GIACCONI [Nob02]. The **Homestake** experiment used radiochemical methods to observe the flux of solar neutrinos ν_e which are generated in the Sun's nuclear fusion processes. The measured flux was compared with predictions from the solar model of that time, and was found to be only about 30% of the expected value [C⁺98]. This discrepancy soon became known as the *solar neutrino problem*, as it was not clear if the used model was incorrect or if the experiment was fallacious.

The problem could not be fully identified until 1998, when the **Super-Kamiokande** experiment reported a direct observation of neutrino oscillations [F⁺98]. The experiment was able to measure the atmospheric neutrino flux of two flavors, ν_e and ν_μ , which could be compared to predicted values. It used elastic scattering on electrons and charged-current reactions on constituents of water to detect neutrinos via Čerenkov light:



If deep inelastic scattering occurs in a CC reaction, a hadronic shower will be created instead of a single proton or neutron. It is possible to distinguish the produced electrons and muons; the latter create a sharper Čerenkov light cone, as electrons are affected by elastic scattering processes inside the water detector. Atmospheric neutrinos are created from cosmic rays that interact with target nuclei in the upper layer of the atmosphere. Depending on the origin of the neutrinos – e. g. an interaction directly above the detector, or on the other side of the Earth – the flight path to the detector differs between a few and several thousand kilometers. This allows to measure the mixing ratio at different oscillation lengths, and the dependency on L/E can be investigated to yield the atmospheric mixing parameters $\Delta m_{atm}^2 = \Delta m_{23}^2$ and $\theta_{atm} = \theta_{23}$.

From 1998 to 2006, the **SNO** experiment measured solar neutrino oscillations by observing the ν_e flux, ϕ_e , and the total flux, $\phi_{e\mu\tau}$. It was able to finally close the case on the solar neutrino problem, as it was shown that the total flux matches the theoretical predictions and the “missing” neutrinos can be explained by oscillation [A⁺01, A⁺02, A⁺05a]. The SNO experiment used a combination of charged-current and neutral-current reactions on deuterons (heavy water) together with elastic scattering:



Note that the CC interaction is only sensitive to e^- and thus provides a direct measurement of the electron neutrino flux. This is due to the rather low energy of the neutrinos emitted by the Sun (lower MeV regime). Incoming $\nu_{\mu,\tau}$ thus have insufficient energy to create a μ^- or τ^- particle in the CC process. The experiment yielded a total neutrino flux of $\phi_{e\mu\tau} = 5.25 \cdot 10^6 \text{ cm}^{-2}\text{s}^{-1} \pm 0.16 \cdot 10^6 \text{ cm}^{-2}\text{s}^{-1}(\text{sys}) \pm 0.12 \cdot 10^6 \text{ cm}^{-2}\text{s}^{-1}(\text{stat})$. The flux of non-electron neutrinos deviates strongly from zero, $\phi_{\mu\tau} = 3.26 \cdot 10^6 \text{ cm}^{-2}\text{s}^{-1} \pm 0.25 \cdot 10^6 \text{ cm}^{-2}\text{s}^{-1}(\text{sys}) \pm 0.38 \cdot 10^6 \text{ cm}^{-2}\text{s}^{-1}(\text{stat})$, indicating that roughly two thirds of solar neutrinos change their flavor until their arrival on Earth. Figure 1.3 shows the combined results from the Super-K and SNO measurements.

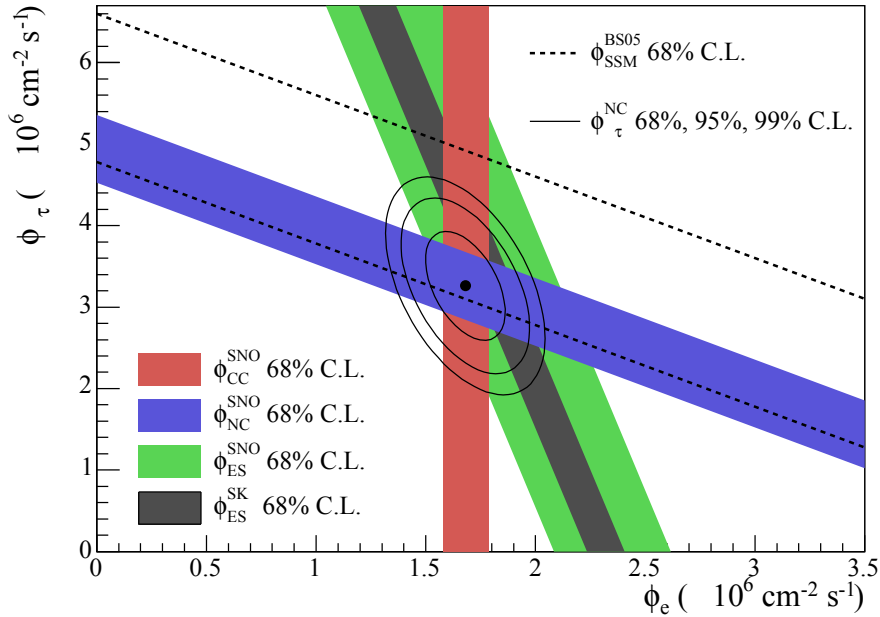


Figure 1.3.: Fluxes of ^8B solar neutrinos. The plot combines data from the SNO and Super-Kamiokande experiments and shows the flux ϕ_e for electron (anti-)neutrinos and $\phi_{\mu\tau}$ for muon and tau (anti-)neutrinos. The results from both experiments show excellent agreement; the solid contour lines show the joint probability for both flavors. The flux also agrees to the prediction by the standard solar model (SSM). Figure from [OG14] and [A⁺05a].

Following reactor experiments like **KamLAND** and accelerator experiments like **K2K** using artificial neutrino sources confirmed the theory of neutrino oscillation and were able to exclude alternative neutrino mixing models due to their ability to discriminate between ν_μ and $\bar{\nu}_\mu$ [A⁺06, G⁺11]. Because recent experiments operate in different regions of the parameter space (ν_α , L/E), all the mixing angles and squared mass-differences of the neutrino flavors can be determined. Recently, the short-baseline reactor experiments **Daya Bay**, **Double Chooz** and **RENO** were able to determine the last missing neutrino parameter, the mixing angle θ_{13} [A⁺12c, A⁺12a, A⁺12b].

Today, all mixing parameters are known except for the CP-violating phase δ and the possible Majorana contribution $\alpha_{1,2}$:

$$\begin{aligned}
\sin^2(2\theta_{12}) &= 0.846(21), && [\text{KamLAND+SBL+solar+accel.}] \\
\Delta m_{21}^2 &= 7.53(18) \cdot 10^{-5} \text{ eV}^2, && [\text{KamLAND+SBL+solar+accel.}] \\
\sin^2(2\theta_{23}) &= \begin{cases} 0.999(2) & [\text{NH}] \\ 1.000(2) & [\text{IH}] \end{cases}, && [3\nu \text{ oscillation}] \\
|\Delta m_{23}^2| &= \begin{cases} 2.42(6) \cdot 10^{-3} \text{ eV}^2 & [\text{NH}] \\ 2.49(6) \cdot 10^{-3} \text{ eV}^2 & [\text{IH}] \end{cases}, && [3\nu \text{ oscillation}] \\
\sin^2(2\theta_{13}) &= 8.5(5), && [\text{DayaBay+DoubleChooz+RENO}] \\
\Delta m_{13}^2 &\approx |\Delta m_{23}^2|.
\end{aligned} \tag{1.11}$$

The terms $\theta_{12}, \Delta m_{21}^2$ are also known as $\theta_{sol}, \Delta m_{sol}^2$ and correspond mainly to solar neutrino mixing; similarly $\theta_{23}, \Delta m_{23}^2$ are known as $\theta_{atm}, \Delta m_{atm}^2$ and correspond mainly to atmospheric mixing. The sign of Δm_{atm}^2 is still unknown; it would allow to distinguish between *normal hierarchy* (NH), where ν_1 is the lightest mass eigenstate, and *inverted hierarchy* (IH), where the lightest eigenstate is ν_3 . In the listing above, the two alternate values for θ_{23} and Δm_{23}^2 refer to the case of normal and inverted hierarchy, respectively. The sign of Δm_{13}^2 , on the other hand, is known from the Mikheyev–Smirnov–Wolfenstein (MSW) effect which modifies the mass eigenstates when neutrinos propagate through matter like Sun or Earth [Wol78, MS86], and implies that $m_1 < m_2$ despite the *absolute* mass being unknown.

1.2.3 Neutrinos in the standard model

Although the formalism of neutrino oscillations had been suggested by B. PONTECORVO already in 1957 [Pon57] and was quickly considered a possible solution to the solar neutrino deficit, only after neutrino oscillations had been confirmed by different experiments this theory became part of the physical canon. F. REINES and R. DAVIS received the Nobel Prize in 1995 and 2002, respectively, decades after their pioneering experiments; the 2015 Nobel Prize was awarded to T. KAJITA and A. McDONALD for confirming the theory of neutrino oscillations at Super-Kamiokande and SNO.

The observation of neutrino oscillations proves non-zero neutrino masses and thus hints at physics beyond the standard model. In the standard model, particle masses are generated by coupling of the left-handed fermion isospin doublet and right-handed fermion singlet to the Higgs doublet; a mechanism known as *Yukawa coupling*. Neutrinos however are left-handed (ν_L) and anti-neutrinos are right-handed ($\bar{\nu}_R$). Hence, there is no right-handed singlet partner to generate masses for the left-handed neutrinos (and vice versa for the anti-neutrinos), which implies that no neutrino masses are generated in the standard model itself.

A possible extension of the model is to postulate a right-handed neutrino to generate Dirac mass terms. This approach would require to add a-priori parameters to the model (e. g. an extremely small coupling constant to generate the small neutrino masses), and is thus rather unsatisfactory. An alternative solution is to generate Majorana mass terms if the neutrino is of the Majorana type. This extension introduces additional mass eigenstates, which results in one heavy right-handed and one light left-handed neutrino per family. This approach is known as the *see-saw type I* mechanism, since the asymmetry of the masses resembles a see-saw where one neutrino pushes away the other one in terms

of their mass, creating an asymmetric mass distribution. The *see-saw type II* mechanism introduces an extra Higgs triplet that generates neutrino masses from symmetry breaking. This Higgs triplet is already included in most super-symmetric extensions of the standard model. With many alternative solutions to create neutrino masses from the standard model, it becomes even more important to achieve a direct measurement of the neutrino mass without depending on the used model. A number of different approaches to determine neutrino masses experimentally will be discussed in the next section.

The neutrino mass is linked to cosmology and therefore an important parameter in the evolution of the universe [A⁺11a]. Today's *relic neutrino* density of 336 cm^{-3} was caused by the decoupling of neutrinos from particle interactions that occurred a short time after the Big Bang, at a temperature of $2.5 \text{ MeV} \approx 3 \cdot 10^{10} \text{ K}$. The *cosmic neutrino background* (CNB) today has a temperature of 1.95 K , slightly smaller than the *cosmic microwave background* (CMB) at 2.73 K . Depending on the absolute neutrino mass, relic neutrinos could contribute a significant amount to the total mass density in the universe.

1.3 Determination of absolute neutrino masses

Different methods to access the absolute neutrino mass scale have been conceived in the recent years after it became clear that neutrinos exhibit non-zero masses. Each method has their own advantages and disadvantages and their sensitivity to the neutrino mass also depends on the hierarchy that is implemented in nature (figure 1.4). At the end of the section, a purely kinematic approach as used by the KATRIN experiment is discussed in more detail.

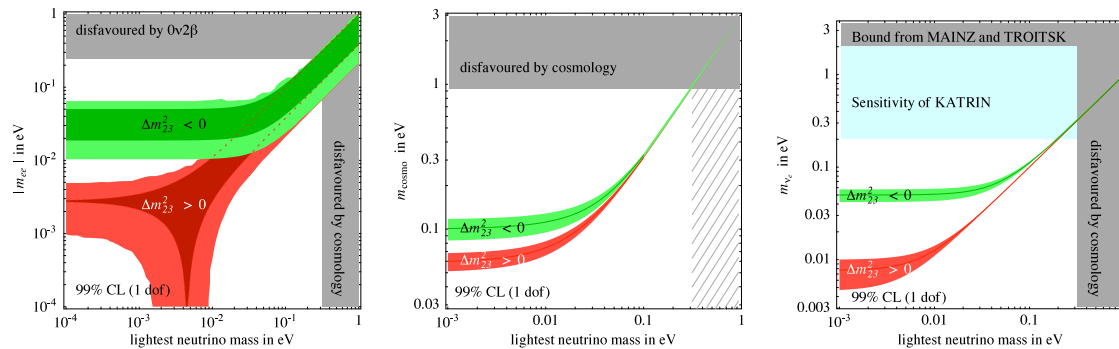


Figure 1.4.: Limits on the neutrino mass for normal and inverted hierarchy. The plots show the neutrino mass measured in $0\nu\beta\beta$ experiments, in cosmological studies, and in kinematic measurements with tritium versus the mass of the lightest neutrino. At rather large masses $m_\nu \gtrsim 0.1 \text{ eV}$ the degenerate case is observed, where the hierarchies cannot be discriminated. Only at small masses it is possible to distinguish between normal ($\Delta m_{23}^2 < 0$) and inverted hierarchy ($\Delta m_{23}^2 > 0$). Figure adapted from [SV05]; note that the data shown is from around 2005.

1.3.1 Cosmological studies

Through their non-zero mass and early decoupling approximately 1 s after the Big Bang, neutrinos played an important role in the structure formation of the universe. The structures we observe today evolved from small density fluctuations in the early universe, which have been modified by interactions with surrounding matter and energy. Due to their small mass neutrinos were highly relativistic particles after their decoupling, which allowed them to smear out any small-scale fluctuations since they only interact gravitationally. They are thus called *hot dark matter*. Because neutrinos decoupled much earlier than photons, their properties are imprinted in the cosmic microwave background (CMB). The structure of the CMB we observe today can be used to examine the scale on which the early neutrinos operated. The scale itself is connected to the neutrino mass, since it defines the free-streaming length of relativistic neutrinos. Additionally, the CMB anisotropy is modified by massive neutrinos, which allows further studies of the neutrino contribution.

The relevant neutrino mass parameter in the cosmological models is the total sum of mass eigenstates:

$$M_\nu = \sum_i m_i. \quad (1.12)$$

This parameter has been investigated by cosmic probes such as **SDSS**, **WMAP** and **Planck**, which studied the CMB anisotropy and other important properties [A⁺14, BM14, PD⁺15]. The measured data has to be compared to the results of rather complex models, however, and the resulting neutrino masses strongly depend on these models [LP06].

A recent combined analysis yields the following limits [OG14]:

$$M_\nu < 0.39 \text{ eV}. \quad [\text{Planck+SDSS+others}] \quad (1.13)$$

1.3.2 Neutrinoless double-beta decay

When the neutrino is of the Majorana type ($\nu = \bar{\nu}$), *neutrinoless double beta-decay* ($0\nu\beta\beta$) becomes possible for certain nuclei. The double beta-decay itself ($2\nu\beta\beta$) is only allowed when the binding energy of the daughter nucleus is larger than the energy of the mother nucleus, and alternative decay paths with two independent beta decays are forbidden. The double beta-decay can be described by two simultaneous beta-decays in the same nucleus, and has been observed in a few isotopes like ⁷⁶Ge. In the $2\nu\beta\beta$ case, two neutrinos are emitted from each beta decay, whereas in the $0\nu\beta\beta$ case one of the decays is modified such that an antineutrino is absorbed instead of a neutrino being emitted. This is possible since both neutrinos are equivalent in the Majorana case; therefore no neutrinos are emitted when this decay occurs.

The $0\nu\beta\beta$ decay would be observed as a sharp line at the endpoint of the beta-electron energy spectrum [GC⁺12]. Since no neutrinos are emitted, the total decay energy is converted to kinetic energy of the emitted electrons, creating in a sharp peak. The $0\nu\beta\beta$ decay rate Γ depends on the squared value of the ‘effective Majorana mass’,

$$\Gamma_{0\nu\beta\beta} \propto \left| \sum_i U_{ei}^2 m_i^2 \right| = m_{\beta\beta}^2. \quad (1.14)$$

This mass is the coherent sum over the three neutrino flavors, and it is possible that some contributions cancel out each other if the phase factors of the PMNS matrix allow. Hence, even if neutrinos are of

the Majorana type, the $0\nu\beta\beta$ signature is not necessarily observed by these experiments. The expected decay rate strongly depends on the nuclear matrix element of the decay, which has to be calculated from a given model. The currently known isotopes where double beta-decay has been observed all have rather complex decay schemes, which leads to considerable systematic uncertainties in their *nuclear matrix elements* (NMEs).

There are experiments such as **GERDA**, **KamLAND-Zen** and **EXO-200** that search for $0\nu\beta\beta$ decay to determine the neutrino mass [A^+13, G^+13a]. Since no direct observation could be achieved yet, currently only lower limits for the half-life of $0\nu\beta\beta$ decay – given that neutrinos are of the Majorana type – are available from these experiments [OG14]:

$$\begin{aligned} T_{1/2}^{0\nu\beta\beta}(^{76}\text{Ge}) &> 2.1 \cdot 10^{25} \text{ yr}, && \text{[GERDA]} \\ T_{1/2}^{0\nu\beta\beta}(^{136}\text{Xe}) &> 3.4 \cdot 10^{25} \text{ yr}. && \text{[KamLAND-Zen,EXO-200]} \end{aligned} \quad (1.15)$$

An upper limit for the neutrino mass can be computed using different NME models, yielding $|m_{\beta\beta}(^{76}\text{Ge})| \leq 0.2 \text{ eV} - 0.4 \text{ eV}$ from the GERDA results [A^+16a] and $|m_{\beta\beta}(^{136}\text{Xe})| \leq 0.11 \text{ eV} - 0.25 \text{ eV}$ from the combined results of KamLAND-Zen and EXO-200 [D^+13a].

A claim of an observed $0\nu\beta\beta$ decay was published in 2006 by the **Heidelberg-Moscow** collaboration at a half-life of $T_{1/2}^{0\nu\beta\beta}(^{76}\text{Ge}) = 2.3 \cdot 10^{25} \text{ yr}$, resulting in a neutrino mass of 0.3 eV [KKK06]. This observation has subsequently been ruled out by other experiments [Mac14].

1.3.3 Supernovae

An approach which is less dependent on the used model is the observation of neutrinos that were generated in cosmic supernovae. The arrival time of the neutrino beam on Earth relative to the photon signal can be used to assess the neutrino mass from a purely kinematic point-of-view. However, since the start time can not be measured, this approach relies to some extent on the supernova model. Kinematic measurements like this operate on an ‘average mass of the electron neutrino’,

$$m_{\nu_e} = \sqrt{\sum_i |U_{ei}|^2 m_i^2}, \quad (1.16)$$

which corresponds to an incoherent sum over the mass eigenstates and are thus not susceptible to cancellations of individual contributions.

Given the scarcity of supernovae that are close enough to Earth to yield a measurable neutrino flux, only one observation has been achieved so far. The supernova SN 1987A, first observed in 1987, took place in the Large Magellanic Cloud at a distance of about $L^* = 168 \cdot 10^3 \text{ ly}$ and allowed for 24 neutrino events to be detected e. g. in the **Kamiokande** experiment [A^+89, P^+10]. It was the closest supernova that was observed on Earth since 1604 (SN 1604). In spite of the small number of detected neutrinos, the measured flux was significantly higher than the background observed before and is also compatible with existing supernova models.

The analysis of the data relies on the idea that all neutrinos have been created at (almost) the same time and left the supernova simultaneously. Since neutrinos only rarely interact with matter, it can be assumed that they were not slowed down in the supernova’s outer shells before entering the vacuum of space. The energy range of the observed neutrinos was determined to 10 MeV to 40 MeV , and all events were observed in a time interval of 13 s . Since massive neutrinos travel slower than light,

their arrival time Δt depends on the neutrino mass m_{ν_e} and their kinetic energy E_ν (assuming that all neutrinos were emitted simultaneously) [AR87]:

$$\Delta t = t_0 \cdot \left(1 + \frac{m_{\nu_e}^2}{2E_\nu^2} \right). \quad (1.17)$$

The propagation time of the supernova light $t_0 = 5.3 \cdot 10^{12}$ s is determined from the distance to earth $L^* = ct_0$. Note that the mass can be determined directly from the energy dependency of the arrival times.

By comparing the spread of arrival times with the observed energies, one can deduce an upper limit of the neutrino mass [OG14]:

$$m_{\nu_e} < 5.8 \text{ eV}. \quad [\text{SN 1987A}] \quad (1.18)$$

Decades have passed since this first – and up to now, only – observation of neutrinos from supernovae. If a supernova was observed today, it is likely that a considerably lower neutrino mass limit could be determined, given the advances in detector technology and the number of available neutrino detectors throughout different experiments.

1.3.4 Kinematic measurements

Another purely kinematic method of determining the neutrino mass is to precisely measure the energy spectrum of beta-decay electrons [D⁺13b]. The observed electron energy ranges from zero to an endpoint $E_0 = Q - E_{rec}$ that depends on the total decay energy Q and the nuclear recoil energy E_{rec} . Because a neutrino is emitted together with the electron, the total energy is shared between both particles. At the endpoint, the electron takes away the maximal amount of available energy. Due to the non-zero rest mass of the neutrino, the actual position of the spectrum endpoint shifts to a lower energy $E_{max} < E_0$. This maximal energy is reduced by the non-zero rest mass of the neutrino that is created in the β -decay. The endpoint energy is therefore linked to the neutrino mass, which can be exploited in a kinematic measurement as indicated in figure 1.5.

In a β^- decay, a mother nucleus (Z, A) is converted to a daughter nucleus $(Z+1, A)$ under the emission of an electron and an electron-antineutrino:

$$(Z, A) \rightarrow (Z+1, A) + e^- + \bar{\nu}_e. \quad (1.19)$$

The resulting energy spectrum can be calculated from *Fermi's golden rule*. For the decay rate in the energy range $(E, E + dE)$ one obtains

$$\frac{dN^2}{dt dE} = \frac{d\dot{N}}{dE} = \frac{2\pi}{\hbar} |M|^2 \rho(E), \quad (1.20)$$

with M denoting the nuclear matrix element of the decay and $\rho(E)$ the phase-space density. The phase space factors for electron and neutrino can be handled separately from the nucleus due to its much larger mass, and neglecting the nuclear recoil energy it follows that

$$\rho(E) = \frac{dn_e}{dE_e} \frac{dn_\nu}{dE_\nu} = \frac{1}{4\pi^4 \hbar^6} \cdot p_e(E + m_e^2) \cdot E_\nu \sqrt{E_\nu^2 - m_\nu^2 c^4}, \quad (1.21)$$

where $E_\nu = E_0 - E$ denotes the total neutrino energy. The nuclear matrix element M can be divided into a hadronic and leptonic part, M_h and M_l :

$$M = G_F \cos \theta_C \cdot M_h \cdot M_l. \quad (1.22)$$

with Fermi's coupling constant G_F and the Cabibbo mixing angle $\theta_C = 13^\circ$. For a super-allowed decay – like in the case of tritium – the leptonic part can be expressed in terms of the normalization volume V for electron and neutrino, and the Fermi function $F(E, Z + 1)$ that describes the interaction between electron and nucleus:

$$|M_l|^2 = \frac{1}{V^2} \cdot F(E, Z + 1). \quad (1.23)$$

A simplified term for the theoretical beta spectrum that does not contain the final states distribution can be written as (using $c = 1$)

$$\frac{dN^2}{dE dt} = A \cdot F(E, Z + 1) \cdot p_e(E + m_e) \cdot E_\nu \sqrt{E_\nu^2 - m_{\nu_e}^2} \cdot \Theta(E_\nu - m_{\nu_e}), \quad (1.24)$$

where A is the signal amplitude

$$A = \frac{G_F^2 \cos^2 \theta_C}{2\pi^3 \hbar^7} \cdot |M_h|^2. \quad (1.25)$$

Although a nuclear matrix element must be calculated to describe the beta spectrum like in the case of neutrinoless double-beta decay, the isotopes used for this kind of kinematic measurement often have a less complicated structure and the matrix element can be computed with smaller uncertainties. There are however a number of smaller corrections which have to be accounted for if one aims to determine the neutrino mass from a kinematic measurement, e. g. the finite mass of the nucleus which affects the momentum transfer.

If these corrections are considered correctly, the neutrino mass can be derived from the location of the spectrum endpoint (figure 1.5). Since the neutrino mass enters the equation in form of the neutrino momentum,

$$p_\nu = \sqrt{(E_0 - E)^2 - m_{\nu_e}^2}. \quad (1.26)$$

the endpoint holds the most sensitive information about the mass m_{ν_e} . The neutrino mass which can be derived from this kind of measurement corresponds to the 'average mass of the electron neutrino' as in the case of supernovae measurements.

If a source with low endpoint in the keV regime is used, a larger fraction of decay electrons contributes to the endpoint region. A low-energetic source is thus beneficial for a kinematic measurement of this type. Additionally, the energy resolution of the experiment is typically increased by choosing a low endpoint; this will be discussed in more detail in the next chapter.

A good choice for a beta source would be ^{187}Re with an endpoint of $E_0 = 2.5$ keV. However, the long half-life of $T_{1/2} = 41 \cdot 10^9$ yr makes it difficult to perform kinematic measurements with spectroscopic energy analysis, since a large fraction of electrons far away from the endpoint is rejected. The resulting statistics thus become extremely small. Hence, experiments like **MARE** which use this isotope typically employ a bolometric setup, where detector and source are in the same volume [Nuc08].

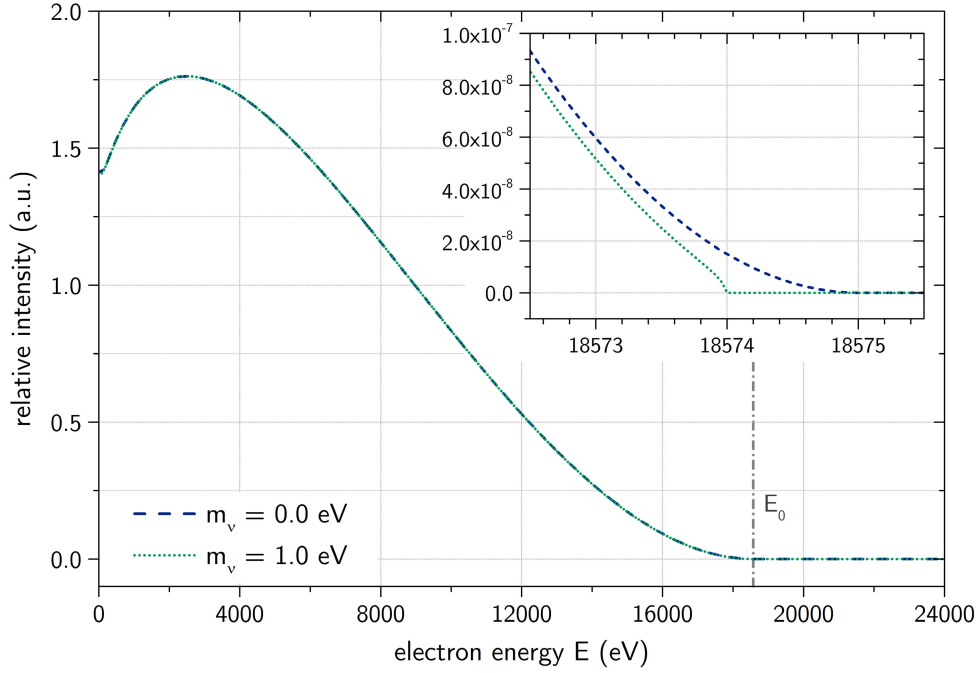
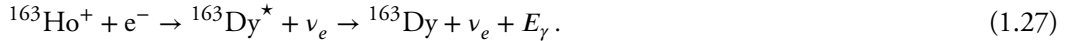


Figure 1.5.: Differential energy spectrum of tritium β -decay. The neutrino mass $m_\nu = m_{\nu_e}$ (1.16) influences the shape of the spectrum close to the endpoint region at $E_0 \lesssim 18574$ keV. In this energy region lies only a small fraction of the emitted electrons, making it necessary to utilize a strong source and a setup with large acceptance angle in order to maximize the neutrino mass sensitivity. Figure from [Kle14].

Another approach is to use isotopes that allow electron-capture processes like ^{163}Ho , which leaves an excited state after an electron-capture process occurred:



The neutrino mass can be determined from the total energy deposited in the detector. This method is used in a bolometric setup in the **ECHo** project [G⁺14].

Yet another approach uses the decay of tritium into helium,



with an endpoint of $E_0 = 18574.3(17)$ eV (second-lowest endpoint energy) for molecular tritium [K⁺05] and a recoil energy of $E_{rec} = 1.72$ eV. In contrast to rhenium with its even lower endpoint, the tritium half-life of $T_{1/2} = 12.3$ yr yields a high source activity with a reasonable amount of radioactive material. This allows to use tritium in a spectrometer-based setup, where decay electrons are analyzed by an electrostatic retarding potential combined with a counting detector.

Two experiments using this approach have been carried out before, the **Mainz** and **Troitsk** experiments [K⁺05, A⁺11b]. Both were using an electrostatic spectrometer to analyze the kinetic energy of the decay electrons, and operated with tritium as a decay source. The energy region close to the tritium endpoint was investigated over several years of measurement time, resulting in upper limits

of [OG14]

$$m_{\nu_e} \leq 2 \text{ eV}. \quad [\text{Mainz+Troitsk}] \quad (1.29)$$

The **KATRIN** experiment is the successor of these two experiments, and is operated in a collaboration which includes former members from Mainz and Troitsk. It follows a similar approach with an electrostatic spectrometer, but aims to improve the sensitivity goal by one order of magnitude down to $0.2 \text{ eV}/c^2$ (90% C. L.) [A⁺05b].

Alternative approaches that rely on kinematic measurements are considered in future experiments that are planned or currently under development, e. g. the **Project8** experiment [A⁺15b]. Here the energy analysis will be performed by measuring synchrotron radiation from decay electrons trapped in a magnetic bottle.

1.4 Thesis outline

This thesis is structured as follows.

Chapter 2 gives an overview of the KATRIN experimental setup with the individual sub-systems. The chapter will focus on the MAC-E filter principle as a key feature of the experiment that is relevant for the two major topics of this thesis. It will also discuss the effect of systematic and statistical uncertainties on the experiment's sensitivity to the neutrino mass.

Chapter 3 explains the simulation and analysis software that is implemented within the KASPER framework, which provided the basis for the analysis of the various measurements that were conducted in the KATRIN SDS commissioning phases and for the detailed simulations that were carried out to support the analysis work. The chapter also aims to give an overview on the various software components like the particle tracking software *Kassiopeia* and the analysis framework *BEANS*. A novel post-analysis called *Peaberry* has been developed during this thesis to provide various analysis methods, and was widely used throughout this work.

Chapter 4 discusses the angular-selective, mono-energetic UV photoelectron source that was further developed and commissioned over the course of this thesis. After explaining the working principle of the electron source and its technical design, the results from commissioning measurements at the monitor spectrometer and at the main spectrometer during the SDS-2 measurement phase are examined to determine many important characteristics of the device. It is shown that the electron source matches its design requirements and achieves angular selectivity with a small energy and angular spread in a MAC-E filter setup. In addition to measurements, *Kassiopeia* simulations with 3D electromagnetic fields were carried out to further investigate the electron acceleration and transport mechanisms that define the electron source's performance. The chapter closes with a discussion on systematic uncertainties and how these affect the analysis results.

Chapter 5 moves on to the second topic of this thesis, the active background removal by a magnetic pulse. This background reduction method was developed during this thesis and implemented at the KATRIN main spectrometer. The chapter discusses the findings of the SDS-1 and SDS-2 measurement phases, where it was verified that the magnetic pulse method is able to remove stored electrons from the main spectrometer. The electron removal processes are investigated with the help of particle-tracking simulations that allow to estimate the background removal efficiency of this method.

Chapter 6 presents a summary of this thesis and gives an outlook on possible future measurements that are related to the thesis topic. The following appendix contains technical drawings, simulation configuration files and analysis code that was used in this work.

The KATRIN experiment

The previous chapter gave a brief overview of the history of neutrino physics as well as current research topics. Since the neutrino mass is still unknown, experiments are currently under development to access the absolute neutrino mass scale. One of these experiments, which uses a purely kinematic approach, is the **Karlsruhe Tritium Neutrino experiment** (KATRIN). It aims to measure the ‘average mass of the electron neutrino’ (1.16) with a sensitivity of $0.2 \text{ eV}/c^2$ (90% C. L.), or provide a discovery potential of $0.35 \text{ meV}/c^2$ for a 5σ -observation [A⁺05b]. The target sensitivity is a factor of 10 lower than current upper limits from kinematic measurements (1.29).

KATRIN uses technologies that are based on its predecessor experiments (Mainz and Troitsk), although many concepts have been improved to reach the much lower sensitivity. One key feature of KATRIN is the electrostatic spectrometer, which employs a technique known as *magnetic adiabatic collimation with electrostatic filtering* (MAC-E) [B⁺81, LS85, P⁺92]. This concept will be explained in detail below (section 2.2), followed by a discussion of KATRIN’s sensitivity to the neutrino mass (section 2.3). First of all, however, a short overview of the experimental setup and its important sub-systems will be given.

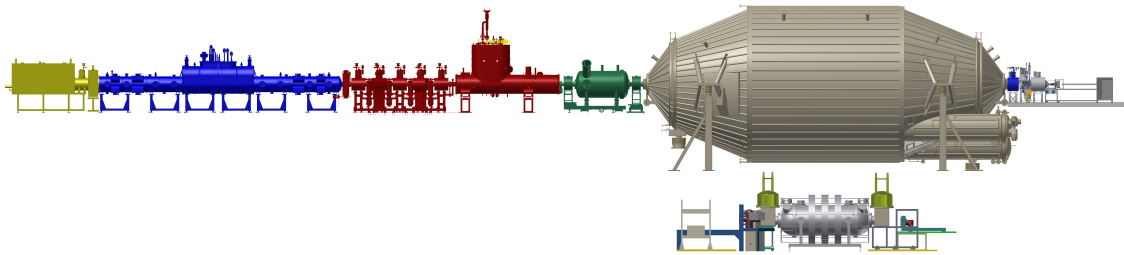


Figure 2.1.: The KATRIN experiment. The main beamline is roughly 70 m long. Its main components are (from left to right): rear section (yellow); windowless gaseous tritium source (blue); differential and cryogenic pumping sections (red); pre-spectrometer (green); main spectrometer (gray); focal-plane detector (blue/gray). The section up to the pre-spectrometer is located in the radiation safety area (tritium laboratory) since it operates with radioactive tritium. The monitor spectrometer shown below is located in an additional experimental hall, but electrically connected to the main spectrometer. It was used before in the Mainz neutrino mass experiment. Figure from [Wol15].

2.1 Experimental setup

The name *KATRIN* already hints at the location of the experimental site: Karlsruhe, Germany – or more specifically, the Karlsruhe Institut für Technologie (KIT). One advantage of this location is the existing infrastructure with the ability to handle the required amounts of gaseous tritium, which is used to generate the beta-decay electrons.

Figure 2.1 shows an overview of the experiment with its major components. The setup can be divided into two main systems: the *source and transport section* (STS) and the *spectrometer and detector section* (SDS). The STS is contained in the area of the Tritium Labor Karlsruhe (TLK), since the radioactive tritium requires specific safety regulations. The SDS contains the spectrometers, which are responsible for energy analysis of the decay electrons, and the detector system. It is located outside of the TLK area, since no tritium is entering this section. The *electromagnetic design* (EMD) features a global magnetic field that forms a flux tube of 191 T cm^2 between the source and the detector. The magnetic field lines guide decay electrons from the source through the spectrometers and to the detector, which is a key feature of the experiment. Many components are operated at high voltage, especially the spectrometers, where the electrostatic retarding potential is applied. The two main sections and their individual components will be outlined in the following paragraphs.

2.1.1 Source and Transport section

The **Rear Section** (RS) contains monitoring and calibration devices that are necessary to monitor the source activity, since unknown fluctuations in the decay rate are a major contribution to the total systematic uncertainty. The RS is also used during commissioning measurements of the beamline, as it contains an electron source that can be used to determine the transmission properties of the full beamline up to the detector. This electron source features a design that is similar to the source presented in this work (chapter 4), and the conclusions drawn from the SDS commissioning measurements provide substantial input to the commissioning measurements of the full beamline. The RS also controls the plasma potential of the gaseous tritium, since the magnetic flux tube connects the detector wafer to the gold-plated *rear wall* (which divides the RS from the WGTS volume) [Bab14].

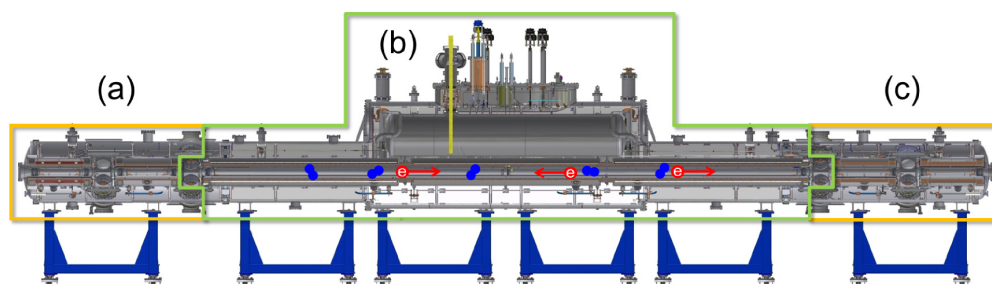


Figure 2.2.: The windowless gaseous tritium source (WGTS). Tritium molecules (blue) are injected into the central section of the 11 m long beam tube (b). The electrons emitted from β -decay (red) are magnetically guided to both ends (c), either hitting the *rear wall* that divides the WGTS from the rear section, or propagating towards the spectrometer section. A first stage of turbo-molecular pumps removes tritium at the end of the beam tube via differential pumping (DPS-1). Figure from [Wan13].

The **Windowless Gaseous Tritium Source** (WGTS) is a section about 11 m in length, where tritium gas is injected from the TLK's tritium loop system (figure 2.2). With a total tritium amount of roughly 20 g at the KATRIN site, the source will emit up to 10^{11} decay electrons towards the SDS per second. Since the total number of tritium nuclei in the beamline decreases over time due to radioactive decays, the tritium gas must be continuously removed, cleaned, and re-injected into the source to achieve a stable source activity. The source is kept at a fixed temperature of 30.00(3) K with a tritium injection pressure of $3.4 \cdot 10^{-3}$ mbar, and reaches a column density of $5 \cdot 10^{17}$ cm $^{-2}$. This column density was chosen specifically to provide a high source activity which allows the experiment to reach a low statistical uncertainty, while limiting electron energy losses inside the source that would increase the systematic uncertainty. The windowless design of the source is another key feature which avoids energy losses and thus increases the neutrino mass sensitivity [B⁺12, P⁺15, Pri13, Fis14].

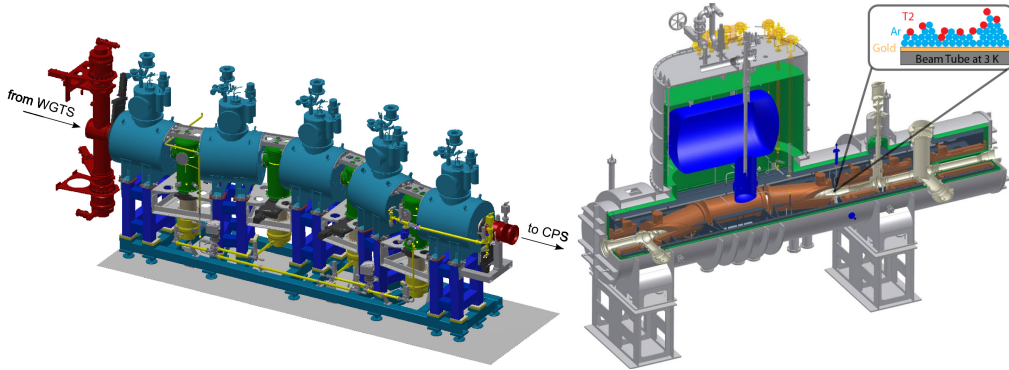


Figure 2.3.: The differential and cryogenic pumping sections (DPS-2/CPS). The electrons and tritium decay products enter a second stage of differential pumping after leaving the tritium source. The kinked beam tube allows the light electrons to follow the magnetic guiding field towards the spectrometer. The heavier ions and molecules are removed by turbo-molecular pumps. A cryogenic pumping section further reduces the remaining tritium flow with the help of an argon frost layer on the inner beam tube. Here tritium and its decay products are removed by cryo-sorption onto the cold surface. Figures from [Gro15].

The **Differential Pumping Section** (DPS-2) and **Cryogenic Pumping Section** (CPS) form the transport section between the WGTS and the spectrometer section (figure 2.3). The main task of these systems is the removal of tritium from the beamline, as the spectrometers operate under *ultra-high vacuum* (UHV) conditions while the source contains a high partial pressure of tritium gas. It is thus crucial to remove tritium and its decay products from the beamline before they enter the spectrometers. The combination of two pumping systems is necessary to reach the design value of 10^{-14} mbar l/s for the gas flow at the beginning of the spectrometer section [L⁺06, G⁺12]. The DPS-2 and CPS follow a first stage of differential pumping (DPS-1) at the end of the WGTS.

The DPS-2 contains two kinks in the beamline, where more heavy ions can't follow the magnetic field lines fast enough and are pumped away by the vacuum system, which uses five *turbo-molecular pumps* (TMPs) that reach a final pressure of $6 \cdot 10^{-10}$ mbar. The lighter electrons which follow the magnetic field lines can move around the kinks, and are thus kept inside the flux tube without being removed. Since charged ions also follow the magnetic field lines to a certain extent, additional electrodes are added to the DPS beamline in order to produce potential barriers and $E \times B$ drifts. By these methods, this first stage of the transport section is expected to reduce the tritium flow by a factor of $2.5 \cdot 10^4$ [L⁺12, Kos12].

The CPS features a similar beamline design, but further reduces the tritium flow by means of an 3 K argon frost layer on the inner beamline walls, where tritium is removed efficiently by cryo-sorption processes. The argon layer becomes saturated during continuous operation, and thus has to be renewed at regular intervals. The CPS is expected to reduce the tritium flow by another factor of 10^9 or better [G⁺10, Jan15].

2.1.2 Spectrometer and Detector section

After leaving the pumping sections, the decay electrons reach the SDS, where they enter a tandem of two MAC-E type spectrometers (figure 2.4). The **Pre-Spectrometer** (PS) (or Prespec) acts as a first filter to reduce the amount of electrons entering the **Main Spectrometer** (MS) (or Mainspec). Both spectrometers operate on high voltage to produce an electrostatic retarding potential close to the tritium endpoint energy ($qU \lesssim 18.6$ keV). The energy analysis of the decay electrons takes place in the MS, where the electrons have to overcome the potential wall formed by the retarding potential. Only a small fraction of electrons produced in the WGTS reaches the detector (i. e. electrons with sufficient energy, $E_e > qU$). One can therefore measure an integral form of the energy spectrum by slightly varying the potential [P⁺92, Val09, Zac14].

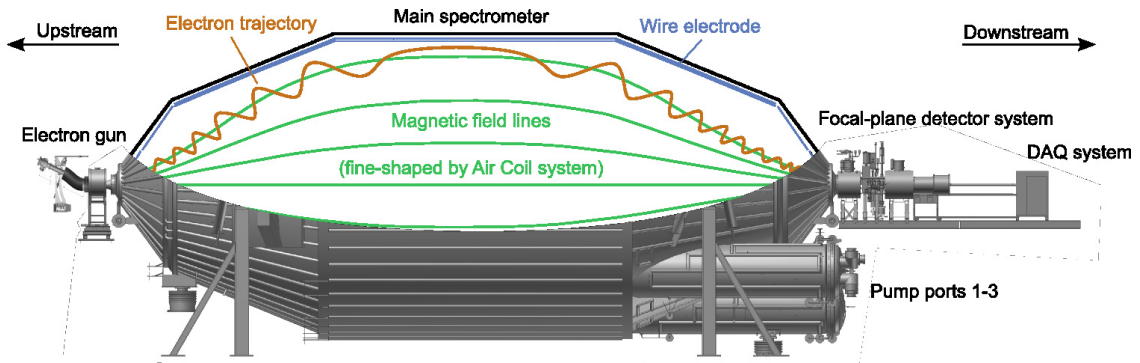


Figure 2.4.: The main spectrometer. The electrons follow the magnetic guiding field towards the detector system, which is created by two superconducting solenoid magnets at the entrance and exit of the spectrometer. An electrostatic retarding potential is implemented by applying a high voltage on the vessel and the wire electrode system. The magnetic fields inside the spectrometer are fine-shaped by an air coil system. The figure shows the SDS-2 setup with the electron source mounted at the upstream side of the spectrometer; in the regular setup the pre-spectrometer connects the main spectrometer to the pumping section. The pre-spectrometer is smaller in dimension, but follows the same design principle. Figure from [Har15].

Although it is possible to operate the spectrometer system without the PS, it is planned to utilize the PS as a pre-filter that cuts away the major fraction of electrons by operating at a retarding potential of about -18.3 kV. This tandem setup of two spectrometers is supposed to avoid negative effects caused by the large amount of roughly 10^{11} s^{-1} electrons from the WGTS entering the MS. As the information about the neutrino mass is only accessible in the spectral region close to the endpoint, the uninteresting low-energy electrons can be safely filtered out without affecting the outcome of the experiment. Both spectrometers operate under *ultra-high vacuum* (UHV) conditions, with the main spectrometer reaching a pressure of down to $1 \cdot 10^{-11}$ mbar. The low pressure minimizes scattering processes of the signal electrons with residual gas, which would increase the systematic uncertainty of the experiment. The UHV level is reached by a combination of TMPs, which are located at three

pump ports that are attached to the main spectrometer vessel, and *non-evaporable getter* (NEG) pumps that are placed inside the pump ports. The vacuum system reaches a total pumping speed of 10^4 l/s by the TMPs and 10^6 l/s for hydrogen by the NEG pumps [A⁺16b, Har15].

The retarding potential is a crucial aspect of the experiment's design, and significantly affects the sensitivity to the neutrino mass (cmp. section 2.3). KATRIN therefore utilizes two independent methods to measure potential fluctuations and determine the absolute retarding potential, without affecting the energy analysis in the main spectrometer itself.

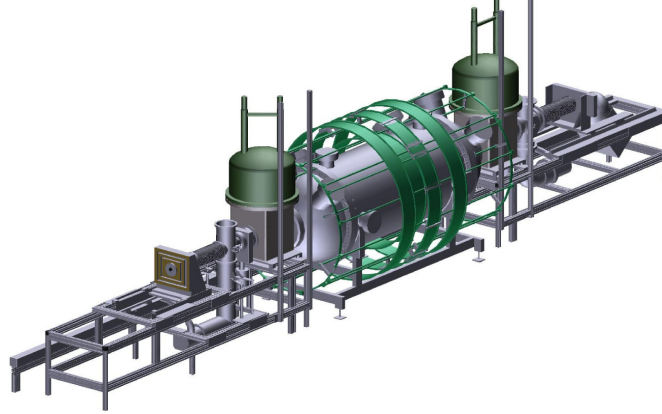


Figure 2.5.: The monitor spectrometer. The spectrometer was refurbished after the Mainz neutrino mass measurements and integrated into the KATRIN setup. Like the pre- and main spectrometer, it is based on the MAC-E filter principle and allows on-line monitoring of the absolute retarding potential. This is achieved by monitoring krypton conversion lines that provide a natural energy standard. Since both spectrometers share the same high-voltage source, changes in the retarding potential are observed as shifts of the line positions. The monitor spectrometer also served as a test setup for the electron source before it was integrated with the main spectrometer SDS-2 setup. Figure from [Kle14].

The first method is a precise readout of the retarding potential by a ultra precise high-voltage divider that was designed specifically for the KATRIN experiment. It is one of the most accurate dividers worldwide. The HV divider is connected to the power supply that provides the high voltage for the MS, and scales down the voltage by a factor of about 2000. This allows to measure the spectrometer high voltage around the nominal value of -18.6 kV with a precise voltmeter operating in the 10 V range, thereby achieving a high accuracy¹. The divider itself is calibrated against a reference divider and a high-voltage source at the *Physikalisch-Technische Bundesanstalt* (PTB) in Braunschweig at regular intervals. In addition to this absolute calibration, it is possible to perform a relative calibration against a precision low-voltage source that delivers a stable electric potential of about 10 V. This source is calibrated against a Josephson voltage standard at the PTB. Both calibration methods are used in combination to account for possible drifts and instabilities in the used electronics [T⁺09, B⁺13b, Bau13]. Additionally, a new absolute calibration method has been developed recently, which allows to perform the full calibration directly at the KATRIN site without the need to transport the high-voltage divider to the PTB. The calibration can thus be performed at smaller time intervals, which further reduces the systematic uncertainty. A full description of the new method is given in [Res17].

1. It is extremely difficult to measure absolute voltages in the kV regime directly.

The second method to observe the stability of the retarding potential is an additional spectrometer, which operates in parallel to the MS and shares the same high-voltage source (figure 2.5). This **Monitor Spectrometer** (MoS) is in fact the spectrometer which was used in the Mainz experiment, and has been relocated to the KATRIN site to be used as a monitoring device. The MoS utilizes a krypton source to provide conversion electrons with precisely known energies, which allows to validate the effective retarding potential against a natural energy standard. Similarly to the energy analysis at the MS, an integral measurement of the krypton spectrum is taken at regular intervals and the observed energy lines are compared with the known line positions. A krypton source was chosen for this purpose, since conversion electrons from the $^{83\text{m}}\text{Kr}$ isotope feature naturally sharp line widths. The conversion line at 17 824.3(5) eV is close to the tritium endpoint and allows a direct measurement of the retarding potential²; other conversion lines at 9 keV and 32 keV are used for regular calibrations of the MoS [S⁺13a, E⁺14, Sle15, Erh16].

The experimental design is based on an integral measurement of the tritium energy spectrum, with the energy analysis taking place in the MS. The **Focal Plane Detector** (FPD) at the end of the beamline thus merely acts as a counting device (figure 2.6). It has an energy resolution of about 1.4 keV FWHM, which is sufficient to investigate the energy spectrum of the detected electrons, and for applying energy cuts in order to reject background events and electronic noise. The FPD consists of a pixelated silicon wafer (PIN diode) with a dead-layer of 100 μm . The wafer is directly connected to a first stage of read-out electronics inside the vacuum chamber, and operates in high-vacuum conditions in the $1 \cdot 10^{-6}$ mbar regime while being cooled down to -30°C in order to reduce electronic noise. Because the wafer and electronics are inside the high-voltage area, the detector signal is fed into the *data-acquisition* (DAQ) system with optical fibers. The DAQ system processes the detector events and distributes the data to the ORCA control software, which takes care of storing the measurement data and provides an interface the operational parameters of the FPD system. The count rate of electrons arriving at the detector is in the range of only 1 cps. The low event rates allow to optimize the DAQ parameters for energy or time resolution³; the FPD features a time resolution of down to 100 ns under nominal conditions. To improve the *signal-to-noise ratio* (SNR) and to be able to observe low-energetic electrons ($E \lesssim 5$ keV), a **Post-Acceleration Electrode** (PAE) is installed in front of the detector wafer. Electrons can thus be accelerated by a positive potential of up to 10 kV, shifting them to higher energies before they reach the detector wafer. The detector system aims at a background level of less than $1 \cdot 10^{-3}$ cps in the signal ROI, and features an active veto system to reduce background from cosmic muons [W⁺14, A⁺15a, Sch14, Har15].

The pixelated wafer surface allows to determine the hit position of the detected electrons; the electron trajectory through the spectrometer can thus be reconstructed to some extent⁴. This feature is important to reach the sensitivity goal: inhomogeneities in both the electric potential and the magnetic field (which can't be completely avoided) would otherwise result in large systematic uncertainties in the energy analysis of the electrons. To investigate these inhomogeneities, commissioning measurements are performed in order to characterize the electromagnetic properties of the MS. The measurements can then be used to apply corrections for each detector pixel and improve the overall sensitivity of the experiment [Gro15, Erh16].

2. The small energy difference to the tritium endpoint allows to post-accelerate the conversion electrons by commercial voltage sources without affecting the accuracy of the measurement.

3. A good time resolution is important for time-of-flight measurements of the observed electrons.

4. This requires the ability to track the electron trajectory from the hit position on the wafer into the spectrometer, which is possible through particle-tracking simulations.

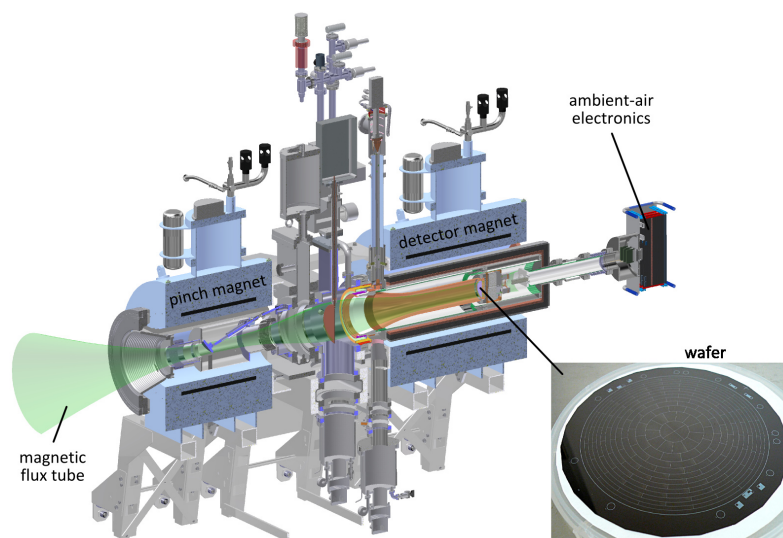


Figure 2.6.: The focal-plane detector system. The detector is mounted at the main spectrometer exit and provides the integral measurement of the tritium β -spectrum by counting the transmitted electrons. The magnetic field is defined by the pinch magnet (which also produces the spectrometer guiding field) and the detector magnet. The electrons are guided onto the pixelated wafer, which allows a spatial resolution of the electron trajectories (and thus can be used to correct for inhomogeneities of the spectrometer transmission properties). A post-acceleration electrode can be used to shift the electron energy in order to improve the signal-to-noise ratio and allows a detection of low-energetic electrons. Figure from [Gro15].

One should note that low-energy background from the spectrometer cannot easily be avoided by technical means: electrons from the spectrometer are accelerated by the retarding potential when they leave the spectrometer volume. Low-energetic background electrons therefore overlap with the signal electrons at the detector, where they both reach energies of about 28.6 keV (at nominal conditions with PAE); it is thus impossible to disentangle the electron signal from the background. Other methods of background reduction must therefore be considered. A short discussion on background reduction techniques is given in section 2.1.4; chapter 5 presents an active background reduction method known as *magnetic pulse*.

2.1.3 Electromagnetic design

Since KATRIN is based on the precise energy analysis of beta-decay electrons, its setup features a well-organized system of electric and magnetic systems (figure 2.7). The electrons generated in the source follow the field lines in the magnetic flux tube towards the detector, passing through numerous subsystems on their way. It has to be ensured that no electrons are lost from a misalignment of the magnetic fields (causing them to hit an inner wall in one of the subsystems). Furthermore, the transport must be completely adiabatic and with minimal energy losses, so that the information about the electron energy is conserved.

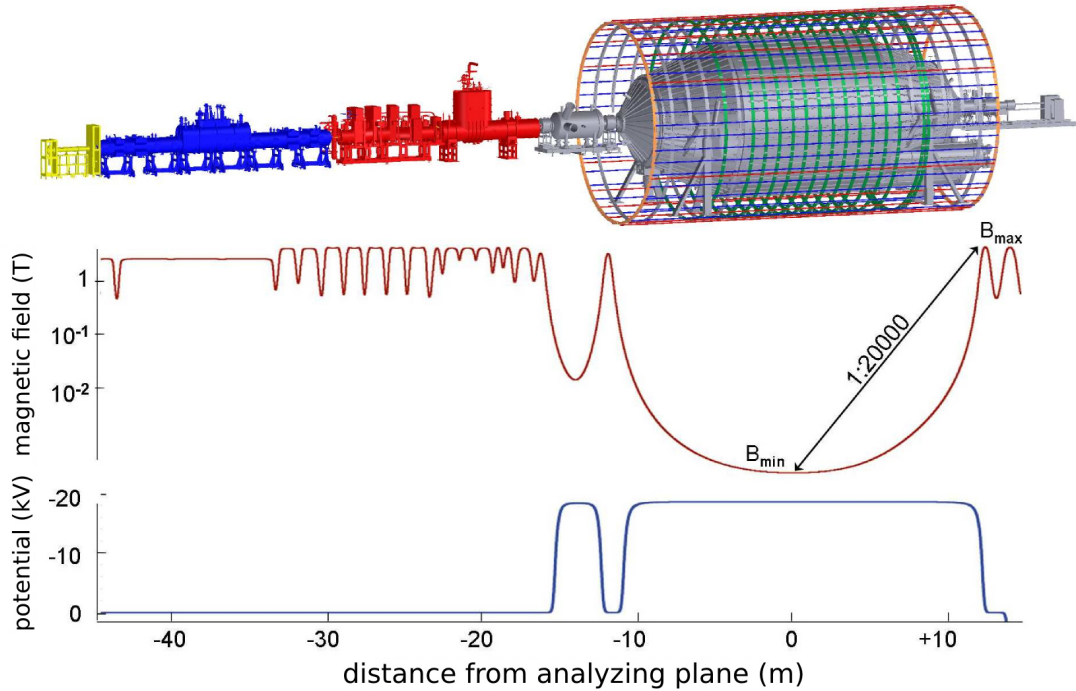


Figure 2.7.: Electromagnetic fields in the KATRIN setup. The magnetic field guides the β -electrons from the source ($B_{src} = 3.6\text{ T}$) through the pumping sections into the spectrometers. At the main spectrometer, the magnetic field drops to its minimal value ($B_{min} = 0.3\text{ mT}$) to achieve an adiabatic collimation of the electron beam. The strongest magnetic field is reached at the pinch magnet at the spectrometer exit ($B_{max} = 6\text{ T}$). The ratio $B_{min}/B_{max} \approx 20\,000$ defines the energy resolution of the main spectrometer. An electric retarding potential is applied at the pre- and main spectrometer to perform an energy analysis of the electrons; the pre-spectrometer is intended to reject the low-energetic electrons that do not contribute to the neutrino mass sensitivity. Note that slightly different settings were used in the SDS-2 measurements. Figure from [Wan13].

Magnetic fields

The magnetic field throughout the experiment is defined by multiple superconducting solenoids operating at field strengths up to 6 T. Inside the WGTS, the magnetic field is 3.6 T and homogeneous over the full source volume; the inner radius is given by the 191 T cm² flux tube, which has to fit inside the beam tube. Solenoids in the pumping sections keep the magnetic field at similar levels towards the spectrometers. Here the flux tube is diverted (kinked) in a way that allows to remove tritium and other gases, as described above. The electrons then reach the spectrometer section, where they first enter the pre-spectrometer through another solenoid, the **Pre-Spectrometer magnet 1 (PS1)**, operating at 4.5 T. Between pre- and main spectrometer, the **Pre-Spectrometer magnet 2 (PS2)** is located; it also operates at 4.5 T. The two PS magnets define the magnetic field inside the pre-spectrometer, where decay electrons can be blocked off from the main spectrometer. The PS2 also defines the field inside the main spectrometer, together with the **Pinch magnet (PCH)** which operates at 6 T. The pinch magnet achieves the highest magnetic field over the KATRIN beamline, and thus “pinches” the flux tube to its smallest radius. After leaving the main spectrometer, the electrons are guided towards the

detector where the last solenoid, the **Detector magnet** (DET) is located. This magnet operates at 3.6 T and ensures that the flux tube is fully mapped onto the pixelated detector wafer [A⁺05b].

Inside the main spectrometer, the magnetic field drops by about 4 orders of magnitude to 0.3 mT (= 3 G). As will be shown in the next section, the varying magnetic field towards the spectrometer's central plane is a key feature of the experiment, and the minimal magnetic field has a direct impact on the resulting energy resolution of the main spectrometer. Additionally, the magnetic field affects the magnetic flux tube inside the spectrometer, and thus affects the field homogeneity as well as the overall background level. The adiabatic electron transport inside the spectrometer must be adiabatic, and the magnetic field minimum must be aligned with the retarding potential [Erh16, Gro15, Wan13].

All these factors make it crucial to control the magnetic field inside the main spectrometer precisely. Two additional magnetic systems that operate with *air coils* are therefore installed at the main spectrometer. The **Low Field Correction System** (LFCS) is designed to adjust the longitudinal magnetic field component over the full length of the main spectrometer. The LFCS consists of 14 air coils that are placed around the spectrometer vessel, with a gap of roughly 1 m between each. The air coils are operated independently at currents up to 100 A, which allows to adjust the minimal magnetic field in the spectrometer in the range of 0.3 mT to 0.9 mT, and provides a method to fine-tune the longitudinal magnetic field⁵. Additionally, the LFCS compensates the longitudinal component of the Earth magnetic field. The remaining two components are compensated by the **Earth Magnetic Field Compensation System** (EMCS). In contrast to the LFCS, the EMCS consists of wire loops that are wound around the spectrometer vessel in longitudinal direction. The wires are arranged in a way that allows to adjust the vertical and horizontal components of the magnetic field. In addition to the compensation of Earth's magnetic field, the EMCS can be used to shift the flux tube center in the spectrometer to align it with the electric field and to reduce background [G⁺13b, E⁺16].

Electric fields

The electric fields at KATRIN are mainly present at the two spectrometers, where an electrostatic retarding potential is applied to perform the energy analysis. The source and pumping sections, on the other hand, operate at ground potential (although local electric fields exist, e. g. at the RS electron source or in the DPS). To apply the retarding potential, the spectrometer vessel is connected to a *high-voltage* (HV) system which provides a voltage of -18.6 kV (up to -35 kV for special measurements). To precisely control the electric potential and to adjust the transmission properties of the spectrometer, an **Inner Electrode** (IE) system is installed at the main spectrometer. The IE consists of a two-layer wire electrode system that is mounted on the inside of the vessel walls and is isolated against the vessel itself. Additionally, the wire layers are isolated against each other; a retarding voltage up to 200 V is typically applied between the wire layers and the vessel walls. The wire layers thus shield the spectrometer volume from low-energy electrons that are created at the inside of the vessel walls, e. g. from radioactive decays or cosmic radiation (muons). The IE also minimizes asymmetries in the electric potential that are caused by the gravitational deformation of the spectrometer vessel. This is possible because the wire system was aligned with a precision of better than 1 mm to form a circular equi-potential surface, which results in a symmetric retarding potential inside the spectrometer [B⁺13c, Val09, Zac14].

The IE is split into two dipole halves in vertical direction, and into independent rings in longitudinal direction. These isolated components can be connected to individual power supplies that operate

5. During the preparation for the SDS-3 commissioning phase (summer 2016), the air coil system has been upgraded to allow currents up to 180 A in order to reach a larger overall magnetic field inside the spectrometer.

on top of the overall vessel voltage, which allows flexible configurations of the electric potential inside the spectrometer. The electric potential variation over the magnetic field lines (which guide the electrons through the spectrometer) is fine-tuned to ensure adiabatic transport, to align the potential maximum with the magnetic field minimum, and to produce the necessary transmission properties. The transmission properties are discussed in more detail in section 2.2.

2.1.4 Background reduction

The background level of the detector system itself is less than 10^{-3} cps by design, which yields a sufficient SNR to reach the sensitivity goal. However, low-energetic background electrons from the spectrometer system overlap with the signal ROI and thus can not be discriminated against (cmp. section 2.1.2). Hence, other methods to reduce the background from the spectrometer have to be investigated.

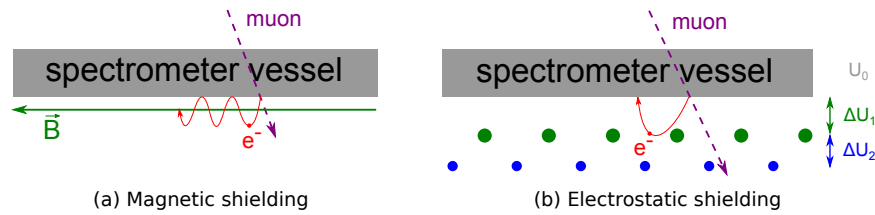


Figure 2.8.: Electromagnetic shielding at the main spectrometer. Cosmic muons and radioactive decays in the stainless steel hull can create free electrons that are emitted into the magnetic flux tube, where they contribute to the observed background level. The majority of these electrons is prevented from entering the flux tube by magnetic shielding (a), which diverts the electron trajectories into the axial direction. A retarding potential between the steel hull and the two layers of the inner-electrode system ($\Delta U_{1,2} \approx 100$ V) provides additional electric shielding (b). Figure from [Gro15].

The background from cosmic muons is significantly reduced by electromagnetic shielding at the main spectrometer. Cosmic muons can easily penetrate the steel hull of the spectrometer vessel and induce electron-emission at the inner surface (figure 2.8). This is true for *all* electrodes inside the spectrometer, but the vessel hull provides the largest target mass for muon interactions. However, electrons created at the vessel surface have to move into the magnetic flux tube to contribute to the background. The magnetic field design prohibits the majority of low-energy electrons from entering the flux tube: electrons follow the magnetic field lines and therefore are confined to a trajectory outside of the active flux tube volume. This *magnetic shielding* effect reduces the background rate from cosmic muons by a factor of 10^5 . Local inhomogeneities in the electromagnetic fields as well as potential fluctuations, however, can produce small “gaps” in the magnetic shield; some electrons are thus able to travel into the flux tube. For this reason, the IE system described above further reduces the electron flow into the flux tube. An electrostatic retarding potential of 100 V is applied between the vessel surface and the first (outer) wire layer, and also between the outer and inner wire layer⁶. Electrons with small energies, which were produced at the vessel hull, are reflected back towards the surface and blocked from the flux tube. A disadvantage of this system is that it adds more parts inside the spectrometer, namely the wire electrode itself and its mounting structure; these parts again provide a target mass

⁶. The experiment is currently operated in “single-wire” configuration, i. e. without an additional retarding potential between the wire layers [H⁺13].

for cosmic muons. The second wire layer is therefore constructed in a way that minimizes the target mass that is directly “visible” from the flux tube. Both layers combined reduce the background from cosmic muons by a factor of 10^2 , so that a net reduction of 10^7 is reached by the electromagnetic shielding [A⁺05b, B⁺13c, Arl09, Val09].

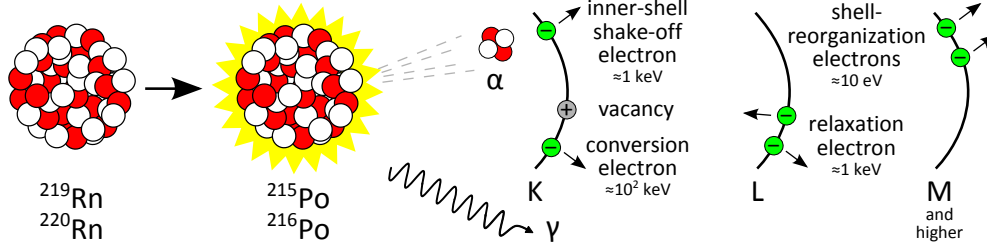


Figure 2.9.: Radon-induced background processes. The radioactive radon isotopes that are abundant at the main spectrometer decay into excited states of polonium nuclei. The excitation energy is dissipated by a variety of processes that emit low- and high-energetic electrons. The short half-life of ^{219}Rn and ^{220}Rn allows these decays to occur inside the magnetic flux tube, where the created electrons can become stored and contribute to the observed background via continuous scattering processes. Since low-energetic secondaries share the energy region with signal electrons, this background cannot be discriminated against. Figure from [Sch13].

Radioactive decays in the steel hull of the spectrometer vessel can also produce electrons that contribute to the observed background. The major source of radioactivity in the steel hull is the isotope ^{220}Rn , which is a natural isotope that can't be easily avoided in industrial processing. Although the stainless steel of the vessel hull was selected for a minimal amount of radioactive isotopes, a small fraction of ^{220}Rn is still abundant. Another isotope of Radon that contributes to the observed background is ^{219}Rn , which is present in the material of the NEG pumps. The radioactive isotopes in the getter material cannot be avoided completely. Radon molecules can thus emanate from the NEG pumps, and travel into the spectrometer volume through the pump ports. Due to the large pumping speed of the TMPs installed at the main spectrometer, most radioactive atoms that get into the spectrometer volume are pumped out before a decay occurs. The half-life of ^{219}Rn , however, is sufficiently small to travel from the NEG pumps into the spectrometer and decay before being pumped out ($T_{1/2}^{219} = 3.96\text{ s}$). The electron spectrum of decay electrons from ^{219}Rn and ^{220}Rn is complex and features a wide energy range from a few eV to several keV (figure 2.9). High-energetic electrons can become magnetically trapped inside the flux tube for several hours, and have a high scattering probability with residual gas. Each scattering event can produce multiple low-energetic secondaries; a single radioactive decay inside the main spectrometer could therefore considerably increase the observed background over several hours [F⁺11, M⁺13, W⁺13, Frä10, Mer12, Wan13].

To reduce this background component, cryogenic baffles have been installed in front of the pump ports. The baffles operate at the temperature of LN_2 ($T_{\text{LN}_2} = 77\text{ K}$), and are designed to block the direct line-of-sight between spectrometer volume and NEG pumps. Radon atoms traveling into the spectrometer are thus guided against the cold surface of the baffles, where they are adsorbed and decay outside the flux tube. The baffles efficiently block radon atoms from the spectrometer volume, and significantly reduce the observed background from radon decays [Gör14, Har15].

Even with these passive background-reduction methods, it could be necessary to remove trapped electrons from the main spectrometer in the case that long-term a rate increase is observed. This is especially important because of the extremely long storage times of high-energetic electrons inside the

spectrometer, which could require to interrupt the current measurement until the background level decreases. The design of the main spectrometer allows to implement two types of active background-reduction techniques, which can be activated dynamically. One method, the **Electric Dipole**, introduces an electric field between the dipole halves of the main spectrometer. The combination of electric and magnetic fields results in an $E \times B$ drift that points mainly in vertical direction. The dipole field thus diverts trapped electrons towards the top/bottom sections of the vessel hull; electrons that hit an electrode surface are removed from the spectrometer volume. A downside of this method is that it is expected to only work efficiently with low-energetic electrons, but is not able to remove the high-energetic primary electrons from nuclear decays. The efficiency is limited by the maximal allowed voltage difference that can be applied between the dipole halves ($\Delta U_{dip} < 1 \text{ kV}$), which results in a maximal dipole field of 100 V/m [Wan13, Hil16].

Another active background reduction method is the **Magnetic Pulse**, which utilizes the magnetic field instead. Here the existing air coil system at the main spectrometer is used to reduce the magnetic field inside the spectrometer. Similarly to the electric dipole, the magnetic pulse diverts stored electrons so that they hit the vessel walls. Because the reduced field affects the magnetic guiding of all electrons regardless of their energy, the magnetic pulse is expected to affect electrons over a wide energy range. It could, however, lead to an increased background afterwards: the diverted field lines allow electrons from the vessel hull to enter the flux tube, where they can become stored and again produce background. An advantageous feature of this method is that it can re-use the existing air coil system. For this purpose, it has to be modified in order to support fast current-switching in the individual air coils, so that a fast reduction of the magnetic field is possible. The magnetic pulse system was developed and tested over the course of this thesis; a detailed discussion is presented in chapter 5.

2.2 The MAC-E filter

The setup of the KATRIN experiment is based around on a key technique known as magnetic adiabatic collimation with electrostatic filtering (MAC-E), a concept that was first published in 1981 [B⁺81] and has been used in numerous experiments [LS85, P⁺92]. The MAC-E filter is used to analyze the energy of beta-decay electrons with a sharp energy resolution of 0.93 eV under nominal conditions and a large (theoretical) acceptance angle of 2π . The method of counting the transmitted electrons with kinetic energies above the filter energy allows to measure the integrated tritium beta spectrum, from which the neutrino mass can be determined.

This section will discuss important properties of the MAC-E filter that are relevant for the KATRIN experiment. The transmission properties of a MAC-E filter can be investigated experimentally with an electron source, which is discussed in chapter 4.

2.2.1 Adiabatic collimation

The key components of the MAC-E filter are the magnet system to provide a magnetic guiding field and the electrode system to create an electric retarding potential. Two super-conducting solenoids at the entrance and exit regions of the spectrometer vessel provide a strong magnetic field in the order of $B_{max} \approx 6$ T. Towards the central plane of the spectrometer, the magnetic field decreases by several orders of magnitude to the minimal magnetic field $B_{min} \approx 0.3$ mT = 3 G (*Gauss*, 1 G = 10^{-4} T) at the central region of the spectrometer. The spectrometer vessel is operated at high voltage $U \approx -18.6$ kV, which creates an electric retarding potential and defines the filter energy qU , where q is the (negative) elementary charge of the electron. The resulting potential wall has a maximum at the central plane of the spectrometer. The magnetic field can be fine-tuned by air coils that are mounted around the spectrometer vessel in order to ensure adiabatic electron transport and to align the potential wall (*analyzing plane*, maximum of the electric potential) with the magnetic field minimum. Figure 2.11 shows a schematic drawing of a MAC-E filter.

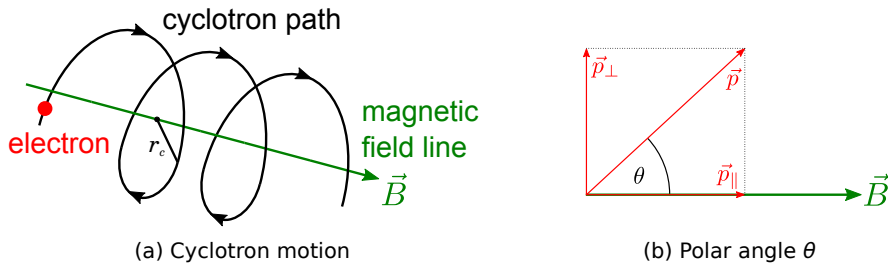


Figure 2.10.: Movement of a charged particle in a magnetic field. A charged particle like an electron follows a circular cyclotron motion around a magnetic field line \vec{B} (“gyration”). Apart from the gyration, the particle is confined to the field line; it can only move in longitudinal direction with momentum p_{\parallel} (if no additional drift occurs). The radius of the circular motion (“cyclotron radius” r_c) depends on the magnetic field and the transversal momentum p_{\perp} . The relation between longitudinal and transversal momentum can be described by the *pitch angle* θ . For $\theta = 0^\circ$, the particle’s kinetic energy is fully stored in the longitudinal component and no gyration occurs. Figure adapted from [Gro15].

Electrons traveling through a magnetic guiding field follow the magnetic field lines on a so-called cyclotron motion, a *gyration* around the field line (figure 2.10). The electron momentum w. r. t. the magnetic field (i. e. the direction of the field line) defines a *pitch angle* that is defined as a polar angle $\theta = \angle(\vec{p}, \vec{B})$. Together with the kinetic energy of the electron, this important parameter can be used to describe the (adiabatic) electron transport through the MAC-E filter. The kinetic energy can be split up into a longitudinal component E_{\parallel} (momentum in direction of the field line) and a transversal component E_{\perp} (momentum contributing to the gyration around the field line):

$$E_{kin} = E_{\parallel} + E_{\perp} \quad (2.1)$$

$$= E_{kin} \cdot (\cos^2 \theta + \sin^2 \theta). \quad (2.2)$$

Signal electrons which enter the spectrometer have kinetic energies of up to $E_{max} = 18.6$ keV, and their kinetic energy is reduced towards the analyzing plane where they have to overcome the potential wall. An electron can be electrically reflected by the retarding potential when its energy becomes extremely small, in which case it leaves the spectrometer through the entrance region instead of being transmitted towards the exit. Given the rather low energy of the decay electrons, $E_{kin} \ll m_e c^2$, it is often convenient to use a non-relativistic approximation where $E_{kin} = \frac{1}{2} m_e v^2$. The Lorentz factor of electrons at the endpoint energy is

$$\gamma_{max} = \frac{1}{\sqrt{1 - \frac{v^2}{c^2}}} = 1 + \frac{E_{kin}}{m_e c^2} = 1.04 \approx 1. \quad (2.3)$$

Since the transversal energy component corresponds to the gyration of the electron, the cyclotron radius can be derived from the Lorentz force,

$$F_L = eB \cdot v_{\perp} = \frac{m_e v_{\perp}^2}{r_c} \quad (2.4)$$

$$\Rightarrow r_c = \frac{\sqrt{2m_e E_{\perp}}}{eB}. \quad (2.5)$$

The transversal energy vanishes for $\theta = 0^\circ$, therefore all electrons with non-zero angles will undergo gyration.

The cyclotron motion of an electron corresponds to a magnetic moment

$$\mu = \frac{e}{2m_e} |\vec{l}| = \frac{E_{\perp}}{|\vec{B}|}, \quad (2.6)$$

where \vec{l} denotes the orbital angular momentum of the electron.

In adiabatic motion, the magnetic moment is conserved [Jac62] and electrons traveling through an inhomogeneous magnetic field will transform their transversal energy according to

$$\mu = \frac{E_{\perp}}{B} = \text{const.} . \quad (2.7)$$

The electron motion is adiabatic when the change in magnetic field over one cyclotron motion is small:

$$\frac{1}{B} \frac{d\vec{B}}{dt} \ll \frac{\omega_c}{2\pi} = \frac{eB}{2\pi\gamma m_e}. \quad (2.8)$$

Here $\omega_c = eB/m_e$ denotes the cyclotron frequency. The condition (2.8) can be derived by evaluating the change in transversal energy, which corresponds to the work done by the electric field over one cyclotron radius,

$$\Delta E_{\perp} = \Delta W_{\perp} = e \oint \vec{E} \cdot d\vec{l} = e \frac{\partial}{\partial t} \int \vec{B} \cdot d\vec{s} \approx e\pi r_c^2 \cdot \frac{\partial B}{\partial t} = \frac{2\pi}{\omega_c} E_{\perp} \cdot \frac{1}{B} \frac{\partial B}{\partial t}, \quad (2.9)$$

assuming that the cyclotron radius r_c does not change significantly over one cyclotron turn. The relation between the two integrals is given by Faraday's law. In adiabatic motion, the relative change $\Delta E_{\perp}/E_{\perp}$ is small, so that the condition

$$\frac{\Delta E_{\perp}}{E_{\perp}} = \frac{2\pi}{\omega_c} \cdot \frac{1}{B} \frac{\partial B}{\partial t} \ll 1 \quad (2.10)$$

yields the adiabaticity condition given above.

One can now derive an equation for the transformation of the pitch angle as introduced in (2.1):

$$\frac{E_{\perp}}{B} = \frac{E'_{\perp}}{B'} \quad (2.11)$$

$$\Rightarrow \sin^2 \theta' = \sin^2 \theta \cdot \frac{B'}{B}. \quad (2.12)$$

The change in pitch angle (or transversal energy) is thus completely defined by the ratio of the magnetic fields.

In the case of the MAC-E filter the magnetic field decreases towards the central plane, which results in a collimation of the electron momenta – electrons that enter the spectrometer with a large pitch angle transform their transversal into longitudinal momentum due to energy conservation, and the pitch angle reaches a minimum at the minimal magnetic field (figure 2.11). The effect reverses when the electrons leave the spectrometer and travel into a region with higher magnetic field, where the pitch angle increases accordingly.

This concept of *adiabatic collimation* is crucial to create an electrostatic spectrometer with a large acceptance angle. As the energy analysis is performed with the retarding potential, only the longitudinal kinetic energy is available to overcome the potential wall ($E_{\parallel} > qU$). Without adiabatic collimation, electrons with large pitch angles would be reflected even if their total kinetic energy is large enough to be transmitted. This would severely limit the acceptance angle and block a large fraction of electrons from the source⁷. As a result, the electron rate available for the neutrino mass measurements would be reduced significantly.

2.2.2 Energy resolution

The MAC-E filter acts as a high-pass filter and transmits electrons above a certain threshold, which is defined by the retarding potential, and provides a theoretical acceptance angle of 2π given the adiabatic collimation of the electron beam. The energy resolution can be derived from these considerations.

Since the minimal magnetic field is always larger than zero, it is impossible to transform the transversal energy completely. Electrons with large pitch angles, $\theta \rightarrow 90^\circ$, therefore require a larger kinetic energy

7. The radioactive decays of tritium in the WGTS produce an isotropic emission spectrum with pitch angles up to 90° .

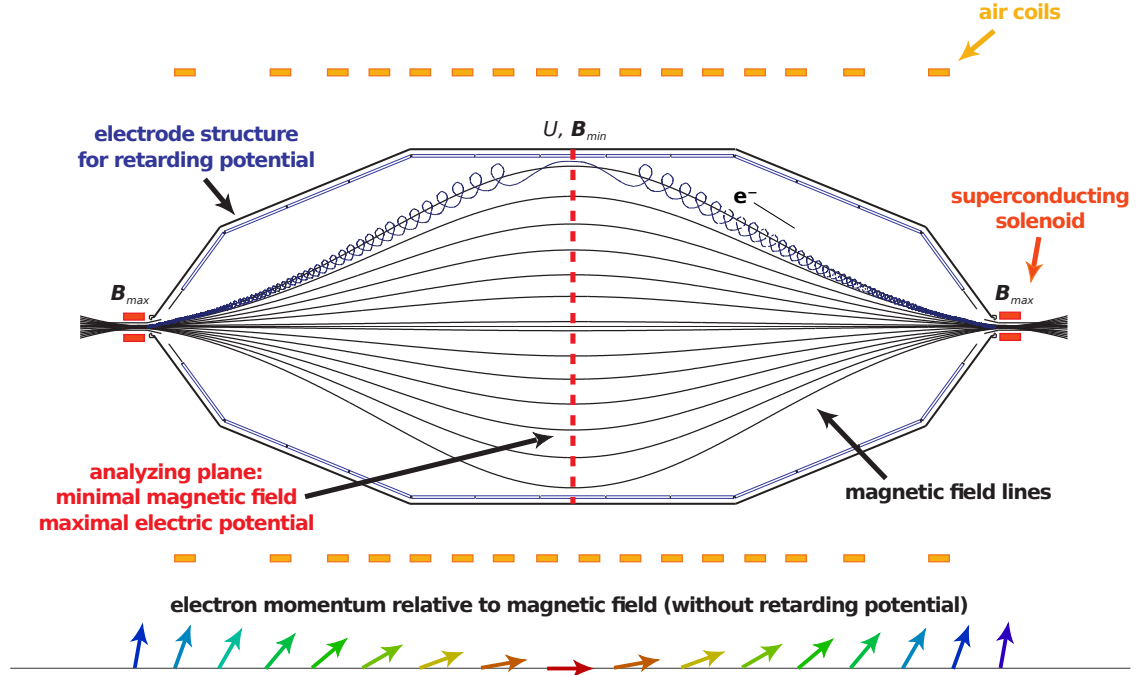


Figure 2.11.: Schematic drawing of a MAC-E filter with its key components. Electrons are guided along the magnetic field lines created by the superconducting solenoids at the spectrometer entrance and exit. The air coil system allows to fine-shape the magnetic field close to the analyzing plane at the center. An electric retarding potential is applied via the vessel hull and the electrode structure so that only electrons with sufficient kinetic energy are transmitted. Only the longitudinal energy is available to overcome the potential wall. Due to the conservation of the magnetic moment, the decreasing magnetic field towards the analyzing plane results in an adiabatic collimation of the electron beam – transversal momentum is converted into longitudinal momentum as the electron propagates into a region with smaller magnetic field; this is shown at the bottom. This technique ensures that electrons with sufficient energy are transmitted even if their longitudinal energy is too low when entering the spectrometer. The combination of a magnetic field with an electric potential thus provides a method for precise energy analysis with a large acceptance angle. Figure adapted from [Val09].

to be transmitted. Assuming that *all* kinetic energy is stored in the transversal component at the entrance magnet, $E_{\perp}^{start} = E_{kin}$ with $\theta_{start} = 90^{\circ}$, one can easily calculate the “missing” longitudinal energy at the magnetic field minimum where the energy analysis takes place. The longitudinal energy spread between electrons with zero and maximal initial pitch angle then corresponds to the energy resolution ΔE ,

$$\Delta E = E_{\perp}^{max} - E_{\perp}^{min} = E_{\perp}^{start} \cdot \frac{B_{min}}{B_{max}} = E_{kin} \cdot \frac{B_{min}}{B_{max}}, \quad (2.13)$$

with the minimal and maximal magnetic fields B_{min} , B_{max} at the spectrometer. Note that $E_{\perp}^{min} = 0$ eV for the minimal pitch angle of 0° .

This calculation is only valid if the electron motion is adiabatic. An important feature of the MAC-E filter to ensure adiabaticity is the early onset of the electric retardation, at a point where the magnetic field has not yet reduced significantly. If the retardation happens too early, however, electrons would be reflected before the energy transformation is completed (a process known as *early retardation*). The

correct shape of the electric potential inside the spectrometer to account for these effects is ensured by a proper design of the spectrometer electrodes [Zac14].

At the KATRIN main spectrometer, the nominal magnetic field settings $B_{max} = 6$ T and $B_{min} = 0.3$ mT result in an energy resolution of $\Delta E = 0.93$ eV at the tritium endpoint energy $E_0 = 18.6$ keV. In the next section, the transmission properties for (signal) electrons are derived.

2.2.3 Transmission properties

A precise knowledge of the transmission properties of the MAC-E filter is important in the design of the KATRIN experiment and necessary to understand many discussions in this thesis, especially regarding the two major topics: reduction of background from stored particles (chapter 5) and measurements with a calibration source used to characterize the main spectrometer (chapter 4).

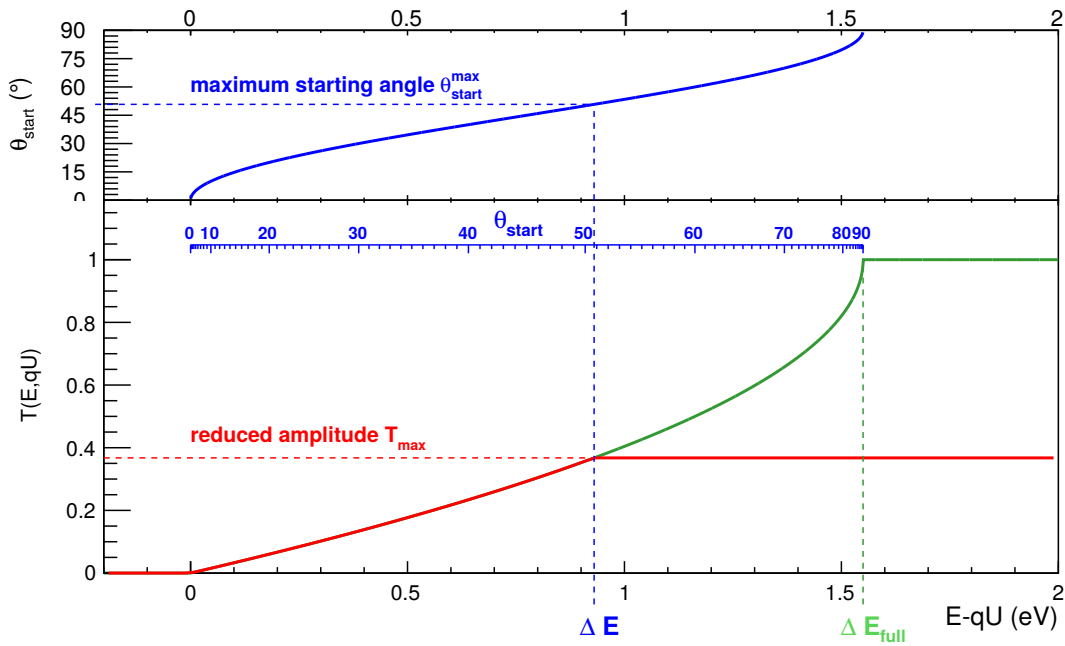


Figure 2.12.: Transmission function of a MAC-E filter. The bottom part shows the transmission probability $T(E, qU)$ according to (2.19). Since a larger electron pitch angle corresponds to less available kinetic energy in the analyzing plane, the surplus energy E must be increased accordingly for $\theta_{start} > 90^\circ$. For isotropic angles, the observed transmission width is $\Delta E_{full} = 1.55$ eV. The pitch angle is shown in the top part and also as an additional axis in the bottom plot. The asymmetric magnetic field setup with $B_{start} < B_{max}$ leads to magnetic reflection of electrons with pitch angles $\theta_{start} \geq \theta_{start}^{max} \approx 51^\circ$. The transmission width is thus reduced to the nominal value $\Delta E = 0.93$ eV, which improves the energy resolution of the spectrometer. Consequently, the transmission amplitude is reduced to $T_{max} < 1$. Figure from [Zac14].

The following discussion is based on the isotropic emission of electrons in the source, which is the case for the WGTS. The transmission function which is derived below is shown in figure 2.12. The calibration source, on the other hand, features a sharp angular resolution and will be discussed later in this thesis.

The basic condition for electrons to be transmitted through the spectrometer can be written as

$$E_{\parallel}(E_0, \theta_0, \vec{r}) - qU > 0. \quad (2.14)$$

where qU defines the filter energy, E_0 the initial kinetic energy and θ_0 the initial pitch angle. As explained above, E_{\parallel} can be computed from E_0, θ_0 if the magnetic fields $B(\vec{r})$ are known. The condition for the electron to reach the end of the spectrometer has to be fulfilled for all points \vec{r} along the electron trajectory.

The initial pitch angle is transformed towards the analyzing plane and defines the remaining transversal energy of the electron at the given retarding potential. The transmission condition (2.14) can be rewritten as

$$E_{\parallel}^{ana} - qU_{ana} = E_0 - E_{\perp}^{ana} - qU_{ana} \quad (2.15)$$

$$= E_0 - E_0 \cdot \sin^2 \theta_0 \cdot \frac{B_{ana}}{B_0} - qU_{ana} > 0, \quad (2.16)$$

where $U_{ana}, B_{ana}, E_{\parallel}^{ana}, E_{\perp}^{ana}$ describe the potential, the magnetic field and the longitudinal/transversal energy at the analyzing plane. This condition allows to compute the transmission probability of an electron entering the spectrometer with given kinetic energy E_0 and pitch angle θ_0 at the magnetic field B_0 .

Because of the energy resolution of the MAC-E filter, electrons with a too large pitch angle at a given energy will not be transmitted. The maximal pitch angle for transmitted electrons θ_{max} can be calculated from (2.15),

$$\theta_0 \leq \theta_{max} = \arcsin \sqrt{\frac{E_0 - qU_{ana}}{E_0} \frac{B_0}{B_{ana}}}. \quad (2.17)$$

The maximal starting angle defines a cone with solid angle $\Delta\Omega$ in which electrons can be transmitted. The transmission probability is given by the ratio of transmitted electrons w. r. t. the full solid angle:

$$\frac{\Delta\Omega}{2\pi} = 1 - \cos \theta_0. \quad (2.18)$$

Using the relation $\cos(\arcsin \sqrt{x}) = \sqrt{1-x}$ yields the transmission function for a MAC-E filter:

$$T(E_0, U_{ana}) = \begin{cases} 0 & \text{for } E_0 < qU_{ana} \\ 1 - \sqrt{1 - \frac{E_0 - qU_{ana}}{E_0} \frac{B_{source}}{B_{ana}}} & \text{for } qU_{ana} < E_0 < qU_{ana} + \Delta E_{full} \\ 1 & \text{for } qU_{ana} + \Delta E_{full} < E_0 \end{cases} \quad (2.19)$$

Here the energy resolution ΔE_{full} corresponds to an isotropic source that produces pitch angles up to 90°. At KATRIN, the signal electrons are created in the WGTS at the initial magnetic field $B_{source} = 3.6$ T. The energy resolution is

$$\Delta E_{full} = E_0 \cdot \frac{B_{ana}}{B_{source}} = 1.55 \text{ eV}, \quad (2.20)$$

which is significantly worse than the design value.

To obtain the design value, one must consider that electrons with an initial pitch angle $\theta_0 > \theta_{max}$ will be magnetically reflected at the magnetic field maximum B_{max} . When the pitch angle reaches 90° , the longitudinal kinetic energy vanishes and the electron is reflected. This *magnetic mirror effect* occurs in addition to the transmission condition (2.19) and limits the acceptance angle of the MAC-E filter according to

$$\theta_0 \leq \theta_{mir} = \arcsin \sqrt{\frac{B_0}{B_{max}}} . \quad (2.21)$$

This condition holds true for the KATRIN setup where the maximal magnetic field B_{max} is reached at ground potential $U = 0$ V; in this case the angle θ_{mir} is independent of the electron's energy.

The bunch of electrons with larger pitch angles is “cut off” from the number of transmitted electrons, and the transmission function (2.19) is modified accordingly:

$$T(E_0, U_{ana}) = \begin{cases} 0 & \text{for } E_0 < qU_{ana} \\ 1 - \sqrt{1 - \frac{E_0 - qU_{ana}}{E_0} \frac{B_{source}}{B_{ana}}} & \text{for } qU_{ana} < E_0 < qU_{ana} + \Delta E \\ 1 - \sqrt{1 - \frac{B_{source}}{B_{max}}} & \text{for } qU_{ana} + \Delta E < E_0 \end{cases} . \quad (2.22)$$

This modified transmission function now features a smaller energy resolution of

$$\Delta E = E_0 \cdot \frac{B_{ana}}{B_{max}} = 0.93 \text{ eV} , \quad (2.23)$$

which corresponds to the design value. The magnetic mirroring effect thus actually improves the energy resolution while reducing the acceptance angle of the spectrometer. This is, however, not a disadvantage of the experiment since electrons with large pitch angles have a higher probability to be affected by energy losses in the source. The systematic uncertainties are therefore improved by the reduced acceptance angle.

The reduced acceptance angle results in a lower signal amplitude,

$$T_{max} = 1 - \sqrt{1 - \frac{B_{source}}{B_{max}}} . \quad (2.24)$$

The magnetic field in the WGTS is $B_{source} = 3.6$ T at nominal conditions and the maximal field at the spectrometer is $B_{max} = 6$ T in the so-called pinch magnet. This results in a maximal pitch angle of $\theta_{source} \leq 51^\circ$ and a transmission amplitude of $T_{max} = 0.37$.

2.2.4 Realistic MAC-E filters

The MAC-E filter provides many advantages for precision measurements of the kinetic energy of electrons. The energy resolution is solely defined by the ratio of magnetic fields B_{min}/B_{max} , which requires a large spectrometer vessel depending on the target resolution. Realistically, the transmission conditions are affected by inhomogeneities in the electric and magnetic fields. These effects will be discussed in the following section.

The magnetic flux is conserved in a magnetic beamline setup,

$$\Phi = \int_0^{r_{max}} \vec{B}(r) d\vec{r} \approx B \cdot A = \text{const.} , \quad (2.25)$$

with r_{max} the flux tube radius at the given magnetic field \vec{B} and A its cross-sectional area. Therefore, when the magnetic field changes, the flux tube radius must adapt accordingly. This explains the large dimensions of the KATRIN main spectrometer, where the magnetic field drops by a factor of 20 000 and the 191 T cm^2 flux tube widens to a radius of almost 5 m at the magnetic field minimum. In contrast, the flux tube radius in the source is only about 4 cm.

The electrostatic retarding potential inside the main spectrometer is created by the vessel hull and the inner electrode system. However, the potential at the analyzing plane is also affected by the ground potential at the entrance and exit regions of the spectrometer, which can not be shielded efficiently. Given the large diameter of the spectrometer vessel, the effective potential in the analyzing plane increases towards the central beam axis where the influence of the vessel hull and inner electrode system is smaller and the influence by the ground potential becomes more dominant. This effect is called *potential depression* (or *potential penetration*), and leads to a position-dependent retarding potential $U_{ana}(r)$. The potential difference along the analyzing plane has been estimated to $\Delta U_{ana} = 1.18 \text{ V}$ at nominal conditions. This value can be reduced by increasing the magnetic field at the analyzing plane, which creates a smaller flux tube but also worsens the energy resolution. Similarly, the magnetic field at the analyzing plane shows a radial dependency due to the varying distance to the spectrometer solenoids and the individual air coils. The *magnetic field depression* has been estimated to $\Delta B_{ana} = 0.05 \text{ mT}$ [Erh16, Gro15].

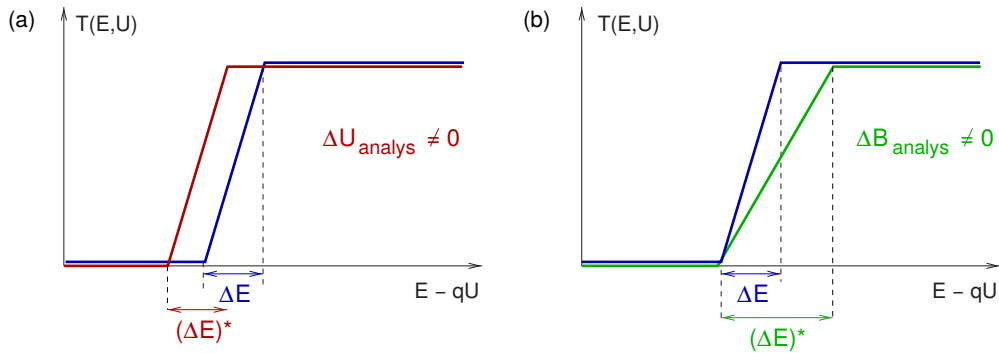


Figure 2.13.: Effects of electromagnetic inhomogeneities on the transmission function. The observed transmission function at the spectrometer is affected by inhomogeneities of the retarding potential (a) and the magnetic field (b) at the analyzing plane. A change in retarding potential results in a shift of the transmission function on the energy axis, but the width is constant ($(\Delta E)^* = \Delta E$). On the other hand, a larger magnetic field increases the width of the transmission function ($(\Delta E)^* > \Delta E$) that also shifts the upper transmission edge to higher energies. The combination of both effects results in a complicated effective transmission function that reduces the energy resolution of the spectrometer. Figure adapted from [A⁺05b].

These two effects lead to inhomogeneities of the transmission properties that depend on the radial position in the analyzing plane (figure 2.13). A change of the electric potential shifts the transmission function to a different energy, and a change in the magnetic field leads to a different transmission width (energy resolution). An “effective transmission function” can be constructed by a superposition of the transmission functions for all \vec{r} . In the case of the KATRIN main spectrometer, this would result in an extremely broad transmission function that would not allow to reach the desired energy resolution.

This issue can be overcome by using a segmented detector, which can resolve the radial position in the analyzing plane to some extent. If the different transmission properties for the single pixels are known, the measured integral energy spectrum can take into account these differences correctly. To be able to perform these corrections, the transmission properties of the main spectrometer must be determined for all detector pixels, which requires a dedicated measurement with a calibration source that creates electrons with sharp energy and angular distributions. The calibration source that is presented in chapter 4 was designed for this purpose, and has been used in the corresponding commissioning measurements at the main spectrometer.

2.3 Sensitivity to the neutrino mass

The KATRIN experiment will determine the neutrino mass by measuring the integrated tritium β -spectrum $\frac{dN_\beta}{dE}(E_0, m_{\nu_e})$, using the MAC-E filter setup that has been discussed above. This purely kinematic method provides a model-independent way of measuring the neutrino mass, but like other experiments it is affected by statistical and systematic uncertainties which limit the resulting sensitivity to the neutrino mass. This section will summarize the major sources for uncertainties at KATRIN and discuss how the uncertainties affect the neutrino mass sensitivity.

2.3.1 Theoretical model of the tritium beta spectrum

In a MAC-E filter setup⁸, the electron rate at the detector depends on the retarding potential U_{ana} , which corresponds to the filter energy qU . Together with the ratio of the magnetic fields B_{min} and B_{max} , the filter energy defines the transmission function $T(E, qU)$.

Uncertainties in the electromagnetic fields thus directly affect the measured electron rate and therefore increase the total systematic uncertainty of the experiment. Furthermore, given the rather high pressure of tritium gas in the WGTS, the β -decay electrons have a high probability of scattering inside the source. It is estimated that only 40% of the electrons leave the source without scattering, and for the majority of electrons at least one scattering event occurs [B⁺12].

Since inelastic scattering will result in a loss of energy, these electrons have a higher chance of being reflected at the MAC-E filter (instead of reaching the detector). The *response function* $R(E, qU)$ accounts for these additional effects (figure 2.14). It is a convolution of the transmission function of the MAC-E filter with a model that describes the energy losses in the source [H⁺17, A⁺05b].

The resulting signal electron rate at the detector \dot{N}_s is then described as

$$\dot{N}_s(qU, E_0, m_{\nu_e}) = N_{tot} \cdot \int_0^{E_0} \frac{dN_\beta}{dE}(E, E_0, m_{\nu_e}^2) \cdot R(E, qU) dE. \quad (2.26)$$

N_{tot} is the total number of tritium nuclei in the source, E_0 the tritium endpoint and m_{ν_e} the neutrino mass.

The previous section explained that low-energy background created at the spectrometer will overlap with the energy region of signal electrons. The background level will thus increase the observed electron rate, resulting in a theoretical spectrum of

$$\dot{N}_{theory}(qU, E_0, m_{\nu_e}, \dot{N}_s, \dot{N}_b) = \dot{N}_s(qU, E_0, m_{\nu_e}) + \dot{N}_b, \quad (2.27)$$

where \dot{N}_s denotes the signal rate (2.26) and \dot{N}_b the background rate.

In the analysis of the neutrino mass measurements, this theoretical model will be fitted to the measured energy spectrum (figure 2.15). The neutrino mass itself is a free parameter in this model. Note that the endpoint energy is also a free parameter here⁹, and can be extracted from the measured spectrum. The

8. Assuming a constant source activity, so that the observed rate is given by the transmission function of the spectrometer.

9. The endpoint energy is not known with sufficient accuracy, and therefore needs to be determined from the actual measurement.

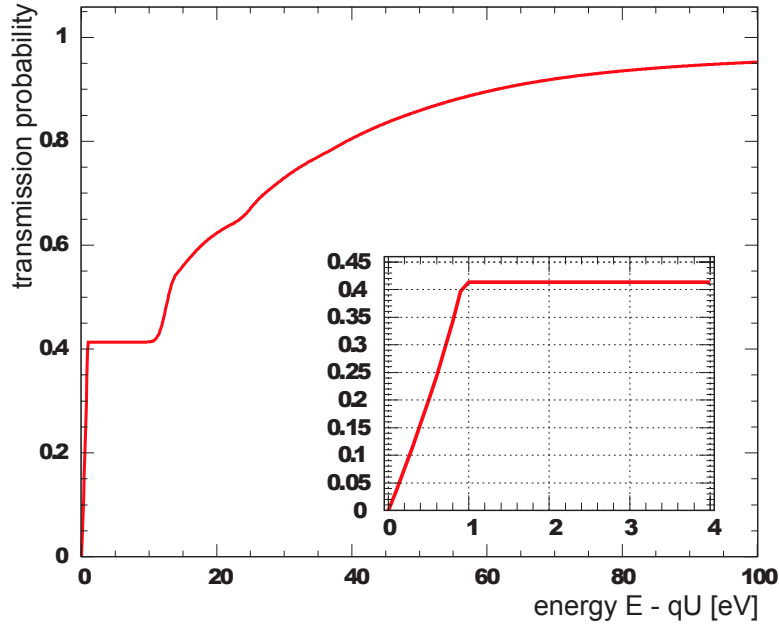


Figure 2.14.: Response function for the KATRIN main spectrometer. The energy loss of electrons in the WGTS is convoluted with the transmission function of the spectrometer. The inset shows electrons with small surplus energies, which are unscattered and reach a transmission plateau of $T_0 \approx 0.41$. Multiple scattering processes become relevant at higher energies and result in the shown broad shape of the response function. Figure from [A⁺05b].

neutrino mass fit will thus use four free parameters: The neutrino mass m_{ν_e} , the endpoint energy E_0 , the background rate \dot{N}_b and the signal rate (or amplitude) \dot{N}_s . The best sensitivity to the neutrino mass is reached in a region of the energy spectrum close to the endpoint. The *measurement time distribution* (MTD) therefore focuses on the endpoint region. However, to be able to determine the remaining free parameters, a smaller fraction of measurement time will also be spent in the region above the endpoint (to determine the background rate) and several eV below the endpoint (to determine the signal rate).

The actual distribution of measurement time at the different filter energies can be optimized to reach the maximal neutrino mass sensitivity, depending on various experimental parameters and estimates of the resulting systematic uncertainties. Monte Carlo simulations with a multitude of “toy experiments” hint that the overall sensitivity could be improved significantly w. r. t. the originally anticipated measurement time distribution; this possibility is currently under investigation [Kle14].

2.3.2 Systematic uncertainties

The experimental layout has been summarized in the previous section; together with the considerations from above, one can acknowledge several major sources of systematic uncertainties in the KATRIN experiment:

- **Transmission function:** The actual shape of the transmission function is affected by many parameters, which leads to a deviation from the theoretical description. Most notably, the radial inhomogeneities of the retarding potential and the minimal magnetic field at the analyzing

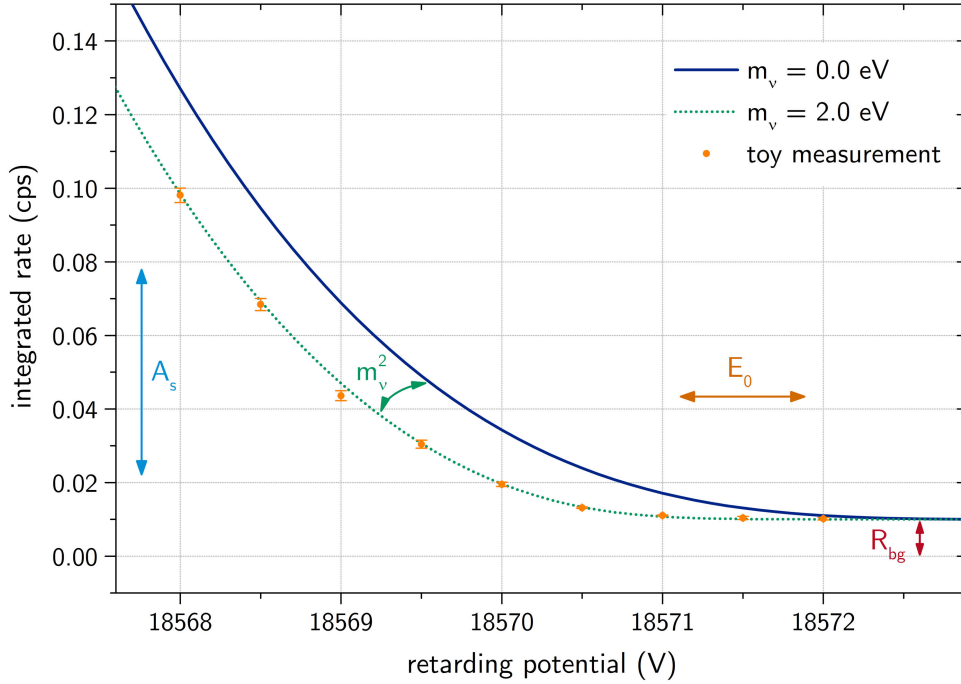


Figure 2.15.: Model parameters of the integral β -spectrum. The observable – the squared neutrino mass m_ν^2 – is extracted from the measured integral energy spectrum by a four-parameter fit. The model includes the signal amplitude A_s and the background level R_{bg} , as well as the position of the endpoint E_0 . The endpoint of the tritium spectrum must be included in the fit since it is not known with sufficient accuracy. The plot compares the energy spectrum for a vanishing neutrino mass with the expected spectrum for a large neutrino mass of 2.0 eV. The contribution of statistical and systematic uncertainties on the total sensitivity can be evaluated by performing so-called *toy experiments* where computed spectra are analyzed by statistical methods. Figure from [Kle14].

plane result in a slightly different transmission function depending on the radial position in the analyzing plane. The largest discrepancy is observed between an electron on the central field line and an electron on a field line at the outer part of the flux tube. Additionally, the axial position of the analyzing point changes slightly for electrons traveling close to the inner electrode system, since the electric potential is affected by the mechanical structure of the electrodes at small distances [B⁺13c].

The segmented detector is able to resolve these effects to some extent, since the single pixels – which correspond to a fraction of the flux tube area in the analyzing plane – can be treated as measuring independent transmission functions. The inhomogeneities are thus limited to a much smaller area of the analyzing plane w. r. t. a non-segmented detector. Although the electric potential and magnetic field in the analyzing plane can be estimated by electromagnetic simulations, precision measurements are required to investigate all possible effects that could influence the transmission function [Erh16, Gro15].

- **Fluctuations of high voltage and magnetic fields:** In addition to the inhomogeneities inside the spectrometer, fluctuations of the power supplies of the high-voltage system, as well as the solenoids and air coils, affect the transmission properties. A crucial parameter is the stability

of the retarding potential, as this directly affects the filter energy and therefore the observed electron rate. The maximal allowed systematic uncertainty from this effect is 0.0075 eV^2 in order to reach the desired sensitivity. Applying this limit to the nominal retarding potential of -18.6 kV leads to a required stability better than 61 mV (which equals 3 ppm) [A⁺05b].

To observe possible fluctuations and long-term drifts of the retarding potential, the KATRIN experiment features two independent methods to monitor the high voltage. The high voltage is continuously monitored by a precision high-voltage divider and a voltmeter operating in the 10 V range. The divider is calibrated against a stable voltage standard in regular intervals. This method allows to observe relative fluctuations of the retarding potential on a short time-scale [B⁺13b, T⁺09, Bau13].

The second method uses another MAC-E filter, the monitor spectrometer, which is connected to the same high-voltage source as the main spectrometer. The monitor spectrometer continuously measures the spectrum of $^{83\text{m}}\text{Kr}$ decay, which provides a natural energy standard with small line width. This second method allows to measure changes of the absolute retarding potential by comparing the positions of the $^{83\text{m}}\text{Kr}$ conversion lines in the energy spectrum [E⁺14, S⁺13a, Sle15].

In addition, a *condensed krypton source* (CKrS) can be moved into the beamline of the main spectrometer at the end of the CPS. This allows to perform regular online calibration runs similarly to the measurements at the monitor spectrometer [Bau13, Dyb17].

The magnetic field is monitored continuously by several fast magnetic field sensors that are mounted on the outer vessel walls. The readout of these sensors allows to construct a three-dimensional model of the magnetic field at the main spectrometer, which can be compared to simulation results using the same parameters as in the real experiment [E⁺16, Erh16].

Another dedicated monitoring system was recently implemented at the main spectrometer: The *mobile sensor unit* (MobSU) is a device equipped with magnetic field sensors. It can move independently around a single air coil mounting structure and thus measures the magnetic field on a circular path around the spectrometer. This measurement can be performed at several axial positions along the spectrometer, which results in another three-dimensional measurement of the magnetic fields [O⁺12].

- **Tritium column density:** The decay rate in the WGTS is mainly determined by the column density of tritium gas inside the source, which also affects the scattering probability of the created electrons. As mentioned already, scattering processes lead to energy losses of the electrons, which affects the observed electron rate. Since a high decay rate is advantageous for the experiment, there is an optimum for the column density which ensures a high decay rate without being affected by too many scattering events. Fluctuations in the column density are a major source of systematic uncertainties, therefore the column density is monitored at regular intervals with an electron source in the Rear Section (which is located on the upstream side of the WGTS). This allows to use electrons with known energy to observe the resulting energy losses [Bab14].

Another approach to monitor the column density is the observation of X-rays that are induced by the decay electrons; this method is realized in the BIXS detector. The forward beam monitor (FBM) measures the “halo” of the decay electrons emitted from the source. The gas composition

inside the source affects the resulting decay rate as well; it is monitored with a Laser-Raman system (LARA) [P⁺15, B⁺12, Fis14].

- **Energy loss function:** The response function discussed above is based on the precise knowledge of energy losses inside the WGTS. Therefore, the actual energy loss function has to be determined from measurements with the Rear Section electron gun. The energy loss function can then be determined from a deconvolution of the measured energy spectrum [H⁺17, A⁺00].
- **Distribution of final states:** Another source of uncertainties is the unknown distribution of final states in the tritium beta decay. The first electronic excited state of the daughter molecule, (³HeT)⁺, has an excitation energy of 24 eV. Due to the high energy resolution of the KATRIN experiment which allows measurements in the small energy region 20 eV below the endpoint, electronic excitations are typically not relevant in the analysis. Rotational-vibrational excitations of the ground state further smear out the sharp edge of the β -spectrum at the endpoint and have to be considered in the analysis. Furthermore, one must take into account other molecules like TH or TD that occur in addition to T and contribute to the systematic uncertainty the final states distribution [OW08, A⁺05b, Kle14].

Together with other sources for systematic uncertainties that have been skipped here for brevity, these effects result in a total systematic uncertainty of $\sigma_{tot,sys} \leq 0.017 \text{ eV}^2$. It is possible to reduce this number significantly by reducing the analyzed energy region, but this will in turn reduce the observed electron rate and thus increase the statistical uncertainty. Therefore an optimum exists where the total sensitivity is affected similarly by both systematic and statistical uncertainties, without being dominated by either one.

2.3.3 Statistical uncertainties

Given a fixed measurement time distribution, the statistical uncertainty is mainly determined by the observed background rate \dot{N}_b . The signal rate \dot{N}_s in a measurement interval \hat{E} , corresponding to a filter energy $qU = E_0 - \hat{E}$, can be approximated and the observed electron rate is given by

$$\dot{N}_{tot}(\hat{E}) = \dot{N}_b + \dot{N}_s \quad (2.28)$$

$$= \dot{N}_b + A \cdot \left(\hat{E}^3 - \frac{3}{2} \hat{E} \cdot \sum_i |U_{ei}|^2 m_i^2 \right). \quad (2.29)$$

A denotes the amplitude of the beta spectrum, and the sum term corresponds to the average mass of the electron anti-neutrino (1.16) that is measured by the experiment. For measurements far away from the endpoint E_0 , the cubic term dominates the signal rate. The linear term is sensitive to the neutrino mass and affects the measured rate for energies close to the endpoint ($\hat{E} \rightarrow 0$).

However at energies *very* close to the endpoint, the background rate will overcast the neutrino mass signal. Further below the endpoint, the signal noise increases according to $\sqrt{\hat{E}^3} = \hat{E}^{3/2}$, and the neutrino mass signal will be dominated by noise. An optimal measurement position exists at \hat{E}_{opt} with $\dot{N}_s(\hat{E}_{opt}) = 2\dot{N}_b$, where the neutrino mass signal has the strongest influence on the measured spectrum [W⁺99, Ott10b]. Using the same approximation, the statistical uncertainty at a data point that is measured at fixed retarding potential U over a time t can be estimated, given that the neutrino mass m_{ν_e} is the only fit parameter:

$$\delta m_{\nu_e}^2 \propto \dot{N}_s^{-4/6} \dot{N}_b^{1/6} t^{1/2}. \quad (2.30)$$

This result shows that the uncertainty decreases faster with the signal rate \dot{N}_s than it rises with the background rate \dot{N}_b . It is therefore advantageous to perform the measurement with a high source activity. The total uncertainty is more difficult to estimate, since it involves multiple measurements at different retarding potentials and also includes more than one fit parameter. A detailed discussion of this topic can be found e. g. in [Kle14].

When the background level is included in the calculation of the neutrino mass sensitivity, the sensitivity worsens quickly as the background level increases. This is especially true for non-Poissonian background, which leads to sudden bursts of increased rate (instead of a rather stable purely Poissonian background level with small fluctuations). This component of background can be caused by nuclear decays in the main spectrometer, which leads to background from stored particles. This emphasizes that it is crucial to reduce stored-particle background as much as possible.

A total background level of less than 0.01 cps is aimed for at the KATRIN experiment, which seems possible given the experience gathered from the predecessor experiments in Mainz and Troitsk. With this background estimate, the resulting statistical uncertainty is $\sigma_{stat} = 0.018 \text{ eV}^2$ within three years of measurement time. This statistical uncertainty could be reduced by increasing the measurement time, but as explained above the systematic uncertainty will then dominate the total uncertainty so that no sensitivity improvement is achieved *per se*. However, an optimization of the measurement time distribution allows to compensate certain systematic effects and background processes (see below).

The total uncertainty of the experiment, given the systematic and statistical uncertainties calculated above, is then

$$\sigma_{tot} = 0.025 \text{ eV}^2 = \Delta m_{\nu_e}^2, \quad (2.31)$$

which corresponds to a neutrino mass sensitivity of $0.2 \text{ meV}/c^2$ at 90% C. L., or a discovery potential of $0.3 \text{ eV}/c^2$ at 3σ ($0.35 \text{ eV}/c^2$ at 5σ) [A⁺05b]. An optimization of the measurement time distribution can considerably improve the sensitivity (figure 2.16).

These considerations emphasize that it is crucial to reach a low background rate in order to determine the neutrino mass at the desired sensitivity. In the following, the major known sources of background in the KATRIN experiment will be summarized.

- **Stored particles:** The MAC-E filter contains an intrinsic trap for electrons created in the spectrometer volume with transversal energies above 1 eV. These electrons can become stored by the magnetic mirror effect, preventing them to leave the spectrometer until their transversal energy has decreased, e. g. from energy losses through synchrotron radiation or scattering with residual gas. During this cool-down phase, several hundred low-energetic secondary electrons can be created, which can become stored as well. Eventually the low-energetic electrons will leave the spectrometer volume and travel towards the detector, where they will energetically overlap with signal electrons and increase the observed background rate.

Stored particles are thus one of the dominating sources of background, and strong efforts have been undertaken to reduce the number of stored particles in the spectrometer as discussed in the previous section [Har15, Gör14]. The magnetic pulse method that is discussed in chapter 5 is an active background reduction technique that has been developed to counteract background from stored electrons. Another method is the application of an electric dipole in the spectrometer volume [Hil16].

In addition to the magnetic mirror effect in the spectrometer, there is also a possibility for creating particle traps from a disadvantageous combination of electric and magnetic fields. These

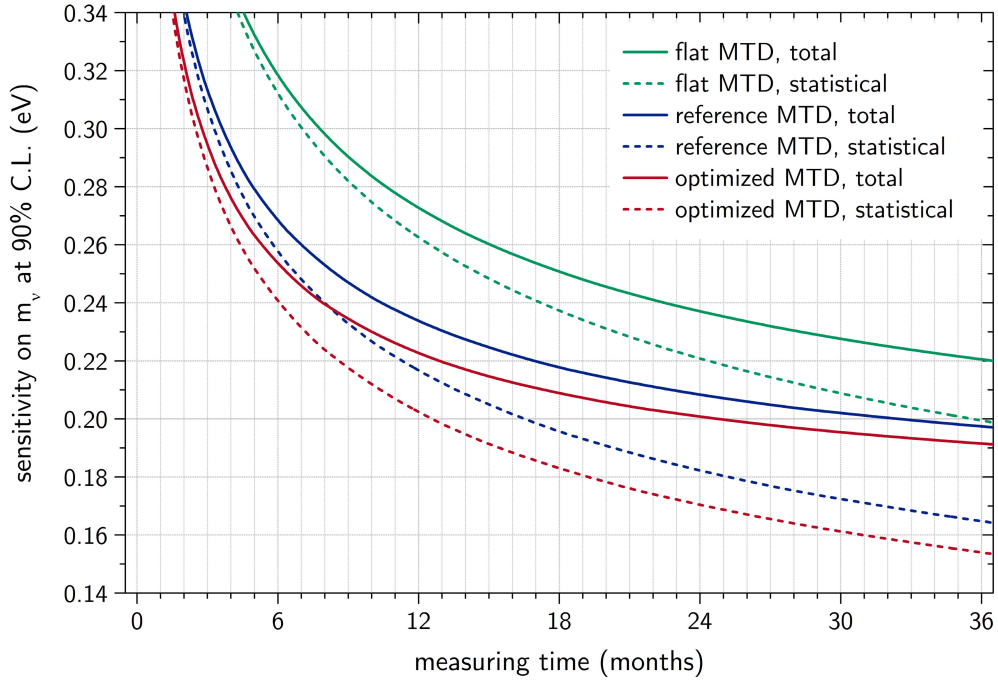


Figure 2.16.: Estimated sensitivity on m_{ν_e} for different measurement time distributions (MTD). The sensitivity improves as the experiment is in operation since the statistical uncertainties decrease as more data is taken (dashed lines). The total sensitivity cannot be better than the systematic uncertainty of $\sigma_{sys} = 0.017 \text{ eV}^2$ (solid lines). Depending on the experimental conditions (e.g. the background level), an optimized MTD can considerably improve the sensitivity. Note that the observable is the *squared* neutrino mass $m_{\nu_e}^2$. Figure from [Kle14].

particle traps can form inside the spectrometer in regions close to the electrodes. Particle traps in the spectrometer can be avoided by a careful electrode design which prevents trapping conditions [Zac14]. An intrinsic particle trap exists between the pre- and main spectrometer when both spectrometer are operated at high voltage. It is however possible to remove stored electrons by inserting a grounded meta rod into the trap volume which will collect and remove the electrons eventually [Hil11, Beh12].

- **Electrons from vessel walls:** The vessel walls of the main spectrometer and the inner electrode system have a large surface that is open towards the flux tube and provide a large target mass for interactions with cosmic particles. Scattering processes of cosmic muons with electrons in the target material can result in electrons being emitted from these surfaces. Radioactive decays in the stainless steel material can emit electrons from the surface as well. Furthermore, at regions where high electric fields are prevalent – like the boundary between inner electrode modules that are operated on different electric potentials – field emission can occur, which will also create free electrons at the electrode surfaces.

The majority of these electrons is shielded by the magnetic field at the main spectrometer, which will divert electrons traveling towards the flux tube, and by the electrostatic shielding of the inner electrode system. The complicated combination of electromagnetic fields close to the inner electrodes and the different electron emission processes lead to a remaining background that

cannot be estimated easily. A background rate from these contributions of less than 10^{-2} cps is aimed for.

- **Detector background:** The detector system itself contributes to the background rate as well by intrinsic noise and by cosmic muons that can produce false detector events. The background from cosmic muons is reduced by a muon veto placed around the detector system, which results in a small detector background of less than 10^{-3} cps.
- **Other background processes:** Another, unexpected background process that became the focus of recent investigations is the thermal excitation of Rydberg atoms or molecules in the main spectrometer. These are highly excited states where at least one electron in the atomic shell has a very large quantum number and thus low binding energy. Because such states are neutral particles where electromagnetic shielding has no effect, they can move freely into the inner spectrometer volume and become ionized by thermal radiation¹⁰, thereby contributing to the observed background.

The Rydberg states originate from the vessel walls, where radioactive decays of implanted ^{210}Pb result in sputtering processes due to the recoil energy of the daughter nucleus. The long-lived ^{210}Pb contamination of the vessel walls results from preceding radioactive decays of natural ^{220}Rn in the spectrometer volume, which leave a daughter nucleus with recoil energies in the 100 keV range that can become implanted into the stainless steel surface of the vessel walls [Har15, Tro17].

While other background processes are well-understood and can be largely suppressed by electromagnetic design, passive and active background reduction methods, the Rydberg background is currently believed to contribute significantly to the observed residual background level of $\mathcal{O}(500)$ mcps, a factor of 50 higher than the design goal. Fortunately, this increase in background level only has a rather small effect on the achieved sensitivity since other operational parameters and the measurement time distribution can be optimized to compensate for the higher background.

10. The spectrometer is typically operated at temperatures around 18 °C.

Simulation and analysis tools

3.1 Introduction

KATRIN is a high precision experiment where electrons from tritium β -decay are guided through a 70 m long beam line that consists of numerous sub-systems. The kinetic energy of the electrons covers a wide range from the tritium endpoint of 18.6 keV into the meV regime at the analyzing plane of the spectrometer. The complex electromagnetic fields affect the electrons on their trajectory towards the detector. Especially at the main spectrometer, small deviations of the fields can have a large effect on the transmission function. Hence, precise knowledge of the electromagnetic conditions is required to reach the experiment's sensitivity to the neutrino mass. It is of great advantage to perform simulations with the experimental setup to examine the transmission properties of the spectrometer, investigate various background processes, or study energy losses inside the tritium sources.

The requirement for a dedicated particle tracking software was realized early in the KATRIN collaboration. Already in 2006, tools to compute electric fields from an electrode geometry (Elcd [Glu11a]) and magnetic fields from a system of coils (Magfield [Glu11b]) were developed. In the beginning these tools were limited to rotational symmetry in the underlying geometries; following extensions allowed to include tilted magnets and non-symmetric electrodes. These field-computation tools were extended by a – in comparison with today's simulation software – less versatile particle-tracking software to compute the propagation of electrons through static electromagnetic fields. The simulation is performed by tracking single electrons in a given geometry, using a discretized trajectory where the equation of motion is solved at each time-step.

To make the simulations more user-friendly and to allow for greater flexibility, in 2009 the independent tools were combined into a single software named *Kassiopeia*, which was developed in a joint effort by the KATRIN collaboration [F⁺17]. *Kassiopeia* allows to define the simulation parameters in a configuration file, which enables the user to change certain aspects of the simulation and compare results at different settings. The software includes a navigation algorithm in order to change simulation parameters dynamically, based on user-defined regions in the geometry. Different methods to compute the propagation of particles are available to improve the speed of the particle-tracking process.

With *Kassiopeia* growing in complexity over time, its developers restructured the software to follow a more modular design. The goal was to make the software more flexible, which is especially important

when simulations of the various KATRIN components are performed. The new design also improves user-friendliness by using a consistent configuration scheme in the individual modules. The restructuring began 2011 and led to the embedding of Kassiopeia into a larger and more general toolkit for simulations and analysis in the KATRIN context: the *KASPER* framework. It is under continuous development by the KATRIN community of software developers, with many improvements and new features having been implemented since its first version.

This chapter aims to give an overview to the various simulation and analysis tools, followed by the presentation of the newly-developed post-analysis framework *Peaberry*. The simulation and analysis results will be presented in chapters 4 and 5.

3.2 KASPER – The KATRIN simulation and analysis framework

In KASPER, the simulation and analysis tasks are handled by different modules, with the framework supplying a common base for the different tools (figure 3.1). The KASPER modules provide access to simulation geometries, compute electromagnetic fields, perform particle tracking, retrieve and analyze measurement data, and even combine measurements with simulations. The framework and its components have been discussed in great detail in [Gro15] with a focus on the simulation software Kassiopeia. The analysis concept and the KASPER modules for handling measurement data have been presented in [Kle14].

- **SSC:** The SSC module provides routines for calculating the tritium β -spectrum and for modeling the tritium source. It is discussed in [Kle14].
- **Kassiopeia:** The particle-tracking software allows to simulate charged particles (like electrons) in electromagnetic fields with high numerical precision. Its design and the core features are summarized in section 3.3.
- **KGeoBag:** The geometry module is responsible for providing geometrical shapes that can be used by other KASPER modules, e. g. Kassiopeia. This module is discussed in section 3.4.
- **KEMField:** This module provides the methods to compute electric and magnetic fields from a given geometry. While it can also be used as a toolkit for stand-alone applications, it is also one of the core modules for Kassiopeia where electromagnetic fields are used as an input to the simulation. The KGeoBag module is used to define the electromagnetic geometry. KEMField provides different methods for field computation. This module and the used algorithms are explained in section 3.5.
- **KaFit:** This module provides various implementations of minimizer and fitting routines, such as MINUIT¹ or Markov Chain Monte-Carlo (MCMC). It also contains tools to study KATRIN's sensitivity to the neutrino mass. The module is also discussed in [Kle14].
- **KTrAP:** KTrAP is a collection of analysis and simulation tools, where many of the KASPER modules listed above are combined. Its main goal is to provide tools for the investigation of the transmission properties of the main spectrometer. It has been used in recent works such as [Kra16, Erh16], and a detailed discussion is available in [Gro15].

1. MINUIT – a physics analysis tool for function minimization, <http://www.cern.ch/minuit/>

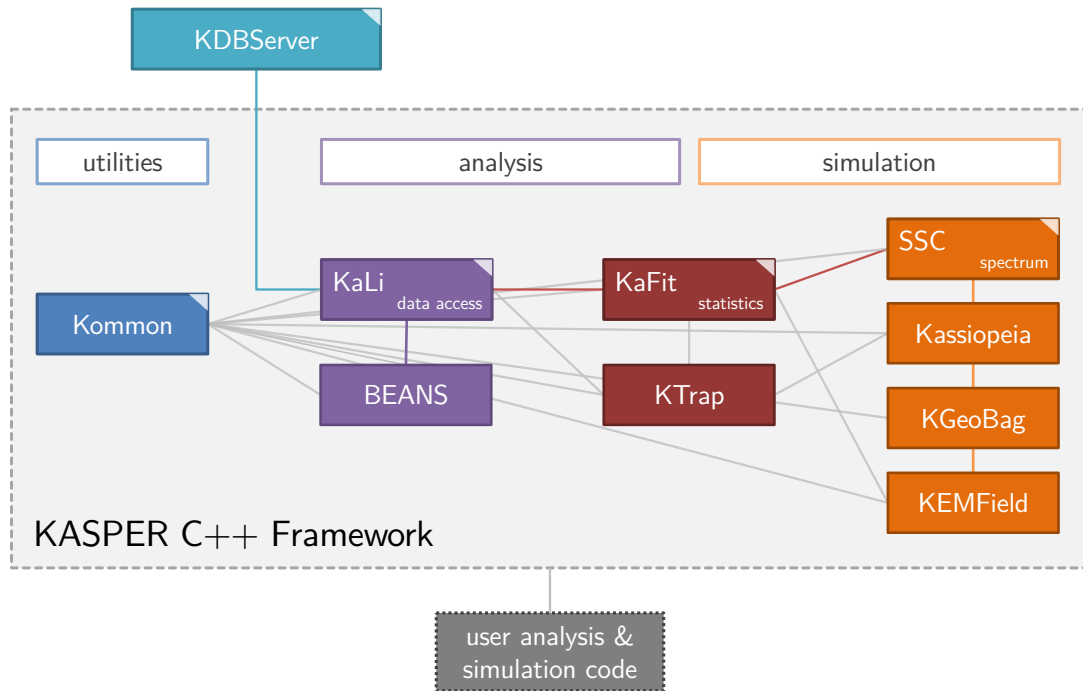


Figure 3.1.: The KASPER framework. The framework contains tools for simulation and analysis tasks, as well as basic utilities that are shared by many pieces of software. It provides an interface between the *user side* where the tasks are executed and the *server side* where input data is stored and processed. The lines indicate the connections (dependencies) between the individual modules. Figure from [Kle14].

- **KaLi:** The Katrin Library provides access to experimental data such as measurement runs or slow-control data. It is used by the analysis software BEANS and also by Kassiopia, where it allows to perform simulations using actual experimental parameters. These features are summarized in section 3.6.
- **BEANS:** The analysis software for KATRIN data is widely used to process measurement data taken with the FPD system. It is also possible to analyze monitor spectrometer measurements, where an independent detector system is used. BEANS allows the user to set up an intuitive *analysis chain* to process the raw data, using concepts derived from functional programming languages. The software and exemplary analysis code is discussed in section 3.7.
- **Kommon:** This core module provides basic features for many of the other KASPER modules. This includes mathematical and physical constants, general mathematics like ordinary differential equation (ODE) solvers or linear algebra routines, and tools for input/output. This module is discussed in detail in [Kle14].
- **KSC:** To make Kassiopia usable for other experiments, the KATRIN-specific code – such as experimental parameters and specialized KASPER code – has been moved into the KSC module. This idea is explained in [Gro15], and the module is skipped in the following.

3.3 The particle-tracking software Kassiopeia

Kassiopeia is a software primarily intended for tracking of charged particles through static electromagnetic fields, especially electrons in the KATRIN main spectrometer where the energy analysis is performed. Figure 3.2 shows the official logo of the software. It is written in C++ and follows a strictly object-oriented design. Numerous software libraries are used to provide specific features, such as ROOT², VTK³, Boost⁴ and GSL⁵. The software was designed for the KATRIN experiment and achieves a high numerical accuracy. It can deal with many peculiarities of the experimental setup, such as the complex electromagnetic design. The modular structure allows to use Kassiopeia in other experiments (e. g. *Project8* [A⁺15b]) and to extend the simulation code if necessary. Basic features like the parsing of configuration files or numerical routines like ODE solvers are provided by the KASPER framework. The computation of electromagnetic fields and access to experimental parameters is also performed in other KASPER modules [F⁺17, Gro15, Fur15].

It is planned to run Kassiopeia simulations continuously during neutrino mass measurements in order to compare the simulated with the measured data. These simulations would include all processes from the creation of electrons in the source to their detection at the detector, as well as electronic interactions in the silicon wafer and the subsequent DAQ processes.



Figure 3.2.: The Kassiopeia logo.

3.3.1 Software design

Kassiopeia's internal structure reflects the strategy that is used for particle-tracking. To simulate a particle in a given simulation geometry, the trajectory is split into discrete steps. The equation of motion is solved at each step in order to compute the position and time of the next step, until the simulation terminates. The combined steps from a particle's creation to its termination form the particle's trajectory.

Each simulated particle is tracked sequentially and independently of each other. A particle is defined by its mass m and its charge q ; other parameters like spin are implemented but not used by any simulations yet. The particle type can be referenced by its particle ID according to the *particle data group* (PDG)⁶. The dynamic properties of the particle – time t , position \vec{x} and momentum \vec{p} – change during propagation. SI units are used in Kassiopeia to avoid inconsistencies; however, energies are given in eV and angles in degrees to make the software more user-friendly.

The particle-tracking and the output of the simulation is organized into four levels (figure 3.3). At the lowest level, the individual **steps** of a simulated particle are considered. Each step is identified by a unique step number which increases while the simulation progresses. The steps that form a single particle's trajectory are grouped into a **track**. Particles that are created according to the configuration are considered *primary* particles. When interactions are included in the simulation, a primary particle can create *secondary* particles which are also processed. All tracks that were created from a single

2. ROOT data and analysis framework, <https://root.cern.ch/>

3. The Visualization Toolkit (VTK), <http://www.vtk.org/>

4. Boost C++ libraries, <http://www.boost.org/>

5. GNU Scientific Library (GSL), <https://www.gnu.org/software/gsl/>

6. Monte Carlo Particle Numbering Scheme, http://pdg.lbl.gov/mc_particle_id_contents.html

primary particle are grouped into an **event**. This allows to distinguish between tracks created by different primaries. On the highest level, all events processed in one Kassiopeia instance are grouped into a single **run**.

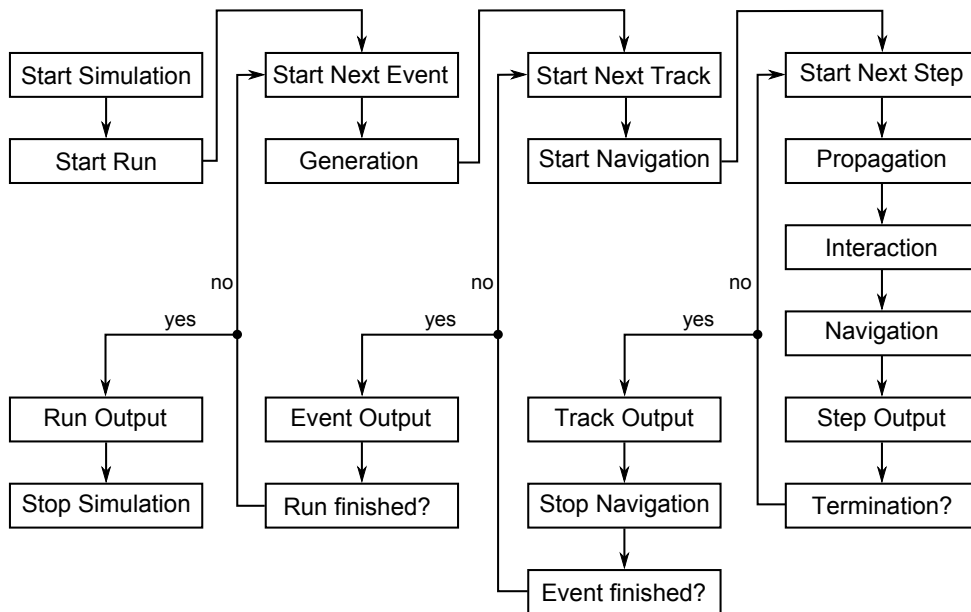


Figure 3.3.: Schematic representation of a Kassiopeia run. The flowchart shows the four major levels that are processed in Kassiopeia: run, event, track and step. All events created during a run are processed sequentially. The individual particle trajectories are represented by discrete steps, where the particle propagates through the simulation geometry according to its properties and the current electromagnetic conditions. Figure from [Gro15].

3.3.2 Kassiopeia configuration

The configuration files for a Kassiopeia simulation include all relevant parameters, such as the geometry that defines navigation regions, electromagnetic fields, and parameters for particle creation and termination. The configuration also includes properties of the application, e.g. the output that is printed on the terminal while the simulation is running. Kassiopeia uses the XML format⁷ in its configuration, which has the advantage of being a human-readable format that is easily parsed by software. The intrinsic tree structure allows nested sections, which provide the user with an intuitive way of setting up the simulation.

A Kassiopeia simulation is started by calling the main application, *Kassiopeia* – or *KatrinKassiopeia* when KATRIN-specific code is used – from a terminal:

```
Kassiopeia [-r variable=value] [options] <configuration.xml>
```

The configuration is provided by the XML file. It is possible to pass variables on the command line to modify simulation settings. Kassiopeia then initializes itself with the provided configuration, prepares its sub-modules which are required for the simulation, and proceed with the particle-tracking until

7. Extensible markup language (XML), <https://www.w3.org/XML/>

all events have been processed. The progress and current state of the simulation can be printed to the terminal.

The XML format is based on so-called *tags* that allow nesting and can contain optional *attributes*:

```
<tag attribute1="value" attribute2="value">
  <nested_tag/>
</tag>
```

In contrast to the official specification of the XML format, Kassiopeia allows multiple *root tags* that are placed on the top level of the file (i. e. without surrounding tags). As the XML file is parsed during the initialization, several text processors can modify its contents *on-the-fly* to implement features like variable replacement or include files.

The details have been discussed extensively in [Fur15] and [Gro15]. A short summary of the core features is given in the following:

- **Variables:** Variables can be defined in the configuration with a *name* and a *value*. The name can be referenced at a later point in the file. Referencing uses a special syntax where the variable name is put in square brackets, which replaces the reference by the current value of the variable. A reference can be used in any XML attribute (e. g. formulas or include directives, see below). This concept provides the user with great flexibility when setting up a simulation.

While *local variables* are only visible in the XML file that is currently being processed, *global variables* are made available to every subsequent XML file in the configuration. This is useful for variables included from other files, e. g. a reference position that is used in other geometry files. A special type are *external variables*, which are essentially global variables that can be overridden at the Kassiopeia command line or by another definition that occurs earlier in the initialization process.

```
<define name="config_path" value="./config/" />
<global_define name="position_absolute_z" value="-1.23" />
<external_define name="start_radius" value="5e-2" />
```

- **Includes:** To allow re-using certain parts of a configuration in different simulations (e. g. an often-used simulation geometry) it is possible to include contents from another file at an arbitrary point in the configuration.

```
<include name="[config_path]/file.xml" />
```

- **Formulas:** Similar to variable references, formula expressions can be used in every attribute where a number is expected. The formula processor uses the ROOT framework and the expression is written out in ROOT syntax; this allows to use ROOT features like special mathematical functions. Formulas use a special syntax where the expression is surrounded by curly brackets. When processed, the expression is replaced with its evaluation result.

```
<define name="start_position_x" value="{[start_radius]*TMath::Cos([angle])}" />
<define name="start_position_y" value="{[start_radius]*TMath::Sin([angle])}" />
```

- **Tags:** Related objects in the configuration can be grouped together with so-called tags⁸. Tags can be referenced later to make their contents available to other configuration objects. One

8. Note that these “tags” are different from the XML tags that are an essential part of the XML syntax.

common example is the grouping of electrode surfaces in the geometry configuration, so that one voltage can be assigned to multiple electrodes.

```
<tag name="electrode">
  <disk_surface name="capacitor_plate_1" z="{[capacitor_position]-0.5*[
    ↪ capacitor_distance]}" r="[capacitor_radius]"/>
  <disk_surface name="capacitor_plate_2" z="{[capacitor_position]+0.5*[
    ↪ capacitor_distance]}" r="[capacitor_radius]"/>
</tag>
```

- **Conditions:** Conditions in Kassiopeia allow for a dynamic configuration. The conditional structures in Kassiopeia are limited to *if*-statements (without *else*-blocks). Its contents are only included when the expression evaluates to *true*. This feature is useful to allow different configurations that can be switched by a single parameter, e. g. to provide different default settings or to activate optional features.

```
<if condition="{[include_extra] eq 1}">
  <include name="[config_path]/optional_file.xml"/>
</if>
```

- **Loops:** A concept similar to conditions are loops, where a configuration block is processed multiple times in sequence. An index variable is incremented while the loop is running, equivalent to a *for*-statement. The loop structure reduces the amount of duplicated content in the configuration files and is often used in geometry definitions where the setup follows a certain pattern, e. g. placing multiple coils for a magnetic field setup.

```
<loop variable="index" start="1" end="2" step="1">
  <cylinder_tube name="coil_[index]" r="{0.5}" z1="{2*[index]-0.5}" z2="{2*[
    ↪ index]+0.5}"/>
</loop>
```

3.3.3 Particle generation

Each track in Kassiopeia begins with the creation of a particle. Primary particles are generated according to the configuration, i. e. defined by the user. Each primary particle starts a new event in the simulation. Secondary particles are generated from interactions of a primary or secondary particle.

The starting conditions of a particle can affect the outcome of the simulation to a large extent. Kassiopeia therefore offers many choices to set these initial conditions with so-called *generators*. In the simplest they set individual parameters: static properties like the particle type – electrons, ions etc. – and dynamic properties like the particle’s kinetic energy, its initial position and direction, and the starting time. The latter is especially relevant for time-dependent simulations (e. g. with electromagnetic fields that change over time). For the position and direction generators, it is possible to use cartesian or non-cartesian (e. g. cylindrical or spherical) coordinate systems. One can define a reference coordinate system, e. g. to start particles on an electrode surface.

These parameter values can be chosen from different distributions to increase flexibility:

- **Fixed value:** The same value is used for each generated particle.

```
<ks_value_fix name="value_fix" value="1"/>
```

- **Value from a list:** Multiple particles are created, using the given values in order.

```
<ks_value_list name="value_list" add_value="1" add_value="2" add_value="3"
↪ add_value="5"/>
```

- **Value from a set:** Multiple particles are created (similar to the list option), but one can define a range and the number of values to generate. The values are evenly distributed over the given range.

```
<ks_value_set name="value_set" value_start="0" value_stop="42" value_count="7"/>
```

- **Uniform distribution:** A random value is picked within the given limits, following a uniform distribution where all values are evenly distributed.

```
<ks_value_uniform name="value_uniform" value_min="0" value_max="1e-6"/>
```

- **Gaussian distribution:** A random value is picked according to a Gaussian distribution with given mean and width. Limits can be provided to constrain the resulting values, e. g. to avoid a negative energy.

```
<ks_value_gauss name="value_gauss" value_mean="0.5" value_sigma="0.2" value_min=
↪ "0" value_max="1"/>
```

- **Cylindrical or spherical distribution:** A random value is picked from a cylindrical or spherical distribution, which is often used with position or direction generator.

The cylindrical distribution is defined by

$$r = \sqrt{\text{uni}(r_{min}^2, r_{max}^2)}, \quad (3.1)$$

whereas the spherical distribution is defined by

$$r = \sqrt[3]{\text{uni}(r_{min}^3, r_{max}^3)}. \quad (3.2)$$

```
<ks_radius_cylindrical name="radius_cylindrical" radius_min="0" radius_max="0.1"
↪ />
```

```
<ks_radius_spherical name="radius_spherical" radius_min="0" radius_max="0.1"/>
```

- **Angular distributions:** Angular distributions are a special case of value generators that are typically used to define the initial direction of a particle. In addition to standard generators like the uniform distribution, one can use a spherical or $\cos \theta$ -distribution to dice a directional angle.

The spherical distribution is defined by

$$\theta = \arccos(\text{uni}(\cos \theta_{max}, \cos \theta_{min})), \quad (3.3)$$

and the $\cos \theta$ -distribution is defined by

$$\theta = \arccos\left(\sqrt{1 - \text{uni}(\sin \theta_{min}, \sin \theta_{max})^2}\right). \quad (3.4)$$

The $\cos \theta$ distribution was implemented for the simulations of the electron source presented in chapter 4.

```
<ks_value_angle_spherical name="angle_isotropic" value_start="0" value_stop="90"
↪ />
<ks_value_angle_cosine name="angle_cosine" value_start="0" value_stop="90"/>
```

- **Value from a histogram:** A ROOT histogram can be loaded into Kassiopeia, and a random value is picked according to the distribution of the histogram. This feature allows to use the outcome of a simulation or measurement as a starting point for new simulations.

```
<ks_value_histogram name="value_histogram" path="AnalysisResults.root" histogram
↪ ="energy_distribution"/>
```

- **Special generators:** Kassiopeia also provides specific generators for complex processes like radioactive decays. Typically there are correlations between different parameters, e. g. energy and direction. By implementing a special generator, these effects can be included in the simulation. One example is a generator that implements the decay of Radon isotopes ^{219}Rn and ^{222}Rn , where a combination of different processes leads to complex energy and angular distributions of the created electrons [Wan13, W⁺13].

The following example combines some available options to generate particles:

```
<ksgen_generator_composite name="electron_source" pid="11">
  <!-- fixed time -->
  <time_composite>
    <time_fix value="0."/>
  </time_composite>
  <!-- gaussian energy (avoid negative energies) -->
  <energy_composite>
    <energy_gauss value_mean="2.5" value_sigma="0.5" value_min="0."/>
  </energy_composite>
  <!-- cylindrical position (random position on equidistant circles) -->
  <position_cylindrical_composite>
    <r_set value_start="0." value_stop="[start_radius]" value_count="10"/>
    <phi_uniform value_min="0." value_max="360."/>
    <z_fix value="[position_absolute_z]"/>
  </position_cylindrical_composite>
  <!-- spherical direction (random polar angle up to 60 degrees) -->
  <direction_spherical_composite>
    <phi_uniform value_min="0." value_max="360."/>
    <theta_spherical angle_min="0." angle_max="60."/>
  </direction_spherical_composite>
</ksgen_generator>
```

3.3.4 Propagation through electromagnetic fields

The propagation of the particles is the core of the particle-tracking simulation. In Kassiopeia, the propagation is computed by solving the equation of motion, which is implemented as first-order differential equation. The integration result is used to update the particle's current parameters, and the simulation proceeds to the next simulation step. The integration is performed by different implementations of the *Runge-Kutta* method [Fur15, Gro15]. A commonly used implementation is the 8th order integrator; it requires 13 evaluations of the equation per step. It is possible to combine

different orders to perform internal error estimation. The choice of integrator significantly affects the simulation performance, especially when complex electromagnetic fields are used.

Exact tracking

The propagation of a charged particle in electromagnetic fields is described by the *Lorentz equation*

$$F_L = m\vec{a} = q(\vec{E} + \vec{v} \times \vec{B}), \quad (3.5)$$

where m is the particle's mass, q its charge, \vec{v} its velocity and (\vec{E}, \vec{B}) the electromagnetic fields at the particle's position. The Lorentz force F_L results in an acceleration (or deceleration) of the particle.

The term can be represented as a set relativistic differential equations [Fur15]:

$$\begin{aligned} \frac{dt}{dt} &= 1, \\ \frac{d\vec{x}}{dt} &= \frac{\vec{p}}{\gamma m}, \\ \frac{d\vec{p}}{dt} &= q \left(\vec{E} + \frac{\vec{p} \times \vec{B}}{\gamma m} \right), \end{aligned} \quad (3.6)$$

where γ is the relativistic Lorentz factor and m the particle's rest mass. The equation of motion has six differential terms which have to be solved at each step of the simulation. This method of propagation is called *exact tracking* in Kassiopeia since no approximations are performed. To accurately represent the particle's trajectory by discrete steps, a small step size is required that often results in a large number of steps to be computed by the simulation.

Continuous physics processes, like energy losses due to synchrotron radiation, can be added to the simulation by extending the equation of motion. These interactions are explained in section 3.3.6.

Adiabatic tracking

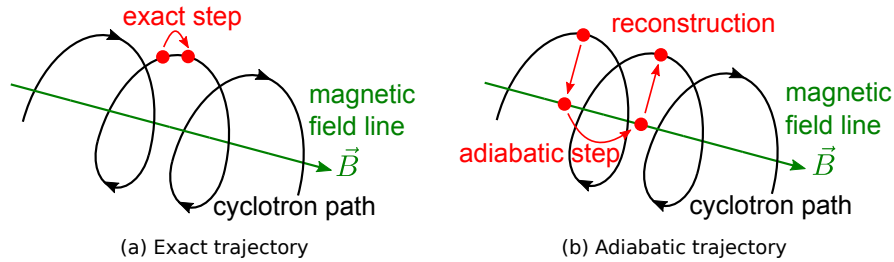


Figure 3.4.: Difference between exact and adiabatic tracking. The adiabatic approximation splits the particle's motion into a longitudinal component along the field line and a transversal component that corresponds to the gyration. In adiabatic tracking only the longitudinal motion is considered, which allows to considerably increase the step size without loss of accuracy. The gyration can be reconstructed from the cyclotron phase and radius; both parameters are known at runtime. Figure from [Gro15].

When a particle is moving adiabatically, it performs a cyclotron motion around a magnetic field line (figure 3.4). If one neglects possible drifts, the particle is fixed to a specific field line. The motion

can then be described by a circular motion around the field line and a longitudinal motion of the so-called *guiding center* \vec{r}_c along the field line. This allows to use a guiding-center approximation for the equation of motion, which relates to the longitudinal movement of the particle's guiding center \vec{r}_c . The integration terms in this case are [Fur15]:

$$\begin{aligned} \frac{dt}{dt} &= 1, \\ \frac{d\vec{r}_c}{dt} &= \frac{p_{\parallel}}{\gamma m} \cdot \frac{\vec{B}_c}{B_c}, \\ \frac{dp_{\parallel}}{dt} &= -\frac{p_{\perp}^2}{2\gamma m B_c} \left(\nabla B_c + q\vec{E}_c \right) \cdot \frac{\vec{B}_c}{B_c}, \\ \frac{dp_{\perp}}{dt} &= \frac{p_{\perp} p_{\parallel}}{2\gamma m B_c} \nabla B_c \cdot \frac{\vec{B}_c}{B_c}. \end{aligned} \tag{3.7}$$

Here \vec{B}_c and \vec{E}_c refer to the magnetic and electric field at the guiding center. This method of propagation is known as *adiabatic tracking* in Kassiopeia.

The main advantage of this approximation is not just the reduced number of integration terms – only two momentum terms are used here – but the possibility to use a larger step size in the simulation. Because the trajectory is now essentially defined by the magnetic field line, the curvature of the trajectory at each step is much smaller than in the case of exact tracking (where the full cyclotron motion is included). Since the number of steps (and thus, step size) strongly affects the required simulation time, adiabatic tracking can often speed up the simulations significantly. It is often used in simulations of the KATRIN beamline where adiabatic electrons are investigated.

To account for possible drifts and to include the cyclotron motion of the particle, the adiabatic tracking can be extended by additional propagation modules. The cyclotron motion is included by computing the cyclotron phase of the particle at each step. The phase is derived from the cyclotron frequency,

$$\frac{d\phi}{dt} = \frac{qB_c}{\gamma m}. \tag{3.8}$$

This allows to compute the actual position of the particle w. r. t. to the guiding center, so that the gyration can be included again in the output while still benefiting from the adiabatic approximation.

A particle moving through electromagnetic fields is also affected by drifts that change the trajectory [Jac62], which is especially relevant for stored particles where the total drift adds up over time. Three types of drifts are present in electromagnetic fields at KATRIN:

- The $\vec{E} \times \vec{B}$ (“E-cross-B”) drift is caused by a combination of electric and magnetic fields. For example, an axial magnetic field together with an azimuthal electric field results in a radial drift; this is the case when the magnetic field at the spectrometer is changed rapidly during the application of a *magnetic pulse* (see chapter 5). The drift is expressed by the drift velocity

$$\vec{v}_{E \times B} = \frac{\vec{E} \times \vec{B}}{B^2}. \tag{3.9}$$

- The $\nabla \vec{B}$ (“gradient-B”) drift is caused by gradients in the magnetic fields. When the particle moves into a region with different magnetic field, the cyclotron radius changes and the circular orbit around the field line is deformed. The drift velocity is given by

$$\vec{v}_{\nabla \vec{B}} = \frac{p_{\perp}}{2q\gamma m} \frac{\vec{B} \times \nabla \vec{B}}{B^3}. \tag{3.10}$$

- The curvature drift is a result of the centripetal force that acts on the particle when it follows a curved field line. The drift velocity is

$$\vec{v}_R = \frac{p_{\parallel}}{q\gamma m} \frac{\vec{R}_c \times \vec{B}}{R_c^2 B^2}, \quad (3.11)$$

where \vec{R}_c is the curvature radius in vector notation (so that it points outwards of an arc that matches the curvature).

In case of exact tracking, these drifts are automatically included since the full Lorentz equation is evaluated. With adiabatic tracking, the drifts have to be computed independently by extending the terms in (3.7), yielding the following integration terms [Fur15]:

$$\begin{aligned} \frac{d\vec{r}_c}{dt} &= \dots + \frac{\vec{E}_c \times \vec{B}_c}{B_c^2} + \frac{2p_{\parallel}^2 + p_{\perp}^2}{q(\gamma + 1)mB_c^3} \cdot \vec{B}_c \times \nabla \vec{B}_c \cdot \frac{\vec{B}_c}{B_c}, \\ \frac{dp_{\parallel}}{dt} &= \dots + \frac{q\gamma m}{p_{\parallel}} \vec{E}_c \cdot \frac{d\vec{r}_c}{dt} - \frac{p_{\perp}^2}{2p_{\parallel}B_c} \cdot \left(\nabla \vec{B}_c \cdot \frac{d\vec{r}_c}{dt} \right) \cdot \frac{\vec{B}_c}{B_c}, \\ \frac{dp_{\perp}}{dt} &= \dots + \frac{p_{\perp}}{2B_c} \left(\nabla \vec{B}_c \cdot \frac{d\vec{r}_c}{dt} \right) \cdot \frac{\vec{B}_c}{B_c}. \end{aligned} \quad (3.12)$$

Magnetic tracking

In addition to adiabatic tracking, which considers the electric field at the particle's position, a strictly magnetic trajectory is available for simulations where the electric field is irrelevant. The equation of motions is then reduced to three terms, neglecting the momentum of the particle:

$$\frac{d\vec{x}}{dt} = \frac{\vec{B}}{B}. \quad (3.13)$$

This method is called *magnetic tracking* and is used to compute field lines in Kassiopeia. It should be noted that although the electric field is not considered in the propagation, it is still possible to compute the electric field at each step to include it in the output. Magnetic tracking is used to investigate the shape of the flux tube and to optimize the electromagnetic fields at KATRIN.

Step size

Since Kassiopeia operates with discrete steps to perform the tracking, the step size is an important parameter that affects both the accuracy and the required time for the simulation. Different *step-size controls* are available in Kassiopeia, which either determine the step size from a fixed value or dynamically adjust the step size within certain limits:

- **Fixed time:** This simple control uses a given constant Δt at each step.

```
<kstraj_control_time name="control_time" time="{1e-6}"/>
```

- **Fixed length:** The step size is computed from the particle's velocity to maintain a fixed step length $\Delta t = v \cdot \Delta s$.

```
<kstraj_control_length name="control_length" length="{1e-3}"/>
```

- **Cyclotron fraction:** The step size is computed as a fraction α of the current cyclotron length. The cyclotron length depends on the particle's angular momentum and the cyclotron frequency,

$$\Delta t = \frac{\alpha}{\omega_c} \quad \text{with} \quad \omega_c = \frac{|q|\vec{B}}{2\pi\gamma m\vec{B}} \quad (3.14)$$

```
<traj_control_cyclotron name="control_cyclotron" fraction="{1. / 64.}" />
```

- **Energy violation:** This is an example of a dynamic step size control where the actual step size Δt is adjusted at each step. The intention behind this control is to avoid a too large violation of energy conservation, $E_{tot} = \text{const.} = E_{kin} + qU$. Because of unavoidable numerical errors in the propagation – caused by the limited accuracy of the integration, the computation of electromagnetic fields etc. – energy is not always fully conserved. The relative energy violation from the current step n to the next step $n + 1$ can be expressed by

$$\delta E = 2 \cdot \left| \frac{(E_{n+1} + qU_{n+1}) - (E_n + qU_n)}{(E_{n+1} + qU_{n+1}) + (E_n + qU_n)} \right|, \quad (3.15)$$

where E and q refer to the kinetic energy and charge of the particle, and U to the electric potential at the particle's position.

The step size control continuously monitors the relative energy violation that will be caused by the next step, and reduces the step size if necessary. To avoid too small step sizes that would unnecessarily increase the computation time, the step size can be increased if energy violation is below a certain limit. The new step size is computed by scaling the current step size by a constant factor α : $\Delta t \leftarrow \Delta t \cdot (1 \pm \alpha)$.

The scaling factor can be defined individually for decreasing and increasing step sizes. By default, the adjustment step is 0.5 for both cases, which will double the current step size if it needs to be increased, or halve the step size if it needs to be decreased. Tuning these parameters allows to reach a valid step size more quickly, especially if the electromagnetic fields at the particle's position change rapidly (e. g. when strong electric field gradients are present). An initial step size can be defined which is used in the first step; typically a cyclotron step size is used here.

This control plays an important role in the simulations of the electron source which have been performed in the course of this thesis (chapter 4). The implementation was therefore extended to allow more control over the resulting step size when this module is used. In addition to the lower and upper limit of the energy violation, now a minimal and maximal step length can be defined as well. These limits add another constraint on the computed step size, and the step control will try to adhere to all given constraints.

Because the conditions at the following step depend on the current step size, the energy violation needs to be re-evaluated in case the step size was adjusted. The control therefore performs a “trial-and-error” approach in a continuous loop to find a valid step size; the current track is terminated if no valid step size was found after a given number of tries (e. g. due to misconfiguration).

```
<traj_control_energy name="control_energy" initial_step="{1e-3}" upper_limit="{1
↪ e-12}" min_length="{1e-6}" max_length="{1e-2}" adjustment_up="0.8"
↪ adjustment_down="0.4" />
```

The following example shows how trajectories are configured with different step size controls:

```
<ktraj_trajectory_exact name="trajectory_exact"/>
  <traj_integrator_rk8 name="integrator_rk87"/>
  <traj_term_propagation name="term_propagation"/>
  <traj_control_cyclotron name="control_cyclotron" fraction="{1. / 64.}"/>
  <traj_control_energy name="control_energy" upper_limit="{1e-12}" min_length="{1e
    ↪ -6}"/>
</ktraj_trajectory_exact>

<ktraj_trajectory_adiabatic name="trajectory_adiabatic"/>
  <traj_integrator_rk8 name="integrator_rk8"/>
  <traj_term_propagation name="term_propagation"/>
  <traj_term_gyration name="term_gyration"/>
  <traj_term_drift name="term_drift"/>
  <traj_control_length name="control_length" length="{1e-3}"/>
</ktraj_trajectory_adiabatic>

<ktraj_trajectory_magnetic name="trajectory_fieldline"/>
  <traj_integrator_rk8 name="integrator_rk8"/>
  <traj_term_propagation name="term_propagation"/>
  <traj_control_time name="control_time" time="{1e-6}"/>
</ktraj_trajectory_magnetic>
```

3.3.5 Navigation inside the simulation geometry

To use complex simulation geometries in Kassiopeia – with the option to split up the simulation volume into different regions and include interactions with geometric shapes – efficient navigation methods are required. Simulation parameters can be adjusted in different regions, e. g. it is possible to activate interactions only in a part of the entire simulation, or to disable the computation of electric fields in a certain volume to speed up the simulation. For this to work, the software needs to know the particle's position within the geometry setup.

The navigation operates on a tree-like structure of spaces and surfaces, which allows to determine the current position inside the geometry at each step. At the beginning of the simulation, the navigation tree is traversed to determine in which section the particle is generated. While the tree is traversed, the simulation parameters are initialized by specific commands that can be executed when a region is entered by the particle. These commands modify certain aspects of the simulation, e. g. add an electric field or change the method of propagation. At each step the navigator checks if the particle moved into another navigation region, in which case the simulation parameters are updated accordingly. If the particle leaves a region afterwards the inverse commands are executed, i. e. a previously added electric field is now removed from the simulation. Surface interactions (section 3.3.6) are triggered by the navigator when a particle hits or crosses a geometric surface.

The following example shows the concept of the tree-like navigation structure, using different commands to reconfigure the simulation while the particle propagates:

```
<ksgeo_space name="space_world" spaces="world">
  <command parent="root_trajectory" field="set_trajectory" child="
    ↪ trajectory_adiabatic"/>
  <command parent="root_terminator" field="add_terminator" child="term_max_steps"/>
```

```

<command parent="root_magnetic_field" field="add_magnetic_field" child="
  ↪ earth_magnetic_field"/>
<geo_space name="space_chamber" spaces="world/chamber">
  <command parent="root_trajectory" field="clear_trajectory" child="
    ↪ trajectory_adiabatic"/>
  <command parent="root_trajectory" field="set_trajectory" child="
    ↪ trajectory_exact"/>
  <command parent="root_terminator" field="add_terminator" child="
    ↪ term_min_energy"/>
  <command parent="root_electric_field" field="add_electric_field" child="
    ↪ electric_quadrupole_field"/>
  <geo_surface name="surface_target" surfaces="world/chamber/target">
    <command parent="root_terminator" field="add_terminator" child="
      ↪ term_death"/>
  </geo_surface>
</geo_space>
</ksgeo_space>

```

3.3.6 Continuous and discrete interactions

Continuous processes like the emission of synchrotron radiation can be included in the simulation by extending the propagation terms. Discrete processes like scattering with residual gas are randomly triggered during propagation, according to their probability of interaction. Surface processes are triggered if the particle interacts with simulation geometry, which requires the navigation capabilities explained above.

Synchrotron radiation

Synchrotron radiation is an important effect to consider when signal or background electrons at the KATRIN experiment are investigated. This process is therefore often included in Kassiopeia simulations. In case of exact tracking, the momentum term (3.7) is extended to [Fur15]

$$\frac{d\vec{p}}{dt} = -\frac{\mu_0 q^4}{6\pi c m} \frac{\vec{p}}{p^2} \left[\gamma \left(E_T^2 + B_V^2 \frac{p^2}{m^2} \right) + \gamma^2 \left(-2E_U B_V \frac{p}{m} \right) + \gamma^3 \left(E_U^2 + E_V^2 \right) \right]. \quad (3.16)$$

μ_0 denotes the vacuum permeability and the indices T, U, V refer to the direction of the momentum \vec{p} , the direction of $\vec{p} \times \vec{B}$, and the normal direction $\vec{V} = \vec{T} \times \vec{U}$.

In case of adiabatic tracking, a simpler term is added to the transversal momentum (which reflects the fact that the energy loss affects the transversal energy of the particle) [Fur15]:

$$\frac{dp_{\perp}}{dt} = -\frac{\mu_0 q^4}{6\pi c m^3} \gamma p_{\perp} \vec{B}_c^2. \quad (3.17)$$

Scattering processes

Non-continuous effects like scattering can be included in Kassiopeia simulations as well. In this case, a finite probability can be determined to randomly trigger an interaction while the particle propagates. Scattering with residual gas atoms is an example of so-called *space interactions*, where the interaction

can happen anywhere inside the given volume. The interaction probability within a given time frame $[0; t]$ can be calculated by

$$P(t) = 1 - \exp\left(-\frac{t \cdot v}{\lambda}\right), \quad (3.18)$$

where v is the velocity of the scattering particle. The mean free path length $\lambda = 1/(n\sigma)$ is defined by the number density of scattering targets n and the scattering cross section σ . The parameters n , σ and v are averaged over the current step. The density can be computed internally by another Kassiopeia, taking into account parameters like temperature and partial pressure.

From (3.18), the average time between two scattering events can be calculated:

$$t_{scat} = -\ln(1 - P(t)) \cdot \frac{\lambda}{v}. \quad (3.19)$$

By drawing the value $P(t)$ from a uniform distribution in the range $[0; 1]$, the simulation decides if a scattering event will occur at the current step: if $t_{scat} > \Delta t$, no interaction occurs; otherwise the step will be re-calculated with a smaller step length $\Delta t = t_{scat}$ to compute the particle's properties at the position of the interaction.

It is possible to include multiple discrete interactions in the simulation, e.g. elastic and inelastic scattering. Weights are assigned to the different processes, based on their individual contribution to the total cross section. If a scattering event resulted in the creation of secondary particles, they will be processed in sequence after the current track has been terminated.

Surface interactions

In addition to space interactions, Kassiopeia also allows to include *surface interactions*. These interactions are triggered if the particle crosses a boundary surface that has been defined in the simulation geometry. A reflection or transmission probability is assigned to the specific surface. Similar to space interactions, the simulation first determines if a surface is crossed at the current step. If that is the case, the current step is re-computed to end at the surface, and the transmission probability is computed. Surface interactions allow to include processes where the particle crosses into another material, e.g. from vacuum into solid silicon at the detector.

The following example shows how synchrotron radiation, scattering with hydrogen gas and diffuse reflection on a surface are configured in Kassiopeia:

```
<kstraj_trajectory_exact name="trajectory_exact">
  <integrator_rk8 name="integrator_rk8"/>
  <term_propagation name="term_propagation"/>
  <control_cyclotron name="control_cyclotron" fraction="{1. / 64.}"/>
  <term_synchrotron name="synchrotron"/>
</kstraj_trajectory_exact>

<ksint_scattering name="scattering_hydrogen">
  <density_constant temperature="300." pressure="1.e-7"/>
  <calculator_constant cross_section="1.e-15"/>
  <calculator_hydrogen elastic="true" excitation="true" ionisation="true"/>
</ksint_scattering>
```

```

<ksint_surface_diffuse name="surface_energy_loss" probability="0.5" transmission_loss
  ↪ ="1.0" />

<disk_surface name="test_disk_surface" z="0" r="1"/>
<surface name="test_disk" node="test_disk_surface"/>
<geo_surface name="test_disk_energy_loss" surfaces="test_disk">
  <command parent="root_surface_interaction" field="set_surface_interaction" child=
    ↪ "surface_energy_loss"/>
</geo_surface>

```

3.3.7 Termination of simulated tracks

When a trajectory is simulated in Kassiopeia, the current track is terminated once a specific exit condition is triggered. These conditions are implemented in Kassiopeia in the form of *terminators*, which are evaluated at the end of each simulation step. When a track is terminated, the simulation continues with the next track (which can be another primary particle or a secondary particle created during the processing of an event). When all events have been processed, the current run is finished and the simulation stops.

Various terminators have been implemented in Kassiopeia. Most of them can be used in many different simulations, while some are specifically designed for a certain task – e. g. a terminator that takes into account the pixelated surface of the FPD. The commonly used terminators will be summarized here shortly.

- **Maximal number of steps:** Triggered once the total number of steps in a track exceeds the given limit:

$$N_{step} \geq N_{max}. \quad (3.20)$$

This is often used in simulations as a “safe guard” terminator which prevents the simulation to run endlessly if no other terminators have been triggered.

```
<ksterm_max_steps name="term_steps" max_steps="1e6"/>
```

- **Minimal/maximal z-position:** Triggered once the particle’s axial position (on the z-axis in Kassiopeia’s coordinate system) exceeds the given limits:

$$z \leq z_{min} \vee z \geq z_{max} \quad (3.21)$$

This is commonly used to stop a particle when it leaves a certain geometry, e. g. the main spectrometer.

```
<ksterm_min_z name="term_z_min" z="-12.2">
<ksterm_max_z name="term_z_max" z="12.2">
```

- **Minimal/maximal r-position:** Triggered once the particle’s radial position $r = \sqrt{x^2 + y^2}$ (distance to the z-axis) exceeds the given limits:

$$r \leq r_{min} \vee r \geq r_{max}. \quad (3.22)$$

Like the previous terminator, this is often used to confine a track to a specific geometry.

```
<ksterm_min_r name="term_z_min" z="2.0">
<ksterm_max_r name="term_z_max" z="5.0">
```

- **Minimal/maximal kinetic energy:** Triggered once the particle's kinetic energy exceeds the given limits:

$$E \leq E_{min} \vee E \geq E_{max}. \quad (3.23)$$

The terminator is useful to focus the simulation on a specific energy regime, i. e. to neglect low-energetic particles that are irrelevant to scattering processes due to an energy threshold.

```
<ksterm_min_energy name="term_energy_min" long_energy="13.6">
<ksterm_max_energy name="term_energy_max" long_energy="1000.">
```

- **Minimal/maximal longitudinal kinetic energy:** Similar to the previous terminator, but considers the longitudinal energy component $E_{\parallel} = E \cdot \cos^2 \theta$ of the particle:

$$E_{\parallel} \leq E_{min} \vee E_{\parallel} \geq E_{max}. \quad (3.24)$$

```
<ksterm_min_long_energy name="term_long_energy_min" long_energy="0.01">
<ksterm_max_long_energy name="term_long_energy_max" long_energy="0.1">
```

- **Maximal time:** Triggered once the time elapsed in the simulation exceeds the given limit:

$$t = \sum_{i=1}^{N_{step}} \Delta t_i \geq t_{max}. \quad (3.25)$$

The time is simply the sum of the individual step sizes. This is often used to skip particle that move slowly in the simulation, e. g. due to misconfiguration of the electromagnetic fields.

```
<ksterm_max_time name="term_time" max_time="1e-6">
```

- **Maximal length:** Triggered once the total length of the particle's trajectory exceeds the given limit:

$$s = \sum_{i=1}^{N_{step}} v_i \Delta t_i \geq s_{max}. \quad (3.26)$$

The length is given by the sum of the individual step lengths, i. e. the product of step size and current particle velocity. Like the "time" terminator, this is often used for debugging.

```
<ksterm_max_length name="term_path_length" max_length="{25.0}">
```

- **Minimal distance:** Triggered once the particle's distance to a given set of surfaces or spaces becomes less than the given limit:

$$\min |\bar{x} - \bar{x}_S| \geq d_{max}. \quad (3.27)$$

The point \bar{x}_S is an arbitrary point on any of the given surfaces $S = \{S_1, S_2, \dots\}$. The terminator is useful to confine simulated particles to regions that are far away from a geometric surface, e. g. to avoid tracks close to an electrode surface (where strong electric fields are present) so that the defined step size becomes too large to produce accurate results.

```
<ksterm_min_distance name="term_distance" min_distance="1e-3" surfaces="
↳ @electrode_tag"/>
```

- **Trapped particle:** Triggered once the particle is reflected more than the given number of times. To determine if the particle has been reflected, the movement direction of the particle along the field line is evaluated:

$$\left(\vec{B} \cdot \vec{p}\right)_{n-1} \cdot \left(\vec{B} \cdot \vec{p}\right)_n < 0. \quad (3.28)$$

The indices n and $n - 1$ refer to the current and the previous step. The direction of motion is given by the product $\vec{B} \cdot \vec{p}$. When the direction changes (i. e. when the term above becomes negative), the reflection count is increased by one. If the number is above a given limit, the particle is terminated. This terminator is mainly useful where stored particles are considered in the simulation.

```
<ksterm_trapped name="term_trapped" max_turns="1"/>
```

- **Secondary particle:** Triggered if a secondary particle was created by the simulation. This terminator is often used when scattering is included in the simulation, but the trajectories of secondary particles are irrelevant.

```
<ksterm_secondaries name="term_secondaries"/>
```

- **Death:** Terminates all particles, which is used either for debugging purposes or in combination with navigation regions. In the latter case, this terminator can be added to a specific volume in which all particles should be terminated, e. g. to focus the simulation on a specific section of the geometry. In combination with the navigation routines (section 3.3.5), this terminator often provides more flexibility than the geometric terminators listed above (such as `max_r`).

```
<ksterm_death name="term_vessel_hull"/>
```

3.3.8 Simulation output

To allow an analysis of simulation results, the data is written to disk while the simulation is running. The parameters of simulated particles are stored using the ROOT file format. ROOT files have the advantage of being capable of handling large amounts of data – which becomes relevant in complex simulations – and providing an efficient tree-like file structure. This allows to include Kassiopeia’s structure – runs, events, tracks and steps – in the output file, which is of great advantage when analyzing the results.

The *step level* output stores the full parameter set of each particle at every step. The trajectory can therefore be restored during analysis and the evolution of a parameter over time can be analyzed. If many steps are simulated, writing step data to disk can result in extreme large files, which can become a disadvantage for the user. The file size can be reduced by including less parameters in the output. For example, it may be sufficient to only store the particle’s position and momentum for later analysis, and disregard other parameters like electromagnetic fields.

In many cases, the step data is not required at all if only the particle state at certain positions is evaluated during analysis. Writing the *track level* to disk only stores parameters at the beginning and end of each track. Additionally it is possible to compute derived values like the minimum, maximum

or the cumulative sum (integral) of a parameter along the trajectory, which can be included in the track output. Examples include the minimal and maximal magnetic field, or the total length of the trajectory. Again, the amount of information can be reduced by storing only a subset of available parameters. Step level output is therefore mostly useful when new simulations are set up and have to be error-checked, or if the user is interested in the actual trajectories of the simulated particles. For other simulations it often makes sense to only include the track level in the output.

The following example shows an output configuration to write track and step data to a ROOT file. The step level output saves the current time, position, kinetic energy and pitch angle of the particle together with the step index. The longitudinal kinetic energy is computed from the kinetic energy and pitch angle according to (2.1), using the built-in analysis logic. At the track level, the output file contains the initial and final position, the total number of steps, and the track index. The maximal pitch angle along the track is also saved. To make the pitch angle at each step available to the track level (so that the maximal value can be determined), the value needs to be defined beforehand in the configuration file.

```
<ks_component_member name="step_final" field="final_particle" parent="step"/>
<ks_component_member name="kin_energy" field="kinetic_energy_ev" parent="step_final"
  ↪ />
<ks_component_member name="pitch_angle" field="polar_angle_to_b" parent="step_final"
  ↪ />
<ks_component_group name="output_step">
  <component_member name="step_id" field="step_id" parent="step"/>
  <component_member name="time" field="time" parent="step_final"/>
  <component_member name="position" field="position" parent="step_final"/>
  <component_member name="kinetic_energy" field="kinetic_energy_ev" parent="
    ↪ step_final"/>
  <component_member name="pitch_angle" field="polar_angle_to_b" parent="step_final"
    ↪ />
  <component_math name="long_kin_energy" term="x0*cos(x1*Math::Pi()/180.)^2"
    ↪ parent="kin_energy" parent="pitch_angle"/>
</ks_component_group>

<ks_component_member name="track_initial" field="initial_particle" parent="track"/>
<ks_component_member name="track_final" field="final_particle" parent="track"/>
<ks_component_group name="output_track">
  <component_member name="track_id" field="track_id" parent="track"/>
  <component_member name="total_steps" field="total_steps" parent="track"/>
  <component_member name="initial_pos" field="position" parent="track_initial"/>
  <component_member name="final_pos" field="position" parent="track_final"/>
  <component_maximum name="max_pitch_angle" group="output_step" parent="pitch_angle"
    ↪ "/>
</ks_component_group>
```

3.3.9 Visualization methods

In addition to the simulation output which can be processed by specific analysis code, Kassiopeia also features powerful visualization tools. Visualization is especially important when complex simulations are performed and many parameters have to be considered. Kassiopeia offers different types of visualization, which either use the drawing capabilities of the ROOT library or the more sophisticated 3D

rendering features of VTK, a toolkit specifically designed for the visualization of large and complex data sets. With VTK it is possible to check the simulation geometry and to examine the particle trajectories even for complex simulations. Electromagnetic fields can be visualized e. g. by colored surfaces, contour lines, vector arrays or field lines. The *ParaView* application⁹ which is built around VTK can be used together with Kassiopeia's capabilities to perform advanced visualizations.

One has to differentiate between the internal visualization that is embedded in Kassiopeia, where the user can investigate the simulation results using a variety of so-called *painters*, and the visualization with external software like ParaView. The output module (section 3.3.8) can be configured to write data to VTK-compatible binary files, similar to the ROOT output. The output can be configured individually for ROOT and VTK; e. g. it is possible to use step level output in VTK files in order to visualize the particle trajectories, but limit the ROOT output to the track level in order to maintain a smaller file size. Additionally, most painters allow to save their contents to a VTK file that can later be accessed in ParaView, e. g. to overlay the particle trajectories with the simulation geometry.

The internal visualization methods of Kassiopeia will be summarized briefly:

- **Geometry:** This painter renders any part of the simulation geometry, referencing the geometric shapes either by name or by tags. This painter also allows to visualize shapes that are not used in the tracking process (i. e. parts that have no physical relevance to the simulation). This painter has been implemented with both ROOT and VTK. In the ROOT painter, the origin and normal of the visualization plane can be defined, resulting in a cut-drawing of the geometry. In the VTK painter, a 3D visualization is performed with the ability to move around in the rendered scene.
- **Tracks:** The track painter will read a ROOT output file that was created by Kassiopeia. It therefore only makes sense to run this painter after the simulation has stopped. It renders the trajectories of simulated particles as polylines, where each vertex corresponds to one step of the simulation. The lines can be colored by any parameter that is available in the output file (e. g. the particle's kinetic energy). In the ROOT painter, the configuration is similar to the geometry painter and the particle tracks will be projected onto the defined visualization plane. The VTK painter performs a 3D visualization, and the tracks can be viewed together with the simulation geometry.
- **Electric potential:** This painter is only available in ROOT, and evaluates the electric potential in a 2D area within the simulation geometry. The results are rendered as a contour plot on top of the visualization plane. Although there is no specific VTK painter, the electric potential and electromagnetic fields can be visualized by computing a 3D field map and saving the results to a VTK file. its contents can be visualized in ParaView, using sophisticated methods like vector glyphs or field lines. A Kassiopeia module to compute such field maps has been implemented over the course of this thesis (section 3.5).
- **Specialized visualization:** Kassiopeia includes additional painters for specific purposes. One example is the FPD painter, where the hit pattern on the pixelated detector surface is visualized. Another example is the Zonal Harmonics painter, which allows to investigate the convergence region of the zonal harmonics approximation that is used in electromagnetic field computations (section 3.5). These painters will be skipped here for brevity.

The following example shows how visualization techniques are configured in Kassiopeia:

9. ParaView: <http://www.paraview.org/>

```

<root_window name="root_visualizer" canvas_width="1024" canvas_height="768">
  <root_pad name="top" xlow="0.02" ylow="0.51" xup="0.98" yup="0.98">
    <root_geometryPainter name="geometry_root" surfaces="@electrode_tag" space="
      ↪ @magnet_tag" plane_normal="1 0 0" plane_point="0 0 0" swap_axis="true"
      ↪ />
    </root_pad>
    <root_pad name="bottom" xlow="0.02" ylow="0.51" xup="0.98" yup="0.98">
      <root_geometryPainter name="geometry_root" surfaces="@electrode_tag" space="
        ↪ @magnet_tag" plane_normal="0 1 0" plane_point="0 0 0" swap_axis="true"
        ↪ />
      </root_pad>
    </root_pad>
  </root_window>

<vtk_window name="vtk_visualizer" frame_size_z="1024" frame_size_y="768">
  <vtk_geometryPainter name="geometry_vtk" surfaces="@electrode_tag" space="
    ↪ @magnet_tag"/>
  <vtk_trackPainter name="tracks_vtk" path="[output_path]" file="Simulation.root"
    ↪ point_object="component_step" point_variable="position" color_object="
    ↪ component_step" color_variable="kinetic_energy_ev"/>
</vtk_window>

```

3.4 The geometry toolkit KGeoBag

The electromagnetic fields used in Kassiopia are most commonly defined by the simulation geometry consisting of electrodes and magnets. Furthermore, the advanced navigation capabilities of Kassiopia rely on a consistent geometry definition. A large fraction of the geometry-handling code was therefore moved out of Kassiopia into a separate module named *KGeoBag*.

The module contains the code to parse a geometry definition from XML configuration files, construct and initialize all geometric parts (“shapes”) with the given parameters, and pass on the resulting geometry to Kassiopia (figure 3.5). By representing the relations between different shapes in a tree, the navigation within the geometry can be performed efficiently [Gro15, Fur15].

3.4.1 Definition of geometric shapes

Shapes resemble the most basic parts from which the simulation geometry is constructed. The available shapes are divided into two groups: surfaces and spaces (volumes). A local coordinate system is maintained for each defined shape, which allows to automatically perform coordinate transformations while navigating in the geometry tree. A shape itself does not include any relations to other shapes and is not yet used by the simulation; it only includes the definition of basic parameters like its position in the local system and its dimension.

In the following example, four shapes are placed in the global coordinate system that is placed at the origin $\vec{x}_0 = (0,0,0)$. Some *tags* are attached to the defined shapes as well (see section 3.3.2).

```

<cylinder_space name="world_space" z1="-25." z2="25." r="10."/>
<tag name="magnet_tag">
  <cylinder_tube_space name="magnet_space" z1="-4.0" z2="4.0" r1="0.6" r2="0.8"/>

```

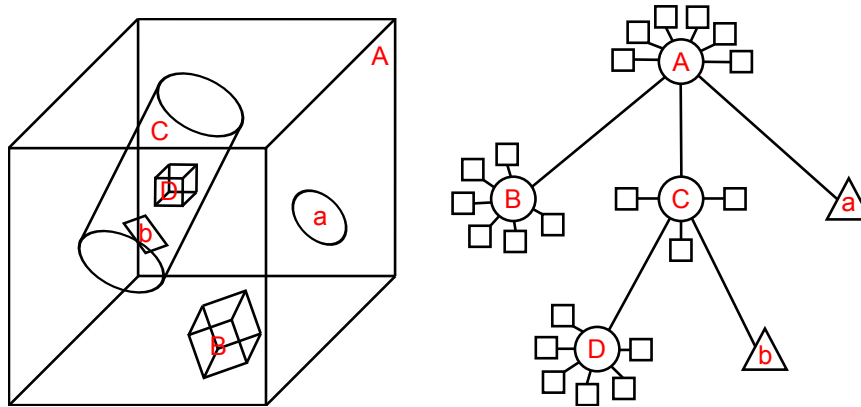


Figure 3.5.: Schematic representation of the KGeoBag geometry tree. KGeoBag allows to define “shapes” (volumes A, B, C, D and surfaces a, b) at arbitrary positions and orientations. All shapes can be nested within each other to resemble the physical structure of a simulation geometry (e. g. electrodes in a vacuum chamber). The geometry and the relation between nested shapes can then be visualized by a tree structure as shown on the right. The navigation routines in Kassiopeia traverse the geometry tree to determine in which part of the geometry a particle is located. The outermost volume is often referred to as the “world volume” since it contains all of the other shapes. Figure from [Gro15].

```

</tag>
<tag name="electrode_tag">
  <cylinder_surface name="cylinder_surface" z1="-4.0" z2="4.0" r="0.5"/>
  <disk_surface name="disk_surface" z="0" r="1e-3"/>
</tag>

```

3.4.2 Placement and nesting of geometric parts

To define the location of a specific shape w. r. t. to other shapes, it needs to be *placed* in the geometry tree. At this point it is possible to define nesting and to collect different shapes in an *assembly*. Assemblies are treated like placed shapes internally, and coordinate transformations are applied to all contained shapes in a common reference frame. This structure allows the user to define the geometric relations in an intuitive way. The simulation geometry for the electron source presented in this work (chapter 4) utilizes these features to a large extent.

Staying with the example code above, the shapes are now placed in the global reference frame. It is possible to place a single shape multiple times, which avoids redundant code in the configuration file. The geometry tree contains the `world` volume at the top level (root node) and branches into the `placed_electrodes` assembly which contains three individual surfaces, and the `placed_magnet` space which refers to a single volume.

```

<space name="electrode_assembly">
  <surface name="placed_disk_a" node="disk_surface">
    <transformation displacement="0 0 0.2"/>
  </surface>
  <surface name="placed_disk_b" node="disk_surface">
    <transformation displacement="0 0 -0.2"/>

```

```
</surface>
<surface name="placed_cylinder" node="cylinder_surface"/>
<space>

<space name="world" node="world_space">
  <space name="placed_magnet" node="magnet_space"/>
  <space name="placed_electrodes" tree="electrode_assembly"/>
</space>
```

Placed shapes are referenced by their full path inside the tree, starting with the root node (e.g. world/placed_electrodes/placed_cylinder). It is also possible to reference shapes by any attached tag, which avoids having to name each shape explicitly every time it is referenced (e.g. world/@electrode_tag).

3.4.3 Extensions of the geometry system

The KGeoBag module features an extension system which allows to process the geometry for use with other modules such as field computation (section 3.5). In this case, each shape needs to have defined some electromagnetic properties like electrode voltage or magnet current. The electric field computation also requires the electrode surfaces to be discretized into smaller sub-elements. The discretization, also known as *meshing*, is performed in KGeoBag and can be configured by additional parameters for each shape.

The following example shows the basic definition of three electrodes and a magnet, using the example configuration from above. A mesh is created for an axially-symmetric geometry (disk and cylinder electrodes as defined above).

```
<electromagnet name="coil_magnet" spaces="world/placed_magnet" current="25.0"/>
<electrostatic_dirichlet name="cylinder_electrode" surfaces="world/placed_electrodes/
  ↪ placed_cylinder" value="0."/>
<electrostatic_dirichlet name="disk_electrode_a" surfaces="world/placed_electrodes/
  ↪ placed_disk_a" value="-100."/>
<electrostatic_dirichlet name="disk_electrode_b" surfaces="world/placed_electrodes/
  ↪ placed_disk_b" value="100."/>

<axial_mesh name="mesh_electrode" surfaces="world/@electrode_tag"/>
```

3.5 The electromagnetic field solver KEMField

With the simulation geometry having been defined in KGeoBag and made available to Kassiopeia, the next thing to focus on is the computation of the electromagnetic fields. Since many particle-tracking simulations at KATRIN deal with complex electromagnetic fields and a high accuracy is desired, a lot of thought has been put into the field solver module *KEMField* [Bar16, Cor14].

The field solver is independent of Kassiopeia and can be used in stand-alone mode for tasks where no particle tracking is required. When used in the context of Kassiopeia, the discretized geometry

is produced by the meshing algorithm in KGeoBag after the geometry has been initialized. The discretized shapes are then passed on to KEMField.

3.5.1 Evaluation of magnetic fields

In principle, no further preparation is necessary to evaluate a magnetic field once the corresponding geometry has been defined and initialized. It is possible to solve for the magnetic field of a coil placed at an arbitrary position in space using direct integration methods. KEMField evaluates the magnetic field using either an integrated form of the Biot-Savart law or elliptic integrals [Glu11b, Cor14].

Since these methods are rather slow and the magnetic field configurations are often symmetric around the beam axis (e. g. when solenoids or air coils are placed central to the beam axis), it is possible to take advantage of an approximation method known as *zonal harmonic expansion*.

Direct method

According to the law of Biot-Savart, a current I in a line segment $d\vec{s}$ placed at the position \vec{r} produces the magnetic field

$$d\vec{B} = \frac{\mu_0}{4\pi} \frac{I d\vec{s} \times \vec{r}}{r^3}, \quad (3.29)$$

with μ_0 the vacuum permeability. Integrating over the line segment gives the resulting magnetic field \vec{B} at an arbitrary position in space. By discretizing complex shapes into N smaller segments of finite length, the total magnetic field can be computed as a superposition of the individual contributions \vec{B}_i :

$$\vec{B}_{tot} = \sum_{i=1}^N \vec{B}_i. \quad (3.30)$$

A better accuracy can be achieved by increasing the number of discretized line segments at the expense of a longer computation time.

Elliptic integration

An alternative method that avoids discretization is provided by *elliptic integration*, which can be numerically computed with high efficiency and is therefore faster than the Biot-Savart method.

For a thin magnetic coil, (3.29) can be expressed by *elliptic integrals* [Car10]:

$$\begin{aligned} K(k) &= \int_0^{\pi/2} \frac{1}{1 - k^2 \sin^2 \theta} d\theta, & \text{(I)} \\ E(k) &= \int_0^{\pi/2} \sqrt{1 - k^2 \sin^2 \theta} d\theta, & \text{(II)} \\ \Pi(n, k) &= \int_0^{\pi/2} \left[(1 - n^2 \sin^2 \theta) \sqrt{1 - k^2 \sin^2 \theta} \right]^{-1} d\theta. & \text{(III)} \end{aligned} \quad (3.31)$$

The roman numbers refer to the elliptic integral of the so-called first, second and third kind. The third term is needed to describe a realistic coil with finite length Z and thickness R .

Using elliptic integrals, the axial and radial components of the magnetic field B_z and B_r can be computed for an infinitesimal thin solenoid,

$$\begin{aligned} B_z &= \hat{B}_z(Z_{max}) - \hat{B}_z(Z_{min}), \\ B_r &= \hat{B}_r(Z_{max}) - \hat{B}_r(Z_{min}), \end{aligned} \quad (3.32)$$

where the terms $\hat{B}_{z,r}$ are given by

$$\begin{aligned} \hat{B}_z &= -\frac{\mu_0 \lambda (z - Z) R}{\pi (r + R) S} \left[K(k) + \frac{R - r}{2R} (\Pi(n, k) - K(k)) \right], \\ \hat{B}_r &= -\frac{\mu_0 \lambda R}{\pi S} \left[2 \frac{E(k) - K(k)}{k^2} + K(k) \right], \end{aligned} \quad (3.33)$$

with the terms

$$\begin{aligned} S &= \sqrt{(r + R)^2 + (z - Z)^2}, \\ k^2 &= \frac{4rR}{S^2}, \\ n^2 &= \frac{4rR}{(r + R)^2}, \end{aligned} \quad (3.34)$$

and the linear current density λ .

Although elliptic integrals allow to compute the magnetic field without need for discretization, the method is still rather slow due to the large number of integration steps involved.

Zonal Harmonic Expansion

For an axially symmetric problem, the *zonal harmonic expansion* provides a much faster method to compute the magnetic field of a coil (figure 3.6). With this method, the magnetic field at a point $p(z, r)$ is expressed by *Legendre polynomials*. One important ingredient is the derivative of the field at so-called *source points* z_i that are located on the symmetry axis [Glu11b].

If the point p is located within the convergence radius ρ_{cen} of the closest source point z_0 , the magnetic field can be expressed by the *central expansion*

$$\begin{aligned} B_z &= \sum_{n=0}^{\infty} B_n^{cen} \left(\frac{\rho}{\rho_{cen}} \right)^n \cdot P_n(u), \\ B_r &= -s \cdot \sum_{n=1}^{\infty} \frac{B_n^{cen}}{n+1} \left(\frac{\rho}{\rho_{cen}} \right) \cdot P_n'(u), \end{aligned} \quad (3.35)$$

with $s = \sin \theta$, $u = \cos \theta$ and ρ the distance between p and z_0 . The symbols P_n and P_n' denote the Legendre polynomial of grade n and its derivative, and B_n^{cen} are the pre-computed source point central coefficients. For small ratios ρ/ρ_{cen} the central expansion converges faster, hence a larger number of source points increases the computation speed as the total convergence region of all source points is

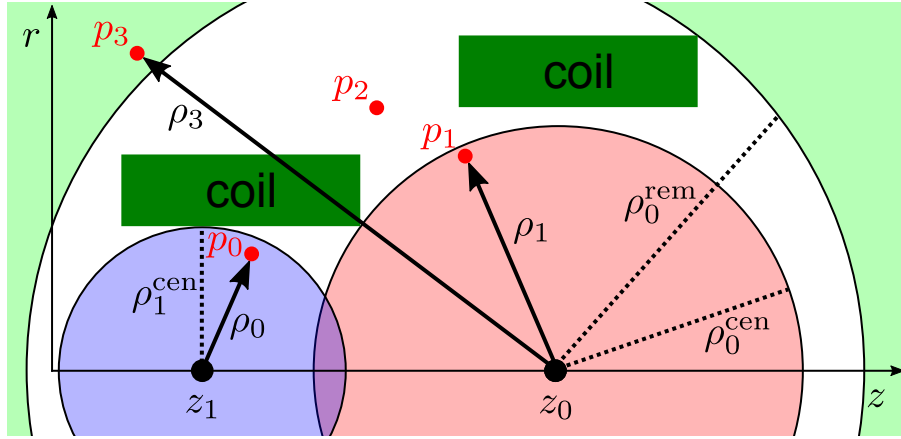


Figure 3.6.: Zonal harmonic approximation to evaluate a magnetic field. For an axially symmetric setup of coils, the so-called “local expansion” allows to compute the magnetic field at points $p_{0,1}$ inside the *convergence radius* $\rho_{0,1}^{cen}$ that is defined by the coil placements. The approximation uses the pre-computed magnetic field (and its derivative) at the *source points* $z_{0,1}$ that are located on the symmetry axis. Similarly, a “remote expansion” allows to apply an approximation to points outside the convergence radius ρ_0^{rem} . The point p_2 outside the shaded areas must be computed by a slower “direct” method such as elliptic integration. A larger number of source points increases the volume where the approximation is valid (e. g. by placing a third source point between z_0 and z_1), but requires more field evaluations during the pre-computation phase. Figure adapted from [Gro15].

larger. Because the values B_n^{cen} have to be computed beforehand for each source point, there is a trade-off between the time required for pre-computing the coefficients and the actual field computations. For a large number of source points, the evaluation is further slowed down since for each evaluation the closest source point needs to be found by comparing the individual distances ρ_i .

Similarly, if the point p is outside the remote convergence radius $\rho_{rem} > \rho_{cen}$, the magnetic field is computed with the *remote expansion*

$$\begin{aligned} B_z &= \sum_{n=2}^{\infty} B_n^{rem} \left(\frac{\rho_{rem}}{\rho} \right)^{n+1} \cdot P_n(u), \\ B_r &= -s \cdot \sum_{n=2}^{\infty} \frac{B_n^{rem}}{n} \left(\frac{\rho_{rem}}{\rho} \right) \cdot P'_n(u). \end{aligned} \quad (3.36)$$

Here B_n^{rem} denotes the source point remote coefficients that have to be computed beforehand. The expansion will again converge faster for smaller ratios ρ_{rem}/ρ .

The implementation of the zonal harmonic expansion in KEMField pre-computes all coefficients for the given source points before the simulation starts. The coefficients are stored in a file that can be re-used for following simulations that use the same field configuration. Compared to elliptic integrals, the zonal harmonic expansion is faster by orders of magnitude and is therefore used in many simulations at KATRIN. However, in some cases the magnetic field can not be evaluated with this method due to a mismatch between ρ_{cen} and ρ_{rem} , e. g. at positions close to a magnetic coil. Instead of aborting the field computation or producing wrong results, KEMField simply falls back to the slower elliptic integration in this case. Dedicated visualization tools (see section 3.3.9) allow to investigate the convergence regions of the zonal harmonic expansion and to optimize the field configuration accordingly.

The following example shows a magnetic field setup in Kassiopeia, making use of the zonal harmonic expansion method. The position of the individual source points is determined automatically from the given geometry, using a density parameter to distribute the source points along the symmetry axis.

```
<ksfield_electromagnet
  name="field_magnet_sds"
  file="MagnetSDSMagnets.kbd"
  system="world"
  spaces="world/@magnet_tag"
>
  <zonal_harmonic_field_solver
    number_of_bifurcations="-1"
    number_of_central_coefficients="500"
    number_of_remote_coefficients="200"
    use_fractional_central_sourcepoint_spacing="true"
    central_sourcepoint_fractional_distance="1.e-2"
  />
</ksfield_electromagnet>
```

3.5.2 Evaluation of electric fields

Electric fields can be computed either directly via integration or by approximated methods like zonal harmonic expansion for axially symmetric geometries [Glu11a, Cor14].

An electrode surface S with given charge density $\sigma_S = \sigma(\vec{r}_S)$ at all points \vec{r}_S on the surface creates an electric potential $\Phi(\vec{r})$ at a given point \vec{r} . Using Green's function, this relation can be expressed as

$$\Phi(\vec{r}) = \frac{1}{4\pi\epsilon_0} \int_S \frac{\sigma_S}{|\vec{r} - \vec{r}_S|} d^2r_S, \quad (3.37)$$

where ϵ_0 is the vacuum permittivity. When multiple electrodes are present, the integral has to be solved for each electrode and the total potential is a superposition of the individual contributions. The integration requires knowledge of the charge densities on all electrodes, which is discussed below.

The zonal harmonics method works the same as in the case of magnetic fields (see above). From the given geometry, the central and remote coefficients are computed for every source point. Depending on the number of electrode segments and the number of source points, the computation time for the coefficients can become rather long. However, the approximation method is often useful when the same axially symmetric geometry is used in many simulations. In this case, the extra time required to prepare the electric fields is compensated by the much faster field evaluation when the simulation is running.

Fast multipole expansion

Another approximation method available in KEMField which has no constraints on symmetry is the *fast Fourier-transform multipole* (FFTM) method. It uses a different approach to approximate and speed up the field evaluation. Instead of computing the individual contributions from each electrode segment for every evaluation of the electric field, multiple segments are combined into *electrode groups* that have the same electric multipole moment as the actual electrodes combined [B⁺15, Bar16].

The relation between the electric potential of an electrode (or electrode group) at the point $\vec{p} = (r, \theta, \phi)$ with charge distribution $\rho(\vec{r})$ and the multipole moment is given by

$$\Phi(r, \theta, \phi) = \sum_{l=0}^{\infty} \sum_{m=-l}^l Q_l^m \frac{Y_l^m(\theta, \phi)}{r^{l+1}}. \quad (3.38)$$

The l -th degree multipole moment of order m is defined as

$$Q_l^m = \int_S r^l \rho(\vec{r}) Y_l^m(\theta, \phi) d^3 r_S, \quad (3.39)$$

with the spherical harmonics term Y_l^m and the sphere S that contains the charge distribution.

Here the potential (and, using a similar relation, the electric field) can be determined from the multipole moments of the given charge distribution without the need to evaluate the individual contributions of the electrodes. The infinite sum in (3.38) is typically cut off at a *degree of expansion* p that can be tuned for optimization. Similar to other methods, there is a trade-off between accuracy and speed: A smaller number of electrodes in a group results in a more accurate result, but the larger number of groups in this case increases the computation time. A detailed presentation of this method is given in [Bar16].

This method would certainly be of advantage for the simulations of the electron source, where no axial symmetry is present (section 4.7). However, it was not used for the simulations presented in this thesis since the FFTM implementation was not yet completely finished and tested when the first electron source simulations were carried out.

Interpolated field map

An alternative, simpler approximation method has been implemented during the course of this thesis. Instead of computing source points or multipole moments of electrode, a 3D field map (“mesh”) is pre-computed within a given volume. The field evaluation is then performed by interpolating between the mesh points (figure 3.7).

This method is extremely straight-forward and thus does not require to tune many parameters for optimal results – the mesh spacing is the only parameter that affects the accuracy for a given electric field. A disadvantage is that it is less optimized to typical setups (e. g. a symmetric geometry or a geometry where electrodes surround a large, empty volume) and its accuracy is inferior to specialized methods like the ones described above. The computation of the 3D field map also requires a long preparation time if a large volume is to be covered by the mesh. The method is therefore mainly focused on debugging purposes or particle-tracking with small step sizes in a strictly confined volume.

The easiest method to compute the electric field between the 8 surrounding mesh points is the so-called *nearest neighbor* method, where the field of the closest mesh point is used. In this case, no interpolation is performed. The accuracy can be improved significantly by using *trilinear* interpolation where the field is averaged between the mesh points, or *tricubic* interpolation which also takes into account the gradient of the electric field. The latter needs to consider 32 mesh points to compute the gradient at each of the 8 corner points. However, the field at each point has been computed beforehand and the computation therefore is essentially reduced to an array look-up with a few mathematical operations. The tricubic interpolation method is therefore preferred as it provides the best accuracy and imposes no drawbacks in terms of computation time.

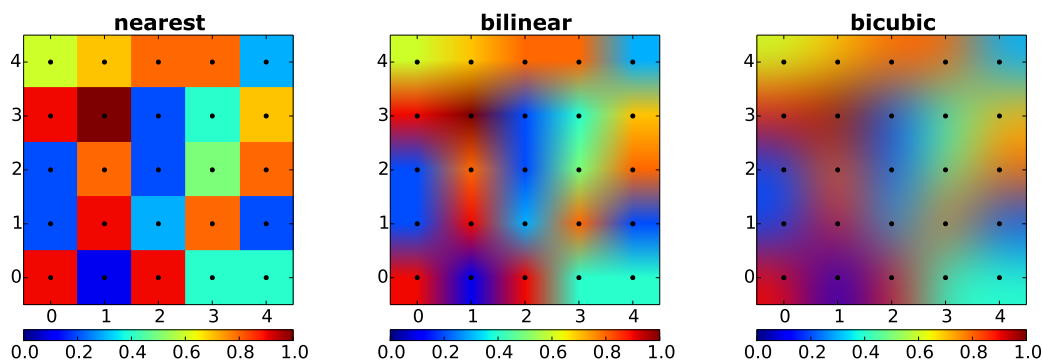


Figure 3.7.: Comparison between three interpolation methods. The left part shows the result without interpolation (“nearest-neighbor”), where the value of the nearest mesh point (black dots) is used. The accuracy can be improved by bilinear and bicubic interpolation, which averages the values between the mesh points and gives a better impression of the original data set. Although this figure shows the case for a 2D data set, the methods can be applied to 3D data as well (called trilinear/tricubic interpolation in this case).

3.5.3 Computation of charge densities

The integrals that are solved to compute the electric field at an arbitrary point in space require that the charge densities on every electrode surface are known beforehand. Although it is possible to initialize the surfaces with charge densities directly, in most cases the problem is defined by a set of given *electrode potentials*. The electric fields between electrodes on different potential redistribute charges; the charge densities thus depend on the defined potentials and on the electrode geometry. KEMField is able to precompute the charge density on the (discretized) electrode segments before evaluating the electric fields [Cor14].

Boundary Element Method

The charge-computation method used in KEMField is known as *boundary element method* (BEM). In contrast to the *finite element method* (FEM) that is often used in other applications, it does not require the complete volume to be discretized. Instead it operates on the *surfaces* of the boundary value problem. It is often faster and more versatile especially for electrostatic problems, where the solution is completely defined by boundary surfaces. In the case of KATRIN the electrostatic problems often feature large volumes with many extremely small electrode segments, e. g. the inner electrode system inside the large main spectrometer vessel (section 2.1). A volume discretization would result in a large number of sub-elements, quickly reaching the technical limits of computation speed and available memory. BEM is thus better suited for these problems, since only the electrode surfaces need to be discretized.

BEM assumes a constant charge density on each electrode segment. The level of discretization is therefore a crucial parameter for this method¹⁰.

¹⁰. KGeoBag’s meshing algorithm takes care of this issue to some extent by using a non-linear discretization of larger electrode surfaces, so that edges (where stronger electric fields are present) are finer discretized than the central region.

The discretization of a surface S into N sub-elements S_j is described by

$$S = \sum_{j=1}^N S_j. \quad (3.40)$$

A larger number of sub-elements results in a better accuracy at the expense of a longer time required to precompute the charge densities and to evaluate the electric fields.

Different methods can be applied to compute the charge densities from known surface potentials. In general, the relation between charge densities σ_j and the electric potential U_j on the N electrode segments can be expressed by the matrix equation

$$U_i = \sum_{j=1}^N c_{ij} \sigma_j, \quad (3.41)$$

where $c_{ij} = C_j(\vec{r}_i)$ are the *Coulomb-matrix elements*

$$C_j(\vec{r}_i) = \frac{1}{4\pi\epsilon_0} \int_{S_j} |\vec{r}_i - \vec{r}_S|^{-1} d\vec{r}_S. \quad (3.42)$$

Equation (3.41) can be solved analytically, e. g. using the Gauss-Jordan algorithm. In this case, the required computation time scales with $\mathcal{O}(N^3)$ and the required memory with $\mathcal{O}(N^2)$. Especially due to common hardware limits of the available memory, the number of sub-elements is limited to about 10^5 with this method.

Robin Hood

An alternative to this method is an iterative approach, the so-called *Robin-Hood* (RH) algorithm. It resembles the actual charge redistribution processes that occur in reality when electrode surfaces are brought close to each other. The redistribution of charges ensures that Gauss's law is satisfied and the electrodes come to an equilibrium condition. In reality, this is an almost instantaneous process; however an implementation in software requires an iterative approach [F⁺12].

At each step of the Robin Hood algorithm a fraction of surface charge is exchanged between the surface elements which differ most from the equilibrium condition (equipotential target). If the algorithm succeeds, the amount of exchanged charge approaches zero asymptotically. Hence, a termination condition needs to be implemented in order to stop the algorithm from running infinitely. In Robin Hood, the user can choose a "target tolerance" which corresponds to the relative charge exchange. If the exchange at some execution step is below the given limit, the iterative process ends. Typical tolerance values lie in the range 10^{-6} to 10^{-10} , depending on the electrode geometry and the required accuracy.

At the start of the iterative process, the charge distributions on all (discretized) electrode segments are randomized. The Coulomb matrix elements (3.42) are then computed for each electrode segment, which can be done either analytically or by exploiting possible approximations. The algorithm then begins to search for the two electrode segments that differ the most from the equipotential target and performs a charge exchange between these electrodes. The amount of charge that needs to be

exchanged is computed as

$$\begin{aligned} U'_m &= U_m + I_{mm} \cdot \delta\sigma_m + I_{mn} \cdot \delta\sigma_n, \\ U'_n &= U_n + I_{nn} \cdot \delta\sigma_n + I_{nm} \cdot \delta\sigma_m, \end{aligned} \quad (3.43)$$

where $U_{m,n}$ is the initial potential on each of the two elements and $U'_m = U'_n$ is the potential after the charge exchange. For this case where only two elements are present, the charge exchange $\delta\sigma_{m,n}$ can be computed fully analytically. The potential on the other electrode segments – which has now changed due to the charge redistribution – is computed again, and the algorithm proceeds with the next step until the termination condition is reached.

For the (typical) case where the electrodes are held at a certain number of different, but fixed potentials (e. g. a plate capacitor where the plates are on two different potentials), a generalization can be made to speed up further computations with altered potentials. This is especially relevant in simulations where an electrode potential is varied between different runs. In this case, the boundary problem can be grouped into sets of electrodes that contains all electrodes that share a common potential. The boundary problem is then rewritten as

$$U_i^k = \sum_{j=1}^{N_k} c_{ij} \sigma_j^k, \quad (3.44)$$

where k denotes the electrode group and N_k is the number of segments in that group.

The charge computation can now be performed with the electrodes in group k held at their common potential Φ_0 , and all remaining electrodes held at ground potential. The process is repeated for all groups, and the total electric potential can be expressed as a superposition of the individual group contributions. This allows to compute the charge distribution for any potential setting Φ_k of a group k without having to perform the iterative charge computation again. The scaled charge density σ_j^* is computed from the known charge densities σ_j^k of the M electrode groups:

$$\sigma_j^* = \sum_{k=1}^M \alpha_k \sigma_j^k, \quad (3.45)$$

with the scale factor $\alpha_k = \Phi_k / \Phi_0$.

With the Robin Hood method, the computation time scales with $\mathcal{O}(n^2)$ and the memory consumption with $\mathcal{O}(n)$. It is therefore often a better alternative to the Gaussian elimination method. It also has the advantage that it is easily parallelizable since the necessary computations at each step are isolated. KEMField supports both MPI¹¹ and OpenCL¹² to allow parallelization on different computer systems. The large-scale parallel architecture of modern GPU devices with hundreds of cores can significantly reduce the time required for a charge density computation. This is especially relevant for large geometries like the detailed 3D model of the main spectrometer, which includes deformations of the vessel hull and contains the complete inner electrode system with more than 20 000 wires and reaches about 6 million electrode elements. The electron source simulations presented in chapter 4 also make heavy use of KEMField's GPU-computing capabilities in order to speed up the 3D field computation.

11. Message Passing Interface Forum, <http://www.mpi-forum.org/>

12. The open standard for parallel programming of heterogeneous systems, <https://www.khronos.org/opencl/>

The following example shows an electric field setup in Kassiopeia, making use of the iterative Robin-Hood algorithm. GPU computation is enabled by the `use_opengl` flag:

```
<ksfield_electrostatic
  name="field_non_axial_egun"
  file="NonAxialEGunElectrodes.kbd"
  system="world/egun"
  surfaces="world/egun/@electrode_tag"
  symmetry="none"
>
  <robin_hood_bem_solver
    tolerance="1e-8"
    cache_matrix_elements="true"
    use_opengl="true"
  />
  <integrating_field_solver
    use_opengl="true"
  />
</ksfield_electrostatic>
```

3.6 Accessing the KATRIN database with KaLi

A large-scale experiment like KATRIN generates a considerable amount of data during its operation, be it detector data from measurements or sensor data that is taken automatically from the various sub-systems.

A general distinction can be made between the actual *run data*, which consists of events observed at the detector systems, and *slow-control data*, which contains the sensor data taken at the site. Run data is taken at a per-event basis: each detector event (e.g. from an electron that was observed) is processed by the DAQ system and stored to disk. Slow-control data is taken continuously at specified intervals on the order of 10 s; it is used to monitor critical parameters like vacuum pressure, baffle temperature or spectrometer voltage. This data is important not only while a measurement is running and its conditions have to be monitored continuously, but also when measurement data is analyzed afterwards.

All data is stored into databases, from where it can be retrieved on- and off-site via internet access. Web interfaces allow to monitor the operational parameters and provide methods for online analysis of measurement data. The *KaLi* module in the KASPER framework provides a combined interface to run data and slow-control values. It is used to retrieve data from the KATRIN servers for analysis [Kle14].

3.6.1 Run data from the detector systems

Currently there are three detector systems in operation at the KATRIN site, all of which are controlled by the ORCA software¹³ (figure 3.8). It manages the DAQ system and handles run files that are created during a measurement.

13. Object-oriented Real-time Control and Acquisition, <http://orca.physics.unc.edu/>

- **Focal-plane detector:** The FPD is the primary detector of the KATRIN experiment. It is located at the end of the main beamline and consists of 148 silicon pixels which can be configured individually via ORCA (e. g. with different gain and threshold values). It also features a 32-channel muon veto system. Additional control channels are available in the DAQ system, which can be used to include reference signals like timing information or lifetime pulser events [A⁺15a].
- **MonSpec detector:** The secondary detector at the monitor spectrometer is intended for online monitoring and calibration of the spectrometer high voltage as explained in section 2.1. Its detector uses 5 individual PIN diodes, the DAQ system is also controlled via ORCA [E⁺14].

The monitor spectrometer is also often used for test measurements related to the commissioning of the KATRIN spectrometers, e. g. for the commissioning of the electron source (section 4.5).

- **Muon panels:** In addition to the detectors above, 8 plastic scintillator panels are set up in the main spectrometer hall to measure the flux of cosmic muons in order to investigate background processes [Har15]. This system is not relevant in the scope of this thesis.

The ORCA software allows to configure many detector parameters online and without hardware reconfigurations. A scripting interface can be used to automate measurements with changing configurations, which is especially important for long-term or “overnight” measurements. Operational parameters of the experiment can be adjusted via a slow-control interface. This feature has been of major relevance for many measurements performed during the spectrometer commissioning phases, including the measurements taken with the electron source (section 4.6) and the magnetic pulse system (section 5.3).

When data taking is initiated (manually or by script), the DAQ system records and processes the detector events. The event data is written to a binary file on the local hard disk by ORCA. Meta data like time stamps of the beginning and end of the data run or the detector configuration is stored together with the run data in a so-called *run header* file. Runs can be split into *sub-runs* by the control software, which is often useful for measurements with changing parameters (such as transmission function measurements).

The DAQ system takes run data in three modes that can be selected by the operator. The amount of data – and thus the size of the resulting run file – depends on the DAQ settings [A⁺15a]:

- **Trace mode:** In this setting, the ADC waveform observed at the detector is stored for each event. With a length of 2048 points per waveform, this setting results in 4 kiB of data being recorded for each event. The maximal event rate is strictly limited to roughly 8 kcps due to the required processing power and bandwidth to store the events to disk at sufficient rate. This setting is mostly used in special measurements, e. g. the investigation of detector properties.
- **Energy mode:** Here only the energy of each event is recorded, as determined by the DAQ system after processing the observed waveform. The system still operates on a per-event basis in this mode, but only stores 12 B per event to disk which is far lower than the 4 kiB in the trace mode. It therefore allows measurements at higher event rates than the trace mode (more than 100 kcps), and is used in the majority of commissioning measurements.
- **Histogram mode:** This setting is intended for measurements at high event rates. An energy histogram is created for each detector channel, merging all events in one (sub-)run. This results in comparatively small file sizes with 8 kiB per channel, regardless of the number of processed events. Event rates up to the Mcps regime are possible in this mode.

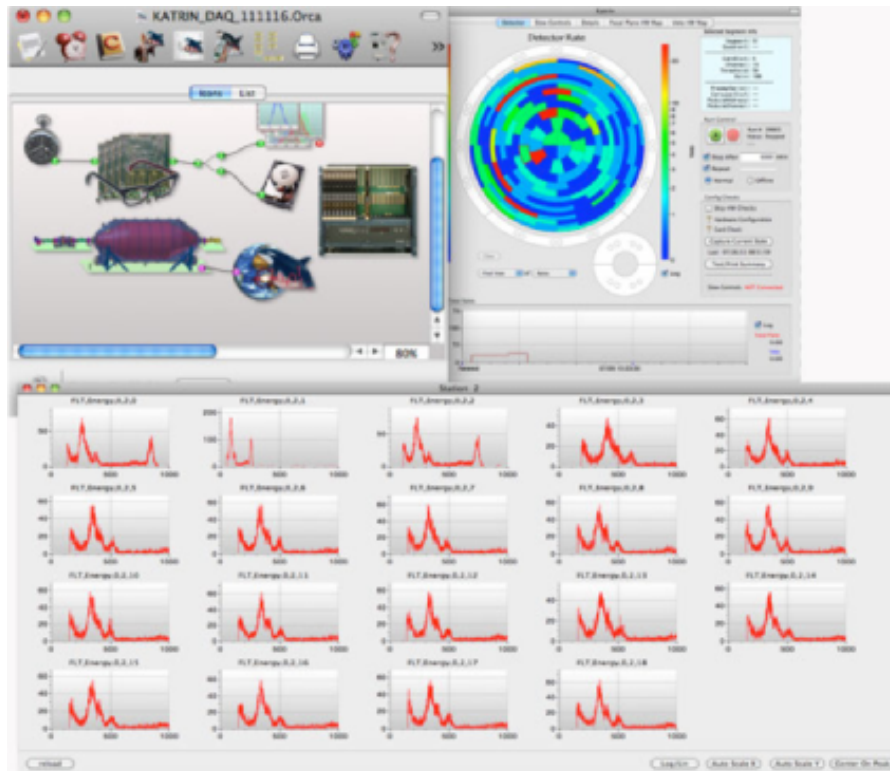


Figure 3.8.: The ORCA software at the FPD system. The DAQ system is configured by individual software modules that control operational parameters, measurement runs, the DAQ hardware etc. (upper left). While data is taken, an event rate is displayed using the FPD pixel mapping (upper right). The window also shows a rough estimate of the total event rate (without any processing) at the bottom and allows to start and stop (sub-)runs. The bottom window shows ADC histograms for several detector channels. Figure from [Kle14].

Typical runs using the energy mode produce files of several 100 MiB. The file sizes can increase to more than 1 GiB for runs with increased event rate, such as measurements with the electron source (at rates of 5 kcps or more on a single pixel) or with artificially increased background sources (e. g. with radioactive sources or at enhanced vacuum pressure).

After a run has been taken and saved to disk, the file is copied to a *redundant array of independent disks* (RAID) server, where it is further processed. The automated processing involves consistency checks, automated conversion into a ROOT tree structure, and merging with data from the FPD veto system (if activated). Both the original and the processed file are stored on the server, together with log files and other information about the automated processing. Meta data about the run configuration is saved independently in the run database. The run data is then made available to analysis software such as BEANS, which is discussed in section 3.7 below.

3.6.2 Sensor data from the slow-control systems

Sensor readings and other operational parameters monitored by the slow-control system are stored in another database. The storage and processing of the data is handled by a web server application

named ADEI¹⁴, which is written in PHP¹⁵. It manages the retrieval of sensor data from the local databases of the slow-control system and merges the data into a global database, from where it can be accessed by analysis software.

In addition, the KATRIN database¹⁶ stores other information relevant to the experiment. In contrast to the run and slow-control databases, it allows changes and updates of the user-generated information. The database holds values related to sensor calibration – which may change over time, therefore requiring the ability to update the database entry – or the assignment of KATRIN numbers¹⁷ to sensor channels [Kle14].

When sensor values are accessed via KaLi, the corresponding *ADEI path* is looked up in the KATRIN database. KaLi then accesses the slow-control database to retrieve the requested sensor value. If a calibration entry is available, KaLi can automatically return a calibrated sensor value. It is also possible to apply certain operations on the server side, such as taking the average or computing the standard deviation of multiple measurements in a given time period. This reduces the amount of data that is transferred to the client system and allows server-side caching of results.

To further reduce the required network traffic, all run and slow-control data is cached on the client system by default. This enables the user to perform *offline analysis* once the necessary data has been transferred to the local system, i. e. without requiring an internet connection. The simulation software *Kassiopeia* contains an interface to retrieve sensor values via KaLi, which allows to set up simulations that use actual experimental parameters.

3.7 Analyzing measurement results with Beans

In principle, the analysis of measurements could be performed with KaLi alone to retrieve and process all data, especially when using KaLi in combination with a plotting and analysis framework like ROOT. There are examples at KATRIN where this approach is implemented, e. g. to analyze measurements of the $^{83\text{m}}\text{Kr}$ conversion line at the monitor spectrometer [E⁺14].

Another, more flexible approach is provided by BEANS (figure 3.9). The software written in C++ is focused on analysis and part of the KASPER framework. It consists of a set of classes that process measurement data for various tasks. It includes methods to retrieve data from the run and slow-control databases, to apply calibrations, to merge and split runs, or to fit a data set [Eno15, Eno13].

Analysis scripts for BEANS can be written in a special file format called *KTF file*, where each analysis step is listed with the corresponding parameters. These files can be set up interactively in a web browser interface provided by VisualBEANS. Alternatively, the available classes can be utilized in a stand-alone application that is written in C++. The latter approach offers more flexibility to the analysis as BEANS classes can be combined with regular C++ code. It also allows user-defined extensions of the BEANS framework (section 3.7.2).

14. KATRIN Data Extraction, <http://katrin.kit.edu/adei-katrin/>

15. PHP: Hypertext Preprocessor, <http://php.net/>

16. KATRIN Database Administrator, <http://katrin.kit.edu/katrin-ng/>

17. The KATRIN numbering scheme allows to uniquely identify every part of the experiment, from sensor and detector channels to hardware pieces. Every KATRIN number follows the scheme *NNN-XXXX-M-nmmn-ZZZZ*, where *NNN* denotes the experimental section, *XXXX* is an alphabetic descriptor, *M* indicates the type of functionality, *nmmn* is a serial number, and *ZZZZ* is a component or channel specifier.

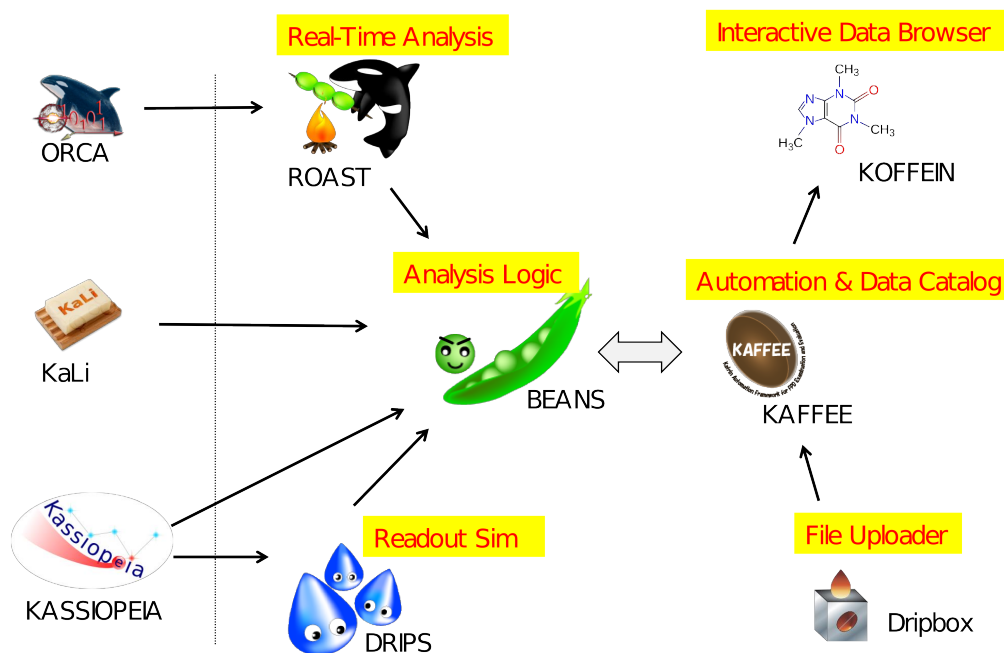


Figure 3.9.: BEANS peripheral software. The analysis logic provided by BEANS can directly process experimental data from KaLi or simulation data from Kassiopieia. Real-time analysis (i. e. while data is taken) is possible through the ROAST module which provides an interface to ORCA. The response of the detector system can be included in simulations via DRIPS. An user interface to BEANS exists through VisualBEANS (not shown here) which allows to configure analysis chains in a web browser. The KAFFEE system automatically applies analysis chains to measurement runs and includes an online file-storage system (Dripbox) and a data viewer (KOFFEIN). Figure from [Eno15].

3.7.1 Analysis with BEANS

To analyze the measurements that are discussed in this thesis, analysis code has been implemented in C++ using the BEANS framework. Although the individual analysis is often specific to the actual measurement, common patterns occur in many analysis scripts. The analysis itself can be viewed as an *analysis chain*, where the output at one step defines the input at the next step. This approach is derived from a concept known as *functional programming*, and allows an intuitive description and implementation of the analysis tasks.

Analysis objects

An analysis chain typically consist the following patterns, which will be shortly discussed here in order to explain the concepts that are utilized to analyze measurements:

- **Event readout:** Before an analysis can be applied, the observed events have to be retrieved from the run data file. When a specific run is analyzed for the first time, the ROOT file containing the event data is retrieved from the run database server with the help of KaLi. Different classes are available for the different event types, e. g. waveform or energy events (section 3.6.1). The retrieved events are added to the analysis chain and processed sequentially by following analysis objects.

```
(beans
  .Append(new KDWaveformEventReadout())
  .Append(new KDEnergyEventReadout())
);
```

- **Energy calibration:** In many cases, the analysis operates on the energy of the individual events. The detector data only contains the corresponding ADC channel for the events, therefore energy calibration has to be applied before the analysis. For the FPD system, calibration measurements are performed with an ^{241}Am source at regular intervals, and the updated calibration data for each detector pixel is added to the calibration database (section 3.6.2) [Har15].

BEANS handles the retrieval of the calibration information from the database server via KaLi, and applies the calibration to each processed event. The time frame to select the corresponding calibration entry is determined automatically from the known time stamp of each event.

```
(beans
  .Append(new KDFpdEnergyCalibration())
);
```

- **Energy, pixel and coincidence cuts:** Data cuts are a common pattern which is used in many analysis scripts. Often the analysis must be limited to a specific energy region called the *region of interest* (ROI). For example, in case of transmission function measurements the analysis includes only the signal electrons which are observed at a defined energy, and for background measurements the analysis often discriminates between low- and high-energy regimes. Additionally, the detector systems have a certain noise level below a defined threshold energy; events in this region are typically excluded from analysis. In BEANS it is possible to select or reject events based on their energy.

Pixel cuts are often applied to take into account the positional information which the pixelated detectors provide. In case of the FPD with 148 pixels organized in 13 pixel rings, the analysis can be limited to a specific region of the flux tube volume in the spectrometer. This is often applied to investigate radial dependencies of the observed rate. In transmission function measurements the electron beam typically only hits one detector pixel, which allows to exclude the irrelevant pixels.

Furthermore, coincidence cuts can be applied to exclude or select events that were observed within a given time frame after an initial event. Examples are the exclusion of accidental coincidences which would affect the analysis result, or required coincidences with a synchronization signal. The latter is used in time-of-flight measurements with the electron source and in measurements where active background reduction methods are combined with a pulsed electron beam (section 5.3).

```
(beans
  .Append((new KDEnergyRangeRejection()
    ->SetRange(0, 5200))
  .Append((new KDPixelSelection()
    ->AddPixel(2))
  .Append((new KDCoincidenceSelection()
    ->SetReferenceChannelGroup(KDChannel::kRef)
    ->SetTimeWindow(-100e-6, 100e-6))
);
```

- **Energy and ADC spectra:** Histograms of the ADC channels or the energies of all processed events represent the observed energy spectrum. ADC spectra are mainly used to calibrate the detector system by comparing the position of measured peaks to a known energy spectrum. In BEANS it is often more helpful to use the energy spectrum, which requires that an energy calibration has been applied beforehand. The energy spectrum allows to perform consistency checks of the measured data and to determine or verify the ROI for energy cuts. BEANS also provides different fit models to analyze the energy spectrum and determine peak positions.

```
(beans
  .Append((new KDAdcHistogram())
    ->SetBin(240, 0, 2400)
    ->SetTitle("ADC spectrum")
    ->SetYAxisLog())
  .Append((new KDEnergyHistogram())
    ->SetBin(250, 5e3, 30e3)
    ->SetTitle("Energy spectrum, 5-30 keV"))
  .Append((new KDPeakFit())
    ->SetSearchRange(10e3, 25e3))
);
```

- **Rate trend graphs and hit maps:** Another basic functionality is the determination of the observed count rate. The time dependency over the full run can be investigated by a so-called *rate trend*, which shows the count rate at specific intervals. Again it is possible to apply fits, e. g. to determine the average rate. The rate pattern on the FPD wafer is also often investigated in background measurements as it can provide important information about the corresponding sources. In BEANS the hit pattern can be visualized by showing the total count rate on each individual detector pixel, using the actual layout of the pixelated wafer.

```
(beans
  .Append((new KDRateTrendGraph())
    ->SetTickWidth(100e-3)
    ->SetTitle("Rate Trend (100 ms bins)"))
  .Append(new KDRateTrendAverage())
  .Append((new KDChannelRateHistogram())
    ->SetSchematicMapping("fpd")
    ->SetTitle("FPD hit map"))
);
```

- **Event tagging:** In addition to data cuts, it is also possible to add *tags* to specific events that are relevant at a later point in the analysis. This is often used with external synchronization signals, such as the start time of electrons generated by the pulsed electron source. In this case, the time-of-flight of the electrons can be determined from the detector arrival time.

```
(beans
  .Append((new KDChannelGroupTagging())
    ->SetTagName("Start")
    ->AddChannelGroup(KDChannel::kRef))
);
```

- **Inter-arrival time histograms:** The *inter-arrival time* is the time between two observed events. Because at higher rates there are more events observed at the detector within the same time frame, the count rate can be determined directly from the inter-arrival time histogram. Fur-

thermore, it allows to investigate the Poissonian nature of the observed events. Electrons created in the pulsed electron source or by radioactive decays cause deviations from the Poissonian behavior, which can be used to discriminate such events.

When the inter-arrival times are determined w. r. t. to a synchronization signal, the resulting histogram represents the time distribution of events observed within each synchronization interval. This feature can be used to create time-of-flight distributions or to combine applications of the active background reduction methods.

```
(beans
  .Append((new KDIntervalHistogram())
    ->SetUnit_ms()->SetBin(100, 0, 1)
    ->SetTitle("1 ms scale")
    ->SetYAxisLog())
  .Append((new KDIntervalHistogram())
    ->SetStartEventTag("Start")
    ->SetStartLatency(1000e-6)
    ->SetTitle("Time-of-flight distribution")
);
```

- **Slow-control values:** Similar to the automated interaction with the run database servers, BEANS also provides an interface to access slow-control values for a specific run. The KaLi module is utilized to retrieve and pre-process data from the slow-control database. Slow-control data often holds crucial parameters for the analysis tasks, e. g. the voltage applied to the spectrometer (which is needed to automatically determine the ROI of signal or background electrons) or the current settings of the electron source. Slow-control values are specified by their KATRIN number (section 3.6.2). It is also possible to apply fits to slow-control data.

```
(beans
  .Append((new KDSlowControlGraph())
    ->SetKatrinNumber("436-WHV-0-9999-0001")
    ->SetValueFactor(-1)
  )
  .Append((new KDLinearFit())
);
```

- **Sub-run splitting:** Most of the BEANS classes can operate on a sub-run level instead of the complete run. This is implemented by splitting the run into a certain number of segments and processing each segment individually in the analysis chain. The segmentation is either already included in the run data file (if sub-runs were created during the data taking ; section 3.6.1), or can be introduced in BEANS (e. g. by splitting the run on synchronization events).

```
(beans
  .Append((new KDDynamicVirtualSubRun())
    ->SetStartEventTag("RefPulse"))
  .Append((new KDEnergyHistogram())
    ->SplitBySubRun())
);
```

- **Run-segment graphs:** This pattern combines many of the elements listed above. A run-segment graph typically consists of one data point per (sub-)run, which is determined from analyzed data. It therefore allows to combine the results from previous analysis objects into a single graph.

A prominent example is the plotting of a transmission function that was measured with the electron source. Such a measurement is divided into sub-runs with fixed electron energy where the event rate is measured for a certain time (typically about 10 s). The energy is varied between each segment, and the observed rate dependency describes the transmission function (section 4.4). In BEANS, the transmission graph is created by splitting the run into sub-run segments, determining the electron energy from the slow-control parameters in each segment, and plotting the observed count rate against the electron energy.

In the example below, the parameters are determined using advanced patterns that extend the BEANS framework; this is explained in section 3.7.2.

```
(beans
  .Append((new KDEGunRunCondition()))
  .Append((new KDEnergyHistogram()
    ->SplitBySubRun()
    ->SetBin(60000, 0, 60000))
  .Append(StatFunction("ElectronRate", ElectronRate))
  .Append((new KDStatTree())->DumpOnFill())
  .Append((new KDRunSegmentGraph()
    ->SetXValue("Condition/EGun/StartVoltage")
    ->SetYValue("ElectronRate")
    ->SetXAxisTitle("surplus energy (eV)")
    ->SetYAxisTitle("electron rate (cps)")
  ));
```

- **Drawing and saving results:** Each histogram or graph that has been created by the analysis chain can be exported to a graphics file, which allows easy investigation of the results. Furthermore, BEANS includes an internal plotting framework to visualize the results while the analysis is running. It is also possible to animate the analysis results while the events are processed. This is especially useful for “real-time analysis” that is performed while data is taken.

```
(beans
  .Append((new KDDraw()
    ->SetImageFileName("TransmissionFunction.png")
  ))
);
```

Executing an analysis script

After the analysis script has been compiled, the program can be executed on the command line. Several built-in options allow to change the amount of output that is printed to the terminal or to store the analysis results into a ROOT file. This feature can be used to apply post-processing (e. g. with the *Peaberry* framework discussed in section 3.8).

The basic terminal commands to analyze a measurement with BEANS are

```
make analysis # g++ -std=c++11 -o analysis $CXXFLAGS $LDLIBS analysis.cxx
./analysis [options] <run> [additional runs ...]
```

Commonly used options are `--output=results.root` to save the analysis results into a ROOT file; `--runlength-limit=seconds` to limit the analysis to a fraction of the total run time¹⁸; and `--offline` to skip the communication with the KATRIN database servers (which allows to perform an analysis without an active internet connection as long as all the necessary data files are present on the local system).

The run number can include a prefix to select the detector system (section 3.6.1), e. g. `fpd20001` for the FPD system or `mos168000` for the monitor spectrometer. By default, the FPD system is assumed. Multiple runs can be merged by using a special syntax in the run number: `20001 ..20005` will consider FPD runs #20001 to #20005 as a single run in the analysis, without the need to list each run individually.

The following example is adapted from the BEANS Cookbook that is available with the KASPER source code¹⁹. It shows the basic functionality of BEANS to generate a raw (uncalibrated) ADC spectrum together with a calibrated energy spectrum from a measurement run. The KATRIN database (section 3.6.2) is accessed to retrieve calibration data, and the file that contains the detector events is downloaded from the run database. The calibrated energy spectrum is also generated for each individual detector pixel.

```
#include <KDBeans.h>

using namespace std;
using namespace katrin;

int main(int argc, char** argv)
{
    KDBeans beans;

    (beans
     .Append(new KDEnergyEventReadout())
     .Append(new KDFpdEnergyCalibration())

     .Append((new KDAdcHistogram())
             ->SetBin(240, 0, 2400)
             ->SetYAxisLog()
             ->SetTitle("ADC, all range, log scale")
            )
     .Append(new KDDraw())

     .Append((new KDEnergyHistogram())
             ->SetBin(800, 0, 80e3)
             ->SplitByChannel()
             ->SetTitle("Energy, E < 80 keV")
            )
     .Append(new KDIndividualPixelDraw())
     .Append(new KDDraw())
```

18. This is often used for testing or debugging analysis scripts or in cases where the run file was corrupted during data-taking.

19. The BEANS Cookbook guides the user in creating analysis chains and contains examples for various analysis tasks. It is available via the KASPER Git repository, <https://nuserv.uni-muenster.de:8443/katrin-git/kasper/tree/develop/Desaster/Examples/Cookbook> (internal site).

```

        .Append((new KDRateTrendGraph()
            ->SetTickWidth(10)
            ->SetTitle("Rate Trend, all range")
        )
        .Append(new KDRateTrendAverage())
        .Append(new KDDraw())
    );

    beans.Build(argc, argv).Start();

    return 0;
}

```

3.7.2 Extensions of the analysis framework

BEANS provides various ways to add user-defined extensions to the framework. Since BEANS uses object-oriented C++ code, it is possible to create derived classes that inherit from BEANS. An often used method is to create a specific **RunCondition**²⁰. This approach offers great flexibility since class methods are executed while measurement data is processed, which allows to modify the analysis at a fundamental level.

Another option is to implement user-defined functions that are called by BEANS during the analysis. This approach does not require to implement a specific analysis class, but also offers limited flexibility. It is thus better suited for less fundamental modifications, e. g. exclusion of specific events or post-processing of BEANS results. The following function types are available:

- **Event function:** The event function is called at each detector event that is processed by BEANS. It thus operates on a fundamental level and allows to modify event parameters (like the energy or time stamp of an event). Single events can be excluded by returning a `false` value, in which case BEANS ignores the event in the following analysis.
- **Pre-run/Post-run function:** These functions are called before or after a run or sub-run is processed. It allows to determine important parameters for the following analysis, e. g. the run length or the number of events observed.
- **Stat function:** This function is called after BEANS has processed measurement data and produced a histogram/graph. Code that modifies the results (e. g. to apply corrections) or derives parameters (e. g. to determine the electron rate from an energy histogram) can be implemented here.

For the analysis of the measurements performed with the electron source, a new `RunCondition` class `KDEGunRunCondition` was implemented²¹. The class determines the electron rate observed at the detector, taking into account multi-electron events (“pile-up”) that occur at higher rates. It also provides methods to access slow-control channels used by the electron source, e. g. to determine the voltage settings. Details of the available slow-control data and the performed measurements are explained in chapter 4.

20. This is done by inheriting from the `KDRunCondition` base class and implementing extensions inside the derived class.

21. All used analysis code is available in the KATRIN Git repository at <https://nuserv.uni-muenster.de:8443/katrin-git/analysisworkspace>

3.8 The post-analysis framework Peaberry

A post-analysis framework called *Peaberry* (abbreviated as **Pb**) written in Python²² has been developed over the course of this thesis. It is intended as an extension to BEANS (not as a replacement), which provides the pre-processed input data. Peaberry is part of the KASPER framework, although it contains no strict dependencies to KASPER modules. In the context of KATRIN, it will typically perform additional analysis using the output from BEANS, where basic analysis (e. g. energy calibration and run splitting/merging) has been performed already. It can also process output from Kassiopia simulations, or be used for stand-alone applications outside the KATRIN framework. The documentation of the Peaberry framework can be generated with *Sphinx*²³ from “docstrings” that are integrated with the source code.

The basic functionality of Peaberry is to provide the user with a ready-to-use framework where measurement and simulation results can be processed, analyzed and plotted. It contains methods to read data from different sources (e. g. ROOT, ASCII or JSON files), to apply fits using a variety of algorithms (e. g. least-squares or MCMC), and to plot the results. Most of these features are utilized from external Python modules that are discussed below.

Dependencies

Peaberry requires the following dependencies on external Python packages, which provide the basic functionality needed for data processing and visualization:

- **NumPy**: This package provides fundamental routines for scientific computing in Python, and is utilized by many other Python packages. It contains efficient array-manipulation functions to handle large data sets and implements a rich set of linear algebra and statistical algorithms. NumPy is distributed as open-source software under the *BSD license*²⁴.
- **SciPy**: The SciPy package extends the capabilities of NumPy for scientific applications. It provides user-friendly and efficient routines for tasks that are often found in natural sciences, e. g. numerical integration, optimization and minimization, linear and vector algebra, or statistical distributions. Like NumPy, it is distributed under the *BSD license*²⁵.
- **Matplotlib**: This plotting library visualizes data sets using various techniques of presentation. It is available under its own open source license, which is based on the *Python Software Foundation license*²⁶.

The following optional dependencies can be fulfilled to activate extension modules in Peaberry:

- **LMFit**: The LMFIt package implements a high-level interface to optimization and minimization problems for Python. It is based on the capabilities of SciPy, which includes a *Levenberg-Marquardt* fit routine. LMFIt allows to use fixed or constrained parameters, supports different fit methods (e. g. *Nelder-Mead* or *Conjugate Gradient*), and can compute confidence intervals

22. Python, <https://www.python.org/>

23. Sphinx: Python documentation generator, <http://www.sphinx-doc.org/en/stable/>

24. NumPy, <http://www.numpy.org/>

25. SciPy library, <https://www.scipy.org/scipylib/>

26. Matplotlib, <http://matplotlib.org/>

for the model parameters based on the F -test. These features will be further explained in section 3.8.3. LMFit is distributed as open source under the *MIT license*²⁷.

- **PyROOT:** The ROOT library contains many methods for minimization problems; one of the most popular is its *MINUIT2* implementation. PyROOT is a set of bindings to access ROOT's features (which is written in C++) directly from Python. Similar to LMFit, MINUIT allows fixed or constrained parameters and includes alternative fit methods like *MIGRAD* or *SIMPLEX*. The computation of confidence intervals is available in *MINOS*. These features will be further explained in section 3.8.3. ROOT and PyROOT are distributed as open source under the *LGPL license*²⁸.
- **emcee, corner:** A completely different approach to fitting is available through the *emcee* package, which implements an affine-invariant Markov-Chain Monte Carlo sampler that can be used to maximize the likelihood of a fit [FM⁺13]. The method has certain advantages that will be further explained below.

The *corner* package implements routines to visualize the outcome of the MCMC sampling process and is especially useful to investigate confidence intervals and correlations of the model parameters. Both modules are distributed as open source under the *MIT license*²⁹.

- **Cython:** Cython is essentially an implementation of Python in C++. It allows to implement algorithms in Python which are then translated to C++, compiled, and made available through the regular Python scripting interface.

At first glance this might not sound overly useful; however, this allows certain speed optimizations which are not possible in Python itself. The main difference is that Python code is interpreted at run time and performs many time-intensive type checks. For code that is executed often at runtime, the resulting speed impact can add up to a level where performance is severely worse than alternative implementations in C or C++.

Re-implementing the Python code in Cython can result in a performance gain of several orders of magnitude. Since the code in the end still uses the Python interface, “cythonized” modules can be easily integrated with other Python modules. Because the Cython-code still contains the Python interface, it is easy to utilize “cythonized” code from other Python scripts. Cython is distributed as open source under the *Apache license*³⁰.

3.8.1 Software design

The Python programming language favors an object-oriented approach for the implementation, the Peaberry package is thus divided into several modules that extend each other (figure 3.10). It is easily possible to create derived classes where specialized code is implemented (e. g. specialized fit models or file handlers to access a specific data format). Some modules are optionally available when the requirements on external Python packages are met. This is the case for modules that extend the core functionality, e. g. MCMC fitting or the interface to read BEANS output.

The different Peaberry modules are explained in the following:

27. LMFit, <http://cars9.uchicago.edu/software/python/lmfit/>

28. ROOT, <https://root.cern.ch/root/>

29. emcee: The MCMC hammer, <http://dan.iel.fm/emcee/current/>

30. Cython: C-extensions for Python <http://cython.org/>

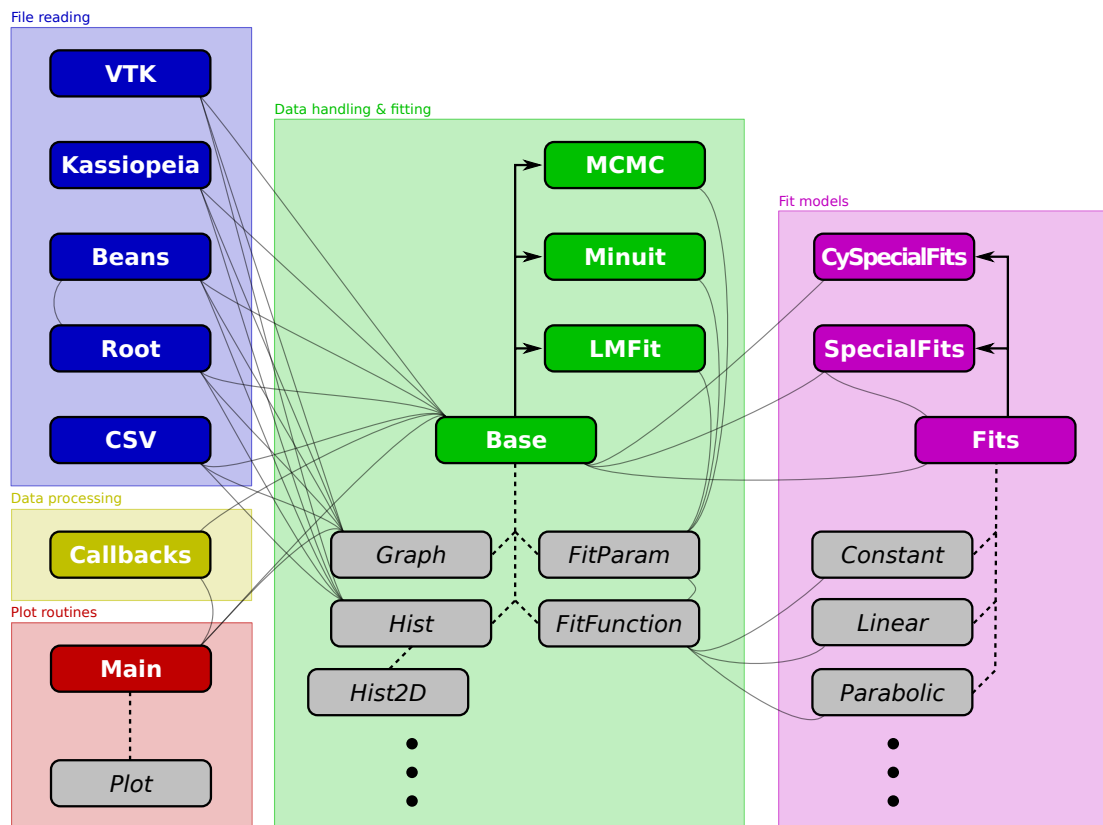


Figure 3.10.: Structure of the Peaberry framework. The framework can be divided into several core sections that implement classes (gray blocks) for basic data handling, fitting and plotting of the data, allow reading from different file formats, and provide various fit methods. The thick black lines indicate extensions of the base modules, e. g. to apply MCMC fitting instead of SciPy’s default method. The thin gray lines indicate dependencies between the modules or classes. Note that only the core classes are shown, others have been skipped for brevity. A complete documentation can be generated by the *Sphinx* toolkit.

- **Base:** In this module, the basic data-handling methods are implemented. This includes the representation of a data set as graph (x- and y-values) or histogram (bins and counts), the base class for all fit models, and a basic fit method which uses SciPy’s default fitting method.

The `Base.Graph` and `Base.Hist` essentially contain arrays that store the data points including their uncertainties (if available). All data-handling routines support asymmetric uncertainties (lower and upper error bars). The classes also provide basic data-manipulation routines, e. g. to combine or scale graphs, stack histograms, or change the ordering of the data points.

The `Base.Fit` class implements basic routines, e. g. to compute the residuals of a fit or to compute the resulting χ^2 and p -values. It allows to apply a least-squares fit to the data, using any (user-defined) fit model that can be implemented elsewhere in the code. SciPy’s default fitting method `optimize.curve_fit` performs a *Levenberg-Marquardt* fit and allows to provide an initial set of fit parameters for the fit. Parameter uncertainties can be derived from the resulting covariance matrix. The method does not support the inclusion of x-errors in the fit, the def-

inition of parameter constraints or the computation of confidence intervals. These advanced features are available in other fit modules that are discussed below.

All fit models are implemented as classes that derive from **Base.FitFunction**, which contains the basic definition of a fit function that operates on a set of data points and a given number of model parameters. The base class provides methods to evaluate the fit function at a given point, which is utilized by Peaberry's fitting and plotting routines. A *fit band* can be drawn in the output plot that visualizes the uncertainty region covered by the fit function. The total uncertainty is computed by varying each parameter independently within a given uncertainty range (e. g. using the 1σ -uncertainties) and taking the minimum and maximum value of all variations.

The fit model utilizes the **Base.FitParam** class, where each model parameter is defined with name, optional unit (for display in the plot's legend), current value, uncertainties, covariances and possible constraints. The value, uncertainties and covariances are updated after a fit has been applied. The constraints are only relevant if supported by the fit method.

- **Main:** This core module is responsible for processing and plotting the data that is analyzed. It is strongly based on the capabilities of the Matplotlib package, which allows to create data plots using a variety of methods to visualize the output.

The module contains one class **Main.Plot**, which defines an output frame where data is visualized. It provides automatic adjustments and routines to plot residuals, draw secondary axes or color bars, and to visualize fit results including their uncertainties.

- **Callbacks:** Different callback functions can be added to the analysis of individual data sets. These functions are executed after the data set has been initialized, but before its contents are plotted. This approach allows a dynamic code structure that can be easily adapted to other analysis tasks.

The module implements several callback functions that are often useful with analysis, e. g. **Callbacks.ApplyFit** to apply a fit to the data set (using the associated fit model and method) or **Callbacks.LoadFitResults/SaveFitResults** to load/save fit results from/to a JSON file³¹. Other callbacks allow to apply numerical differentiation or integration or to compute a moving average of the data.

- **Fits:** This module contains a set of basic fit models, e. g. **Fit.Constant** (zero-order polynomial, i. e. constant value), **Fit.Linear** (first-order polynomial, i. e. linear function with offset) or **Fit.Parabolic** (second-order polynomial with offset). Exponential functions (decay curves) and Gaussian distributions and their integrated forms (error functions) are also implemented here.
- **SpecialFits:** Fit models that are specialized for KATRIN are moved into this module, which allows to release Peaberry to the public without containing KATRIN-specific code (an approach similar to KSC; see section 3.2). Many fit models that are used with the electron source are implemented in this module, e. g. the Fowler model to determine a work function of a metallic material (section 4.2).
- **CySpecialFits:** This module contains "cythonized" versions of fit models specific to KATRIN, which is currently limited to transmission function models. These fit models involve multiple

31. JavaScript Object Notation, <http://www.json.org/>

integrations of rather complex mathematical expressions, which are significantly slowed down in Python. Using the Cython implementation, a speed benefit of up to two order of magnitude is observed.

- **CSV:** This module implements the data handlers **CSV.Graph/Hist** for plain-text data files, e. g. the *comma-separated values* (CSV) format that can be used with various spreadsheet software or other whitespace-separated formats that are often used with *Gnuplot*³².
- **Root:** This module contains the data handlers **Root.Graph/Hist** to read graphs or histograms from a ROOT file; including a fit that can be associated with the ROOT graph. The module also implements a fit class that provides an interface to ROOT's fitting capabilities.
- **Beans:** Here an extension of the Root module is implemented, which provides a more user-friendly interface to ROOT output that is produced by BEANS (section 3.7). The classes **Beans.Graph/Hist** are used to access a specific graph or histogram in BEANS output.
- **Kassiopeia:** This is another extension of the Root module, which provides access to output files from Kassiopeia simulations that are stored in the ROOT format. To utilize the event-based structure of the simulation output (with steps, tracks etc.; cmp. section 3.3.8), the module implements an iterative reader **Kassiopeia.KassiopeiaReader**. It also allows a filtering of the file contents to reduce memory consumption. The classes **Beans.Graph/Hist** are used to access specific fields in the Kassiopeia output tree.
- **VTK:** Similar to the Kassiopeia module, this module is intended to read simulation data directly from a VTK output file. This is mainly useful when Kassiopeia output is split between the ROOT and VTK formats, e. g. writing track data to a ROOT file and step data to a VTK file. To access step data in this case, the class **VTK.VTKReader** implements an iterative reader that retrieves specific data sets from the VTK file.
- **LMFit:** This module implements an extension of the basic Fit class which makes use of the advanced features that LMFIt provides. The implementation in **LMFit.Fit** is transparent to the user: the fit method can be easily switched by replacing `Base.Fit(Fits.xyz` with `LMFit.Fit(Fits.xyz)` in the analysis script. The LMFIt package and its benefits are further discussed in section 3.8.3).
- **MINUIT:** The ROOT framework contains an implementation of the well-known MINUIT code that was originally written in Fortran. The corresponding C++ implementation in ROOT is known as *MINUIT2*. Like other specialized fit methods that are available in Peaberry, this module extends the basic Fit class and provides an interface to MINUIT's capabilities via **MINUIT.Fit**. Similarly to LMFIt it extends the basic functionality of **Base.Fit**. The MINUIT2 software is discussed in section 3.8.3.
- **MCMC:** Markov-Chain Monte Carlo methods utilize Bayesian statistics and provide a completely different approach to fitting problems. This Peaberry module uses the *emcee* implementation of an MCMC sampler. The **MCMC.Fit** class provides an extension of **Base.Fit** that uses MCMC sampling to perform a fit. MCMC and the sampler provided by *emcee* are discussed in section 3.8 and 3.8.3.

32. Gnuplot, <http://www.gnuplot.info/>

3.8.2 Analysis procedure

The basic procedure to process and display a data set is as follows: An instance of the **Plot** class is created, and data sets (**Graph** or **Histogram**) are added. Each data set contains a number of data points, which can be created from scratch (e. g. using a mathematical expression), read from an input file, or derived from existing data. A fit can be associated with a data set; it is defined by a combination of the *fit model* (e. g. linear, parabolic, or more specialized functions) and the *fit method* (e. g. least-squares, MINUIT, or MCMC). Callback functions are added to process the data in order to apply a fit or to pre-/post-process the data. The callback functions are executed in order, either automatically by the **Plot** object before drawing or manually by the script.

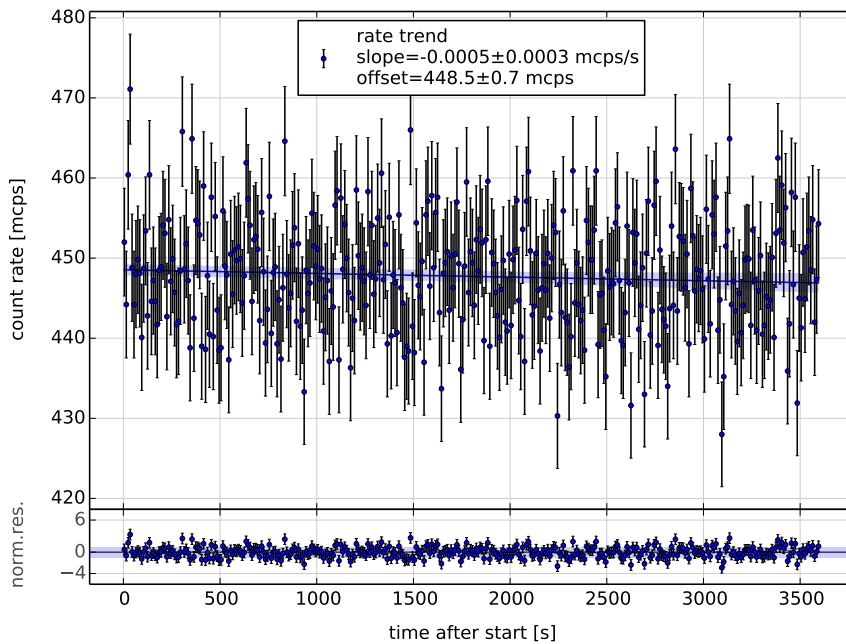


Figure 3.11.: Example output of a Peaberry analysis run. The analysis script shown in this section was applied to a SDS-2 measurement run (#fpd20001). The rate trend graph has been produced by BEANS beforehand with a tick width of 10 s. A linear fit was applied to the graph in Peaberry, yielding a vanishing slope and an average rate of 448.5(7) mcps at $\chi^2/\text{ndf} = 1.05$.

The following example shows the basic features of Peaberry, reading a data set from a BEANS file and applying a linear fit before drawing the results and saving the output to PDF and PNG files (figure 3.11). The data file used in the example can be generated with the BEANS analysis script shown at the end of section 3.7.1.

```
#!/usr/bin/env python
import Peaberry as Pb

# create Plot instance
p = Pb.Main.Plot("")
p.setLabels(xlabel="time after start [s]", ylabel="count rate [mcps]")
p.setStyle('plot', dict(residuals=True, grid=True))

# create linear fit model, define initial parameters
```

```

f = Pb.Base.Fit( Pb.Fits.Linear() )
f.fitfunc.setFitValues(dict(slope=0.0, offset=500))
f.fitfunc.setParamUnits(dict(slope="mcps/s", offset="mcps"))

# create graph from BEANS output, add fit model
g = Pb.Beans.Graph("rate trend", plot=p, fit=f)
g.fromBeans(filename="fpd20001.root", plotname="TrendGraph00")

# add callbacks to apply fit and save results
g.addCallback(Pb.Callbacks.ApplyFit)
g.addCallback(Pb.Callbacks.SaveFitResults)

# process data and save plot to graphics file
p.generate()
p.savePlot("fpd20001")

```

3.8.3 Fit methods

A core feature of Peaberry is the ability to apply fits to data sets. For the measurements and simulations presented in this thesis, Peaberry was used to analyze the results and apply fits in order to derive the required parameters. It is important to compare the results of different fit methods to verify that their implementation is correct (figure 3.12 and table 3.1).

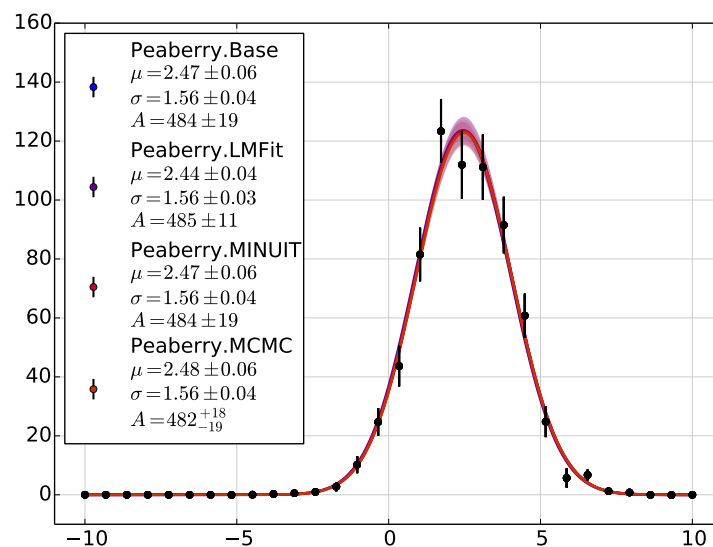


Figure 3.12.: Comparison of different Peaberry fit methods. An exemplary data set with 30 data points following a normal distribution with $\mu = 2.5$, $\sigma = 1.5$ was fitted using the different methods available in the Peaberry framework. The data points are randomly shifted on the y -axis to impose an artificial error and make the example more realistic. The results are all in agreement with each other, including the estimated uncertainties. Note that MCMC in this case determined an asymmetric confidence interval. The MINUIT fit was performed with MINOS to compute uncertainties.

Table 3.1.: Results from different Peaberry fit methods.

parameter		truth	SciPy	LMFit	MINUIT	MCMC
mean	μ	2.5	2.47(6)	2.44(4)	2.47(6)	2.48(6)
width	σ	1.5	1.56(4)	1.56(3)	1.56(4)	1.56(4)
amplitude	A	500	484(19)	485(11)	484(19)	482(18)
	χ^2	—	32.32	32.72	32.32	32.34
	χ^2/ndf	—	1.197	1.212	1.197	1.198

The fit process

In general, a fit method tries to minimize the sum of the residuals – the quadratic difference between the fit result and the actual observation at each data point. This can be expressed in the context of *chi-square statistics*, where it is assumed that the probability for an observation x at an expected value μ is approximated by a normal distribution,

$$p(x|\mu, \sigma) = \frac{1}{\sigma\sqrt{2\pi}} \cdot \exp\left(-\frac{(x - \mu)^2}{2\sigma^2}\right). \quad (3.46)$$

Here $\mu = \mu(\vec{\Theta})$ is the estimated value that is defined by the vector of free parameters $\vec{\Theta}$, and σ is the standard deviation of the observed value.

The *likelihood* $L(\vec{\Theta}|\vec{N})$ of a set of model parameters $\vec{\Theta}$, given a particular set of observations \vec{N} , equals the probability $P(\vec{N}|\vec{\Theta})$ to observe the outcome \vec{N} , given a set of parameters $\vec{\Theta}$. It can be expressed by the product of the probabilities of n individual observations N_i :

$$P(\vec{N}|\vec{\Theta}) = \prod_{i=1}^n p(N_i|\vec{\Theta}) = L(\vec{\Theta}|\vec{N}). \quad (3.47)$$

The likelihood is maximized for the parameter set $\vec{\Theta}$ which produces the highest probability to observe the outcome \vec{N} .

A fit routine thus tries to vary the parameter set in order to find the maximum likelihood, which corresponds to the best fit of the given model to the observed data. In practice, the likelihood is often written as negative *log-likelihood*, which is numerically more convenient as (3.47) reduces to a sum of probabilities:

$$-\ln L(\vec{\Theta}|\vec{N}) = -\ln \prod_{i=1}^n p(N_i|\vec{\Theta}) = -\sum_{i=1}^n \ln p(N_i|\vec{\Theta}). \quad (3.48)$$

Using chi-square statistics, the likelihood $-2\ln L = \chi^2$ can be constructed from (3.46),

$$-2\ln L = \sum_i \left(\frac{x_i - \mu_i(\vec{\Theta})}{\sigma_i}\right)^2 + \dots = \chi^2, \quad (3.49)$$

where σ_i is the statistical uncertainty of the observation x_i . In case of Poissonian-distributed observations (e. g. in count rate experiments), the uncertainty is given by $\sigma = \sqrt{N}$ where N is the number of observed counts. Common implementations of fit routines are based on the minimization of the χ^2 value, using different techniques (fit methods) to vary the model parameters $\vec{\Theta}$.

LMFit

LMFit is a Python package for advanced fitting, which extends the fitting capabilities of SciPy. It uses an object-oriented structure to define the model parameters and the minimizer method [NS⁺16].

The main advantages of LMFit over SciPy's standard tools are:

- Support for constrained parameters (i. e. lower or upper limits), and the possibility to temporarily fix parameters during the fit.
- Many supported fit methods in addition to the *Levenberg-Marquardt* algorithm that is often used by fit software such as *Gnuplot*. One example is the slower, but more robust *Nelder-Mead* (simplex) algorithm, which applies randomization and is thus more tolerant of local minima.
- Computation of confidence intervals (i. e. parameter uncertainties) by applying a so-called *F-test* to each independent parameter. This method is especially important when parameters are highly correlated or when their χ^2 profile is not parabolic. In both cases, the standard uncertainty estimation using the covariance matrix is insufficient and may underestimate the actual uncertainties.

The implementation of constrained parameters follows the approach of *MINPACK-1* (which is also used by MINUIT). In order to allow the fitter to evaluate the full parameter space, it is required to transform the “external” (constrained) parameters \bar{p} to unconstrained “internal” parameters \bar{p}_{int} that can be varied freely during the fit process. The transformation is described by three equations:

$$p = \begin{cases} p_{min} + (\sin p_{int} + 1) \cdot \frac{p_{max} - p_{min}}{2} & \text{for } p = [p_{min}; p_{max}], \\ p_{max} + 1 - \sqrt{p_{int}^2 + 1} & \text{for } (p = -\infty; p_{max}], \\ p_{min} - 1 + \sqrt{p_{int}^2 + 1} & \text{for } p = [p_{min}; \infty). \end{cases} \quad (3.50)$$

Confidence intervals can be computed via *F-tests*, which compare the “null model” (the best-fit result) with alternate models where one of the parameters is varied while the remaining parameters are fixed. The F-test is defined by

$$F(P_{fix}, N - P) = \left(\frac{\chi^2}{\chi_0^2} - 1 \right) \cdot \frac{N - P}{P_{fix}}, \quad (3.51)$$

where χ_0^2 corresponds to the best-fit result and χ^2 to the alternative model. N is the number of data points, P the number of fit parameters, and $P_{fix} = P - 1$ the number of fixed parameters in the alternate model. The free parameter is varied until the difference in the χ^2 values cannot be explained anymore by statistical effects from the reduced degrees of freedom. This method relies on a repeated evaluation of the fit model around the best-fit result, and is thus more robust than deriving the confidence interval from the covariance matrix where a parabolic shape of the parameter's confidence regions is assumed. For complex fit models, the uncertainties computed by this method are therefore more accurate.

In Peaberry's implementation of the LMFit class, the χ^2 value is computed from the fit model μ with free parameters $\bar{\Theta}$ and the given data set (\bar{x}, \bar{y}) with (optional) uncertainties $(\bar{\sigma}_x, \bar{\sigma}_y)$.

$$\chi^2 = \sum_i \left(\frac{y_i - \mu(x_i, \bar{\Theta})}{\sigma_i} \right)^2. \quad (3.52)$$

Uncertainties for the abscissa (x-values) are typically not included in χ^2 -fits using this definition since only the differences on the ordinate (y-axis) are considered, i. e. $\sigma_i = \sigma_{y,i}$. To include $\sigma_{x,i}$ values in the fit, the gradient of the fit model at the data point (x,y) is used to scale the uncertainty σ_x to an effective ordinate uncertainty which is then added to σ_y :

$$\sigma_i = \sigma_{y,i} + \sigma_{x,i} \cdot \left. \left| \frac{d\mu(x_i, \bar{\Theta})}{dx} \right| \right|_{x=x_i} . \quad (3.53)$$

MINUIT

In addition to LMFit it is possible to use the features of MINUIT in Peaberry. The ROOT framework contains a C++ implementation of the software called *MINUIT2*. It is made available to Python scripts via the *PyROOT* bindings. Similarly to LMFit, MINUIT provides advanced fit methods and an improved estimation of confidence intervals. MINUIT is widely used in scientific applications [JR75].

In comparison with other fit software, MINUIT2 has many advantages:

- Written in the platform-independent C++ language and thus available on many systems.
- Excellent numerical accuracy and computational performance (equivalent to the original MINUIT implementation in Fortran).
- The possibility to use constrained or fixed parameters. MINUIT uses the *MINPACK-1* method, which is also utilized by LMFit as shown in (3.50).
- Different methods to minimize the χ^2 value of the problem. By default, MINUIT uses the *MIGRAD* algorithm which is suitable for many fit problems. Alternate options include the *SIMPLEX* method, which is an implementation of the robust Nelder-Mead algorithm, or a combination of the two.
- Different approaches to estimate parameter uncertainties, such as the default methods *MIGRAD* and *HESSE*, or the more advanced *MINOS* algorithm.

The *MIGRAD* fit algorithm is an implementation of the Davidon–Fletcher–Powell algorithm, which is based on Newton’s method to find the roots of a given function. The algorithm starts with a quasi-random solution to the problem, and iteratively changes the solution to converge to the optimal result. A disadvantage is that it depends on knowledge of the first derivatives of the fit model, which is problematic when the derivatives can not be computed numerically with sufficient accuracy. It is known that iterative methods of this kind do not necessarily converge to the *global* minimum, but may fall into a local minimum instead. *MIGRAD* can be used in combination with *SIMPLEX*, which is more tolerant of local minima.

By default, MINUIT derives parameter uncertainties from the covariance matrix that is computed by *MIGRAD* or *HESSE*. The uncertainties correspond to the square root of the diagonal elements of the matrix; parameter correlations can be estimated from the matrix as well. Alternatively it is possible to compute parameter uncertainties by *MINOS*, which takes into account any parameter correlations and non-linearities of the fit model. *MINOS* uses an approach known as *non-parabolic log-likelihood*, which evaluates the fit function around the best-fit result to compute a confidence interval. It is thus similar to the F-test method available in LMFit, but uses a different mathematical background.

The implementation of the MINUIT fit method in Peaberry uses the same χ^2 value as the LMFit module (3.52), and allows to include x-errors according to (3.53).

MCMC

A completely different approach to fitting is available in Peaberry via *Markov Chain Monte-Carlo* (MCMC) sampling, which is based on the Bayesian understanding of statistics. Since MCMC methods sample from the actual probability distribution of χ^2/ndf or $\ln L$ as defined in (3.49), they provide an intuitive and accurate estimation of confidence intervals. They are also more tolerant of local minima than many other algorithms and can deal with multi-dimensional problems where highly correlated parameters occur. These problems are usually hard to solve for classical frequentist-based methods. MCMC is used in many scientific applications, e. g. in astroparticle physics [FM⁺13, GW10].

The main difference between Frequentism and Bayesianism is the definition of probability. Frequentists define probability as a *limiting case in repeated measurements*, which is thus viewed as *frequencies of events* that were observed. Bayesians on the other hand relate probability to a *statement about confidence* of a certain observation, which is thus viewed as *knowledge about events*. There is an ongoing philosophical debate between the two schools of statistics, and a full discussion is out of the scope of this thesis. A practical introduction to both concepts is given e. g. in [Van14].

MCMC methods have been developed to provide a practical approach to Bayesianism in statistical analysis. Although for simple problems it is easy to compute Bayesian results analytically, it is often required to perform numerical integrations to perform Bayesian analysis in high-dimensional parameter spaces. MCMC describes a class of algorithms which can efficiently determine a probability distribution from a given set of parameters by drawing random samples, such that the resulting points are distributed according to the posterior. A first implementation of MCMC was published by N. METROPOLIS et al. in 1953 [M⁺53] and the concept has been extended to a rich set of different algorithms since then, each with their own advantages and disadvantages.

The name “MCMC” relates to the core principle of these algorithms. The random sampling of the distribution is referred to as *Monte-Carlo*, which is used in many applications where statistical analysis is performed by drawing from a numerically computed probability distribution (e. g. in particle simulations)³³. Monte-Carlo methods are applicable as long as the posterior distribution can be computed efficiently and does not require any knowledge about the underlying prior distribution. To apply Monte-Carlo methods in a statistical context, another feature is needed: A *Markov Chain* is a stochastic process that is completely defined by the transition probability between two steps. An important feature is that the probability is defined only by the current state of the chain (i. e. the model parameters at the current iteration) and does not depend on earlier steps. In MCMC algorithms this feature is used to modify the “random walk” behavior of the Monte-Carlo method so that it follows the underlying probability distribution: the Markov Chain ensures that points in the parameter space with higher probabilities are sampled more frequently, and the resulting sampling density reflects the probability distribution.

MCMC methods do not depend on the definition of the posterior distribution, and can therefore be used in minimization problems similar to “classical” fit algorithms. When the posterior distribution

33. A simple example of this method is the computation of the value of π : Random positions in a two-dimensional coordinate system are generated, and the points that lie inside a circle are counted: $x^2 + y^2 \leq 1$. Given enough samples, the area covered by the points inside the circle can be determined and the value of π is derived from this area. This algorithm notably relies only on the geometry of the circle, and does not include any assumptions about the meaning of π itself.

is defined by the χ^2 value of the fit, the MCMC sampling will converge towards the parameter region where χ^2 is minimized. In most fit problems, this value can be easily computed since it is completely defined by the observed data and the fit model. The method is tolerant against local minima due to the random sampling and parameter correlations are automatically included in the sampling process.

MCMC typically operates on the log-likelihood from (3.49),

$$L = \prod_{i=1}^n \frac{1}{\sqrt{2\pi\sigma_i^2}} \exp\left(-\frac{(x_i - \mu_i)^2}{\sigma_i^2}\right), \quad (3.54)$$

$$\ln L = -\frac{n}{2} \sum_{i=1}^n \ln(2\pi\sigma_i^2) + \frac{(x_i - \mu_i)^2}{\sigma_i^2}, \quad (3.55)$$

with $\mu_i = \mu(x_i, \bar{\Theta})$ the value of the fit function given the model parameters $\bar{\Theta}$, and σ_i the statistical uncertainty according to (3.53). A maximization of $\ln L$ then corresponds to the minimization of χ^2/ndf .

Since the actual value of the log-likelihood is irrelevant to the maximization, the log-likelihood is typically implemented as

$$\ln L(\bar{\Theta}) = -\frac{1}{2} \sum_{i=1}^n \left(\frac{x_i - \mu_i}{\sigma_i}\right)^2 + 2 \ln(\sigma_i). \quad (3.56)$$

This definition is also used in Peaberry with the emcee sampler.

The posterior probability distribution, which is sampled by the MCMC algorithm, is defined by

$$\ln p(\bar{\Theta}) = \ln L(\bar{\Theta}) + \ln p_0(\bar{\Theta}), \quad (3.57)$$

where p_0 is a prior that can be used to include information that is known *a priori* in the fit. In the simplest case, $\ln p_0 = 0$, no information is added and only the likelihood defines the probability distribution. In Peaberry, the prior can be used to implement parameter constraints in the sampling process: the value $\ln p_0 = -\infty$ is used when a parameter is outside user-defined limits, moving the probability $\ln p$ to negative infinity. This prevents the MCMC sampler to access this region of the parameter space.

A well-known MCMC implementation is the *Metroplis-Hastings* algorithm named after N. METROPOLIS and W. HASTINGS [Has70]. It is a generalization of the classic Metroplis algorithm that quickly became the standard implementation for MCMC methods. The algorithm computes the *proposal distribution* $P(\bar{x}, \bar{y})$ for each step of the Markov Chain, which depends on the current position in the parameter space \bar{x} and the next (proposed) position \bar{y} which is randomly selected. The proposed step $\bar{x} \rightarrow \bar{y}$ is carried out according to the *acceptance probability*

$$p_A = \min\left(1, \frac{p(\bar{y}) \cdot P(\bar{x}, \bar{y})}{p(\bar{x}) \cdot P(\bar{y}, \bar{x})}\right), \quad (3.58)$$

where $p(\bar{x})$ is the posterior probability distribution. The value p_A compares the proposed with the inverse step, and thus ensures that the chain converges towards the maximum of the distribution. Occasionally a step is performed that decreases the probability – this is an essential feature which results in a sampling of the posterior distribution with sufficient coverage³⁴. If the proposal is not accepted,

34. Note that if the chain converges too fast, only little information about the posterior distribution can be gathered.

a new random value for \bar{y} is drawn and the procedure repeats. As the Markov Chain proceeds, the sampling steps map out the underlying parameter space. Their density is higher in regions where the posterior distribution (the log-likelihood $\ln L$) is maximized.

Affine-invariant MCMC sampling

Peaberry uses the so-called *affine-invariant MCMC ensemble sampler* proposed by J. GOODMAN and J. WEARE [GW10], which is provided by the *emcee* package [FM⁺13]. In contrast to other widely used MCMC algorithms like the “classic” MH sampler (see above), *emcee* processes many individual sampling chains in parallel. The chains start with slightly different initial parameter values and can thus quickly explore a large section of the posterior distribution (figure 3.13).

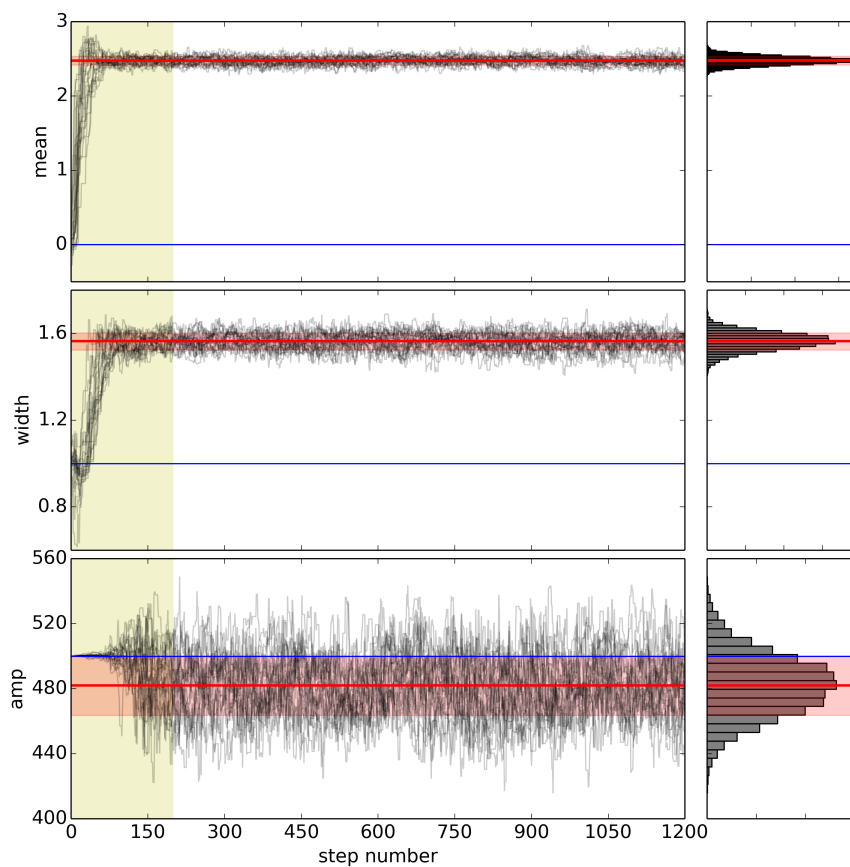


Figure 3.13.: MCMC trace plot with affine-invariant sampling. The plot shows the evolution of the sampling chains over 1200 iterations for each fit parameter (cmp. table 3.1). The affine-invariant sampler in this case uses 20 chains that run in parallel to provide better coverage of the parameter space and faster convergence. The horizontal lines indicate the initial parameter value (blue) and the fit result with its estimated confidence interval (red). The first 200 iterations are discarded as a “burn-in” phase (yellow region), where the chains converge towards the likelihood maximum. The fit result is determined from the projection of the non-discarded sampling steps as shown on the right. The median and the confidence region are determined from the median and 1σ -quantile of the projection histogram.

The individual states of the K parallel chains are defined by so-called *walkers* $S = X_k$, and the proposal distribution of each walker k is given by the state of the remaining $K - 1$ walkers in the ensemble. The computation of a proposal step for each walker is called a *stretch move* since it includes information from all chains in the ensemble. This approach often results in faster convergence towards the maximum likelihood and requires none or only little fine-tuning of the sampling process. The algorithm is efficient in applications such as fitting and has been utilized in many recent publications, e. g. for the analysis of astrophysical observations. A complete discussion of the actual sampling process and the differences to the Metropolis algorithm, however, is out of the scope of this thesis.

The posterior distribution is sampled by individual steps in the parallel chains. Due to the convergence criteria, the sampling will at some point reduce to a random walk around the likelihood maximum, which is typically reached after a sufficient number of steps have been performed. The necessary number of steps (or *chain length*) depends on the minimization problem and is difficult to estimate beforehand. However, since MCMC is an iterative process, one can investigate the convergence over time to find a point where stable conditions are reached. Any additional sampling after this point can be used to determine the posterior distribution close to the likelihood maximum. The earlier steps in the so-called *burn-in* phase are typically discarded from later analysis. The posterior distribution of a given fit parameter is then determined from a projection of the single steps into histogram (see right part of figure 3.13). The best-fit result is given by the median value of the histogram which corresponds to the maximum likelihood. Similarly, the confidence interval can be estimated from its width and shape e. g. by computing the standard deviation or 1σ -quantiles. Quantiles are more robust against outliers (similar to median versus average) and allow to determine asymmetric uncertainties. Accordingly, the MCMC fit results are computed as {16%, 50%, 84%} quantiles of the posterior distribution for each model parameter in Peaberry.

Parameter correlations can be investigated if the individual steps are projected against two parameters (figure 3.14). This results in a two-dimensional view of the posterior distribution. The correlation can be computed directly from the posterior distribution according to the covariance

$$\text{cov}(x,y) = \frac{1}{n^2} \cdot \sum_i^n \sum_{j>i}^n (x_i - x_j)(y_i - y_j), \quad (3.59)$$

where (x, y) are the two model parameters for which the covariance is computed and n is the total number of steps (after discarding the burn-in phase).

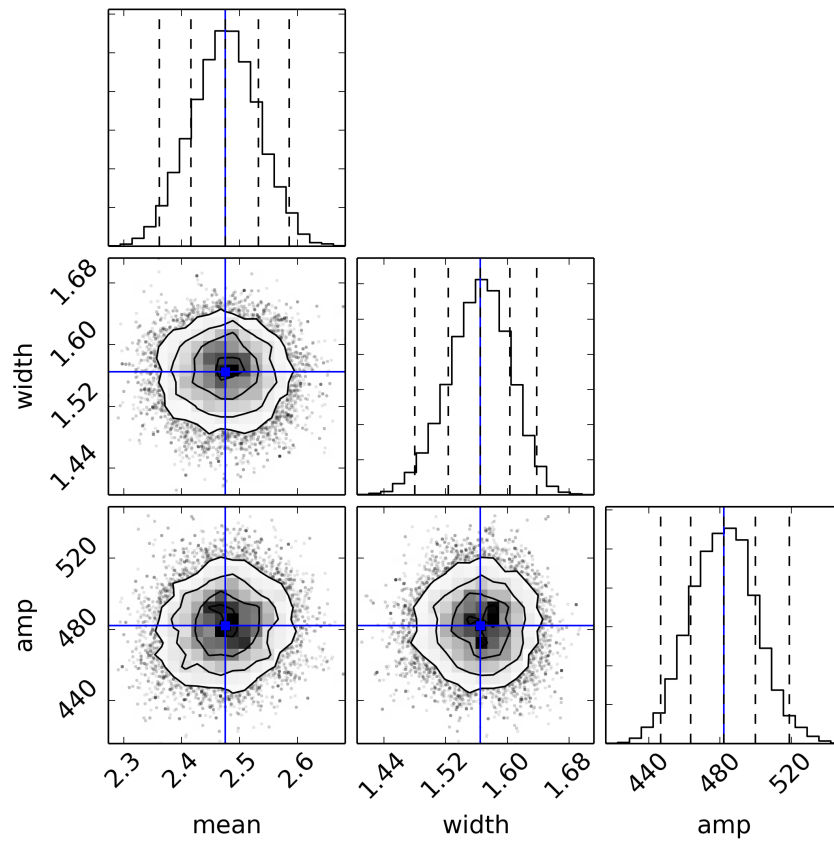


Figure 3.14.: MCMC corner plot after affine-invariant sampling. Here the parameter samples that result from the MCMC process are plotted against each other to investigate parameter correlations. The shown histograms correspond to the chain projections shown on the right in figure 3.13. The dashed lines indicate the 1σ - and 2σ -width that are determined via quantiles. The blue lines indicate the median of the histograms, i. e. the fit results. The circular shape of the correlation plot for all parameter combinations indicate that in this example, the fit parameters are not correlated. Deviations from the circular shape indicate correlations. Note that with MCMC, correlations do not affect the accuracy of the fit results and can be investigated directly from the parameter samples, as the sampling process maps out the χ^2/ndf or $\ln L$ parameter space directly.

A calibration source for the commissioning of the KATRIN main spectrometer

As noted in a previous chapter, it is crucial to determine the transmission properties of the MAC-E filter used for the energy analysis of tritium beta-decay electrons. The transmission properties are affected by the interplay of the electric and magnetic fields at the spectrometer, and the actual transmission function also depends on the radial position in the analyzing plane. Although a lot of studies can be performed using particle tracking simulations, a precise knowledge of the effective transmission function can only be gained from actual measurements at the spectrometer.

To investigate the energy resolution and the influence of the electron pitch angle on the transmission probability, a calibration source is required that features a line width much smaller than the energy resolution of the spectrometer and a small angular spread with well-defined pitch angles of the emitted electrons. Hence, a mono-energetic and angular-selective electron source is needed that can be placed in front of the main spectrometer entrance to provide an electron beam that is used to investigate the spectrometer properties.

The requirements and the design of such a calibration source are discussed in this section, as well as measurements at the KATRIN main and monitor spectrometers and corresponding simulations to further study the characteristics of the provided electrons. The analysis of the monitor spectrometer measurements and corresponding simulations are also published in a paper [B⁺17a].

4.1 Spectrometer transmission properties for a calibration source

To understand the design criteria and the results from the various measurements with the calibration source, it is helpful to start with a discussion of the electron creation and transport processes inside the source. The principles discussed in this section apply to any kind of MAC-E filter and only depend on the electromagnetic conditions. The source has been used at the main spectrometer and the monitor spectrometer, where the magnetic fields are set up differently. The details of the experimental setup will be discussed at a later point in this chapter.

4.1.1 Transmission function with an angular-selective electron source

The measurement principle with a calibration source is based on the fact that an electron beam with defined energy and pitch angle is guided into the spectrometer entry magnet, from where the electrons undergo the adiabatic transformations discussed in section 2.2. This allows to scan the available range of kinetic energies and pitch angles at defined steps and investigate their influence on the transmission properties of the spectrometer. For these measurements, the electron source is placed at a point upstream of the entry magnet.

To discuss the effect on the transmission properties with such an electron source, it is not required to know the exact details of the electron transport between the source and the magnet. Hence in this section, we will assume that an electron beam with the required properties is provided that starts in the entry magnet at the magnetic field B_0 . The relevant parameters for the electron beam generated by the calibration source are the initial kinetic energy E_0 with an energy spread σ_E and the initial pitch angle θ_0 with an angular spread σ_θ .

The kinetic energy of the electrons in the analyzing plane of the spectrometer defines the transmission probability. The energy is defined by the starting voltage U_{start} of the electron source, $E_0 = qU_{start}$, where q is the (negative) elementary charge of the electron. Electrons are transmitted if their energy is larger than the electric potential in the analyzing plane U_{ana} . The analyzing plane potential can only be determined indirectly by measurements e. g. with an electron source. For practical reasons, the transmission function is drawn in terms of the voltage difference between the spectrometer (actually the voltage of the inner wire electrode in a typical MAC-E filter) and the electron source, $U_{start} - U_{spec}$. The voltage difference corresponds to the so-called *surplus energy* of the electrons, which can be used to describe the transmission probability:

$$E = q\Delta U = q(U_{start} - U_{spec}). \quad (4.1)$$

Since only the longitudinal component $E_{\parallel} = E \cdot \cos^2 \theta$ is available to overcome the retarding potential, the transmission probability also depends on the pitch angle θ of the electrons due to the adiabatic collimation (2.7). This results in a shift of the transmission function to larger surplus energies as the pitch angle increases.

Due to the definition in (4.1), the observed transmission function is also shifted by the *potential depression* of the spectrometer that corresponds to the difference between spectrometer voltage and analyzing plane potential, $\Delta U_r = U_{ana} - U_{spec}$. The potential depression depends on the spectrometer geometry and on the radial position of the electron in the analyzing plane (i. e. the magnetic field line). This has been investigated in [Erh16, Gro15]. At the monitor spectrometer it also depends on the spectrometer voltage due to the different setup. For the measurements presented later in this chapter, the value ΔU_r is typically constant over all measurements¹. Any shift of the transmission function that is not related to the energy or pitch angle of the electrons is therefore neglected in the description below.

Mono-energetic isotropic source

For the case of an *isotropically* emitting electron source with small line width, the width of the transmission function is defined by the energy resolution of the main spectrometer ΔE according to (2.22).

1. Except for measurements at the monitor spectrometer with reduced voltage, this is noted whenever relevant.

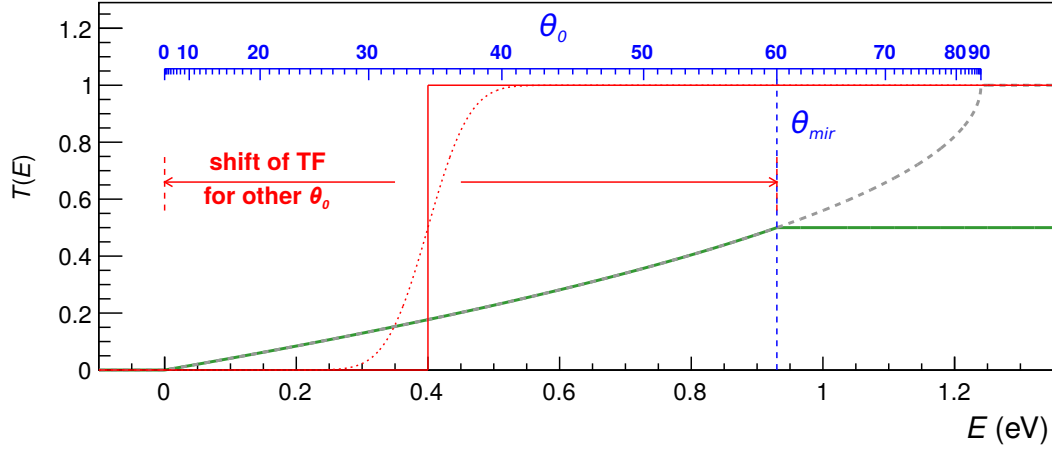


Figure 4.1.: Transmission function for different calibration sources. A mono-energetic, isotropic source produces a broad transmission function that goes from zero surplus energy ($E = 0$) to $E = \Delta E^{iso}$ (dashed gray line). At the main spectrometer, magnetic reflection limits the starting angle to $\theta_0 \lesssim 60^\circ$, which reduces the transmission width to $\Delta E = 0.93$ eV at nominal conditions (green line). The width thus corresponds to the energy resolution of the MAC-E filter. A source with angular selectivity where the starting angle θ_0 is well-defined, the transmission function reduces to a step function (red line) since all electrons above a certain energy threshold are transmitted. The position of the transmission function shifts with the starting angle θ_0 which affects the kinetic energy of the electrons in the analyzing plane. A finite energy or angular spread broadens the step function to a so-called error function. Note that this model of the transmission function is simplified and does not take into account all relevant effects, especially for non-Gaussian energy and angular distributions. Figure adapted from [Zac14].

The initial pitch angle in this case is $\theta_0 = 0^\circ$ to 90° . Assuming a narrow electron beam, so that the electrons start at a spot-like position, the deformation of the transmission function due to electromagnetic inhomogeneities can be neglected. The basic transmission condition has been derived in section 2.2:

$$T(E) = \begin{cases} 0 & \text{for } E_0 < qU_{ana} \\ 1 - \sqrt{1 - \frac{E_0 - qU_{ana}}{E_0} \frac{B_0}{B_{ana}}} & \text{for } qU_{ana} < E_0 < qU_{ana} + \Delta E \\ 1 - \sqrt{1 - \frac{B_0}{B_{max}}} & \text{for } qU_{ana} + \Delta E < E_0 \end{cases} . \quad (4.2)$$

In a setup where the magnetic field at the source is lower than the maximal magnetic field along the beam line, $B_0 < B_{max}$ like at the main spectrometer, electrons with large pitch angles are magnetically reflected and thus cut off from the transmission function.

$$\theta_0 < \theta_{mir} = \arcsin \sqrt{\frac{B_0}{B_{max}}} . \quad (4.3)$$

The energy resolution is then given by $\Delta E = qU_{ana} \cdot B_{ana}/B_{max}$. The equations above are still valid in a symmetric magnetic field setup with $B_0 = B_{max}$, where no reflection occurs. Both cases are shown in figure 4.1.

Mono-energetic source with angular selectivity

The observed transmission function is different in the case of a calibration source with angular selectivity, where the pitch angle is well-defined with a small angular spread. In this case, both E_0 and θ_0 can be assumed to be fixed for a single transmission function measurement. Hence, *all* emitted electrons with sufficient surplus energy $E > 0$ in the analyzing plane are transmitted and the transmission function reduces to a step-function for a mono-energetic and mono-angular source (also shown in figure 4.1).

The term $T(E)$ describes the transmission probability at a given surplus energy E of the electrons, i. e. the transmission function:

$$T(E) = \begin{cases} 0 & \text{for } E < 0 \\ 1 & \text{for } E > 0 \end{cases}. \quad (4.4)$$

Source with energy and angular distribution

If the electron energy E_0 is Gaussian-distributed with a distribution function $\eta(E)$ and the angular spread is neglected, the transmission function is broadened by the energy spread σ_E . It changes to an integrated form of a Gaussian function, the so-called *error function*:

$$T'(E) = \frac{1}{2\pi\sqrt{\sigma_E}} \cdot \exp\left(-\frac{(E - E_0)^2}{2\sigma_E^2}\right) = \eta(E), \quad (4.5)$$

$$T(E) = \int_E^{\infty} T'(\epsilon) d\epsilon = \frac{1}{2} \left[1 + \operatorname{erf}\left(\frac{E - E_0}{\sqrt{2}\sigma_E}\right) \right] \quad (4.6)$$

$$\text{with } \operatorname{erf}(x) = \sqrt{2\pi} \int_0^x e^{-\tau^2} d\tau. \quad (4.7)$$

The term $T(E)$ now describes the transmission probability for a mono-angular source with energy spread σ_E . The positive sign in front of the error function $\operatorname{erf}(x)$ is by convention; it ensures that the transmission function rises with increasing E . The resulting transmission function is shown in figure 4.1 for an arbitrary pitch angle θ_0 . The position is shifted according to the pitch angle, which allows to scan the transmission properties of the MAC-E filter.

If the pitch angles also follows some distribution $\zeta(\theta)$, the width of the transmission function is further increased. The surplus energy depends on the pitch angle θ due to the adiabatic collimation (2.7). Hence, the angular spread σ_θ effectively increases the energy spread σ_E in (4.6). The magnitude of this effect depends on the energy resolution of the MAC-E filter that defines the strength of the collimation. For large pitch angles that are close to the limit of magnetic reflection, $\theta_0 \rightarrow \theta_{mir}$ (4.3), the part of the angular distribution with pitch angles above θ_{mir} is completely cut off from the transmission function. This effect leads to an additional deformation of the observed transmission function.

Analytical description of the transmission function

The transmission function for different energies and pitch angles can be computed analytically by combining the energy spread with the angular spread [Gro15]. The transmission function $T(E)$ is then

determined by integrating the underlying distribution $T'(E)$, which combines the energy distribution $\eta(E)$ with the angular distribution $\zeta(\theta)$. The angular integral yields a scaling factor A that takes into account the electrons that are transmitted for the given pitch angle:

$$T'(E) = \eta(E) \cdot \underbrace{\int_0^{\theta_{max}(E)} \zeta(\theta) d\theta}_A. \quad (4.8)$$

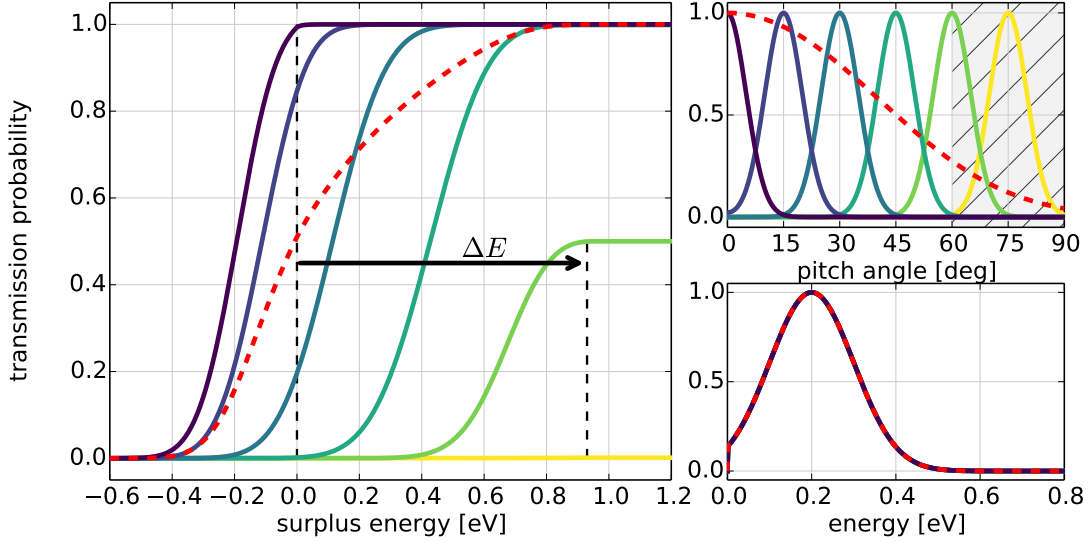


Figure 4.2.: Analytical transmission functions at different pitch angles. The main plot shows the transmission functions computed with the analytical model (4.10), using the angular distributions shown on the upper right and the energy distribution shown on the lower right. The transmission functions shift to larger surplus energies as the pitch angle of the electrons increases, as indicated by the different solid lines. The dashed region in the angular distribution marks the region where magnetic reflection occurs ($\theta_{mir} = 60^\circ$). The observed shift corresponds to the energy resolution ΔE of the spectrometer. For comparison, a quasi-isotropic angular distribution is indicated by the dashed red line. In this case, no angular selectivity is achieved and the energy resolution cannot be investigated.

The angular distribution is integrated over the range of pitch angles that can be transmitted for an electron with given energy E ,

$$0^\circ \leq \theta_0 < \theta_{max}(E) = \min \left(\arcsin \sqrt{\frac{E_0}{qU_{ana}} \cdot \frac{2}{\gamma + 1} \cdot \frac{B_0}{B_{ana}}}, \arcsin \sqrt{\frac{B_0}{B_{max}}} \right), \quad (4.9)$$

where γ is the Lorentz factor for the electrons entering the spectrometer with kinetic energy E_0 . Since the electrons are retarded at the analyzing plane, the Lorentz factor here reduces to $\gamma_{ana} \approx 1$ and can be left out in the equation. In an asymmetric magnetic field setup with $B_0 < B_{max}$, magnetic reflection (4.3) must be considered here as well; this is done in the second term in $\theta_{max}(E)$. The min-function ensures that both transmission conditions that limit the transmitted pitch angles are taken into account.

Following (4.6), the transmission function $T(E)$ is then given by integrating the term $T'(E)$ over the complete energy range. This general description includes the transmission functions derived above:

$$T(E) = \int_E^\infty T'(\epsilon) d\epsilon = \int_E^\infty \eta(\epsilon) \int_0^{\theta_{max}(\epsilon)} \zeta(\theta) d\theta d\epsilon. \quad (4.10)$$

Using this analytical approach to integrate the energy and angular distributions has the advantage that it includes *all* effects that influence the observed transmission function, especially the correlation between the pitch angle in the analyzing plane and the kinetic energy of the electrons (adiabatic collimation) that results in the energy-dependence of $\theta_{max}(E)$. It is thus ideally suited to describe the measured transmission functions that are discussed later in this chapter. The approach has been used in other works as well [Erh16, Gro15]. In simpler descriptions, e. g. using an error function (4.6), it is difficult to include the contribution of the angular distribution correctly.

Figure 4.2 shows transmission functions that were computed using this approach with a Gaussian energy and angular distribution. As expected, the transmission function shifts towards positive surplus energies as the pitch angle increases, and magnetic reflection occurs when the pitch angle grows too large.

Transmission function at reduced voltage

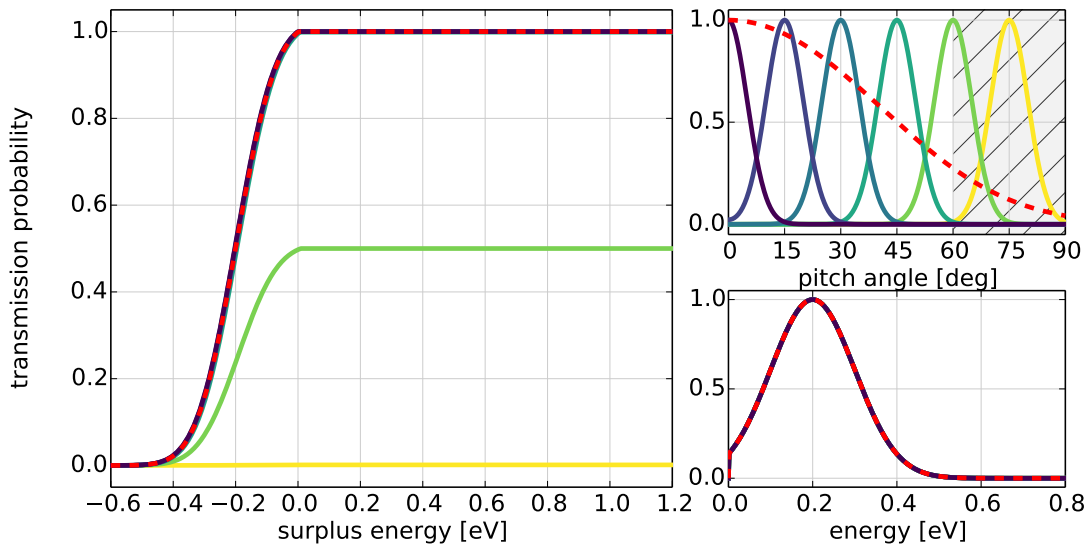


Figure 4.3.: Analytical transmission functions at different pitch angles at reduced voltage. The main plot shows the transmission functions computed with the analytical model (4.10) as in figure 4.2. In this case the spectrometer voltage was reduced to 200 V (and the electron energy scaled accordingly). The transmission functions are now only affected by the energy distribution of the electrons. This also implies that the isotropic emission profile (dashed red line) shows no difference to the narrower angular distributions (solid lines). Since magnetic reflection occurs independently of the energy, electrons are still cut off from the transmission function if $\theta_0 > \theta_{mir}$.

Because of the contribution of the angular spread through the integral in (4.10), it is difficult to disentangle this effect from the actual energy spread of the calibration source in a measurement. However,

an important characteristic of the MAC-E filter can be used to overcome this problem: The energy resolution depends not only on the magnetic fields, but also the spectrometer voltage (filter energy) U_{ana} (2.23).

Hence, a transmission function can be measured at a substantially lower voltage than the nominal high voltage setting of $E_0 \approx 18.6 \text{ keV} = qU_{ana}$. The contribution of the angular spread is reduced in this case and the MAC-E filter can now examine the energy distribution of the electrons without being affected by the angular spread. The commissioning measurements used $E_0 \approx 200 \text{ eV}$ for this purpose, which results in an improved energy resolution of roughly 0.1 eV at nominal magnetic fields. This is shown in figure 4.3.

The analytical model also allows to freely choose the underlying distributions, so that one could use non-Gaussian distributions here as well. It will be shown later that a realistic description of the electron source requires the use of such modified distributions (section 4.2). Figure 4.4 shows the corresponding transmission functions for different energy distributions. A calibration source with small angular spread like the device presented here is fully dominated by the energy distribution if the pitch angle θ_0 is sufficiently small.

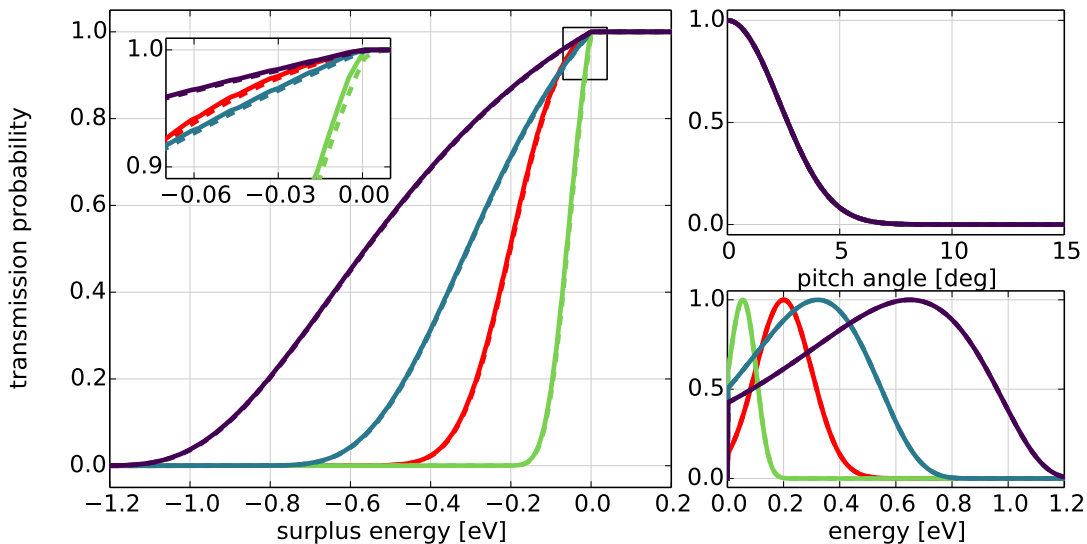


Figure 4.4.: Analytical transmission function with different energy distributions. For an electron source with small angular spread, the observed transmission function is dominated by the energy distribution of the electrons. The analytical model allows to include non-Gaussian energy distributions as well (colored lines) that agree better with the measurements discussed later. For comparison, a Gaussian distribution is shown as well (red line). The energy distribution can be measured directly if the spectrometer is operated at reduced voltage (solid lines). The transmission function is modified at nominal high voltage, where the influence of the angular distribution increases (dashed lines). This is especially apparent close to the transmission edge as shown in the inset. However, for a small angular spread this deviation is extremely small and can typically be neglected in the analysis of measurement data. Note that the position of the transmission edge (upper edge of the transmission function) does not change for different energy distributions, since the upper edge corresponds to $E = 0$ in the energy spectrum where the distributions are cut off. This is typically the case for transmission function measurements with the electron source presented here.

Sensitivity to the spectrometer work function

The “classic” definition of the electron surplus energy (4.1) is based on the voltage difference $\Delta U = U_{start} - U_{spec}$, which is monitored by a difference voltmeter. During a transmission function measurement, the starting voltage U_{start} at the electron source back plate is varied around U_{spec} to adjust the kinetic energy of the electrons. The transmission function is then determined by measuring the observed electron rate at the detector in dependency of the surplus energy, $\dot{N}(E = q\Delta U)$.

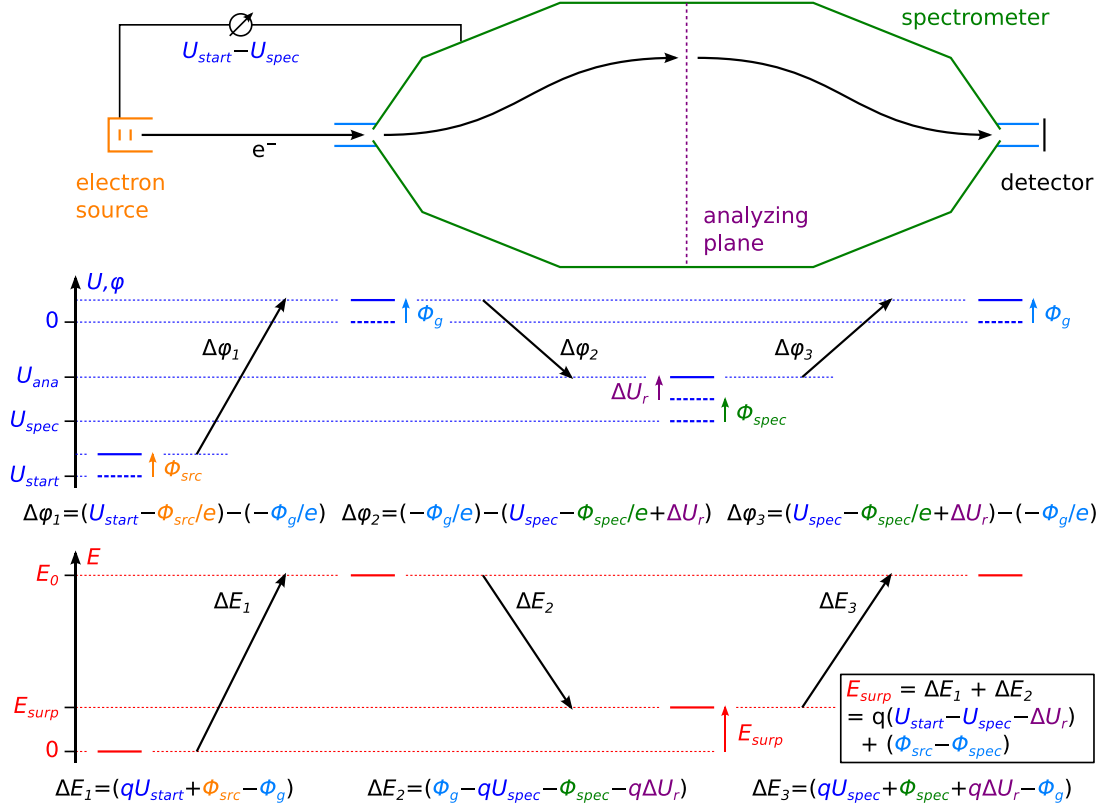


Figure 4.5.: Electron surplus energy in the main spectrometer. The figure shows the electric vacuum potential ϕ , the electrode voltage U and the kinetic energy E of the produced electrons at several points in the experimental setup. In contrast to the “classic” definition (4.1), the *surplus energy* of the electron in the analyzing plane E_{surp} is affected by contributions from the *potential depression* ΔU_r , and the *work function* of the electrodes. See running text for a detailed description.

However, the *actual* surplus energy – the kinetic energy of the electrons in the analyzing plane – is modified by other contributions. This is explained in figure 4.5, which schematically shows the electric potential U and the kinetic energy E of the electrons at several points in the experimental setup:

- Electrons are created at the electron source back plate with a kinetic energy $E \approx 0$ eV. The vacuum potential at the back plate is given by the starting voltage U_{start} and the work function Φ_{src} , which modifies the vacuum potential ϕ_{start} according to

$$\phi_{start} = U_{start} - \frac{\Phi_{src}}{e}, \quad (4.11)$$

where e is the elementary charge.

- The electrons (with charge $q = -e$) are accelerated against the ground electrodes ($U_g = 0$ V) at the spectrometer entrance, where they reach their nominal kinetic energy E_0 . The gained energy corresponds to the potential difference $\Delta\phi_1 = \phi_{start} - \phi_g$ so that $\Delta E_1 = q\Delta\phi_1$. The influence of the work function must be considered here again, shifting the ground potential to $\phi_g = 0 \text{ V} - \Phi_g/e$. The kinetic energy of the electrons is then

$$E = E_0 = q\Delta\phi_1 = q \left[\left(U_{start} - \frac{\Phi_{src}}{e} \right) - \left(0 - \frac{\Phi_g}{e} \right) \right] \quad (4.12)$$

$$= qU_{start} + \Phi_{src} - \Phi_g. \quad (4.13)$$

- After entering the spectrometer, the electrons are decelerated by electrostatic retarding potential U_{ana} , which is minimal at the analyzing plane. It is given by the spectrometer voltage $U_{spec} \approx -18.6$ kV and shifted to more positive values by the *potential depression*. The potential depression is a result of the spectrometer design and implements a radial dependency of the retarding potential at the analyzing plane, $U_{ana}(r) = U_{spec} + \Delta U_r(r)$. Furthermore, the work function Φ_{spec} of the spectrometer must be considered here. The retarding potential is

$$\phi_{ana} \equiv U_{ana} = U_{spec} - \frac{\Phi_{spec}}{e} + \Delta U_r. \quad (4.14)$$

The kinetic energy of the electrons is reduced from E_0 to E_{surp} by the potential difference $\Delta\phi_2 = \phi_{ana} - \phi_g$. The actual surplus energy of the electrons in the analyzing plane results to

$$E = E_{surp} = q\Delta\phi_2 = q \left[\left(0 - \frac{\Phi_g}{e} \right) - \left(U_{spec} - \frac{\Phi_{spec}}{e} + \Delta U_r \right) \right] \quad (4.15)$$

$$= q \underbrace{(U_{start} - U_{spec} - \Delta U_r)}_{\Delta U} + \underbrace{(\Phi_{src} - \Phi_{spec})}_{\Delta\Phi}. \quad (4.16)$$

The surplus energy thus corresponds to the “classic” definition with $\Delta U = U_{start} - U_{spec}$ (4.5), which is now modified by the work functions Φ_{src} and Φ_{spec} and by the potential depression ΔU_r . The potential depression depends only on the spectrometer geometry and the electrode configuration (which are both fixed in a typical transmission measurement) and the radial position in the analyzing plane. The radial position can also be assumed to be constant due to the small size of the emission spot at the electron source photocathode; it only changes if the electron source is moved to a different magnetic field line during a measurement.

Note that in the case of a non-zero pitch angle, $\theta > 0$, the longitudinal energy is reduced according to (2.1). This effect is visible in a transmission function measurement, but not relevant to this discussion since it effectively reduces the kinetic energy E_0 by a certain value.

The value $\Delta U = U_{start} - U_{spec}$ is measured directly in the high-voltage setup of the electron source². A transmission function measurement is thus sensitive to the *work function difference* between source and spectrometer,

$$\Delta\Phi = \Phi - \Phi_{spec}, \quad (4.17)$$

where $\Phi = \Phi_{src}$ is the work function of the photocathode. If its value is known e. g. from a dedicated measurement, the spectrometer work function Φ_{spec} can be determined. It is of

2. The read-out is achieved by a difference voltmeter (DVM) that is integrated with the slow-control system.

interest for commissioning and neutrino mass measurements, since the work function directly affects the retarding potential (which is responsible for the energy analysis of the electrons) and any instabilities could affect the sensitivity of the experiment.

- After passing the analyzing plane the electrons propagate towards the detector. They are accelerated again by the retarding potential and reach their nominal kinetic energy E_0 at the spectrometer exit. Since the electrons are merely counted to determine the transmission function, their energy at the detector is irrelevant to the measurement.

4.1.2 Requirements for a calibration source

The calibration source discussed in this section allows various measurements dedicated to understanding the transmission properties of the KATRIN main spectrometer and other important characteristics, as well as related measurements of other subsystems at the KATRIN setup. Furthermore, the measurements with a MAC-E filter allow investigations of the source properties itself, e. g. the measurement of the energy distribution as explained above. Possible measurements are:

- **Transmission properties of the MAC-E filter:** A straight-forward measurement with the calibration source is the determination of the transmission function of a MAC-E filter like the main spectrometer. The source allows to measure the transmission function against the electron energy for a fixed pitch angle, and can therefore be used to determine the energy resolution of the spectrometer by investigating the shift of the transmission function towards larger pitch angles. A series of similar measurements can be conducted at different positions in the analyzing plane if the calibration source can be moved around the magnetic flux tube. This technique can be used to investigate inhomogeneities of the transmission properties over the full area of the analyzing plane.

The measurement can be repeated at different settings of the filter energy qU_{ana} or the magnetic fields B_{min} , B_{max} . This allows to further investigate the characteristics of the spectrometer and to verify the theoretical description of the adiabatic electron transport in a MAC-E filter.

If the spot-size of the electron beam on the detector wafer is smaller than a single pixel, the calibration source can resolve transmission properties on a sub-pixel scale. A single detector pixel will measure an effective transmission function that is affected by small-scale inhomogeneities of the electromagnetic fields at the analyzing plane that lead to a slightly increased transmission width. These affects can be investigated with the calibration source if enough measurement time is available to perform such a detailed transmission scan.

- **Integrity of the inner electrode system:** When the electron source is moved to an outer position of the flux tube, the electrons will follow a field line with a large radial distance to the spectrometer axis. This trajectory brings them close to the wires and mounting structure of the inner electrode system. If the distance to these structures is sufficiently small, the transmission function can resolve local differences in the electric potential close to the electrodes. By performing an azimuthal scan, this method allows to check for broken wires or other issues with the inner electrode system.

Azimuthal scans also allow to check for influences of the vessel deformation on the homogeneity of the retarding potential. The massive steel hull of the main spectrometer is deformed by gravity, so that it features an elliptical shape. Although the inner electrode system was designed

to correct the non-circular shape of the vessel hull and provide a symmetric potential in the analyzing plane, a residual contribution from the deformed vessel is still possible. Comparing the measured transmission functions at different azimuthal positions allows to investigate this effect.

- **Early retardation and adiabaticity:** With the energy and pitch angle being free parameters, the MAC-E filter can be tested for unwanted effects like early retardation that can occur for electrons with large pitch angles. Since early retardation is typically prevented by adjusting the configuration of the spectrometer voltage, it depends on the interplay between the electrons and the electromagnetic conditions at the spectrometer. Investigating early retardation can be used to further optimize the spectrometer settings.

The adiabatic electron transport in the spectrometer can also be verified with the calibration source. For electrons with large energies above the filter energy, it is expected that the propagation is not fully adiabatic. This non-adiabaticity also has important effects on high-energetic stored particles and needs to be considered for models of the background caused by stored particles in the main spectrometer.

- **Time-of-flight studies:** If the electron source is operated in a pulsed mode, it is possible to measure the electron time-of-flight – the difference between the arrival time at the detector and the start time at the source. This method has the advantage that electrons are not only affected by the electromagnetic conditions at the analyzing plane – a single electron can either be transmitted or not – but over the complete trajectory. Time-of-flight data therefore carries more information, and this measurement technique can be combined with the measurements discussed above to get a more detailed understanding of the spectrometer properties. It is especially useful in combination with the wire integrity scans, as it allows to check the electrode system farther away from the analyzing plane as well.

Additionally, such measurements provide a nice opportunity to investigate the differential measurement mode of the MAC-E filter: In contrast to the standard “integral” mode, the energy spectrum determined from time-of-flight data does not require to perform multiple measurements at fixed filter energies close to the tritium endpoint. This technique would require a known starting time of the electrons, which is difficult to implement for the tritium source that is used in neutrino-mass measurements [S⁺13b].

- **Detector properties:** Since the parameters of the generated electrons are known, the electron source can be used to investigate properties of the detector system such as backscattering or its energy resolution. Backscattering is an effect where electrons arrive at the detector wafer, but are reflected before depositing their kinetic energy in the silicon material of the detector wafer. Backscattered electrons can be reflected again between the detector and the analyzing plane until they are eventually absorbed at the detector wafer. The backscatter effect strongly depends on the electron pitch angle, and can be investigated with an angular-selective source.
- **Work function of the spectrometer:** The energy distribution of the electrons emitted from the calibration source depends on the work function of the photocathode material, which modifies the observed transmission function. The surplus energy of the electrons is typically modified by the *work function difference* between electron source and spectrometer, $\Delta\Phi = \Phi - \Phi_{spec}$, as shown in figure 4.5.

If the work function of the calibration source is known with sufficient precision, the observed shift of the transmission function allows to determine the spectrometer work function. It is thus possible to investigate the work function stability over time, provided that the work function of the source can be measured regularly.

Due to its flexibility, the calibration source allows many more measurements that can help to understand the properties of the spectrometer or to investigate subsystems like the detector. The above list is therefore by no means complete, but lists measurement ideas that have been carried out during the commissioning measurements or are planned for the near future.

In order to perform these measurements, the electron source needs to fulfill certain requirements. It is especially important to achieve a small energy and angular spread to use the source for the commissioning of the KATRIN main spectrometer. These requirements will be discussed here shortly.

- **Energy spread:** The energy spread of the electrons emitted from the calibration source directly affects the ability to determine the transmission properties of the MAC-E filter. A given energy spread σ_E will contribute to the width of the transmission function. To be able to scan investigate the effects of different pitch angles $\theta_0 = 0^\circ$ to 90° on the transmission function, the energy spread must be significantly smaller than the energy resolution of the spectrometer. If this is not the case, the transmission functions for different pitch angles would be smeared out and overlap each other so that no conclusive results can be obtained.
- **Angular spread:** The angular distribution in the spectrometer entry magnet is translated into a narrower distribution at the analyzing plane due to the adiabatic collimation of the electrons. A non-zero pitch angle at the analyzing plane corresponds to a “missing” kinetic energy that affects the transmission probability of the electrons accordingly. The angular spread σ_θ therefore contributes to the transmission width. A small angular spread is therefore required to resolve the transmission functions for different pitch angles, which allows to determine the energy resolution of the MAC-E filter.
- **Spot size:** Inhomogeneities in U_{ana} and B_{min} at the analyzing plane affect the transmission properties of the MAC-E filter, depending on the electron’s position at the analyzing plane. A small size of the electron emission spot is required to limit the area that is covered by the emitted electrons at the analyzing plane, which contributes to the observed transmission function. A small spot size is also advantageous to investigate characteristics of the detector system such as backscattering or cross-talk between pixels. When the electron source is used to check the integrity of the wire electrode system, a small spot size improves the spatial resolution of the scan.
- **Variable position:** To allow a mapping of the values (U_{ana}, B_{min}) at the analyzing plane, the electron source must be movable around the full 191 T cm² flux tube. This allows to create electrons on different magnetic field lines that cover the full area of the analyzing plane. This feature implies that the source is mounted on a *manipulator system* which can adjust the position of the emission spot w. r. t. to the spectrometer system. A movable source is also important for the wire integrity scan, where electrons are required to travel on outer field lines through the spectrometer.
- **Pulsed mode:** When the electron source is operated in pulsed mode, the starting time of the electrons is known within certain limits. Together with the arrival time at the detector, which is readily available at the DAQ system, the time-of-flight of the electrons can be measured.

The pulse length of the electron beam must be short compared to the pulse period in order to determine the starting time with sufficient accuracy. It is beneficial to run the electron source in pulsed mode during normal measurements as well, as the time-of-flight information is complementary to the measurement. In the case of transmission function studies, the time-of-flight data could provide additional insights into the spectrometer characteristics.

- **Electron rate:** It should be possible to adjust the produced electron rate since different measurements have different requirements. For example, the investigation of the transmission properties profits from a high electron rate as this reduces the required measurement time. Other measurements, however, are negatively affected by high electron rates, such as the investigation of backscattering at the detector or the time-of-flight studies. Furthermore, the electron rate is limited by the given dead-time of the detector system which leads to unwanted pile-up of electron events if the rate becomes too high.

4.2 Principle of the photo-electron source

The intention behind the electron source and its requirements have been explained in the previous section. This section will now discuss the implementation of the photo-electron source to meet these requirements. Especially the two key features – small energy spread and the ability to generate electrons with well-defined pitch angles – will be explained in detail. The electron source presented here has been developed over the recent years [Zac14, Val09] and its design principles have been discussed in several publications [B⁺17a, B⁺14a, V⁺11, V⁺09].

4.2.1 Electron creation by UV light

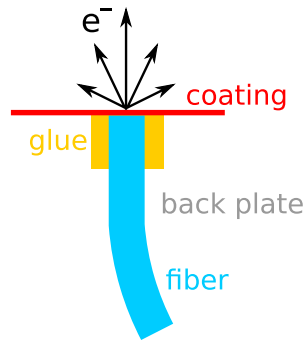


Figure 4.6.: Schematic drawing of the electron source photocathode. The electron source uses the photoelectric effect to generate electrons of defined energy from a photocathode. The photocathode consists of a thin metallic coating (e. g. silver or gold with a thickness of 20 nm to 40 nm) on the aperture of an optical fiber. It is glued into a stainless steel holder which can be mounted inside the electron source setup. The fiber guides UV light into the setup to illuminate the photocathode from behind. The electrons are emitted in forwards direction, where they are further accelerated by an electric field (see figure 4.10). Figure from [Zac14].

The electron source is based on the emission of electrons from a metal surface by the photoelectric effect (figure 4.6). This well-known principle that was first discovered by H. HERTZ [Her87] in 1886 and was further investigated by A. EINSTEIN [Ein05]. To describe the effect in the context of quantum mechanics, Einstein introduced the photon as the quantum state of light. The *Planck equation*, $E = h\nu = hc/\lambda$ where h is the *Planck constant*, links the photon's energy E with its frequency ν .

Neglecting an energy distribution of the electrons, the energy of the electrons in the material needs to be increased above the *work function* Φ to allow the electron to leave the surface. The energy of the released electron is then defined by the frequency of the incident UV light (or its wavelength) and the work function of the photocathode material:

$$E_e = h\nu - \Phi > 0. \quad (4.18)$$

Due to the energy distribution of the electrons in the material, the released electrons have a kinetic energy in the range $0 < E_e \leq h\nu - \Phi$. Hence, the energy spread of the source can be minimized by choosing an UV wavelength that matches the work function. This concept has been discussed in [Zac14], and the electron source was designed with this idea in mind.

4.2.2 The photoemission process

Because of the large impact of the work function on the electron emission, the effects occurring in the photocathode material that lead to the emission of electrons from its surface will be discussed here shortly. The first quantitative description of the photoemission process has been developed by R.H. FOWLER in 1931, who developed a model that considered a free electron gas inside the photocathode material from which electron can be emitted [Fow31]. The Fowler model was considerably extended in the works of C.N. BERGLUND and W.E. SPICER, where the well-known three-step model of photoemission was introduced [BS64b,BS64a]. The discussion below is largely based on this model. Although it uses certain simplifications and has been developed more than 50 years ago, it is still often useful to describe photoemission on a generic level and is often applicable without significant loss of accuracy. Nowadays a more detailed understanding of the process is available through methods like *X-ray photon spectroscopy* (XPS) or *Auger electron spectroscopy* (AES).

In the classic description of the photoeffect where a free electron gas is assumed, the emission of electrons by incident light is not possible due to the conservation of momentum [GB76]. The initial and final momentum of an electron with energy E_0 in the material, p_i and p_f , is given by

$$p_i = \sqrt{2m_e E_0 + hv/c}, \quad (4.19)$$

$$p_f = \sqrt{2m_e(E_0 + hv/c)}, \quad (4.20)$$

where hv is the photon energy. Due to the conservation of momentum and possible momentum loss inside the material, $p_f \leq p_i$, this yields the condition

$$\frac{hv}{m_e c^2} + 2\sqrt{\frac{2E_0}{m_e c^2}} \geq 2. \quad (4.21)$$

However, this condition is typically impossible to fulfill since $hv \ll m_e c^2$ and $E_0 \ll m_e c^2$. Photoemission from a material is therefore only possible if the electron momentum is modified e. g. by the force field close to the photocathode surface. The electron emission is therefore constrained to the surface, and emission from the bulk material cannot play a role in the photoeffect for small photon energies.

A general description of the photoemission process in metallic and non-metallic materials is available through the Berglund/Spicer model where the process is divided into three steps [BS64b]:

1. An electron in the conduction band (or valence band in a non-metallic material) is excited by UV light. This step is typically dominated by the properties of the bulk material since the excitation depends on the density of initial and final states.
2. The electron is transported to the surface. At this stage, both bulk and surface material play a significant role. The transport can be affected by inelastic scattering processes and may feature the release of Auger electrons. The overall process strongly depends on the photon energy.

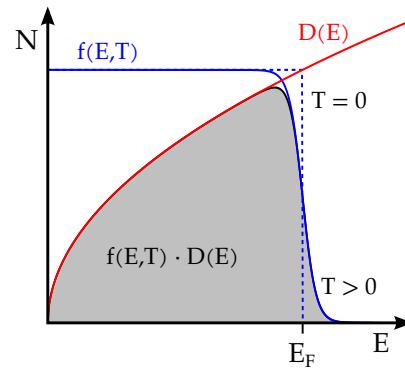


Figure 4.7.: Density distribution in a free electron gas. The distribution is governed by the Fermi-Dirac distribution $f(E,T)$ and the density of states $D(E)$. Both effects combined result in a typical asymmetric shape of the distribution with a tail towards lower energies [Kit88].

- The electron is emitted from the surface into the surrounding vacuum. At this step, the work function defines if the electron is released at all: The kinetic energy of the electron into the direction of the surface normal must be sufficiently large to reach the vacuum energy level.

A review of this simplified model and a more thorough discussion that also investigates effects like the directional photoemission or the final states interactions of the excited electrons is available in [GB76].

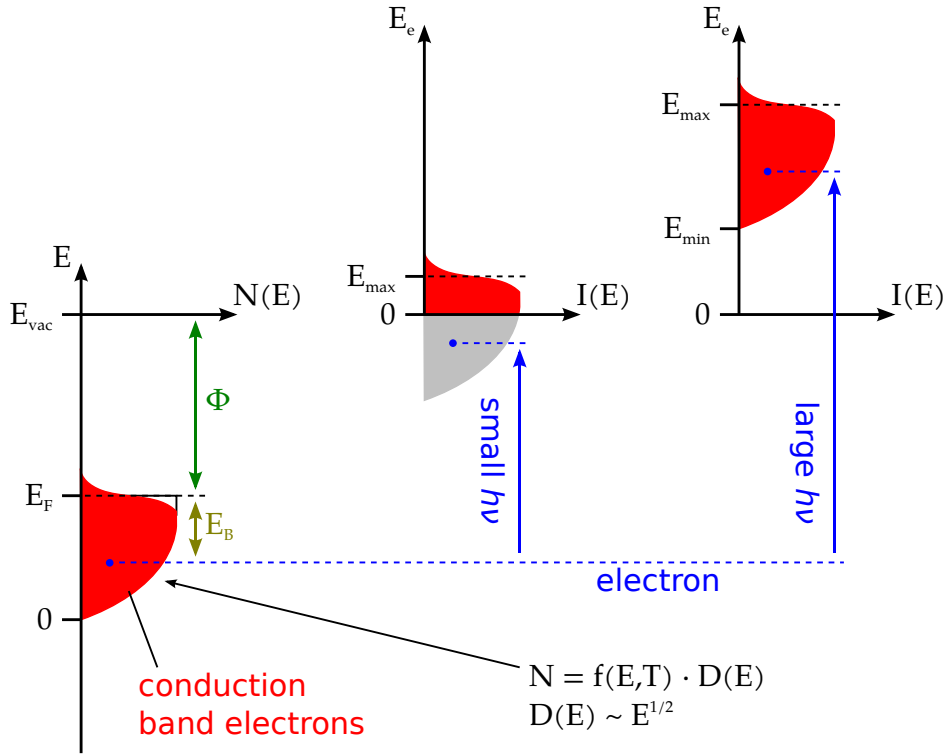


Figure 4.8.: Schematic picture of the photoemission process. *Left:* The figure shows the conduction band electrons in the photocathode bulk material (red). Their distribution $N(E)$ is given by the Fermi-Dirac distribution $F(E,T)$ and the density of states $D(E) \propto \sqrt{E}$ (figure 4.7). The distance of the Fermi edge E_F to the vacuum level E_{vac} corresponds to the work function Φ . An incident photon of energy $h\nu$ moves an electron in the conduction band (blue) towards the vacuum level. The process can be viewed as shifting the complete conduction band to higher energies. *Middle:* For small $h\nu$, the energy distribution of the emitted electrons is cut off at $E_e = 0$ since not all electrons reach the vacuum level. Only a fraction of conduction band electrons is emitted, resulting in a small energy spread and low electron yield $I(E)$. *Right:* If the photon energy is sufficiently large, the all conduction band electrons can be emitted. The energy spread and the electron yield increases accordingly. Figure adapted from [Zac14].

The first step is dominated by the electronic structure inside the photocathode material. The density of states $N(E)$ can be divided into core levels with large binding energies (above 20 eV) and the conduction band, where the binding energy is significantly lower. In this picture, the work function is defined by the *Fermi energy* of the electrons in the material, E_F , and the vacuum energy level, E_{vac} . The Fermi energy corresponds to the upper edge of the conduction band at $T = 0$; at temperatures $T > 0$ the edge is smeared out according to Fermi-Dirac statistics [Kit88].

The energy of the conduction band electrons around the Fermi energy is given by the Fermi-Dirac distribution $f(E,T)$ and the density of states $D(E)$,

$$N(E) = f(E,T) \cdot D(E). \quad (4.22)$$

with

$$f(E,T) = \left[\exp\left(\frac{E - E_F}{k_B T}\right) + 1 \right]^{-1}, \quad (4.23)$$

where k_B is the Boltzmann constant, and

$$D(E) = \frac{1}{2\pi^2} \cdot \left(\frac{2m_e}{\hbar^2}\right)^{3/2} \cdot E^{1/2} \propto \sqrt{E}. \quad (4.24)$$

The distribution is shown schematically in figure 4.7 and features a tail towards lower energies $E < E_F$, and the Fermi edge is smeared out at $T > 0$. At $T = 300$ K, the width of the Fermi edge is about 0.1 eV so that photoemission is possible even for $h\nu < \Phi$ to some extent.

Using this picture, the energy of an emitted electron can be written as

$$E_e = h\nu - \Phi - E_B > 0, \quad (4.25)$$

where E_B is the binding energy w. r. t. the Fermi level E_F . The maximum electron energy is then given by $E_{max} = h\nu - \Phi$ if the smearing around E_F due to the Fermi distribution is neglected. For the case that no scattering processes occur during the electron transport to the surface and the work function on the surface is constant, the energy spectrum of the emitted electrons follows the energy distribution of the conduction band – the incident photon merely shifts the energy of the conduction band electrons into the vacuum regime as depicted in figure 4.8. For small photon energies, only the least-bound states of the conduction band can leave the photocathode. For larger photon energies, the energy distribution becomes broader and strongly asymmetric.

4.2.3 Electron yield and the Fowler model

The Berglund/Spicer model is based on the earlier description by Fowler, which investigates the electron emission rate from the photocathode in dependency of the UV photon energy (or their wavelength) [Fow31]. The model is valid at wavelengths close to the threshold energy Φ and has been widely used in theoretical and experimental investigations of the photoemission process [DuB32]. The Fowler model can be used to determine the work function of a photocathode *in-situ* by a dedicated measurement of the *electron yield* at varying wavelengths, which is utilized in the commissioning measurements of the electron source described in this chapter.

For photon energies close to the Fermi edge of the photocathode material, the photo-current is dominated by the Fermi-Dirac distribution and the density of states of the conduction band electrons (see above). Assuming a constant work function and neglecting any corrections, the photo-current can be described as a free electron gas with Fermi-Dirac statistics. The number of electron states in the velocity range $[u, u + du]$, $[v, v + dv]$, $[w, w + dw]$ is given by

$$n(u,v,w) \, dudvdw = 2 \left(\frac{m_e}{h}\right)^3 \cdot \left[\exp\left(\frac{\frac{1}{2}m_e(u^2 + v^2 + w^2) - E_F}{k_B T}\right) + 1 \right]^{-1} \, dudvdw. \quad (4.26)$$

The coordinate system is chosen so that u corresponds to the normal of the photocathode surface. The velocity component in this direction must be sufficient to overcome the work function, $\frac{1}{2}m_e u^2 > \Phi$.

The number of electrons in the velocity range $[u, u + du]$ is

$$\bar{n} du = 2 \left(\frac{m_e}{h} \right)^3 \cdot \int_0^\infty \int_0^{2\pi} \left[\exp \left(\frac{\frac{1}{2}m_e(u^2 + v^2 + w^2) - E_F}{k_B T} \right) + 1 \right]^{-1} \rho d\rho d\theta \quad (4.27)$$

$$= \frac{4\pi k_B T}{m_e} \left(\frac{m_e}{h} \right)^3 \cdot \ln \left[1 + \exp \left(\frac{E_F - \frac{1}{2}m_e u^2}{k_B T} \right) \right]. \quad (4.28)$$

The number of emitted electrons can now be calculated by integrating over the interval with sufficient velocity, $\frac{1}{2}m_e u^2 \geq E_{vac} - h\nu$:

$$N = \int_{u_0}^\infty \bar{n} du \quad \text{with } u_0 = \sqrt{\frac{2(E_{vac} - h\nu)}{m_e}}. \quad (4.29)$$

This integral cannot be solved analytically. With an expansion in $\mu = (h\nu - \Phi)/k_B T$ one obtains

$$N = 2\sqrt{2\pi} m_e^{3/2} h^{-3} \frac{k_B^2 T^2}{\sqrt{E_{vac} - h\nu}} \cdot \xi(\mu), \quad (4.30)$$

where $\xi(\mu)$ is the so-called *Fowler function*:

$$\xi(\mu) = \begin{cases} e^\mu - \frac{e^{2\mu}}{4} + \frac{e^{3\mu}}{9} + \dots & (\mu \leq 0) \\ \frac{\pi^2}{6} + \frac{1}{2}\mu^2 - \left(e^{-\mu} - \frac{e^{-2\mu}}{4} + \frac{e^{-3\mu}}{9} - \dots \right) & (\mu > 0) \end{cases}. \quad (4.31)$$

The resulting photo-current I corresponds to the integral over the energy distribution of the emitted electrons $I(E)$ as shown in figure 4.8. In a simplified model where corrections to the electron transport within the material are neglected, it can be written as

$$I = \int_0^\infty I(E) dE \propto \frac{T^2}{\sqrt{E_{vac} - h\nu}} \cdot \xi(\mu) \quad \text{with } \mu = \frac{h\nu - \Phi}{k_B T}. \quad (4.32)$$

As expected, the photo-current depends on the photon energy, since more electrons are released if the energy is large. The shape of I plotted against the wavelength $\lambda = c/\nu$ shows a prominent exponential behavior for photon energies $h\nu > \Phi$. For photon energies approaching the work function, the photo-current quickly reduces to zero.

Hence, one can determine the work function of a photocathode by measuring the electron yield at varying wavelengths in a so-called *Fowler measurement*. This approach allows to determine the work function of a photocathode that is mounted in an operational setup, in contrast to alternative methods like a *Kelvin-probe measurement*. The energy spread of the released electrons can be minimized by choosing a wavelength that is close to the corresponding work function, $h\nu \gtrsim \Phi$, on cost of the achieved electron rate.

4.2.4 Work function of realistic surfaces

In typical experimental setups, the work function of the material is influenced by a variety of independent factors. It is difficult to determine a matching wavelength from theoretical values alone. The design of the electron source therefore features different UV light sources that allow to adjust the wavelength during measurements, so that a minimal energy spread can be achieved if necessary. As it will be shown later in this chapter, even with small wavelengths around 260 nm the resulting energy spread is well within the required limits and considerably smaller than the spectrometer's energy resolution. Increasing the wavelength will also result in reduced electron rate due to the strong exponential shape of the Fowler function. The trade-off between small energy spread and sufficient electron rate therefore has to be considered when measurements are carried out.

The electron source presented in this thesis uses poly-crystalline silver or gold as photocathode material, which is brought onto a fiber surface by an evaporation process. While the work function has been determined to 5.1 eV for gold and 4.0 eV for silver under laboratory conditions³ [Eas70], *in situ* measurements with the electron source show a substantially lower work function well below 4 eV for both materials [Zac14, Win14, Bus14]. The measured work functions are consistent and have been verified in multiple measurements with different photocathode materials. The discrepancy to the "laboratory" results must therefore be explained by changes of the properties of the photocathode surface and the bulk material [S⁺95].

Various effects that influence the work function have been discussed in detail in [Zac14] and will be summarized here shortly:

- **Impurities:** Adsorbed foreign atoms that sit on the photocathode surface, or impurities in the bulk material from high-energetic implanted ions, have been shown to result in significant changes of the work function [DS73, She92]. This is explained by the additional dipole fields that are induced by the additional atoms, which affect the band structure of the photocathode material.

The effect can be described by an effective work function

$$\Phi_{eff} = \Phi + \delta\Phi_{ads}, \quad (4.33)$$

where $\delta\Phi_{ads}$ is the change due to the adsorbed atoms. It can be positive or negative and reaches values of more than 1 eV. In some measurements, extreme values of $\delta\Phi_{ads} = -2.3$ eV have been observed. Surface impurities, which are certainly expected when the photocathode is operated under non-UHV vacuum conditions ($p \approx 1 \cdot 10^{-7}$ mbar) over a prolonged time, can therefore explain the reduced work function that is observed at the electron source.

- **Inhomogeneities:** When poly-crystalline surfaces are used for the photocathode, the surface properties can be described by several *patches* with specific work functions Φ_i that correspond to the crystal orientation of each patch. Impurities affect each patch independently, and the effective work functions $\Phi_{eff,i}$ can be different between two patches.

At a sufficiently large distance from the surface $r_0 \gg d_i$ where d_i is the patch size, the surface can be described by an average work function

$$\bar{\Phi} = \sum_i f_i \Phi_i, \quad (4.34)$$

3. Typically the photocathode is prepared, cleaned over several hours, and directly used in the measurement under extreme UHV conditions. This ensures a work function that is unaffected by surface effects, e. g. impurities.

where f_i corresponds to the fractional area of the patch i w. r. t. the total surface area. The escape process of the electrons, however, is likely to be affected by the individual work functions of each patch, since the local surface properties play a strong role in the photoemission process. The photoemission over the complete surface area is dominated by patches where the work function is smaller, since here a larger electron yield is achieved according to (4.32).

- **Surface roughness:** The electron source uses a photocathode stainless-steel surface that is manually polished and then covered with a thin layer (20 nm to 40 nm) of the photocathode material. The polishing is performed with fairly large grain sizes down to 0.1 μm , and investigations with a microscope showed that a perfectly plain surface can not be assumed [Zac14].

The surface roughness is described by the curvature radius of irregularities at the surface, which is therefore expected to be comparable to the granularity of the polishing paste that was used. Measurements showed that the surface roughness can have large effects on the work function,

$$\Phi_{eff} = \Phi + \Delta\Phi_r, \quad (4.35)$$

with $\Delta\Phi_r \leq 0.5$ eV for poly-crystalline copper [LL05]. It is expected that the values for poly-crystalline gold or silver are comparable to this value, since the surface roughness causes similar modifications of the local fields.

- **Electric fields:** External electric fields at the surface reduce the work function by the *Schottky effect* [DS73]. The effect describes the modification of the vacuum energy level E_{vac} . Under normal conditions, the vacuum level is reached for a distance $r \rightarrow \infty$ from the surface by the image charge potential V_{mir} in front of the surface. An external electric potential V_{ext} results in an effective potential $V_{eff} = V_{mir} + V_{ext}$, which features a maximum at distance r_0 , and decreases towards infinity.

The work function, which depends on the vacuum energy level E_{vac} , is then modified to

$$\Phi_{eff} = \Phi - \delta\Phi_{sch} \quad \text{with} \quad \delta\Phi_{sch} = -V(r_0) = \sqrt{\frac{qE}{4\pi\epsilon_0}}, \quad (4.36)$$

where E is the external field strength, ϵ_0 is the vacuum permittivity and q the elementary charge.

At the electron source described in this thesis, a field strength up to 500 kV/m is reached at the electron emission spot, which yields a fairly low value of $\delta\Phi_{sch} \approx 25$ meV. However, the local electric field can be significantly increased by the surface roughness, which can be described as

$$E = \beta \cdot E_0, \quad (4.37)$$

where β is the so-called *roughness factor*. It depends on the local curvature radius of the surface. The actual value of this factor is hard to estimate, but it is believed that $\beta = 10$ to 50 can be easily achieved [Zac14].

Since all these effects play a significant role at the electron source – manual preparation of the surface, long-term operation under vacuum conditions, electric fields at the plate setup – large deviations to the theoretical work function can be expected. When the single effects are combined, deviations of more than 1 eV can easily be inferred.

4.2.5 Description of the energy spectrum

The energy distribution of the emitted electrons can be described with the help of the three-step model of the photoeffect discussed above (figure 4.8). In this model, the energy distribution features an edge at $E_{max} = h\nu - \Phi$ that is described by the Fermi distribution (4.23). At a temperature of 300 K, the edge is smeared out by about 0.1 eV. Due to the energy distribution of the conduction band electrons, the energy spectrum of the emitted electrons features a tail towards lower energies (cmp. figure 4.7), resulting in a strongly asymmetric shape. Since only electrons with positive energy are released from the photocathode material, the energy spectrum is cut off at $E = 0$ for small photon energies $h\nu$.

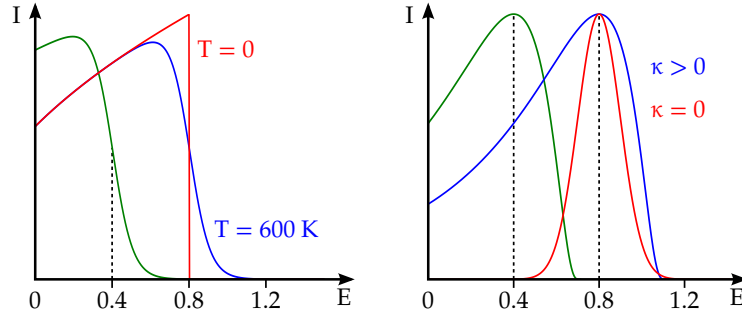


Figure 4.9.: Alternative models to describe the photo-electron energy spectrum. *Left:* Following the discussion in this section, the energy spectrum can be described by a shifted Fermi distribution with an edge E_{max} and a \sqrt{E} -like tail towards lower energies. *Right:* A more general description can be achieved with a *generalized normal distribution*, which is essentially an asymmetric extension of the standard normal distribution. A shape parameter κ describes the asymmetry, and $\kappa = 0$ corresponds to the normal distribution.

Fermi distribution

Following the discussion in section 4.2.2, the energy distribution can be described by a shifted Fermi distribution with edge $E'_F = E_{max} = h\nu - \Phi$ that is combined with a low-energy tail which follows a \sqrt{E} -like behavior (figure 4.9). This energy distribution can be written as

$$\eta_F(E > 0) = \sqrt{\frac{1 + \tau E - E_{max}}{1 + E_{max} \cdot (\tau - 1)}} \cdot \left[\exp\left(\frac{E - E_{max}}{k_B T'}\right) + 1 \right]^{-1}, \quad (4.38)$$

where τ is a shape parameter that describes the slope of the low-energy tail. The effective temperature $T' \geq T$ allows to include a possible broadening of the distribution due to energy losses during electron transport. One advantage of this model is that the shifted Fermi edge E_{max} can be determined directly from the fit, and there are no obvious correlations between the parameters.

However, during the analysis of the measurements it became clear that a more general model is better suited⁴ to describe the observed transmission functions. The model (4.38) is therefore not used in the analysis of the measurements.

4. The main issue is that the Fermi-based model takes too strict assumptions about the shape of the energy distribution, which often results in the fit to produce erroneous results.

Generalized normal distribution

A more general approach to describe the resulting energy resolution can be achieved with a Gaussian-like distribution. While one could simply use the symmetric normal distribution, the energy spectrum becomes strongly asymmetric for larger photon energies $h\nu$. This is expected from the photoemission model discussed above, where energy distribution follows the shape of the conduction band and at higher energies a larger fraction of conduction band electrons is emitted.

It therefore makes sense to describe the distribution by an asymmetric Gaussian function. For the sake of simplicity, the so-called *generalized normal distribution* of the second kind [HW97] is used (figure 4.9). The distribution is an extension of the normal distribution and features an additional asymmetry parameter κ that describes its *skewness*. When this parameter approaches zero, the generalized Gaussian takes on the symmetric form of the simple Gaussian.

The energy distribution of the emitted electrons can thus be described by a generalized Gaussian with mean energy \hat{E} , width σ'_E and shape κ :

$$\eta(0 < E < E_{lim}) = \frac{1}{\sqrt{2\pi}} \cdot \begin{cases} \frac{1}{\sigma'_E} \cdot \exp\left(-\frac{1}{2} \left[\frac{E - \hat{E}}{\sigma'_E}\right]^2\right) & (\kappa = 0) \\ \frac{1}{\sigma'_E - \kappa(E - \hat{E})} \cdot \exp\left(-\frac{1}{2\kappa^2} \cdot \ln\left[1 - \kappa \frac{E - \hat{E}}{\sigma'_E}\right]^2\right) & (\kappa \neq 0) \end{cases} \quad (4.39)$$

The width σ'_E can be converted into a Gaussian width σ_E that allows a comparison with the normal distribution (see below). The main advantage of this distribution over (4.38) is that it is more general and allows to include possible deformations of the energy spectrum. A disadvantage of this model is that the parameters are correlated – a larger value κ increases the effective width of the distribution, which must be compensated by a smaller value σ'_E . However, given its generality, this model is favored to describe the measured transmission functions that are discussed later in this chapter. The distribution $\eta(E)$ is therefore used in the analytical model of the transmission function (section 4.1.1), which is then fitted to the measurement data.

The maximal energy E_{lim} in (4.39) is only relevant if $\kappa \neq 0$. In this case, the distribution $\eta(E)$ only has limited support up to a specific energy due to its definition:

$$E_{lim} = \begin{cases} \infty & (\kappa \leq 0) \\ \hat{E} + \frac{\sigma'_E}{\kappa} & (\kappa > 0) \end{cases} \quad (4.40)$$

The distribution assumes the symmetric shape of the normal distribution for $\kappa \rightarrow 0$. However, the width σ'_E cannot be compared directly to the width of a typical normal distribution. To allow a direct comparison of these values, the parameters have to be transformed for $\kappa \neq 0$ to derive a Gaussian width σ_E . Similarly, the asymmetry parameter κ can be converted into the standard skewness γ :

$$\sigma_E = \frac{\sigma'_E}{\kappa} \cdot \sqrt{e^{\kappa^2}(e^{\kappa^2} - 1)} \quad (4.41)$$

$$\gamma = \frac{3e^{\kappa^2} - e^{3\kappa^2} - 2}{(e^{\kappa^2} - 1)^{3/2}} \cdot \text{sgn}(\kappa). \quad (4.42)$$

When this conversion is performed with values that result from a fit of the energy distribution, the parameter uncertainties have to be considered correctly according to error propagation.

4.2.6 Imprinting of a well-defined pitch angle

The design of the electron source allows to emit electrons at a defined pitch angle θ w. r. t. the magnetic field lines \vec{B}_0 at the emission spot. In general, the direction of electrons emitted from a flat photocathode surface follows a $\cos \theta$ -distribution [PB02]. Hence, the pitch angles cover the complete range between 0° and 90° . To produce a well-defined angle, the pitch angles have to be collimated into a narrower angular distribution.

This is achieved by a *non-adiabatic acceleration* of the emitted electrons. In contrast to the adiabatic motion of the electrons (2.7), this allows to change the transversal kinetic energy E_\perp (and accordingly, the pitch angle θ) independently of the magnetic field. From the Lorentz equation $F_L = q(E + vB)$ it is clear that the electrostatic acceleration against the magnetic field line is only possible while the electron has not gained a large amount of kinetic energy, $v \approx 0$. The acceleration therefore must be achieved by a strong electric field close to the photocathode.

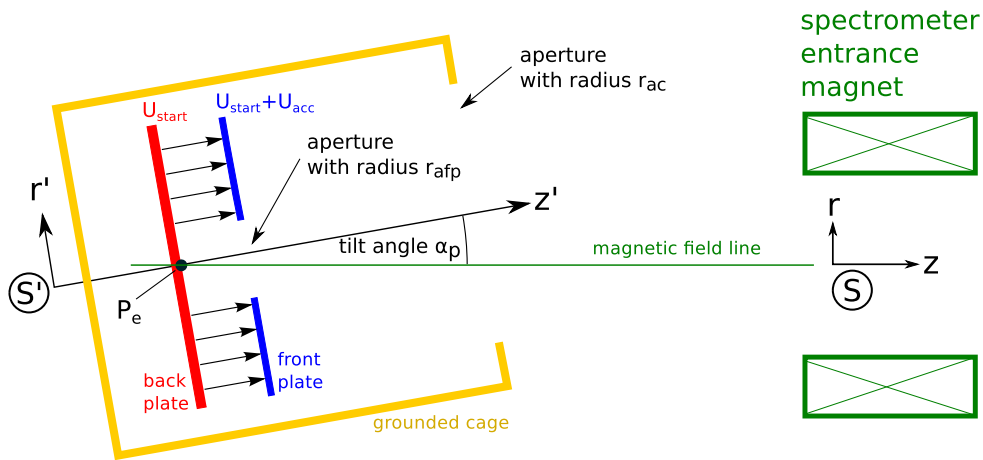


Figure 4.10.: Schematic drawing of the electron source setup. The design of the electron source features a setup similar to a plate-capacitor with two plates where a acceleration voltage U_{acc} is applied. The electrons are generated by the photoelectric effect from a photocathode on the back plate (see figure 4.6). A *starting voltage* U_{start} is applied on the back plate that defines the kinetic energy of the produced electrons, which are accelerated against ground potential after passing the front plate. The plate setup is mounted inside a grounded cage in order to shield the electric field between the plates from outside influences. The grounded cage with the plates can be tilted against the direction of the magnetic field by the so-called *plate angle* α_p . The non-adiabatic acceleration by the electric field imprints a well-defined pitch angle on the produced electrons, a feature known as *angular selectivity*. Figure from [Zac14].

For this reason, the electron source features a setup similar to a plate-capacitor as shown in figure 4.10. The photocathode surface is located at the center of a larger stainless steel plate. A second plate of the same dimensions with an aperture in the center is placed in front of the photocathode at a short distance. These two plates are called the *back plate* and *front plate*, respectively. The back plate is operated on a negative electric potential $U_{back} = U_{start} \gtrsim -18.6\text{ kV}$ that defines the kinetic energy of the electrons after acceleration against the surrounding ground potential, $E_{kin} = qU_{start}$. The front plate is operated on a more positive potential, so that a potential difference $U_{acc} = U_{front} - U_{back} \leq 5\text{ kV}$ is introduced between the plates. The emitted electrons are thus accelerated by a strong electric field

(up to 500 kV/m or more) towards the front plate, while their kinetic energy is low. The aperture in the front plate allows the electrons to leave the plate-capacitor setup and enter the beamline towards the spectrometer.

The plates are parallel to each other and mounted inside a grounded cage to ensure a homogeneous electric field that is shielded against outside influences. The complete setup can be tilted by a *plate angle* α_p against the direction of the magnetic field. In this case, the non-adiabatic acceleration achieves a defined pitch angle of the produced electrons that can be selected by tilting the setup and that depends on the electromagnetic conditions at the electron source (especially the magnetic fields).

This setup achieves a collimation of the electron beam with an angular spread in the spectrometer entry magnet of typically less than 5° . Under nominal conditions – i. e. a useful setup of the magnetic fields at the source and the entry magnet and while operating at $U_{start} \approx -18.6$ kV – this allows to produce pitch angles in the isotropic range $\theta_0 = 0^\circ$ to 90° in the entry magnet. It is thus possible to determine the transmission properties of an attached MAC-E filter like the KATRIN main spectrometer, as discussed earlier in this section.

Angular distribution

One can assume that the collimation through non-adiabatic acceleration results in a Gaussian distribution of the electron pitch angles at the end of the source cage. This is verified by corresponding simulations (section 4.8). For small pitch angles $\theta \rightarrow 0^\circ$ one must consider that the pitch angle cannot reach negative values due to its definition as a polar angle. Any angular distribution that spans into the negative regime is thus “wrapped” into positive direction, resulting in a deformation of the otherwise symmetric Gaussian distribution [Gro15].

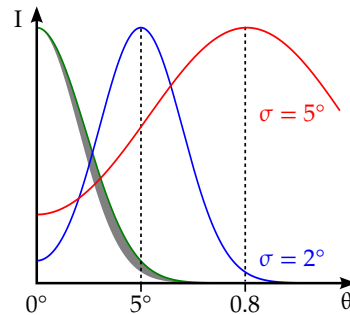


Figure 4.11.: Gaussian model to describe the photo-electron angular spectrum. The collimated angular spectrum of the emitted electrons can be described by the sum of two symmetric Gaussian distributions. For small pitch angles, $\theta \rightarrow 0^\circ$, the distribution becomes asymmetric since the pitch angle cannot take on negative values, resulting in a “wrapping” of the negative part of the angular distribution into the positive regime. The gray area indicates the broadening of the angular distribution due to this effect.

Taking this effect into account, the angular spectrum can be described by the sum of two Gaussian functions with mean angle $\hat{\theta}$ and width σ_θ (figure 4.11). The two functions are placed symmetrically

around the 0° -axis:

$$\zeta(0^\circ \leq \theta \leq 90^\circ) = \frac{1}{\sqrt{2\pi}\sigma} \cdot \left[\exp\left(-\frac{(\theta - \hat{\theta})^2}{2\sigma_\theta^2}\right) + \exp\left(-\frac{(\theta + \hat{\theta})^2}{2\sigma_\theta^2}\right) \right]. \quad (4.43)$$

The shape of this distribution is essentially Gaussian unless the mean angle $\hat{\theta}$ approaches 0° and the “wrapping effect” occurs. In that case, the distribution becomes increasingly asymmetric. This is in agreement with data from simulations and measurements that verify this effect.

The angular distribution (4.43) is used together with the energy distribution (4.39) in the analytical model of the transmission function (4.10) that has been derived above. The analytical model thus uses a realistic description of the energy and angular distribution of the electrons, and is thus well-suited to describe the transmission function measurements discussed in section 4.4.

4.2.7 Adiabatic electron transport towards the spectrometer

After leaving the grounded source cage, the emitted electrons propagate adiabatically towards the spectrometer where they reach the spectrometer entry magnet. The adiabatic transformation (2.7) increases the pitch angle as the electrons travel into the higher magnetic field at the spectrometer entrance. Since the motion is adiabatic, the pitch angle transformation depends only on the ratio of the magnetic fields at the end of the electron source and in the spectrometer magnet:

$$\sin \theta_0 = \sin \theta_{source} \cdot \frac{B_0}{B_{source}}. \quad (4.44)$$

The acceleration processes and the electron transport towards the spectrometer, which possibly influence the resulting distributions, can be investigated by measurements and particle-tracking simulations. Both approaches have been employed in the context of the commissioning measurements at the KATRIN main spectrometer, and will be discussed in the remainder of this chapter.

4.3 Design of the electron source

The electron source has been continuously developed and improved over the recent years [V⁺09, V⁺11, B⁺14a, B⁺17a]. This section explains the technical design of the source, followed by a description of the reworked slow-control system.

In the first commissioning phase of the KATRIN spectrometer and detector section (SDS-1, 2013), the electron source was mounted for the first time at the main spectrometer. It was used to determine important parameters like the effective retarding potential in the analyzing plane [Gro15]. It allowed to determine many characteristics of the MAC-E filter and was utilized in related measurements, e. g. to verify the integrity of the inner-electrode system [Bar16]. The SDS-1 setup is shown in figure 4.12.

However, the key feature of *angular selectivity* – the production of electrons with well-defined pitch angles – was not fully achieved in the SDS-1 measurement phase. Although angular selectivity had been proven to work in a test setup at WWU Münster [Zac14], the different electromagnetic conditions at the KATRIN site had unforeseen effects on the electron transport inside the source. Consequently, the angular distribution of the produced electrons was considerably broader than expected. It was therefore impossible to achieve an angular spread sufficiently small to investigate the spectrometer transmission properties in full detail. Furthermore, the integration with the KATRIN slow-control system was not fully implemented yet, and it was not possible to perform automated overnight measurements without the need for manual adjustments by the measurement operators.

During the preparations for the second commissioning phase (SDS-2, 2014–2015), the electron source design was reworked and improved. Especially the issues that prevented angular selectivity to work were closely investigated. To reduce the angular spread of the electrons, the front plate aperture was reduced from a diameter of 24 mm to 6 mm in coordination with particle-tracking simulations that indicated an improvement of the electromagnetic conditions [Zac14]. The properties and the stability of the photocathode was further examined to ensure successful long-term operation during the SDS-2 measurements [Bus14]. The actuation of the plate setup – which is required to imprint a defined pitch angle on the produced electrons – was reworked to utilize pressured-air linear motors in combination with a precise read-out of the plate angle. The design allows to remotely tilt the source cage to an arbitrary polar and azimuthal angle. Furthermore, the high voltage design of the electron source and the corresponding infrastructure (power supplies

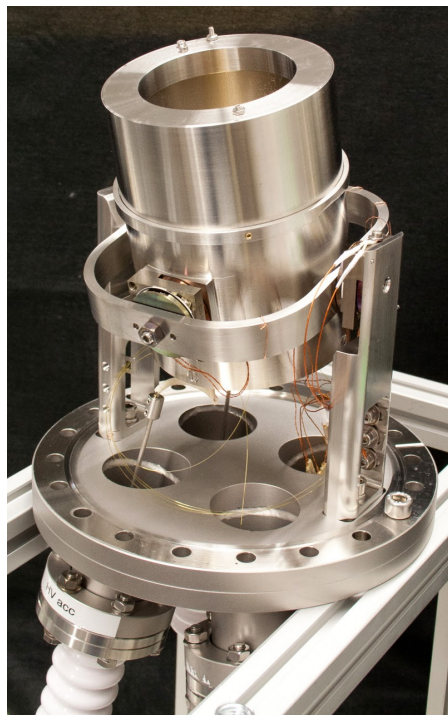


Figure 4.12.: The electron source in the pre-SDS-2 setup. The source cage containing the plate-capacitor setup with the photocathode is installed in a gimbal mount and can be tilted against two axes. The complete system is mounted on a vacuum flange that allows the source to be installed in different setups. The flange also contains the feed-throughs for high voltage, UV light and mechanical plate actuation. Image from [Zac14].

etc.) was improved to allow remote operations. Figure 4.13 shows the SDS-2 setup of the electron source.

The slow-control interface of the complete system – including the various auxiliary devices like the UV laser and the UV-LED setup – was revised to allow better integration with the KATRIN slow-control system [Jos13]. The optical system was improved to utilize several UV LEDs which that can be switched remotely to allow automated measurements at selected UV wavelengths in combination with a monochromator [Pot13].

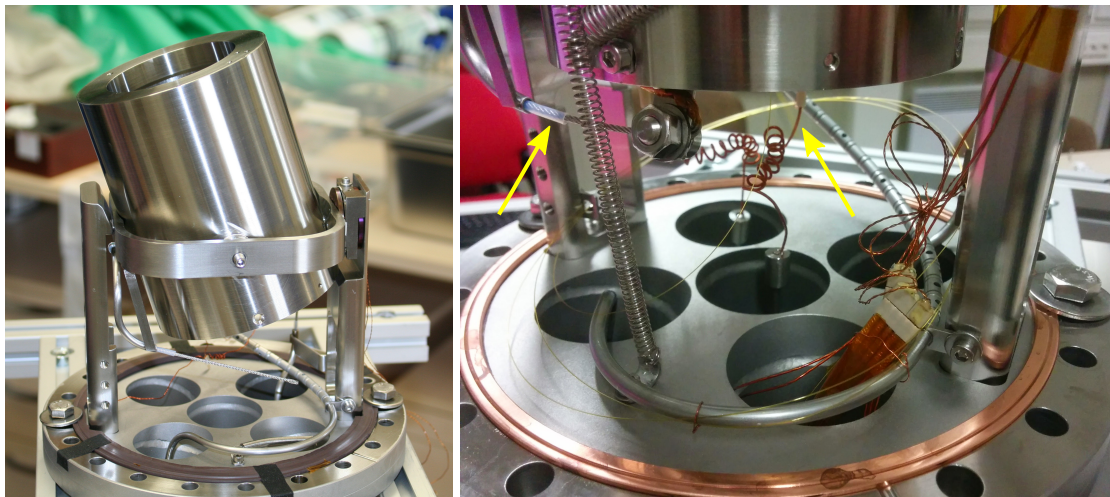


Figure 4.13.: The improved electron source setup in the SDS-2 phase. The most apparent change is related to the plate actuation, which is now performed by linear motors that are installed on the ambient-air side of the vacuum flange. The linear motion is converted into a tilt motion of the source cage via Bowden cables. The high voltage wires have been reworked to remove the ceramic insulators that were used in the original setup and caused voltage stability issues (cmp. figure 4.14).

Another crucial improvement was the re-design of the HV wires inside the source, which connect the back and front plate to the corresponding feed-throughs on the vacuum flange. In the original design that was used in the SDS-1 measurement phase, the Kapton wires have been additionally insulated with a layer of small ceramic tubes. Instabilities of the HV system that were encountered during measurements were attributed to issues with the HV cabling, which were investigated during the SDS-2 preparations. To spot any occurring HV breakdowns that are typically accompanied by an electric discharge, a digital camera was mounted on a window in the vacuum flange. This allows an optical monitoring of the conditions at the back side of the source cage (i. e. pointing away from the direction of the electron beam). Using this approach it became clear that the ceramic parts enclosing the wire can induce voltage breakdowns, since they accumulate charge during HV operation. Once enough charge has been accumulated, a visible discharge occurs that clearly affects the high-voltage stability (figure 4.14). This issue was resolved by removing the ceramics from the wire and by switching to wires with larger diameter to reduce the electric field strength at their surface.

The revised system was tested in preparation measurements at the KATRIN monitor spectrometer (“MoS”) before the start of the SDS-2 measurements. This preparation phase allowed detailed functionality tests of key features of the electron source (especially angular selectivity) in a real MAC-E filter setup. The electromagnetic conditions at the monitor spectrometer are comparable to the main spectrometer, so that the source properties determined in the MoS measurements provided substantial

input for the SDS-2 measurement phase. The results from both measurement phases are discussed in section 4.4.

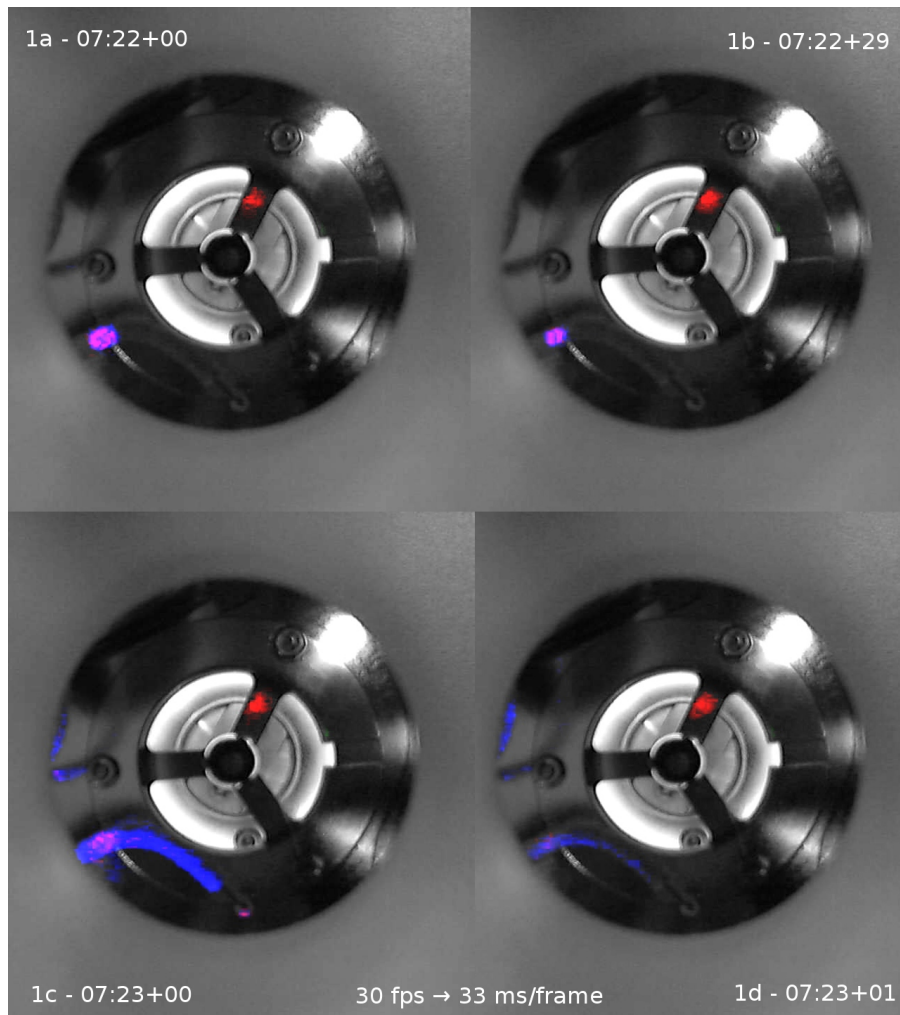


Figure 4.14.: Electric discharge caused by charge build-up on ceramic insulators. The original electron source design used Kapton-insulated wires to connect the back/front plate to the high voltage power supply. The wires were additionally covered with small ceramic insulator tubes to improve voltage stability. Investigations with a digital camera at a vacuum window showed that this design can result in electric discharges due to charge build-up at the ceramics, which leads to voltage breakdowns and affects the high voltage stability. The shown pictures correspond to four single frames taken with the camera (the notation mm:ss+nn indicates m=minute, s=second, n=frame) at 30 fps frame rate. The images were digitally enhanced for a better visibility of the discharge, which is seen here as blue light. The pictures clearly show that the light emission corresponds to the Kapton wires at the bottom left of each image. The discharge disappears quickly after less than 0.1 s (note that images 1b–d are only two frames apart). The circular bright shape at the center of each image is the backside of the source cage with the photocathode. The small red dot is a reflection from camera LED that is not related to the electron source.

4.3.1 Technical implementation

Mechanical design

The technical design of the electron source is developed around the plate-capacitor setup depicted in figure 4.10. Electrons are created on a photocathode on the so-called *back plate* which is operated on a starting voltage $U_{start} = U_{back}$. The emitted electrons are accelerated towards the *front plate*, which is operated on a positive voltage difference $U_{acc} = U_{front} - U_{back} \leq 5$ kV w. r. t. the back plate.

The setup uses two stainless steel disks with radius $r_p = 30$ mm for both plates, which form two parallel electrode surfaces that resemble a plate capacitor (figure 4.15, left). The plates are placed at a distance $d = 10$ mm, resulting in an electrostatic acceleration field of up to $E_{acc} = U_{acc}/d = 500$ kV/m. Both plates were electro-polished before installation to improve the stability under high-voltage operation. Additional HV conditioning is typically performed before the source is brought into operation. The front plate has a thickness $d_{fp} = 2$ mm and features an aperture of $r_{afp} = 3$ mm to allow the accelerated electrons to pass through. The thickness of the back plate is $d_{bp} = 3$ mm. It features an aperture at its center to install a photocathode holder (see below). The mechanical design ensures that the surface of the photocathode aligns with the surface of the back plate and is centered w. r. t. the front plate aperture. The plates are insulated against each other and against the grounded cage by *polyether ether ketone* (PEEK) tubes that also hold the setup in place. The grounded source cage which surrounds the plate setup has an inner radius of $r_c = 50$ mm with an aperture of $r_{ac} = 35$ mm at the front end.

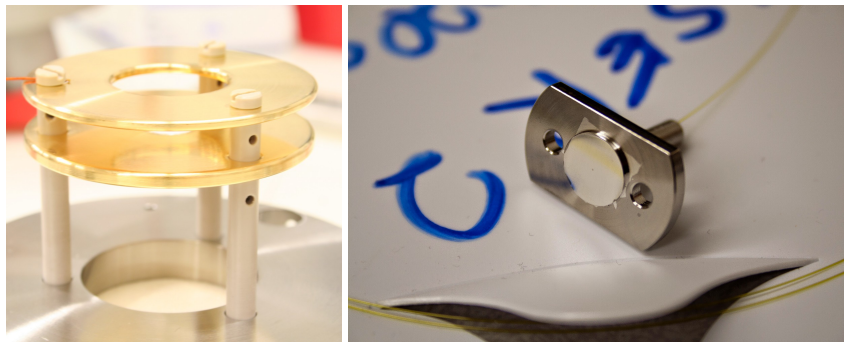


Figure 4.15.: The plate-capacitor setup and the photocathode. *Left:* An acceleration voltage up to 5 kV is applied between the two plate electrode depicted here (bottom: back plate; top: front plate). The electrodes are held in place by three columns of PEEK insulators. The plate setup is mounted on the backside of the grounded source cage (figure 4.12). The photocathode is mounted into an aperture at the back plate, so that emitted electrons are accelerated towards the front plate and leave the source cage in forwards direction. Note that this image shows the SDS-1 design with a front plate aperture of 24 mm diameter, which was reduced to 6 mm in the SDS-2 setup. *Right:* The photocathode consists of a thin optical fiber (diameter 200 μ m) that is glued into a stainless steel holder. The front surface of the holder with the glued-in fiber is polished and coated with a photocathode material, e. g. silver or gold (thickness 40 nm and 20 nm). Incident UV light that is guided through the fiber releases electrons from the photocathode due to the photo-electric effect, which occurs at wavelengths around 300 nm depending on the photocathode work function. Images from [Zac14].

The photocathode holder consists of a stainless steel plate that has a small aperture to glue in an optical fiber of 200 μ m diameter (figure 4.15, right). The fiber connects to an optical vacuum feed-through and guides the incident UV light to the photocathode. After the fiber is glued in, the holder

with the fiber is manually polished to create a flat front surface. The photocathode material (e. g. gold) is then deposited on the surface by *electron beam physical vapor deposition* (EBPVD), which allows to create a uniform material layer of defined thickness on the order of several nm. During operation of the electron source, the photocathode coating is back-illuminated by UV light from the fiber to induce a photoelectric effect that releases electrons from the surface. The MoS and SDS-2 measurements used different gold photocathodes with a coating layer of 20 nm thickness. The early SDS-2 measurements (up to 12/2014) used a silver photocathode with 40 nm thickness⁵ before the photocathode was replaced in a maintenance break.

The grounded cage is gimbal-mounted to allow independent tilting in two axes. Since it contains the plate electrodes together with the photocathode, the complete system can be tilted without affecting the electric fields that accelerate the emitted electrons. This is especially important for the acceleration field between the plates to ensure a consistent electron acceleration with different tilt angles. If the source cage is tilted, the electrons are accelerated against the direction of the magnetic field to imprint a defined pitch angle, as discussed in the previous section. The center of rotation is aligned with the emission spot on the back plate (center of the photocathode). This design ensures that the magnetic field line that the emitted electrons follow does not change when the cage is tilted. This allows consistent measurements at different tilt angles without affecting other operational parameters. A precise monitoring of the tilt angle is achieved by piezo-electric motors (Attocube ANR240) that feature a resistive readout of the absolute rotation angle with an accuracy of 0.05°. Note that these motors do not provide sufficient torque to tilt the source cage under vacuum conditions, which makes it necessary to implement another method of actuation. The SDS-2 design therefore uses two linear motors (Bibus Tesla 1620) that are driven by pressured air and allow operation in a strong magnetic field⁶. The motors are mounted on the outside of the vacuum chamber, and their motion is brought into the source cage by two linear feed-throughs on the chamber flange. Bowden cables connect the inside of the feed-throughs to each axis of the gimbal mount. The design allows to tilt both axes independently, so that an arbitrary polar/azimuthal angle can be reached. The polar angle is mechanically limited to roughly 16° due to the dimensions of the source cage and the surrounding vacuum chamber. The linear motors are controlled by a software implemented in LabView, which also takes care of the transformation between the cartesian and the polar coordinate system for the tilt angle⁷.

Electromagnetic design

The electron source generates electrons by photo-emission from incident UV light on a photocathode. The emitted electrons are accelerated by a strong electrostatic field. The actual propagation of the electrons is defined by the combination of electric and magnetic fields according to the Lorentz force, $F = q(E + v \cdot B)$. A magnetic field of $B_{start} = 30$ mT is typically reached at the photocathode; the actual value depends on the experimental setup. The strong electric field of up roughly 500 kV/m results in a non-adiabatic acceleration of the electrons, which imprints a defined pitch angle. The plate setup is therefore essential to achieve angular selectivity. The non-adiabatic acceleration is only possible while the contribution of the electric field is substantially larger than the velocity-dependent contribution of the magnetic field. As the electrons are quickly accelerated to a kinetic energy of 5 keV towards the

5. The thickness was increased to compensate the lower density of silver, which is roughly 50% of the density of gold.

6. Field strengths of more than 30 mT are typically reached at the experimental site.

7. The measurements typically use the polar/azimuthal system since it allows an easier comparison of the operational parameters. The tilting itself is based on the two-axial system that follows the motor actuation, and is typically oriented so that it aligns to the horizontal/vertical axes of the experimental system.

front plate and the strong electric field vanishes afterwards, the magnetic field takes over the electron propagation from here. From this point on the electrons move adiabatically towards the spectrometer entry magnet. At the SDS-2 setup, a magnetic field of $B_0 = B_{PS2} = 4.5 \text{ T}$ is reached in the PS2 entry magnet. The MoS setup features a stronger field of $B_0 = B_{max} = 6 \text{ T}$. The pitch angle that is reached in the entry magnet depends on the ratio B_{start}/B_0 according to the adiabatic transformation (2.7).

Electrons that are reflected before reaching the detector – either by the electric retarding potential at the analyzing plane of the spectrometer or by the strong magnetic fields at the spectrometer magnets – can be trapped between the electron source and the spectrometer. Trapped electrons can induce a Penning discharge, which typically has disastrous consequences for the photocathode and likely requires a maintenance break to bring the system back into operation.

To avoid a build-up of stored electrons and a subsequent discharge, a dipole electrode is placed in the beamline between the source cage and the spectrometer. The electric field \vec{E} induced by the electrode results in a drift of the electrons according to

$$\vec{v}_{drift} = \frac{\vec{E} \times \vec{B}}{B^2}, \quad (4.45)$$

with \vec{B} the magnetic field at the dipole electrode. Since the magnetic field is almost fully oriented in axial direction and the dipole electrode is designed to achieve a vertical electric field, the resulting drift is in horizontal direction.

The MoS measurements used a half-shell dipole electrode that spans 170° at a radius $r_{dip} = 30 \text{ mm}$, and a similar half-shell electrode of 33.5 mm radius was used in the SDS-2 measurements. In both settings the dipole electrode is operated at a high voltage of $U_{dip} \leq 4 \text{ kV}$. Corresponding measurements confirmed that the electrode removes trapped electrons efficiently and allows a safe operation of the electron source (see section 4.4.2).

Optical system

The optical system provides UV light for the photocathode and is thus a crucial component of the overall setup. The complete system is set up in an optically sealed box (“UV box”), where the UV light is created and guided into the electron source through an optical fiber of $200 \mu\text{m}$ diameter (figure 4.16). One can choose between two UV light sources, a high-intensity laser or a system of LEDs that allows measurements at different wavelengths.

The primary light source is a frequency-quadrupled Nd:YVO₄ laser (InnoLas mosquito-266-0.1-V) which provides UV light of 266 nm (1 nm FWHM) at high intensity ($< 10 \text{ mW}$ output power). The laser is operated in pulsed mode (using a fast Q-switch) with pulse widths of $< 20 \text{ ns}$ typically. The pulse frequency can be varied from between 40 kHz and 100 kHz , where lower pulse frequencies increase the intensity of the UV light. The intensity also depends on the pumping laser diode current of 6 A to 8 A . It can be further adjusted by an internal attenuator ($\lambda/2$ -plate with polarizing filter). Additionally it is possible to further reduce the intensity by a mounting a *neutral density* (ND) filter in the optical beamline. The measurements typically use a 1% filter to achieve a reasonable electron rate at the detector (several kcps) with the electron source. Under nominal conditions, the 100 kHz setting with a current of 6 A (MoS) or 7 A (SDS-2) was used. The short pulse width allows time-of-flight measurements with a precisely known starting time of the electrons; this feature was utilized in several measurements.

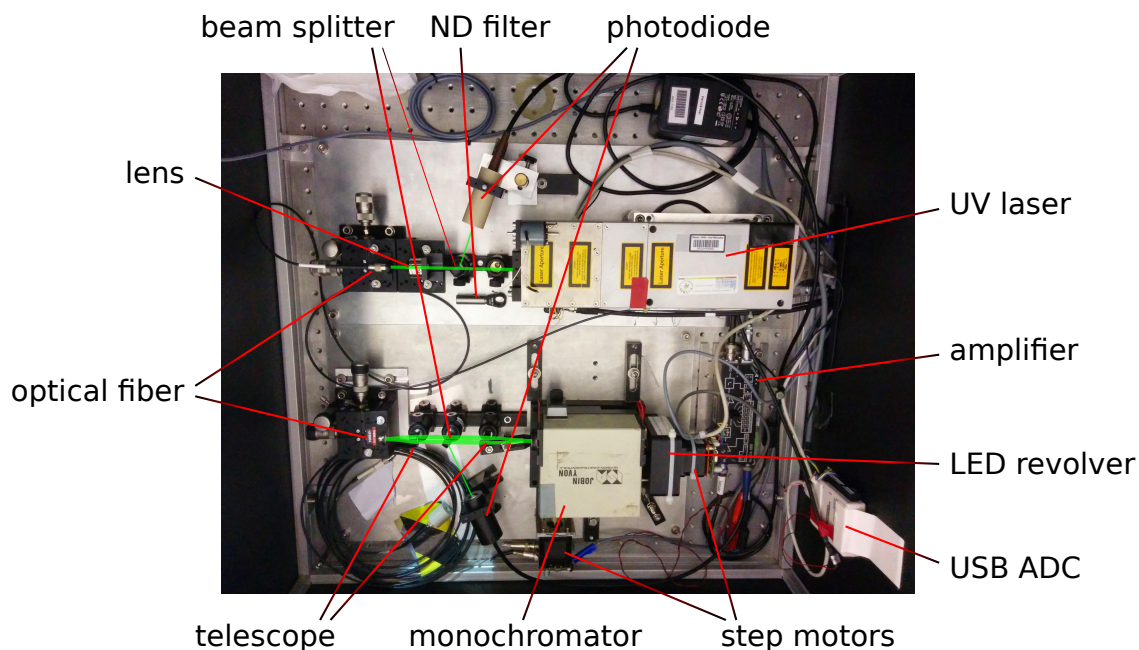


Figure 4.16.: The optical system. The “optics box” of the electron source contains all devices related to the production of UV light. The box is optically sealed to allow operating a class-3 laser system under standard laboratory conditions without special restrictions. The green lines in this picture indicate the optical paths. The section at the top contains the UV laser (right), a photodiode that monitors the light intensity (center), and an aspheric lens to focus the light into the fiber aperture (left). The optical fiber guides UV light into the electron source system. An amplifier (far right) is used to convert the photodiode current into a voltage that can be measured with a LabView-controlled ADC device. The bottom section contains the LED system that can be used as an alternative to the laser. It features a revolver setup to operate multiple UV-LEDs (right), a monochromator to select a specific wavelength (center), another photodiode and a two-lens optical telescope to focus the light beam. Again, the UV light is focused into an optical fiber that connects to the electron source. With this setup it is possible to quickly switch between the two light sources, depending on the measurement requirements.

A fraction of UV light (around 2%) is coupled out by a beam splitter (Thorlabs BSF05-A) to monitor the light intensity with a photodiode (OSI UV-035EQ). The signal of the photodiode is amplified, read out by an ADC and monitored by the control system. It can be used to observe the stability of the UV light and apply corrections if necessary⁸. The laser light is focused into a $\varnothing 200\text{ }\mu\text{m}$ optical fiber by an aspheric lens. The fiber connects to an optical feed-through on the source flange to guide the UV light to the photocathode.

Alternatively, an array of LEDs can be used to provide UV light. The LEDs are mounted on a rotator (“revolver”) that is moved by stepper motor; this allows to place a selected LED on the optical axis. The setup uses six different ball-lens UV-LEDs (Roithner UVTOP260–310) with peak wavelengths between 265 nm and 305 nm and 12 nm FWHM. The LEDs couple into a monochromator with 4 nm FWHM to select an arbitrary wavelength. The monochromator is also operated by a stepper motor to allow remote operation. The control software provides an interface to both motors, so that it is

⁸. Changes in light intensity affects the achieved electron rate accordingly. The electron rate can be normalized to the photodiode signal to correct this effect. The correction must include the wavelength-dependent reflectance of the beam splitter and the quantum yield of the photodiode.

possible to perform measurements at an arbitrary wavelength $\lambda = 250$ nm to 330 nm from the available LEDs. Due to the Gaussian-like emission profile of the LEDs, the light intensity diminishes quickly if wavelengths far off the peak wavelength are selected.

The LEDs are driven by a function generator (“pulser”) that provides a voltage up to 10 V. The internal $50\ \Omega$ resistor of the device is used to limit the LED current. The pulser allows to operate the LEDs at arbitrary pulse frequencies and widths. The pulser setting affects the achieved light intensity, so that the parameters can be tuned to match the requirements of the measurement that is performed. Typically, a voltage of 8.5 V is used with a pulse frequency of 100 kHz (to match the laser setting) and 10% duty cycle (1000 ns pulse width). In this case the LEDs receive a peak current of 200 mA, which averages to 20 mA given the duty cycle in pulse mode and thus conforms to the LED specifications. Although time-of-flight measurements are also possible with LEDs, the laser is typically used due to the significantly shorter pulse length. LED measurements are mainly used in dedicated measurements, where wavelength-dependent effects are investigated.

As with the laser, a beam splitter with a photodiode is used to monitor the light intensity. The divergent light beam emitted from the monochromator is focused by an optical telescope that consists of two convex lenses. The light is then guided into an optical fiber that is compatible with the one used for the laser. An on-line calibration of the monochromator is possible by monitoring the light intensity of a given UV LED at different wavelengths, i. e. by determining the emission profile. If the emission profile of the LED is known (e. g. from an earlier reference measurement), a possible offset of the monochromator wavelength can be corrected. This approach has been used in the measurements discussed later (section 4.4). For the reference measurement, the monochromator was calibrated beforehand with the known wavelength of the laser as a reference.

Since both light sources (laser and LEDs) are set up independently in the UV box, they can be switched by connecting a different optical fiber to the electron source (cmp. figure 4.16). The corresponding photodiode has to be connected manually to the amplifier if a monitoring of the intensity is desired.

4.3.2 Integration with other systems

The slow-control software that was developed for the SDS-2 measurements allows to adjust and monitor the majority of operational parameters (figure 4.17). The software is implemented in LabView and grouped into the different sub-systems that are required to operate the electron source (figure 4.18). At the SDS-2 setup, the software was integrated with the existing slow-control system of the KA-TRIN main spectrometer⁹. This allowed a remote control of the electron source that is consistent with other systems and provided the possibility for scripted measurements, where the parameters are automatically adjusted by the run-control software ORCA (cmp. section 3.6.1). The system was tested beforehand at the MoS setup, where the parameters were controlled directly via the LabView user interface.

The following parameters are available in the slow-control software:

- **Dipole electrode:** In contrast to the power supplies for the starting and acceleration voltage that are integrated with the overall HV system, the dipole power supply is directly controlled by the software. The power supply provides two output channels; one is used to generate a positive voltage up to 4 kV for the dipole electrode. The control software allows to set and read

9. The integration uses so-called *shared variables* that can be accessed from an external location in a computer network.

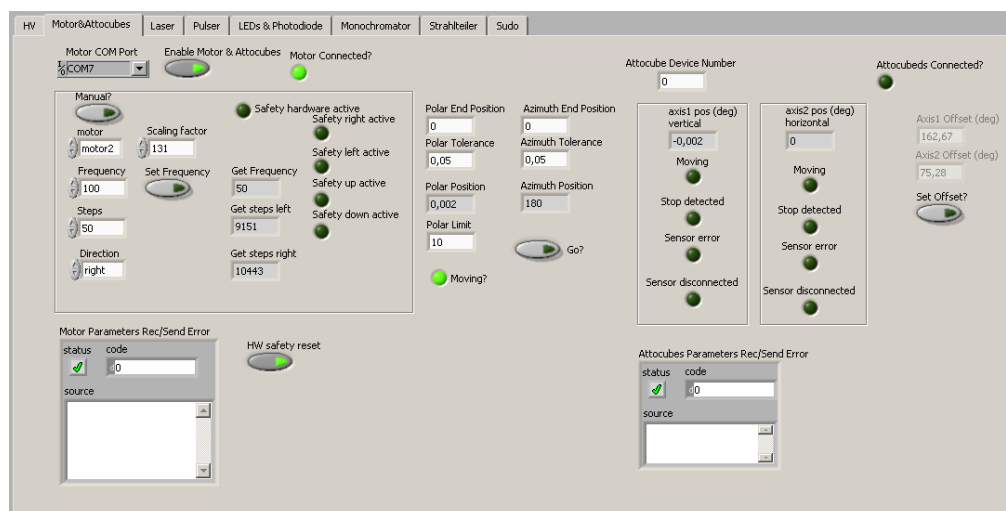


Figure 4.17.: The control software to operate the electron source. The LabView software that was implemented for electron source measurements allows to change all relevant operational parameters, such as the tilt angle of the plate setup, the selected wavelength of the monochromator, or the dipole electrode voltage. The software runs continuously on a *control PC* that is mounted in the control rack (see figure 4.18). Remote operation is possible via so-called *shared variables* in the LabView implementation, which integrate the electron source with the existing slow-control system at the KATRIN site. It is thus possible to perform fully automated measurements, where parameters are controlled by ORCA run scripts that also manage the data taking.

back the voltage, and to monitor the electrode current (which is useful to investigate the HV stability).

- **Plate actuation:** The tilt angle of the source cage can be adjusted either by setting the angles of the two independent axes, or by setting a polar and azimuthal angle. The software automatically performs a conversion between the coordinate systems. To tilt the source cage to the desired position, the software performs an iterative movement where each step is calculated as an angular distance between current and target position. The software moves the linear motors until the distance is smaller than a given tolerance. The absolute tilt angle (i. e. the “zero position”) must be determined beforehand in a dedicated measurement (section 4.4.4).
- **UV laser:** The laser is controlled over a USB interface. For the operation of the electron source, it is possible to adjust the pulse frequency and the diode current. A “stand-by” flag can be used to quickly toggle the light emission. The laser system monitors the temperature of the laser diode and the two frequency-doubling crystals (“SHG/FHG”, second/fourth harmonic generator). The temperature monitoring is especially important while the components are brought to operational temperature (“warm-up”). In this phase the light intensity shows considerable fluctuations that can be monitored by the photodiode.
- **UV LEDs:** To select a desired LED with a given wavelength as a light source, the control software operates the two stepper motors for the LED revolver and the monochromator. It is possible to select one of the six available LEDs by their peak wavelength and to move the monochromator to an arbitrary wavelength. The current position of both stepper motors is monitored to verify that the target has been reached. The software allows to adjust the calibration of both motors to ensure that the desired wavelength is selected.

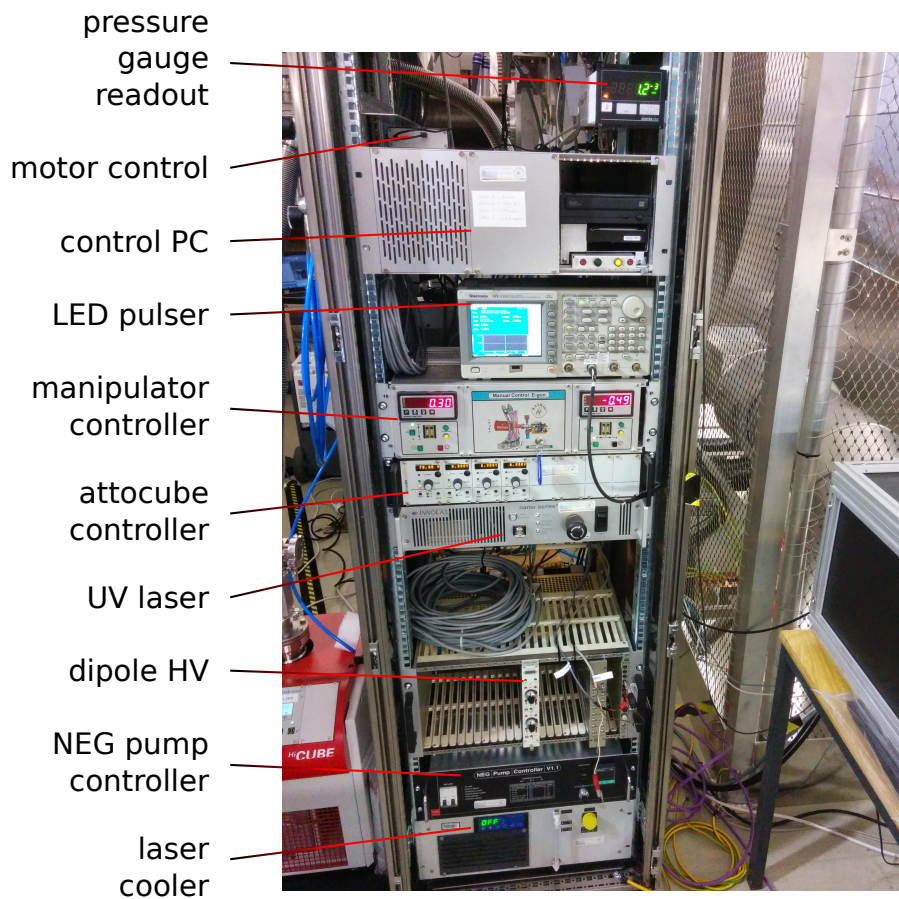


Figure 4.18.: The electron source control rack used in SDS-2 measurements. The control rack contains various auxiliary devices that are necessary to operate the electron source. Examples include the laser controller and the laser cooling system, the frequency generator to operate the UV-LEDs („LED pulser”), or the control PC that runs the LabView software. The control rack was installed next to the electron source at the spectrometer entrance and the optics box. The control PC is integrated with the KATRIN slow-control system via a local network connection. A reference trigger signal from the laser controller or the LED pulser is fed into the DAQ system via a BNC cable to provide start time information for time-of-flight measurements.

- **Photodiode:** The photodiodes inside the UV box allow to monitor the intensity of the UV light that is produced by either the laser or the LEDs. The amplified voltage signal of the selected photodiode is measured by a USB device (NI USB-6008) that is integrated with LabView. The signal is evaluated at an interval of 1 s typically and made available to the KATRIN slow-control system. Note that due to limitations of the data rate in the slow-control system, a monitoring interval of 10 s is used here. The high-resolution data can be accessed via logfiles that are stored to disk by the LabView software.

Independent control softwares are used to control the HV system of the electron source (starting and acceleration voltage) and the movement of the UHV manipulator (position of the electron source in the flux tube). The latter is required to investigate the transmission properties of the main spectrometer over the complete analyzing plane. The UHV manipulator was not used in the MoS measurements. In both cases, the LabView software was implemented already for the SDS-1 measurements and only

slightly adjusted for the SDS-2 phase. It was integrated with the overall KATRIN slow-control system at the main spectrometer together with the new control software discussed above, so that a full remote operation of the electron source could be achieved.

4.4 Measurement principles and analysis strategies

This thesis focuses on the commissioning of the electron source with its revised design (see section 4.3) during the second commissioning phase of the KATRIN spectrometer and detector section (SDS-2) in 2014–2015. Preparation measurements have been carried out at the KATRIN monitor spectrometer (MoS) in summer 2014, as well as functionality tests in a laboratory setup at WWU Münster.

The different measurements are discussed in this section (MoS: section 4.5, SDS-2: section 4.6). An investigation of the expected uncertainties is presented in section 4.9. First of all, however, important measurement principles that have been applied during the commissioning measurements will be shortly explained.

4.4.1 Electron rate

A basic measurement of the electron source functionality is the investigation of the achieved electron rate. When the electron source is operated in full transmission ($E = qU_{start} \gg qU_{ana}$) and at zero angle¹⁰ ($\alpha_p = 0^\circ$), the observed rate only depends on the used light source since *all* electrons reach the detector. The electromagnetic settings of the spectrometer do not affect the observed rate in this case.

The produced electron rate depends on several factors: The number of emitted electrons is proportional to the intensity of the incident UV light at the photocathode since photoemission is a statistical process where each photon of sufficient energy has a specific probability to release an electron from the photocathode material. The probability is mainly determined by the difference between photon energy (depending on its wavelength) and work function of the photocathode, where a larger difference increases the electron yield and therefore the observed electron rate. The light intensity depends on the used light source: In case of the laser ($\lambda = 266$ nm), the intensity is controlled by the laser settings (pump laser diode current and pulse frequency). It is attenuated both internally (by a polarizing filter) and externally (by a ND filter), and the parameters can be tuned to achieve the desired rate. The laser intensity increases with the diode current and decreases with the pulse frequency (since a higher frequency corresponds to shorter pulses where less photons are emitted). In case of the LEDs the intensity depends on the used LED (which have different emission profiles), the pulser settings (voltage and pulse width) and the monochromator position. The LED emission profiles have been determined at the beginning of the SDS-2 measurements as shown in figure 4.19.

It is possible to monitor the light intensity by a photodiode that is installed at the optical system of the electron source. Here one must consider the wavelength dependency of the photodiode and the beam splitter, which directs a fraction of UV light onto the photodiode for monitoring. This allows to determine relative changes in light intensity from the photodiode signal, which is especially important where measurements at different wavelengths are performed (e. g. to determine the work function of the photocathode, see section 4.4.8 below). The analysis presented here includes the necessary corrections wherever appropriate. The UV light is further attenuated before it reaches the photocathode, e. g. by the optical couplings; it is, however, assumed that these intensity losses are constant over time and do not depend on the used light source.

10. At non-zero plate angles, magnetic reflection could occur which blocks electrons from being transmitted regardless of their kinetic energy.

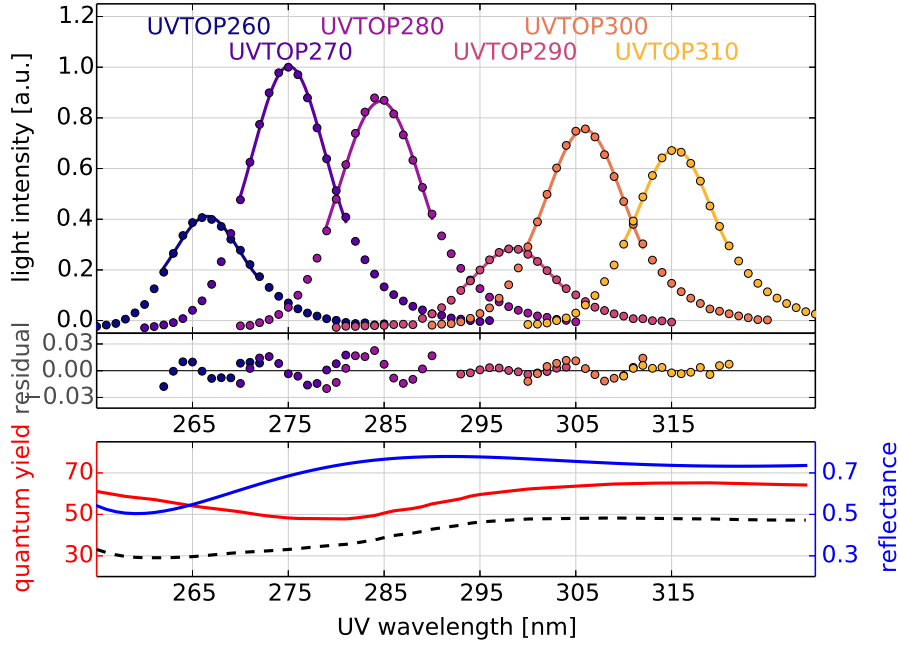


Figure 4.19.: Emission profiles for the LEDs used at the MoS and SDS-2 setups. The shown emission profiles for six LEDs were determined by measuring the voltage of the photodiode which is used to monitor the light intensity. The monochromator used to select a specific wavelength for each data point was calibrated beforehand against the reference wavelength of the laser ($\lambda = 266(1)$ nm). Around the peak intensity the emission profile can be described by a Gaussian distribution, which allows to determine the peak wavelength. The bottom plot shows the quantum yield of the photodiode and the reflectance of the beam splitter in the optical beamline. The dashed black line indicates the combined correction factor by which the photodiode voltage has to be divided to correctly determine the light intensity (all values given in %).

In general, the electron rate achieved with the laser is larger than with the LEDs due to the significantly higher light intensity of the laser. If a higher electron rate is desired in a measurement that uses LEDs, the LEDs can be operated at a large pulse width. This is, however, not useful in measurements where a pulsed electron beam with a narrow time distribution is required (e. g. time-of-flight measurements). Hence, the regular measurements performed at the SDS-2 setup always used the laser to provide UV light. LEDs were only used for dedicated measurements at selected wavelengths.

The stability of the electron rate is affected by light intensity fluctuations – e. g. due to warm-up effects or natural instabilities of the laser system. These fluctuations can typically be corrected by normalizing the observed rate to the photodiode signal. Changes of the surface conditions at the photocathode (i. e. changes of the work function) can result in a slow drift of the observed electron rate that cannot be explained by light intensity fluctuations. If the work function changes over time, it affects the electron yield for a given UV wavelength which changes the observed electron rate accordingly. Earlier measurements during the SDS-1 commissioning phase and at the test setup at WWU Münster indicate that the rate typically shows a slow decrease while the electron source is in operation. It is assumed that this is caused by cleaning of the photocathode surface due to ion bombardment under vacuum conditions.

It is therefore interesting to monitor the rate stability over different time periods in order to investigate these effects. Corresponding measurements have been performed at the MoS setup (section 4.5.2) and at the SDS-2 setup (section 4.6.2).

Determining the electron rate

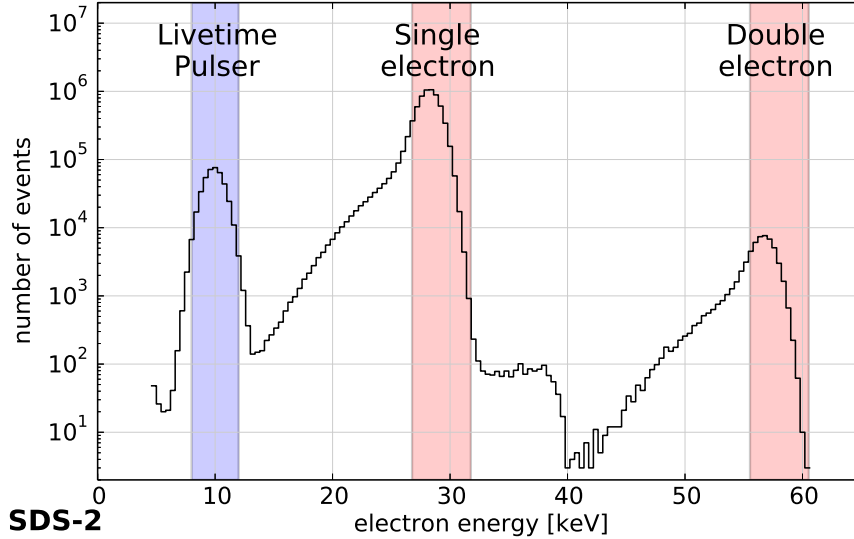


Figure 4.20.: Typical electron energy spectrum at the SDS-2 setup. During measurements with the electron source, the energy spectrum typically shows one or more electron peaks at an energy that is defined by the starting voltage $U_{start} \approx U_{spec} \geq -18.6$ kV, the post-acceleration voltage $U_{PAE} \leq 10$ kV and the detector bias voltage $U_{bias} = 120$ V. At higher rates, multi-electron peaks are observed due to event pile-up at the detector. The corresponding region-of-interest (ROI) is located at $E_1 = q(U_{start} - U_{PAE} - U_{bias}) = 28.72$ keV for the single-electron peak in measurements at nominal conditions. The ROI is multiplied by a factor of 2, 3, ... for multi-electron peaks. A ROI window of $[-2$ keV; 3 keV] is used to select events that are assumed to originate from the electron source. A livetime pulser was used during the commissioning measurements, which is located at an energy $E_{pulser} = 10$ keV at nominal conditions. For zero-voltage measurements, the pulser peak is moved to 40 keV to avoid overlaps with the electron energy spectrum. A ROI window of $[-2$ keV; 2 keV] is used for the pulser peak. Note that due to inaccuracies in the determined livetime when using the pulser signal and the typically low electron rates $\dot{N} \lesssim 5$ kcps, the livetime was determined directly from the recorder run time in each measurement. It is believed that this approach yields a more accurate electron rate than when including the livetime pulser information. Runs: 24750

In the analysis performed in this work, an alternative approach to determine the electron rate in a measurement is used. Typically, one can determine the electron rate e. g. from the energy spectrum of the observed electrons during a given time interval Δt . After the region-of-interest (ROI) has been determined by considering the kinetic energy of the electrons at the detector, one can simply sum up all observed electron events in the ROI to retrieve the number of counts N , from which the electron rate $\dot{N} = N/\Delta t$ can be determined. In case of the electron source, multi-electron events are observed at higher rates: In this case, the detector cannot discriminate between multiple electrons that arrive at the detector within a short time frame due to its intrinsic deadtime. In this case, the total energy from all the coincident electrons is recognized by the detector, and multi-electron peaks are seen in the energy spectrum. This effect is known as *pile-up* and more pronounced at high electron rates, where

higher electron multiplicities are observed. For two-electron events (i. e. with an electron multiplicity of 2), the corresponding ROI in the energy spectrum is at twice the nominal electron energy due to the energy summation. The ROI must be extended accordingly, and to determine a correct rate the multiplicities must be taken into account correctly. Figure 4.20 shows a typical energy spectrum during electron source measurements.

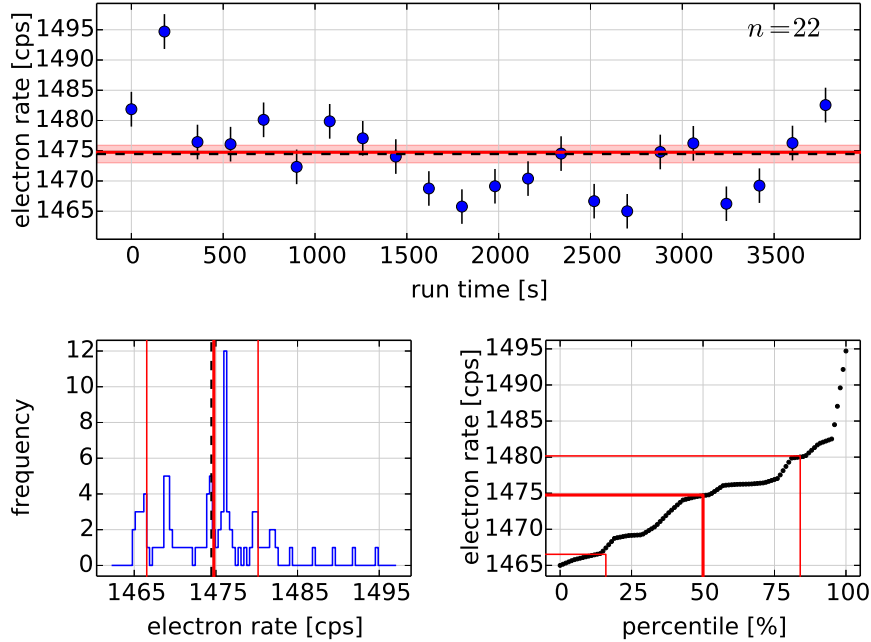


Figure 4.21.: Determining the electron rate by percentiles from a measured rate trend. A typical measurement run contains multiple data points ($n = 22$ in this example) that show a fluctuating electron rate (top). The electron rate for each data point was determined from the corresponding energy spectrum (cmp. figure 4.20). Instead of simply averaging the observed rate over the total run length (dashed black line), one can create a rate projection histogram (bottom left). The histogram shows the distribution of the electron rate during the run and can be analyzed with statistical method to determine a median (average rate) and a width (rate uncertainty). One numerically robust method to determine these values is via percentiles (bottom right). Percentiles are computed from a given data set and describe how the histogram area (from 0% to 100%) develops w. r. t. the measured value (in this case the electron rate). The percentile plot shows this procedure; each percentile value is mapped to the corresponding rate to determine the median (50% percentile) and the 1σ -width (16% and 84% percentiles, since $1\sigma = 68\%$). These values are indicated by the solid/dashed red lines in each plot. This method allows to determine the rate uncertainty from actually observed rate fluctuations (instead of relying e. g. on a Poisson-distributed electron rate). It is possible to adjust the number of data points that are spread over the total run (i. e. change the sampling interval): While this long-term stability run uses a sampling interval of 180 s, typical electron source measurements use a sampling time of 2 s due to their much shorter run length of $\mathcal{O}(10\text{ s})$. Note that to ensure that the determined rate is independent of the number of data points n , the histogram width that was determined from percentiles is scales by a factor $1/\sqrt{n}$.

Especially at lower electron rates – e. g. in a transmission function measurement at low surplus energy, before the nominal rate is achieved – it is difficult to correctly determine an electron rate and the corresponding statistical uncertainty. For transmission function measurements, the uncertainty is not only given by actual fluctuations of the electron rate at the source, but can be increased by other effects

such as voltage fluctuations – to which the observed transmission function is extremely sensitive as the observed rate depends on the electron energy – or short-term variations of the photocathode surface conditions. Hence, the alternative approach that was used in this thesis tries to consider the actual rate fluctuations that are observed at the detector to determine the statistical uncertainty of the electron rate that is observed in a given time interval Δt . To do so, the electron rate is first determined at a smaller sub-interval $\tau < \Delta t$, yielding a sequence of electron rates that correspond to each time step $[0; \tau)$, $[\tau; 2\tau)$ and so on. If τ is sufficiently small, one can create a *rate projection histogram* of the sub-interval rates. The median of the histogram is then identified with the average rate that was observed during the full time interval Δt , and the width of the histogram corresponds to the statistical rate uncertainty. Both values can be determined easily from a given histogram by its (16%, 50%, 84%)-percentiles [NIS12]. The 16% and 84% values correspond to twice the 1σ -width of the histogram¹¹. This procedure is shown in figure 4.21 for an exemplary stability run that was taken during the SDS-2 measurement phase.

Because this method considers the rate fluctuations that were actually observed at the detector during a given time interval, it is believed that this approach gives a better estimation of the statistical uncertainty of the electron rate. Furthermore, the median – and similarly, the 1σ -uncertainty that is computed from histogram percentiles – is more robust than the mean (which is computed from averaging the data), especially if the rate projection histogram is asymmetric. Such asymmetries can arise from large short-term fluctuations in the electron rate (e. g. if the starting voltage did not yet reach its setpoint at the beginning of a measurement run) or at low electron rates (since the electron rate cannot become negative). A comparison between the “classic” method and the alternative approach that is used in this work shows that in most cases, the determined electron rate and its estimated uncertainty are typically comparable, except in the aforementioned case where short-term fluctuations or low rates occur.

4.4.2 Dipole efficiency

The dipole electrode in front of the electron source chamber is intended to remove any trapped electrons when the source is operated in non-transmission mode, i. e. with electron energies $E_0 = qU_{start} < qU_{ana}$. In this mode, electrons are reflected by the retarding potential of the spectrometer; they can thus become stored between the negative electric potentials at the photocathode and the spectrometer. If the electron density in the trap region increases above a certain threshold, a Penning discharge could ignite, with possible disastrous consequences for the photocathode. Such discharges are a reasonable explanation for stability issues that were encountered during the SDS-2 measurements (see section 4.6.7). Under nominal conditions, the dipole electrode is expected to remove trapped electrons efficiently so that any Penning discharges are prevented.

The removal efficiency of the dipole electrode can be investigated by comparing transmission functions measured in order of decreasing and increasing surplus energy, $E = q\Delta U = q(U_{start} - U_{ana})$ (“out-of transmission” and “into transmission”). If the trapped electrons are removed by the dipole field, the observed transmission functions will show similar characteristics with comparable electron rates. However, if the electron-removal is insufficient, a hysteresis effect between the two measurement directions will occur and the observed electron rate will differ between the two measurement directions. This effect can be explained by the continuous filling of the trap from the beginning of the

11. The 1σ -width includes 68% of the histogram’s area. The 84%- and 16% percentile yield the lower and upper limit of this range, since $84\% - 16\% = 68\%$.

measurement in the case of increasing surplus energy (“into transmission”), since the surplus energy at the beginning is too small for electrons to be transmitted. Electrons with a given energy will therefore stay trapped until they have lost enough kinetic energy (e. g. through synchrotron radiation) or they are eventually removed by the dipole field. Due to scattering processes with electrons of higher kinetic energy – generated at a later time during the measurement – some of the stored low-energetic electrons can be “kicked” to a higher kinetic energy. These electrons then have a higher chance of being transmitted to the detector, which results in an increased electron rate. On the other hand, the effect does not occur when the measurement is performed in inverse direction (“out-of transmission”), where the electrons are transmitted from the beginning due to their higher surplus energy. This hysteresis effect is explained and thoroughly investigated in [Wie16].

The observed rate hysteresis is therefore linked to interactions between stored electrons, which allows to investigate the amount of electrons stored between the source and the spectrometer. By comparing transmission function measurements that were performed in different scanning directions, the removal efficiency of the dipole electrode can be investigated directly. The dipole efficiency has been investigated during the test measurements at the MoS setup, where a clear hysteresis effect is observed for small dipole voltages (see section 4.5.3).

4.4.3 Time-of-flight

The electron source is operated in pulsed mode under nominal conditions, so that the electron beam is emitted in bunches of certain length. The *time-of-flight* (ToF) Δt from the photocathode to the detector wafer can be determined by comparing the measured arrival time, t_1 , to the known start time of the electrons, t_0 . While the arrival time for each electron event is determined automatically by the DAQ system, the start time is reconstructed from a reference trigger signal that is generated at the electron source. The setup either uses a function generator (“pulser”) to drive the LEDs that provides a second output channel for the reference signal, or uses the TTL trigger signal that is provided by the laser system.

The electron beam is pulsed with the given frequency (20 kHz to 100 kHz for the laser, up to 100 kHz for the LED pulser) and a specific pulse length (< 20 ns for the laser; adjustable from 100 ns to 1000 ns for the LEDs). The reference signal is generated in synchronicity with the start of the pulse and fed into the DAQ system through a BNC cable. In order to be processed by the DAQ electronics, the signal has to be down-scaled in frequency¹² and converted to an optical input signal. The total delay w. r. t. to the start of the pulse is created by the BNC cable, down-scaler and optical converter. It is further increased by the internal filtering of the DAQ system due to the different waveforms of a typical electron event and the TTL reference signal. The waveform dependency shifts the trigger time, i. e. the time stamp of a recorded event, and must be considered as well to determine the correct ToF. All the individual delays can be determined by direct measurements or by investigating the recorded DAQ event waveforms. For the SDS-2 setup, a trigger delay of $\tau = 1270$ ns has been determined [BE14]. The ToF of the transmitted electrons is then given by

$$\Delta t = t_1 - t_0 - \tau. \tag{4.46}$$

The time-of-flight measurement mode has been used in a variety of SDS-2 commissioning measurements, e. g. to verify the integrity of the inner-electrode system at the main spectrometer [Bar16] or to

12. The down-scaling is necessary to limit the rate that is processed at the DAQ system, typically a scaling factor of 1:128 is used. This down-scaling is considered and automatically corrected in the BEANS analysis.

investigate time-focusing methods that could increase the sensitivity of the experiment [Ful16]. This thesis, however, focuses on the design and commissioning of the electron source itself, where ToF data is not relevant and will not be discussed further.

4.4.4 Zero angle

The design of the electron source allows a tilting of the plate-capacitor setup against the direction of the magnetic field in order to imprint a well-defined pitch angle on the produced electrons. This feature is known as *angular selectivity* and allows to produce pitch angles $\theta = 0^\circ$ to 90° in the spectrometer entry magnet. Since the produced pitch angle is influenced by numerous effects, such as the alignment of the electromagnetic field at the photocathode, it is important to determine the absolute tilt angle α_p where the minimal pitch angle is produced; this position is known as the “zero angle”, $\alpha_p = \alpha_0$. A precise readout of the tilt angle for the two independent tilt axes (horizontal and vertical) is possible with an accuracy of 0.5° .

To perform a zero-angle measurement, the electron source is operated “on transmission”, i. e. with a constant surplus energy $qU_{start} = qU_{ana} + \Delta U$. In this setting, the transmission probability (2.22) strongly depends on the electron pitch angle. The observed electron rate thus becomes extremely sensitive to the pitch angle, and a small variation of the source tilt angle – which changes the pitch angle accordingly – results in a different electron rate. The zero angle is then determined by varying the tilt angle on each independent axis while monitoring the electron rate. Since a smaller pitch angle results in a larger transmission probability, the maximum of the observed rate dependency corresponds to the “zero angle” setting where the pitch angle is minimal.

To improve the accuracy of the measurement, the data points taken at different tilt angles are fitted with a Gaussian distribution that describes the rate dependency close to the zero angle with reasonable accuracy. For each tilt axis, the determined peak position is used to correct the adjust the tilt angle offset in the electron source slow-control software. After the correction has been applied, a tilt angle $\alpha_p = 0^\circ$ corresponds to the “zero angle” setting where the minimal pitch angle is produced. Corresponding measurements have been performed at the MoS setup (section 4.5.4) and at the SDS-2 setup (section 4.6.3).

It should be noted that the zero angle must be re-calibrated whenever the operational parameters, e. g. the acceleration potential U_{acc} or the dipole voltage U_{dip} , have been changed. For example, the measurements performed at the MoS setup have shown that the dipole voltage significantly affects the resulting zero angle. Similar influences exist for the starting voltage U_{start} or the magnetic field B_0 at the photocathode. This behavior is also confirmed by particle-tracking simulations of the electron source (section 4.8.7).

The analysis of the zero angle measurements is carried out in *Peaberry*. A Gaussian fit model (with offset) is used to describe the electron rate dependency on the plate angle α_p ,

$$\dot{N}(\alpha_p) = A \cdot \exp\left(-\frac{(\alpha_p - \alpha_0)^2}{2\sigma_\alpha^2}\right) + b, \quad (4.47)$$

with amplitude A , mean α_0 (the zero angle position), width σ_α and background b . The fit is carried out with MINUIT2 in combination with MINOS to determine the parameter uncertainties (cmp. section 3.8.3)

4.4.5 Magnetic reflection

In addition to zero-angle measurements, the produced pitch angles can be investigated by observing the magnetic reflection of electrons. Magnetic reflection occurs when the pitch angle reaches 90° before being fully transmitted to the detector, i. e. when the electron moves into a region with higher magnetic field (so that the adiabatic transformation (2.7) increases the pitch angle). The effect is observed as a sudden drop in the observed electron rate if the tilt angle at the electron source reaches a certain threshold. The threshold angle depends on the ratio between the magnetic field at the photocathode, B_0 , and the highest magnetic field along the electron trajectory, $B_{max} \gg B_0$.

The magnetic reflection measurement is performed by setting the electron source in full transmission ($qU_{start} \gg qU_{ana}$), so that the electron rate is not affected by the transmission properties of the spectrometer. In this setting, the observed rate can only be reduced by magnetic reflection (assuming that a stable electron rate is produced at the source). When the tilt angle at the electron source is increased and magnetic reflection occurs, the electron rate decreases as more electrons are magnetically reflected. The tilt angle where the rate-drop occurs corresponds to a pitch angle of 90° in the magnet, and the rate dependency can be typically described by an error function.

Since the rate depends on the produced pitch angle in this measurement mode, the observer rate dependency allows to investigate the angular distribution of the produced electrons. Since magnetic reflection is extremely sensitive to the produced pitch angle, this measurement technique can also investigate possible asymmetries e. g. due to misalignments of the magnet system or due to asymmetries in the electromagnetic fields at the source. Since the effect is completely independent of the transmission properties of the spectrometer, this method that can be used to characterize the electron source in addition to other methods such as zero-angle or transmission measurements. Corresponding measurements that examine various influences on the magnetic reflection have been performed at the MoS setup (section 4.5.5) and in the SDS-2 phase (section 4.6.4).

The analysis of the magnetic reflection measurements uses the *Peaberry* framework. An error function is fitted to the data points in order to determine the reflection angle and the angular spread,

$$\dot{N}(\alpha_p) = A \cdot \frac{1}{2} \left[1 - \operatorname{erf} \left(\frac{\alpha_p - \alpha_{max}}{\sqrt{2}\sigma_\alpha} \right) \right] + b, \quad (4.48)$$

with amplitude A , mean α_{max} (the reflection angle), width σ_α and background b . The width σ_α describes the angular spread in terms of the tilt angle α_p and can be used to investigate the angular distribution of the produced electrons (in terms of pitch angle θ). The fit uses MINUIT2 with MINOS to determine the parameter uncertainties.

4.4.6 Energy spread

The energy spread of the produced electrons – occasionally also called “line width” – has a major effect on the observed transmission functions. To allow investigations of the spectrometer transmission properties, the energy spread must be significantly smaller than the energy resolution of the main spectrometer (cmp. section 2.2). The energy distribution of the electron source can be measured independently by operating the spectrometer at low voltage (“zero voltage” setting at $U_{ana} \approx -200$ V). In this case, the angular emission characteristics of the electron source only have a negligible effect

on the measured transmission function, due to the improved energy resolution of the spectrometer at this setting¹³.

As indicated by the measurements that are presented in this thesis, the angular spread achieved by the electron source at the zero-angle setting is sufficiently small to determine the energy distribution even at high voltage ($U_{ana} \approx -18.6$ kV). However, a dedicated measurement at “zero voltage” provided a more direct approach to the energy distribution and likely produced more accurate results. Furthermore, the zero-voltage measurement can be used to investigate the work function of the spectrometer. Corresponding measurements at low and high voltage have been performed in the SDS-2 phase (section 4.6.5). At the MoS setup it was only possible to perform high-voltage measurement due to the different experimental setup (section 4.5.6).

To determine the energy distribution from a transmission function measurement, the analytical transmission model (section 4.1.1) is used in the *Peaberry* framework. The energy distribution is described by a generalized (asymmetric) normal distribution (4.39) with mean energy \hat{E} , width σ'_E and shape parameter κ_E (section 4.2.5). The width can be converted to an energy spread σ via (4.41); this value is comparable to the width of a symmetric normal distribution. The upper limit of the energy E_{max} , i. e. the maximal electron energy that is produced at the photocathode, can be derived from the energy distribution as well. The angular distribution is described by a combination of two normal distributions (4.43) that are symmetrically placed around $\theta = 0^\circ$ with mean angle $\pm\hat{\theta}$ and angular spread σ_θ (section 4.2.6).

The energy distribution is typically determined from a transmission measurement performed at zero angle ($\alpha_p = 0^\circ$). In this case, the fit uses a fixed angular distribution with $\hat{\theta} = 2^\circ$ and $\sigma_\theta = 1^\circ$. Since the transmission model is only weakly sensitive to the angular distribution at the zero-angle setting, the parameter values $\hat{\theta}$, σ_θ have negligible influence on the resulting transmission function. The parameters above were therefore chosen to produce accurate fit results.

On the other hand, the position of the transmission edge (equivalent to $E = 0$ eV in the energy distribution) is an important parameter in the analytical model. The edge position also shows strong correlations to other parameters (see section 4.9 where this effect is investigated). In order to improve the accuracy of the fit results, the edge position is determined beforehand by an iterative approach and then kept fixed in the actual transmission function fit.

The fit is performed with MCMC (implemented in *emcee* [Van14]), using 8000 steps for the burn-in phase (which are discarded) and 2000 steps to evaluate the outcome of the fit. The affine-invariant MCMC method that is used here evaluates 100 parallel Markov chains to sample from the log-likelihood parameter space of the fit model. A transmission function fit typically completes within a few hours and provides good numerical stability, i. e. it is not strongly affected by variations of the initial parameters, which is an advantage over alternative (typically faster) methods such as *MINUIT*. Using MCMC, the fit result is evaluated directly from the log-likelihood samples. The fit result includes possible correlations and provides an accurate estimate of the parameter uncertainties (cmp. section 3.8.3).

13. The energy resolution scales with the spectrometer voltage and is therefore improved by a factor of roughly 100 by reducing the voltage from -18.6 kV to -200 V.

4.4.7 Angular spread

Especially at non-zero tilt angles, $\alpha_p > 0^\circ$, the angular distribution of the produced electrons affects the observed transmission function in addition to their energy distribution. Both the kinetic energy and the pitch angle of the electrons define the longitudinal energy (2.1) in the analyzing plane of the spectrometer. Due to the adiabatic collimation of the MAC-E filter, the impact of the angular spread is considerably smaller than the effect of the energy spread (cmp. section 2.2). The influence of the angular spread scales with the energy resolution of the spectrometer and disappears if the spectrometer is operated at low voltage. By comparing transmission function measurements performed at high voltage ($U_{ana} \approx -18.6 \text{ kV}$) with measurements of the energy distribution at “zero voltage” ($U_{ana} \approx -200 \text{ V}$), it is possible to investigate the angular distribution of the electrons independently of the energy distribution.

The electron source achieves “angular selectivity”, i. e. produces electrons with well-defined pitch angles θ . Transmission function measurements at different tilt angles α_p at the electron source allow to investigate how the angular distribution is affected by increasing tilt angles. As the produced pitch angle θ increases with α_p , the observed transmission function shifts to larger surplus energies. This is explained by the smaller amount of longitudinal kinetic energy at the analyzing plane at larger pitch angles, which is compensated by increasing the kinetic energy of the electrons. The produced pitch angles and the observed shift w. r. t. to the zero-angle setting depend on the spectrometer properties (especially the magnetic fields), which allows to investigate its energy resolution. Such measurements have been carried out at the MoS setup (section 4.5.6) and at the SDS-2 setup (section 4.6.5).

The angular distribution is determined with the analytical transmission model, similar to the energy spread measurements described above. The fit uses the same model distributions and is performed via MCMC. In this case, however, the energy distribution is kept fixed during the fit with parameters that were determined beforehand from an independent energy spread measurement (preferably at “zero voltage”, where the energy distribution can be determined accurately). Generally speaking, the analysis approach is to determine the energy distribution from a dedicated measurement at zero angle and then use the fitted energy distribution as input to analyze measurements performed at non-zero tilt angles, in order to determine the angular distribution.

4.4.8 Work function

The work function of the photocathode has a prominent effect on the energy spread that can be achieved with the electron source. Photoemission of electrons occurs if the photon energy of incident light is larger than the work function Φ of the photocathode material. The minimal energy spread is therefore produced when the UV wavelength matches the work function, and it increases if the wavelength is reduced. In the case of the electron source, the work function is modified by various effects such as surface impurities, electric fields (cmp. section 4.2.4) or the non-zero temperature of the photocathode. Furthermore, these effects are often time-dependent so that the work function changes while the electron source is in operation.

Because the work function defines important parameters of the electron source like the energy spread of the produced electrons, it is therefore useful to perform an *in situ* work function measurement – i. e. under conditions that are equivalent to normal operation. Such a measurement is possible with the method conceived by Fowler, where the electron yield Y is determined in dependency of the

wavelength λ . The electron yield describes the number of emitted electrons per incident photon; it is therefore important to normalize the observed electron rate to the light intensity. The optical system of the electron source at the MoS and SDS-2 setups allows to monitor the intensity of the UV light by a photodiode (section 4.4.1), so that the observed electron rate can be normalized to the photodiode signal. The normalized rate is then proportional to the electron yield and can be investigated by the Fowler method. This approach has been applied successfully in earlier measurements with the electron source [Zac14, Win14, Bus14].

The analysis of the Fowler-type measurement applies a fit that is based on Fowler's description of the electron yield in dependency of the wavelength,

$$Y(\lambda) = A \cdot \xi(\mu) \cdot T^2, \quad (4.49)$$

$$\mu = \frac{2\pi hc \lambda^{-1} - \Phi}{k_B T}, \quad (4.50)$$

with the amplitude A , work function Φ and effective temperature T . The term $\xi(\mu)$ is the Fowler function (4.31) and k_B is the Boltzmann constant. The analysis of the measurements presented here uses a fixed temperature $T = 291 \text{ K} = 18^\circ\text{C}$, which corresponds to the average temperature of the climate-controlled main/monitor spectrometer hall. The temperature is therefore assumed to match the temperature of the photocathode. Preliminary analysis showed that including the temperature as a free parameter in the fit does not improve the fit results, and it is believed that a fixed value in this case improves the stability and accuracy of the fit.

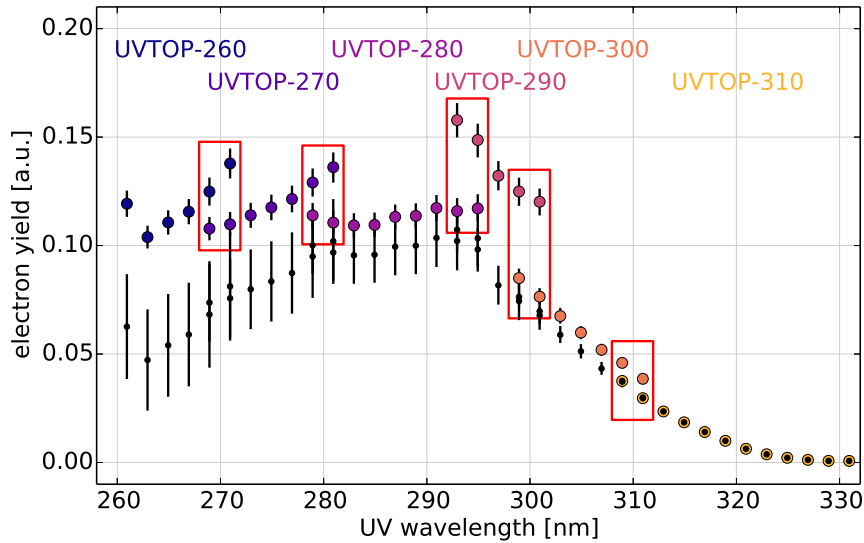


Figure 4.22.: Measured electron yield before and after corrections. Due to small mechanical misalignments of the individual UV-LEDs, intensity changes are observed that cannot be corrected by the photodiode readout. The changes are visible as sudden jumps in the measured electron yield when LEDs are switched that prevent a correct analysis of the data (colored data points). To solve this issue, overlapping data points are measured (indicated by the red boxes) so that the jumps between different LEDs can be resolved and the electron yield corrected. The correction starts at the largest wavelength and increases the error bars towards the left side, since the uncertainties cumulate with each jump (small black data points). After the correction, the measured electron yield can be described by the Fowler model.

One issue that had to be solved for this analysis is that multiple UV-LEDs are used to scan the full wavelength range (roughly 260 nm to 330 nm). The LED revolver mount (cmp. section 4.3.1) allows to automatically switch between different LEDs and place them on the optical axis, where the light enters the monochromator to select a specific wavelength. However, due to small mechanical misalignments of the individual LEDs, the position on the optical axis differs slightly for each LED. Due to the complicated optical setup with monochromator, two-lens telescope and beam splitter, even a small displacement affects the coupling of UV light into the 200 μm optical fiber. This effect creates differences in light intensity at the photocathode that cannot be monitored by the photodiode (since the photodiode measures the intensity *before* the light is coupled into the fiber). As a result, several “jumps” are observed in the measured electron yield whenever LEDs are switched as visible in figure 4.22. To overcome this issue, the measurement was refined to include overlapping data points: some wavelengths are used twice with two different LEDs, e. g. a wavelength of 300 nm from the UVTOP-295 and UVTOP-305 LEDs. Since theoretically the overlapping data points should show the same electron yield, this approach can be used to resolve the intensity differences that affect the observed electron rate. The measurements presented here use two overlapping wavelengths between each adjacent pair of LEDs and automatically scales the electron rate to minimize the observed rate differences, which is shown in the figure.

The downside of this method is that the error bars at the individual data points increase since the uncertainties cumulate with each correction step. To minimize this effect, the automated correction procedure always starts at the largest wavelength (close to the work function threshold), where the Fowler model is most sensitive to the work function. The larger error bars at smaller wavelengths, on the other hand, have negligible effect on the fit result. The whole procedure is shown in figure 4.22, where the original data is compared with the corrected electron yield.

In addition to the direct work function measurement by the Fowler method, it is possible to determine the work function from the observed energy distribution. The energy spread that is achieved, i. e. the width of the distribution, relates to the difference between photon energy and work function, $E_{max} = h\nu - \Phi$. By examining the energy distribution of the produced electrons in a transmission function measurement (see section 4.4.6 above), one can determine the work function without the need to perform a dedicated Fowler-type measurement of the electron yield. The results of both methods have been compared at the MoS setup (section 4.5.8) and at the SDS-2 setup (section 4.6.6) for different photocathodes and wavelengths, and are in agreement with each other.

4.5 Measurements at the monitor spectrometer

In the SDS-1 measurement phase, the electron source was primarily intended to study the transmission properties of the main spectrometer. However, as it turned out while performing the measurements, the crucial feature of *angular selectivity* could not be achieved. This prevented a complete investigation of the transmission properties as planned [Gro15, Zac14].

After the completion of the SDS-1 measurements, the issues with angular selectivity were investigated and the design of the electron source was improved accordingly (cmp. section 4.3). The electron source was operated in a lab setup at WWU Münster (cmp. [Zac14, Win14]) during this period for maintenance work, software and hardware upgrades, and several test measurements [Jos13, Pot13, Bus14].

Prior to the SDS-2 commissioning phase, a period of test measurements at the monitor spectrometer was conducted in order to verify the complete functionality of the electron source. This dedicated commissioning phase was intended to prevent similar issues that were encountered during SDS-1, where the source had not been tested beforehand in a MAC-E filter setup. The monitor spectrometer provides conditions that are similar to the main spectrometer, making it an excellent tool to investigate the electron source characteristics.

The measurements at the monitor spectrometer are discussed in this section. Many concepts developed at this stage were extremely relevant for the SDS-2 measurements (section 4.6). The knowledge gained about the electron source properties proved to be of great advantage when operating the source at the main spectrometer later on.

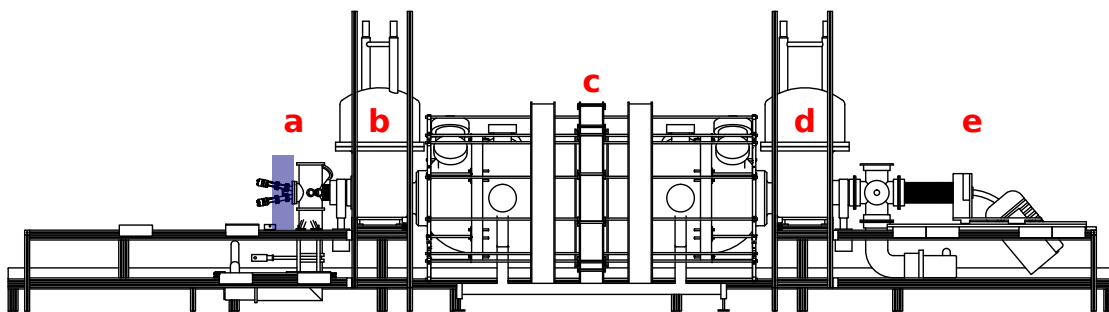


Figure 4.23.: Electron source setup at the monitor spectrometer (MoS). The electron source (a) was mounted directly on the upstream (source-side) flange of the beam tube. The distance to the center of the spectrometer entry magnet (b) was determined to 0.625 m by a manual measurement; the distance between magnet housing and the inner coil was determined from CAD drawings. This distance is also implemented in the simulation geometry (section 4.7). A LN₂-cooled five-pixel PIN diode is used as the detector (e). The MoS features a symmetric magnetic field setup with $B_{max} = 6$ T at the spectrometer entrance and exit (b,d), and $B_{min} = 0.38$ mT in the analyzing plane (c) of the MAC-E filter. The magnetic field at the photocathode of the source was measured with a hall probe, yielding a field of $B_{start} = 21$ mT under nominal conditions. The field can be enhanced to $B_{start}^+ = 28$ mT with an additional air coil that is installed next to the source on the upstream side (indicated by the blue area).

4.5.1 Experimental setup

The monitor spectrometer is a MAC-E filter with similar characteristics as the main spectrometer. The overall experimental setup is shown in figure 4.23 and the setup of the electron source in figure 4.24. The main difference is the smaller magnetic flux (and thus, a considerably smaller vessel diameter of only 1 m to contain the flux tube at nominal magnetic field), and a symmetric magnetic field setup with $B_{max} = 6$ T at the spectrometer entrance and exit¹⁴. In contrast to the main spectrometer measurements, where the source could be moved around the flux tube by an UHV manipulator, the electron source was directly attached to the beam tube at the spectrometer entrance at the MoS setup. This made the alignment procedure less difficult as the position of the source w. r. t. the spectrometer was fixed (cmp. section 4.8.1). The monitor spectrometer features a five-pixel PIN diode to observe electrons, and the detector is cooled by LN₂ to reduce the noise level. The achieved electron rates in this setup are typically in the range 0.5 kcps to 5 kcps on a single pixel, so that the signal-to-noise ratio is always sufficient for transmission function measurements. Adjustments of the MoS setup were therefore not required.

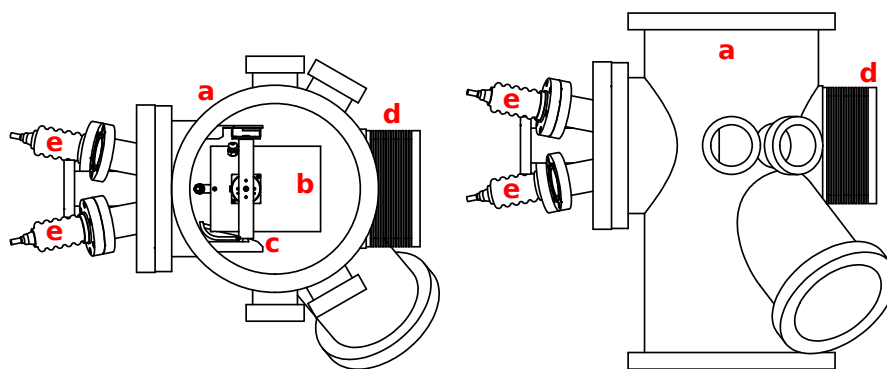


Figure 4.24. Electron source chamber at the monitor spectrometer (MoS). To mount the electron source into the MoS beamline, the vacuum chamber (a) that is installed for ellipsometry measurements with a ^{83m}Kr source [B⁺13a] was adopted. The source features a source cage (b) on a gimbal mount (c). The grounded cage contains the plate-capacitor setup and shields the electric fields at the photocathode from outside influences. It can be tilted against two independent axes (vertical and horizontal) to produce electrons with well-defined pitch angles. The electrical, optical and mechanical feed-throughs (e) at the vacuum flange connect to the high voltage power supplies, the optical system and the pneumatic linear motors. The produced electrons are accelerated against the grounded beam tube (d), which connects to the spectrometer entrance.

Magnetic field setup

However, after some basic functionality tests it turned out that the magnetic field at the electron emission spot was lower than expected. This was caused by a mismatch between the simulations that had been performed in preparation of the measurement phase, and the actual conditions at the spectrometer¹⁵. This was later verified by direct field measurements with a hall probe, showing a magnetic field of $B_{start} = 21$ mT at the position of the photocathode in contrast to the expected value

14. At the main spectrometer, the entry magnet is operated at a smaller field than the pinch magnet at the exit.

15. The main problem was that the distance of the electron source w. r. t. the spectrometer was expected to be smaller. The magnetic field at the photocathode was thus smaller than expected due to the larger distance to the entry magnet.

of roughly 30 mT [B⁺14b]. Although the electron source can be operated without severe limitations at this field strength, the test measurements required conditions similar to the main spectrometer in order to verify the electron source functionality. Eventually the issue was solved by mounting an additional air coil in close vicinity to the electron source, which increases the magnetic field at the emission spot to $B_{start}^+ = 28$ mT. This creates electromagnetic conditions that are sufficiently close to the main spectrometer setup where $B_{start}^{SDS} = 29$ mT is achieved.

Many measurements discussed below were performed with this *enhanced field setting*. On some occasions, the air coil was intentionally ramped down to perform measurement at the smaller magnetic field of 21 mT. These measurements allowed to investigate the source properties at different magnetic fields.

High voltage setup

The high-voltage (HV) system is a crucial part of the experimental setup, as the kinetic energy of the electrons as well as the acceleration processes (and thus, angular selectivity) are largely defined by the applied electric potentials. The HV setup was constructed at WWU Münster and integrated with the MoS setup prior to the measurements. It features multiple devices that are mostly set up inside a dedicated HV cage that is operated at high voltage (up to -18.6 kV) and isolated against ground potential¹⁶.

To minimize possible voltage fluctuations between the spectrometer and the electron source, which would increase the uncertainties in a transmission function measurement, the HV system uses the voltage of the spectrometer vessel $U_{spec} \gtrsim -18.6$ kV as a reference voltage. A series of a (negative) power supply and a (positive) battery allows to vary the starting voltage at the photocathode (back plate) in the range $\Delta U = -1160$ V to 90 V without adjusting the power supply's polarity. It is thus possible to perform transmission measurements (where the voltage is typically varied by roughly 5 V around U_{spec}) and also dedicated measurements at higher surplus energies of more than 1 keV. The voltage difference $\Delta U = U_{spec} - U_{start}$ is monitored by a difference voltmeter (DVM). The DVM read-out corresponds to the electron surplus energy $E = q\Delta U$ and is therefore one of the important slow-control parameters during measurements. The additional acceleration voltage that is applied between the front and back plate is necessary to achieve angular selectivity. An additional power supply mounted outside the HV cage produces an offset voltage at the front plate, $U_{acc} = U_{front} - U_{start} \leq 5$ kV. The dipole electrode is operated by a completely independent power supply (not shown in the figure) that is controlled directly by the slow-control software. The power supply achieves a dipole voltage up to 4 kV, and the dipole electrode is typically operated at $U_{dip} \leq 4$ kV in the MoS setup.

The slow-control system of the electron source (section 4.3.2) was still under development at this stage. However, many core features were already available and could be thoroughly tested during the measurement phase. The automated remote control of the starting voltage U_{start} , the remote actuation of the plates that adjusts the plate angles α_p and α_{az} , and the control of the dipole voltage U_{dip} was extremely helpful to carry out the measurements. The optical system could be monitored and controlled by the slow-control software to some extent, e. g. to control the UV wavelength in LED measurements or to monitor the light intensity. The functionality tests at the monitor spectrometer

16. This technique allows to use standard devices that do not have to fulfill any special regulations regarding the operation at high voltage of several kV. Inside the HV cage, the potential differences are the same as if all devices are operated at ground potential.

therefore also served as a test case for the slow-control software that was – after some improvements – also used in the SDS-2 measurement phase.

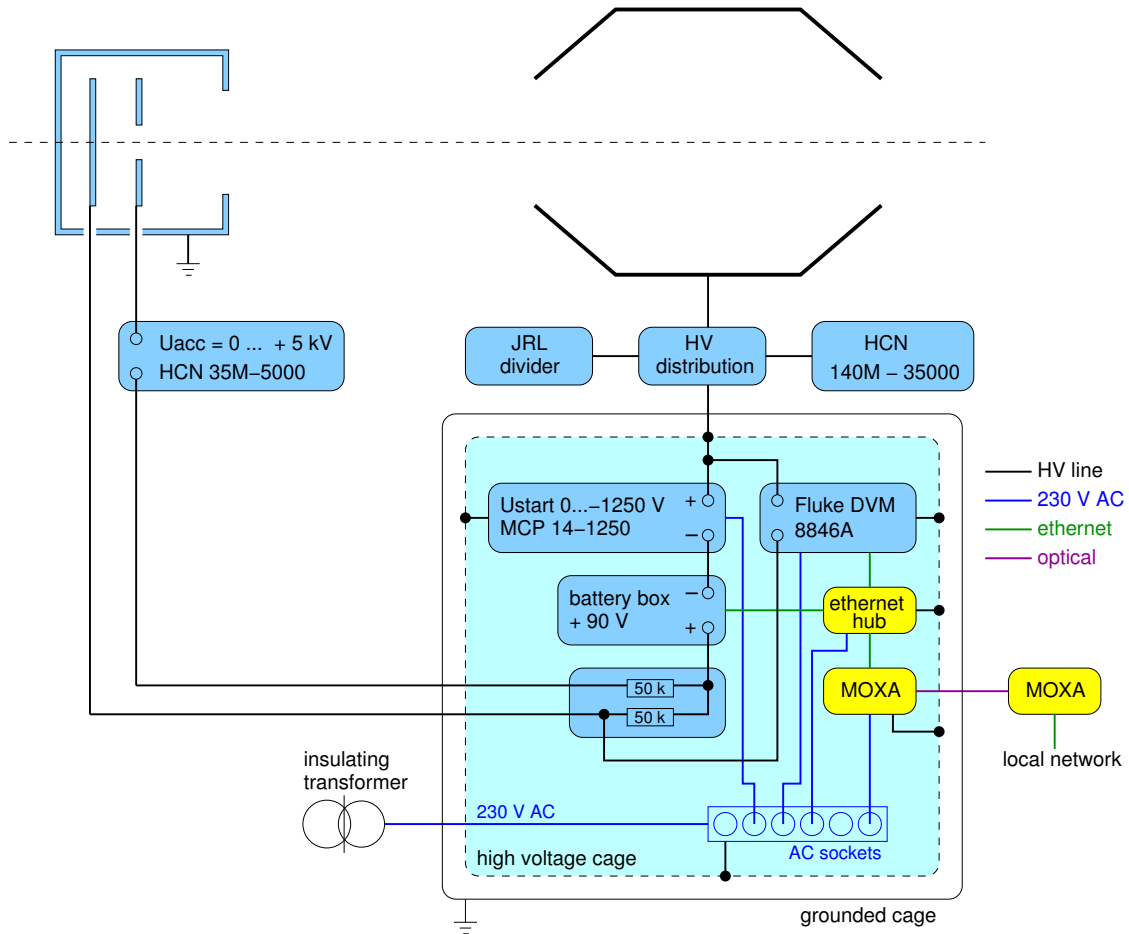


Figure 4.25.: High voltage setup at the monitor spectrometer (MoS). The electron source operates on a relative potential offset to the spectrometer's retarding potential to minimize voltage fluctuations that would affect the kinetic energy of the emitted electrons. The starting voltage U_{start} at the photocathode is defined as an offset to the vessel voltage U_{spec} at the spectrometer, using a combination of a power supply (MCP 14-1250) and a 90 V battery that allows to use a voltage range $U_{start} - U_{spec} = -1160 \text{ V}$ to 90 V. This voltage difference is monitored by a voltmeter (DVM), as it relates to the surplus energy of the produced electrons. The acceleration voltage U_{acc} between front and back plate of the source is implemented as an additional offset $U_{front} - U_{back} = U_{acc} \leq 5 \text{ kV}$, using another power supply (HCN 35M-5000). The SDS-2 measurements at the main spectrometer use the same setup. Figure kindly provided by V. Hannen [B⁺14b].

4.5.2 Rate stability

The short- and long-term stability of the achieved electron rate is an important aspect of the electron source, especially when it is used in the commissioning measurements of the main spectrometer. Long-term changes of the nominal electron rate could require a re-adjustment of the operational parameters if a stable electron rate is required. For the transmission function runs and related mea-

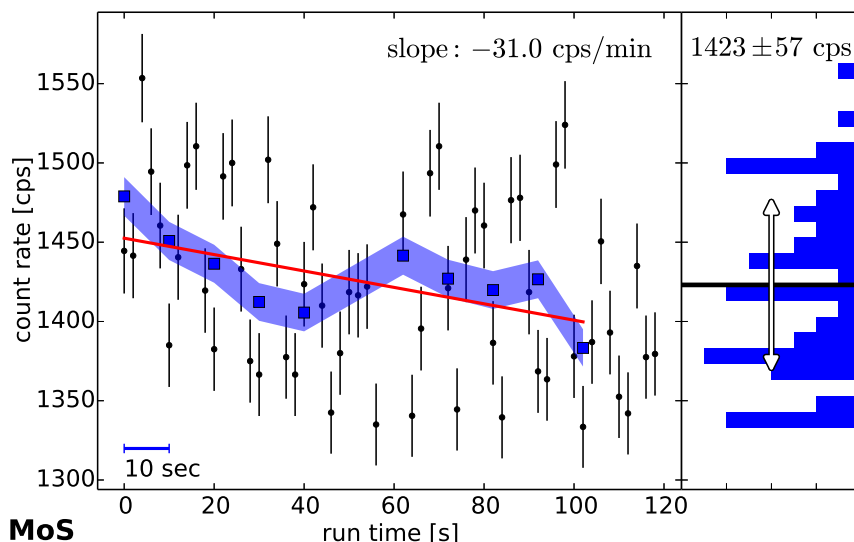


Figure 4.26.: Electron rate stability at the MoS setup. The electron rate was measured in two consecutive 1-minute runs, using the UV laser at nominal settings (100 kHz pulse frequency, 6 A diode current). The spectrometer operated at nominal settings with high voltage ($U_{spec} = -18.6$ kV). The standard rate analysis uses a sampling time of 2 s (black points), yielding an average rate of $1423(57)$ cps over the complete run set. The uncertainty is estimated from the 1σ -width of the rate projection histogram that is shown on the right; it is slightly above the expected uncertainty from Poisson statistics (38 cps). The electron rate decreases with a slope of $29.2(67)$ cps/min in this run set, corresponding to 2% rate reduction per minute. This decrease is caused by fluctuations in UV light intensity due to warm-up effects at the laser; it is therefore not directly related to stability of photocathode. The averaged rate in 10 s-bins is shown for comparison (blue squares). The averaging reduces the observed uncertainty at each data point, as indicated by the uncertainty band (blue).

Runs: 167676–167677

measurements, however, the absolute rate is often insignificant since the observed rate is typically fitted and normalized to the average nominal rate. These measurements therefore only require a stable rate during a single data run (typically on the order of 15 min) and a sufficient rate of 0.5 kcps to 5 kcps to achieve a sufficient signal-to-noise ratio. Short-term fluctuations or drifts of the electron rate, on the other hand, are more critical and could have negative effects on the measurement results. Especially a rate drift over short time periods of a few minutes would cause a deformation of the observed transmission function, which would increase the systematic uncertainty of the measurement.

Fluctuations in UV light intensity naturally have a strong effect on the produced electron rate. For this reason, the intensity is monitored by a photodiode inside the optics box where the laser and LEDs are mounted (section 4.3.1). This allows to check for sufficient stability and to correct the observed rate by normalizing to the photodiode signal, if necessary. The electron rate could also be affected by other processes such as changing conditions at the photocathode (e. g. a work function drift). These effects can only be investigated by observing the electron rate over an extended time range, while the electron source is in stable operation. Measurements during the SDS-1 commissioning phase revealed a slowly decreasing electron rate (resulting in a notable decrease on a timescale of hours) [Gro15]. This was explained by a continuously increasing work function of the photocathode, which reduces the amount of electrons being emitted at a given wavelength (electron yield). The work function is affected by surface impurities and other factors (cmp. section 4.2) that can change during operation, which

is likely the cause for these observations. Similar effects were also observed in test measurements at WWU Münster. At the monitor spectrometer, the rate stability was only investigated in a few dedicated measurements due to time constraints that required to put more focus on transmission measurements and other commissioning tasks. Figure 4.26 shows the short-term rate stability in a run set of 2 min length. A rate decrease of 29.2(67) cps/min is observed at a nominal rate of 1423(57) cps; this corresponds to a 2% decrease per minute. This drift is significantly larger than observed in the SDS-1 measurements, where the long-term stability was investigated on several occasions. The shown stability measurement was performed with the UV laser at 6 A and 100 kHz pulse frequency. Warm-up effects of the laser and the corresponding fluctuations in UV light intensity can explain the observed drift, which is also indicated by the photodiode signal. A longer warm-up time or a measurement with LEDs could therefore reduce the rate decrease. Note that this measurement was performed at the beginning of the MoS measurement phase where not all parameters had been optimized, so that the photodiode readout suffers from a low signal-to-noise ratio in this case.

A more detailed investigation of the achieved rate stability was performed in the SDS-2 measurement phase, where the photodiode signal was also taken into account to disentangle light intensity fluctuations from the actual rate drift (section 4.6.2).

4.5.3 Dipole voltage

The dipole electrode that is mounted inside the beam tube towards the spectrometer is an important feature of the electron source. It is intended to remove electrons that are trapped between the back plate (photocathode) and the analyzing plane or the spectrometer entry magnet. Trapping is likely to occur if the source is not operated in full transmission or if magnetic reflection occurs, in which case emitted electrons will be reflected before arriving at the detector. In this case it is possible for a charge build-up to occur which (in the worst case) can induce a Penning discharge – with possibly disastrous consequences for the photocathode [Wie16].

The dipole electrode creates an asymmetric electric field between the electron source and the spectrometer entry magnet. The field points in vertical direction, inducing a horizontal force on passing electrons that is caused by the $E \times B$ -drift. Stored electrons that pass the dipole field several times in a short time period are thus forced against the inner surface of the beam tube, which removes them from the flux tube. Because the drift force depends on the electric and magnetic field, it is difficult to estimate if all stored electrons can be removed before a Penning discharge occurs. Hence, it is important to investigate the removal efficiency of the dipole electrode by dedicated measurements. This can be achieved by measuring transmission functions in order of increasing and decreasing surplus energy and compare the observed electron rates, as explained in section 4.4.

Figure 4.27 shows transmission functions measured at three different dipole voltage $U_{dip} = 1.0\text{ kV}, 1.5\text{ kV}, 2.0\text{ kV}$ with increasing and decreasing energies. The spectrometer and the electron source were operated at nominal settings (high voltage, laser at 6 A/100 kHz). Electrons become trapped when the surplus energy is below roughly 0.5 eV in this case; the actual threshold depends on the operational parameters. If trapped electrons are present, a hysteresis effect between the two transmission function runs is observed, resulting in a difference in nominal rate (i. e. the average rate in full transmission). A pronounced hysteresis effect is observed at the fairly low (and insufficient) dipole voltage of 1 kV. The effect reduces considerably as the dipole voltage is increased and disappears

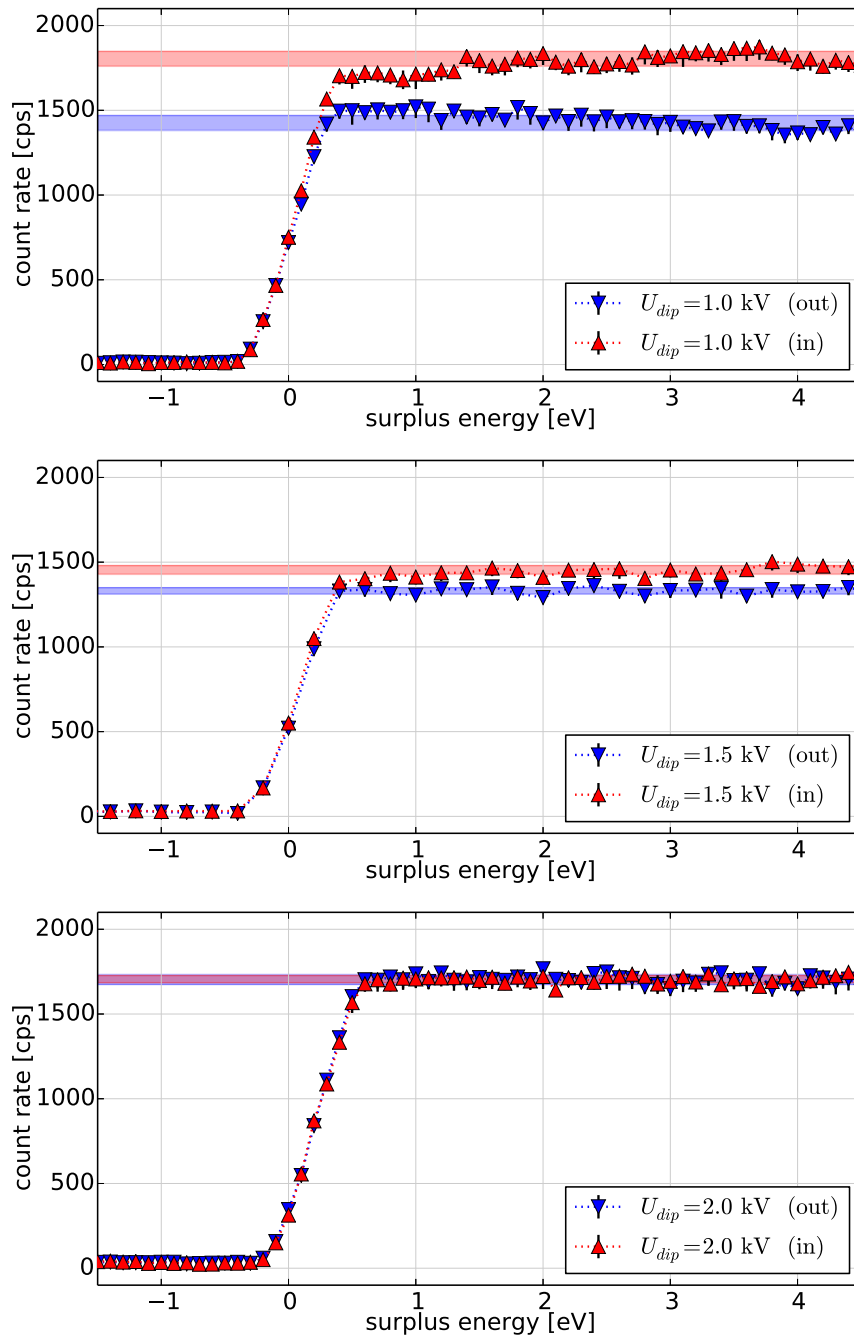


Figure 4.27.: Transmission functions with different dipole voltages at the MoS setup. The efficiency of the dipole electrode can be investigated by comparing transmission function that are measured in direction of increasing and decreasing surplus energy (“in” versus “out”). A hysteresis effect is observed if electrons are stored at the electron source. The colored horizontal bars indicate the nominal electron rate (where full transmission is reached) for each measurement. A pronounced hysteresis effect is seen at a small dipole voltage ($U_{dip} = 1$ kV). It disappears completely when the voltage increases to 2 kV. This shows that the dipole electrode is able to remove stored electrons at this setting, while a lower voltage is clearly insufficient. Runs: 167681,167682,167718,167719,167771,167772

completely 2 kV, indicating that the removal efficiency of the dipole electrode at 2 kV is sufficient to prevent any charge build-up.

Table 4.1 lists the rate differences $\Delta\dot{N} = |\dot{N}_{out} - \dot{N}_{in}|$ between the two transmission runs at each investigated setting, as indicated by the shaded horizontal bars in the figure. The nominal rate was determined by averaging the observed rate for surplus energies $qU \geq 1$ eV, corresponding to the average rate full transmission. Since the dipole voltage of $U_{dip} = 2$ kV is considered sufficient to remove stored electrons from the beam tube, it was used as the nominal setting in the following measurements at the MoS setup.

Table 4.1.: Observed hysteresis effect between transmission functions at different dipole voltages.

U_{dip}	\dot{N}_{out}	\dot{N}_{in}	$\Delta\dot{N}$	$\overline{\Delta\dot{N}/\dot{N}}$
1.0 kV	1425(44) cps	1804(44) cps	379(88) cps	23.5%
1.5 kV	1330(20) cps	1454(26) cps	124(45) cps	8.9%
2.0 kV	1704(30) cps	1706(21) cps	2(50) cps	0.1%

4.5.4 Zero angle

Nominal magnetic field

The so-called zero angle corresponds to the setting of the plate (tilt) angle where the minimal pitch angle is produced in the spectrometer entry magnet. Due to effects that influence the angular selectivity – the acceleration, dipole and starting voltages, the magnetic fields at the emission spot and in the magnet, etc. – it is necessary to determine the correct zero angle for a specific set of operational parameters by a dedicated measurement. The measurement is performed by independently scanning the vertical and horizontal plate angle (α_v, α_h) while the electron source is operating at a surplus energy of roughly 0 eV, i. e. “on” the transmission function. At this point the observed electron rate is extremely sensitive to changes in the produced pitch angle. For practical reasons a surplus energy setting is chosen where the observed electron rate is about half the nominal rate (in full transmission). The plate angle where a rate maximum is observed for a specific tilt axis corresponds to the zero angle, since the lowest pitch angle corresponds to maximal transmission probability. This approach¹⁷ is described in section 4.4.

Figure 4.28 shows the zero angle at nominal magnetic field ($B_{start} = 21$ mT at the photocathode). The measurements were performed at nominal spectrometer (-18.6 kV) and electron source settings (laser at 6 A/100 kHz). The dipole electrode was operated at 1.5 kV, 2.0 kV. In the shown measurements, the correct zero angle is unknown after the source was mounted in front of the monitor spectrometer. A clear rate dependency on the plate angle w. r. t. a specific axis is observed for both tilt axes. At small plate angles like in this case, the observed rate can be fitted accurately by a Gaussian distribution. The position of the rate maximum corresponds to the *zero-angle offset*; this value is then used as a correction term in the slow-control software that operates the tilt actuation motors of the electron

17. An alternative approach would be to perform a magnetic reflection measurement (see below), which is also sensitive to the produced pitch angle and covers a wider range up to $\theta = 90^\circ$ in the entry magnet. Corresponding simulations (section 4.8.11) indicate that this method could be more accurate than a zero-angle measurement, and thus should be preferred in future commissioning phases.

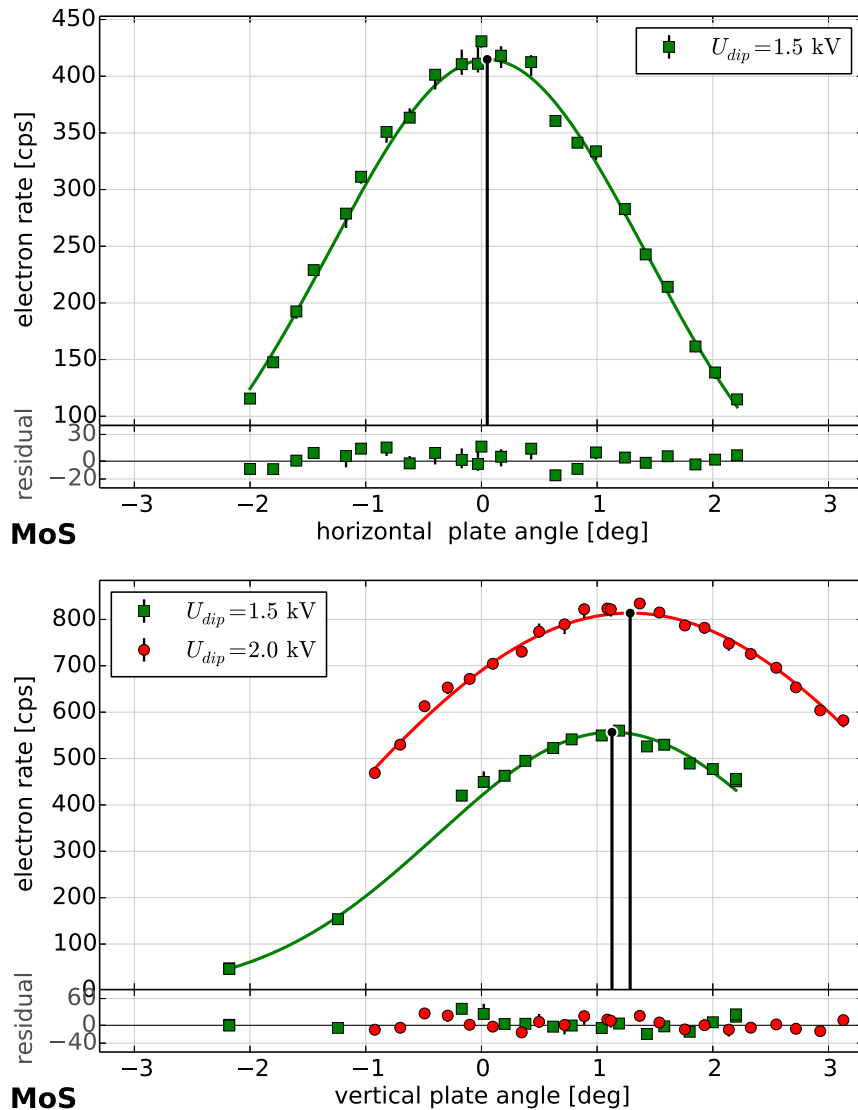


Figure 4.28.: Zero angle with nominal magnetic field at the MoS setup. The zero-angle offset at the current source setting can be determined by measuring the electron rate while varying the plate angle α_p in each tilt axis. The measurement is performed “on” the transmission edge, $U_{start} \approx U_{ana}$, where the electron rate is sensitive to changes in the electron pitch angle. The rate maximum then indicates the setting where the minimal pitch angle is produced, and its position is used as an offset-correction in the slow-control software of the electron source. After correction, the minimal pitch angle is achieved at $\alpha_p = 0^\circ$. It was found that the zero-angle depends on the dipole voltage, which needs to be considered in corresponding measurements. The plot at the bottom shows that a change in dipole voltage by 500 V (25%) results in a zero-angle shift of 0.16° .

Runs: 167747–167770,167730–167746,167867–167888

source. The corresponding fit results are shown in table 4.2. Clearly it is important to perform the offset correction with the correct sign: A positive zero-angle offset indicates that the actual zero angle is at a *larger* value of α_p . Consequently, the offset must be *added* to the value that is currently used in the software in order to achieve the minimal pitch angle at $\alpha_p = 0^\circ$.

The measurement procedure has to be performed for both tilt axes. Once the corrected offsets are implemented into the slow-control software, they are used for all following measurements (which improves usability of the software and prevents mistakes from wrongly applying zero-angle offsets). However, if the operational parameters of the electron source change so that the produced pitch angle is affected, the new zero angle must be determined again. This is the case e. g. for a changed dipole voltage, which is shown in the bottom part of figure 4.28. Here the zero-angle measurements was performed on the vertical axis at another dipole voltage (2 kV), and a significant deviation of 0.16° is observed between the two settings. An equivalent measurement on the horizontal axis showed no such effect, i. e. the zero-angle position is independent of the dipole voltage. This can be explained by the asymmetric electric dipole field which is oriented in vertical direction, given the design of the dipole chamber (where the dipole electrode is mounted at the bottom of the beam tube). The stray dipole field influences the electric field inside the electron source chamber where the electron acceleration occurs, so that the resulting pitch angle is modified and the zero-angle position changes. This effect has been further investigated by simulations (section 4.8.7) and is now well understood.

Enhanced magnetic field

When the additional air coil is used to enhance the magnetic field at the photocathode, the electron acceleration process is modified as well. The non-adiabatic acceleration is a result of the electric and magnetic field near the emission spot working against each other (cmp. section 4.2.6). A change in the magnetic field affects the produced pitch angle and thus the zero angle.

To investigate this effect, another zero-angle measurement was performed on the vertical axis after ramping the air coil to $I_{coil} = -35$ A; the negative sign here is by convention. The measurement was performed at otherwise nominal settings and with the previously determined zero-angle setting. The measurement therefore determines the *change* in zero angle due to the increased magnetic field. The measurement result (zero-angle offset for the vertical axis) is therefore seen as an additional correction to the value determined above, and must be implemented into the slow-control software accordingly for measurements at enhanced magnetic field. The fit results are shown in table 4.2 together with the earlier measurement results.

The measurement at enhanced field shows that the roughly 33% higher magnetic field (21 mT \rightarrow 28 mT) results in a considerable zero-angle shift of -0.39° on the vertical axis, which is larger than the effect from a changed dipole voltage (33% increase, 1.5 kV \rightarrow 2.0 kV). An equivalent measurement on the horizontal axis indicated that the effect here is marginal; the observed shift is within the uncertainty of the fit results. The magnetic field therefore primarily affects the vertical zero angle, which could again be explained by the stray field of the dipole electrode. The asymmetry of the electric field in vertical direction that is caused by the dipole has a large impact on the electron acceleration, as indicated by the results discussed above. The electron acceleration in general is a complex process that depends strongly on the electromagnetic conditions, and the dipole field could thus easily amplify the dependency on the magnetic field.

Table 4.2.: Measured zero angle offsets at different dipole voltages and magnetic field settings.

U_{dip}	I_{coil}	χ^2/ndf	$\Delta\alpha_{0,v}$	χ^2/ndf	$\Delta\alpha_{0,h}$
1.5 kV	0 A	4.29	1.128(1)°	5.28	0.050(6)°
2.0 kV	0 A	2.91	1.285(9)°	—	—
	-35 A	0.71	-0.384(65)°	—	—

Zero-angle offset correction

In the MoS measurements, only the nominal dipole setting ($U_{dip} = 2$ kV) and the enhanced magnetic field setting ($B_{start}^+ = 28$ mT) was used for regular measurements. However, the magnetic field was reduced by ramping down the additional air coil for dedicated measurements where the influence of the magnetic field was investigated. This requires to modify the zero-angle offset in the slow-control software whenever necessary.

For measurements at nominal magnetic field ($B_{start} = 21$ mT), the zero-angle offsets in the slow-control software were updated from their initial (and arbitrary¹⁸) values

$$\alpha_{0,h}^* = 75.28^\circ, \quad \alpha_{0,v}^* = 162.67^\circ, \quad (4.51)$$

to

$$\alpha_{0,h}^* = 75.332^\circ, \quad \alpha_{0,v}^* = 163.796^\circ. \quad (4.52)$$

The * indicates that these values are internal values that are only used by the software, and not actual plate angles. For regular measurements at enhanced magnetic field, the values were again updated to

$$\alpha_{0,h}^* = 75.332^\circ, \quad \alpha_{0,v}^* = 163.310^\circ. \quad (4.53)$$

Note that only the vertical zero-angle offset changed here, as discussed above. Differences between these adjustments and the values given in table 4.2 are due to the refined analysis and fitting methods that were used to process the measurement results for this thesis.

4.5.5 Magnetic reflection

Nominal magnetic field

Magnetic reflection measurements provide an alternative method to investigate the pitch angles produced by the electron source. In contrast to the zero angle measurement, which operates near the minimal pitch angle, this type of measurement determines the *maximal* pitch angle that is transmitted. Electrons are reflected if they reach $\theta = 90^\circ$ before reaching the detector. The measurement principle is described in section 4.4. As soon as the plate tilt angle reaches $\alpha_p \rightarrow \alpha_{max}$ where the maximal pitch angle is produced, a steady rate decrease is observed due to the finite angular spread of

18. The offsets correspond to earlier measurements at a different setup, before the electron source was mounted at the MoS setup.

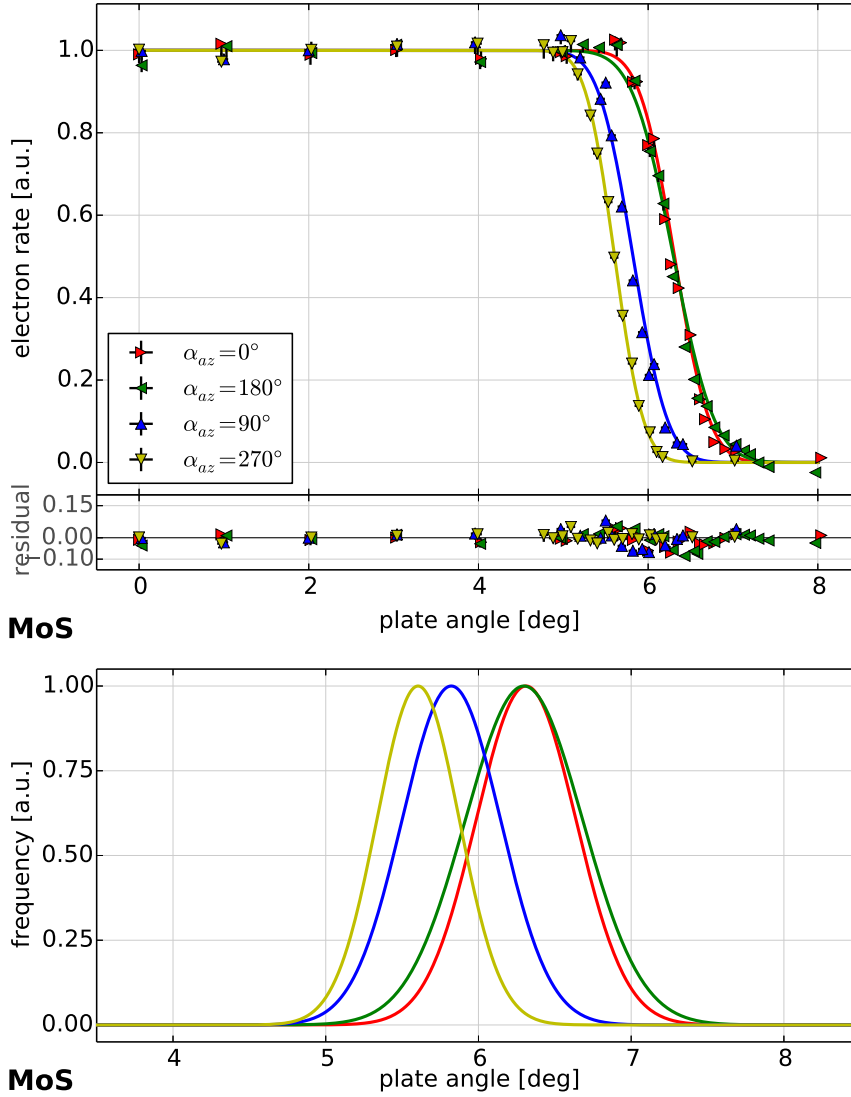


Figure 4.29.: Magnetic reflection with nominal magnetic field at the MoS setup. The plot shows the observed electron rate in dependency of the plate angle α_p with $U_{dip} = 2$ kV. The measurement as performed in four azimuthal tilt directions ($\alpha_{az} = 0^\circ, 180^\circ, 90^\circ, 270^\circ$) and used the nominal magnetic field ($B_{start} = 21$ mT). Magnetic reflection at the entry magnet occurs at $\alpha_p \approx 6^\circ$. A discrepancy between the two tilt axes (vertical: $\alpha_{az} = 90^\circ, 270^\circ$; horizontal $\alpha_{az} = 0^\circ, 180^\circ$) is seen, which can be explained by phase effects that influence the electron acceleration processes. The observed asymmetry on the vertical axis is likely caused by an incorrect zero-angle setting, despite the offset correction that has been performed beforehand. Runs: 167889–167911,167912–167938,167940–167958,167959–167980

the created electrons. The angular distribution is dominated by a Gaussian shape; the rate decrease can therefore be modeled by an error function. At its center, $\alpha_p = \alpha_{max}$, half of the emitted electrons are magnetically reflected and the angle α_{max} is called the *reflection angle*.

Similar to the zero-angle measurement, this method can be applied to determine the zero-angle of the plate setup, i. e. to align the electron source with the magnetic field so that a minimal pitch angle

is produced at $\alpha_p = 0^\circ$. It provides a higher accuracy due to the larger scanning range¹⁹. A zero-angle offset effectively shifts the produced pitch angles into a specific direction – i. e. increases or decreases the produced pitch angle, depending on the azimuthal direction – and therefore causes an asymmetry. Such an asymmetry causes a difference in the determined values of α_{max} along a given tilt axis (horizontal or vertical), and can be resolved in a magnetic reflection measurement. Since the measurement operates at large pitch angles close to 90° , the adiabatic transformation towards the spectrometer magnet enhances any asymmetry in the pitch angle, which further contributes to the improved accuracy w. r. t. to a zero-angle measurement.

Unfortunately, this novel approach was not taken into account in the MoS and SDS2-2 measurements as its benefits over the zero-angle method became clear only during the analysis of the measurements. As it turns out, the limited accuracy of the zero-angle measurements results in a remaining asymmetry that had not been fully corrected during the commissioning measurements of the electron source. This asymmetry can be clearly observed in the magnetic reflection measurements.

Figure 4.29 shows the results of the magnetic reflection measurements at nominal magnetic field ($B_{start} = 21$ mT without the additional air coil) in the four major azimuthal directions (up/down/left/right). The measurements were performed at nominal settings ($U_{spec} = -18.6$ kV, $U_{acc} = 5$ kV, $U_{dip} = 2$ kV, laser at 6 A/100 kHz). The reflection angles are determined by an error-function fit. The angular distributions are shown at the bottom of the figure; they correspond to the derivative of the fit curves. Note that the angles are given in terms of plate tilt angle α_p (not pitch angle θ) here that was varied during the individual measurements. However, the reflection angle α_{max} corresponds to the maximal pitch angle $\theta = 90^\circ$ in the entry magnet. Furthermore, one can assume that the pitch angle θ_0 produced at the electron source depends linearly on the plate tilt angle, which is confirmed by simulations (section 4.7):

$$\theta_0 = f(\alpha_p) = k \cdot \alpha_p. \quad (4.54)$$

The adiabatic transformation between θ_0 at the electron source and θ in the entry magnet can then be written as

$$\theta = \arcsin\left(\alpha_p \cdot k \frac{B_{max}}{B_0}\right) \quad (4.55)$$

$$= \arcsin\left(\frac{\alpha_p}{\alpha_{max}}\right), \quad (4.56)$$

where the factor k and the ratio of the magnetic fields B_{max}/B is constant in regular measurements. The transformation in (4.56) is allowed since $\theta = 90^\circ$ at $\alpha_p = \alpha_{max}$ by definition.

Using the above equation, one can now derive an *effective angular spread* σ_θ^* from the width σ_α of the magnetic reflection curve that was measured:

$$\sigma_\theta^* = \theta_{max} - \theta_{low} \quad (4.57)$$

$$= 90^\circ - \arcsin\left(\frac{\alpha_{max} - \sigma_\alpha}{\alpha_{max}}\right), \quad (4.58)$$

where θ_{low} corresponds to the lower bound (1σ -width) of the angular distribution. Note that due to the behavior of the arcsin-term, this width can only be computed for the lower half of the angular

19. The reflection measurement typically uses plate angles around -12° to 12° on the tilt axis; the zero angle measurement only uses a range of -2° to 2° .

distribution, i. e. for pitch angles below 90° . Assuming that the distribution is symmetric (which is confirmed by simulations), the resulting width can be used as a rough estimate for the angular spread. Table 4.3 lists the measurement results and the effective angular spread that has been determined using this approach. It can be compared with other measurements that investigate the angular spread directly, such as the angular-selective transmission function measurements discussed later on (section 4.5.6).

Enhanced magnetic field

Figure 4.30 shows a magnetic reflection measurement at enhanced magnetic field ($B_{start}^+ = 28 \text{ mT}$ with the additional air coil), otherwise using the same settings as the measurements above. Due to the reduced field, the reflection angles shift from the previously determined values around 6° to roughly 10° here. This effect is expected from the adiabatic transformation (4.56), which produces larger pitch angles θ as the magnetic field B_0 at the electron source increases. At the given settings, the ratio of the magnetic fields increased by about 30% in this measurement ($28 \text{ mT}/6 \text{ T} = 0.0047$ versus $21 \text{ mT}/6 \text{ T} = 0.0035$ before). Due to the larger pitch angles of the created electrons, magnetic reflection occurs at a smaller plate tilt angle α_p . The results of this measurement series are given in table 4.3. Like before, an effective angular spread in the entry magnet has been determined from the width of the fitted error function.

Unfortunately, this measurement series was carried out before the new zero angle for enhanced magnetic field had been determined²⁰. The measurements were thus performed operated at a slightly shifted zero angle (about 0.4° , see section 4.5.4 above). This offset contributes to the observed asymmetry and explains why the reflection curves for a given tilt axis are not well aligned. This is especially visible when comparing the horizontal axis scans between the two magnetic field settings, where the measurement at enhanced fields shows a considerably larger asymmetry.

Table 4.3.: Measured reflection angles at different magnetic field settings.

I_{coil}	α_{az}	χ^2/ndf	α_{max}	σ_α	σ_θ^*
0 A	0°	1.07	$6.31(1)^\circ$	$0.33(2)^\circ$	$18.5(9)^\circ$
	180°	1.57	$6.30(2)^\circ$	$0.38(1)^\circ$	$20.1(8)^\circ$
	90°	1.53	$5.82(2)^\circ$	$0.32(2)^\circ$	$19.1(11)^\circ$
	270°	0.35	$5.60(2)^\circ$	$0.27(2)^\circ$	$17.8(15)^\circ$
	weighted average:			$0.341(4)^\circ$	$19.06(10)^\circ$
-35 A	0°	0.71	$10.06(2)^\circ$	$0.39(3)^\circ$	$16.0(10)^\circ$
	180°	0.88	$11.13(3)^\circ$	$0.39(3)^\circ$	$15.2(12)^\circ$
	90°	1.89	$9.56(2)^\circ$	$0.40(2)^\circ$	$16.7(9)^\circ$
	270°	0.82	$9.73(2)^\circ$	$0.40(3)^\circ$	$16.6(10)^\circ$
	weighted average:			$0.396(1)^\circ$	$16.20(7)^\circ$

²⁰. Actually, it only became clear after these measurement that the zero-angle had changed due to the different magnetic field.

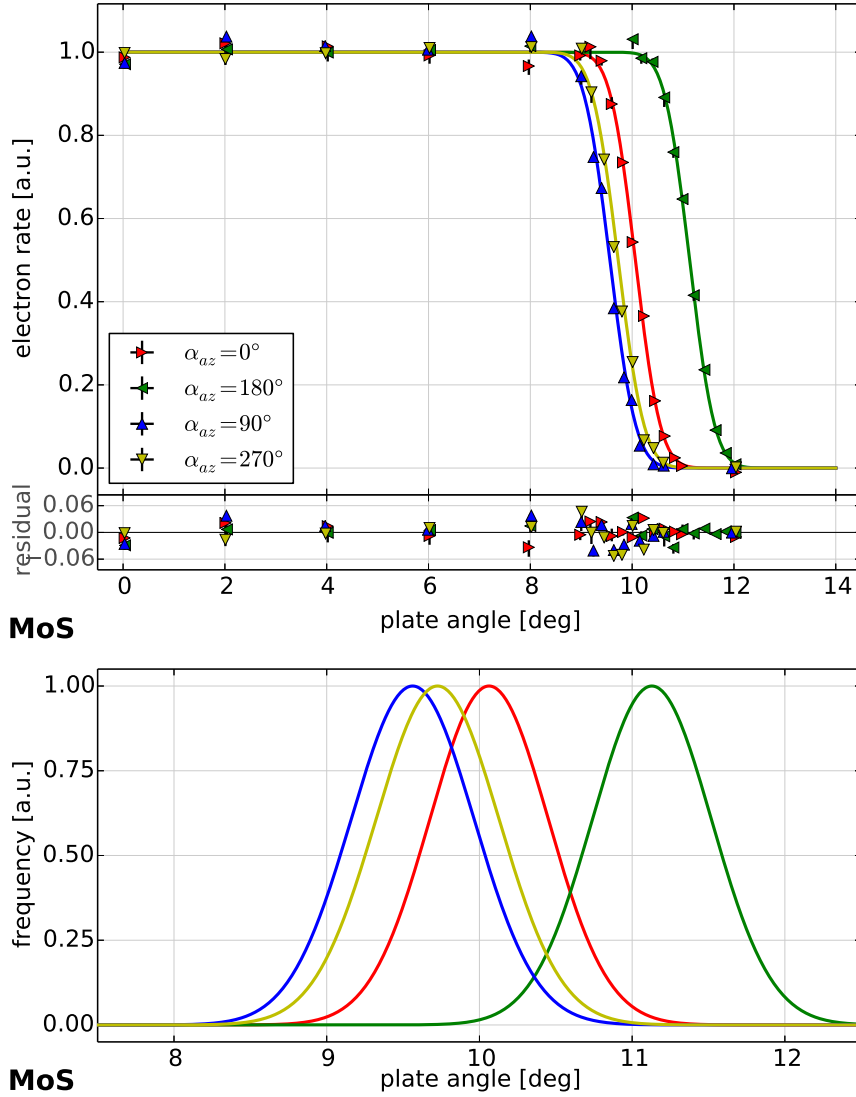


Figure 4.30.: Magnetic reflection with enhanced magnetic field at the MoS setup. The plot shows the observed electron rate in dependency of the plate angle α_p with $U_{dip} = 2\text{ kV}$ and $\alpha_{az} = 0^\circ, 180^\circ, 90^\circ, 270^\circ$. In contrast to figure 4.29, this measurement used the enhanced magnetic field setting ($B_{start}^+ = 28\text{ mT}$). The reflection angle shifts to larger values around 10° due to the higher magnetic field at the photocathode, which reduces the magnetic field ratio B_{start}^+/B_{max} . Again, an asymmetry between the azimuthal directions is observed. Note that this setting was performed with the zero-angle setting for nominal magnetic field, which increases the asymmetry.

Runs: 168013–168029,168030–168047,168049–168063,168064–168078

Pitch angle asymmetries

From the measurement results discussed above, one can now compare the reflection angle α_{max} , the width of the reflection curve σ_α , and the effective angular spread σ_θ^* between the individual tilt axes. This allows to investigate asymmetries in the produced pitch angles.

Two types of asymmetry are observed here:

- An asymmetry between the reflection angles on a single tilt axis (horizontal or vertical) indicates an incorrect zero-angle setting. If the source is operated with a small (non-zero) zero-angle offset – e. g. due to improper alignment or the limited accuracy of a zero-angle measurements – the produced pitch angles will systematically shift in one direction, corresponding to the sign of the offset.

Since the magnetic reflection measurement is more sensitive to the produced pitch angle for the reasons explained above, even small zero-angle offsets can become clearly visible. Consequently, it is possible to use the magnetic reflection measurement to determine the zero-angle with better accuracy, although this approach was not used in the MoS and SDS-II measurements presented here. It should, however, be considered for future measurements with similar setups.

The observed asymmetry of the reflection angle corresponds to the zero-angle offset, since both values relate to the plate tilt angle of the electron source. The offsets for the two independent tilt axes are defined as

$$\Delta\alpha_{0,h} = \Delta\alpha_{max} = \alpha_{max}(0^\circ) - \alpha_{max}(180^\circ), \quad (4.59)$$

$$\Delta\alpha_{0,v} = \Delta\alpha_{max} = \alpha_{max}(90^\circ) - \alpha_{max}(270^\circ). \quad (4.60)$$

- An asymmetry between the average reflection angles for each tilt axis, on the other hand, cannot be explained simply by a zero-angle offset since the actuation of the two axes is independent. Hence, a zero-angle offset on one axis cannot create an asymmetry on the other axis.

Instead, the deviation must be explained by actual differences in the electron-acceleration processes in the source. The asymmetric electric field of the dipole electrode, for example, is known to affect the electron acceleration inside the source chamber. Another contribution is caused by phase-effects, i. e. a dependency of the produced pitch angle on the initial azimuthal angle of the electrons created in the source. These effects are believed to play a significant role in the electron-acceleration processes, which is also indicated by simulations (see section 4.8.5). This azimuthal dependency in combination with the asymmetric electric field could explain the observed asymmetry in the produced pitch angles.

This type of asymmetry can be described by the difference between the average reflection angle of each tilt axis,

$$\Delta\alpha_{h-v} = \Delta\alpha_{max} = \frac{1}{2} \cdot \{ [\alpha_{max}(0^\circ) + \alpha_{max}(180^\circ)] - [\alpha_{max}(90^\circ) + \alpha_{max}(270^\circ)] \}. \quad (4.61)$$

Both types of asymmetries were evaluated from the measurements discussed above; the resulting values are given in table 4.4. The observed asymmetries $\Delta\alpha_h, \Delta\alpha_v$ for the two tilt axes indicate that the zero-angle offset determined from the corresponding measurements is not entirely correct. Especially the horizontal axis shows a significant asymmetry at the enhanced field setting, which has already been noted before. On the other hand, the asymmetry $\Delta\alpha_{h-v}$ between the tilt axes are comparable for both magnetic field settings, with the reflection angle α_{max} on the horizontal axis being generally larger. This indicates that the pitch angle that is produced at azimuthal plate angles $\alpha_{az} = 0^\circ, 180^\circ$ (horizontal axis) is systematically smaller than for $\alpha_{az} = 90^\circ, 270^\circ$ (vertical axis). This observation is in agreement with the idea that phase-effects modify the produced pitch angle with an azimuthal dependency.

In a similar approach, the effective angular spread in the entry magnet σ_θ^* can be investigated for asymmetries as well, using equivalent definitions of (4.59), (4.60) and (4.61). The results are also

listed in table 4.4 and show consistency over all measurements within a 2% margin. This corresponds to a maximal deviation of 1.6° for the angular spread at maximal pitch angle, $\theta = 90^\circ$.

Table 4.4.: Observed asymmetries in the reflection angle measurements.

asymmetry	I_{coil}	$\Delta\alpha_{max}$	$\Delta\sigma_\alpha$	$\Delta\sigma_\theta^*$
horizontal axis	0 A	$0.01(3)^\circ$	$-0.05(3)^\circ$	$-1.6(2)^\circ$
	-35 A	$-1.07(5)^\circ$	$0.05(4)^\circ$	$1.3(3)^\circ$
vertical axis	0 A	$0.22(4)^\circ$	$0.00(6)^\circ$	$0.8(2)^\circ$
	-35 A	$-0.16(4)^\circ$	$0.00(5)^\circ$	$0.1(2)^\circ$
between axes	0 A	$0.59(7)^\circ$	$0.06(7)^\circ$	$0.9(4)^\circ$
	-35 A	$0.95(9)^\circ$	$-0.01(11)^\circ$	$-1.1(4)^\circ$

Influence of the acceleration voltage

The pitch angle that is produced by the electron source not only depends on the plate angle, but also on other parameters like the acceleration voltage U_{acc} that is applied between the front and back plate. The working principle of the electron source is based on the non-adiabatic acceleration of the emitted electrons and thus requires a strong electric field to imprint a defined pitch angle (cmp. section 4.2.6). The produced pitch angle is therefore strongly related to the electromagnetic conditions near the photocathode.

Hence, instead of varying the plate angle α_p in order to observe magnetic reflection, it is also possible to investigate the pitch angle by varying the acceleration voltage U_{acc} . Under nominal conditions, the electron source is operated at $U_{acc} = 5$ kV. When a setting is used where the plate tilt angle is slightly above the reflection angle, $\alpha_p \gtrsim \alpha_{max}$, the majority of electrons is magnetically reflected before reaching the detector. One can now steadily reduce U_{acc} , thereby reducing the produced pitch angles, so that the electron signal re-appears at the detector as the amount of reflected electrons decreases. The lower acceleration voltage essentially shifts the produced angular distribution into the regime $\theta < 90^\circ$. The transmission probability for the emitted electrons increases accordingly. The observed rate dependency on U_{acc} can again be described by an error function that corresponds to the angular distribution of the electrons.

Figure 4.31 shows a magnetic reflection measurement with $U_{acc} = 5$ kV to 1 kV at otherwise nominal settings, using the nominal magnetic field without air coil. At this setting, magnetic reflection occurs at $\alpha_{max} = 6.3^\circ$ for $\alpha_{az} = 0^\circ$ and $U_{acc} = 5$ kV. At a plate angle $\alpha_p = 7^\circ > \alpha_{max}$, all electrons are reflected so that the detector observes only background. As expected, reducing the acceleration voltage results in a rate increase up to the nominal rate of several kcps, which is reached at $U_{acc} \approx 3$ kV. This confirms that the produced pitch angle depends on the acceleration voltage. The non-adiabatic acceleration in the plate setup of the electron source is less efficient at lower voltages, so that the produced pitch angle becomes smaller in this case. Interestingly, magnetic reflection is observed again at low acceleration voltages $U_{acc} \leq 1$ kV. This behavior is explained by the fact that angular selectivity ceases at these small field strengths (below 100 kV/m), so that a sharp angular distribution is no longer achieved. Instead, the distribution becomes extremely broad and starts to follow the initial $\cos \theta$ -distribution

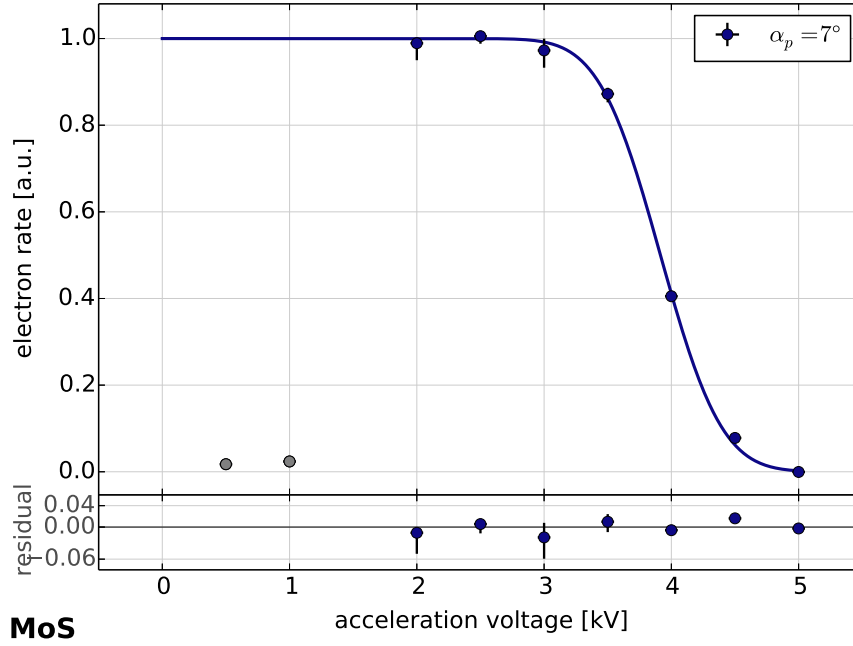


Figure 4.31.: Magnetic reflection measured by varying the acceleration voltage at the MoS setup. The plot shows the observed electron rate in dependency of the acceleration voltage $U_{acc} = 0.5$ kV to 5 kV with $U_{dip} = 2$ kV. The measurement was performed at a non-zero plate angle to increase its sensitivity to the acceleration voltage ($\alpha_p = 7^\circ, \alpha_{az} = 0^\circ$) and uses the nominal magnetic field setting ($B_{start} = 21$ mT). The electron rate shows a similar behavior as in typical magnetic reflection measurements (figure 4.29f.), since the reduction of U_{acc} changes the produced pitch angle. The rate can be described by an error function to examine the angular distribution of the electrons. At low acceleration voltage $U_{acc} \leq 1$ kV, the resulting angular distribution becomes extremely broad as angular selectivity ceases in this voltage range. In this case, a large fraction of electrons is emitted with large pitch angles and magnetically reflected at the entry magnet, which explains the observed rate reduction in this setting. Runs: 167986–167994

of the electrons emitted from the photocathode. In this case, a considerable fraction of produced electrons with large pitch angles is magnetically reflected, and the observed rate decreases accordingly.

Because the measurement described here investigates the angular distribution of the electrons quite similarly to the regular magnetic reflection measurement discussed above, one can apply the same analysis methods here as well. Again it is possible to estimate an effective angular spread σ_θ^* of the electrons from the with σ_U of the fitted error function. The only difference to (4.56) is that instead of the reflection angle α_{max} there now is a voltage \hat{U}_{acc} that corresponds to $\theta = 90^\circ$, i. e. to the center of the fitted error function:

$$\theta = \arcsin\left(\frac{U_{acc}}{\hat{U}_{acc}}\right). \quad (4.62)$$

Following the approach in (4.58), the effective angular spread in this case can then be estimated by

$$\sigma_\theta^* = 90^\circ - \arcsin\left(\frac{\hat{U}_{acc} - \sigma_U}{\hat{U}_{acc}}\right). \quad (4.63)$$

This relation again uses the fact that \hat{U}_{acc} corresponds to 50% of the electrons being reflected, i. e. where an average pitch angle of $\theta = 90^\circ$ is produced. The result of this measurement is given in table 4.5. The estimated angular spread of $\sigma_\theta^* \approx 26^\circ$ is somewhat larger than the results from the regular magnetic reflection measurements above, where an average angular spread of 19° was determined. The observed deviation is likely caused by modifications to the shape of the angular distribution due to the changed acceleration processes at lower voltages. In general, the results seem to be in agreement, especially if one considers the rather larger uncertainties.

Table 4.5.: Measured magnetic reflection in dependency of acceleration voltage.

I_{coil}	α_{az}	α_p	χ^2/ndf	\hat{U}_{acc}	σ_U	σ_θ^*
0 A	0°	7°	0.22	3.91(3) kV	0.38(6) kV	25.5(31) $^\circ$

Influence of the dipole voltage

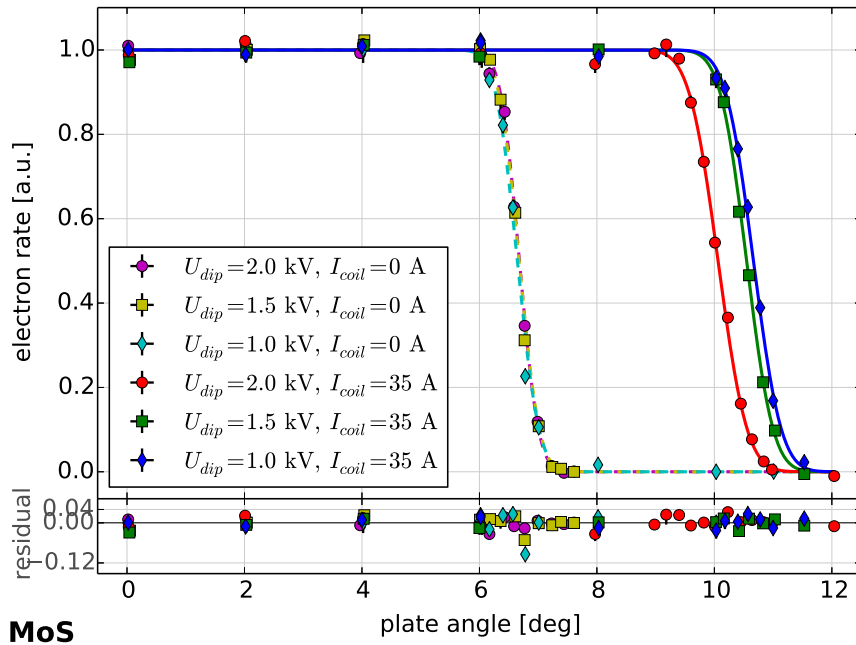


Figure 4.32.: Magnetic reflection with different magnetic field and dipole settings at the MoS setup. The plot shows the observed electron rate in dependency of the plate angle for different dipole voltages $U_{dip} = 1$ kV to 2 kV. The measurement was performed at both magnetic field settings with $\alpha_{az} = 0^\circ$. At nominal magnetic field ($B_{start} = 21$ mT), the dipole voltage does not seem to affect the reflection angle $\alpha_{max} \approx 6^\circ$. At enhanced magnetic field ($B_{start}^+ = 28$ mT), a consistent increase in α_{max} as the dipole voltage is reduced, which indicates that the dipole voltage affects the produced pitch angle to some extent. Runs: 168124–168135, 168136–168147, 168175–168186, 168013–168029, 168148–168159, 168160–168172

In addition to the previous discussions, magnetic reflection measurements can also be used to investigate how the dipole electrode affects the produced pitch angles. This is especially useful since magnetic reflection is extremely sensitive to small variations in the pitch angle close to α_{max} , and therefore achieves a higher sensitivity than e. g. zero-angle measurements.

Figure 4.32 shows two series of magnetic reflection measurements at dipole voltages $U_{dip} = 1.0\text{ kV}, 1.5\text{ kV}, 2.0\text{ kV}$. The measurements were performed at both nominal and enhanced magnetic field, and otherwise nominal settings ($U_{spec} = -18.6\text{ kV}, U_{acc} = 5\text{ kV}$). At nominal magnetic field ($B_{start} = 21\text{ mT}$), the three reflection curves are well-aligned and show no dependency on the dipole voltage. At enhanced magnetic field ($B_{start}^+ = 28\text{ mT}$), a systematic shift to larger reflection angles is observed as the dipole voltage is reduced. The observed increase in the reflection angle α_{max} indicates that the produced pitch angle becomes smaller, so that magnetic reflection is only achieved at larger plate angles α_p . The corresponding analysis results are shown in table 4.6. The effective angular spread σ_θ^* has been determined using (4.56) and (4.58), as discussed above. The angular spread is consistent over each measurement series where the magnetic field is constant. Furthermore, there is no significant deviation observed between the two field settings. This indicates that although changes to the dipole voltage affect the produced pitch angle, the shape of the angular distribution stays consistent. The observed variations in the pitch angle can therefore be viewed as simply scaling the range $[0; \alpha_{max})$ without affecting the underlying distribution in θ .

Table 4.6.: Measured reflection angles in dependency of the dipole voltage at different field settings.

I_{coil}	α_{az}	U_{dip}	χ^2/ndf	α_{max}	σ_α	σ_θ^*
0 A	0°	2.0 kV	0.42	6.68(3)°	0.26(3)°	15.9(19)°
		1.5 kV	0.73	6.68(3)°	0.27(3)°	16.4(17)°
		1.0 kV	0.58	6.64(2)°	0.29(2)°	17.0(13)°
-35 A	0°	2.0 kV	0.71	10.06(2)°	0.39(3)°	16.0(10)°
		1.5 kV	0.76	10.55(4)°	0.35(4)°	14.9(15)°
		1.0 kV	0.72	10.66(4)°	0.37(4)°	15.2(17)°

4.5.6 Energy and angular distributions

Energy distributions

A transmission function that has been measured with the electron source is well described by the analytical model described in section 4.1. The transmission function is then defined by the underlying energy and angular distributions of the electrons in the spectrometer entry magnet. These distributions can be investigated by spectroscopic measurements with a MAC-E filter²¹. The measurements at the MoS setup allowed to examine the source properties in detail, e. g. by varying operational parameters like the acceleration voltage or the wavelength of the incident UV light. It is thus possible to investigate how various parameters affect the produced energy and angular distributions.

The two distributions can be completely disentangled by performing a reference measurement at reduced spectrometer voltage. The improved energy resolution of the spectrometer in this case makes the observed transmission function independent of the angular distribution. Instead, it is fully defined by the energy distribution of the electrons, which allows to determine the energy spread directly

21. For the commissioning measurements of the electron source, the MAC-E filter was used as a spectrometer to characterize the source. Vice versa, with known source properties one can determine the transmission properties of a MAC-E filter.

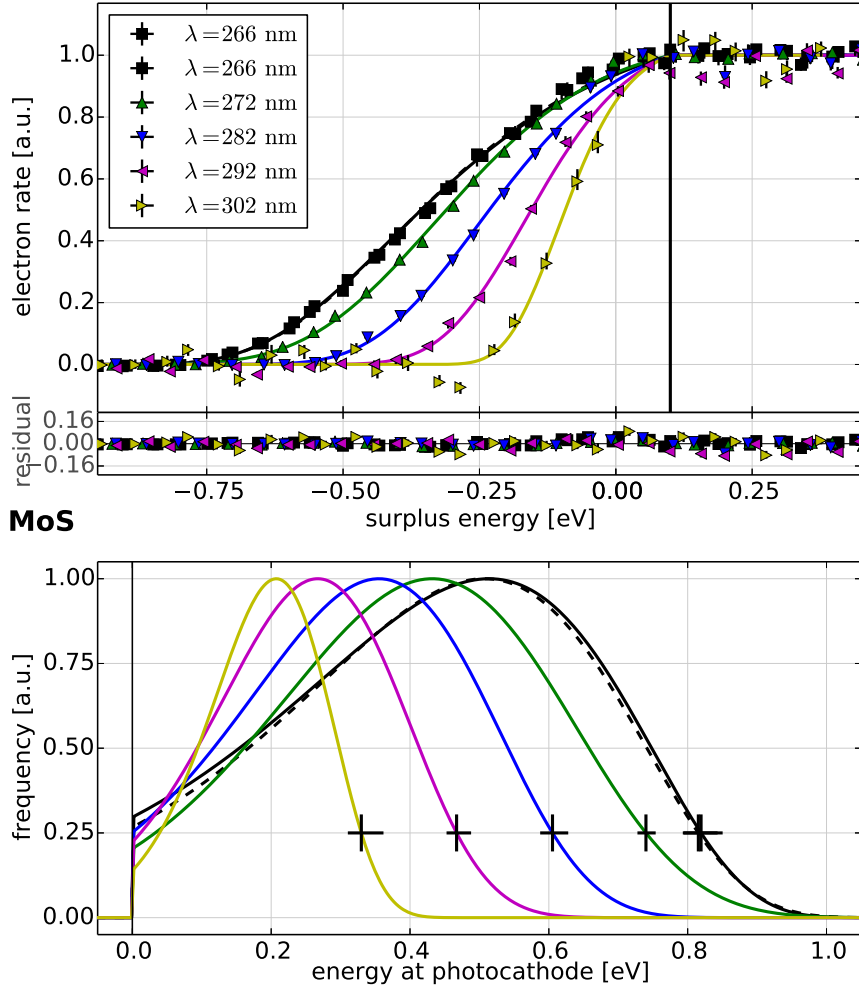


Figure 4.33.: Energy spread with different wavelengths at the MoS setup. The first plot shows transmission function measurements at different wavelengths $\lambda = 262$ nm to 302 nm at zero-angle ($\alpha_p = 0^\circ$). The measurements were performed at nominal magnetic field ($B_{start} = 21$ mT) and at high voltage ($U_{spec} = -18.6$ kV). The width of the observed transmission functions decreases with larger wavelengths, which is expected from the photoemission model where the maximal energy of the emitted electrons is given by $E_{max} = h\nu - \Phi$. Since the work function Φ was constant over the measurements, the energy spread of the electrons is determined by the photon energy $h\nu = hc/\lambda$. The observed transmission functions are fitted with the analytical transmission model (4.10). The transmission edge is located at $q\Delta U_0 = 0.10$ eV in this measurement series, as indicated by the vertical black line. The second plot shows the corresponding energy distributions that are included in the analytical model. As the wavelength increases, the upper limit of the distribution shifts towards smaller energies, which is equivalent to a smaller energy spread. The position of the upper limit E_{max} (indicated by black crosses) can be used to determine the photocathode work function directly from this type of measurement, instead of requiring a dedicated measurement series.

Runs: 167983,167984,168204,168189,168194,168297

from the width of the measured distribution. Following this approach, it is possible to determine the angular spread by comparing the energy distribution to transmission function measurements per-

formed at high voltage, where the angular distribution becomes relevant. This technique is described in section 4.4.

Ideally, the energy distribution measurement is performed at the lowest possible voltage (“zero voltage”); a value of $U_{spec} = -200$ V is typically used for convenience²². However, the detector at the monitor spectrometer is only sensitive to electron energies above roughly 6 keV [E⁺ 14]. Hence, in order to perform measurements at “zero voltage”, it is necessary to shift the electron energy above this threshold. Unfortunately, this is not possible at the monitor spectrometer where no post-acceleration setup exists²³. The measurements are therefore limited to electron energies $qU_{start} \gtrsim 8$ keV, where the spectrometer is operated at a reduced voltage of $U_{spec}^- = -9.3$ kV. A precise energy distribution measurement is therefore not possible at the MoS setup.

However, the energy distribution can be investigated if the electron source is operated at zero-angle ($\alpha_p = 0^\circ$). In this case, the effect of the angular spread on the observed transmission function is marginal due to the efficient adiabatic collimation of pitch angles in the MAC-E filter. The transmission function is therefore mostly sensitive to the energy distribution and can be describe by the analytical model if a fixed angular distribution is assumed. According to particle-tracking simulations, the values $\hat{\theta} = 2^\circ$ and $\sigma_\theta = 1^\circ$ for the mean pitch angle and the angular spread are used in the analysis presented here. Because of the low sensitivity to the angular distribution, the exact values of these parameters do not play a significant role for the transmission function as long as the measurement is performed at small pitch angles (cmp. section 4.9.2). It is thus possible to investigate the energy distribution and the energy spread regardless of the limitations that are present at the MoS setup.

Figure 4.33 shows transmission functions that were measured with different UV wavelengths at $\alpha_p = 0^\circ$ (zero angle). The measurement was performed at nominal magnetic field ($B_{start} = 21$ mT) and standard spectrometer settings ($U_{spec} = -18.6$ kV, $B_{min} = 0.38$ mT, $B_{max} = 6$ T). The UV light was provided by a laser ($\lambda = 266$ nm) or by UV-LEDs ($\lambda = 272$ nm, 282 nm, 292 nm, 302 nm). The position of the transmission edge was determined to $q\Delta U_0 = 0.10(1)$ eV for the analysis (cmp. section 4.9.2); it corresponds to the point where the transmission function reaches the full amplitude.

A clear decrease in transmission width is observed for increasing wavelengths. This corresponds to the smaller energy spread that is achieved as the photon energy (or wavelength) approaches the work function of the photocathode and is therefore expected. Note that the measurements at 292 nm, 302 nm are affected by low statistics due to the small electron rates that are achieved at these LED settings²⁴. The bottom of the figure shows the corresponding energy distributions that are used in the analytical model. The two measurements performed with the laser are in good agreement. The energy spread σ_E reduces considerably for larger wavelengths, from about 310 meV at 266 nm to 90 meV at 302 nm. The observed decrease is also consistent over the individual measurements. A measurement at a larger wavelength (312 nm) would have been possible with the LED setup and would have further reduced the energy spread, but was skipped due to time constraints.

In addition to determining the energy spread σ_E from the (generalized) normal distribution that is used to describe the energy distribution (cmp. section 4.2.5), it is also possible to derive an *effective energy spread* E_{max} from the width of the distribution directly. The energy of the emitted electrons

22. The voltage of the spectrometer vessel is reduced to 0 V, while the inner-electrode system stays at -200 V offset to the vessel potential.

23. The main spectrometer features a post-acceleration electrode in front of the detector, which allows low-energy measurements.

24. The statistical uncertainties could be reduced by increasing the measurement time, or by tuning the optical system to higher intensity (e. g. by increasing the pulse width).

is limited by the difference between photon energy $h\nu$ and the photocathode work function Φ . The upper limit of the distribution (above the position of the maximum) therefore corresponds to the value $E_{max} = h\nu - \Phi \geq 0$. In the analysis discussed here, the upper limit is defined as the energy where the normalized distribution drops to 25% of its height. This is indicated by the black crosses in the figure. The value of 25% has been chosen to yield consistency between the work functions determined using this approach and the result of direct measurements by the Fowler method (see section 4.5.8 below). With this definition, the fraction $[0; E_{max}]$ of every distribution includes at least 95% of its total integral. The value E_{max} therefore corresponds to the maximal observed energy of 95% of the emitted electrons, and is thus a valuable quantity to describe the effective energy spread that is achieved by the electron source.

Table 4.7 lists the peak energy \hat{E} , the energy maximum E_{max} (corresponding to the effective energy spread) and the energy spread σ_E for the measurements at different wavelengths. The energy spread has been computed from the model parameters of the energy distribution (generalized normal distribution) and corresponds to the 1σ -width of a normal distribution. This conversion to an equivalent symmetric distribution allows to compare the results to earlier measurements that were analyzed differently, e. g. the transmission function measurements in [Zac14].

Energy distributions at reduced voltage

As discussed above, the measurements performed at nominal conditions can be compared with transmission functions measured at reduced spectrometer voltage. Although it is not possible to perform measurements at electron energies well below 10 keV, the reduced voltage improves the energy resolution of the MAC-E filter and thus reduced the contribution of the angular spread to the observed transmission function. Hence, the low-voltage measurement allows to further investigate the energy spread and to compare the determined energy distributions. Additionally, if the effect of the angular distribution is indeed marginal for measurements performed at zero-angle (see above), the transmission functions measured at different spectrometer voltages must be comparable in width and shape.

Figure 4.34 shows the two transmission functions from above (measured at $U_{spec} = -18.6$ kV) in comparison with a single measurement performed at $U_{spec}^- = -9.3$ kV. All three measurements were performed at zero angle ($\alpha_p = 0^\circ$) and with the laser at a wavelength of $\lambda = 266$ nm. The observed energy distributions are in excellent agreement, and all relevant parameters (peak energy, energy spread, energy maximum) are consistent within their uncertainties. The corresponding fit results are given in table 4.7 and compared with the results from above. The observation that the determined energy distribution is independent of the spectrometer voltage proves that the contribution of the angular spread is marginal for this type of measurement. Otherwise, a clear deviation between the distributions measured at different spectrometer voltages would be visible. The assumption that the energy distribution can be determined from a high-voltage measurement at zero-angle is therefore correct.

This measurement series also showcases another important feature of the transmission function measurements. At the MoS setup, the reduced spectrometer voltage shifts the observed transmission function to larger surplus energies, which is clearly seen in figure 4.34. This shift corresponds to a smaller kinetic energy of the electrons in the analyzing plane (which is compensated by increasing the surplus energy in order to reach transmission). In the case that is discussed here, the transmission edge moves from 0.10(1) eV at $U_{spec} = -18.6$ kV to 0.24(1) eV at $U_{spec}^- = -9.3$ kV. This clearly is not an effect of the electron source, but is instead related to the so-called potential depression of the spectrometer (section 2.2.4), which modifies the retarding potential U_{ana} in the analyzing plane.

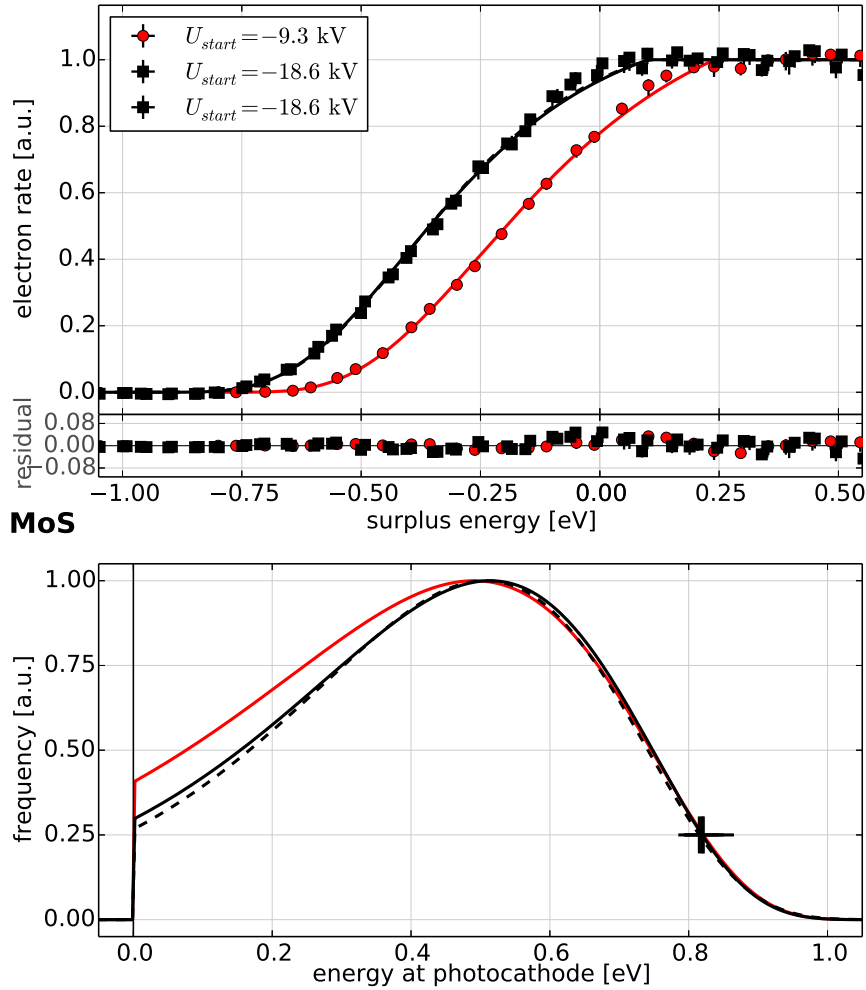


Figure 4.34.: Energy spread with different starting voltages at the MoS setup. The plot compares transmission functions that were measured at nominal and at reduced spectrometer voltage ($U_{spec} = -18.6$ kV, -9.3 kV) with nominal magnetic field and at zero-angle. The depicted high voltage runs are the same as in figure 4.33. The reduced voltage shifts the transmission function to larger surplus energies (i. e. to the right in this plot), since the potential depression ΔU_r of the spectrometer decreases. Apart from this shift, the observed transmission functions are practically identical. The shift can therefore be described by a change in the transmission edge position $q\Delta U_0$, and no influence from the angular spread of the emitted electrons is observed in this setting. Runs: 167983,167984,168296

At the monitor spectrometer, the strength of the potential depression depends on the absolute spectrometer voltage. It can be determined with sufficient accuracy by Kassiopia simulations, where the electric potential inside the spectrometer is evaluated. The resulting potential depression is 0.30 V at -18.6 kV and 0.16 V at -9.3 kV, yielding a difference of 0.14 eV. This simulated value is in excellent agreement with the observed shift of 0.14(2) eV.

Table 4.7.: Measured energy distributions at different wavelengths.

U_{ana}	λ	χ^2/ndf	\hat{E}	E_{max}	σ_E
-18.6 kV	266.0(10) nm	1.39	0.42(1) eV	0.82(2) eV	0.31(5) eV
		1.40	0.43(1) eV	0.82(2) eV	0.28(4) eV
	272.4(22) nm	1.18	0.40(1) eV	0.74(1) eV	0.22(2) eV
	282.4(22) nm	1.23	0.32(1) eV	0.61(2) eV	0.19(3) eV
	292.4(22) nm	3.38	0.25(1) eV	0.47(2) eV	0.14(3) eV
	302.4(22) nm	3.46	0.19(1) eV	0.33(2) eV	0.09(7) eV
-9.3 kV	266.0(10) nm	0.45	0.37(3) eV	0.82(4) eV	0.37(6) eV

Angular distributions

In addition to the energy distribution of the emitted electrons, it is also possible to examine the angular distributions of the electrons in the spectrometer entry magnet by transmission function measurements. The pitch angle θ in the spectrometer entry magnet depends on the plate tilt angle α_p due to the electron-acceleration processes that provide the electron source with angular selectivity. Electrons can be magnetically reflected if their pitch angle reaches 90° before arriving at the detector. Due to the symmetric magnetic fields at the MoS setup ($B_{max} = 6$ T at the spectrometer entrance and exit), magnetic reflection typically occurs in front of the entry magnet before the electrons enter the spectrometer.

In order to use the electron source as a calibration device for the commissioning of a MAC-E filter (i. e. in SDS commissioning measurements), it is necessary to achieve variable pitch angles that cover the full range of $\theta = 0^\circ$ to 90° in the magnet. This allows to investigate the pitch angle dependency of the transmission function and thus determine the transmission properties of the spectrometer. In this context, the measurements at the MoS setup also served as a test case for the following SDS-2 measurements.

Due to the angular dependency, the observed transmission function in high-voltage measurements shifts to larger surplus energies if the pitch angle increases. This is due to the non-perfect collimation of the electron beam in a MAC-E filter (section 2.2.1). The observed shift between a measurement at $\theta = 0^\circ$ and $\theta = 90^\circ$ corresponds to the spectrometer's energy resolution (2.13). It can be resolved with an electron source if the produced energy and angular spread is sufficiently small (cmp. section 4.1.1). This feature is utilized in the SDS-2 measurements to determine the energy resolution of the main spectrometer for different electron trajectories [Erh16].

Figure 4.35 shows transmission functions measured at enhanced magnetic field ($B_{start}^+ = 28$ mT) and nominal spectrometer settings ($U_{spec} = -18.6$ kV, $B_{min} = 0.38$ mT, $B_{max} = 6$ T). The measurement was performed with the laser (266 nm, 6 A/100 kHz). In this measurement series, the plate angle was increased in 2° steps in the range $\alpha_p = 0^\circ$ to 11° . The figure shows a measurement on the horizontal plate tilt axis ($\alpha_{ax} = 0^\circ$); an equivalent measurement in reverse direction ($\alpha_{ax} = 180^\circ$) is skipped here for brevity.

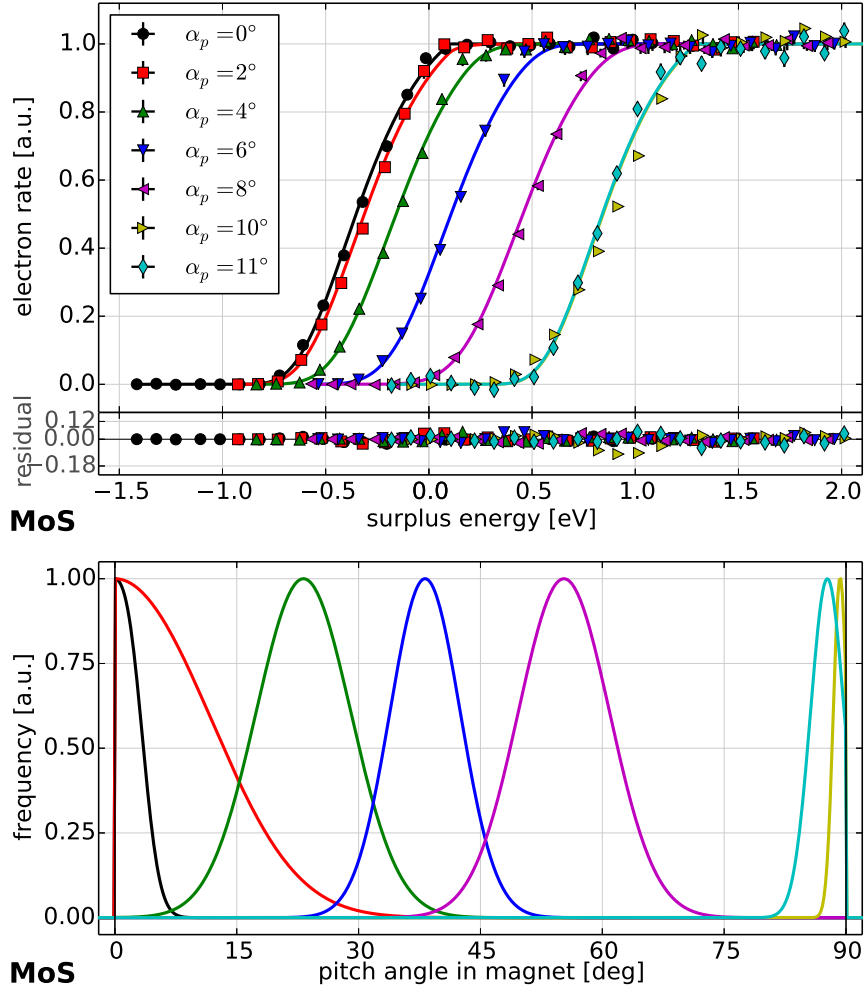


Figure 4.35.: Angular selectivity with $\alpha_{az} = 0^\circ$ at the MoS setup. The plot shows transmission functions that were measured with different plate angles α_p at nominal spectrometer settings ($U_{spec} = -18.6$ kV, $\Delta E = 1.18$ eV) and enhanced magnetic field at the source ($B_{start}^+ = 28$ mT). The measurements used the UV laser at $\lambda = 266$ nm; an energy distribution for this setting has been determined beforehand. As expected, the transmission functions shift towards higher surplus energies for larger plate angles as a result of the increasing pitch angle θ of the electrons. This proves that angular selectivity is achieved, and the electron source produces electrons with well-defined pitch angles. The observed transmission functions are again fitted with the analytical model (4.10). The underlying angular distributions for each measurement are shown at the bottom. The pitch angle in the entry magnet increases from roughly 0° to 90° , where magnetic reflection occurs. In the $\alpha_p = 11^\circ$ measurement the majority of electrons is already reflected, which causes the observed deviation from the analytical fit model.

Runs: 168103,168104,168105,168107,168108,168109,168110

From the given spectrometer settings one expects an energy resolution of

$$\Delta E = qU_{ana} \cdot \frac{B_{min}}{B_{max}} = 1.18 \text{ eV}. \quad (4.64)$$

The observed transmission functions clearly show the expected shift as the pitch angle increases towards the reflection angle $\alpha_{max} = 10^\circ$ (this value has been determined beforehand by a magnetic

reflection measurement, see section 4.5.5 above). Like before, the transmission functions were fitted with the analytical model. In this case, however, the analysis used a fixed energy distribution that was determined beforehand from reference measurements at zero-angle²⁵

At $\alpha_p > 10^\circ$, a large fraction of electrons is already magnetically reflected. The observed rate at $\alpha_p = 11^\circ$ is only 213 cps, corresponding to a reduction of 89% w. r. t. to the nominal rate of 1897 cps in this measurement series. Due to finite angular distribution of the electrons, the electron signal does not fully disappear yet since some electrons are produced with $\theta \lesssim 90^\circ$ here. However, the partial reflection deforms the observed angular and energy distributions, since reflected electrons do not contribute to the observed transmission function. This explains the deviation from the analytical model that is observed. The overlap of the transmission functions for $\alpha_p = 10^\circ, 11^\circ$ indicates that the reflection angle $\theta = 90^\circ$ has been reached at this point, and it is not possible to shift the transmission function to larger surplus energies. The observed shift therefore corresponds to the energy resolution of the monitor spectrometer:

$$\Delta E = q (\Delta U_0(\theta = 90^\circ) - \Delta U_0(\theta = 0^\circ)) \quad (4.65)$$

$$= 1.20(3) \text{ eV} - 0.00(5) \text{ eV} = 1.20(8) \text{ eV} , \quad (4.66)$$

where ΔU_0 refers to the position of the transmission edge, i. e. the point where the transmission function reaches its nominal amplitude. The result is in full agreement with the expected energy resolution (4.64). The measurement at $\alpha_{az} = 180^\circ$ yields an energy resolution of 1.20(6) eV and is therefore consistent with this result. The asymmetry in the produced pitch angles that was observed earlier (see above) is visible here as well, resulting in generally larger pitch angles for fixed values of α_p in the 180° direction of the plate tilt angle.

The measurements also show that the width and shape of the transmission function does not change significantly from increasing the pitch angle (except for larger angles $\alpha_p > \alpha_{max}$ where magnetic reflection occurs). This is expected because the transmission width is dominated by the energy distribution of the electrons (with an energy spread of $\sigma_E \approx 0.3 \text{ eV}$ in this case). Consequently, the contribution from the angular distribution is marginal. One can estimate the effect of the angular spread by the known energy resolution of the spectrometer from the transmission condition (2.15). At $\Delta E = 1.2 \text{ eV}$, the effective energy spread in the analyzing plane after the collimation by the MAC-E filter is 51 meV for $\theta = 45^\circ$ and $\sigma_\theta = 5^\circ$. This is the maximal value that can be achieved; it decreases if θ approaches 0° or 90° . The actual energy spread of the produced electrons of is considerably larger with $\sigma_E \approx 100 \text{ meV}$ to 300 meV for the available light sources.

The observed angular spread for different plate tilt angles α_p is consistent over the complete measurement series, achieving values of $\sigma_\theta \leq 6^\circ$ over the full range of pitch angles up to $\theta = 90^\circ$. The fit results for $\theta = 0^\circ, 90^\circ$ are affected by large uncertainties, in contrast to measurements performed at intermediate pitch angles. This is explained by the low sensitivity of the fit model to changes in pitch angle (and angular spread) if the pitch angle itself is close to the minimum or maximum. In general, the pitch angle in the intermediate range has a more pronounced effect on the transmission function than near the endpoints of the angular spectrum, since in this case the effective angular spread (after collimation by the MAC-E filter) is larger. One can estimate this effect by comparing the transmission function shift that is produced by varying the pitch angle,

$$\Delta E_\theta = q (\Delta U_0(\theta + \Delta\theta) - \Delta U_0(\theta)) . \quad (4.67)$$

25. Specifically, in this case the average of the energy distributions measured with the laser at $U_{spec} = -18.6 \text{ kV}$ and $\alpha_p = 0^\circ$ was used, cmp. table 4.7).

For a minimal pitch angle $\theta = 0^\circ$, a variation by $\Delta\theta = 10^\circ$ shifts the transmission functions by 36 meV towards higher surplus energy. At $\theta = 40^\circ$, the corresponding shift is 209 meV, which is substantially larger. This example also serves as another confirmation that the transmission function is fully dominated by the energy distribution of the electrons for measurements performed at zero-angle ($\theta \approx 0^\circ$), which has been exploited earlier.

Table 4.8.: Measured angular distributions at different plate angles.

α_{az}	α_p	χ^2/ndf	$\hat{\theta}$	σ_θ	ΔE_θ
0°	0°	1.09	1.7(13)°	2.0(13)°	0.00(5) eV
	2°	1.07	5.7(34)°	9.3(26)°	0.01(12) eV
	4°	1.12	23.2(3)°	5.8(8)°	0.19(1) eV
	6°	1.31	38.2(2)°	4.3(5)°	0.46(1) eV
	8°	1.50	55.3(3)°	5.6(4)°	0.81(1) eV
	10°	10.9	89.3(8)°	0.8(7)°	1.20(3) eV
	11°	1.57	87.7(18)°	2.1(16)°	1.20(6) eV
180°	2°	1.57	4.5(30)°	10.6(15)°	0.01(10) eV
	4°	1.30	19.9(3)°	6.4(8)°	0.14(1) eV
	6°	1.79	36.2(2)°	4.7(5)°	0.42(1) eV
	8°	2.19	51.9(2)°	5.7(3)°	0.74(1) eV
	10°	15.3	89.8(3)°	13.0(3)°	1.20(1) eV
	11°	4.48	89.4(6)°	0.6(5)°	1.20(2) eV

Influence of the acceleration voltage

The influence of the acceleration voltage on the produced pitch angle has already been investigated in the context of magnetic reflection measurements (section 4.5.5). Transmission function measurements can be used to further examine this influence. This allows to determine the angular distribution (mean pitch angle $\hat{\theta}$ and angular spread σ_θ in the entry magnet) in dependency of the acceleration voltage.

Figure 4.36 shows transmission function that have been measured at varying acceleration voltages $U_{acc} = 1.5$ kV to 5.0 kV. The measurement was performed at enhanced magnetic field ($B_{start} = 28$ mT) and nominal spectrometer settings ($U_{spec} = -18.6$ kV, $B_{min} = 0.38$ mT, $B_{max} = 6$ T). To increase sensitivity to the produced pitch angle θ , the measurement was performed at $\alpha_p = 11^\circ > \alpha_{max}$, where the majority of emitted electrons is magnetically reflected (see above). Since the pitch angle decreases at lower acceleration voltages, the transmission functions shifts to smaller surplus energies for $U_{acc} \rightarrow 3.0$ kV. When the voltage is further reduced, however, the pitch angle increases again and the transmission function shifts back towards larger surplus energies. The corresponding fit results are listed in table 4.9. The transmission functions were fitted again with the analytical model, using the previously determined energy distribution for the laser at $\lambda = 266$ nm. The table also lists the transmission function shift ΔE_θ that was introduced in (4.67).

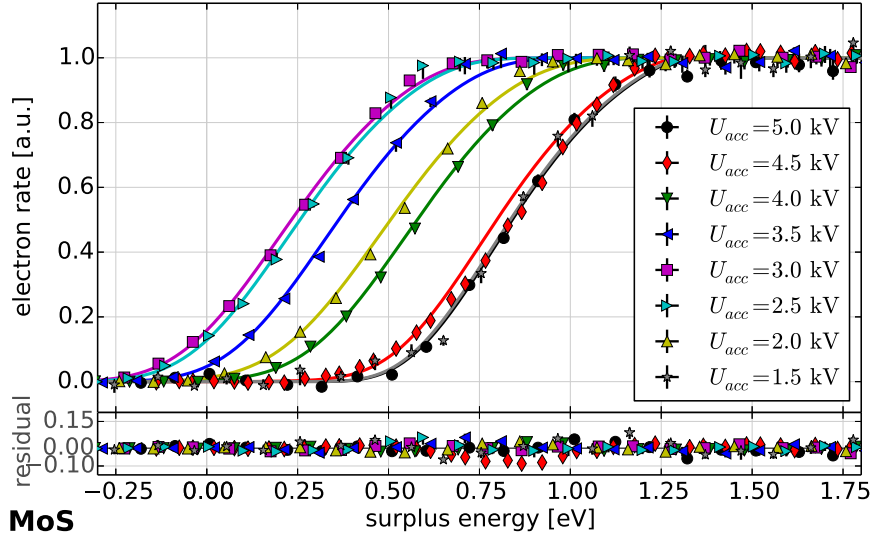


Figure 4.36.: Angular selectivity with reduced acceleration voltage at the MoS setup. The plot shows transmission functions for $\alpha_{az} = 0^\circ$ and $\alpha_p = 11^\circ$ at different acceleration voltages $U_{acc} = 5.0\text{ kV}$ to 1.5 kV . The measurement used the enhanced magnetic field and nominal high voltage at the spectrometer. At the plate angle $\alpha_p = 11^\circ$, the majority of electrons is magnetically reflected for $U_{acc} = 5\text{ kV}$. By reducing the acceleration voltage, the pitch angle of the produced electrons decreases and a shift of the observed transmission function towards lower surplus energies is observed. This is in agreement with magnetic reflection measurements that were performed at varying acceleration voltage (section 4.5.5). While the pitch angle decreases for $U_{acc} \rightarrow 3\text{ kV}$, for even lower acceleration voltages an increasing pitch angle is observed. This is also in agreement with magnetic reflection measurements, and can be explained by changes to the electron acceleration processes.

Runs: 168110,168192,168111,168196,168112,168199,168113,168203

The measurements show that a minimal pitch angle is produced at $U_{acc} \approx 3.0\text{ kV}$ in this setup, instead of decreasing towards $U_{acc} = 0\text{ V}$. This behavior is explained by considering how the pitch angles are produced in the electron source; this has been discussed in section 4.5.5 above. When the acceleration voltage is decreased, the non-adiabatic acceleration becomes less effective due to the lower electric field at the photocathode, which results in smaller pitch angles being imprinted on the emitted electrons. However, if the voltage is reduced below a certain threshold, the collimation of the electron beam in the source is severely impaired, and the observed angular distribution becomes extremely broad. The produced mean pitch angle therefore increases again, which is seen in the transmission function shift.

It should be noted that a measurement of this type would achieve maximal sensitivity to changes in pitch angle around $\theta = 45^\circ$, as discussed earlier. This means that it would be better to perform the measurement at smaller plate tilt angles $\alpha_p < \alpha_{max}$, which would also avoid the problem that the observed transmission function is deformed due to magnetic reflection. This can be seen especially in the measurement at $U_{acc} = 4.5\text{ kV}$, where the fit results show large uncertainties due to the deformation (see table 4.9). For possible future measurements of this type it is therefore suggested to reduce the plate tilt angle to a point where no reflection occurs at the nominal acceleration voltage of $U_{acc} = 5\text{ kV}$ (e. g. $\alpha_p \approx 8^\circ$ in the setup discussed here).

Table 4.9.: Measured angular distributions at acceleration voltages.

α_p	U_{acc}	χ^2/ndf	$\hat{\theta}$	σ_θ	ΔE_θ
11°	5.0 kV	1.57	87.7(18)°	2.1(16)°	1.20(6) eV
	4.5 kV	6.50	89.5(5)°	11.7(3)°	1.20(2) eV
	4.0 kV	0.81	62.1(3)°	6.3(5)°	0.94(1) eV
	3.5 kV	1.20	50.6(3)°	4.8(5)°	0.72(1) eV
	3.0 kV	1.26	44.3(2)°	5.1(4)°	0.58(1) eV
	2.5 kV	1.13	45.4(3)°	4.6(7)°	0.61(1) eV
	2.0 kV	1.37	58.0(3)°	6.5(4)°	0.86(1) eV
	1.5 kV	1.51	86.3(26)°	3.0(22)°	1.19(9) eV

Produced pitch angles

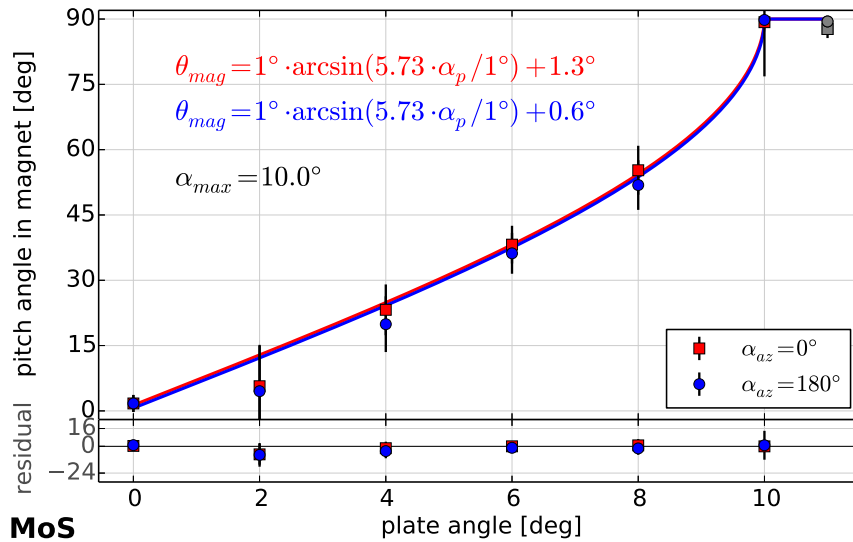


Figure 4.37.: Produced pitch angles with different plate angle at the MoS setup. The plot shows the pitch angle θ in the spectrometer entry magnet in dependency of the plate angle α_p , using data from transmission function measurements at $\alpha_{az} = 0^\circ, 180^\circ$ that have been discussed above (cmp. figure 4.35f). The observed behavior can be described by a model that is based on the adiabatic transformation of the pitch angle towards the entry magnet, which contains an arcsin-term that results in the observed non-linear dependency. For both measurement series the fit yields a reflection angle $\alpha_{max} = 10^\circ$ where magnetic reflection occurs ($\theta \rightarrow 90^\circ$). This is in excellent agreement with the magnetic reflection measurements discussed in section 4.5.5). Runs: 168103–168123

The measurements discussed so far showed that the electron source achieves angular selectivity and can produce electrons with well-defined pitch angles. The resulting pitch angle θ in the spectrometer entry magnet can be selected by tilting the plate setup around the plate angle α_p , but also depends on other operational parameters like the acceleration voltage U_{acc} that affects the electron-acceleration

processes inside the source. Another major influence comes from the ratio of the magnetic fields at the electron source and in the entry magnet, B_0/B_{max} .

It is therefore interesting to analyze the measurement results gathered at the MoS setup and investigate the dependency of the pitch angle on the plate tilt angle. Due to the adiabatic transformation of the pitch angles towards the entry magnet, this dependency can be described by an arcsin-function [Zac14, Gro15],

$$\theta(\alpha_p) = \arcsin(\beta \cdot \alpha_p) + \theta_{min}, \quad (4.68)$$

where $\beta = k \cdot \sqrt{B_0/B_{max}}$ describes the dependency on the magnetic fields; k is a constant that describes the pitch angle θ_0 that is produced at the end of the source before the adiabatic transformation sets in. One can assume that this pitch angle depends linearly on the plate tilt angle, $\theta_0 = k \cdot \alpha_p$, which is also confirmed by simulations (see section 4.8.4). This model for $\theta_0(\alpha_p)$ was also used in the analysis of the magnetic reflection measurements (section 4.5.5 above). The offset θ_{min} describes the minimal pitch angle that is produced by the source at $\alpha_p = 0^\circ$ (zero-angle). Due to a misalignment with the magnetic field, it is possible for θ_{min} to be non-zero.

Figure 4.37 shows the pitch angles that are produced for different values of α_p and α_{az} , using the results of the transmission function fits discussed in section 4.5.6. The plot shows the mean pitch angle $\hat{\theta}$ in the entry magnet that was determined by the fit; the error bars correspond to the angular spread σ_θ . Both measurements (in different azimuthal directions) are well described by the arcsin-model (4.68) and show consistent results. The reflection angle α_{max} can be calculated directly from the model; it corresponds to the value of α_p where $\theta(\alpha_p) = 90^\circ$:

$$\alpha_{max} = \frac{1}{\beta} \cdot \sin(90^\circ - \theta_{min}). \quad (4.69)$$

Both measurements yield a consistent value of $\alpha_{max} = 10.0^\circ$, which is also in agreement with the magnetic reflection measurements discussed earlier. The pitch angle asymmetry between the two azimuthal directions is reflected in the slightly different values for θ_{min} , where a difference of $1.3^\circ - 0.6^\circ = 0.9^\circ$ is observed.

The produced pitch angles can also be analyzed for their dependency on the acceleration voltage U_{acc} , based on the transmission function measurements discussed above. Figure 4.38 shows the fit results for $\hat{\theta}$ and σ_θ , using the measurements listed in table 4.9. A clear dependency on U_{acc} is observed with a minimum around $U_{acc} = 3$ kV, which is expected from the discussion in section 4.5.6. Similar to (4.68), the dependency $\theta(U_{acc})$ can be described by an arcsin-model. The model has been modified to reflect the symmetric shape of the dependency that is visible in the figure:

$$\theta(U_{acc}) = \arcsin(\beta \cdot |U_{acc} - \hat{U}_{acc}|^2) + \theta_{min}. \quad (4.70)$$

The additional fit parameter \hat{U}_{acc} corresponds to the position where the minimal pitch angle is produced, i. e. the center of the quadratic fit curve at. Note that it is not clear why (4.70) shows a quadratic dependency on $U_{acc} - \hat{U}_{acc}$, rather than e. g. a linear dependency. It was, however, found that the quadratic behavior best matches the measurement data. Furthermore, the corresponding simulations are in agreement with this model (see section 4.8.8).

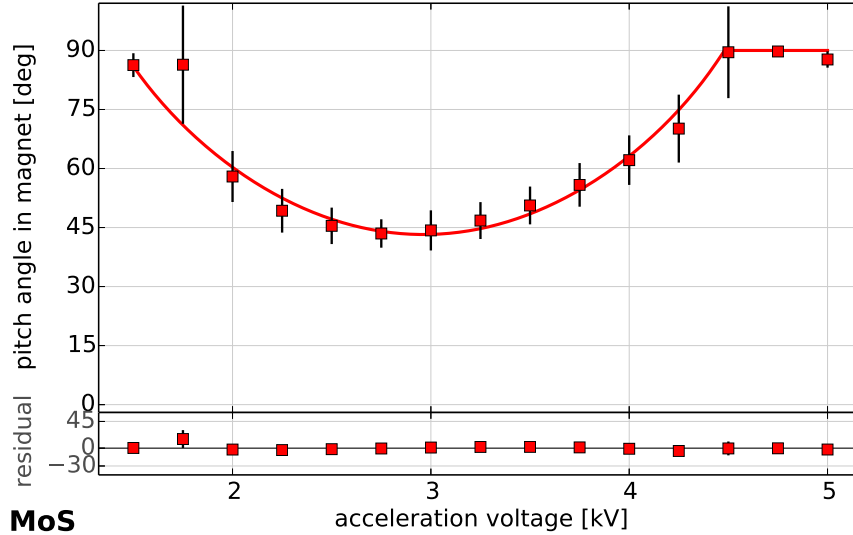


Figure 4.38.: Produced pitch angles with different acceleration voltages at the MoS setup. The plot shows the pitch angle θ in dependency of the acceleration voltage U_{acc} . Again, the plot uses data from transmission function measurements (cmp. figure 4.36). To describe the observed behavior, the model used in figure 4.37 is adapted to include a quadratic dependency on the acceleration voltage. The fit model (4.70) is in good agreement with the data. A minimal pitch angle is achieved at $U_{acc} = 2.96(5)$ kV with the used magnetic field setting. Runs: 168110–168113,168190–168203

4.5.7 Azimuthal transmission scans

The previously discussed measurements indicated that the produced pitch angle depends on the azimuthal plate tilt angle α_{az} to some extent. This was observed in both the zero-angle measurements (section 4.5.4) and the magnetic reflection measurements (section 4.5.5). To further examine the observed asymmetry, additional transmission function measurements were carried out for the four main azimuthal directions $\alpha_{az} = 0^\circ, 180^\circ, 90^\circ, 270^\circ$. As discussed earlier, the transmission function shifts to lower or higher surplus energies if the pitch angle changes. These dedicated measurements are therefore suitable to resolve the pitch angle dependency on α_{az} .

Figure 4.39 shows the four measurements at $\alpha_{az} = 0^\circ, 180^\circ, 90^\circ, 270^\circ$. To improve their sensitivity to the produced pitch angle²⁶, a plate tilt angle of $\alpha_p = 6^\circ$ was used here. The measurement was performed at enhanced magnetic field and nominal spectrometer settings.

It is clearly seen that the transmission functions do not align for different values of α_{az} , which is attributed to changes in $\theta = \theta(\alpha_{az}, \alpha_p)$ and thus confirms the pitch angle asymmetry. An asymmetry between opposite tilt directions is observed for both independent tilt axes of the electron source. Furthermore, the transmission functions that correspond to the vertical axis ($\alpha_{az} = 90^\circ, 270^\circ$) are generally shifted to larger surplus energies by roughly 0.1 eV. This indicates that the pitch angle that is produced at a given tilt angle α_p by tilting the vertical axis is larger than for the horizontal axis. This confirms the pitch angle dependency on α_{az} and is in agreement with the earlier observations.

²⁶. As discussed earlier in this chapter, the effect of small changes in θ on the transmission function is maximal at $\theta = 45^\circ$, i. e. at intermediate plate angles α_p .

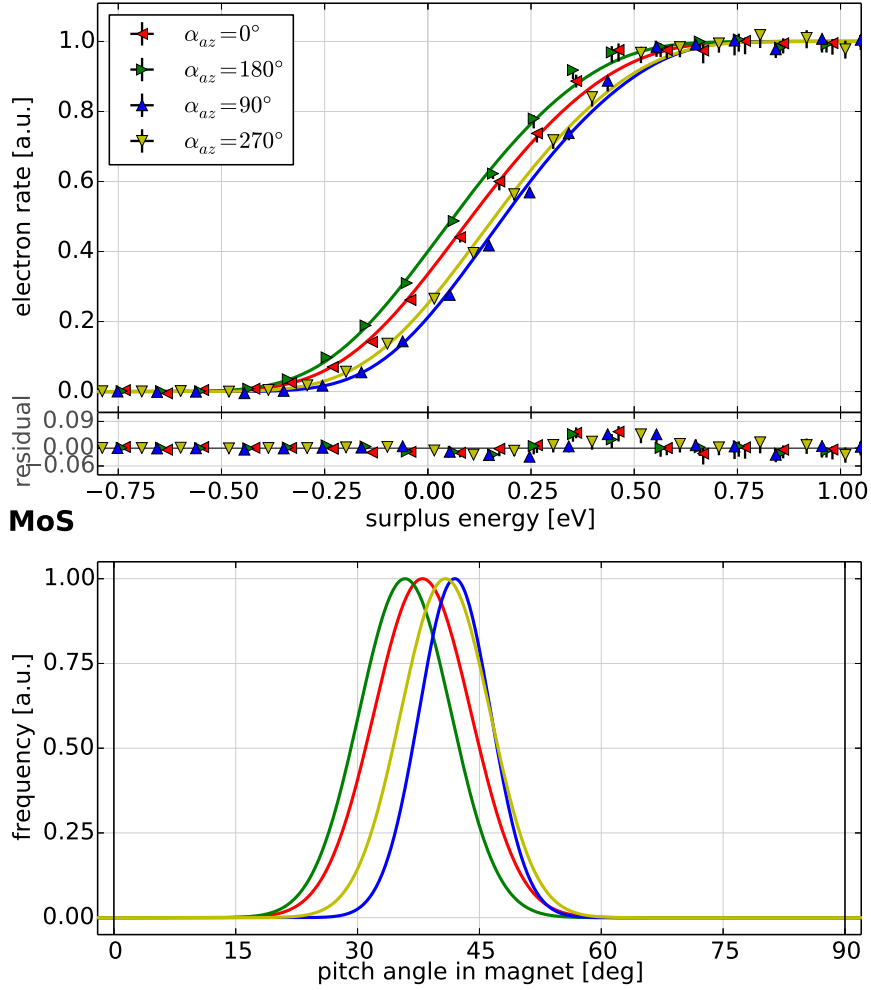


Figure 4.39.: Azimuthal-dependent transmission measurements with $\alpha_p = 6^\circ$ at the MoS setup. The plot shows transmission functions that were measured at different azimuthal directions $\alpha_{az} = 0^\circ, 180^\circ, 90^\circ, 270^\circ$ with enhanced magnetic field. The sensitivity to the produced pitch angle is improved by increasing the plate angle to $\alpha_p = 6^\circ$. The observed shift between the transmission functions is explained by small differences in the electron acceleration process that change the produced pitch angle. An asymmetry is observed between the two independent tilt axes, as well as a smaller asymmetry between opposite directions on each axis. The observed asymmetries are in agreement with magnetic reflection and zero-angle measurements. The underlying angular distributions are shown below, which clearly show that the observed asymmetry can be explained by differences in the produced pitch angle. While the mean pitch angle $\hat{\theta}$ depends on α_{az} , the angular spread σ_θ (1σ -width of the distribution) is consistent over the four measurements. Runs: 168205,168206,168207,168208

Table 4.10 lists the corresponding fit results, using the same methods that have been applied before (analytical model fit with pre-determined energy distribution). The achieved mean pitch angle $\hat{\theta}$ and angular spread σ_θ are generally consistent over all measurements, differing only by a few degrees. On average, a pitch angle of 39.31° is achieved at the given plate tilt angle of $\alpha_p = 6^\circ$ with an angular spread of $5.5(1)^\circ$. The observed asymmetry in θ between the horizontal and vertical axis is $\Delta\theta = 4.5(6)^\circ$.

Table 4.10.: Measured angular distributions for different azimuthal angles.

α_p	α_{az}	χ^2/ndf	$\hat{\theta}$	σ_θ
6°	0°	6.10	38.0(3)°	6.0(6)°
	180°	1.58	35.8(3)°	5.7(4)°
	90°	1.03	42.0(3)°	4.4(5)°
	270°	1.06	40.8(3)°	5.5(5)°
weighted average:			39.3(1)°	5.5(1)°

Azimuthal dependency of the transmission function

To further examine the observed pitch angle dependency $\theta(\alpha_{az}, \alpha_p)$, one would ideally perform a series of transmission function measurements at several azimuthal tilt angles (e. g. $\alpha_{az} = 45^\circ$) and at different values for α_p . However, the given time constraints in the MoS measurement phase did not allow to carry out such a large number of measurements²⁷. Hence, a different approach was used to investigate the pitch angle asymmetry within the available time frame. When the electron source is operated “on” the transmission function ($U_{start} \approx U_{ana}$, i. e. at roughly 50% of the nominal rate; cmp. section 4.4), the observed electron rate is sensitive to changes in θ (which is also exploited for the zero-angle measurements). By operating the electron source in this mode while varying the azimuthal tilt angle α_p , one can relate the changes in electron rate to changes in pitch angle. Since only one data point (rate measurement) is taken at each setting of (α_{az}, α_p) – instead of tens of data points for a full transmission scan – this measurement can be performed in a rather short time frame.

Figure 4.40 shows the result of such a measurement that was performed at a plate angle of $\alpha_p = 8^\circ$ and in 10° steps of α_{az} . As before, the measurement was performed at enhanced magnetic field ($B_{start} = 28$ mT) and nominal spectrometer and source settings ($U_{spec} = -18.6$ kV, $U_{acc} = 5$ kV, $U_{dip} = 2$ kV). Note that the plot uses a polar projection to get a clearer representation of the azimuthal dependency. The observed rate dependency shows a prominent “dumb-bell shape” that can be roughly described by a sinuoid function

$$\dot{N}(\alpha_{az}) = a \cdot \cos^2 \alpha_{az} + b, \quad (4.71)$$

where a and b are the signal amplitude and background. This simple model represents the clear asymmetry between the horizontal and vertical tilt axis, where the pitch angle produced at a given plate angle α_p on the vertical axis is considerably larger than on the horizontal axis²⁸. This is in agreement with the azimuthal transmission function measurements discussed above, where the same relation was found.

Although the simple sinusoid model (4.71) matches the observed asymmetry between the tilt axes, a better agreement to the measurement data can be achieved by extending the fit model to a combination of two sinusoids, and by including a tilt angle offset ϕ_0 that rotates the fit curve in azimuthal direction:

27. A single transmission measurement took roughly 15 min at the MoS setup. An azimuthal scan in 10° -degree steps would thus have taken another full day of measurement time.

28. A larger pitch angle results in a smaller observed rate since the transmission probability reduces with increasing pitch angle.

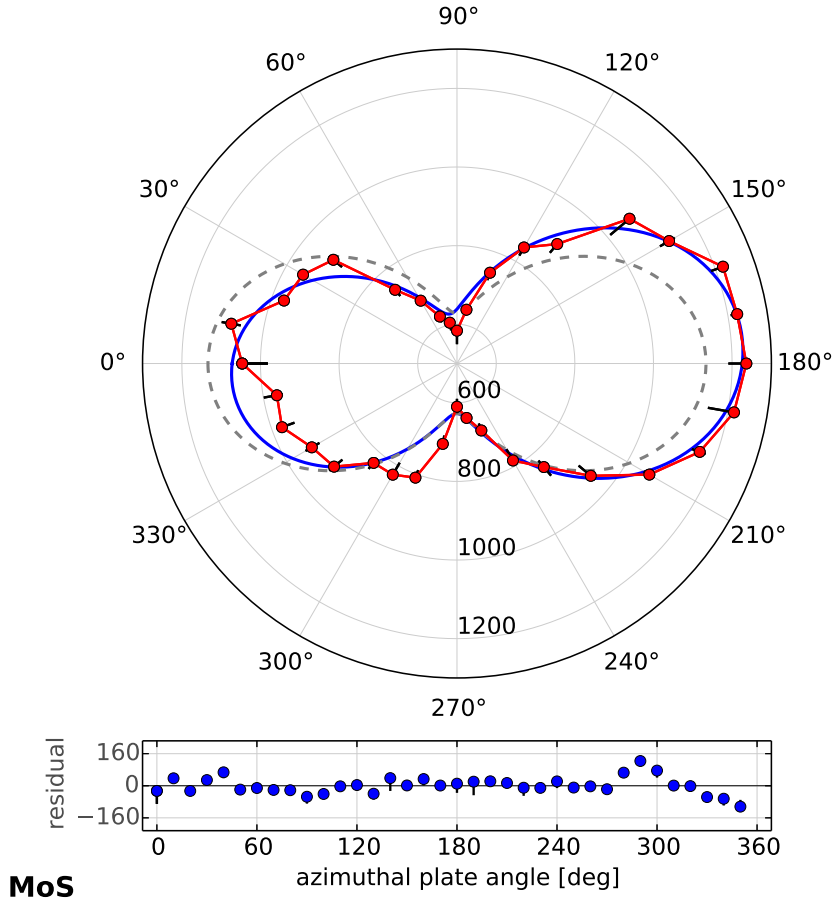


Figure 4.40. Azimuthal transmission-edge scan with $\alpha_p = 8^\circ$ at the MoS setup. The plot shows the electron rate at different azimuthal tilt angles $\alpha_{az} = 0^\circ$ to 360° . A polar coordinate system (radial axis: electron rate in cps) is used to give a better representation of the data. The azimuthal axis uses the experimental coordinate system with 0° pointing right and 90° pointing up. The measurement was performed “on” the transmission edge ($U_{start} \approx U_{ana}$) where the rate is sensitive to differences in pitch angle, and at $\alpha_p = 8^\circ$ where a pitch angle of roughly 55° is achieved. The observed “dumbbell-shape” can be described by a simple sinusoidal fit model (4.71) (dashed gray line). A better agreement to the data is achieved by an extended model (4.72) that includes asymmetries (solid blue line).

Runs: 168260–168295

$$\dot{N}(\alpha_{az}) = a_1 \cdot \cos(\alpha_{az} + \phi_0) + a_2 \cdot \cos^2(\alpha_{az} + \phi_0) + b. \quad (4.72)$$

The parameters $a_{1,2}$ are the individual signal amplitudes and b is the background. The fit result from this model is indicated by the solid blue line in figure 4.40. The improved fit yields a considerably better agreement to the observed rate variation. The corresponding fit results for the two models are given in table 4.11.

Essentially, the additional first-order sinuoid in (4.72) creates an asymmetry between opposite azimuthal directions, which reflects the higher rate that is observed for $\alpha_{az} \approx 180^\circ$. This is also in agreement with earlier measurements, where small differences in the produced pitch angles in opposite tilt directions on a given axis were observed. The tilt angle offset ϕ_0 that has been added to

the fit model reflects the fact that the observed rate dependency is not fully mirror-symmetric. This effect could be explained by phase effects that influence the electron-acceleration processes inside the source. The produced pitch angle thus depends on many factors, such as the electric and magnetic fields near the photocathode (including possible asymmetries and misalignments). Hence, one can easily imagine that the azimuthal position of the minimal (or maximal) pitch angle is not perfectly aligned with the tilt axes. Another effect that could be relevant here is the Lorentz force due to the electrons moving in a magnetic field, and $E \times B$ drifts that are caused by the combination of electric and magnetic fields in the source. Unfortunately it is extremely difficult to fully explain these observations without detailed, complex particle-tracking simulations that investigate these effects. Given the limited time available, this option was not further pursued here.

Table 4.11.: Fit results for the azimuthal transmission-edge scan.

α_p	χ^2/ndf	a_1	a_2	b	ϕ_0
8°	17.8	—	506.4(79) cps	627.2(38) cps	—
	5.53	-7.3(132) cps	516.5(80) cps	631.5(38) cps	$-4.7(5)^\circ$

4.5.8 Photocathode work function

The electron source is based on the principle of electron emission by the photo-electric effect (section 4.2). The *work function* of the photocathode is an extremely important parameter, as it controls several characteristics of the device. The energy spread of the emitted electrons is defined by the difference between work function and photon energy (wavelength of the UV light). Furthermore, simulations indicate that the angular spread of the electrons that is achieved in the spectrometer entry magnet relates to the energy spread and is thus also influenced by the work function (cmp. section 4.8.5).

At the MoS setup, a gold (Au) photocathode of 20 nm thickness was used in all electron source measurements. The expected work function for poly-crystalline gold is approximately 5.1 eV [Eas70]. This value is typically determined under laboratory conditions, where the surface is prepared and completely cleaned from impurities under ultra-high vacuum conditions just before the measurement. Earlier measurements at the WWU Münster test setup indicated that the *actual* work function of the photocathode is modified by numerous effects, such as surface impurities or electric fields; this has been discussed earlier in section 4.2.4). Under these conditions, the work function is typically decreased by more than 1 eV [Zac14, Win14, Bus14]. Independent reference measurements confirm work functions around 4.2 eV for gold surfaces that have been exposed to air [S⁺95].

To determine the actual value of the work function and fully characterize the electron source, a direct measurement is therefore required. Although it is possible to measure the work function of a surface by specialized methods such as a *Kelvin probe* measurement, these results might not be applicable to the actual setup where the conditions are different and could change over time. Hence, the ideal method to determine the work function is an *in situ* measurement where the photocathode is probed while being mounted at the MoS setup. Such a method has been conceived by R. FOWLER in 1931 [Fow31]. It is based in a measurement of the observed electron rate (more specifically, the electron yield) in dependency of the UV wavelength, as describe by the *Fowler function* (4.31). The electron source uses an optical system where multiple UV-LEDs are used in combination with a monochromator to provide UV light, which allows to vary the wavelength over a wide range $\lambda \approx 260 \text{ nm}$ to 320 nm . The

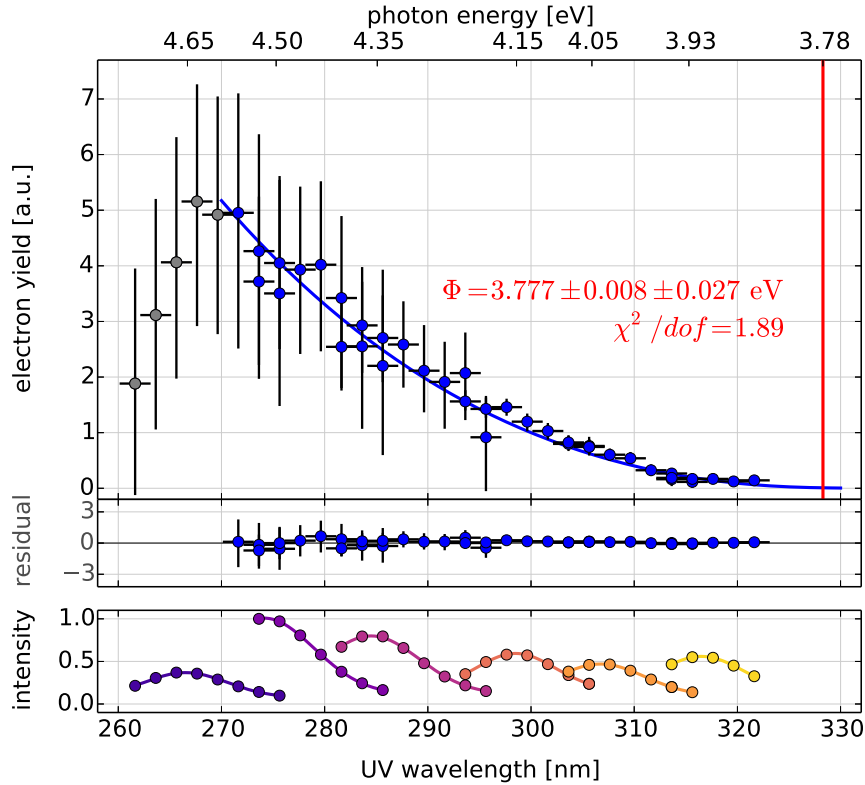


Figure 4.41.: Work function measurement at the MoS setup. A measurement of the electron yield in dependency of the UV wavelength allows to determine the *in situ* work function of the photocathode. The data is fitted with a model of the photocurrent (4.32) that was conceived by Fowler [Fow31]. At wavelengths close to the work function threshold, the data is well described by this model. The resulting work function for the gold photocathode used in this measurement is $\Phi = 3.777(8)$ eV, which is considerably lower than the expected value of 5.1 eV for a clean surface prepared under laboratory conditions. This discrepancy is explained by the dominating surface effects that reduce the observed work function. At lower wavelengths far away from the threshold, the Fowler model cannot describe the photoemission process accurately. Additional effects that become relevant at larger photon energies are not included in this model. This explains the deviation that is observed for wavelengths $\lambda < 270$ nm; this data range has been excluded from the fit. Runs: 168209–168254

work function Φ is then determined by fitting the Fowler function to the observed electron yield²⁹. The details of this “Fowler measurement” are discussed in section 4.4.

Figure 4.41 shows the result of a Fowler measurement performed at the MoS setup. All six UV-LEDs were used to cover the wavelength range $\lambda = 261.4$ nm to 321.4 nm. The wavelength at each data points was selected by a monochromator with an uncertainty (filter width) of 1.5 nm. To precisely determine the actual wavelengths used in this measurement, the monochromator was calibrated against a reference measurement of the LED emission curves (figure 4.19). This results in an offset $\Delta\lambda = -2.6(7)$ nm, which has already been included in the λ values given here. The wavelength range corresponds to photon energies of $h\nu = 4.74$ eV to 3.86 eV. A combined systematic uncertainty on the

²⁹. The electron yield corresponds to the electron rate emitted from the photocathode at a given UV light intensity. In the setup used here it is determined by normalizing the observed electron rate to the light intensity, which is monitored by a photodiode. The normalization takes into account the wavelength-dependent quantum efficiency of the photodiode and the reflectance of the beam splitter used to divert UV light to the photodiode.

wavelength of 2.2 nm, resulting from the filter width and the uncertainty of the calibration, is included in the analysis. This value is equivalent to 0.03 eV to 0.04 eV uncertainty in the photon energy.

The Fowler function fit yields a work function of

$$\Phi_{MoS,Au} = 3.777 \text{ eV} \pm 0.027 \text{ eV}(\text{sys}) \pm 0.008 \text{ eV}(\text{stat}). \quad (4.73)$$

The given statistical uncertainty results directly from the fit, the systematic uncertainty corresponds to the monochromator and the wavelength calibration. The measured work function is more than 1 eV lower than the expected value from reference measurements under ideal conditions (5.1 eV [Eas70]). This is in agreement with earlier Fowler measurements that were performed with the electron source in different setups.

The figure shows that for small wavelengths $\lambda \lesssim 270 \text{ nm}$, the Fowler model cannot describe the observed electron yield. In fact, the Fowler function (4.31) has been derived only for wavelengths close to the work function threshold, and is thus invalid for wavelengths far below the corresponding work function. The three-step model of the photoemission process developed by W.E. SPICER and C.N. BERGLUND [BS64b, BS64a] extends the description by Fowler by discriminating between effects inside the bulk material, such as scattering processes of electrons before emission, and the electron release from the surface. To explain the observed effect – a decrease in electron yield w. r. t. to the expectation by the Fowler model if the photon energy rises above a certain threshold – one could therefore argue that higher photon energies also increase the scattering probability for electrons inside the photocathode material. Even if elastic scattering processes do not change the energy of the excited electron, they could easily change its direction. Since only the longitudinal kinetic energy (in direction of the surface normal) is available to move the electron to the surface where it can be released (cmp. section 4.2.2), such scattering processes could likely reduce the electron yield sufficiently to explain the observed effect.

Energy distribution

It is possible to compare the measured work function value with the energy distributions that were determined from transmission function measurements (see section 4.5.6 above). The maximal kinetic energy of the emitted electrons is given by the difference between photon energy $h\nu$ and the work function Φ (with $\nu = c/\lambda$). Because of the finite energy distribution of the electrons (which is related to the band structure of the photocathode material), electrons can be emitted with smaller energies as well. The observed electron energy E_e is then given by

$$0 \text{ eV} < E_e \leq E_{max} = h\nu - \Phi^\dagger. \quad (4.74)$$

This relation gives rise to the *effective energy spread* E_{max} that has been defined in section 4.5.6). If the photon energy $h\nu$ is known, the observed energy spread can therefore be used to determine the work function. Hence, this approach creates an alternative method to the Fowler measurement. To avoid confusion with the work function Φ that is determined by the Fowler measurement, the work function determined by the alternative method is written as Φ^\dagger here. Under ideal conditions, both methods are expected to yield the same value, i. e. $\Phi \equiv \Phi^\dagger$.

Table 4.12 shows the resulting work functions Φ^\dagger that were determined by (4.74) from the transmission function measurements at different wavelengths λ . The results are compared to the Fowler-based work function Φ . As expected, both methods generally yield comparable work functions with an absolute difference $|\Phi - \Phi^\dagger| \leq 0.05 \text{ eV}$. There is some indication for a systematic shift towards smaller

values of Φ^\dagger for larger wavelengths, which is possibly due to unaccounted systematic effects in the analysis of the energy distribution from which E_{max} is determined. However, within the given uncertainties all results are consistent. A further investigation would require to reduce the statistical uncertainty of the results (i. e. to extend the measurement time) as well as the systematic uncertainty (i. e. to improve the accuracy of the used wavelengths) to yield more accurate results.

The weighted average of the work function is

$$\overline{\Phi^\dagger}_{MoS,Au} = 3.810 \text{ eV} \pm 0.02 \text{ eV(sys)} \pm 0.001 \text{ eV(stat)} \quad (4.75)$$

over the measurement series with different wavelengths, which is in full agreement with the result of the Fowler measurement. The given systematic uncertainties result from the analytical transmission model (see section 4.9).

It has thus been verified that an *in situ* work function is possible either by performing a Fowler-type measurement at varying wavelength, or by examining the energy distribution of the emitted electrons in a transmission function measurement at one or more selected wavelength(s). The latter approach could be especially useful if the available measurement time is limited, since the energy distribution is typically measured in combination with regular transmission function measurement that investigate the transmission properties of the MAC-E filter. With this method, no extra measurement time is required to determine the work function. The Fowler measurement, on the other hand, requires a dedicated measurement series. Especially for large wavelengths close to the threshold, where the achieved electron yield (and thus, the electron rate) is extremely small, long measurement times are necessary to achieve sufficient statistics. An advantage of the Fowler method is that it likely produced more reliable results, as the analysis does not rely on modeling the energy distribution to determine the maximal electron energy.

For future commissioning measurements at the KATRIN experiment, it is strongly suggested to consider the possibility of regular work function measurements with the alternative method that was discussed here. It can be easily combined with Fowler measurements that are performed at longer intervals, so that the possible time-dependency of the work function can be investigated accurately.

Table 4.12.: Comparison of the determined work functions for a gold photocathode.

λ	$E_\gamma = h\nu$	χ^2/ndf	E_{max}	$\Phi^\dagger = E_{max} - h\nu$	$\Delta\Phi = \Phi^\dagger - \Phi$
266.0(10) nm	4.66(2) eV	1.39	0.82(2) eV	3.84(4) eV	0.05(7) eV
		1.40	0.82(2) eV	3.84(4) eV	0.05(7) eV
272.4(22) nm	4.55(4) eV	1.18	0.74(1) eV	3.81(5) eV	0.02(8) eV
282.4(22) nm	4.39(4) eV	1.23	0.61(2) eV	3.79(5) eV	0.00(8) eV
292.4(22) nm	4.24(3) eV	3.38	0.47(2) eV	3.77(5) eV	-0.02(8) eV
302.4(22) nm	4.10(3) eV	3.46	0.33(2) eV	3.77(5) eV	-0.02(8) eV
weighted average:				3.810(1) eV	0.03(3) eV

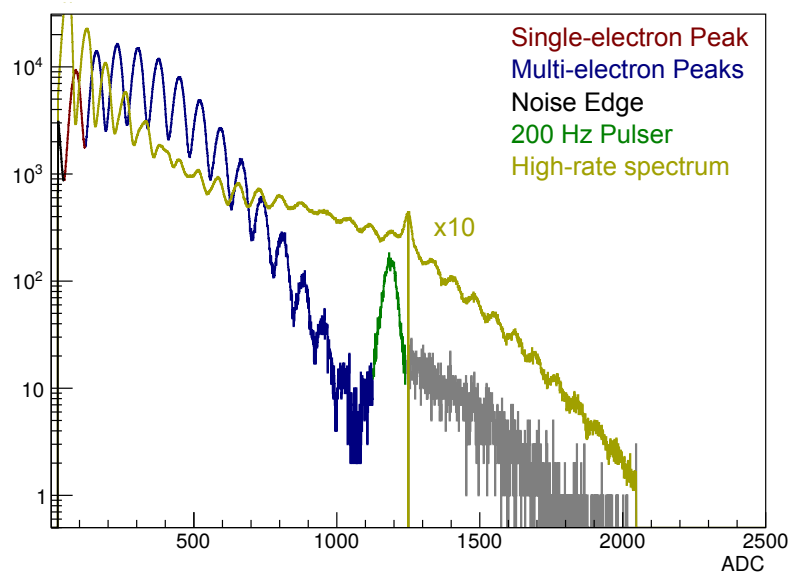


Figure 4.42.: Typical energy spectrum in high-rate measurements at the MoS setup. The energy spectrum contains a single-electron peak next to the noise edge of the detector, which is followed by several multi-electron peaks at increasing multiplicities $k = 2, 3, \dots$. The artificial signal of the livetime pulser is located near ADC channel #1200. Large electron rates increase the observed multiplicities, as multiple coincident electrons arrive at the detector in a single event due to its finite time resolution. At extremely high rates, the multi-electron peaks dominate the energy spectrum, and the spectrum is influenced by additional effects like a shifting detector baseline. This makes “classic” rate analysis (summing up the areas of each electron peak) increasingly difficult. Note that the shown high-rate spectrum is scaled down by a factor of 10 for easier comparison.

4.5.9 Maximal electron rate

Depending on the light intensity that is achieved by the optical system, the electron source typically produces electron rates around 5 kcps. The optical system allows to vary the rate in a large range (typically 0.1 kcps to 10 kcps). When using UV-LEDs, rates in the kcps range can only be achieved by increasing the pulse width to $\mathcal{O}(1 \text{ us})$. The achieved rates provide a good compromise between sufficient statistics and short measurement times, as well as good signal-to-noise ratio and low pile-up of events at the detector. For some dedicated measurements, however, it is useful to increase the achieved electron rate beyond these typical limits³⁰

The test measurements at the MoS setup provided a great opportunity to investigate the maximal electron rate that can be achieved with the electron source. To increase the produced electron rate, the optical system was tuned to maximal light intensity by adjusting the internal attenuator (polarizing filter) of the laser; the 1% ND-filter in the optical beam line was kept to avoid readjustments of the lens system. The laser was also switched to maximal output power at a diode current of 8 A and 40 kHz pulse frequency. The light intensity increases nearly linearly with the diode current and increases exponentially towards shorter pulse lengths [Win14]. For this measurement, the electron source was

³⁰. A planned SDS-2 measurement was to use the electron source as a high-rate source to simulate the effects induced by electrons from tritium β -decay. The WGTS will emit up to 10^{11} electrons per second into the main spectrometer (without pre-spectrometer), which could result in an increased background rate.

operated in full transmission ($qU \approx 10$ eV) and at zero-angle ($\alpha_p = 0^\circ$), so that all emitted electrons reach the detector.

A disadvantage of these high electron rates is the extreme pile-up at the detector system. The pile-up is caused by multiple electrons arriving at the detector in the same time frame, so that single events cannot be distinguished. Multi-electron peaks appear in the energy spectrum, according to the total deposited energy that scales with the number of coincident electrons. A typical energy spectrum that is observed at high electron rates is shown in figure 4.42, where several multi-electron peaks can be seen. At even higher rates, the multi-electron peaks begin to dominate the energy spectrum, as also indicated in the figure. The pile-up makes it more difficult to accurately determine the achieved electron rate. In regular measurements, the rate is determined by summing up the events in the individual electron peaks, taking into account their respective multiplicity ($k = 1, 2, \dots$). At high rates, however, this method fails since the spectrum is severely deformed due to the response of the detector system, which results e. g. in a shifted baseline. Hence, a description of the spectrum by individual electron peaks becomes increasingly inaccurate.

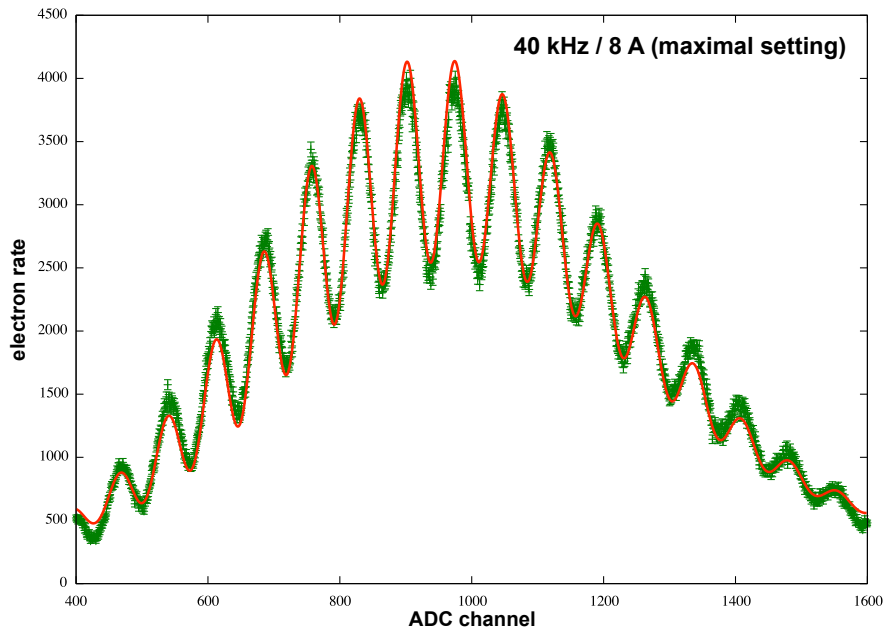


Figure 4.43.: Poisson fit model for high-rate measurements. The electron energy spectrum that is shown here is dominated by multi-electron peaks with high multiplicities, which makes it difficult to accurately determine the total electron rate. An alternative analysis method that is based on a Poisson distribution of the individual electron peaks allows to determine the average electron multiplicity n , which yields accurate rate estimations even in extreme cases like it is shown here. The plot shows the ADC spectrum and the Poisson-based fit (4.76) for the laser setting that achieves the maximal electron rate (40 kHz/8 A). The fit yields an average multiplicity $n = 13.2$, resulting in a total electron rate of $\dot{N} = n \cdot f_{las} = 528$ keps. Note that this plot does not show the entire ADC spectrum (channels numbers 0 to 2500) to give a clearer representation of the fitted data. Runs: 168638

To overcome these issues, an alternative approach has been implemented that allows to determine a correct electron rate even if the detector suffers from large pile-up [Beh14, BW14]. The analysis assumes a Poisson distribution of multi-electron peaks, where the distance between peaks is given by the electron energy and multiplicity ($E_k = E_1 \cdot k$ with $E_1 = E = qU_{start}$). The individual peaks are

described by Gaussian distributions that are superimposed on the Poisson distribution. The observed energy spectrum is then described by a function

$$\frac{d\dot{N}}{dE}(\epsilon) = \sum_{k=1}^N P_n(k) \cdot f(\epsilon, k, E_1, a_k, \mu_k, \sigma_k) + b, \quad (4.76)$$

$$P_n(k) = \frac{n^k}{k!} \cdot e^{-n}, \quad (4.77)$$

$$f(\epsilon, k, E_1, a, \mu, \sigma) = \frac{a}{\sqrt{2\pi}\sigma} \cdot \exp\left(-\frac{[\epsilon - (\mu + kE_1)]^2}{2\sigma^2}\right). \quad (4.78)$$

The global parameters here are the expectation value of the Poisson distribution n , the position of the first (single-)electron peak E_1 , and the background b ; ϵ corresponds to the energy bins in the spectrum. The number of peaks N must be determined from the observed energy spectrum beforehand. Each Gaussian distribution for a peak at multiplicity k has individual parameters, namely the amplitude a , the peak position μ and the width σ . The total number of free parameters in this fit is therefore $n_{par} = 3N + 3$.

The expectation value n can be viewed as the average number of electrons that is emitted in a single laser pulse at the electron source, and thus corresponds to the *average multiplicity* of the released electrons. Since the laser pulse frequency f_{las} is known as an operational parameter, the achieved electron rate is then simply computed as

$$\dot{N} = n \cdot f_{las}. \quad (4.79)$$

An example of such a Poisson-based fit is shown in figure 4.43. The fit yields a multiplicity of $n = 13.2$ at maximal laser intensity (pulse frequency 40 kHz and diode current of 8 A). This results in a total electron rate of $\dot{N}_{max} = 13.2$ according to (4.79). The analysis here uses the ADC spectrum with channel numbers $x = [0; 2500)$ instead of the energy bins (so that no energy calibration is required). This is completely equivalent to the energy spectrum, as the actual energy of the observed electrons is irrelevant to the fit method.

Figure 4.44 shows the electron rates that were achieved at different laser settings at the electron source. The rates are compared between the “classic” approach where the electron peaks are summed up, and the alternative “Poisson” method. As expected, both methods yield comparable results at low rates. At higher rates, however, the issues with the classic method become apparent and the deviation between the results is clearly visible. At pulse frequencies $f \leq 60$ kHz, the rates determined by the classic method is above the results from the Poisson method because the detector dead-time is wrongly estimated due to the large pile-up. Because the Poisson method does not rely on the area of the individual electron peaks to determine the rate, the electron rate can be determined more accurately even if extreme pile-up is observed. The method is therefore less influenced by side effects like baseline shifts and produces consistent results at higher rates.

The highest rate that was achieved in this measurement series is $5.28 \cdot 10^5$ cps at maximal output power of the laser (8 A, 40 kHz), according the Poisson-based analysis. This corresponds to 13.2 electrons being emitted per laser pulse. The rate could be further increased by removing the ND filter from the optical beam line, thereby reaching $5 \cdot 10^7$ cps (100-fold increase). Although this is still considerably lower than the 10^{11} cps emitted from the WGTs, a high-rate measurement with the electron source at the main spectrometer would allow first investigations of possible negative side effects from high electron rates.

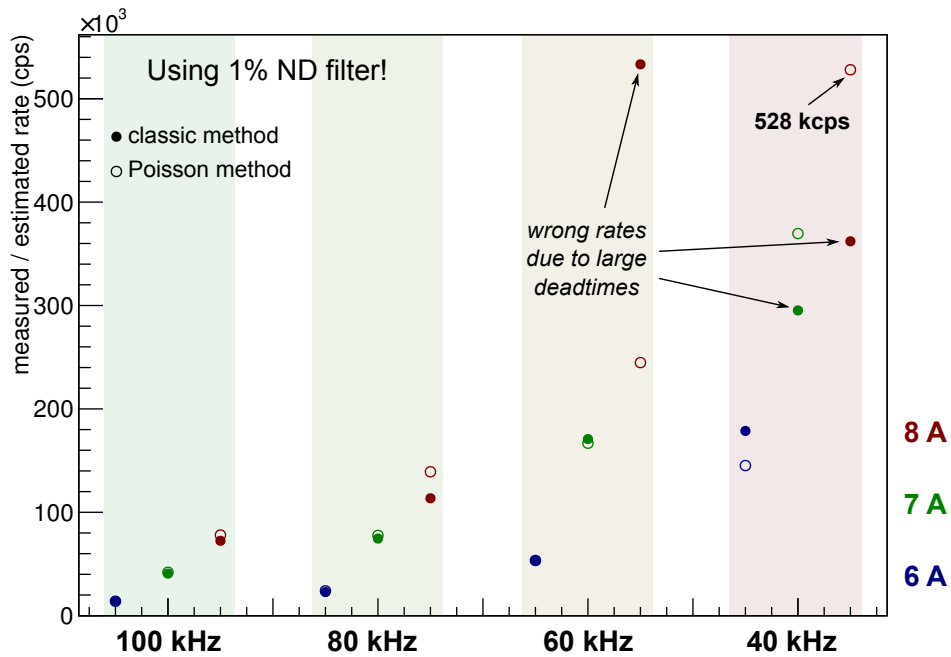


Figure 4.44. High-rate measurement at the MoS setup. The plot shows the electron rates that were determined for different laser settings, using the “classic” method where the energy spectrum is examined directly and the “Poisson” method that uses a fit model (4.76) to determine the electron multiplicity. The observed rate depends on the laser setting, since the UV light intensity increases with higher diode currents and lower pulse frequencies. At extremely high electron rates, the classic approach fails to estimate the observed rate accurately (filled circles). This is prominently seen at the 8 A setting, where the estimated rate at 40 kHz is lower than at 60 kHz despite the higher light intensity. In contrast, the alternative method yields consistent results over the different laser settings, and is therefore believed to be more accurate. The maximal electron rate that is achieved at the highest laser setting is 528 kcps. By removing the 1% ND-filter from the optical beamline, one could further increase this value by a factor of 100.

Runs: 168628–168638

4.5.10 Summary

Before moving on to the SDS-2 commissioning measurements, the results from the test phase at the MoS setup will be summarized shortly. The dedicated measurement phase with roughly 1 month of time available for functionality tests and first source commissioning measurements was deemed necessary after the issues that were encountered during SDS-1 (see section 4.8.12 for quick summary). Although the electron source has been shown to work as expected in the laboratory setup at WWU Münster, some features could not be reproduced after installation at the main spectrometer. The MoS setup now provided an opportunity to verify the functionality of the source in a MAC-E filter setup with conditions similar to the main spectrometer.

The measurements proved to be extremely beneficial for the following SDS-2 commissioning phase, as many important characteristics like the produced energy and angular spread, magnetic reflection at the spectrometer magnet, and angular selectivity as a key feature could be investigated. Furthermore, many measurement and analysis procedures were further developed during the MoS phase, such as the determination of the zero-angle offset and the dipole efficiency, or the investigation of magnetic reflection under different conditions. The analysis of transmission functions were based on a simple error-function model during the measurement phase; the analytical model utilized in this thesis was implemented at a later stage during SDS-2.

The MoS setup also featured many components that were used directly or with minor modifications for the SDS-2 phase. One example is the HV setup with multiple power supplies that allows to control the surplus energy of the produced electrons with high precision. The improved tilt actuation of the electron source with pressured-air linear motors is a design that was developed and tested at WWU Münster during the preparations for SDS-1 [Bus14], and was now used at a MAC-E filter for the first time. The optical system was improved to allow measurements with variable wavelengths using an UV-LED revolver setup [Pot13]. The LabView-based slow-control software was still under development at this stage, but had many important features available for testing, e. g. the motor control for plate actuation or an interface to the optical system [Jos13].

4.6 Measurements at the main spectrometer

One major goal of the SDS-2 commissioning measurements was to determine the transmission properties of the main spectrometer and to study the inhomogeneity of the retarding potential and the magnetic field over the analyzing plane [Erh16]. These measurements could not be performed completely in the SDS-1 commissioning phase that was carried out earlier due to multiple technical issues [Zac14, Gro15].

The improved design of the electron source allowed to determine these crucial parameters in the SDS-2 phase. The device has been verified to work in various test measurements at the monitor spectrometer (section 4.5). The test setup allowed to characterize many important source parameters, such as the achieved energy and angular spread or the work function of the photocathode. Many measurement and analysis techniques that were developed during the test measurements were extremely valuable to perform and analyze the SDS-2 measurements. The analytical model of the transmission function (section 4.1.1), which is used in this thesis to describe the observed transmission functions, was further developed during the analysis of SDS-2 measurement data.

Before determining the main spectrometer's transmission properties, it was first necessary to perform a commissioning of the electron source at the SDS-2 setup. Often it is possible to compare the results to measurements performed at the MoS setup, e. g. in case of the photocathode work function (see section 4.6.6 below).

4.6.1 Experimental setup

The main spectrometer is a MAC-E filter with an expected energy resolution of 0.93 eV under nominal conditions. In contrast to the monitor spectrometer, it features an asymmetric magnetic field setup where the entry magnet is operated at a lower magnetic field than the pinch magnet at the exit. In the SDS-2 commissioning phase, the magnetic fields were set up as $B_{max} = 5.1$ T at the pinch magnet, $B_{PS2} = 4.5$ T at the entry magnet, and $B_{min} = 0.38$ mT in the analyzing plane of the spectrometer. This results in an energy resolution of $\Delta E_{SDS2} = 1.22$ eV, considering the cut-off angle of $\theta_{max} = 70^\circ$ due to magnetic reflection at the pinch magnet. In some dedicated measurements at low spectrometer voltage ($U_{spec} = -200$ V), the minimal magnetic field was increased to $B_{min}^+ = 0.9$ mT in the analyzing plane. This special setting is indicated when these particular measurements are discussed.

In contrast to the monitor spectrometer, the SDS-2 setup also allowed measurements at low electron energies well below 10 keV due to the post-acceleration electrode that is installed in front of the FPD system. This is an important feature for the electron source commissioning, since it allows to accurately determine the energy distribution of the produced electrons without any influence by the angular distribution (cmp. section 4.5.6). For this purpose, the retarding potential (and accordingly, the starting voltage at the source) was reduced to $U_{spec}^- = -200$ V instead of the nominal $U_{spec} = -18.6$ kV.

In the SDS-2 setup, the magnetic field at the electron emission spot (the photocathode) is combination of the magnetic field of the PS1 magnet (upstream side of the source) and the PS2 magnet (spectrometer entry magnet, downstream side between source and spectrometer). The PS2 magnet is required to provide the magnetic guiding field in the spectrometer. The PS1 magnet is used to contract the magnetic flux tube at the electron source³¹ so that the movable source covers the complete

31. Later during neutrino mass measurements, the PS1 and PS2 magnets create the guiding field in the pre-spectrometer.

magnetic flux tube. With the PS1 magnet operated at $B_{PS1} = 3.0\text{ T}$, the magnetic field at the photocathode is $B_{start} = 29\text{ mT}$. This value is comparable to the conditions of the monitor spectrometer, where $B_{start} = 28\text{ mT}$ at enhanced magnetic field (cmp. section 4.5.1). Hence, it is expected that the electron source achieves a similar angular spread as at the MoS setup.

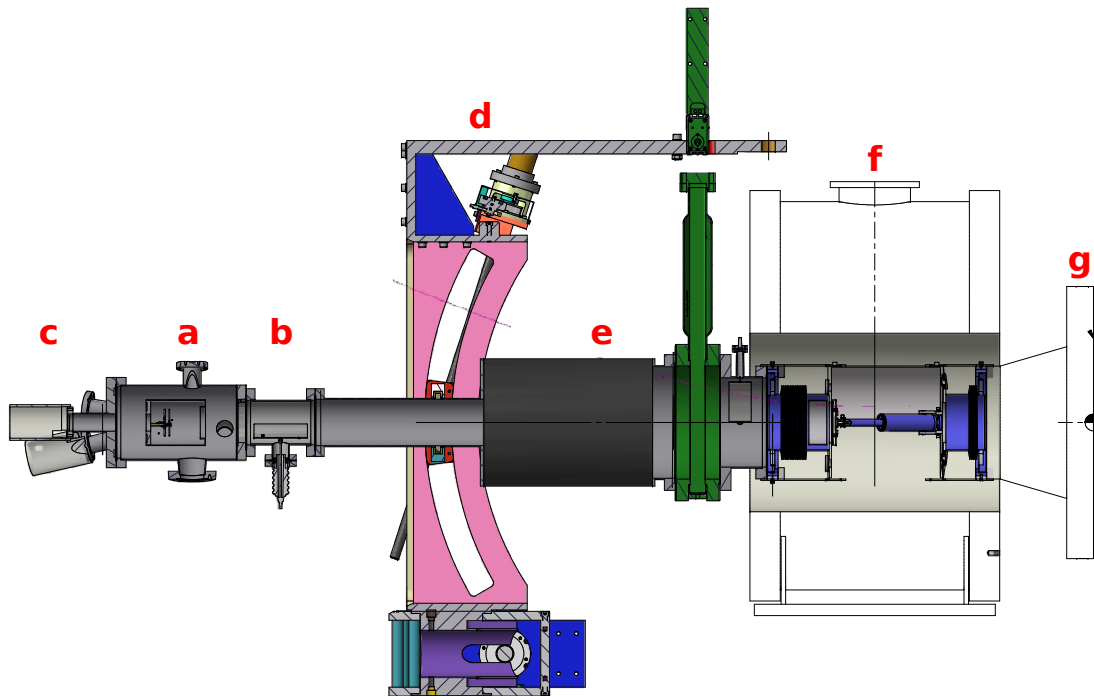


Figure 4.45.: Electron source setup with manipulator at the main spectrometer (SDS-2). The electron source is mounted in a vacuum chamber (a) that connects to a dipole chamber (b) and the beam tube towards the spectrometer (g). The connections for high voltage, UV light and mechanical actuation of the source (c) are located on the vacuum flange. The overall setup is similar to the MoS setup, but here the source chamber including all its components can be moved in two dimensions by the UHV manipulator (d) to position the source anywhere in the magnetic flux tube. A bellow (e) connects the movable beamline to the spectrometer entry magnet (f).

The electron source is mounted on a UHV manipulator in order to perform measurements at variable positions w. r. t. the complete magnetic flux tube (figure 4.45). This is required to investigate the inhomogeneity of the transmission function over the analyzing plane and allows to determine the transmission properties for each detector pixel. The manipulator tilts the complete electron source (vacuum chamber and beam tube) to polar angles up to 20° . This range is sufficient to cover the complete flux tube due to the contraction of the magnetic flux tube by the PS1 magnet. The electric field inside the source are not affected by this movement. The electron acceleration processes in the source therefore do not depend on the manipulator tilt angle. However, the magnetic field at the photocathode change due to its radial gradient at the emission spot. Measurements and simulations show that the magnetic field drops from roughly 29 mT at the central manipulator position (“on-axis”) to 25 mT at maximal manipulator angle. The magnetic field measurements and the procedures that were performed to align the electron source with the experimental setup are discussed in section 4.8.1.

The high-voltage system of the electron source uses the same setup as in the MoS measurements (see figure 4.25). The starting voltage U_{start} is defined relative to the spectrometer voltage U_{spec} to avoid

fluctuations of the electron surplus energy. The voltage difference is monitored by a DVM that is placed inside the HV cage; this value corresponds to the surplus energy of the produced electrons $q\Delta U = U_{start} - U_{spec}$. Due to the potential depression in the main spectrometer and other effects, the retarding potential in the analyzing plane U_{ana} is typically more positive than the spectrometer potential, $U_{ana} \gtrsim U_{spec}$ (cmp. section 2.2.4). This results in a measurable shift of the transmission function towards higher surplus energies. The transmission function measurements with the electron source allow to investigate this difference in detail, and the corresponding measurements are discussed in section 4.6.5. Like at the MoS setup, the dipole electrode in front of the electron source is controlled by an independent power supply, which is integrated with the slow-control system of the electron source. Investigations of the dipole efficiency show that a dipole voltage $U_{dip} = 3$ kV is sufficient to remove any stored electrons. This measurement used the same approach as in the MoS measurement phase (section 4.5.3) and is not further discussed here.

The slow-control system of the electron source was further developed after the end of the MoS measurements, and has been integrated with the existing system at the main spectrometer that also control other sub-systems. All relevant operational parameters – high voltage, manipulator and plate angles, UV light sources etc. – can be controlled by ORCA scripts, which allows fully automated measurements that run overnight. Although not all measurements could be performed as planned due to multiple hardware- and software-related issues (see section 4.6.7), the SDS-2 measurements allowed a detailed characterization of the electron source. The source was used in many related measurements, such as determining the main spectrometer transmission properties [Erh16], verifying of the integrity of the inner-electrode system [Bar16] or investigating trapped particles between electron source and analyzing plane of the spectrometer [Wie16]. Furthermore, the source was used to study active background reduction methods (section 5) or time-focusing time-of-flight methods [Ful16].

4.6.2 Rate stability

The stability of the electron rate is an important parameter for every measurement that is performed with the electron source. A typical transmission run takes around 15 min in total, with 10 s per data point during which the starting voltage at the electron source is constant. Any rate instability within this time frame could negatively affect the measurement result. The electron rate is mainly defined by the intensity of the incident UV light (at higher intensity, more photons are available to induce photoemission) and the difference between UV wavelength and work function of the photocathode (a larger difference increases the electron yield, cmp. section 4.2.2). Both parameters are subject to change over time, e. g. due to intensity fluctuations from warm-up effects or due to a slow drift of the work function caused by changing conditions at the photocathode surface. Here it is important to distinguish between random rate fluctuations and long-term rate drifts. The optical system of the electron source allows to monitor the light intensity with a photodiode; however, this approach cannot be used to observe changes of the work function or of components outside the optical system (e. g. the vacuum feed-throughs for the optical fiber). It is therefore useful to perform stability measurements, where the produced electron rate is monitored over an extended time frame and its fluctuations and possible drifts can be examined.

Figure 4.46 shows a stability run at nominal SDS-2 settings (laser at 266 nm, 100 kHz, 6 A). The electron source was operated in full transmission ($q\Delta U \approx 10$ eV) to ensure that all electrons reach the detector. The electron rate is monitored in 10 s intervals in the analysis and shows typical Poisson fluctuations. By averaging the observed rate over a longer time frame of 3 min, these fluctuations can

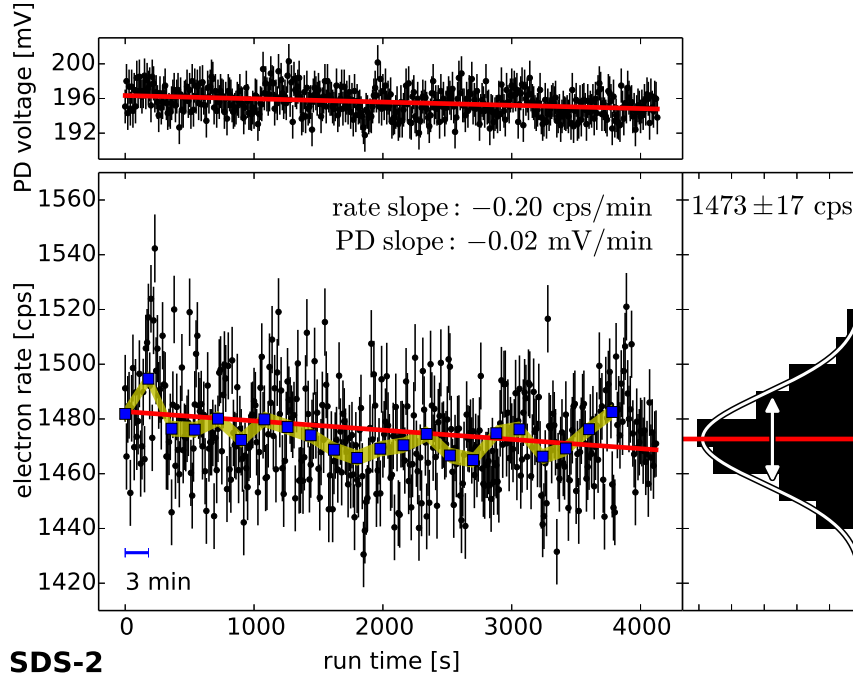


Figure 4.46.: Electron rate and photodiode stability at the SDS-2 setup. The plot shows a stability measurement at nominal SDS-2 settings with the laser at 100 kHz/6 A. The source was operating in full transmission (surplus energy $q\Delta U \approx 10$ eV). The observed electron rate is monitored in 10 s intervals (black points). As expected, the rate projection histogram (right side) follows a normal distribution. The average rate over the complete 70 min run is 1473(17) cps, as determined from the median and 1σ -width of the histogram. A small rate drift of -0.20 cps/min (-138 ppm/min) is observed (red line: linear fit result). One can reduce the statistical uncertainty by increasing the bin size e. g. to 3 min (blue squares with yellow uncertainty band), yielding an average rate of 1474(7) cps. The photodiode signal that corresponds to the UV light intensity is shown at the top (in 10 s bins). The long-term intensity drift of -115 ppm/min is comparable to the rate drift and the likely cause for the observed decrease over time. The short-term intensity fluctuations do not seem to be correlated with rate fluctuations (see figure 4.47). Runs: 22450

be significantly reduced³². The histogram on the right side of the figure shows the *rate projection*, i. e. the distribution of the 10 s data points over the complete measurement. As expected, it resembles a normal distribution where the majority of data points is close to the mean value. A statistical uncertainty can be determined from the 1σ -width of the distribution. This yields an average electron rate of $\bar{N} = 1473(17)$ cps. The observed width is in agreement with the expectation from Poisson statistics,

$$\Delta\bar{N} = \frac{\sqrt{\bar{N} \cdot t}}{t} = \sqrt{\frac{\bar{N}}{t}} = \sqrt{\frac{1473 \text{ cps}}{10 \text{ s}}} = 12 \text{ cps}. \quad (4.80)$$

By increasing the sampling time to 3 min, the stability can be improved since the fluctuations average out over the extended time frame. By doing so, an average electron rate of $\bar{N}_{3min} = 1474(7)$ cps is achieved. The uncertainty of 7 cps is now larger than expected from Poisson statistics, which yields

32. This is important for long-term measurements where data points are taken at longer intervals than in a typical transmission run.

$\Delta\dot{N}_{3min} = 3$ cps. This observation can be explained by intensity fluctuations that become more relevant on this timescale of several minutes, so that the observed rate fluctuation is an effect of both Poisson rate fluctuations and random intensity fluctuations. This can be seen by comparing the blue/yellow curve in the figure with the photodiode signal at the top, which shows similar relative deviations to the long-term drift (red lines) and therefore indicates some correlation between the two parameters rate and intensity.

The observed rate drift can be described by a linear rate decrease. Fitting a linear model to the data points yields a decrease of 0.20(1) cps/min (or 11.5 cps/h) for the measurement run, which corresponds to a relative drift of 138 ppm/min. The electron rate is stable on a sub-percent level over a typical run length of 15 min.

Influence of fluctuations in light intensity

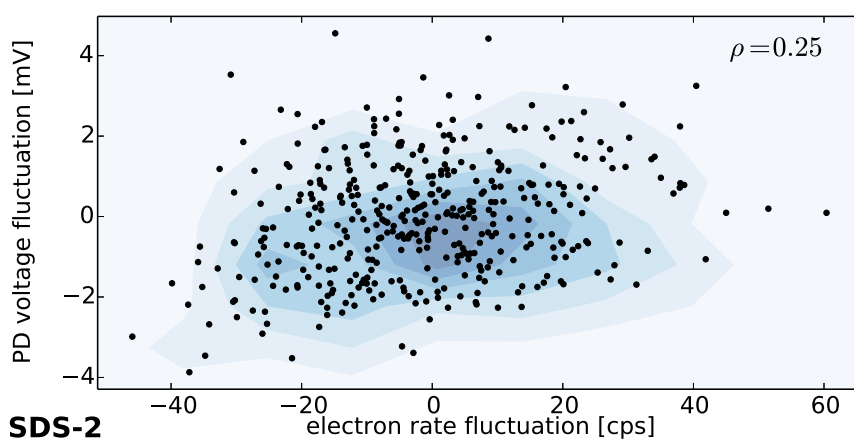


Figure 4.47.: Correlation between electron rate and photodiode voltage at the SDS-2 setup. The plot shows the correlation between the electron rate and the monitored light intensity (photodiode signal), both in 10 s bins. The data points correspond to the observed fluctuations, i. e. the difference between the measured values and the linear drift that was determined from a fit (cmp. figure 4.46). The long-term drift is therefore excluded from this plot. Contour lines are added to visualize the density of the data points. Although the electron rate depends on the light intensity (since the UV light is responsible for the photoemission of electrons), the observed short-term fluctuations are clearly uncorrelated ($\rho = 0.25$). This indicates that the photodiode signal is dominated by noise that overshadows the actual (smaller) intensity fluctuations. Runs: 22450

It is now interesting to see if the rate decrease is related to changes in UV light intensity. The photodiode signal, shown at the top of the figure³³, shows a drift of $-0.023(4)$ mV/min or 115 ppm/min. This is consistent with the observed rate drift. One can therefore argue that the rate decrease is correlated to a reduction in light intensity, which can be explained by warm-up effects of the laser system. Long-term effects such as work function changes are expected to operate on longer timescales, and are therefore not observed in this measurement (see below for an investigation of these long-term effects).

The intensity fluctuations that are observed in the photodiode signal do not seem to be correlated with the rate fluctuations, so that the 1% stability level that was determined for 10 s bins cannot be improved by monitoring the intensity. Figure 4.47 shows a correlation plot between the two

³³. The photodiode current is converted to a voltage signal by a FEMTO amplifier that is part of the optical system.

parameters (intensity and rate). Contour lines were added to give a better visual representation of the point density. Note that the linear drift has been excluded in this plot by subtracting the linear rate/intensity decrease from the data points, so that only the short-term fluctuations are considered. The plot shows that the data points are essentially random distributed, which indicates that there is indeed no strong correlation between the intensity and rate fluctuations. A possible explanation is the rather high noise level of the photodiode and the signal amplifier, which creates additional fluctuations that are independent of the light intensity.

It would be easily possible to normalize the observed electron rate to the photodiode signal, which would make the rate independent of rate drifts caused by a slowly changing light intensity (e. g. warm-up effects). However, this would also increase the statistical uncertainties (since two observables are combined) and actually results in larger fluctuations of the normalized rate (since rate fluctuations are uncorrelated to intensity fluctuations, as discussed above). Since the electron rate is stable on a sufficient level with negligible drifts over typical run lengths of less than one hour, no further corrections have been applied in the analysis of measurement data. The only exception are the direct work function measurements after the Fowler method (section 4.6.6), where such a normalization is required to determine the electron yield.

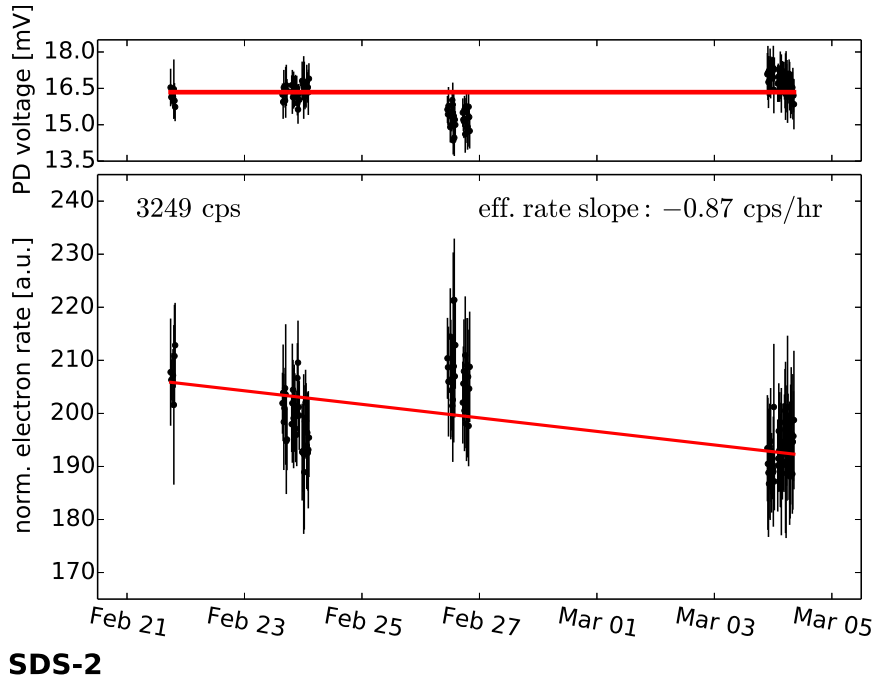
Long-term stability

In addition to the short-term rate stability (on a scale of minutes to hours), one can also investigate the long-term stability (over a scale of several days). During the SDS-2 measurements, no dedicated long-term stability runs were performed due to the limited time available to complete the measurement schedule. However, it is possible to use the available data from transmission measurements instead. A typical transmission run starts at low surplus energy (no transmission) and proceeds into full transmission. Hence, at the end of one such run the nominal electron rate is observed at the detector. This information can therefore be used to investigate the rate stability over multiple runs, if only the last few data points of each run are considered.

Figure 4.48 shows the long-term stability of a total of 67 transmission runs that were carried out over several days. During these runs, the electron source was moved around the flux tube with the UHV manipulator to investigate the transmission properties of the spectrometer. However, since this does not affect the electron rate if the source is operated in full transmission, this run series matches the criteria for an investigation of the long-term rate. Each data point in the figure corresponds to the average rate of the last 60 s of a single transmission run, where the electron rate does not depend on the spectrometer characteristics and the nominal rate is observed.

The photodiode signal, shown at the top of the figure, is rather stable at 16.34(2) mV over the complete time frame. Some systematic shifts are visible between individual measurement series (i. e. different days), which is likely caused by warm-up effects³⁴. To investigate the rate drift without influence from changes in light intensity, the figure shows the normalized electron rate (observed electron rate divided by the photodiode voltage). Since in this case the investigated time frames are much longer than in the measurements discussed earlier in this section, it is believed that short-term intensity fluctuations average out and do not influence the observed electron rate significantly.

³⁴. Depending on the measurement schedule, the laser was not always in operation for an extended time period before starting the transmission measurements. It is thus difficult to determine the role that warm-up effects play in each individual measurement series.



SDS-2

Figure 4.48.: Electron rate over multiple days at the SDS-2 setup. One can examine the long-term stability of the source from regular transmission function measurements that were performed over several weeks. The plot shows the nominal rate at the end of selected transmission runs under nominal conditions with the laser operating at 100 kHz/SI7A. Each data point corresponds to the average electron rate in the last 60 s of a run, where the source was operating in full transmission. The investigated time frame of roughly two weeks shows a consistent rate decrease of 0.87 cps/hr (268 ppm/hr). The nominal electron rate at the beginning is 3249 cps.
Runs: 22880–22886,23014–23021,23032–23058,23172–23200,23436–23449,23454–23485

The analysis yields a consistent rate drift of $-0.053(4)$ 1/hr for the normalized electron rate. By considering an effective rate of $\dot{N} = 3249$ cps this value can be converted into an actual rate drift, which yields a decrease of $0.87(7)$ cps/hr (268 ppm/hr). This value corresponds to a decrease of $20.9(17)$ cps/day, which is considerably smaller than the short-term drift that was determined above (11.5 cps/h or 276 cps/day). Due to the normalization procedure, the long-term drift is independent of intensity changes and is therefore attributed to actual changes in electron emission, i. e. to a reduction in electron yield. It is believed that this is an effect of work function changes, where a work function increase results in a smaller electron yield (cmp. section 4.6.6). This is in agreement with earlier measurements at WWU Münster and during the SDS-1 measurement phase, where a long-term rate decrease was also observed [Zac14, Gro15].

4.6.3 Zero angle

One important aspect of the electron source commissioning measurements is to determine the *zero-angle* where the minimal pitch angle θ is achieved in the spectrometer entry magnet. This calibration is necessary to correctly perform measurements that rely on angular selectivity, such as magnetic reflection and transmission function measurements. The approach is described in section 4.4, and corresponding measurements were also performed at the MoS setup (section 4.5.4). The electron

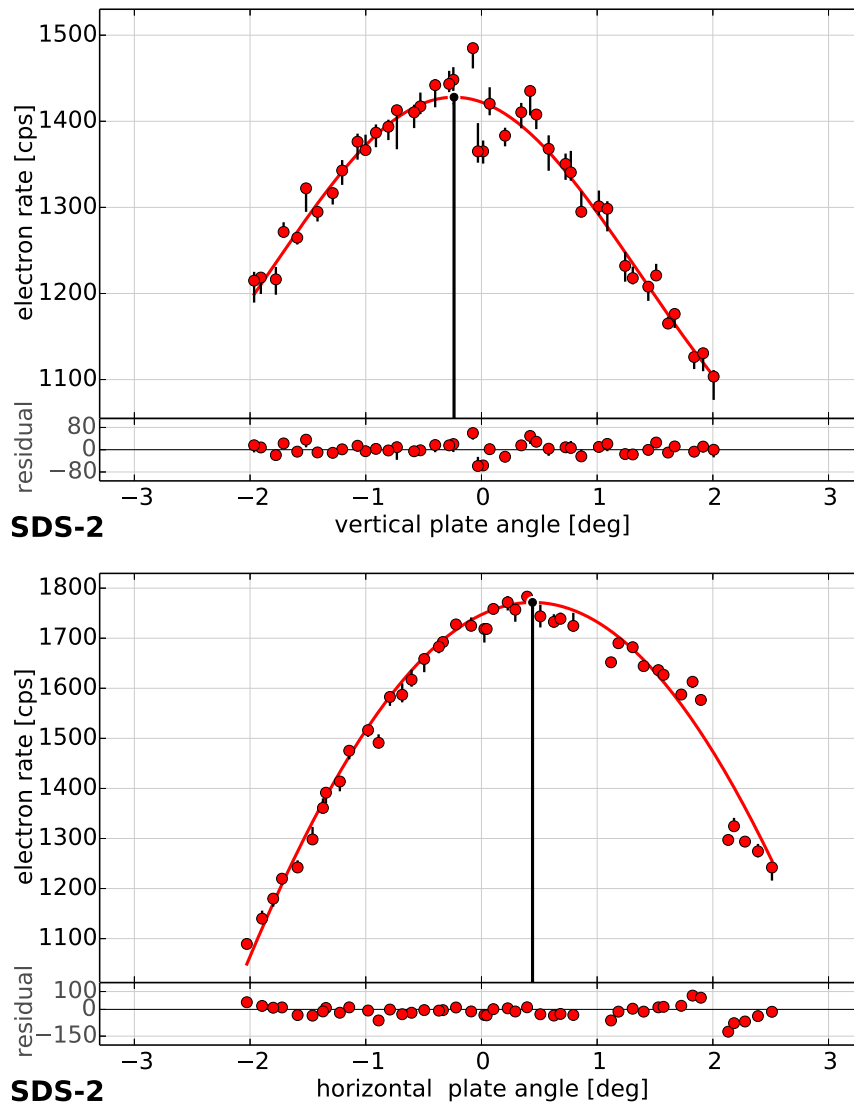


Figure 4.49.: Zero angle after the maintenance break at the SDS-2 setup. The plots show zero-angle measurements for the two independent tilt axes, where the tilt angle α_p was varied at nominal conditions ($U_{spec} = -18.6\text{ kV}$, $U_{acc} = 5\text{ kV}$, $U_{dip} = 3\text{ kV}$). The rate dependency follows a normal distribution where the position of the rate maximum indicates the zero-angle offset (this is in agreement with MoS results, cmp. figure 4.28f.). The determined offset is used in the slow-control software of the electron source to perform an offset correction. The zero-angle measurement was repeated after the maintenance break in early 2015 to account for the changed conditions after the photocathode replacement. The earlier measurement performed in 11/2014 is not shown here.

Runs: 22414-22416,22417-22418

source was installed at the main spectrometer in 11/2014, and first commissioning measurements without high voltage (i. e. $U_{spec} = -200\text{ V}$) were carried out. Due to severe stability issues at the electron source (high voltage breakdowns, rate fluctuations etc.; see section 4.6.7), the source needed to be dismantled in 01/2015 to perform maintenance work at WWU Münster. The electron source

was then re-installed in 02/2015, so that another zero-angle measurement had to be performed before continuing with the planned measurements.

Figure 4.49 shows the zero angle offsets for the vertical and horizontal tilt axes that were determined after the re-installation. The measurement was performed at high voltage ($U_{spec} = -18.6$ kV) and at nominal spectrometer and source settings ($U_{acc} = 5$ kV, $U_{dip} = 3$ kV, laser at 100 kHz/8 A). The determined offsets are added to the reference values that are used internally in the slow-control software of the source. This corrects the tilt angle on both axes so that the zero-angle $\alpha_p = 0^\circ$ corresponds to the minimal pitch angle in the spectrometer entry magnet. The offsets are listed in table 4.13. Note that the dipole voltage has a significant impact on the zero-angle, as observed during the MoS measurements. At the SDS-2 setup, however, this effect is uncritical because all measurements were performed at fixed settings (with the exception of measurements at reduced spectrometer voltage, see section 4.6.5).

The corresponding reference values in the slow-control software were updated accordingly to

$$\alpha_{0,h}^* = 75.14^\circ, \quad \alpha_{0,v}^* = 163.41^\circ. \quad (4.81)$$

All measurements that were performed from 02/2015 until the end of the SDS-2 commissioning phase in 04/2015 use these values, which applies to all magnetic reflection and transmission function measurements that are discussed in this section. Note that the work function measurement in 11/2014 does not depend on the zero-angle to produce correct results (see section 4.6.6).

Table 4.13.: Measured zero angle offsets before and after maintenance break.

phase	U_{dip}	χ^2/ndf	$\Delta\alpha_{0,v}$	χ^2/ndf	$\Delta\alpha_{0,h}$
02/2015	3.0 kV	2.41	$-0.237(14)^\circ$	17.1	$0.442(6)^\circ$

4.6.4 Magnetic reflection

Nominal conditions

Magnetic reflection of electrons occurs when their pitch angle reaches 90° along their trajectory. In the MoS measurements with a symmetric magnetic field setup (section 4.5.5), electrons are typically reflected at the spectrometer entry magnet where the electrons encounter the maximal magnetic field. In the asymmetric setup of the main spectrometer, the maximal magnetic field is reached in the pinch magnet at the spectrometer exit with $B_{max} = 5.1$ T. The magnetic field in the PS2 magnet at the spectrometer entrance is lower at $B_{PS2} = 4.5$ T. Electrons can therefore be magnetically reflected either at the pinch magnet or the PS2 magnet, depending on their initial pitch angle. Since only electrons that reach the detector are observed, the magnetic field of the pinch magnet defines the maximal pitch angle that can be transmitted. Consequently, electrons that are transmitted through the PS2 magnet can be reflected at the pinch magnet if their pitch angle is too large. Since in this thesis the angular distribution is always evaluated at the point of the spectrometer entry magnet (PS2 in this case), the maximal angle that can be transmitted from the PS2 magnet to the detector is defined by the relation

$$\theta < \theta_{mir} = \arcsin\left(\sqrt{\frac{B_{PS2}}{B_{max}}}\right) = 69.9^\circ. \quad (4.82)$$

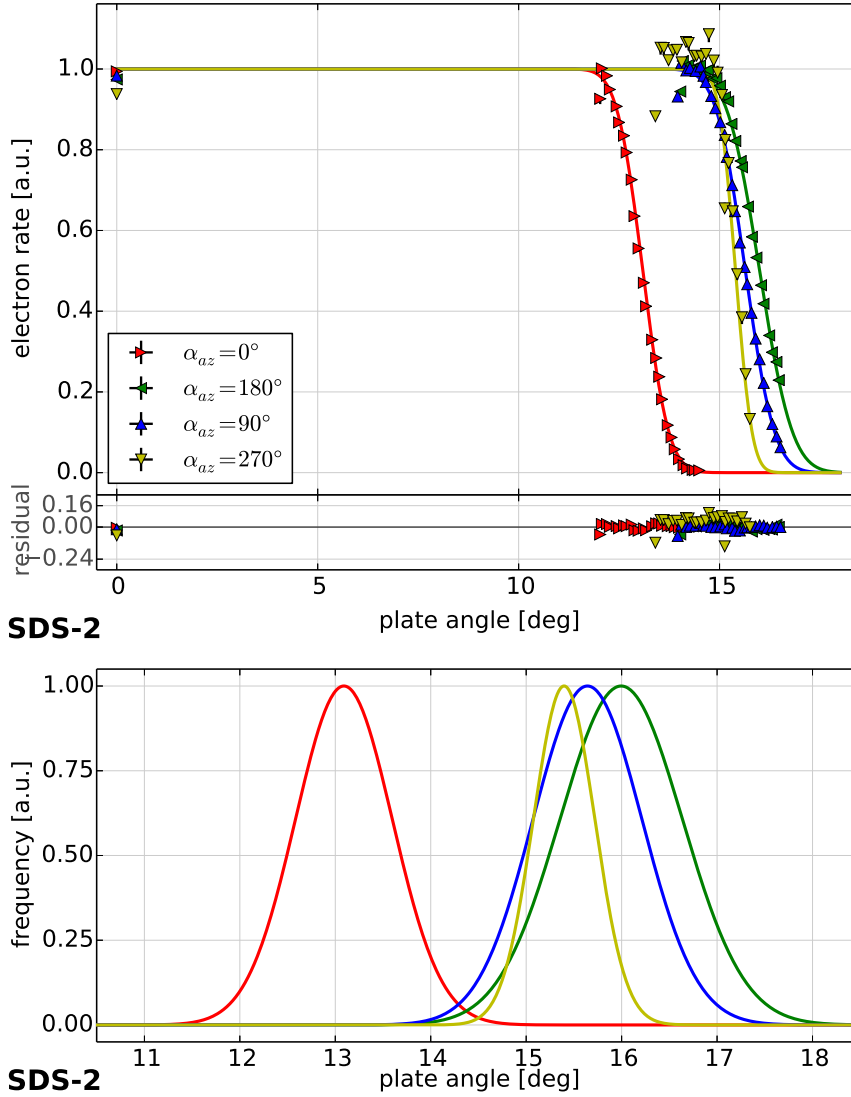


Figure 4.50.: Magnetic reflection under nominal conditions at the SDS-2 setup. The plot shows the observed electron rate in dependency of the plate angle α_p in four azimuthal directions ($\alpha_{az} = 0^\circ, 180^\circ, 90^\circ, 270^\circ$). The measurement was performed at nominal conditions ($U_{spec} = -18.6$ kV, $U_{acc} = 5$ kV, $U_{dip} = 3$ kV). Magnetic reflection occurs at $\alpha_p \approx 15^\circ$. A large deviation is observed on the horizontal axis, where reflection is reached at $\alpha_p \approx 13^\circ$ for $\alpha_{az} = 0^\circ$. This asymmetry is attributed to an inaccurate zero-angle setting, which affects the produced pitch angle. A similar observation (although less pronounced) was made at the MoS setup (figure 4.30). The bottom plot shows the corresponding angular distributions in terms of α_p , as determined by the error-function fit. The observed angular spread is consistent between the measurements. The measurement at $\alpha_{az} = 270^\circ$ suffers from missing data points for $\alpha_p > 16^\circ$, which explains the observed discrepancy.

Runs: 22420,22424,22425,22427–22428

The angular distribution in the entry magnet with $0^\circ \leq \theta < 90^\circ$ is therefore cut off at $\theta = 70^\circ$ due to magnetic reflection at the pinch magnet.

The magnetic reflection measurement determines the reflection angle α_{max} , i. e. the plate tilt angle at the electron source that achieves a pitch angle $\theta = \theta_{mir}$ in the entry magnet; this approach is explained in section 4.4. The MoS measurements showed that after finding the correct zero-angle (so that $\alpha_p = 0^\circ$ achieves the minimal pitch angle in the entry magnet), an asymmetry between the reflection angles α_{max} for the different tilt axes can be observed. In principle, such asymmetries should not occur since the zero-angle measurement already aligns the source w. r. t. the magnetic fields. However, the MoS results indicate that this alignment does not remove asymmetries entirely. Since a magnetic reflection measurement is more sensitive to small changes in the produced pitch angle for $\alpha_p \lesssim \alpha_{max}$, it can be used to verify the previously determined zero-angle and to investigate any possible asymmetries of the produced pitch angle.

Figure 4.50 shows measured reflection curves for different azimuthal plate angles $\alpha_{az} = 0^\circ, 180^\circ, 90^\circ, 270^\circ$ that correspond to the two tilt axes. The measurement was performed at nominal settings ($U_{spec} = -18.6$ kV, $U_{acc} = 5$ kV, $U_{dip} = 3$ kV, laser at 100 kHz/8 A). In comparison with the MoS results, the reflection angle α_{max} is always larger as an effect of the different magnetic fields: The ratio between the initial and the maximal magnetic field

$$\frac{B_{start}}{B_{max}} = \frac{29 \text{ mT}}{5.1 \text{ T}} = 0.0057 \quad (4.83)$$

is 21% larger than at the MoS setup at enhanced magnetic field ($B_{start}^+ = 28$ mT). Since the reflection angle is largely defined by this ratio due to the adiabatic transformation (2.7) of the pitch angle between source and entry magnet, larger plate tilt angles α_p are necessary to reach the same pitch angle θ in the magnet. The tilt angle is mechanically limited to $\alpha_p \leq 16^\circ$, which explains why not all reflection curves could be measured completely (as seen in the figure). This has a negative effect on the accuracy of the fit, but fortunately it is still possible to determine the angular distribution and the reflection angle with reasonable accuracy. The angular distributions (in terms of plate angle α_p , cmp. section 4.5.5) is shown at the bottom of the figure. The fit results for this measurement series are listed in table 4.14.

The individual reflection curves for $\alpha_{az} = 90^\circ, 180^\circ, 270^\circ$ overlap and produce comparable reflection angles around 16° . A strong discrepancy (asymmetry) is only observed for the measurement at $\alpha_{az} = 0^\circ$, where reflection is reached roughly 3° earlier. This asymmetry is considerable larger than in comparable measurements at the MoS setup. It can be explained by an improper zero-angle setting (e. g. due to inaccurate measurement data or due to human error when applying the correction). The asymmetry can be quantified by the difference between the reflection angles for different tilt axes according to (4.61). The corresponding values are given in table 4.15.

As with the MoS measurements, it is possible to determine the effective angular spread (4.63) from the observed reflection curves. This calculation is explained in section 4.5.5. The corresponding angular spread σ_θ^* is also given in table 4.15. It is consistent with results from the MoS setup over different tilt directions α_{az} , with a combined weighted average of $\bar{\alpha}_{max} = 15.4^\circ$ for the SDS-2 setup and $\bar{\alpha}_{max}^{MoS} = 19.1^\circ$ for the MoS setup. This consistency is expected, since the electron acceleration mechanisms are similar, with only small differences in the electromagnetic conditions inside the source. Note that the discrepancy that is observed for $\alpha_{az} = 270^\circ$, were a substantially smaller angular spread is determined, is likely caused by the bad fit (note the large χ^2 value) due to the missing data points above $\alpha_p \gtrsim 16^\circ$.

Table 4.14.: Measured reflection angles.

α_{az}	χ^2/ndf	α_{max}	σ_α	σ_θ^*
0°	1.32	13.09(2)°	0.51(2)°	16.0(5)°
180°	11.5	16.00(8)°	0.64(6)°	16.3(18)°
90°	4.85	15.64(2)°	0.57(3)°	15.5(7)°
270°	39.5	15.40(4)°	0.32(3)°	11.7(14)°
weighted average:		14.80(3)°	0.518(12)°	15.38(16)°

Table 4.15.: Observed asymmetries in the reflection angle measurements.

asymmetry	$\Delta\alpha_{max}$	$\Delta\sigma_\alpha$	$\Delta\sigma_\theta^*$
horizontal axis	-2.91(10)°	-0.05(3)°	-1.6(2)°
vertical axis	0.24(6)°	0.25(6)°	3.8(21)°
between axes	-0.97(16)°	0.45(9)°	2.5(23)°

Influence of the starting voltage

At the end of the SDS-2 measurement phase, the spectrometer voltage was changed to $U_{spec} = -5.6\text{ kV}$ to -8.6 kV to measure transmission functions at reduced voltage. Although the actual reason for this unusual setting were sudden issues with the high voltage stability (see section 4.6.7), this allowed to investigate the influence of a reduced starting voltage $U_{start} \approx U_{spec}$ on the produced pitch angles. Since the starting voltage affects the electron acceleration mechanisms between the source and the entry magnet, it is expected that a different voltage setting also affects the pitch angle of the electrons.

Figure 4.51 shows reflection curves that were measured at four different starting voltages $U_{start} = -8.6\text{ kV}$ to -5.6 kV at otherwise nominal conditions (see above); the spectrometer voltage was changed accordingly. The measurements are compared in the figure with a reference measurement at $U_{start} = -18.6\text{ kV}$ that was carried out earlier. The measurements show a clear shift of the reflection angle α_{max} from the nominal value of roughly 16° to considerably smaller values of 7° and less. The corresponding fit results are listed in table 4.16. Note that the electron rate in the reduced-voltage setting shows rather large fluctuations due to the mentioned stability issues. This explains the larger χ^2 values of the fit results that are observed here.

Nonetheless, all observed reflection curves can be described by error functions. The effective angular spread has been computed following the approach explained above. This measurement shows that a reduced starting voltage not only increases the produced pitch angles – visible as a shift of the reflection angle α_{max} to smaller values – but also increases the angular spread from 16° to more than 20° . This shows that the acceleration mechanisms between the source and the entry magnet are indeed influenced by changes in starting voltage, and the observed behavior is in agreement with the expectations.

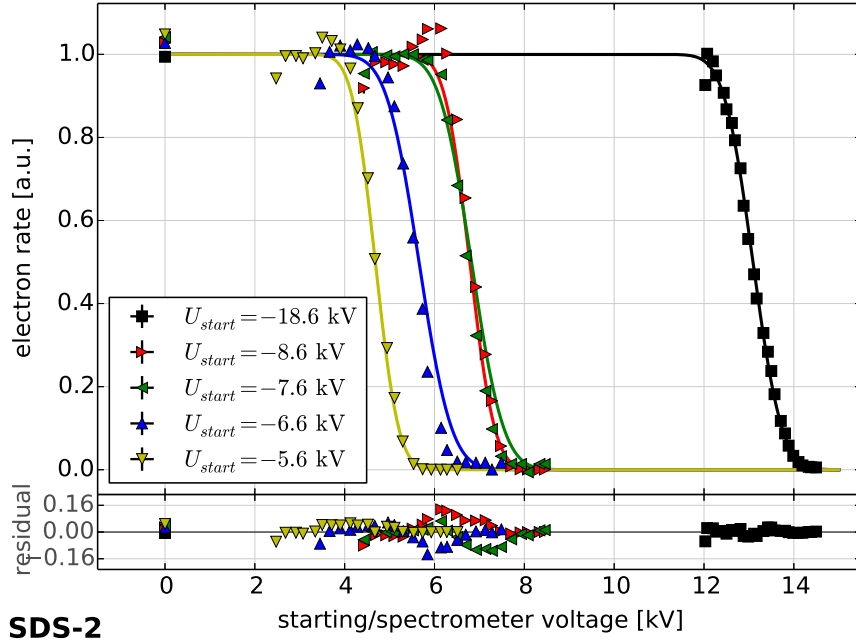


Figure 4.51.: Magnetic reflection with reduced voltage at the SDS-2 setup. The plot shows the observed electron rate in dependency of the plate angle α_p for different spectrometer voltages $U_{spec} = -18.6 \text{ kV}, -8.6 \text{ kV}, -7.6 \text{ kV}, -6.6 \text{ kV}, -5.6 \text{ kV}$ with $\alpha_{az} = 0^\circ$. The measurement was performed in full transmission (surplus energy $q\Delta U \approx 10 \text{ eV}$); the starting voltage scales with the spectrometer voltage ($U_{start} = U_{spec} + \Delta U$). The reflection angle α_{max} where magnetic reflection occurs shifts from 16° at nominal high voltage to less than 8° at reduced voltage. This is in agreement with the expectation that the lower starting voltage influences the electron acceleration processes, resulting in an increased pitch angle of the produced electrons. The observed shift is inconsistent at $U_{start} = -7.6 \text{ kV}$, where a smaller value of α_{max} would be expected. Runs: 22420,23756,23757,23758,23759

Table 4.16.: Measured reflection angles at reduced voltage.

α_{az}	U_{start}	χ^2/ndf	α_{max}	σ_α	σ_θ^*
0°	-18.6 kV	1.32	13.09(2) $^\circ$	0.51(2) $^\circ$	16.0(5) $^\circ$
	-8.6 kV	19.7	6.78(2) $^\circ$	0.44(1) $^\circ$	20.7(7) $^\circ$
	-7.6 kV	14.3	6.82(2) $^\circ$	0.56(1) $^\circ$	23.4(7) $^\circ$
	-6.6 kV	19.4	5.65(2) $^\circ$	0.57(1) $^\circ$	25.9(8) $^\circ$
	-5.6 kV	14.0	4.68(2) $^\circ$	0.41(2) $^\circ$	24.1(11) $^\circ$

4.6.5 Energy and angular distributions

Energy distributions with Ag photocathode

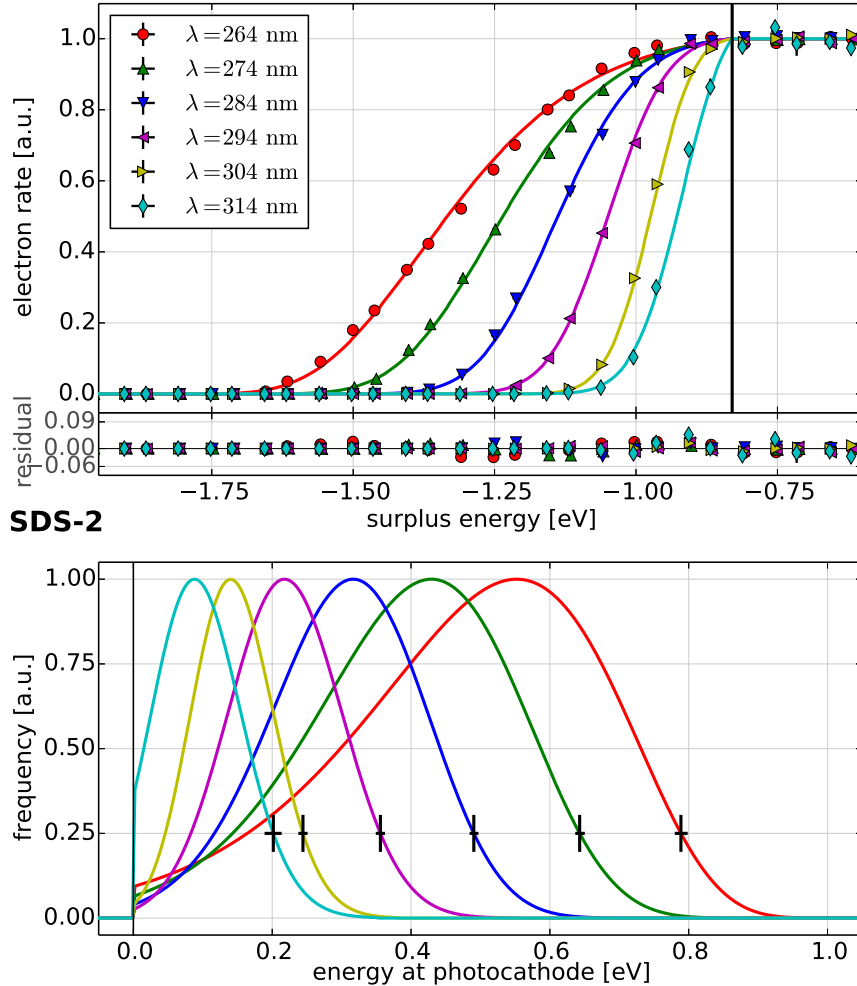


Figure 4.52.: Energy spread with different wavelengths at the SDS-2 setup (silver photocathode). The plot shows transmission function measurements at different wavelengths $\lambda = 264$ nm to 314 nm for the silver photocathode used until 12/2014. The measurement was performed at zero-voltage ($U_{spec} = -200$ V, $U_{acc} = 100$ V) and zero-angle ($\alpha_p = 0^\circ$). The transmission width decreases with larger wavelengths, as expected from the photoemission principle. This is in agreement with corresponding MoS measurements (figure 4.33). The observed transmission functions are well described by the analytical model (4.10). The vertical black line marks the position of the transmission edge at $q\Delta U_0 = -0.83$ eV; it corresponds to a kinetic energy $E_e = 0$ eV of the emitted electrons. The bottom plot shows the underlying energy distributions that were determined from the analytical model. The upper limit E_{max} (black crosses) shifts to smaller energies with increasing wavelengths, which reduces the observed energy spread.

Runs: 20896,20871,20872,20873,20874,20897

Transmission function measurements at “zero voltage” ($U_{start} \approx U_{spec} = -200$ V) allow to determine the energy distribution of the produced electrons. Due to the improved energy resolution of the MAC-E filter at the lower retarding potential, such measurements are independent of the angular

distribution of the electrons, which allows to disentangle these two contributions. This approach is discussed in section 4.4. At the SDS-2 setup, the energy resolution improves from 1.39 eV to 0.015 eV in the zero-voltage setting (nominal magnetic field: $B_{min} = 0.38$ mT, $B_{max} = 5.1$ T).

The MoS measurements showed that it is also possible to accurately determine the energy distribution at nominal spectrometer voltage ($U_{spec} = -18.6$ kV, see section 4.5.6), since the contribution from the angular spread at small pitch angles is negligible. The SDS-2 setup now allows to verify this observation, as the different voltage settings can be compared directly.

Figure 4.52 shows several zero-voltage transmission functions that were measured at otherwise nominal settings ($U_{spec} = -200$ V, $B_{max} = 5.1$ T, $B_{start} = 29$ mT), but with increased magnetic field ($B_{min} = 0.9$ mT). Since the spectrometer is operated at zero-voltage, which improves its energy resolution to 35 meV, the higher field does not affect the measurement. The electron source operated at nominal settings as well, but with a reduced acceleration voltage ($U_{dip} = 3$ kV, $U_{acc} = 100$ V). This is necessary to avoid a potential maximum at the front plate of the electron source ($U_{front} = U_{start} + U_{acc} = -200$ V + 5 kV > 0) that could result in an electron trap inside the source with a possible risk of discharges. Reducing the acceleration voltage ensures that the ground potential at the spectrometer entrance is the most positive potential ($U_{front} = -200$ V + 100 V < 0). The measurement was performed at different wavelengths $\lambda = 264.3$ nm to 314.3 nm with the silver photocathode (Ag), which was used at the electron source from 11/2014 to 12/2014. The photocathode was later replaced after a maintenance break (see below).

Agreeing to the results of MoS measurements, the observed transmission width decreases significantly for larger wavelengths. This decrease corresponds to the smaller energy spread, as the photon energy $h\nu = hc/\lambda$ approaches the work function Φ of the photocathode. The observed transmission functions are described accurately by the analytical fit model with a pre-determined edge position $\Delta U_0 = -0.83(1)$ eV, as indicated by the vertical black line in the figure. The edge position was kept fixed in the model fit to avoid a systematic bias that results from correlations between the energy parameters and the edge position; this is discussed in section 4.9. The measurement data also shows that the change in energy spread only moves the *lower* bound of the transmission function (small electron rates) towards the transmission edge. The edge position itself is not affected as it does not depend on the energy spread. This is expected since the transmission edge corresponds to an electron energy of $E_e = 0$ eV at the photocathode, which is independent of the energy distribution (and thus, the photon energy of the incident UV light).

The energy distributions that are shown at the bottom of the figure are comparable to the MoS results, showing a similar shape where the width (e. g. FWHM) and the asymmetry decreases for larger wavelengths. The energy spread σ_E (corresponding to the 1σ -width) decreases from about 210 meV at 264 nm to 60 meV at 304 nm. Table 4.17 shows the corresponding energy distribution parameters for this measurement series: the mean energy \hat{E} , the effective energy spread σ_E (equivalent to the 1σ -width of a normal distribution) and the energy limit E_{max} of the energy distribution. The energy limit corresponds to the position where the energy distribution drops to 25% of its nominal height, as is indicated by the black crosses in the bottom of figure 4.52. The measurement at 314 nm is affected by the too large step size of the surplus energy – there are too few data points that cover the actual transmission function – and thus produces rather large parameter uncertainties in the fit.

The determined energy spreads are considerably smaller than at the MoS setup, if one compares similar wavelengths. The reason is the different photocathode material – silver instead of gold at the MoS –

which has a roughly 0.1 eV larger work function (see section 4.6.6 below). Due to the relation

$$E_{max} = h\nu - \Phi = hc/\lambda - \Phi, \quad (4.84)$$

the larger work function reduces the observed energy spread at a given wavelength. As with the MoS measurements, it is also possible to determine the photocathode work function directly from this relation by considering the energy limit E_{max} that is determined from the energy distribution. The corresponding results are discussed in section 4.6.6 below.

Table 4.17.: Measured energy distributions for Ag photocathode at different wavelengths.

λ	χ^2/ndf	\hat{E}	E_{max}	σ_E
264.3(22) nm	1.53	0.496(4) eV	0.789(7) eV	0.210(17) eV
274.3(22) nm	0.97	0.403(3) eV	0.643(4) eV	0.156(8) eV
284.3(22) nm	0.78	0.307(4) eV	0.490(4) eV	0.113(5) eV
294.3(22) nm	0.62	0.219(4) eV	0.356(4) eV	0.082(4) eV
304.3(22) nm	0.72	0.144(4) eV	0.244(4) eV	0.060(8) eV
314.3(22) nm	0.76	0.092(9) eV	0.202(10) eV	0.065(15) eV

Energy distributions with Au photocathode

After the replacement of the silver photocathode with a new gold photocathode (Au) during the maintenance break in 01/2015, its work function was determined again with the established approach. Since the new photocathode likely has a different work function, one expects a different energy spread that can be observed in zero-voltage transmission function measurements. This new photocathode was used for the remainder of the SDS-2 measurement phase (02/2015 to 04/2015).

Figure 4.53 shows the corresponding measurements with the Au photocathode, using the same spectrometer and source settings as before. The position of the transmission edge was determined to $\Delta U_0 = -1.19(1)$ eV in this measurement series, which is considerably smaller than before. This edge shift will be discussed in the next section. The wavelengths $\lambda = 265.8$ nm to 315.8 nm used here are slightly different than in earlier measurements due to a changed monochromator calibration³⁵. The observed transmission functions and the underlying energy distributions are generally comparable to the earlier measurements with the Ag photocathode. Table 4.25 lists the corresponding fit results, using the same methods as discussed above.

The difference in wavelength for each UV-LED ($\Delta\lambda = 1.5$ nm) is smaller than the estimated uncertainty of the fit parameters. These parameters can therefore be compared to earlier measurements without much loss of accuracy. With the new photocathode, the energy spread decreases from about 280 meV at 266 nm to 70 meV at 316 nm. The values are consistent with the MoS results where a gold photocathode was used as well, and are substantially larger than the results using the silver photocathode. Table 4.19 lists a comparison between the energy parameters determined at the different setups.

³⁵. The monochromator is operated mechanically by a step-motor, which easily results in small changes in the calibration. The re-calibration was performed by comparing the emission spectrum of the UV-LEDs with a reference measurement, see section 4.4.

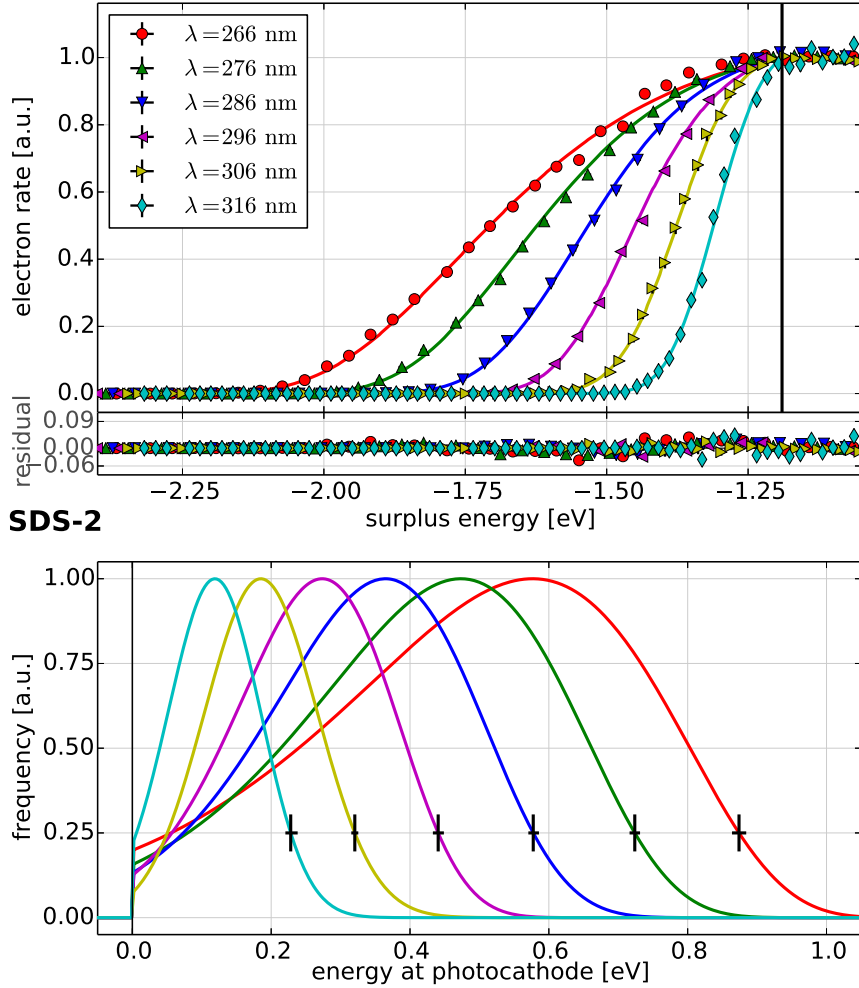


Figure 4.53.: Energy spread with different wavelengths at the SDS-2 setup (gold photocathode). The plot shows transmission functions at different wavelengths $\lambda = 266$ nm to 316 nm at zero-voltage and zero-angle ($U_{spec} = -200$ V, $U_{acc} = 100$ V, $\alpha_p = 0^\circ$) for the gold photocathode used since 02/2015. The overall behavior is consistent with the results from an earlier measurements using the silver photocathode (figure 4.52). The vertical black line again indicates the transmission edge, which has shifted to $q\Delta U_0 = -1.19$ eV here. The underlying energy distributions are shown at the bottom. For comparable wavelengths, the energy distributions are consistent with the results for the silver photocathode and with earlier measurements at the MoS (figure 4.33) where another gold photocathode was used. The energy spread and the photocathode work function can be determined from the upper limit E_{max} of the energy distributions (black crosses). Runs: 23201,23202,23203,23204,23205,23207

Note that the wavelength given in this table is approximated to allow an easier comparison between the different measurement series.

The observed transmission functions, including the underlying energy distributions and the position of the transmission edge, are all consistent with a measurement series that was performed in 02/2015 under the same conditions. These measurements, however, used a larger surplus energy step size and thus are affected by larger uncertainties. These results are in agreement with the discussion above, but are skipped here for brevity.

Table 4.18.: Measured energy distributions for Au photocathode at different wavelengths.

λ	χ^2/ndf	\hat{E}	E_{max}	σ_E
265.8(20) nm	3.28	0.493(4) eV	0.874(8) eV	0.284(15) eV
275.8(20) nm	1.92	0.421(3) eV	0.724(5) eV	0.213(10) eV
285.8(20) nm	4.80	0.336(3) eV	0.578(5) eV	0.158(8) eV
295.8(20) nm	0.61	0.256(3) eV	0.441(6) eV	0.119(11) eV
305.8(20) nm	6.17	0.185(3) eV	0.320(3) eV	0.081(2) eV
315.8(20) nm	3.18	0.118(5) eV	0.228(7) eV	0.067(7) eV

Table 4.19.: Determined energy parameters for different setups and different wavelengths.

approx. λ	SDS-2/Au σ_E	SDS-2/Ag σ_E	MoS/Au σ_E
265 nm	0.284(15) eV	0.210(17) eV	0.31(5) eV
275 nm	0.213(10) eV	0.156(8) eV	0.28(4) eV
285 nm	0.158(8) eV	0.113(5) eV	0.22(2) eV
295 nm	0.119(11) eV	0.082(4) eV	0.19(3) eV
305 nm	0.081(2) eV	0.060(8) eV	0.14(3) eV
315 nm	0.067(7) eV	0.065(15) eV	0.09(7) eV

Work function of the main spectrometer

Between the two SDS-2 measurements performed in 11/2014 and 3/2015, the transmission edge shifted from $-0.83(1)$ eV to $-1.19(1)$ eV, which is almost a 50% difference. The transmission edge corresponds to the electrons that are emitted with “zero-energy” from the photocathode, $E_e \approx 0$ eV. Its position, as observed in a transmission measurements, is defined by the potential depression of the main spectrometer, $\Delta U_r > 0$, and the difference between the work function Φ of the photocathode and the (effective) work function Φ_{spec} of the main spectrometer electrodes,

$$\Delta\Phi = \Phi - \Phi_{spec}. \quad (4.85)$$

The potential depression caused by the ground potential at the spectrometer entrance and exit, and causes an offset between the voltage applied to the spectrometer, U_{spec} , and the actual retarding potential in the analyzing plane, $U_{ana} = U_{spec} + \Delta U_r$. The work function difference results in an additional shift of the observed transmission edge. If the potential depression is known e. g. from electromagnetic simulations, one can resolve changes in $\Delta\Phi$ between different measurements. If the photocathode work function is known as well from a dedicated measurement), the spectrometer work function can be investigated. The relation between the different parameters (U_{ana} , ΔU_r , $\Delta\Phi$ etc.) has been discussed in section 4.1.1 and is visualized in figure 4.5.

One can assume the value ΔU_r to be constant for the analysis given here³⁶. For an “on-axis” transmission function measurement – where the electrons follow a field line close to the spectrometer axis and arrive at a central detector pixel, which is the default setting for the measurements discussed here – the value $\Delta U_r = 1.30$ V has been computed by Kassiopeia simulations (see section 3.3). Neglecting a possible work function difference, $\Delta\Phi \equiv 0$, the transmission edge aligns with the value of the potential depression, $\Delta U_0 = \Delta U_r$. For all transmission function measurements at the main spectrometer, the edge position is therefore expected to be at -1.30 eV. Consequently, any additional shift that is observed must correspond to a work function difference between the electron source photocathode and the main spectrometer electrodes.

Two measurement series that were carried out in 11/2014 and 03/2015 (beginning and end of the SDS-2 commissioning phase, see above) are investigated here for this effect. The results are summarized in table 4.20. From the different edge positions mentioned at the beginning of this discussion ($q\Delta U_0 > q\Delta U_r = -1.3$ eV) it is already clear that a work function difference $\Delta\Phi > 0$ exists. This difference is considerably smaller in the later measurement, where an edge position $q\Delta U_0 = -1.19$ eV was observed.

Since the photocathode work function has been determined in independent measurements (Fowler method, see section 4.6.6 below), it is possible to compute the absolute value of the spectrometer work function $\Phi_{spec} = \Phi - \Delta\Phi$. This yields a value

$$\Phi_{spec} = 3.65(4) \text{ eV} \quad (4.86)$$

at the end of the SDS-2 measurements (in 03/2015), where a gold photocathode with a work function $\Phi = 3.76(3)$ eV was used. When applying the same method to the earlier measurement in 11/2014, one must consider the changed work function of the photocathode³⁷, which yields an absolute work function change of $\Delta\Phi_{src} = -0.09(5)$ eV between 11/2014 and 03/2015. Combining this value with the observed transmission edge shift of $\Delta(q\Delta U_0) = 0.36(2)$ eV, an absolute spectrometer work function change of

$$\Delta\Phi_{spec} = \Delta(q\Delta U_0) - \Delta\Phi_{src} = 0.27(7) \text{ eV} \quad (4.87)$$

is observed over the examined time frame of roughly 3 months, which is equivalent to a 7% change.

A reasonable explanation is given by the sensitivity of the work function to surface impurities. It is known that such impurities can have significant effects on the work function of different materials (e. g. [She92] or [DS73]), and similar effects have been observed at the photocathode (cmp. section 4.2.4).

If one assumes that the electrode surfaces inside the main spectrometer were not completely clean at the beginning of the SDS-2 measurements, the observed time-dependency can be explained. It is possible that impurities on the electrode surfaces, such as components of the residual gas, were removed over the time frame of 100 d between the two measurements series. This argument is supported by the fact that the spectrometer vessel was not baked out before the start of the SDS-2 phase, so that residual gas components like hydrogen were likely adsorbed onto the electrode surfaces. Measurements at the beginning of SDS-2 that are sensitive to the spectrometer work function were therefore affected by such impurities. Continuous vacuum pumping during the measurement phase removed these impurities over time, so that measurements at a later time observed a changed work function. Hence,

36. The potential depression only depends on the spectrometer geometry and the settings of the inner electrode system, which have not changed over the different measurements.

37. The earlier measurement used a silver photocathode that was later replaced in a maintenance break.

a transmission edge shift is seen between measurements that were performed over the course of the SDS-2 commissioning phase. This time-dependency is also indicated in figure 4.54, which shows the vacuum pressure during the SDS-2 measurement phase. A pressure decrease from $2.9 \cdot 10^{-9}$ mbar to $5.0 \cdot 10^{-10}$ mbar between the two work function measurements is observed, as indicated by the vertical lines.

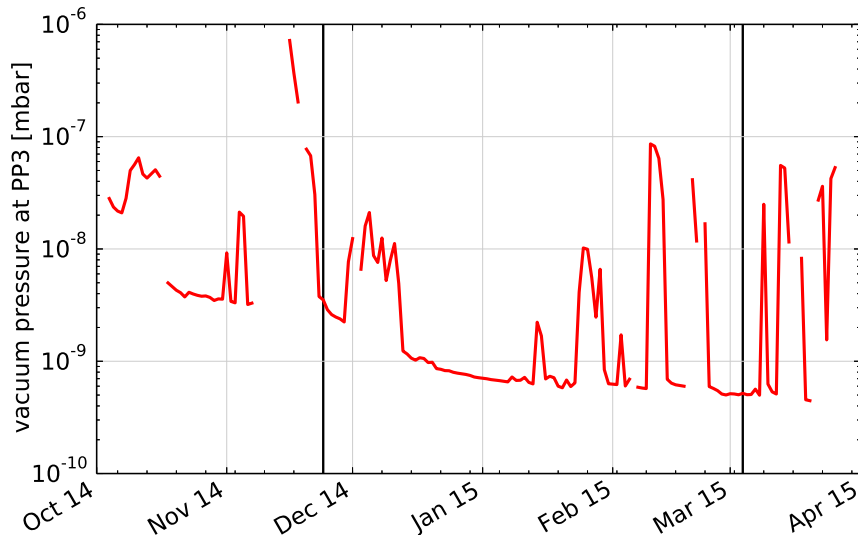


Figure 4.54.: Vacuum pressure during the SDS-2 measurement phase. The plot shows the daily average of the vacuum pressure p_{PP3} at pump-port 3 of the main spectrometer over several months of data-taking. Note that the pressure gauge was located in the vacuum system behind the LN₂-cooled baffles, so that the actual pressure in the main spectrometer is considerably lower. Occasional pressure increases are caused by dedicated measurements at modified vacuum conditions, e. g. when using radioactive sources (cmp. section 5.3.5). The two vertical lines indicate the time of the two work function measurements that were performed in 11/2014 and 03/2015. The pressure decreased from $2.9 \cdot 10^{-9}$ mbar to $5.0 \cdot 10^{-10}$ mbar in this time period. The observed work function change between the two measurements is likely related to this pressure difference. It is believed that hydrogen and other impurities were removed from the electrode surfaces at the main spectrometer due to the continuous vacuum pumping.

The spectrometer work function of 3.39(4) eV to 3.65(4) eV that was determined here is in agreement with the expected work function of 4.4 eV for stainless steel [P⁺92], if one considers that the work function is heavily influenced by impurities, surface roughness, electric fields and other effects. These effects also play an important role at the electron source. In case of stainless steel, the work function also depends on the alloy composition³⁸ [Wil66]. The observed reduction by about 1 eV w. r. t. the expected value for stainless steel is comparable to observed differences for the silver and gold photocathodes at the electron source, where a reduction of 0.5 eV to 1.5 eV was measured. The observed increase of the spectrometer work function due to continuous vacuum pumping – and thus, the removal of surface impurities – is also in agreement with independent studies. In [She92] it was found that a small exposure of a platinum surface to hydrogen increases its work function, whereas a larger exposure results in a considerable reduction.

38. In addition to iron, stainless steel typically consists of roughly 20% chromium, 10% nickel and smaller amounts of other materials. See e. g. https://www.dew-stahl.com/fileadmin/files/dew-stahl.com/documents/Publikationen/Werkstoffdatenblaetter/RSH/1.4429_en.pdf.

Conclusively, if one assumes a small amount of impurities at the beginning of the SDS-2 phase that was reduced over time, thus increasing the work function Φ_{spec} , and also considers that effects such as surface roughness can considerably modify the work function, the observed time-dependency of the spectrometer work function can be explained. It is expected that similar effects can be observed in upcoming commissioning measurements at the KATRIN experiment, and it is advised to perform work function measurements on a regular basis to investigate its stability over time. This is also important for later neutrino-mass measurements, since any change in Φ_{spec} also affects the retarding potential U_{ana} .

Table 4.20.: Observed work function change over the SDS-2 measurement phase.

measurement	$q\Delta U_0$	$\Delta\Phi$	$\Phi = \Phi_{src}$	Φ_{spec}
11/2014	-0.83(1) eV	0.47(1) eV	3.855(28) eV	3.385(38) eV
03/2015	-1.19(1) eV	0.11(1) eV	3.764(26) eV	3.654(36) eV
difference:	-0.36(2) eV	-0.36(2) eV	-0.091(54) eV	0.269(74) eV

Energy distributions at high voltage

The MoS setup only allowed measurements of the energy distribution at non-zero voltages, $U_{spec} \leq 8$ kV. The determined energy distributions that were determined with this setting are in agreement with the SDS-2 results discussed above, where a zero-voltage setting was used. It is, however, not entirely clear how much the MoS measurements were affected by the angular spread. The SDS-2 setup allows transmission function measurements at different spectrometer voltages, so that energy distributions at zero-voltage can be compared to the results from high-voltage measurements. A similar comparison of MoS measurements at -18.6 kV and -9.3 kV already indicated that the contribution of the angular spread to the observed transmission function is negligible in the used setting (section 4.5.6).

Figure 4.55 shows transmission function measurements that were performed at $U_{spec} = -18.6$ kV (nominal setting) and $U_{spec} = -200$ V (“zero-voltage”). For the high-voltage measurement, the magnetic field in the analyzing plane was increased to $B_{min}^+ = 0.9$ mT to increase the sensitivity to the angular spread³⁹. Both measurements used the zero-angle setting $\alpha_p = 0^\circ$ and were performed at otherwise nominal settings (magnetic fields, UV light source). As discussed earlier, the acceleration voltage of the electron source was reduced to $U_{acc} = 100$ V in the zero-voltage setting. Although this results in an extremely large angular spread of the electrons due to the missing electric acceleration field, this effect is not relevant here since the angular spread does not contribute to the transmission function at zero-voltage. The figure shows that the transmission functions for both voltage settings overlap almost exactly, which is also the case for the underlying energy distributions that were determined using the analytical transmission model. To include the angular distribution of the electrons, a mean pitch angle $\hat{\theta} = 2^\circ$ with an angular spread $\sigma_\theta = 1^\circ$ was used in the model. The energy parameters (mean energy \hat{E} , energy spread σ_E) are consistent between the different settings. The results are compared in table 4.21, where \hat{E}^0 and σ_E^0 refer to the zero-voltage case.

39. The higher field results in an energy resolution of 3.28 eV at the main spectrometer, so that changes in pitch angle have a larger effect on the observed transmission functions.

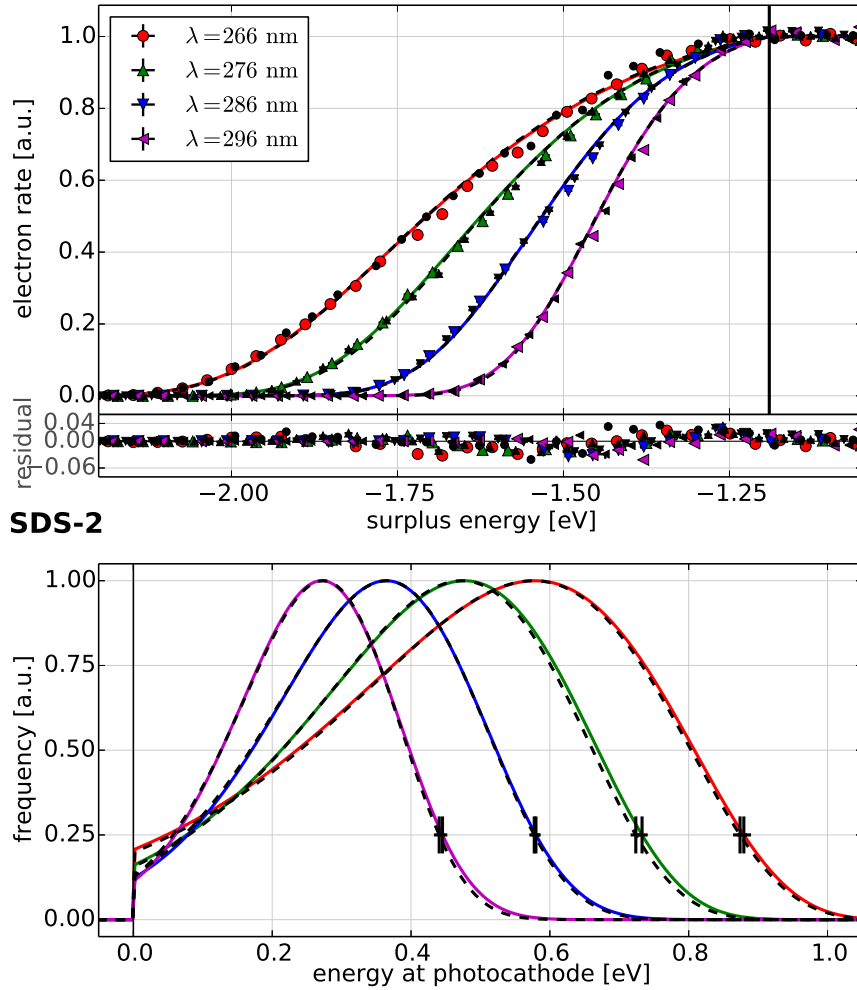


Figure 4.55.: Energy spread with different wavelengths at the SDS-2 setup. The plot shows transmission functions at different wavelengths $\lambda = 266$ nm to 296 nm with the gold photocathode at $\alpha_p = 0^\circ$. The measurement was performed at nominal high voltage ($U_{spec} = -18.6$ kV, $U_{acc} = 5$ kV) and at increased magnetic field ($B_{min} = 0.9$ mT). The smaller black data points and the dashed lines show the zero-voltage measurements from figure 4.53 for comparison. This allows to investigate the effect of the angular spread, which contributes to the observed transmission function in the high voltage setting. The plot shows that the transmission functions observed at high voltage and zero-voltage are in full agreement for the investigated wavelengths. No systematic deviation due to the angular spread is seen in this measurement series, which confirms results from similar MoS measurements at reduced voltage (section 4.5.6).
Runs: 23208,23209,23210,23211

These results completely verify the approach that was used in the MoS measurements, where the energy distributions for later analysis were determined from high-voltage measurements. It is therefore possible to determine the energy distribution of the produced electrons with sufficient accuracy by measuring transmission functions at high voltage. Dedicated zero-voltage measurements are not required to determine the energy spread and related parameters of the electron source, since the contribution of the angular spread to the transmission width is marginal due to the good energy resolution of the spectrometer. Note that this is only valid for an electron source that achieves angular selectivity with

a small angular spread, so that a zero-angle measurement at $\alpha_p = 0^\circ$ produced pitch angles $\theta \approx 0^\circ$ in the spectrometer entry magnet. Larger pitch angles will affect the transmission function and diminish the accuracy of the measurement. Furthermore, this approach only works if the energy spread of the electrons fully dominates the transmission function, as otherwise the angular spread becomes more relevant. This was not investigated here, since only measurements at small wavelengths (266 nm) were compared, where the achieved energy spread is rather large. One also needs to assume an angular distribution to describe the observed transmission function with the analytical model, from which the energy distribution can be derived. Fortunately, the analytical model is not overly sensitive to the actual angular distribution at small pitch angles, so that the assumed angular distribution does not have a significant effect on the fit result.

Conclusively, although it is possible to determine the energy distribution directly from a measurement at nominal high voltage, one needs to include many assumptions about the working principle and the characteristics of the electron source. It is therefore advised to not only rely on high-voltage measurements, especially if accuracy of the results is crucial (e. g. to determine the spectrometer transmission properties). A better approach is to use the high-voltage measurements in addition to zero-voltage runs, e. g. to perform stability monitoring of the energy distribution (and the photocathode work function) on a regular basis.

Table 4.21.: Comparison of energy distributions for Au photocathode at different voltage settings.

λ	χ^2/ndf	\hat{E}	σ_E	$\hat{E} - \hat{E}^0$	$\sigma_E - \sigma_E^0$
265.8(20) nm	1.73	0.493(4) eV	0.290(14) eV	0.000(8) eV	0.01(3) eV
275.8(20) nm	4.25	0.424(3) eV	0.216(10) eV	0.003(6) eV	0.00(2) eV
285.8(20) nm	2.76	0.339(3) eV	0.156(7) eV	0.003(6) eV	0.00(2) eV
295.8(20) nm	3.27	0.258(3) eV	0.118(6) eV	0.002(6) eV	0.00(2) eV
weighted average:				0.003(1) eV	0.01(1) eV

Angular spread

After the energy distribution of the produced electrons has been determined by measurements at zero- or high voltage (see above), the observed transmission functions can be investigated with the analytical model to determine the angular distribution as well. This approach uses the energy distribution that was determined for a given wavelength and the pre-determined position of the transmission edge as input to the analytical model, from which the parameters of the angular transmission are determined in a fit.

Figure 4.56 shows transmission functions that were measured at high voltage ($U_{spec} = -18.6$ kV) with increased magnetic field ($B_{min}^+ = 0.9$ mT) and at zero-angle ($\alpha_p = 0^\circ$) with different wavelengths $\lambda = 265.8$ nm to 295.8 nm and otherwise nominal settings. The measurements investigated here are the same runs as shown in figure 4.55, but a different fit model is applied here to determine the angular distribution. The fit results are given in table 4.22. Note the rather large uncertainties for the angular parameters (mean pitch angle $\hat{\theta}$, angular spread σ_θ) that are determined by the MCMC fit. This is caused by the small contribution of the angular distribution to the transmission function at

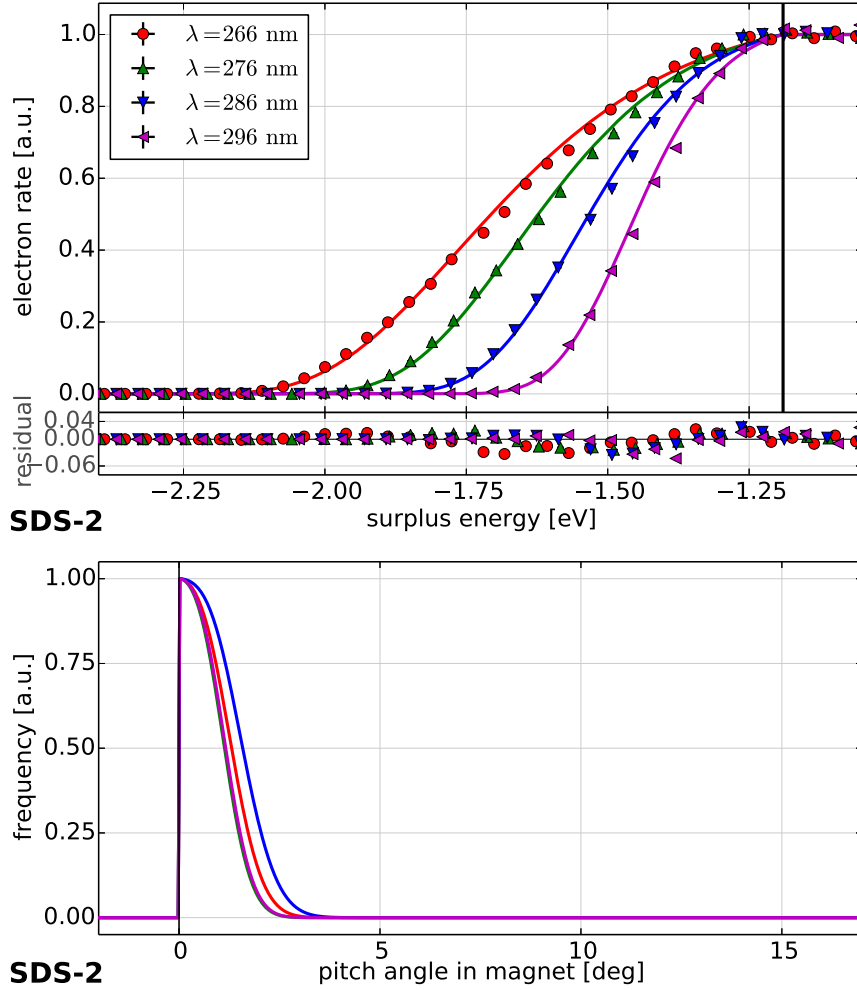


Figure 4.56.: Angular spread with different wavelengths at the SDS-2 setup. The plot shows transmission functions at different wavelengths $\lambda = 266$ nm to 296 nm with the gold photocathode at $\alpha_p = 0^\circ$. The measurement was performed at nominal high voltage with increased magnetic field ($U_{spec} = -18.6$ kV, $U_{acc} = 5$ kV, $B_{min}^+ = 0.9$ mT). Similar to the zero-voltage measurements (figure 4.53), the transmission width decreases with larger wavelengths. The similarity between the measurements at different voltages indicates that the influence of the angular spread is extremely small at the zero-angle setting. The transmission functions are again well described by the analytical transmission model (4.10). Note that in contrast to figure 4.55 which shows the same data sets, the fit here was performed with an energy distribution that was determined from corresponding zero-voltage measurements. The bottom plot shows the underlying angular distributions that were determined from the analytical model. The obtained angular spread and the mean pitch angle of the produced electrons is comparable between the different wavelengths, which indicates that the UV wavelength does not affect the angular distribution of the electrons. Runs: 23208,23209,23210,23211

zero-angle that has been discussed earlier. A more detailed discussion of this systematic effect is given in section 4.9.

The determined mean angle $\hat{\theta}$ and the angular spread σ_θ are consistent for the different wavelengths. This is expected since the angular distribution does not depend on the wavelength of the UV light, in

contrast to the energy distribution of the emitted electrons. The angular spread is generally small at the zero-angle setting, with an average value of $\bar{\sigma}_\theta = 0.69(4)^\circ$. The small angular spread is interesting for the discussion above, where it was argued that the energy distribution can be determined from a high voltage measurement due to the negligible effect of the angular spread. One can estimate what effect a given angular spread has on the observed transmission function. Since the electron pitch angles are collimated towards the analyzing plane of the spectrometer, the effective energy spread at this position depends on the angular distribution of the electrons,

$$\Delta E_\perp^{max} = E_0 \cdot \sin^2(\hat{\theta} + \sigma_\theta) \cdot \frac{B_{min}^+}{B_{PS2}}, \quad (4.88)$$

where $\hat{\theta}$ and σ_θ describe the mean pitch angle and the angular spread in the spectrometer entry magnet (at $B_{PS2} = 4.5$ T in this case), $E_0 \approx 18.6$ keV is the electron energy in the magnet, and $B_{min}^+ = 0.9$ mT the magnetic field in the analyzing plane. With a mean pitch angle and angular spread of 2° , the effective energy spread in the analyzing plane is only $\Delta E_\perp^{max} \approx 7$ meV even with the increased magnetic field. This is small compared to the actual energy spread of the electrons at small wavelengths ($\sigma_E \approx 300$ meV, see above). Hence to yield an observable effect in this setting, the value $\hat{\theta} + \sigma_\theta$ would need to be larger than 10° (resulting in an effective energy spread of $\Delta E_\perp^{max} = 112$ meV = $\mathcal{O}(\sigma_E)$). At larger wavelengths, however, where the energy spread reduces significantly, the value ΔE_\perp^{max} is comparable to the energy spread already at small values of $\hat{\theta}$ and σ_θ . Consequently, the observed transmission function becomes more sensitive to the angular distribution even at zero-angle $\alpha_p \approx 0^\circ$.

This result further establishes the result from the previous section, where it was found that the effect of the angular spread on the transmission width is negligible for the zero-angle setting if the energy spread of the electrons is large, i. e. for measurements performed with the laser at $\lambda = 266$ nm (nominal setting). For measurements at different settings, however, one must consider the angular spread in the analysis as well. This is possible in the analytical model, which includes the angular distribution of the electrons. It should be noted that the best accuracy is always achieved by performing measurements at zero-voltage, where the angular spread does not affect the transmission function regardless of the source characteristics.

Table 4.22.: Measured angular distributions for Au photocathode at different wavelengths.

λ	χ^2/ndf	$\hat{\theta}$	σ_θ
265.8(20) nm	1.72	0.6(5) $^\circ$	0.7(5) $^\circ$
275.8(20) nm	4.18	0.5(10) $^\circ$	0.6(9) $^\circ$
285.8(20) nm	2.75	0.8(6) $^\circ$	0.8(6) $^\circ$
295.8(20) nm	3.43	0.6(5) $^\circ$	0.6(5) $^\circ$
weighted average:		0.65(6) $^\circ$	0.69(4) $^\circ$

Angular selectivity

In addition to a small energy spread of the emitted electrons, angular selectivity is another key feature of the electron source. To precisely determine the spectrometer transmission properties, the electron source must produce electrons with selected pitch angles and with a small angular spread. The angular

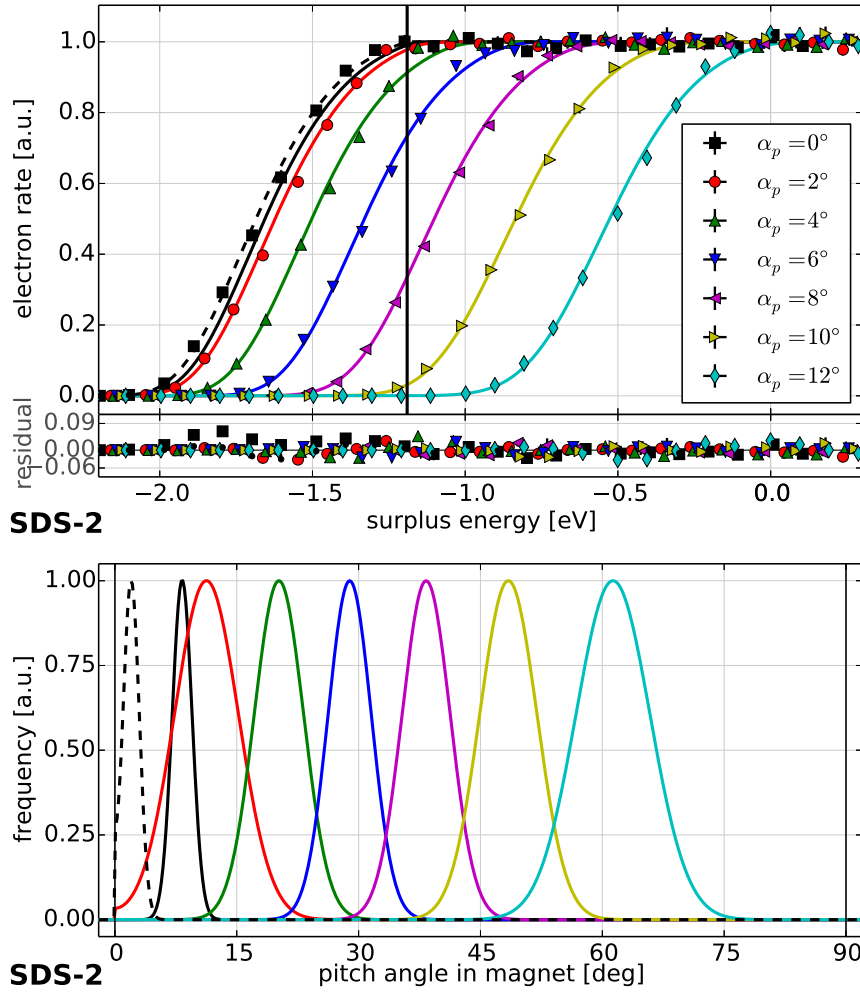


Figure 4.57.: Angular distributions with different plate angles at the SDS-2 setup. The plot shows transmission functions at different plate angles $\alpha_p = 0^\circ$ to 12° with the gold photocathode at $\alpha_{az} = 0^\circ$ and nominal spectrometer settings ($U_{spec} = -18.6$ kV, $U_{ana} = 5$ kV, $B_{min} = 0.38$ mT). The measurements were performed with the laser ($\lambda = 266$ nm), for which an energy distribution has been determined beforehand in a zero-voltage measurement. As expected, the transmission functions shift towards larger surplus energies with increasing plate angle. The observed shift corresponds to the energy resolution of the spectrometer (4.89). If one considers that the $\alpha_p = 12^\circ$ setting produces pitch angles $\theta \approx 60^\circ < \theta_{max}$, the shift is in agreement with the expected energy resolution (4.90). The bottom plot shows the underlying angular distribution that were determined by the analytical transmission model (4.10). Since electrons with $\theta \geq \theta_{max} = 70^\circ$ are magnetically reflected at the pinch magnet, the investigated range is limited to θ_{max} and larger pitch angles up to 90° are not observed here.

Runs: 22475,22481,22480,22479,22478,22477,22476

distribution of the electrons can be determined from transmission function measurements, again using the analytical transmission model. Earlier measurements at the MoS setup verified that the electron source achieves angular selectivity with an angular spread of better than 6° (section 4.5.6).

Figure 4.57 shows transmission functions that were measured at nominal settings with high voltage ($U_{spec} = -18.6$ kV) and at different plate angles $\alpha_p = 0^\circ$ to 12° with $\alpha_{az} = 0^\circ$. The measurements

used the laser as a light source (266 nm, 100 kHz/8 A). The energy distribution of the electrons for this setting has been determined beforehand (see above) and is used in the analytical model. As expected, the observed transmission functions show a shift towards higher surplus energies for increasing pitch angle, which results from larger pitch angles θ that are achieved in the spectrometer entry magnet. For the different values of α_p the transmission functions are clearly separated, indicating that angular selectivity is achieved. The surplus energy shift between $\alpha_p = 0^\circ$ and $\alpha_p = 12^\circ$ in this measurement series is $\Delta U_\theta = 1.14(3)$ eV.

Table 4.23 lists the corresponding fit results with the angular parameters – mean pitch angle $\hat{\theta}$ and angular spread σ_θ – that are determined by the analytical model. The table also shows the effective shift of the transmission function ΔU_θ , which corresponds to the distance of the transmission edge at a given setting of α_p to the reference value 0 eV (zero-angle, $\Delta U_\theta = 0$). It is not entirely clear why the pitch angle $\hat{\theta} \approx 8^\circ$ for the $\alpha_p = 0^\circ$ setting is substantially larger than expected⁴⁰, although this can be explained by the aforementioned insensitivity of the analytical model to the angular distribution for small pitch angles. This likely causes the fit to yield a larger value for $\hat{\theta}$, as this parameter does not have a large effect on the outcome at this setting. Assuming a fixed angular distribution with $\hat{\theta} = 2^\circ$ and $\sigma_\theta = 1^\circ$, one can achieve a better match to the measurement data, reducing the χ^2 value from 3.75 to 1.31; this is shown at the bottom of the table. This result is in better agreement with the expectation that $\alpha_p = 0^\circ$ produces a minimal pitch angle $\hat{\theta} \gtrsim 0^\circ$. Using this model, the observed shift of the transmission function increases to $\Delta U_\theta^* = 1.17(1)$ eV.

The observed transmission function shift corresponds to the energy resolution of the main spectrometer. The measurement result can thus be compared to the expected value that results from the magnetic field setting. With a magnetic field of $B_{min} = 0.38$ mT at the analyzing plane and $B_{PS2} = 4.5$ T at the spectrometer entrance, one would expect an energy resolution of 1.49 eV according to (4.64). However, at the SDS-2 setup one must consider the magnetic reflection at the pinch magnet ($B_{max} = 5.1$ T), which cuts off electrons with pitch angles $\theta > 70^\circ$ from the transmission function (cmp. section 2.2.2). The resulting energy resolution is then

$$\Delta E = qU_{ana} \cdot \frac{B_{min}}{B_{max}} = qU_{ana} \cdot \frac{B_{min}}{B_{PS2}} \cdot \sin^2 \theta_{max} = 1.39 \text{ eV} \quad \text{with } \theta_{max} = \arcsin\left(\frac{B_{PS2}}{B_{max}}\right) = 69.9^\circ. \quad (4.89)$$

The expected value is thus considerably larger than the observed shift of 1.17(1) eV. This is explained by the fact that the measurement does not cover the complete range of pitch angles up to $\theta = \theta_{max} = 69.9^\circ$ in the entry magnet, but only reaches angles up to 61.3° according to table 4.23. To compare the measurement result with the expected energy resolution, one can modify (4.89) to use the maximal angle that was achieved in the measurement, which yields

$$\Delta E^* = qU_{ana} \cdot \frac{B_{min}}{B_{PS2}} \cdot \sin^2 61.3(4)^\circ = 1.21(1) \text{ eV}. \quad (4.90)$$

This value is still somewhat larger than the observed shift of 1.17(1) eV, but is in general agreement to the measurement result. The observed discrepancy is 0.04(2) eV.

The achieved angular spread σ_θ is comparable to the MoS results. At the SDS-2 setup, the angular spread ranges from 1.5° to 4.5° , depending on the pitch angle $\hat{\theta}$. The increase in angular spread with larger pitch angles is caused by the adiabatic transformation (4.55) of the electron pitch angle towards the magnet, which has a nonlinear behavior due to the arcsin-term.

40. At this zero-angle setting, a pitch angle close to 0° should be achieved.

This measurement series shows that the electron source is able to produce electrons with well-defined pitch angles and a small angular spread of less than 5° at the SDS-2 setup, and thus confirms the results from the MoS measurements. This allows to use the electron source to investigate the transmission properties of the main spectrometer with high accuracy, and to determine the retarding potential U_{ana} and the magnetic field B_{min} in the analyzing plane. The results of these commissioning measurements are discussed in [Erh16].

Table 4.23.: Measured angular distributions for Au photocathode at different plate angles.

α_{az}	α_p	χ^2/ndf	$\hat{\theta}$	σ_θ	ΔU_θ
0°	0°	3.75	8.3(6)°	1.2(10)°	0.03(2) eV
	2°	0.71	11.3(9)°	3.9(18)°	0.06(3) eV
	4°	1.52	20.2(2)°	3.0(7)°	0.18(1) eV
	6°	0.59	28.9(2)°	2.7(5)°	0.35(1) eV
	8°	1.01	38.3(2)°	3.0(3)°	0.58(1) eV
	10°	0.79	48.4(2)°	3.5(3)°	0.85(1) eV
	12°	1.64	61.3(4)°	4.5(4)°	1.17(1) eV
	* 0°	1.31	2.0°	1.0°	0 eV

Produced pitch angles

Angular selectivity allows to produce electrons with well-defined pitch angles by tilting the electron source against the magnetic field, i. e. by varying the plate tilt angle α_p . The dependency between the pitch angle θ in the magnet and the tilt angle α_p can be described by a model (4.55) that considers the adiabatic transformation of the pitch angle between the electron source and the spectrometer entry magnet. This model was derived in section 4.5.5, and it was shown that it is in agreement with the MoS measurement results.

Figure 4.58 shows the pitch angles $\hat{\theta}$ (which were determined in the section above from the analytical transmission model) in dependency of the plate angle $\alpha_p = 0^\circ$ to 12° . Except for the data point at $\alpha_p = 0^\circ$ where the determined pitch angle is substantially larger than expected, the observed dependency is in good agreement with the fit model (4.55).

Magnetic reflection at the spectrometer entry magnet is reached at $\alpha_p \approx 14^\circ$; this corresponds to the point where θ reaches 90° . The higher magnetic field at the pinch magnet results in an additional cut-off of pitch angles above $\theta_{max} = 69.9^\circ$ according to (4.89), as indicated by the shaded area in the figure. Hence, only electrons with pitch angles $\theta < \theta_{max}$ in the entry magnet can be transmitted to the detector. The maximal plate angle that still emits observable electrons therefore reduces to $\alpha_{max} = 13.0(10)^\circ$, which is indicated by the dashed vertical line. This result is in agreement with the reflection angle of $13.09(2)^\circ$ that was observed in a magnetic reflection measurement for $\alpha_{az} = 0^\circ$ (see section 4.6.4).

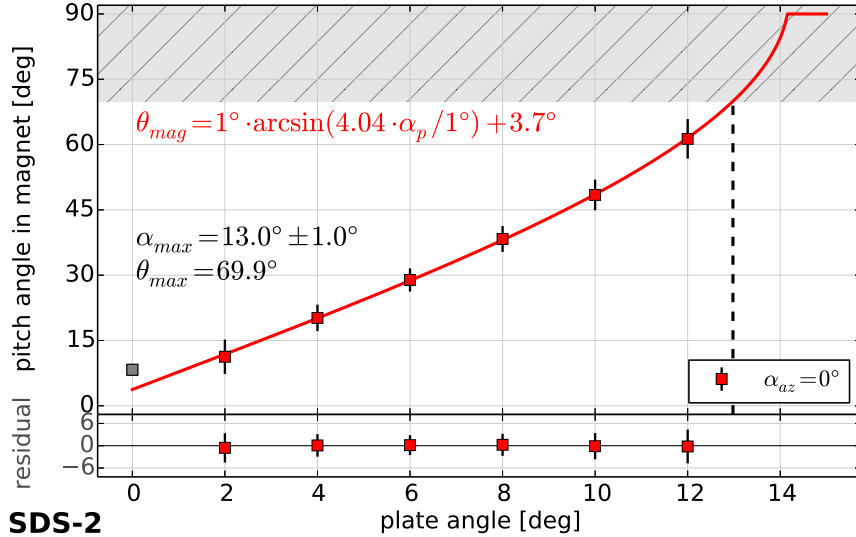


Figure 4.58.: Produced pitch angles with different plate angle at the SDS-2 setup. The plot shows the produced pitch angles in the spectrometer entry magnet θ in dependency of the plate angle α_p for the gold photocathode at $\alpha_{az} = 0^\circ$. The pitch angles were determined by fitting transmission functions with the analytical model (4.10) (table 4.23). The observed behavior is described by a model (4.55) that is based on the adiabatic transformation of the pitch angle. The non-linear dependency is caused by the arcsin-term in this model. The shaded area at the top indicates pitch angles $\theta \geq \theta_{max} = 69.9^\circ$ that are magnetically reflected at the pinch magnet. The reflection angle α_{max} up to which electrons are transmitted to the detector therefore shifts to a smaller value, as indicated by the dashed vertical line. The obtained value of $\alpha_{max} = 13.0^\circ$ is in agreement with magnetic reflection measurements, where a value of 13.1° was determined (cmp. figure 4.50). Runs: 22475–22481

4.6.6 Photocathode work function

The Fowler method allows to determine the work function of the photocathode that is used in the electron source (see section 4.2.3 and 4.4). This approach has been employed in earlier measurements, e. g. at the MoS setup where a work function of $\Phi_{MoS} = 3.777 \text{ eV} \pm 0.026 \text{ eV}(\text{sys}) \pm 0.008 \text{ eV}(\text{stat})$ was found for the gold photocathode. This value is significantly smaller than the reference values around 5 eV [Eas70], which is explained by effects like surface impurities that decrease the observed work function. In the SDS-2 measurements, a silver photocathode was used in the beginning of the measurement phase until it was replaced by a gold photocathode during a maintenance break (see section 4.6.7). Although this was unfortunate for the planned measurements, it allowed to perform several work function measurements and to compare the different photocathode materials in the same setup.

Silver photocathode

Figure 4.59 shows the work function measurement for the silver photocathode, which was performed in 11/2014. The measured was performed at zero-voltage at the spectrometer and reduced acceleration voltage ($U_{spec} = -200 \text{ V}$, $U_{acc} = 100 \text{ V}$, $U_{dip} = 3 \text{ kV}$). Since the measurement is only based on counting the number of emitted electrons, it is expected that the spectrometer and source settings do not influence the measurement result. The electron yield was determined by normalizing the observed

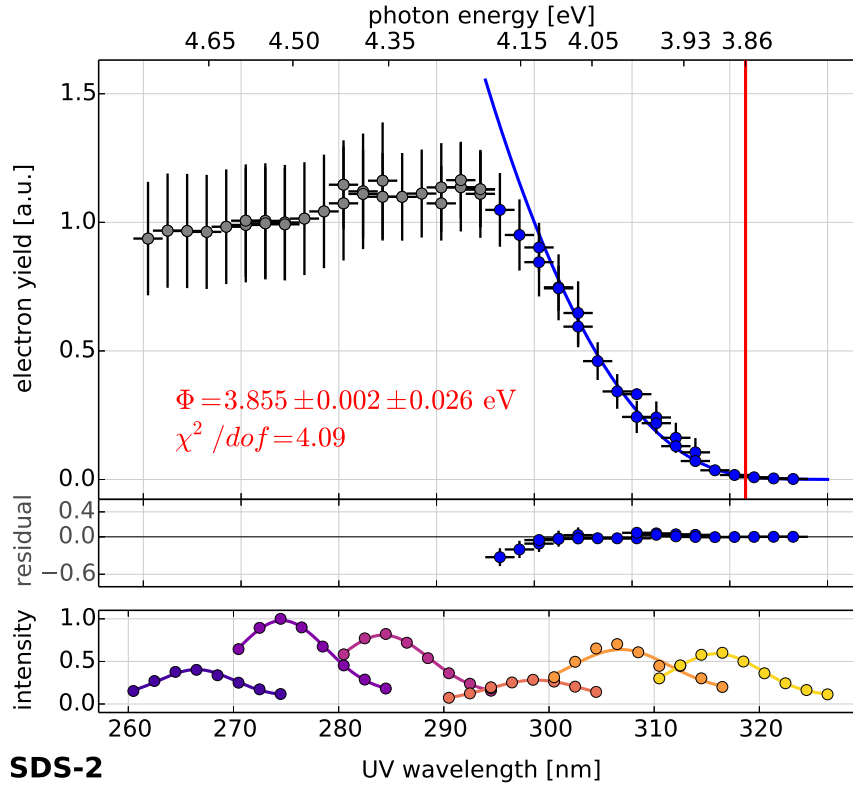


Figure 4.59.: Work function measurement with Ag photocathode at the SDS-2 setup. The plot shows a measurement of the electron yield in dependency of the wavelength, which allows to determine the work function of the silver photocathode in an *in situ* measurement following the Fowler method [Fow31]. The measurement data is well described by the Fowler model (4.32) at wavelengths near the work function threshold ($\lambda \gtrsim 295$ nm). The resulting work function is $\Phi = 3.855(2)$ eV, which is considerably lower than the reference value of 4.2 eV for a clean silver surface under laboratory conditions. The deviation can be explained by surface effects that modify the work function (see section 4.2.4). In case of the silver photocathode, the measured work function is likely affected by the silver oxide layer on the surface that is expected to form after exposure to ambient air (e. g. during photocathode installation). The observed discrepancy between Fowler model and measurement data at small wavelengths is consistent with earlier observations at the MoS setup (figure 4.41).

Runs: 20763–20813

electron rate to the light intensity that is monitored by a photodiode, taking into account additional corrections that result from switching between different UV-LEDs. This procedure is explained in section 4.4. The data for wavelengths above 295 nm is described accurately by the Fowler model of the electron yield (4.32). The fit yields a work function of

$$\Phi_{SDS2,Ag} = 3.855 \text{ eV} \pm 0.026 \text{ eV}(\text{sys}) \pm 0.002 \text{ eV}(\text{stat}) \quad (4.91)$$

for the silver photocathode. The given systematic uncertainty corresponds to the filter width of the monochromator and the uncertainty of the wavelength calibration, as discussed in section 4.5.8.

The observed work function is significantly smaller than values expected from independent reference measurements, which are around 4.0 eV for a clean surface under laboratory conditions at ultra-high vacuum [Eas70]. Furthermore, the work function is slightly larger than the work function for a gold photocathode that was determined at the MoS setup, although for a gold surface one would expect

a higher work function. This deviation can again be attributed to surface effects, which result in a reduction of the work function. The observed difference of roughly 0.15 eV w. r. t. to the reference value is smaller than the observed difference for a gold photocathode (1.3 eV at the MoS). This can be explained by the fact that silver, in contrast to gold, builds an oxide surface layer when exposed to air. It is believed that the silver oxide further modifies the surface conditions, which increases the work function and reduces the observed deviation to the reference value [She92]. Hence, the work function observed in this *in situ* measurement is only slightly smaller than the expected value for a clean surface.

The observed deviation between the Fowler model and the measured electron yield for smaller wavelengths is a result of additional effects that occur at higher photon energies $h\nu = hc/\lambda$, which are not considered in the Fowler model. These effects were explained in section 4.5.8, and a similar behavior was observed at the MoS setup. Since the Fowler function is fully dominated by the electron yield at wavelengths close to the work function threshold, these deviations do not affect the accuracy of the fit result. The data points for wavelengths $\lambda < 295$ nm are therefore excluded from the analysis.

It should be noted that if the electron source is operated continuously under vacuum conditions, the silver oxide layer could significantly decrease over time. If this is the case, one would expect a time-dependency of the work function (and thus, the electron yield at a given wavelength). Such a time-dependency could be determined by repeated work function measurements in regular intervals. This was not considered in the SDS-2 measurement phase due to time constraints, and eventually the silver photocathode was replaced during the maintenance break in 01/2015.

Gold photocathode

After the photocathode replacement, the work function of the new gold photocathode was determined in 03/2015 again using the Fowler method. Figure 4.60 shows the measurement, which was now performed at nominal spectrometer and source settings ($U_{spec} = -18.6$ kV, $U_{acc} = 5$ kV, $U_{dip} = 3$ kV). The resulting work function can be compared directly to the MoS result, where another gold photocathode was investigated at the same electromagnetic conditions at the electron emission spot. Indeed, the observed behavior is similar to the MoS measurement and also to the measurement discussed above with a silver photocathode. Again, one notices a deviation to the Fowler model (4.32) for small wavelengths $\lambda < 295$ nm for the reasons mentioned earlier. The wavelength where this deviation comes into place is larger than at the MoS setup (about 270 nm, cmp. figure 4.41), which is attributed to the fact that a different photocathode is used here (although the material is the same). The work function that results from this measurement is

$$\Phi_{SDS2,Au} = 3.764 \text{ eV} \pm 0.024 \text{ eV}(\text{sys}) \pm 0.002 \text{ eV}(\text{stat}), \quad (4.92)$$

which is in excellent agreement to the MoS result and consistent within the given uncertainties.

The two work function measurements with a gold photocathode under similar conditions confirm that the observed discrepancy to the reference value of 4.2 eV to 5.1 eV [Eas70, She92] is not an issue with the measurement procedure or the analysis, but a physical effect that results from changes in the surface conditions of the photocathode. The fact that the work functions for silver and gold do not show a large difference – which would be expected from the reference values for a clean surface – indicates the photocathode used in the electron source is fully dominated by surface effects such as impurities, which were discussed in section 4.2.4. The work functions determined using the Fowler

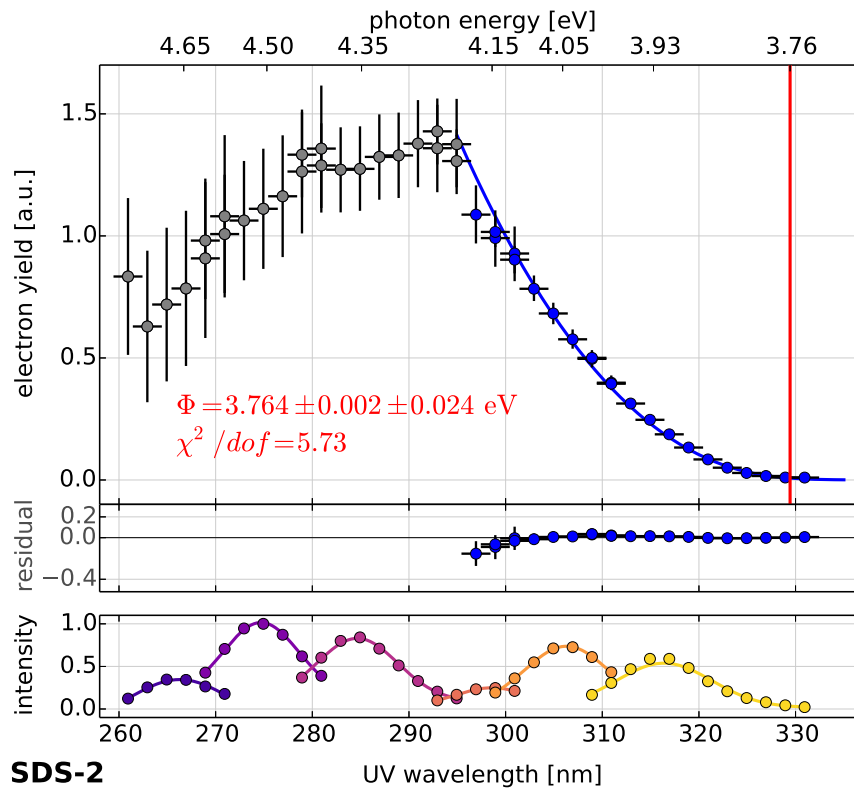


Figure 4.60.: Work function measurement with Au photocathode at the SDS-2 setup. The plot shows a second *in situ* work function measurement for the gold photocathode that was performed a few months after the measurement shown in figure 4.59. The resulting work function is $\Phi = 3.764(2) \text{ eV}$, which is comparable to a MoS measurement where a work function of $3.777(8) \text{ eV}$ was determined for a gold photocathode. Note that the SDS-2 setup used a new gold photocathode that is different from the one used at the MoS setup. It was installed after the maintenance break in 02/2015. The obtained value is considerably below the reference value of 5.1 eV for a cleaned and prepared gold surface. This is in agreement with other measurements and can be explained by surface effects. The deviation between Fowler model and data points at small wavelengths is expected and consistent with earlier observations.

Runs: 23509–23554

model are also consistent with results from an alternative method, where the work function is instead determined directly from the observed energy distribution of the electrons (see below).

Alternative method

As a complementary method to the Fowler measurement, the work function can be determined from the energy distribution of the emitted electrons. The method is based on the relation between electron energy E_e , photon energy $h\nu$ and work function Φ of the surface,

$$0 < E_e \leq E_{max} = h\nu - \Phi. \quad (4.93)$$

This approach was established in the analysis of the MoS measurements, and it was shown that it yields results that are consistent with the direct measurement using the Fowler method (see section 4.5.8).

The same method can be applied to the energy distribution measurements that were performed at the SDS-2 setup, using the data that was analyzed earlier in section 4.6.5. 4.24 shows the determined work functions for the silver photocathode and table 4.25 for the gold photocathode. The value Φ^\dagger corresponds to the result from the alternative method, which is compared to the Fowler result Φ in the tables. The weighted average of the results for different UV wavelengths yield a work function

$$\overline{\Phi^\dagger}_{SDS2,Ag} = 3.846 \text{ eV} \pm 0.020 \text{ eV(sys)} \pm 0.002 \text{ eV(stat)}, \quad (4.94)$$

$$\overline{\Phi^\dagger}_{SDS2,Au} = 3.749 \text{ eV} \pm 0.020 \text{ eV(sys)} \pm 0.001 \text{ eV(stat)}. \quad (4.95)$$

The given systematic uncertainties result from the analytical transmission model, which is discussed in section 4.9 below. These values are fully consistent with the Fowler results. Conclusively, both complementary methods can be used together to investigate the work function of the photocathode. The Fowler method allows to precisely determine the work function in an *in situ* measurement, which was shown to produce consistent results. The method based on the energy distribution provides a possibility for monitoring the work function stability at regular intervals without consuming extra measurement time (if typical transmission function measurements are performed).

As it was mentioned section 4.6.5, additional energy distribution measurements were performed at the SDS-2 setup with a larger step size during the transmission function run; these measurements are skipped here again for brevity. The analysis using this data yields an average work function of 3.751(1) eV for the gold photocathode, which is in full agreement with the result above.

Table 4.24.: Comparison of the determined work functions for a silver photocathode.

λ	$E_\gamma = h\nu$	χ^2/ndf	E_{max}	Φ^\dagger	$\Delta\Phi = \Phi^\dagger - \Phi$
264.3(22) nm	4.69(4) eV	1.53	0.789(7) eV	3.90(5) eV	0.04(8) eV
274.3(22) nm	4.52(3) eV	0.97	0.643(4) eV	3.88(3) eV	0.02(6) eV
284.3(22) nm	4.36(3) eV	0.78	0.490(4) eV	3.87(3) eV	0.01(6) eV
294.3(22) nm	4.21(3) eV	0.62	0.356(4) eV	3.85(3) eV	-0.01(6) eV
304.3(22) nm	4.07(3) eV	0.72	0.244(4) eV	3.83(3) eV	-0.03(6) eV
314.3(22) nm	3.94(3) eV	0.76	0.202(10) eV	3.74(4) eV	-0.12(7) eV
weighted average:				3.846(2) eV	-0.06(4) eV

Table 4.25.: Comparison of the determined work functions for a gold photocathode.

λ	$E_\gamma = h\nu$	χ^2/ndf	E_{max}	Φ^\dagger	$\Delta\Phi = \Phi^\dagger - \Phi$
265.8(20) nm	4.66(4) eV	3.28	0.874(8) eV	3.79(5) eV	0.02(8) eV
275.8(20) nm	4.50(3) eV	1.92	0.724(5) eV	3.78(4) eV	0.01(7) eV
285.8(20) nm	4.34(3) eV	4.80	0.578(5) eV	3.76(4) eV	-0.01(7) eV
295.8(20) nm	4.19(3) eV	0.61	0.441(6) eV	3.75(4) eV	-0.02(7) eV
305.8(20) nm	4.05(3) eV	6.17	0.320(3) eV	3.73(3) eV	-0.04(6) eV
315.8(20) nm	3.93(3) eV	3.18	0.228(7) eV	3.70(4) eV	-0.05(7) eV
weighted average:				3.749(1) eV	-0.03(2) eV

4.6.7 Stability issues

Despite the successful measurement phase at the SDS-2 setup, where the source was commissioned and characterized [Wie16] and important parameters of the main spectrometer could be determined [Kra16, Erh16, Bar16], the performance of the electron source was overshadowed by occasional stability problems. Especially after the first measurements at the beginning of the SDS-2 phase, serious issues with the high voltage stability of the source required to perform a maintenance break, before the source could be operated again. At the end of the SDS-2 measurements another breakdown occurred, which prevented to continue the planned measurements at high voltage. Due to the limited time available at this late stage of the SDS-2 commissioning phase, it was not possible to perform another maintenance break. Hence, the source could only be operated at reduced voltage for the remainder of the measurements.

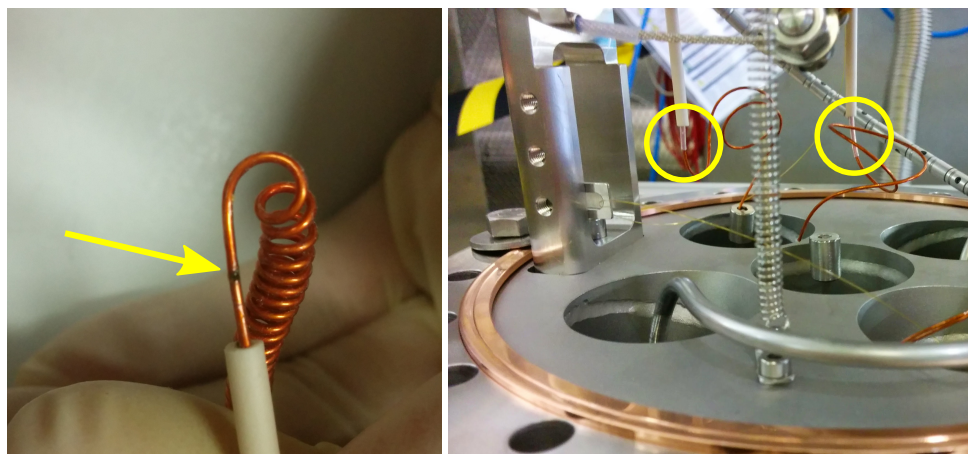


Figure 4.61.: Issues with Kapton-insulated high voltage wire at the electron source. The sharp ends of the ceramic insulators can break the thin Kapton insulation layer of the high voltage wire that are used inside the electron source. The setup was improved by adding another layer of Teflon tube between the Kapton wires and the ceramic insulators, as seen in the image on the right.

In the following, a short time line of the observed problems is given. The steps that were carried out during the maintenance break are discussed as well.

- **2014/10:** The source was installed at the main spectrometer and prepared for vacuum pump-down. A final pressure of $p = 4.2 \cdot 10^{-7}$ mbar was reached on November 7th, after which the valve between electron source and main spectrometer could be opened for the first time [Ran14].
- **2014/11:** The source was successfully conditioned for high-voltage operation by applying a voltage up to 25 kV (positive/negative polarity) on the plates. At this time it was not possible yet to perform measurements with the main spectrometer on high voltage. Hence, the first commissioning measurements were performed with $U_{start} \approx -200$ V.
- **2014/12:** Configuration problems with the high voltage system at the electron source prevented operation with $U_{start} \approx -18.6$ kV. The main reason was the interconnection between power supplies at the main spectrometer vessel and at the source setup, which resulted in a too large current flow observed at the back plate power supply (MCP, cmp. figure 4.25). The issues could be resolved by adjusting the setup accordingly, so that HV operation was possible from now on.

Unfortunately, on December 19th an extreme increase of the electron rate was observed when ramping the source voltage up to -18.6 kV, reaching more than 80 kcps at the FPD. This was only observed with the electron source electrically connected to the high voltage system. Furthermore, these electrons were emitted without any incident UV light on the photocathode, indicating a problem with the electrical system. Changes of the dipole voltage and the electron surplus energy showed no significant effect on the high rate.

Another high voltage conditioning was performed at the electron source, where stable operation was reached with 25 kV positive voltage on the source plates. With negative polarity like under nominal operation, voltage breakdowns occurred already at voltages of 5 kV or less. These problems could not be resolved by repeated conditioning attempts, and a maintenance break at the beginning of 2015 was deemed necessary.

- **2015/01:** To perform maintenance on the internal setup of the source, it was dismantled from the main spectrometer and the photocathode was replaced. The examination indicated that the photocathode material (silver) has been sputtered away, likely due to ion bombardment caused by electrons trapped at the electron source. High voltage conditioning was performed successfully with voltages up to 25 kV and -20 kV after re-assembling and re-mounting the source again.

After first test measurements with the new silver photocathode, more stability issues at high voltage were observed. Another on-site maintenance break showed a broken insulation of the Kapton wires that are used to connect the source plates to the HV feed-throughs at the source flange. It is believed that the sharp end of the additional ceramic insulation cuts into the Kapton layer when the source cage is tilted. The setup was therefore improved to include an additional layer of Teflon between the Kapton wire and the ceramic tube (figure 4.61).

Albeit the successful conditioning that was performed after resolving these issues, the electron source could not be brought back into operation at this time. The FPD observed an electron rate of around 2.5 kcps without any voltage on the electron source, that dropped to 500 cps with a small voltage on the dipole electrode. Since this behavior is unexpected, it was decided to dismantle the electron source completely and perform test measurements and maintenance in the test setup at WWU Münster. During this maintenance break, the photocathode was

replaced with a newly prepared gold cathode, which was used for the remainder of the SDS-2 measurements.

- **2015/02:** Performing an extended maintenance phase at the WWU Münster lab proved to be advantageous as the stability issues under high-voltage operation could be finally resolved (see below). The source was mounted again at the SDS-2 setup. After replacing a broken Kapton wire in the electron source, another conditioning was performed successfully which eventually allowed to redo the commissioning measurements with the electron source and carry out the planned measurements.

Although the electron source now could be operated as planned and measurements were running continuously, on some occasions measurements had to be restarted due to crashes of the ORCA software that controls the DAQ system and the experimental conditions (section 3.6). The actual issue causing these crashes could not be resolved during the SDS-2 measurements. It is believed that either the rather high electron rate of roughly 5 keps (in comparison with background measurements where the rate is typically below 1 cps) or the continuous variation of operational parameters through ADEI (e. g. the starting voltage) caused problems with the stability of the software. The crashes were especially problematic when they occurred during automated overnight measurements, which required the operators to get to the experimental site in order to restart the measurement.

- **2015/03:** The electron was in continuous operation after the maintenance break. On March 6th, after the source has been disconnected for overnight background measurements, new issues arose that made it impossible to reach nominal high voltage with the electron source. A drastic rate increase was observed after ramping the system to -18.6 kV: following some minutes of the expected low rate that is consistent with background, the observed rate at the FPD reached 2.5 keps without any incident light at the electron source. The high rate disappeared again when reducing the voltage, and the effect was observed consistently when ramping the voltage several times. This limited the following measurements to voltages between -200 V and -10 kV, where the observed rate was still small enough to allow continuous operation. The plan for the remaining measurements was adjusted accordingly.

Although the exact cause of this unexpected issue could not be determined, it is believed that the electron source was not disconnected properly from the high voltage system for the overnight break. If the source plates were still connected to the power supplies while the dipole voltage was correctly ramped down, a Penning trap could have been created at the electron source. Consequently, one or more Penning discharges could have occurred that have severe effects on the photocathode, as observed before. Since the valve to the main spectrometer was closed during the overnight measurements, these Penning discharges would have happened completely undetected by the operators. If this is the case, the electron source was likely affected by the discharges, causing issues similar to the ones observed at the beginning of SDS-2. Due to the limited time available at this point, it was decided to not perform another maintenance break, but perform the remaining measurements at a reduced voltage instead.

Maintenance break during SDS-2

The electron source was disassembled on January 23rd, 2015 and shipped back to WWU Münster afterwards for extended maintenance. The goal was to mount the source in a dedicated laboratory

test setup that was also utilized during development. All relevant parts of the source setup were exchanged before installation: the ceramic insulators at the plates, the PEEK insulators between the plates, and the Kapton wires for high voltage. The Kapton wires were partially insulated with a Teflon tube to protect the thin Kapton layer against the sharp edges of the ceramics. During a high-voltage conditioning cycle it was possible to reach 26 kV on both plates without any problems [BHO⁺15].

However, the detector at the test setup indicated strong field emission at voltages of -15 kV or less, which is in agreement to earlier measurements at the KATRIN site where similar effects were observed. At the nominal voltage of -18.6 kV, an electron rate of 140 kcps was measured at the test setup. Further examinations showed that the electrons are emitted not from the photocathode or the plate setup, but from somewhere close to the HV feed-throughs that are located behind the emission spot (if looking from the detector towards the source). The problem was eventually narrowed down to a contamination of the ceramic insulators of the feed-throughs that could be removed by thorough manual cleaning with Almecco and ethanol/isopropanol. Interestingly, the contamination on the ambient-air side of the system caused severe electron emission *inside* the setup, i. e. on the vacuum side. It is not clear which processes cause the observed effect, although it is assumed that short-term voltage fluctuations on the insulator surface that are caused by the contamination can couple into the feed-through and cause field-emission processes on the vacuum side.

Repeated measurements after the cleaning process showed that the issue was finally resolved, and a low electron rate of 0.2 cps was observed when the electron source was grounded. The rate was therefore decreased by 6 orders of magnitude by cleaning the outer surface of the HV feed-through insulators.

4.6.8 Summary

The commissioning of the electron source at the SDS-2 setup took place after a test phase at the MoS setup, which allowed to investigate many important characteristics of the device and verify the functionality of many components. During installation at the main spectrometer, the UHV manipulator and the electron source with the optical system, the HV setup etc. was integrated with the existing slow-control system to allow automated remote measurements. The source was also prepared for ToF measurements with the pulse electron beam, by integrating a reference trigger signal into the DAQ system that allows to determine the start time of the electrons. The complete source setup could be controlled via the ORCA software that also manages the data-taking and provides an interface to other systems, such as the detector and the DAQ or the HV system of the main spectrometer. The source was also integrated with a PCS 7 control system⁴¹ that handles critical components with safety implications like the vacuum system.

Unfortunately, serious stability issues were encountered after the first successful commissioning that took place in 11/2014. This required an extended maintenance break, during which the photocathode was replaced and the HV setup at the source was reworked. The source was shipped to WWU Münster to perform maintenance work and then re-installed at the SDS-2 setup in 02/2015, where the commissioning was performed again. Although not all planned measurements could be carried out due to the reduced measurement time after the maintenance break and new stability issues at the end of the SDS-2 phase, the electron source measurements overall were successful.

The source was commissioned and characterized in detail with many dedicated measurements, such as the investigation of the transmission function at different voltages and wavelengths. It was also utilized by other measurements, not only for the commissioning of the main spectrometer were the retarding potential and the magnetic field over the analyzing plane could be determined [Erh16], but also to investigate the influence of HV instabilities on the spectrometer properties and for tests of the post-regulation system [Kra16], or to verify the integrity of the inner-electrode system of the spectrometer [Bar16]. Other measurements examined a novel ToF measurement mode with time-variant electric field [Res17, Ful16] and studied the spectrometer transmission properties with a shifted analyzing plane [Dyb17]. The electron source was also used in combination with the magnetic pulse to investigate its timing characteristics (chapter 5 in this work).

41. Siemens SIMATIC PCS 7, <http://www.siemens.de/pcs7>

4.7 Particle-tracking simulations

To achieve a better understanding of the electron source and the electron-transport processes inside the device, particle-tracking simulations were carried out with the software *Kassiopeia* (section 3.3). These simulations allow to investigate the electromagnetic design of the electron source, and to determine the expected energy and angular distributions of the emitted electrons. While the energy spread is fully defined by the properties of the photocathode and the photoemission process (see section 4.2), the angular spread at the spectrometer entrance largely depends on the electromagnetic conditions at the source. Hence, one can assess the produced pitch angles through simulations. The simulation results also provide important input parameters for the measurement analysis, which was discussed earlier in this chapter.

The simulations focus on the SDS-2 setup, where the electron source was used for the commissioning of the main spectrometer. A detailed investigation of the electron acceleration and transport mechanisms at different electromagnetic conditions is presented in section 4.8. A smaller set of simulations was also performed for the MoS setup, in order to compare the results between the different setups and to better understand the measurement results from both systems. The electron source simulation geometry and the necessary configuration files have been implemented into the KASPER framework⁴².

In this section, the implementation of the electron source geometry into *Kassiopeia* with its relevant parameters and the analysis of the simulation results will be discussed.

4.7.1 Implementation into *Kassiopeia*

The advanced capabilities of *Kassiopeia* and the geometry toolkit *KGeoBag* (section 3.4) allows to create an accurate simulation model of the electron source. This model includes all relevant electrodes and has the ability to tilt the source cage against the magnetic field lines (figure 4.62). The simulation geometry that was developed for this thesis is based on a *computer-aided design* (CAD) drawings of the electron source. The design has been created in *Autodesk Inventor*⁴³ and was used for the development of the electron source [B⁺14b, Zac14, Val09].

For the simulations, the level of detail must be reduced significantly to avoid performance issues. Sections that are far away from typical electron trajectories, or sections that are closed off from the beamline, have no impact on the simulation results and can therefore be excluded in the geometry model. Other sections can often be simplified by neglecting details that are only relevant to the mechanical design, e. g. screws or wires. The electrode geometry therefore consists only of the vacuum chamber with beam tube, the grounded source cage with the plate setup, and the dipole electrode in front of the source. The geometry is discretized in order to compute electric fields with *KEMField* using the boundary-element method (section 3.5). Note that due to the half-shell design of the dipole electrode (which breaks axial symmetry) it is not possible to utilize approximations such as zonal harmonics, which would greatly improve the simulation performance. However, by utilizing GPU acceleration⁴⁴, the required computation time to evaluate electric fields can be significantly

42. KASPER is accessible via the KATRIN Git repository at <https://nuserv.uni-muenster.de/gitlab/katrin-git/kasper> (internal site).

43. Inventor – Mechanical design and 3D CAD software, <http://www.autodesk.com/products/inventor/>

44. The simulations presented here use OpenCL-based acceleration on a Nvidia Tesla C1060 graphics processing unit.

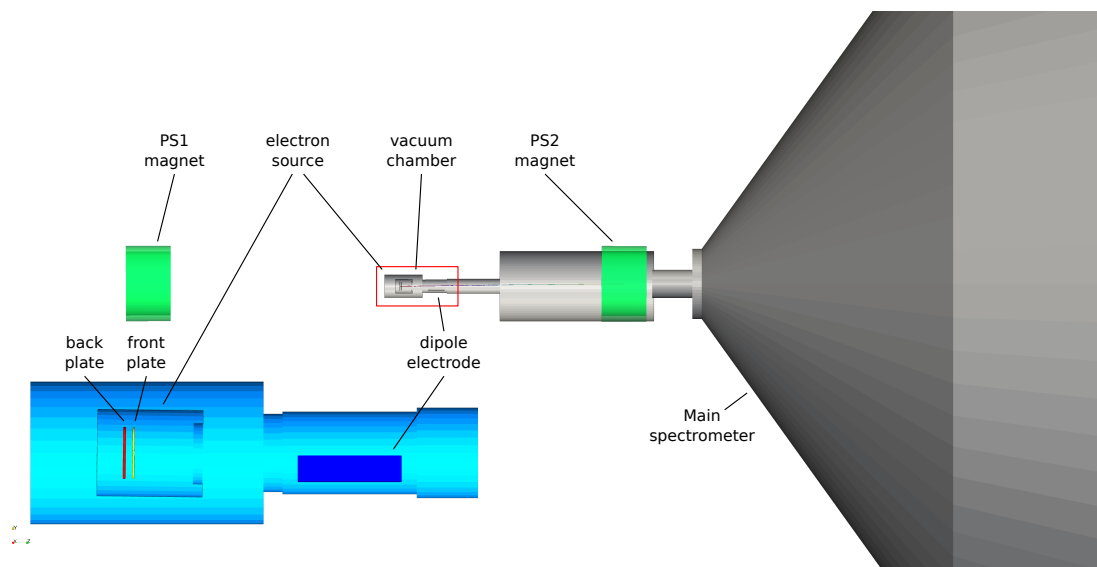


Figure 4.62.: Simulation geometry of the SDS-2 setup. The geometry is based on CAD drawings of the electron source (appendix A) and includes corrections from alignment measurements. The overall design resembles the experimental setup (figure 4.45) and includes the plate-tilt mechanism and the UHV manipulator. The electrode geometry has been simplified to include only relevant parts (e. g. the plate-capacitor setup), which improves speed and accuracy of the field computations. The tiltable source cage with the plate setup is placed inside the grounded vacuum chamber with the attached beam tube. The dipole electrode is included in this setup, which breaks axial symmetry. The complete electron source setup can be moved according to the UHV manipulator design (not shown here). In Kassiopeia simulations, electrons are started at the emission spot on the back plate (photocathode) and propagate towards the spectrometer entrance. The simulation stops at the center of the entry magnet (PS2 in case of the SDS-2 setup), where important parameters like the energy and angular distributions of the electrons can be evaluated.

reduced. This allows to generate sufficient statistics in Monte-Carlo simulations in a reasonable time frame⁴⁵.

Simulation geometry of the electron source

The geometry model is implemented with the XML configuration file format that is used throughout Kassiopeia. The individual geometric shapes are created in local coordinate frames, and then combined into assemblies where their relative position is defined. The assemblies typically resemble specific parts of the setup, such as the vacuum chamber. The geometry is mainly implemented with cylindrical surfaces, disks and annuli (i. e. disks with apertures). The dipole electrode is modeled by an extruded surface of an arc-shaped line segment (which allows to implement such an asymmetric shape), and the back and front plate of the electron source uses a combination of disk and annulus parts with rotated surfaces that model the rounded edges (fillets) of the plates. This accurate implementation is especially important for the front plate aperture, where the distance between electrode and electron trajectory is only a few mm.

⁴⁵. Depending on the simulation parameters, it typically takes between 30 s and 3 min to compute a single electron trajectory from the emission spot on the photocathode to the spectrometer entry magnet.

The individual shapes are combined into electrode groups that share a common electric potential. This uses the tagging system that is available in KGeoBag, which allows to specify the actual potential for a given group later in the configuration file and thus disentangles the geometry model from the simulation parameters. The different electrode groups are the *ground electrodes* (vacuum chamber, beam tube etc.), the *front and back plates*, and the *dipole electrode*. The voltage parameters of the electron source – $U_{start} = U_{back}$, $U_{front} = U_{back} + U_{acc}$, and U_{dip} – can thus be defined directly for each simulation run.

The electrode surfaces are discretized using the automated meshing system that is provided by KGeoBag (figure 4.63). The mesh parameters are defined for each geometric shape, so that the discretization level can be adapted to focus on electrode segments that have a larger influence on the simulation result (i. e. segments that are closer to the electron beam). This optimizes both the accuracy and the performance of the simulation. The charge densities of the electrode segments are then computed by the iterative GPU-accelerated Robin Hood algorithm (section 3.5) with a relative precision of 10^{-8} , which takes about 40 min typically for a given source geometry. Re-computation is necessary when the setup changes, e. g. when the plate tilt angle α_p is changed or when the source is moved by the UHV manipulator. Changes in the electric potentials often do not require a full re-computation, since it is possible to utilize the superposition principle.

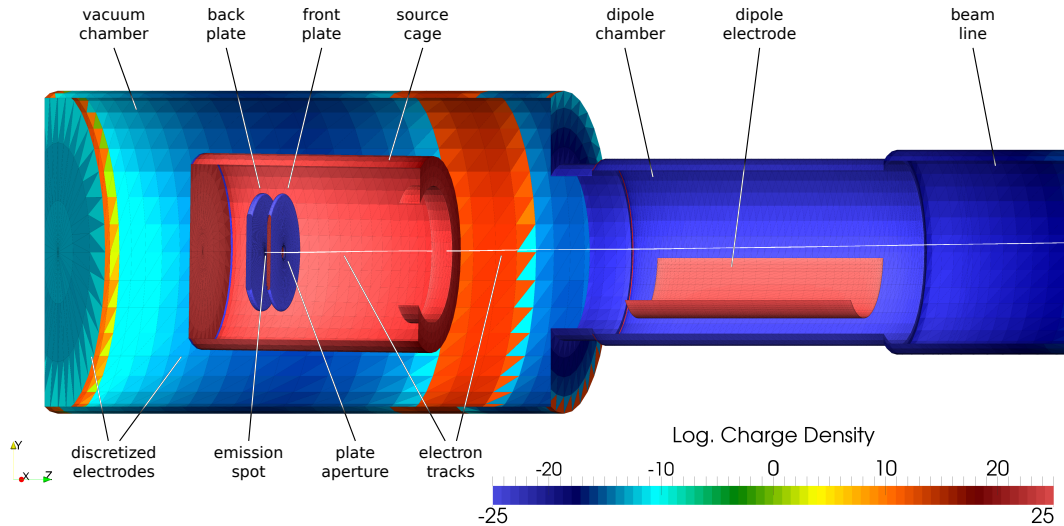


Figure 4.63.: Electrode geometry of the electron source. The image shows the discretized electrode geometry of the electron source (excluding the beam tube towards the spectrometer). The individual electrode segments are colored by their logarithmic charge density $\sigma^* = \text{sgn}(\sigma) \cdot \log(1 + |\sigma \cdot 10^{16} \text{ m}^2/\text{C}|)$ that was computed by KEMField with the Robin Hood algorithm (section 3.5). KEMField assumes a constant charge density on each segment; the level of discretization therefore affects the accuracy of the field computation if field gradients are present. To further improve the simulation accuracy, the electrode segments close to the electron trajectory are finer discretized. Note that the logarithmic coloring exaggerates the differences in charge density between the electrode segments; this coloring scheme was chosen to give a better representation of the KEMField results.

The source geometry that was used in this thesis features almost 40 000 discretized electrode segments in total, which are mostly distributed to the back and front plate and the dipole electrode, which have

the most significant effect on the simulation. The discretization has been optimized for accuracy by comparing simulations using different discretization parameters⁴⁶.

The geometric shapes are nested into so-called *assemblies*, which resemble the mechanical design of the electron source. For example, the back plate assembly uses two disk surfaces (front and back surface of the plate) that are connected by a rounded edge (fillet of the lateral surface). The nesting also follows the source design: The back and front plate assemblies are put into the grounded source cage assembly, which in turn is put into the vacuum chamber assembly. Similarly, the dipole electrode is nested into the dipole chamber that is connected to the vacuum chamber. The grounded cage with the plate setup can be tilted in two independent axes (horizontal and vertical), which allows to change the plate tilt angle α_p . The tilting is equivalent to the real electron source, so that measurement parameters can be applied directly to the simulation.

Similarly, the UHV manipulator that allows to move the source around the magnetic flux tube at the SDS-2 setup has been included in the geometry model. Changing the manipulator tilt angle moves the source along one independent circular path for each tilt axis. Dedicated alignment measurements were carried out at the SDS-2 setup to improve the accuracy of the simulations; these measurements have been included in the used geometry model. For the MoS setup, no accurate alignment data is available; however in this case, the alignment is less complicated since the UHV manipulator was not used in this setup and the source is always positioned central to the spectrometer axis.

Another important aspect of the simulations are the magnetic fields. The magnet geometry was already implemented in Kassiopeia for the MoS and SDS-2 setup, and could be re-used for the electron source simulations. At the SDS-2 setup, the magnetic field at the source is defined by the PS2 magnet at the spectrometer entrance and the PS1 magnet behind the electron source. The PS1 magnet was moved towards the source for the commissioning measurements, since it is required to contract the magnetic field lines so that the UHV manipulator movement covers the complete magnetic flux tube. The placement of the PS1 and PS2 magnets has been adjusted according to the alignment measurements. At the MoS setup, the magnetic field at the source is normally only defined by the spectrometer entry magnet. Since no alignment measurements are available, the magnet positioning in the existing model is assumed to be correct. To enhance the magnetic field at the photocathode in order to achieve conditions that are similar to the SDS-2 setup, an additional air coil⁴⁷ was used in the MoS measurements. The coil was placed behind the electron source with a minimal distance to the emission spot to reach the required magnetic field. The coil was implemented into the MoS geometry model following the parameters from given in [Hil11].

Configuration of the simulation software

The simulated electron tracks must start extremely close to the photocathode to fully include the non-adiabatic acceleration in the strong electric field. This acceleration is most effective at a small kinetic energy of the electrons, which is the case only at a small distance to the back plate. On the other hand, a certain minimal distance must be kept in order to accurately compute the electric field near the electrode surface. In the simulations presented here, a *starting distance* of 10 nm to the back plate surface was used, following earlier investigations in [Zac14]. This setting provides a good compromise

46. In general, a discretization level is considered “good” if lowering the number of discretized segments does not produce a mismatch between simulation results. Otherwise the discretization is too coarse and needs to be refined.

47. The coil itself was manufactured at WWU Münster for earlier measurements at the KATRIN pre-spectrometer, and has been re-used for this purpose.

between the accuracy of the electron-tracking and the accuracy of the field evaluations, when using the given discretization level at the emission spot.

The accuracy of the simulation is in general strongly affected by the used *step size*. Since the simulation computes the electron trajectory by a series of discrete steps, numerical inaccuracies can result from too large step size, especially when strong field gradients are present. The electron tracking over the first few mm of the simulated trajectory is quite delicate to the non-adiabatic acceleration, which makes the initial step size a crucial parameter of the simulation. To achieve optimal results even with changing simulation parameters (e. g. acceleration voltage) and to avoid using too small step sizes, which would unnecessarily slow down the simulation, a new method to determine the step size has been implemented for this thesis (see section 3.3.4). This dynamic step size monitors the energy violation between two discrete steps and reduces the step size if the violation becomes too large⁴⁸. The step size is further controlled by absolute limits that prevent the step size from becoming too small or too large. The simulations in this thesis used a lower and upper limit for the relative energy violation of 10^{-15} and 10^{-5} , and absolute step size limits of 10 nm and 1 mm. The step size is further constrained to an upper limit of $r_c/12$, where r_c is the cyclotron radius of the electron. This prevents inaccuracies when using the exact tracking method in Kassiopeia, which could occur even if the determined step size is within the other mentioned limits. Similar to the discretization level, simulation runs with different step size settings were compared to optimize these parameters and to verify the consistency of the simulations.

Since the transmission function that is observed in a measurement is fully defined by the electron properties in the spectrometer entry magnet (e. g. their energy and angular distributions), it is not necessary to compute trajectories through the entire spectrometer and up to the detector. Hence, the simulations stop when the simulated electron reaches the center of the entry magnet, which considerably reduces the required simulation time. The simulations show that the electrons move adiabatically towards the entry magnet after they have left the source chamber with the dipole electrode. One could therefore switch from exact to adiabatic tracking in the beam tube to speed up the simulation. However, in order to correctly include the *cyclotron phase* of the electrons⁴⁹, the simulations rely on exact tracking without any approximations up to the entry magnet. Since earlier simulations showed that *phase effects* often play a significant role at the electron source [Zac14], it is important to fully include these effects to produce accurate simulation results.

The overall electric field vanishes inside the grounded beam tube that leads to the spectrometer entry magnet. Hence in this region, the electric field $\vec{E} \approx 0$ can be removed from the simulation and the step size is switched to a value that only depends on the cyclotron radius. Since this step size reduces significantly as the electron moves into the higher magnetic field at the entry magnet, a large amount of simulation time is spent in the beam tube where no interesting effects are observed. Removing the electric field improves this condition, as the electric field computation is orders of magnitude slower than computing magnetic fields. The electric field is removed at a point in the geometry model where the electric potential has reduced sufficiently, which introduces an absolute error of $< 10^{-5}$ eV in the electron's kinetic energy (due to the fact that the potential cannot become zero). Since this error is much smaller than other estimated uncertainties of the simulation, this procedure does not affect the simulation results in a measurable amount.

⁴⁸. Energy is typically not entirely conserved in these simulations due to the limited numerical accuracy.

⁴⁹. The cyclotron phase corresponds to the azimuthal angle ϕ between the electron momentum and the magnetic field. It is defined by the initial azimuthal angle of an electron emitted from the back plate and changes during propagation. It is also affected by inhomogeneous electromagnetic fields along the trajectory.

Simulation parameters

Several parameters can be modified to perform simulations at different settings. These parameters are defined in the geometry model and the simulation configuration as so-called *external variables*, which have certain default values that can be overridden at the command line. This allows a flexible configuration where parameters can be modified automatically by run scripts that carry out a series of simulation runs. Table 4.26 lists the commonly used parameters and their default values.

The simulation results are written to ROOT data files by Kassiopeia (section 3.3.8). The PyROOT interface⁵⁰ provides access to simulation results in Python scripts. Python features a large collection of modules that can be used for data analysis, such as NumPy, SciPy and Matplotlib. The *Peaberry* framework that was developed over the course of this thesis (section 3.8) was used to perform the analysis of simulation results, using similar methods that were applied to measurement data for analysis.

Table 4.26.: Important parameters of the electron source simulations and their default values.

Parameter	Description	SDS-2 default	MoS default
generator	generator type	gauss_cosine	
egun_line_mean	mean energy	0.2 eV	
egun_line_width	energy spread	0.2 eV	
egun_angle_spread	angular spread	90°	
egun_start_radius	radial spread	100 μ m	
egun_start_distance	distance to back plate	10 nm	
hillencoil_current	extra air coil current	<i>MoS only</i>	-35 A
egun_backplate_voltage	start voltage	-18.61 kV	
egun_acceleration_voltage	acceleration voltage	5 kV	
egun_dipole_voltage	dipole voltage	3 kV	2 kV
egun_plates_vertical_angle	ver. plate angle	0°	
egun_plates_horizontal_angle	hor. plate angle	0°	
egun_plates_vertical_angle_zero	ver. plate zero angle	-0.32°	-0.12°
egun_plates_horizontal_angle_zero	hor. plate zero angle	0.77°	0.17°
egun_vertical_angle	ver. manipulator angle	0°	
egun_horizontal_angle	hor. manipulator angle	0°	
egun_offset_x	alignment x-correction	-0.0072 m	0 m
egun_offset_y	alignment y-correction	-0.0168 m	0 m
egun_beamspot_offset_x	photocathode x-offset	0 m	
egun_beamspot_offset_y	photocathode y-offset	0 m	

50. PyROOT, <https://root.cern.ch/pyroot>

4.8 Simulations of the MoS and SDS-2 setups

From the working principle and the design of the electron source it is known that the strong electric field between the back and front plate achieves a non-adiabatic acceleration of the electrons which are emitted at the back plate. The non-adiabatic propagation violates the conservation of the magnetic moment and thus allows to imprint a defined pitch angle on the electrons. This process can be viewed as the electric field pulling against the magnetic field, which is fully described by the Lorentz equation

$$\vec{F} = q(\vec{E} + \vec{v} \times \vec{B}). \quad (4.96)$$

It is clear that the net effect of the electric field \vec{E} decreases as the electron gains kinetic energy $E_{kin} \propto v^2$. Hence at some distance from the back plate, the magnetic field \vec{B} essentially takes over the propagation and the electron proceeds towards the spectrometer in adiabatic motion.

These effects can be investigated in detail with particle-tracking simulations. Although earlier simulations performed in [Zac14] already discussed these effects with the help of simulations, the used geometry model did not include all important details such as the dipole electrode, and were limited to an axially symmetric geometry⁵¹. The new simulation results that are presented in this chapter intend to answer open questions that could not be solved yet, and to investigate affects that have not been considered so far. Furthermore, the electron acceleration strongly depends on the initial longitudinal and transversal of the electrons that are emitted at the back plate. The initial energy and angular distributions therefore must be fully considered in the simulations.

This section will discuss simulations that were performed with the setup described in section 4.7.1. Detailed studies have been carried out to answer the following questions:

- How do the electromagnetic fields affect the electron acceleration and transport towards the spectrometer magnet?
- How are the energy and angular distributions in the spectrometer magnet produced?
- How are the well-defined pitch angles produced, and how does the acceleration voltage affect the electron-beam collimation?
- What is the effect of the dipole electrode on the produced pitch angles?
- How do small misalignments of the electron source (e. g. the position of the emission spot) affect the electrons?

The goal of the simulations is to produce results that can be compared to measurement data taken at the MoS and SDS-2 setups, and to get a detailed understanding of the electron acceleration and transport processes inside the electron source. Simulations also provide important input parameters for the analysis of measurements, as shown e. g. in [Erh16]. Furthermore, a better knowledge of the source will certainly be helpful for possible future measurements with the electron source discussed in this thesis or with similar devices, such as the electron source at the KATRIN Rear Section that will be used in the upcoming commissioning measurements of the experiment.

⁵¹. The reason is that these simulations were performed at a time where Kassiopeia did not include the necessary features yet.

4.8.1 Alignment with the experimental setup

The experimental setup of the electron source for the MoS and SDS-2 measurement phases was discussed in sections 4.5.1 and 4.6.1. It is necessary to align the electron source with the MAC-E filter and with the magnetic guiding field to ensure that key features such as angular selectivity can be achieved. An accidental misalignment in the SDS-1 measurement phase in 2013 resulted in substantial problems with the source operation⁵². To avoid similar problems in the SDS-2 phase, special care was taken to optimize the alignment between the electron source, the magnet system and the main spectrometer.

It is especially important to determine any remaining misalignment in order to perform particle-tracking simulations that reproduce the experimental conditions. Hence, precision measurements of the position of relevant components (e. g. the source vacuum chamber) and their tilt angles against a reference coordinate system were carried out at the SDS-2 setup. These measurements used a FARO system⁵³, which can determine the distance and relative tilt of measurement points against a reference system. These measurements allow to include corrections in the existing SDS-2 simulation geometry, so that the misalignment of the PS1 and PS2 magnets and the exact position of the electron source are fully considered. The measurement results are listed in appendix A.

Table 4.27 lists the results of the FARO measurements [EBO15] and the corresponding alignment parameters that are used in Kassiopeia simulations of the electron source. To determine the correct alignment parameters, some details must be considered:

- The upstream⁵⁴ side of the entry flange of the main spectrometer is used as a common reference point in CAD drawings, FARO measurements and Kassiopeia simulations. The reference point is located on the central spectrometer axis by definition. With this reference point it is possible to integrate the FARO results (which contains only distances, but no absolute positions) into the simulation geometry.
- The coordinate system for the FARO measurements corresponds to the one used in CAD drawings, but is different from the system that is used in Kassiopeia simulations. In the CAD system, z points towards the source and x points in eastward direction; in the simulation system z points towards the detector and x points westwards. The distances measured in different directions must therefore be corrected accordingly.
- The tilt angles measured by the FARO system are given as a tilt angle of a plane against a given reference axis, e. g. a measurement at the xz -plane returns the tilt against the y -axis. The resulting angles are therefore *not* Euler angles and would need to be transformed. However, KGeoBag also supports the so called “axis-angle” format to tilt geometric shapes against a coordinate system; here one defines a tilt axis and then uses the tilt angle against that axis. Hence, the FARO tilt angles can be included directly in the simulation geometry. Because the coordinate systems differ between the FARO system and the simulation geometry (see above), the tilt angles change their sign.

52. The source was placed at a wrong distance to the main spectrometer and the PS2 magnet, which resulted in too low magnetic fields at the source. Subsequently, magnetic reflection at the spectrometer could not be achieved within the scanning range of the plate tilt angle $\alpha_p \leq 16^\circ$. These issues have been discussed in [Gro15] and [Zac14].

53. FARO 3D measurement technology, <http://www.faro.com>

54. *Upstream*: towards the source; *Downstream*: towards the detector.

Table 4.27.: Alignment parameters of the electron source and PS magnet system.

parameter	value	description	source
z_{ref}	-11.613 75 m	reference point	CAD
z_{PS2}	-12.104 689 m	pos. of PS2 magnet	FARO: $\Delta Z = 490.939$ mm
Δx_{PS2}	0.000 539 m	hor. offset of PS2 magnet	FARO: $\Delta X = -0.539$ mm
Δy_{PS2}	0.000 313 m	ver. offset of PS2 magnet	FARO: $\Delta Y = 0.313$ mm
α_{PS2}^h	-0.043°	hor. tilt of PS2 magnet	FARO: $\alpha_{XZ} = 0.043^\circ$
α_{PS2}^v	-0.013°	ver. tilt of PS2 magnet	FARO: $\alpha_{YZ} = 0.013^\circ$
z_{PS1}	-14.660 234 m	pos. of PS1 magnet	FARO+CAD: $\Delta Z = 3606.484$ mm + 560 mm
Δx_{PS1}	-0.001 234 m	hor. offset of PS1 magnet	FARO: $\Delta X = 1.234$ mm
Δy_{PS1}	0.003 264 m	ver. offset of PS1 magnet	FARO: $\Delta Y = 3.264$ mm
α_{PS1}^h	0.082°	hor. tilt of PS1 magnet	FARO: $\alpha_{XZ} = -0.082^\circ$
α_{PS1}^v	-0.070°	ver. tilt of PS1 magnet	FARO: $\alpha_{YZ} = 0.070^\circ$
z_{egun}	-13.702 294 m	pos. of electron source	FARO+CAD: $\Delta Z = 2220.894$ mm - 132.35 mm
Δx_{egun}	0.000 19 m	hor. offset of el. source	FARO: $\Delta X = -0.190$ mm
Δy_{egun}	0.000 19 m	ver. offset of el. source	FARO: $\Delta Y = 0.190$ mm
α_{egun}^h	-0.077°	hor. tilt of el. source	FARO: $\alpha_{XZ} = 0.077^\circ$
α_{egun}^v	-0.078°	ver. tilt of el. source	FARO: $\alpha_{YZ} = 0.078^\circ$
Δz_{UHV}^h	1.379 903 m	hor. manipulator center	FARO: $\Delta Z = 729.509$ mm
Δz_{UHV}^v	1.376 892 m	ver. manipulator center	FARO: $\Delta Z = 726.498$ mm

- The magnets are placed within the simulation geometry using their center as reference point. The FARO measurements determined the distance of the downstream side of PS2 housing against the reference point at the spectrometer, and the distance between the upstream side of the PS1 housing to the downstream side of the PS2 housing. In both cases, only one side of each magnet was used in the measurement due to the limited range of the FARO device. To retrieve the center position of the PS1 and PS2 magnet, one must consider the length of the housing, which is 560 mm according to CAD drawings. The magnet position in the simulation geometry is therefore a combination of FARO results and CAD drawings. Note that the table below lists the PS1 and PS2 magnets with the position of their respective upstream side; the 280 mm distance to their center is taken into account internally in the Kassiopeia simulation geometry.
- The simulation geometry positions the electron source using the emission spot on the photocathode as reference point. The FARO measurement, however, can only determine the distance of the nearby upstream flange of the source vacuum chamber to the reference point at the main spectrometer. The distance of 132.35 mm between source flange and photocathode must therefore be included to determine the source position in the simulation geometry. As with the magnet system, the given distance is determined from CAD drawings.

- The FARO results show that the UHV manipulator, which allows to move the source within the magnetic flux tube, has different centers of rotation for the two tilt axes. In the reference design, the center of rotation should be the same for both axes. The observed different of about 3 mm has been included accordingly in the simulation geometry.

Alignment measurements

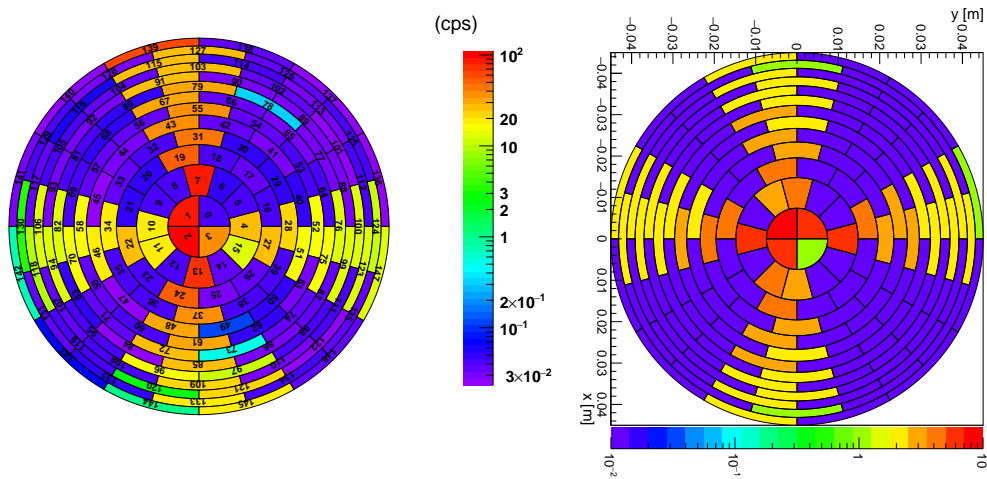


Figure 4.64. Line-scan measurement and corresponding simulation in the SDS-2 setup. The line-scan measurement (left) is performed by sweeping the tilt angle of the UHV manipulator in the range -20° to 20° and observing the hit position of the electrons on the detector. By comparing the simulation result to measurement data, an alignment offset can be determined that is then used in the simulation geometry. With the obtained offset, the simulated hit pattern (right) reproduces the measurement result to a large extent. A deviation is only observed for large tilt angles at the bottom of the wafer, where the electron beam hits adjacent pixels. Since measurements are typically limited to manipulator angles of less than 17° , this discrepancy is not significant. Note that variations in color between the two figures are due to the fundamental differences between measurement (where an average electron rate is measured) and simulations (where single detector hits are observed).

The thorough alignment measurements only determine the exact positioning of the electron source w. r. t. the spectrometer and the PS magnet system. However, the residual offset of the emission spot w. r. t. the silicon wafer at the detector cannot be resolved with these measurements. The tilt angle and the position of the detector system and the wafer itself was determined in independent alignment measurements at the FPD system, but it is difficult to precisely determine the alignment between the source and the detector by mechanical measurements alone (especially when considering the distance of more than 20 m between both systems). Furthermore, there could be tilts of the solenoid coils (at the PS magnets and pinch magnet) w. r. t. the spectrometer axis that are not accounted for⁵⁵. More accurate results can be achieved by conducting alignment measurements with the produced electron beam at the SDS-2 setup.

A so-called “line scan” measurement is performed by moving the electron source along the flux tube with the UHV manipulator, while electrons are emitted into the spectrometer. The scan is performed for the horizontal and the vertical manipulator axis, resulting in a prominent cross-like detector hit

⁵⁵. The FARO measurement can only determine the tilt of the magnet housing, which is not necessarily aligned to the coils inside.

pattern as the electron beam moves over the wafer. The result is shown on the right side of figure 4.64, where the UHV manipulator was moved from -20° to 20° on each axis [BEK⁺15]. The arrangement of the detector pixels on the wafer allows to reconstruct the line on which the electron beam is moving. By doing this for both axes, a crossing point can be determined that corresponds to the central position of the manipulator (i. e. where the tilt angle is zero on both axes). This yields the effective offset between the electron source and the detector wafer.

To reconstruct the scan line, one can reasonably assume that the manipulator angle changes with a constant velocity due to the technical design⁵⁶. The total number of electron hits in a single detector pixel therefore only depends on the time during which electrons arrived at the given pixel, according to the achieved electron rate and the movement speed of the manipulator. A comparison of the number of hits in adjacent pixels then allows to determine the position of the scan line with high accuracy, as described in [Gro15, Har15]. This analysis is repeated for the FPD pixel rings #0 (“bulls-eye” at the center) and #1 for the four azimuthal scan directions used in the measurement. The resulting position of the crossing point is

$$\Delta x_{hit} = -0.82 \text{ mm}, \quad (4.97)$$

$$\Delta y_{hit} = -2.82 \text{ mm}, \quad (4.98)$$

on the FPD wafer. The source–detector alignment was therefore considerably improved w. r. t. the SDS-1 measurement phase, where an offset of $\Delta x = -3.28 \text{ mm}$ and $\Delta y = -3.34 \text{ mm}$ has been determined following the same method [Gro15].

A similar strategy is employed to include this remaining misalignment into the simulation geometry. Electrons were tracked from the source to the detector at different manipulator angles (-20° to 20°) to observe a hit pattern on the detector wafer. This method is more complex than simply taking the measured misalignment that was discussed above and including the position of the crossing point in the simulation geometry. However, it allows to examine any possible mismatch between simulations and measurements, which could result from inaccuracies in the simulation geometry (which is largely based on CAD drawings). By comparing the simulated hit pattern to the one that was observed in the line-scan measurement, one can include additional corrections in order to reproduce the experimental conditions. In the end, the same detector pixels should be hit when a given manipulator position is used in both measurements and simulations.

The simulated hit pattern (after including these corrections) is shown on the left side of figure 4.64. The line-scan simulation reproduces the measurement result when the electron source geometry is shifted by

$$\Delta x_{sim} = -7.2 \text{ mm}, \quad (4.99)$$

$$\Delta y_{sim} = -16.8 \text{ mm} \quad (4.100)$$

in the simulations w. r. t. the spectrometer axis. This adds another xy -offset in the simulation geometry that is superimposed on the results of the FARO measurements. The need for this additional correction can be explained by differences between the simulation geometry and the real experimental setup, which have not been accounted so far. The produced hit pattern is compared with the result of the line-scan result in the next section.

⁵⁶. The manipulator uses screw drives that are moved by pressured-air motors. The motors run at constant speed until the desired target position is reached.

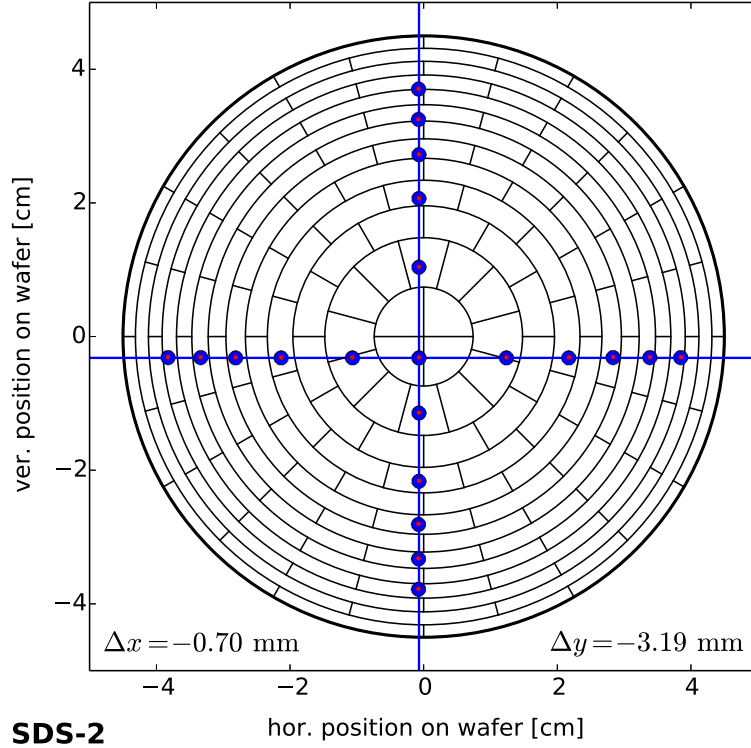


Figure 4.65.: Pixel mapping simulation for selected detector pixels in the SDS-2 setup. The “pixel mapping” describes the relation between a manipulator angle and the hit position on the detector. The plot shows the exact hit positions that were produced by simulations after implementing the alignment results. The investigated manipulator positions correspond to the cross-like scanning pattern that was used in the SDS-2 spectrometer commissioning measurements. The crossing point of the two tilt axes (indicated by the thin blue lines) measures the misalignment between electron source and detector wafer in the simulations. The resulting offset (noted at the bottom of the figure) is in agreement with the result from the line-scan measurement (cmp. figure 4.64).

The commissioning measurements of the electron source that are presented in this work were always performed at the central manipulator position, i. e. with the emission spot of the electron source on the spectrometer axis. Other measurements that determined the spectrometer transmission properties required to move the manipulator to off-axis positions [Erh16]. These measurements were performed at selected detector pixels in a cross-shaped pattern to investigate possible inhomogeneities over the spectrometer’s analyzing plane [BEK⁺15, BEW⁺15]. In order to further investigate the alignment of the electron source w. r. t. the detector, the exact hit positions of the electron beam on the detector wafer were determined for the used manipulator positions. The results are shown in figure 4.65.

Using the simulation geometry with all the corrections discussed so far, the detector hit pattern yields a crossing point position of

$$\Delta x_{hit,sim} = -0.70 \text{ mm}, \quad (4.101)$$

$$\Delta y_{hit,sim} = -3.19 \text{ mm}. \quad (4.102)$$

This result is in agreement with the line-scan measurements discussed above. The observed deviation of $< 0.5 \text{ mm}$ is within the uncertainty of the pattern-matching method that was employed here. Its

accuracy is mainly limited by the size of the detector pixels and by their arrangement on the wafer, since only full detector pixels can be compared between the line-scan measurements and the corresponding simulations⁵⁷. One can estimate the uncertainty by observing changes in the hit pattern if the alignment offsets are varied. The estimated uncertainty is then 1.7 mm for the horizontal and 0.5 mm for the vertical axis. The difference between the axes is a result of the pixel arrangement, which makes the method more sensitive to changes in vertical direction.

The discussion so far only considered the SDS-2 setup. At the MoS setup, the manipulator was not used as the measurement goal was to verify the source functionality, and not to determine any spectrometer properties. A precise alignment between source and spectrometer is therefore not essential for these test measurements. Furthermore, the source was mounted on the upstream beamline flange of the MoS – where in regular measurements a $^{83\text{m}}\text{Kr}$ source is attached – so that the source is always central to the spectrometer axis. Hence, there are no xy -offsets expected and the simulation geometry is constructed accordingly. The most relevant alignment parameter here is the distance between the spectrometer entry magnet and the source flange since it defines the magnetic fields at the electron source. A distance of 2.635 m between the source and the spectrometer’s analyzing plane was determined, combining manual measurements and CAD drawings of the MoS setup [B⁺14b, Beh14].

Magnetic field at the emission spot

The alignment of the simulation geometry for the SDS-2 and MoS setups has been verified by comparing the magnetic field at the electron emission spot – which has a large influence on the produced pitch angles and the overall functionality of the source – to measurement results. The measurements have been performed at both setups before the electron source was mounted into the vacuum chamber. This allowed to use a hall probe that measures the magnetic field directly at the position of the emission spot. A special mounting device was mounted at the vacuum chamber flange to achieve an exact positioning of the probe w. r. t. the source setup.

At the SDS-2 setup, the magnetic field was measured for different manipulator angles at nominal magnetic fields ($B_{PS1} = 3.0\text{ T}$, $B_{PS2} = 4.5\text{ T}$). At the MoS setup, the measurement was performed for nominal magnetic field ($B_{max} = 6\text{ T}$ at the entry magnet) and at enhanced magnetic field (with $I_{coil} = -35\text{ A}$ on the additional air coil). Figure 4.66 compares the simulated to the measured values for both setups.

The simulated fields are in good agreement with the measured values at both setups. The nominal magnetic field is 29.3 mT at the SDS-2 setup and 21.0 mT at the MoS setup. At enhanced magnetic field, the MoS setup achieves 27.9 mT at the emission spot, which is comparable to the SDS-2 value. When moving to off-axis positions at the SDS-2 setup the measured magnetic field decreases by several mT, which has important consequences for the performance of the electron source⁵⁸. The figure shows a significant deviation between the measured magnetic field at different manipulator positions and the corresponding simulated values, especially for negative angles on both tilt axes. This deviation can be explained by a remaining misalignment between the magnet system and the electron source. Although the position and tilt of the PS magnets were determined in FARO measurements with good accuracy, the alignment of the actual solenoid coils inside the magnet housing is difficult

57. In a measurement, the hit position is only known on a per-pixel basis. In simulations, sub-pixel accuracy can be achieved since the exact position of each electron is known.

58. The pitch angle of the produced electrons strongly depends on the initial magnetic field; a lower magnetic field results in the production of larger pitch angles at the same operational parameters.

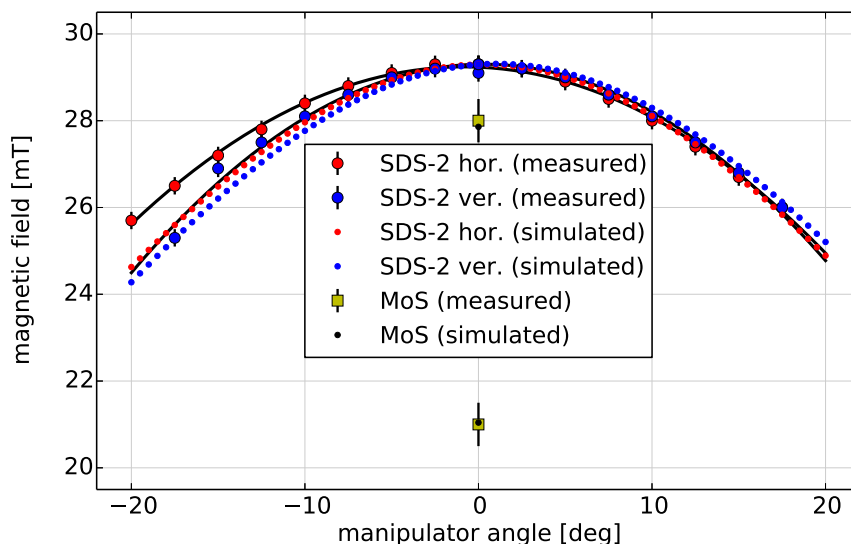


Figure 4.66.: Comparison of simulated and measured magnetic fields at the SDS-2 and MoS setups. At the SDS-2 setup, the magnetic field was measured at several manipulator positions. At the MoS setup where no manipulator was used, two measurements were performed at nominal and enhanced magnetic field (cmp. section 4.5.1). The simulations for both setups (indicated by the smaller data points) show that the computed field at the center is in agreement with the measurement data. For the SDS-2 setup, the simulated value of 29.3 mT precisely matches the measurement result; for the MoS setup the simulated value of 21.0 mT (27.9 mT at enhanced field) is in good agreement with the measured value of 21.0 mT (28.0 mT). A deviation is observed at the SDS-2 setup for off-axis manipulator positions, especially at large negative manipulator angles on the horizontal axis. This deviation is not relevant for the simulations discussed in this work, as the source commissioning measurements were all carried out at the central manipulator position.

to determine. One therefore can assume that some unknown misalignment of the magnetic fields is present, which becomes more complicated when considering that two magnets with independent alignments are responsible for the observed magnetic field.

It would be possible to reduce the observed deviation by optimizing the alignment between electron source and magnet system by comparing the magnetic fields and taking into account the off-axis manipulator positions as well. The procedure could be automated by implementing a minimizer algorithm that modifies the alignment parameters of the simulation in order to bring simulation and measurement into agreement (e. g. using MCMC fit methods). Up to 15 free parameters would need to be included in this process: The three-dimensional position of each PS magnet and of the source (3×3 parameters); and their respective tilt angles against the horizontal and vertical axis (3×2 parameters). This possibility was, however, not further investigated in the course of this thesis due to its complexity and the limited time available. It should also be noted that the observed deviation is irrelevant for this thesis, as the manipulator was only set to central positions in the source commissioning measurements and the corresponding simulations. Only if electron source simulations at off-axis manipulator positions are performed, the observed differences must be taken into account.

4.8.2 Electromagnetic conditions in the electron source

An important aspect of the electron acceleration and transport towards the spectrometer are the electromagnetic conditions inside the electron source. The magnetic guiding field provides the field lines which the emitted electrons follow through the spectrometer up to the detector. The strong electric field between the plate electrodes at the source achieves a non-adiabatic acceleration of the electrons, which imprints a well-defined pitch angle on the electrons that enter the spectrometer. Hence, to better understand these processes one must investigate the electromagnetic conditions at the electron source.

Electric potential and magnetic field

Figure 4.67 shows the electric potential and the magnetic field between the photocathode of the electron source and the spectrometer entry magnet for the MoS and SDS-2 setups. At the SDS-2 setup, the source is mounted on the UHV manipulator and the distance between the emission spot and the center of the entry magnet is 1.6 m at the central manipulator position. Under nominal conditions, the magnetic field at the emission spot is $B_{start} = 29.3$ mT with the back plate on a potential of $U_{start} = -18.6$ kV, an acceleration voltage of $U_{acc} = 5$ kV between the front and back plate, and a dipole voltage of $U_{dip} = 3$ kV. The emitted electrons are accelerated towards the ground potential at the spectrometer entrance after leaving the source. At the MoS setup, the distance to the entry magnet is 0.6 m and the magnetic field at the emission spot is only $B_{start} = 21.0$ mT under nominal conditions. The field can be increased to 27.9 mT using an additional air coil, which achieves conditions that are comparable to the SDS-2 setup. The figure shows the same starting and acceleration voltages as above, but the dipole voltage is only $U_{dip} = 2$ kV at the MoS setup, according to the nominal operational parameters.

The figure shows that the electric potential reaches ground level inside the source chamber (i. e. at a distance $d \leq 12.2$ cm from the emission spot; see inset). The electrons therefore have reached almost their full kinetic energy $E = qU_{start}$ when leaving the source chamber. The electric dipole field results in a localized increase of the electric potential to positive values. After passing the dipole electrode, the electrons move inside the grounded beam tube where no strong electric fields are present (cmp. section 4.7.1). The overall magnetic field is larger at the MoS setup due to the higher magnetic field in the spectrometer entry magnet (6 T vs. 4.5 T in SDS-2). Both setups use the same source setup and the plate setup where the electron acceleration occurs is shielded from outside influence by the grounded cage. The only difference that affects the electrons is therefore the magnetic field, which influences the produced pitch angles. This will be investigated in more detail in the following sections.

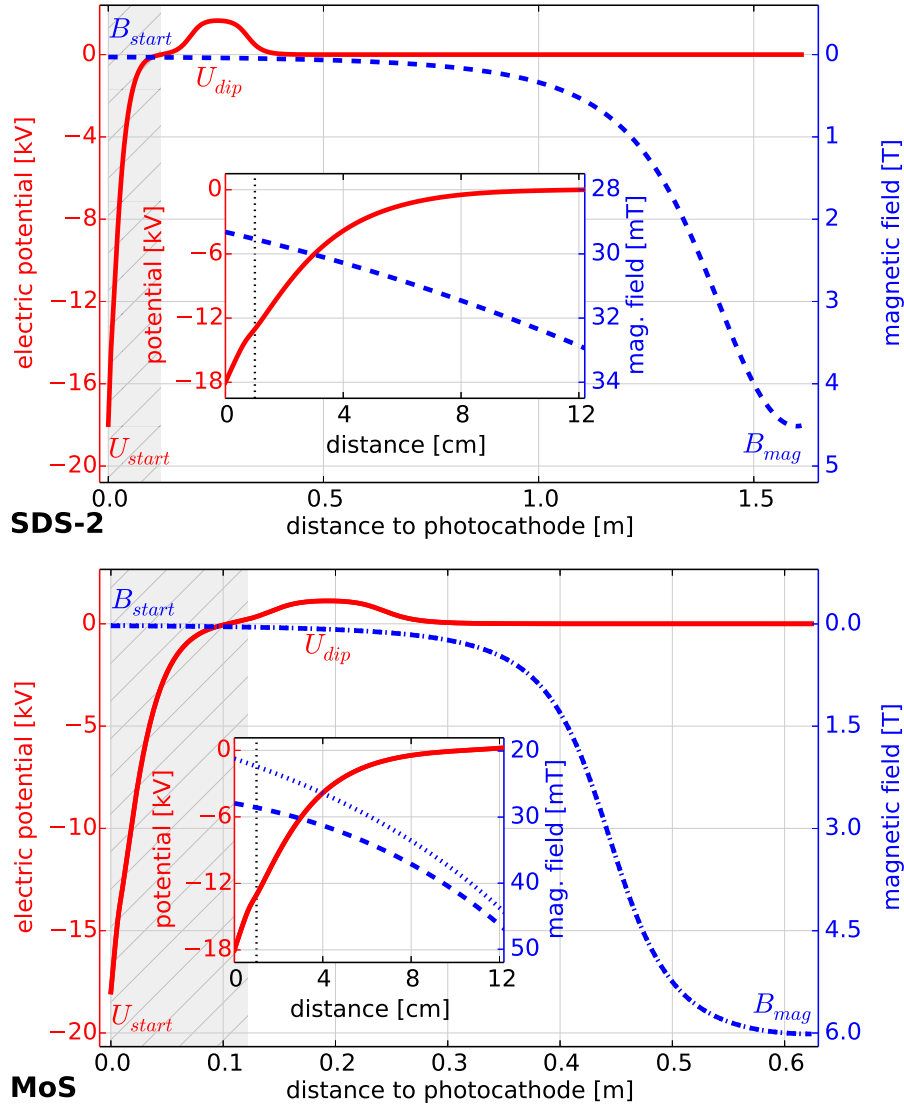


Figure 4.67.: Electromagnetic conditions at the electron source in the SDS-2 and MoS setups. The plots show the electric potential (red, left axis) and the magnetic field (blue, right axis) between the photocathode and the spectrometer entry magnet. The inset shows the conditions inside the grounded source cage (distance $d \leq 12.2$ cm from the emission spot; the region is indicated in gray in the main plot). The dotted vertical line in the inset marks the position of the front plate ($d = 10$ mm). *Top:* SDS-2 setup under nominal high voltage conditions ($U_{start} = -18.6$ kV, $U_{acc} = 5$ kV, $U_{dip} = 3$ kV, $B_{start} = 29.3$ mT, $B_{mag} = B_{PS2} = 4.5$ T). *Bottom:* MoS setup under nominal conditions at enhanced magnetic field (as above, with $U_{dip} = 2$ kV, $B_{start}^+ = 27.9$ mT, $B_{mag} = B_{max} = 6$ T). The dotted blue line shows the nominal magnetic field without enhancement by the additional air coil ($B_{start} = 21.0$ mT).

Electron energy

The electron pitch angle is related to its longitudinal and transversal kinetic energy according to (2.1). The longitudinal energy is affected by the electric field (potential gradient), which accelerates elec-

trons in longitudinal direction so that they gain kinetic energy. The transversal energy changes due to electrostatic acceleration and the gradient of the magnetic field. By investigating both components of an electron's kinetic energy (or its momentum), one can gain more insight into the electron acceleration processes at the source. Both components are influenced by the axial and the radial electric field close to the emission spot. In this discussion, the axial electric field corresponds to the component in normal direction of the back plate and the radial field to the component in perpendicular direction to the normal. Hence, if electrons are emitted in direction of the normal, their longitudinal energy is modified by the axial field and their transversal energy by the radial field. The process changes accordingly if electrons are emitted in other directions, where the radial and axial fields then influence both energy components. In this section, only electrons that start in normal direction of the back plate (photocathode) are considered.

Figure 4.68 shows the longitudinal and transversal kinetic energy of electrons that are created at small and large plate tilt angles ($\alpha_p = 0^\circ, 10^\circ$) for the SDS-2 setup; similar conditions are observed at the MoS setup. Inside the grounded cage (see inset), the longitudinal energy of the electron does not depend on the tilt angle. This is expected since the electric potential gradient is the same regardless of the plate angle, because the grounded cage shields the electric acceleration field from outside influences. The transversal energy, on the other hand, shows a completely different behavior when the plate setup is tilted against the magnetic field. While at zero-angle ($\alpha_p = 0^\circ$) the transversal energy stays constant at $E_\perp = 0$ eV – the pitch angle is $\theta = 0^\circ = \text{const.}$ since the electron is emitted into the direction of the magnetic field – the non-adiabatic electron acceleration increases the transversal energy to a maximum of $E_\perp \approx 150$ eV, thus imprinting a non-zero pitch angle on the electron. The maximum is reached at the front plate, where the longitudinal energy reaches $E_\parallel \approx 5$ keV. The pitch angle that is reached at this point is then increased by the adiabatic transformation (2.7) as the electrons moves into a higher magnetic field at the spectrometer entrance.

The electric dipole field has practically no effect on the longitudinal or transversal energy, since the electron motion is already fully adiabatic when it passes the dipole electrode⁵⁹. For *stored* electrons that pass the dipole electrode multiple times before being removed, however, the dipole field has a more pronounced effect and moves the electrons towards the beam tube walls. For a more detailed investigation of this effect, see [Wie16].

The bottom part of the figure shows the axial and radial electric fields, as defined above. For electrons emitted in normal direction to the back plate (photocathode), the axial field only influences the longitudinal electron energy and the radial field is responsible for the observed increase in transversal energy. As expected, the axial field is not influenced by tilting the plate setup since it is a result of the plate-capacitor setup, where a nearly homogeneous linear field is created by the acceleration voltage U_{acc} . Due to the small distance between the plates ($d = 10$ mm), a linear acceleration field of about 600 kV/m is achieved at the emission spot.

The radial field is extremely small at zero-angle ($\alpha_p = 0^\circ$) and reaches values of 10 kV/m at the emission spot. It is larger than zero since the electric field between the plates is not entirely homogeneous due to the aperture in the front plate. The small radial field explains why the electrons do not gain transversal kinetic energy in the zero-angle setting. For larger tilt angles ($\alpha_p = 10^\circ$ in the figure), the radial field reaches considerably higher values of up to 120 kV/m at the emission spot. Furthermore, the radial

⁵⁹. Note that this does not imply that the dipole field has absolutely no effect on the produced electrons: The stray electric field is extremely asymmetric due to the half-shell electrode design and modifies the electric acceleration field at the source. Consequently, the acceleration process is influenced by the dipole field and small differences in the produced pitch angles can be observed.

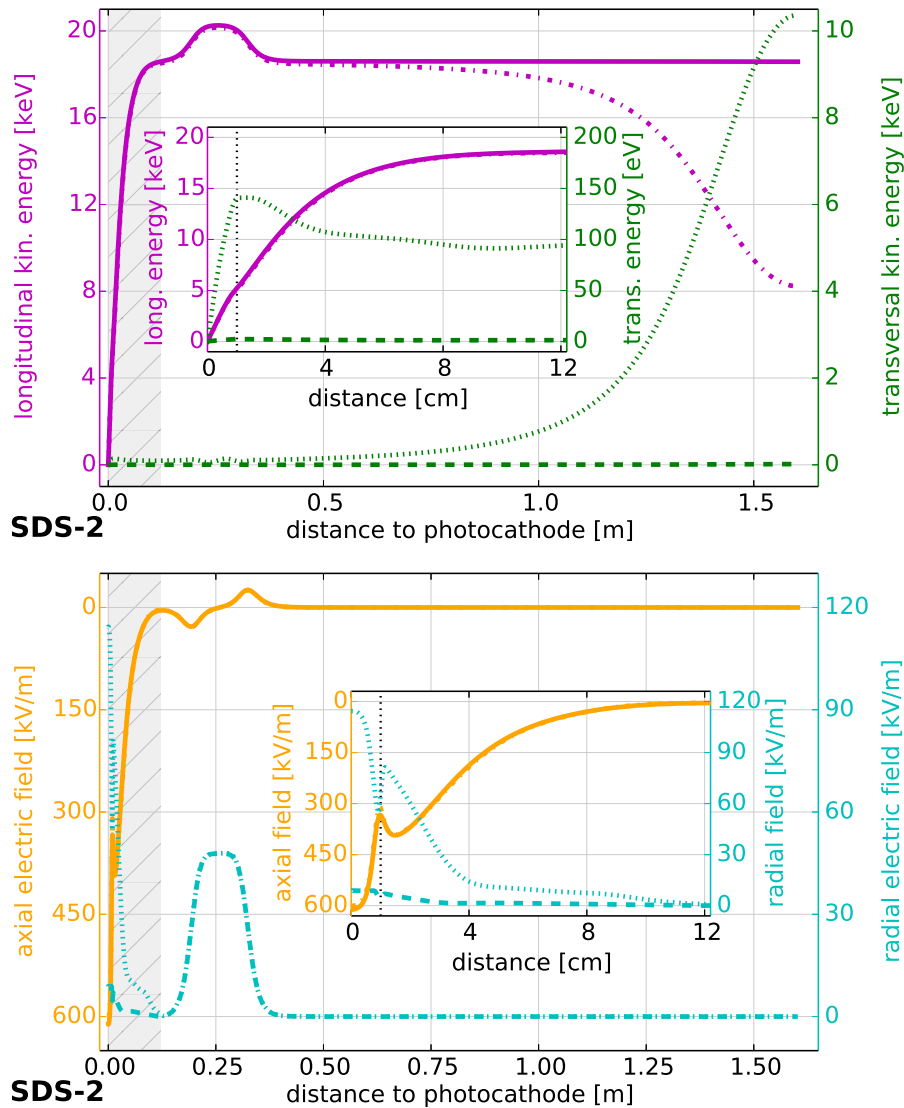


Figure 4.68.: Electron transport at the electron source in the SDS-2 setup. The plots show the kinetic energy of an electron that is started at the photocathode in forwards direction (initial momentum aligned with the normal of the photocathode surface) and the electric fields that act upon the electron. The insets show the conditions inside the grounded source cage. *Top:* Longitudinal (magenta, left axis) and transversal energy (green, right axis) of the electron. The solid/dashed lines correspond to a plate angle $\alpha_p = 0^\circ$ (zero-angle); the dotted lines to a larger plate angle $\alpha_p = 10^\circ$. The non-zero plate angle results in an increased transversal energy of the electron, which corresponds to a larger pitch angle. This effect is called *angular selectivity*. *Bottom:* Axial (orange, left axis) and radial electric field (cyan, right axis) along the electron trajectory. The axial field (in direction of the spectrometer axis) that accelerates the electron mainly in longitudinal direction is not changed by different plate angles. The radial field increases significantly with larger plate angles and results in the observed gain in transversal energy that imprints a defined pitch angle on the electrons.

field now affects electrons over a larger path length (up to roughly 4 cm from the emission spot, as shown in the inset). The net acceleration in radial direction is therefore significantly larger when the plate setup is tilted against the magnetic field, so that the emitted electrons gain more transversal

energy and consequently reach larger pitch angles at the end of the source chamber. Hence, the feature of angular selectivity is reproduced in the simulations and can be explained by the interplay of axial and radial electric fields together with the magnetic guiding field.

Accuracy of the simulation

The tracking of electrons in complex electromagnetic fields (e. g. with strong gradients or high asymmetry) is a delicate process. Especially during the non-adiabatic acceleration, where the electrons gain several keV of kinetic energy over a distance of a few cm, numerical errors can affect the simulation and produce invalid results. It is therefore important to verify that the accuracy of the particle-tracking process is sufficient. Numerical inaccuracies can arise in the computation of the electromagnetic fields due to used approximations and due to limited precision from the finite discretization, and also during the numerical integration of the equation of motion that is performed to compute the particle trajectory.

A verification of the simulation process is possible by checking the *energy conservation*. Every physical process conserves the total energy, $E_{tot} = E_{kin} + qU$ for a particle in an electromagnetic field. The energy violation due to numerical inaccuracies can be defined as the absolute difference to a reference value,

$$\Delta E_{tot} = E_{tot}(\vec{r}) - E_{tot}(\vec{r}_0), \quad (4.103)$$

where \vec{r} is the particle's current position and \vec{r}_0 its starting point at the emission spot. With this definition, one can examine energy conservation over a particle trajectory. If the total energy is conserved perfectly, ΔE will always be zero; numerical inaccuracies that influence the total energy are seen as deviations from this value.

Figure 4.69 shows the energy violation for electrons that are emitted under nominal conditions at the SDS-2 setup. The figure compares the zero-angle setting ($\alpha_p = 0^\circ$) to higher plate tilt angles $\alpha_p = 5^\circ, 10^\circ, 15^\circ$ to investigate any differences due to changes in the acceleration processes. The plot clearly shows that for zero-angle electrons, the total energy violation is always less than 1 meV up to the spectrometer entry magnet. The top of the figure shows the step size that used in the simulation to examine if changes in step size affect energy conservation or cause other inaccuracies. Close to the photocathode where strong field gradients are present, the step size is dynamically adjusted to improve the simulation accuracy⁶⁰. For electrons started at higher plate angles, the observed energy violation increases to roughly 10 meV. A sudden jump is observed at a distance $d = 0.09$ m from the emission spot, where the step size switches to a considerably larger value to speed up the simulation. Interestingly, the energy violation reduces again if the plate angle is further increased.

The observed energy violation is within the uncertainty of typical measurements to which the simulations can be compared (e. g. transmission function measurements). It is thus insignificant to the simulation, and one can expect that the simulation results are comparable to corresponding measurements. However, it would be possible to achieve a substantial improvement in accuracy by reducing the step size of the simulation, if one accepts the trade-off in simulation speed. Due to the limited available time for the simulations presented in this chapter and the large number of different simulation settings, this possibility was not further investigated.

60. This novel feature was implemented into Kassiopeia during the course of this thesis; cmp. section 3.3.4.

Another quantity that describes the simulation accuracy is the *orbital magnetic moment*, $\gamma\mu = E_{\perp}/B$. It is conserved in adiabatic motion (cmp. section 2.2.1), and any deviation from this behavior can be used to describe the *non-adiabaticity* of the electron propagation,

$$\Delta(\gamma\mu) = \frac{E_{\perp}(\vec{r},t)}{B(\vec{r},t)} - \frac{E_{\perp}(\vec{r}_0)}{B(\vec{r}_0)}. \quad (4.104)$$

with the same quantities as in (4.103). If the particle moves fully adiabatically, the value $\Delta(\gamma\mu)$ is always zero. Again, one can examine the non-adiabaticity over a simulated electron trajectory to investigate numerical inaccuracies⁶¹.

The bottom of figure 4.69 shows the non-adiabaticity (4.104) in the SDS-2 setup (note that here a logarithmic axis is used). As expected, a rapid deviation from adiabaticity by several order of magnitude is observed for non-zero plate angles α_p , as the electron is accelerated against the direction of the magnetic field. As discussed above, this non-adiabatic acceleration is responsible to achieve angular selectivity. At larger plate angles, the non-adiabaticity increases considerably as a result of the larger radial electric field and the electron's higher transversal energy. After the acceleration phase, the electron propagation is nearly adiabatic and the magnetic moment approaches a constant value. However, another significant deviation from adiabaticity is observed at the dipole electrode, where the strongly asymmetric electric field moves the electron trajectory in vertical direction and thus influences the electron's transversal energy.

The deviation at $d \approx 0.36$ m that is observed for $\alpha_p = 0^\circ$ is another interesting detail of the electron propagation. At this point, the pitch angle decreases due to adiabatic transformation (2.7) of the pitch angle in the decreasing magnetic field. However, the pitch angle is defined as a *polar angle* and thus cannot become negative. Hence, wherever the pitch angle would decrease below 0° along the track, it becomes positive instead and increases after this "turning point". This effect influences the angular distribution of the produced electrons at low plate angles α_p , where the effect occurs more frequently due to the typically small pitch angles in this setting. This is discussed in more detail below.

The discussed investigation of the energy violation and the non-adiabaticity verified that the simulation works as expected and does not suffer from significant numerical inaccuracies. Hence, particle-tracking simulations can produce results that are comparable to the measurements if the setup is configured correctly (no errors in the electromagnetic fields, precise alignment etc.). These simulations allow to examine important details of the electron propagation at the source, e. g. the evolution of the pitch angle as the electron moves towards the spectrometer entry magnet.

61. Note that to investigate the adiabaticity of a propagating particle, the simulation must use the *exact tracking* model to produce meaningful results. The *adiabatic tracking* assumes adiabatic propagation, so that $\gamma\mu = \text{const.}$ by definition; cmp. section 3.3.4

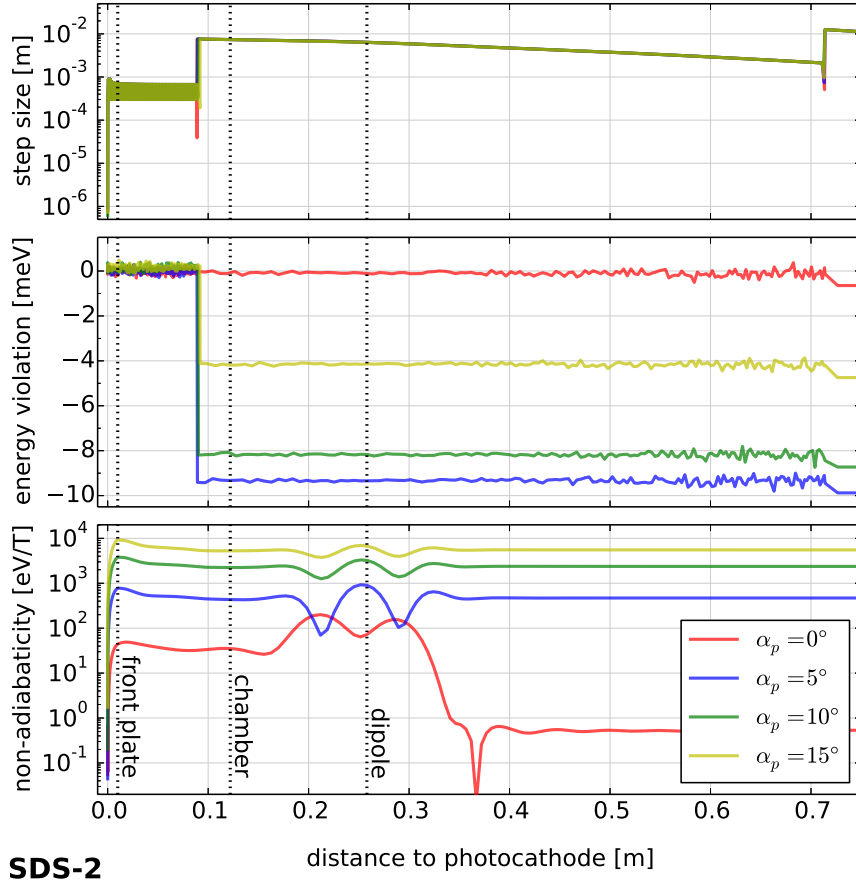


Figure 4.69.: Step size, energy violation and non-adiabaticity in the electron source simulations at the SDS-2 setup. The plots show the discrete step size of the simulation (top), the energy violation ΔE_{tot} according to (4.103) (middle), and the non-adiabaticity $\Delta(\gamma\mu)$ according to (4.104) (bottom). All values are plotted against the distance d from the emission spot for simulation runs at different plate angles $\alpha_p = 0^\circ, 5^\circ, 10^\circ, 15^\circ$. The dotted vertical lines indicate the position of the front plate ($d = 10$ mm), the end of the grounded source cage ($d = 12.2$ cm), and the center of the dipole electrode ($d = 25.8$ cm). The step size scales from a few hundred nm at the emission spot to several cm towards the end of the spectrometer entrance. It is dynamically adjusted to optimize accuracy and speed of the simulation. The total energy violation due to numerical inaccuracies is $\sum \Delta E_{tot} < 10$ meV and thus insignificant when considering the typical measurement uncertainties. At non-zero plate angles, a sudden energy violation is observed when increasing the step size at $d \approx 0.09$ m, which is related to the used navigation method in Kassiopeia. The non-adiabatic electron acceleration at the photocathode is reflected in a strong violation of adiabaticity in this section, which is a key feature of the source design and therefore expected. Non-adiabatic propagation is also observed at the dipole electrode due to its extremely asymmetric electric field. The magnetic moment approaches a constant value as the electron propagates towards the spectrometer entrance in adiabatic motion ($d \gtrsim 0.5$ m).

4.8.3 Electron transport between source and spectrometer magnet

One of the most important properties of the produced electrons is their pitch angle in the spectrometer entry magnet. Angular selectivity with a small angular spread are key features of the electron source, which are essential to perform the commissioning measurements of the main spectrometer. The evolution of the pitch angle between the photocathode and the spectrometer entry magnet can be investigated in detail with particle-tracking simulations.

Figure 4.70 shows the pitch angle of multiple electron tracks that are emitted from the photocathode at different plate angles $\alpha_p = 0^\circ$ to 16° , as indicated by the color scale. The figure compares the conditions at the SDS-2 setup with the MoS setup. The electrons were created with a random initial energy that follows a normal distribution with $\mu = \sigma = 0.2$ eV at the photocathode and with random initial polar angle to the normal direction of the photocathode surface, following a $\cos \theta$ -distribution with angles up to 90° . These settings are the default of the simulations discussed in this chapter, and are always used unless indicated otherwise. The figure shows that the electron beam is collimated into a narrow angular distribution at a distance $d \approx 0.05$ m from the emission spot, i. e. the pitch angles decrease from their range up to 90° (according to the $\cos \theta$ -distribution) to considerably smaller values with a smaller spread. After the electrons leave the source and move on towards the entry magnet, the pitch angles increase again due to the adiabatic transformation (2.7). The angular spread of the produced electrons can be estimated from the figure for each given plate angle α_p by the width of the colored bands. It is observed that the angular spread in the entry magnet is rather constant for plate angles $\alpha_p \leq 10^\circ$; this will be further discussed below.

Magnetic reflection occurs when the pitch angle reaches 90° before passing the entry magnet, and this effect is clearly visible by the trajectories with $\alpha_p > 12^\circ$ that end at the top of the plot instead of continuing to the right side. The pitch angle where magnetic reflection occurs is different at the MoS setup due to the different magnetic fields. Note that for the SDS-2 setup, magnetic reflection also occurs at the pinch magnet at the end of the spectrometer so that electrons that pass the entry magnet can still be reflected before reaching the detector; this limits the maximal pitch angle that is transmitted from the entry magnet to $\theta_{max} = 70^\circ$ (see section 4.6.1).

The inset in figure 4.70 focuses on the pitch angle evolution inside the grounded cage of the electron source where the electrons undergo electrostatic acceleration ($d \leq 12.2$ cm from the emission spot). The inset uses a logarithmic distance axis to emphasize the effects that occur close to the photocathode surface, where the electric acceleration field is maximal. Again it can be seen that the electron beam is collimated and reaches a small angular spread within a few mm of their trajectory. Already at a distance of only 1 mm from the photocathode, the electrons reach a narrow angular distribution although their initial angle follows a $\cos \theta$ -distribution. The pitch angle further decreases towards the front plate at $d = 10$ mm due to the gain in longitudinal kinetic energy that results from the linear acceleration field. After passing the front plate, the electrons begin to move adiabatically as they are further accelerated to their maximal kinetic energy of 18.6 keV. The pitch angle further decreases as the transversal energy remains almost constant in this region (due to the small magnetic field gradient over the short distance of a few cm) and the longitudinal energy increases. The asymmetric electric field of the dipole electrode (around $d = 0.25$ cm at the SDS-2 setup) affects the electron pitch angles only locally. As mentioned earlier, the net effect on electrons that pass the dipole electrode only one – i. e. electrons that are not stored between source and spectrometer – is negligible for the discussion of the produced electrons.

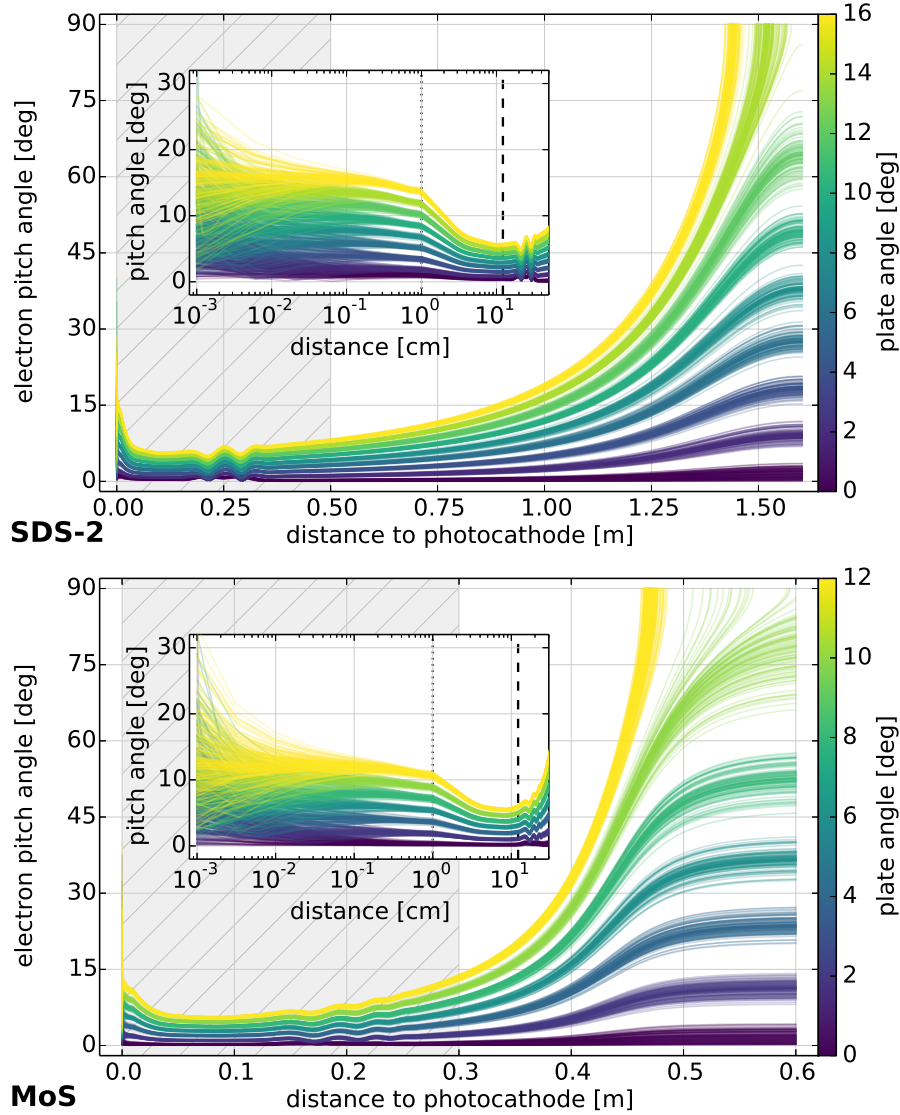


Figure 4.70.: Simulated electron trajectories in the SDS-2 (top) and MoS (bottom) setups. The plots show the pitch angle of 100 electrons that were tracked from the emission spot to the spectrometer entry magnet at different plate angles $\alpha_p = 0^\circ$ to 16° . The simulation was performed at nominal conditions ($U_{start} = -18.6$ kV, $U_{acc} = 5$ kV, $U_{dip} = 2$ kV, 3 kV in SDS-2/MoS). The MoS simulation used the enhanced magnetic field setting. The inset shows the conditions inside the grounded source cage (distance $d \leq 12.2$ cm from the emission spot, note the logarithmic axis); this region is indicated in gray in the main plot. The vertical lines mark the position of the front plate (dotted) and the end of the source cage (dashed). For all plate angles, the initial angular distribution is collimated towards the front plate, where the electrons show a defined pitch angle with small angular spread. The ongoing acceleration inside the source cage further decreases their pitch angle; it reaches a minimum close to the end of the source cage. The pitch angle is locally affected by the electric dipole field ($d \approx 26$ cm in SDS-2) and increases towards the spectrometer entrance due to the adiabatic transformation (2.7). Electrons that achieve a too large pitch angle are reflected before reaching the entry magnet ($\alpha_p > 12^\circ$ in SDS-2, the maximal angle depends on the electromagnetic conditions).

Zero voltage

The figure above showed the conditions at nominal high voltage settings ($U_{start} = -18.6\text{ kV}$ and $U_{acc} = 5\text{ kV}$). It is now interesting to compare this case with the conditions at the zero-voltage setting that was often used during the commissioning measurements ($U_{start} = -200\text{ V}$, $U_{acc} = 100\text{ V}$).

Figure 4.71 shows the pitch angles for electrons started with the same parameters as above at different plate angles in the SDS-2 setup. In this case where the acceleration voltage U_{acc} is reduced, angular selectivity cannot be achieved and the produced electrons have a broad angular distribution that is considerably larger than in the case of high voltage. This is seen clearly in the plot, and the influence of different plate angles on the produced electrons is marginal since the electron beam is not collimated efficiently. With the small acceleration voltage, the electrons are only accelerated adiabatically so that no defined pitch angle is imprinted. The pitch angle still decreases after the electrons are emitted from the photocathode due to the aforementioned gain in longitudinal energy by the electrostatic acceleration against ground potential. The most important difference in this setting is that the plate angle α_p has practically no influence on the pitch angle θ in the spectrometer entry magnet.

It should be noted that transmission function measurements that are performed at this setting – e. g. to determine the energy distribution of the produced electrons – typically use a reduced spectrometer voltage $U_{spec} \approx U_{start}$ as well, so that its energy resolution is drastically improved. In this case, the large angular spread of the electrons does not affect the observed transmission function.

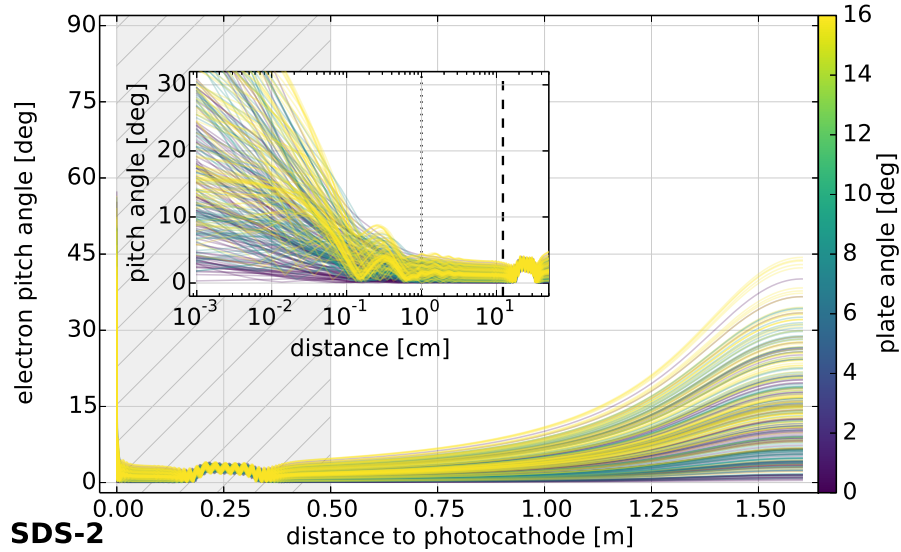


Figure 4.71.: Simulated electron trajectories at zero voltage in the SDS-2 setup. The plot shows the pitch angle of 100 simulated electrons at different plate angles $\alpha_p = 0^\circ, 8^\circ, 16^\circ$. The simulation was performed at the same conditions as shown in figure 4.70, but at zero-voltage ($U_{start} = -200\text{ V}$, $U_{acc} = 100\text{ V}$). Due to the missing acceleration field at the photocathode in this setting, angular selectivity is not achieved and the initial angular distribution is not collimated efficiently, in contrast to the high voltage case. The pitch angle in the spectrometer entry magnet does not depend on the used plate angle and shows a large angular spread.

4.8.4 Produced pitch angles in the spectrometer magnet

The produced angular distributions of the electrons in the spectrometer entry magnet at different settings are of special relevance to understand the feature of angular selectivity. Furthermore, the simulated angular distributions can provide important input for the analysis of measurement data. Due to the working principle of the MAC-E filter (section 2.2), the angular distributions directly affect the observed transmission functions. By comparing transmission functions that were measured at nominal high voltage and at zero-voltage, one can disentangle the angular distribution from the energy distribution in a measurement. The results that were discussed in section 4.5.6 (MoS) and section 4.6.5 (SDS-2) can now be compared with simulations.

Figure 4.72 shows the angular distributions that are produced under nominal conditions at the MoS and SDS-2 setups. It uses the same color scheme as the figures above, where each color corresponds to a different plate angle α_p ; this is also indicated at the top of each plot. The angular distributions shifts to larger pitch angles as the plate angle is increased, while the shape and width of the distributions stays essentially constant until large pitch angles above roughly 60° are reached. Here the arcsin-behavior of the adiabatic transformation (4.55) comes into play, which results in a non-linear dependency between the produced pitch angle θ and the plate angle α_p .

Pitch angles of 90° cannot be reached due to magnetic reflection. Electrons that are magnetically reflected before reaching the entry magnet do not contribute to the observed angular distribution, and consequently the angular distributions at larger plate angles are considerably deformed. This effect is especially visible at the MoS setup (bottom of the figure), where magnetic reflection is reached at $\alpha_p = 10^\circ$. A fraction of electrons is reflected in this case, and the distribution becomes strongly asymmetric. Another effect is responsible for the asymmetric distribution for $\alpha_p = 0^\circ$, where pitch angles close to 0° are produced. Because the pitch angle is a polar angle – and thus cannot reach negative values by definition – the part of the distribution that would normally extend below 0° (i. e. to negative values) is “wrapped around” into the positive regime instead. This creates an asymmetric distribution with a mean (or median) that is shifted towards higher pitch angles.

In general, the produced angular distributions are comparable for a given pitch angle [*sic!*], which means that the angular spread σ_θ is essentially defined by the mean pitch angle $\hat{\theta}$ regardless of the setup. The only difference between the two setups is that a different pitch angle is produced for the same plate angle α_p , which results from the different magnetic fields and the effect of the adiabatic transformation (4.55).

The pitch angles that are produced at different plate angles α_p are listed in table 4.28 (limited to even values $\alpha_p = 0^\circ, 2^\circ, \dots^\circ$ here for the sake of brevity). One can derive an *effective starting angle* θ_{start}^* that corresponds to the initial pitch angle that would produce the given pitch angle θ in the magnet. The two values are related by the adiabatic transformation model (4.55) that depends on the ratio of the magnetic fields,

$$\theta_{start}^* = \arcsin \left(\sin \theta_{mag} \cdot \sqrt{\frac{B_{start}}{B_{mag}}} \right) \approx \theta_{mag} \cdot \sqrt{\frac{B_{start}}{B_{mag}}}, \quad (4.105)$$

where B_{start} is the field at the emission spot and B_{mag} the field in the spectrometer entry magnet. The SDS-2 setup reaches a ratio $B_{start}/B_{mag} = 6.51$ and the MoS setup a ratio of 4.65. The conversion to θ_{start}^* allows to compare the produced pitch angle in different setups independently of the effects of adiabatic transformation, which is especially useful if different magnetic fields are present in the entry magnet. Hence, one would expect θ_{start}^* to be the same for both setups at a given plate angle α_p . A

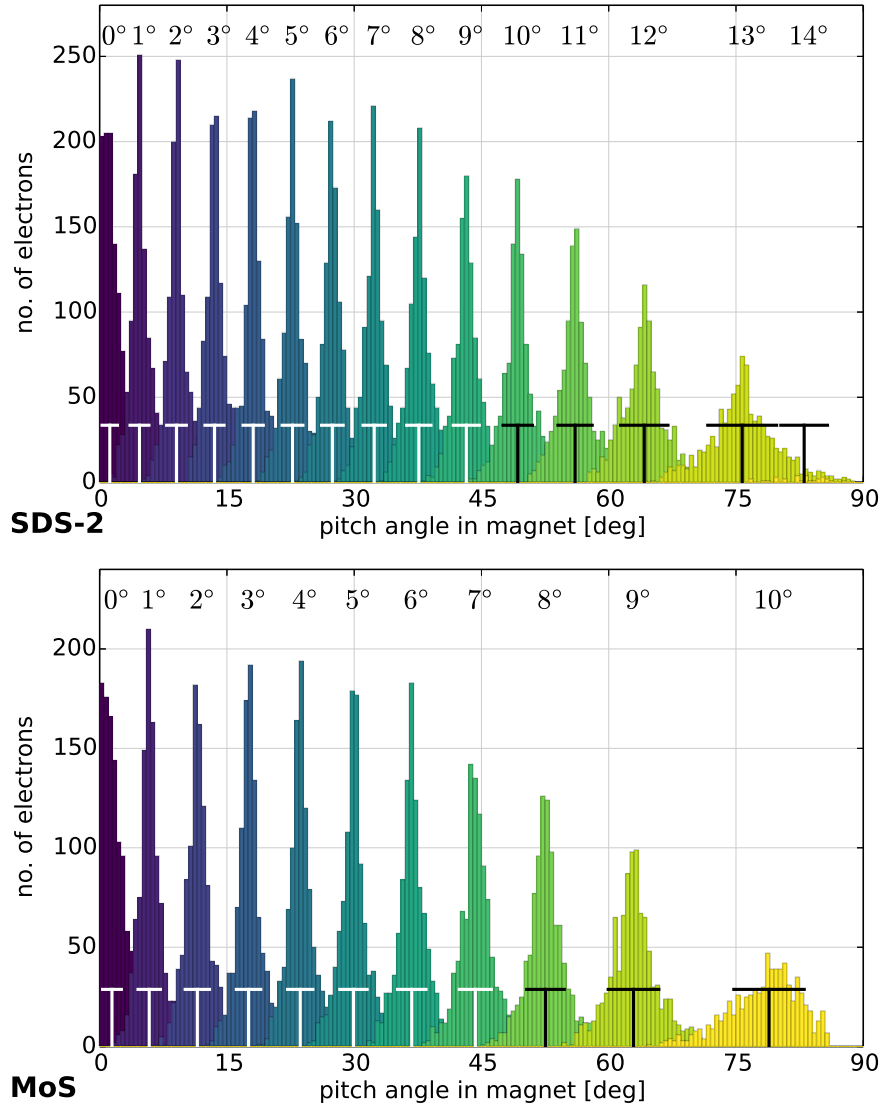


Figure 4.72.: Simulated angular distributions for different plate angles in the SDS-2 and MoS setups. The plots show the angular distributions that are produced in the spectrometer entry magnet under the same conditions as in figure 4.70 for different plate angles at $\alpha_{az} = 0^\circ$. The plots use the same color scheme to indicate the plate angle, which is also noted at the top of each plot. The T-like markers at the bottom of each distribution indicate their median and their 1σ -width, i. e. the produced pitch angle and the angular spread. A sharp angular distribution is achieved at each plate angle setting due to angular selectivity at the electron source. The shape and width of the distributions are comparable over the investigated range of pitch angles, except for large pitch angles close to the magnetic reflection limit. When magnetic reflection is reached, the upper tail of the distribution is partially cut off and the distribution is deformed accordingly.

slight discrepancy is observed due to the different initial magnetic field B_{start} in both setups, which influences the efficiency of the non-adiabatic acceleration close to the photocathode.

Table 4.28.: Simulated pitch angles at different plate angles for $\alpha_{az} = 0^\circ$.

setup	α_{az}	α_p	θ_{mag}	$\theta_{0,eff}$
SDS-2	0°	0°	1.2(10) $^\circ$	0.1(1) $^\circ$
		2°	9.1(11) $^\circ$	0.7(1) $^\circ$
		4°	18.1(10) $^\circ$	1.4(1) $^\circ$
		6°	27.4(12) $^\circ$	2.1(1) $^\circ$
		8°	37.6(13) $^\circ$	2.8(1) $^\circ$
		10°	49.3(16) $^\circ$	3.5(1) $^\circ$
		12°	64.2(26) $^\circ$	4.2(1) $^\circ$
		14°	83.0(28) $^\circ$	4.60(3) $^\circ$
MoS	0°	0°	1.5(12) $^\circ$	0.1(1) $^\circ$
		2°	11.5(13) $^\circ$	0.8(1) $^\circ$
		4°	23.6(13) $^\circ$	1.6(1) $^\circ$
		6°	36.8(15) $^\circ$	2.3(1) $^\circ$
		8°	52.5(19) $^\circ$	3.1(1) $^\circ$
		10°	78.9(42) $^\circ$	3.8(1) $^\circ$

Dependency on the plate angle

The relation between the produced pitch angle θ and the plate angle α_p can be described by the adiabatic transformation model (4.55) that has been derived earlier in this thesis.

Figure 4.73 shows this relation for the two experimental setups at nominal conditions, according to simulations. Each data point corresponds to the median pitch angle that is produced at a given plate angle, and the error bars indicate the 1σ -width of the corresponding angular distribution. The data points are fitted with the adiabatic transformation model, from which the reflection angle α_{max} can be determined as indicated in the figure. The first and last data points are excluded from the fit in each case for the reasons mentioned above: While the last data point at large pitch angles typically suffers from magnetic reflection, which deforms the angular distribution and shifts the observed median to a lower value, the first data point at $\alpha_p = 0^\circ$ shows a deviation towards larger pitch angles since the pitch angle cannot reach negative values and the distribution is “wrapped” into the positive regime. The remaining data points, however, are in excellent agreement with the fit model.

To investigate differences between the different azimuthal tilt directions of the plate setup, figure 4.74 compares the produced pitch angles for azimuthal plate angles $\alpha_{az} = 0^\circ, 180^\circ, 90^\circ, 270^\circ$ at the SDS-2 setup. A small deviation in the resulting reflection angle α_{max} is observed due to phase effects during the electrostatic acceleration of the electrons, which influence the produced pitch angle. Such phase effects have also been observed in the commissioning measurements, although the observed deviation was larger; this is discussed in more detail at the end of this section.

Table 4.29 lists the corresponding fit results. The slope value in the arcsin-term – which describes the dependency of the pitch angle θ on the plate angle α_p – is nearly equal for different azimuthal angle in the SDS-2 setup. Hence, the observed asymmetry in the pitch angle θ and the reflection

angle α_{max} is fully described by a different offset value. At the MoS setup where the magnetic field at the spectrometer entrance is higher, magnetic reflection is reached at a smaller plate angle α_{max} . This behavior is reproduced by the larger slope parameter in the fit result, which causes a large pitch angle for a given plate angle setting.

The reflection angles α_{max} that were determined here from simulation results match the results from magnetic reflection measurements at the SDS-2 and MoS setups. However, the observed asymmetry between different azimuthal directions α_{az} of the plate angle was up to 3° in the measurements, whereas the simulation results for α_{max} are essentially all in agreement. Possible causes for this discrepancy are evaluated in sections 4.8.10ff.

The simulations also allow to investigate the pitch angle θ_{src} that is produced at the end of the grounded source cage. At this point, the non-adiabatic acceleration ceases but the adiabatic transformation does not yet affect the pitch angle due to the rather small magnetic field gradient inside the source chamber (cmp. figure 4.70 where the pitch angle increase towards the entry magnet becomes apparent only at distances $d \gg 0.1$ m from the emission spot). The resulting values for θ_{src} are also shown in figure 4.73 and table 4.28. It shows a strictly linear behavior on the plate angle α_p , and the corresponding data points can be described by a linear fit model. Again, the first data point has been excluded from the fit due to the observed deviation towards larger pitch angles (for the same reason as discussed above).

The produced pitch angles and the linear dependency on α_p are comparable for both experimental setups, which is expected since the starting magnetic field B_{start} at the emission spot was chosen specifically to be similar in both cases. The smaller reflection angle α_{max} that is observed at the MoS setup is therefore fully explained by the higher magnetic field in the entry magnet, which causes magnetic reflection to occur at smaller initial pitch angles.

Table 4.29.: Fit results of simulated pitch angles at different azimuthal plate angles.

setup	α_{az}	θ_{src}	θ	α_{max}
SDS-2	0°	$0.33 \cdot \alpha_p + 0.2^\circ$	$\arcsin(4.28 \cdot \alpha_p) + 0.7^\circ$	$12.5(5)^\circ$
	180°	$0.33 \cdot \alpha_p + 0.2^\circ$	$\arcsin(4.20 \cdot \alpha_p) + 0.4^\circ$	$12.8(4)^\circ$
	90°	$0.33 \cdot \alpha_p + 0.5^\circ$	$\arcsin(4.20 \cdot \alpha_p) + 0.6^\circ$	$12.8(4)^\circ$
	270°	$0.34 \cdot \alpha_p - 0.3^\circ$	$\arcsin(4.27 \cdot \alpha_p) + 0.5^\circ$	$12.6(5)^\circ$
MoS	0°	$0.38 \cdot \alpha_p + 0.1^\circ$	$\arcsin(5.67 \cdot \alpha_p) + 0.2^\circ$	$10.1(12)^\circ$

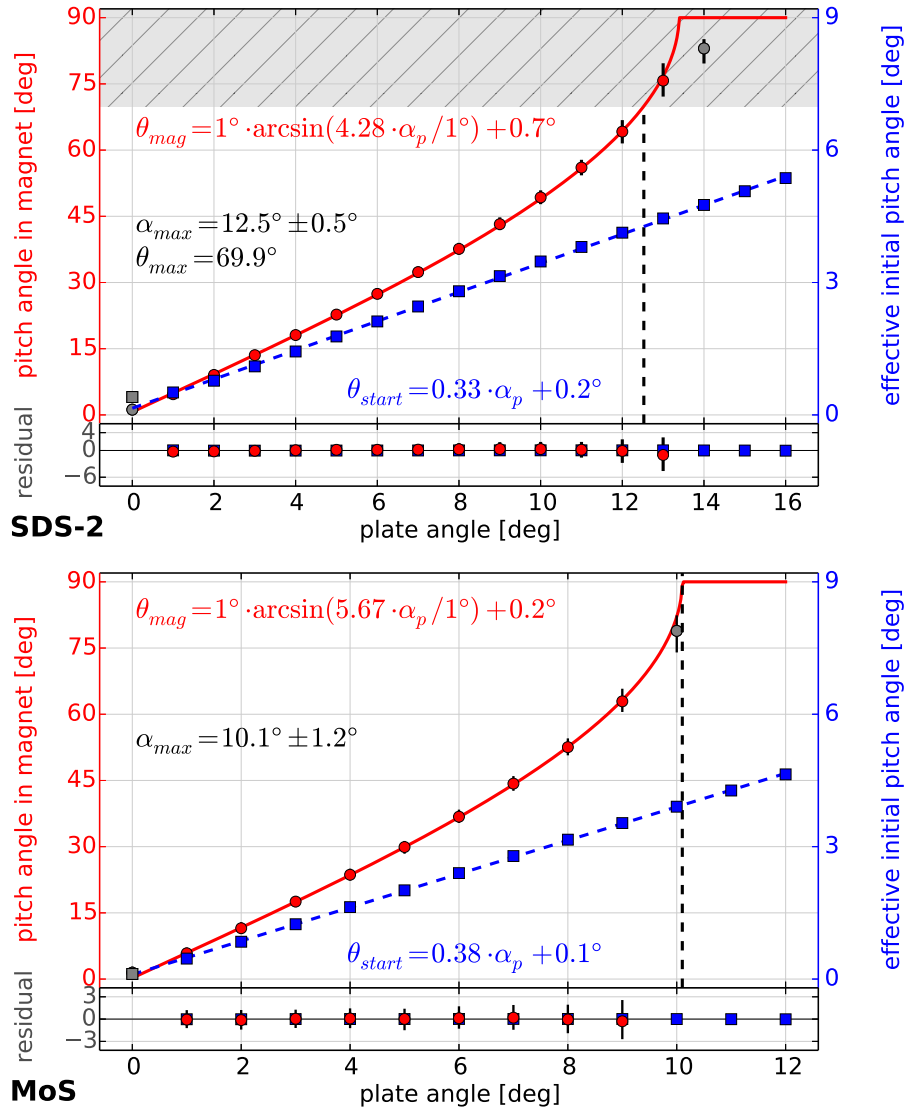


Figure 4.73.: Simulated pitch angles for different plate angles in the SDS-2 and MoS setups. The plots show the relation between the plate angle α_p and the pitch angle θ_{mag} that is reached in the spectrometer entry magnet (red, left axis). The pitch angle θ_{source} at the end of the source cage is shown for comparison (blue, right axis; note the different scale). The simulation uses the results shown in figure 4.72. The pitch angle at the source cage shows a linear dependency to the plate angle as a result of the increasing transversal energy of the produced electrons as the source is tilted (cmp. figure 4.68). The first data point (zero-angle $\alpha_p = 0^\circ$) is excluded from the fit, since the underlying angular distribution is asymmetric and produces a systematic bias towards larger values of θ_{source} . The pitch angle in the magnet follows an arcsin-behavior due to the adiabatic transformation (4.55). Again the first data point is excluded for the same reason. The last data point is also excluded since the angular distribution is deformed due to magnetic reflection. Simulations at other azimuthal plate angles ($\alpha_{az} = 90^\circ, 180^\circ, 270^\circ$) indicate that the produced pitch angles θ_{source} and θ_{mag} are modified by asymmetries in the electron acceleration process, which is caused by misalignments of the electromagnetic fields. A similar effect was observed in SDS-2 measurements (figure 4.58). At the SDS-2 setup, electrons with $\theta_{mag} \geq 69.9^\circ$ cannot reach the detector due to magnetic reflection at the pinch magnet; this is indicated by the gray area at the top of the plot.

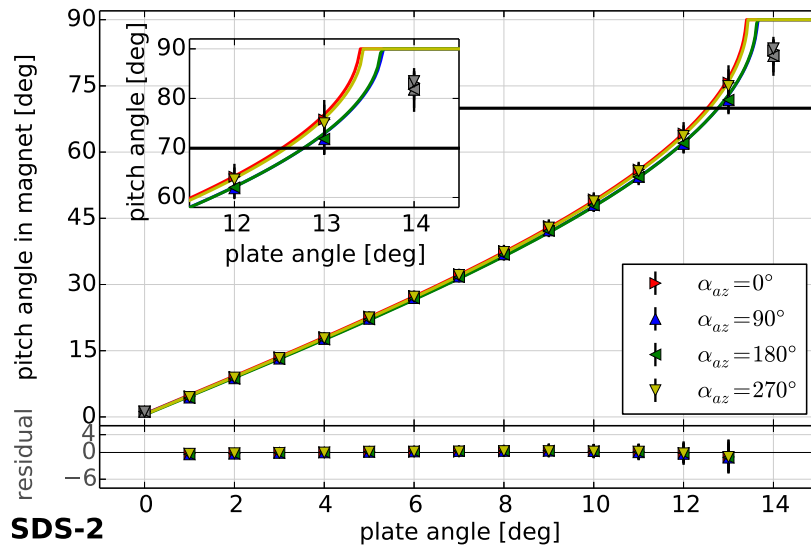


Figure 4.74.: Simulated pitch angles for different plate angles in the SDS-2 setup. The plot shows the relation between the plate angle α_p and the pitch angle θ_{mag} in the spectrometer entry magnet for different azimuthal tilt directions $\alpha_{az} = 0^\circ, 180^\circ, 90^\circ, 270^\circ$. The horizontal black line marks the cut-off at $\theta_{max} = 69.9^\circ$ due to magnetic reflection at the pinch magnet. An asymmetry in the produced pitch angles is observed between the different azimuthal directions, which is reflected in a different reflection angle α_{max} (see table 4.29). The reflection angle corresponds to the point where the pitch angle reaches θ_{max} , i. e. where the data points cross the horizontal line that is shown in this plot.

4.8.5 Energy and angular distributions

Zero voltage

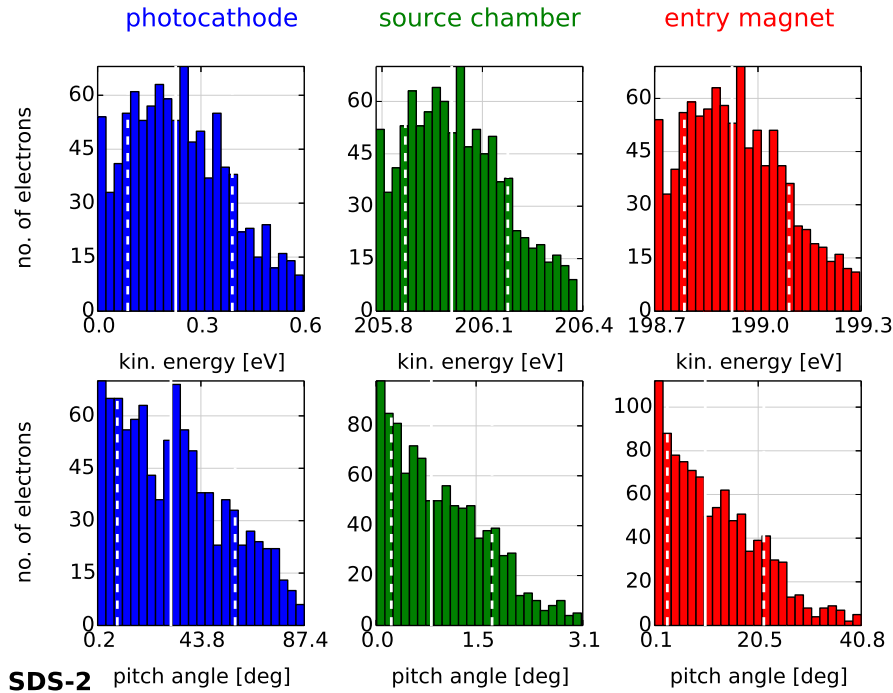


Figure 4.75.: Simulated energy and angular distributions at zero voltage in the SDS-2 setup. The plot shows the energy (top row) and angular distributions (bottom row) of 1000 simulated electrons that were started at the photocathode (left) with the shown initial distributions (normal distribution with $\mu = \sigma = 0.2 \text{ eV}$ for the energy, $\cos \theta$ -distribution for the angle). The distributions at the end of the grounded source cage (center) and in the spectrometer entry magnet (right) are shown for comparison. The vertical white lines indicate the median and the 1σ -width of the distributions. In the zero voltage setting that is shown here ($U_{start} = -198.7 \text{ V}$, $U_{acc} = 100 \text{ V}$), angular selectivity is not achieved and the angular distribution is not collimated into a sharp peak. A large angular spread is observed in the entry magnet. The energy distribution is not affected by the electron acceleration and transport mechanisms in the source. It is reproduced in the spectrometer entry magnet, so that the energy distribution observed in transmission function measurement corresponds to the initial energy distribution of the emitted electrons.

A better understanding of the effects that were discussed above can be gained from a closer look at the angular and energy distributions of the produced electrons at different operational parameters. The two distributions in the spectrometer entry magnet are extremely relevant for the commissioning measurements of the electron source, as they influence the observed transmission function according to the analytical model (section 4.1.1).

At first the conditions in the zero-angle setting will be investigated. Figure 4.75 shows the energy and angular distributions of 1000 simulated electrons that were started at the photocathode with $U_{start} \approx -200 \text{ V}$, $U_{acc} = 100 \text{ V}$ and $U_{dip} = 3 \text{ kV}$ in the SDS-2 setup at nominal magnetic field. The distributions are evaluated at three positions: the emission spot (showing the initial distributions that are assumed for the simulation); the end of the source chamber (grounded source cage at a distance

$d = 12.2$ cm from the emission spot; here the electrons have reached their maximal kinetic energy); and the spectrometer entry magnet. The initial distributions shown here are also used in other simulations that are discussed in this section, unless indicated otherwise. They use an initial kinetic energy that is normal-distributed with $\mu = \sigma = 0.2$ eV (limited to 0.0 eV to 0.6 eV) and $\cos\theta$ -distributed initial polar angles w. r. t. the normal of the photocathode surface that reaches angles up to 90° . The figure shows the distributions that are produced at the zero-angle setting with $\alpha_p = 0^\circ$.

The energy distribution is shifted to larger energies as the electrons are accelerated on their way towards the spectrometer entrance, but the shape and width of the distribution is unaffected by this acceleration. This verifies that it is possible to investigate the *initial* energy distribution of the produced electrons by analyzing the energy distribution in the entry magnet. As the electrons proceed towards the analyzing plane of the spectrometer, their kinetic energy decreases and the observed transmission function reflects the initial energy distribution. This has been discussed in detail in section 4.1.1.

The angular distribution, however, is compressed significantly as the electrons are accelerated. The maximal pitch angle that is observed reduces from 90° to 3° at the end of the source chamber. Note that this collimation towards smaller pitch angles occurs even with a low acceleration voltage of $U_{acc} = 100$ V in the zero-voltage setting. Although angular selectivity is not available in this setting (cmp. section 4.8.3), a small angular spread of less than 2° is achieved at the end of the source chamber. The adiabatic transformation towards the entry magnet then results in an increase of the pitch angle, which produces a rather larger angular spread with a maximal pitch angle of roughly 40° . Hence, even at zero-voltage the initial angular spread is reduced by a factor of about 2 due to the electron acceleration processes inside the source. Interestingly, the shape of the angular distribution does not seem to be affected by the pitch angle transformation.

High voltage

One can now compare the distribution at the zero-voltage setting with the results under nominal conditions at high voltage. Figure 4.76 shows the energy and angular distributions at the three positions that were examined above, now with $U_{start} \approx -18.6$ kV and $U_{acc} = 5$ kV. In this setting, angular selectivity is achieved and the source produces electrons with a small angular spread. Again, the figure shows the results for the zero-angle setting with $\alpha_p = 0^\circ$.

For the energy distribution, the same effects as in the zero-voltage case are observed. The distribution shifts to higher energies due to the electron acceleration, but does not change its shape and width. It is therefore possible to investigate the initial energy distribution at high voltage as well, if one considers the angular spread of the electrons in the analysis of measurement data. This method has been applied at the MoS setup (section 4.5.6) and the SDS-2 setup (section 4.6.5).

In contrast, the angular distribution now shows a completely different behavior than at the zero-voltage setting. Due to the higher acceleration voltage, the electron beam is collimated efficiently and reaches a sharp angular distribution at the end of the source chamber. The angular spread that is observed here is less than 0.2° and the angular distribution is symmetric around a mean pitch angle of 0.4° . The distribution is therefore considerably narrower than in the zero-voltage case, which results from the non-adiabatic acceleration that imprints a defined pitch angle on the electrons. As before, the adiabatic transformation towards the entry magnet increases the pitch angle again. However, since the pitch angle at the end of the source chamber is extremely small, the transformation does not produce the large pitch angles in the magnet that were seen in the zero-voltage simulation. The highly

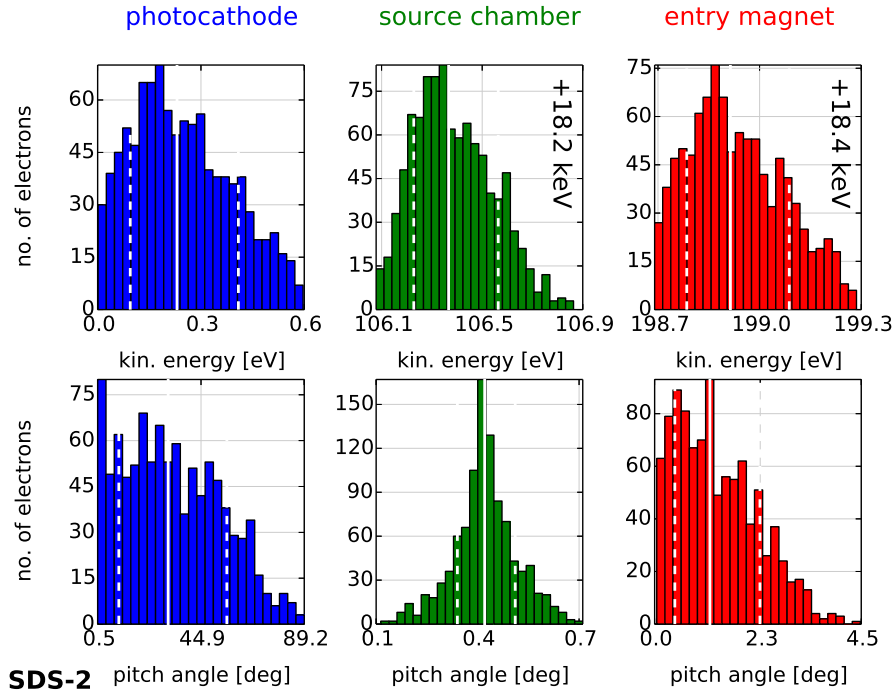


Figure 4.76.: Simulated energy and angular distributions at high voltage in the SDS-2 setup. The plot is similar to figure 4.75, but shows the resulting distributions at nominal high voltage ($U_{start} = -18\,598.7\text{ V}$, $U_{acc} = 5\text{ kV}$). At this setting, angular selectivity is achieved and the angular distribution is collimated into a sharp peak at the end of the source cage. The angular spread increases towards the spectrometer entry magnet due to adiabatic transformation (2.7) in the magnetic field. The shape of the angular distribution is modified in this case, since the produced pitch angle θ cannot become negative due to its definition as polar angle. The distribution is therefore “wrapped” into the positive regime and becomes asymmetric. As in the zero-voltage case, the energy distribution is completely unaffected by the electron transport towards the entry magnet.

asymmetric distribution in the magnet can again be explained by the fact that the pitch angle cannot reach negative values because it is defined as a polar angle. As seen in figure 4.70, the pitch angle is further decreased after the electrons pass the end of the source chamber, until at some point the low tail of the angular distribution stretches into the negative regime. As it is impossible to realize negative pitch angles, the corresponding fraction of the angular distribution is wrapped into the positive regime. The resulting angular distribution is then a superposition of the original distribution in the positive regime and the negative fraction that is mirrored at 0° , which results in the asymmetric shape that is observed. Due to this effect, the median⁶² (and mean) of the angular distribution has a systematic bias towards larger values if the original distribution extends into the negative regime. Hence, the simulations and measurements discussed here never yield a median pitch angle of 0° , even at the zero-angle setting with angular selectivity.

The kinetic energy and pitch angle of the simulated electrons in the spectrometer entry magnet are listed in table 4.30 for different operational parameters and simulation settings. The first line in the table refers to the nominal setting ($U_{start} \approx -18.6\text{ keV}$, $U_{acc} = 5\text{ kV}$, $U_{dip} = 3\text{ kV}$ as used in the

⁶². The median and 1σ -width of a given distribution can easily be computed from its (16%, 50%, 84%)-percentiles. This is the preferred method for the analysis discussed in this thesis.

measurements and default energy and angular distribution). The comparison between different initial angular distributions ($\cos \theta$ or spherical/isotropic) shows that the angular distribution in the magnet is heavily influenced by the initial setting. For example, using a spherical distribution in the simulation results in a considerably larger angular spread⁶³.

Furthermore, a broader initial energy distribution (e.g. with $\mu = \sigma = 0.5 \text{ eV}$) also increases the produced pitch angle and the angular spread. This interesting correlation will be further investigated below. The energy distribution in the entry magnet, on the other hand, only depends on the initial distribution and is not influenced by the electron acceleration and transport mechanisms (except for the observed energy shift due to the gain in kinetic energy). The initial energy distribution of the electrons is therefore fully reproduced in the entry magnet.

Non-zero pitch angles

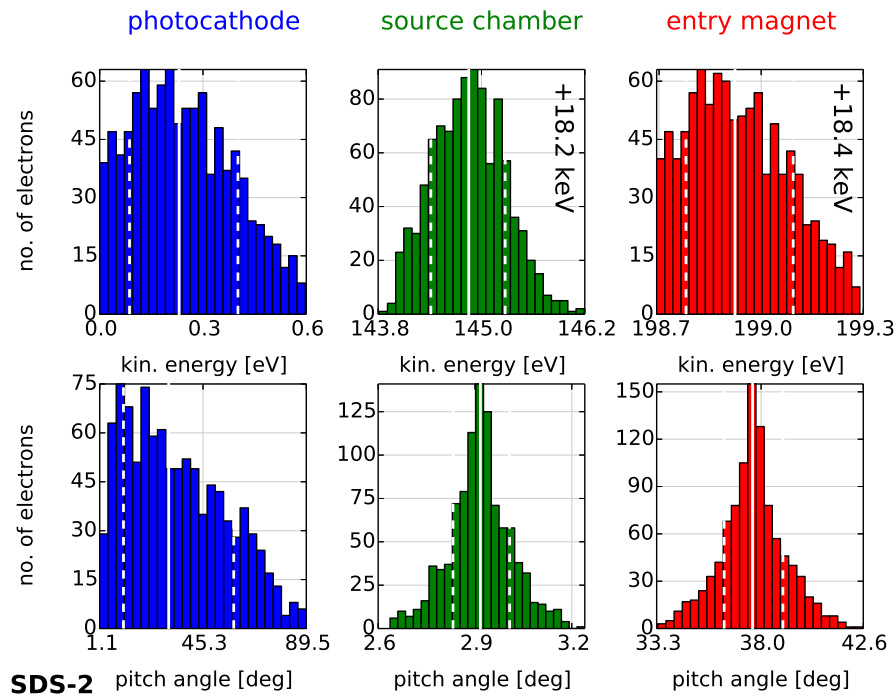


Figure 4.77.: Simulated energy and angular distributions at high voltage and increased plate angle in the SDS-2 setup. Similar to the previous figures, the plot shows the energy and angular distributions produced by the electron source. Here the distributions at a non-zero plate angle of $\alpha_p = 8^\circ$ in the high voltage setting are shown. In this case, angular selectivity still collimates the angular distribution into a sharp peak at the end of the source cage, but the produced pitch angles are significantly larger ($\hat{\theta}_{source} = 2.9^\circ$ instead of 0.4° at zero-angle). This is of course expected from the tilting against the magnetic field line. The pitch angle in the spectrometer entry magnet is again increased due to adiabatic transformation. This shows that by tilting the source to different plate angles α_p , one can produce defined pitch angles of roughly 0° to 90° in the entry magnet. Even at this setting with non-zero plate angle, the energy distribution in the entry magnet corresponds to the initial energy distribution of the electrons.

⁶³. Independent measurements have indicated that electrons that are emitted from a photocathode in a plate-capacitor setup follow a $\cos \theta$ -distribution [PB02]; this setting is therefore used by default.

The effect of non-zero plate angles ($\alpha_p > 0^\circ$) can also be investigated by simulations. Figure 4.77 shows the energy and angular distribution in the nominal setting (see above), but with a plate angle $\alpha_p = 8^\circ$. As before, the shape and width of the energy distribution at the entry magnet is not affected by the acceleration and transport mechanisms in the electron source. The energy distribution at the end of the source chamber, however, shows a considerable deformation and has a larger energy spread than the initial distribution. This deformation is caused by the fraction of electrons that has not yet reached its maximal kinetic energy at this point. The effect is therefore related to the chosen position to examine the distributions at the end of the source chamber. Moving the analysis point to a larger distance $d > 12.2$ cm from the emission spot would yield an energy distribution that is comparable to the initial one. The observed effect is therefore purely caused by the analysis and not a physical effect. This is also suggested by the fact that the distribution in the entry magnet closely follows the initial distribution again.

The angular distribution at the end of the source chamber again shows a similar peak-like shape as seen in figure 4.76 at zero-angle, but the median of the distribution is now shifted to a pitch angle of 2.9° due to the increased plate angle α_p . In this case where the produced pitch angles are much larger than 0° , the “wrap-around” effect of the pitch angle at $\theta \rightarrow 0^\circ$ is not observed and the angular distribution in the magnet is fully symmetric.

An important conclusion from this analysis is that the energy distribution in the spectrometer entry magnet is not affected by changing the starting voltage U_{start} or tilting the source to $\alpha_p > 0^\circ$. It is thus possible to consider the energy and angular distributions as two independent contributions to the observed transmission function. This is the underlying approach on which the analytical transmission model that was derived in section 4.1 is based upon.

Reduced voltage

Finally, one can compare the distributions at nominal high voltage with the results for a reduced starting voltage. Some of the commissioning measurements at the MoS setup were performed at half the nominal voltage to determine the energy distribution experimentally, and a similarly reduced voltage setting was also used at the end of the SDS-2 measurement phase. Figure 4.78 shows the energy and angular distributions for $U_{start} = -9.3$ kV for the SDS-2 setup at otherwise nominal settings ($U_{acc} = 5$ kV, $U_{dip} = 3$ kV, $\alpha_p = 0^\circ$). As expected, the energy distribution is again unaffected by the electron acceleration. For better comparison with figure 4.76, the energy distributions in the figure use an offset of 9.0 keV or 9.1 keV so that the distributions can be compared visually. The angular distribution is now shifted to significantly higher pitch angles due to the changed acceleration processes at the smaller starting voltage. The shape of the distribution is again comparable to the above results and again shows a peak-like structure.

To understand how the produced pitch angles are affected by the starting voltage, one must consider that the pitch angle θ of an electron is defined by the ratio between its longitudinal kinetic energy E_{\parallel} and its transversal energy E_{\perp} according to (2.1):

$$\frac{E_{\perp}}{E_{\parallel}} = \frac{\sin^2 \theta}{\cos^2 \theta} = \tan^2 \theta \quad \Rightarrow \quad \arctan \sqrt{\frac{E_{\perp}}{E_{\parallel}}} = \theta. \quad (4.106)$$

The transversal energy is largely defined by the acceleration field at the photocathode and the initial pitch angle of the electron, as discussed in section 4.8.2 above. The transversal energy is therefore *not* changed by reducing the starting voltage, as long as the acceleration voltage U_{acc} between the plates

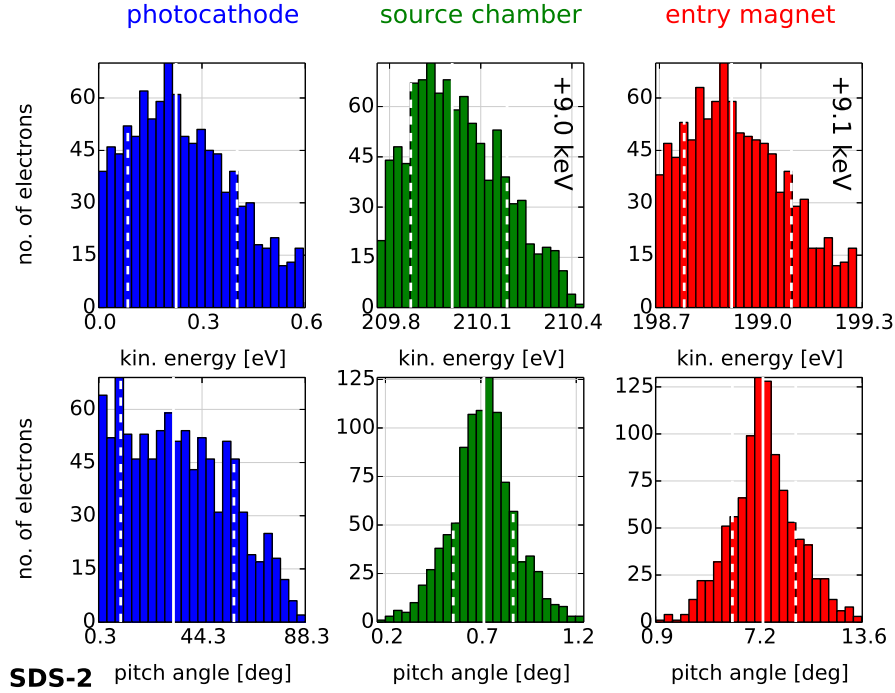


Figure 4.78.: Simulated energy and angular distributions at reduced voltage in the SDS-2 setup. For comparison with figure 4.76 at high voltage, this plot shows the resulting distributions at reduced starting voltage ($U_{start} = -9289.7$ V, $U_{acc} = 5$ kV) and zero-angle $\alpha_p = 0^\circ$. Similar settings were used occasionally in the SDS-2 and MoS measurements. In comparison with the high voltage setting, the produced pitch angle at the end of the source cage and in the spectrometer entry magnet is considerably larger ($\theta_{mag} = 7.2^\circ$ instead of 1.2° at high voltage). This is explained by the smaller longitudinal energy which the electron gains as it is accelerated towards ground potential, while the transversal energy is nearly the same due to the source design. However, the increase in θ_{mag} is larger than expected from this effect, which indicates that the zero-angle has changed in this special setting. This results in an additional shift in the produced pitch angle.

is the same. The longitudinal energy, however, corresponds to the starting voltage since the electrons gain a kinetic energy $E_{\parallel} = qU_{start}$ as they propagate towards the spectrometer entrance. Reducing the starting voltage therefore reduces the longitudinal energy, and hence produces a larger pitch angle.

The effect of a reduced starting voltage can therefore be estimated from (4.106) above. Assuming a reasonable value of $E_{\perp} = 10$ eV at the zero-angle setting, the produced pitch angle in the magnet is $\theta = 1.3^\circ$ at nominal high voltage ($E_{\parallel} = 18.6$ keV). By reducing the starting voltage to half this value, the produced pitch angle increases to 1.9° . Apparently this value is much smaller than the simulation result of $\theta = 7.2^\circ$ that is shown in the figure above. To explain this deviation, one must consider that the electrostatic acceleration fields inside the source chamber are likely affected by the voltage reduction, which would have an additional effect on the produced pitch angle. The reduced voltage therefore causes a systematic shift of the produced pitch angle. This shift can be explained by a changed zero-angle, which is also indicated by additional simulations which are skipped here for brevity. A changed zero-angle implies that any calibration that has been performed beforehand at nominal conditions becomes invalid if the measurement is performed at reduced starting voltage, which has severe implications for measurements and simulations. This effect is further examined in section 4.8.9.

Table 4.30.: Simulated kinetic energies and pitch angles at different simulation setting in the SDS-2 setup.

setting	angle	energy	U_{acc}	U_{dip}	E_{mag}	θ_{mag}
18.6 kV	0° to 90° (cos θ)	$\mu = \sigma =$ 0.2 eV	5 kV	3 kV	18 598.91(15) eV	1.20(93)°
		$\mu = \sigma =$ 0.1 eV			18 598.81(8) eV	0.87(69)°
		$\mu = \sigma =$ 0.5 eV			18 599.24(40) eV	1.75(156)°
	0° to 90° (spher.)	$\mu = \sigma =$ 0.2 eV	5 kV	3 kV	18 598.94(16) eV	2.09(102)°
200 V	0° to 90° (cos θ)	$\mu = \sigma =$ 0.2 eV	100 V	3 kV	198.93(15) eV	10.1(95)°
		$\mu = \sigma =$ 0.1 eV			198.81(8) eV	7.3(61)°
		$\mu = \sigma =$ 0.5 eV			199.26(40) eV	16.3(155)°
	0° to 90° (spher.)	$\mu = \sigma =$ 0.2 eV	100 V	3 kV	198.94(15) eV	19.4(96)°

4.8.6 Correlation between kinetic energy and pitch angle

Energy distributions

Up to this point, the energy and angular distributions have been investigated independently of each other. The simulations also allow to examine possible correlations between these two important parameters, and the following sections discuss how these correlations affect the distributions that are observed in the spectrometer entry magnet.

Figure 4.79 shows a correlation plot between the initial energy distribution (at the emission spot; top right) and the final energy distribution (in the entry magnet; bottom left). The colors indicate the initial pitch angle of the simulated electrons, which follows a $\cos \theta$ -distributed (top left). The figure therefore allows to examine the correlation between the two energy distributions (bottom right) and how the correlation is affected by the angular distribution (indicated by the colors). As discussed above, the energy distribution is merely shifted to a higher kinetic energy in the entry magnet while its shape and width does not change. This is reflected in the correlation plot, where a purely linear behavior is observed and the determined correlation is maximal with $\rho = 1.0$. The colors indicate that the energy distribution is not affected by the angular distribution, since electrons from the complete range of pitch angles (0° to 90°) contribute to full energy distribution, i. e. the observed energy distribution shows both light and dark colors without any preference for specific energies.

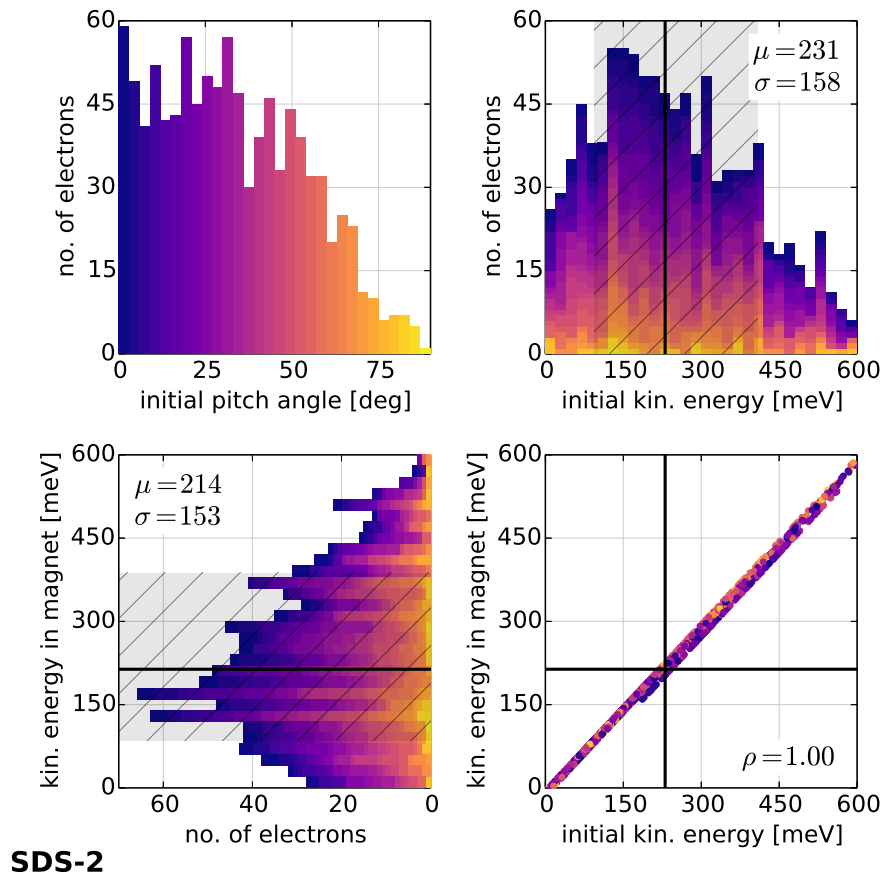
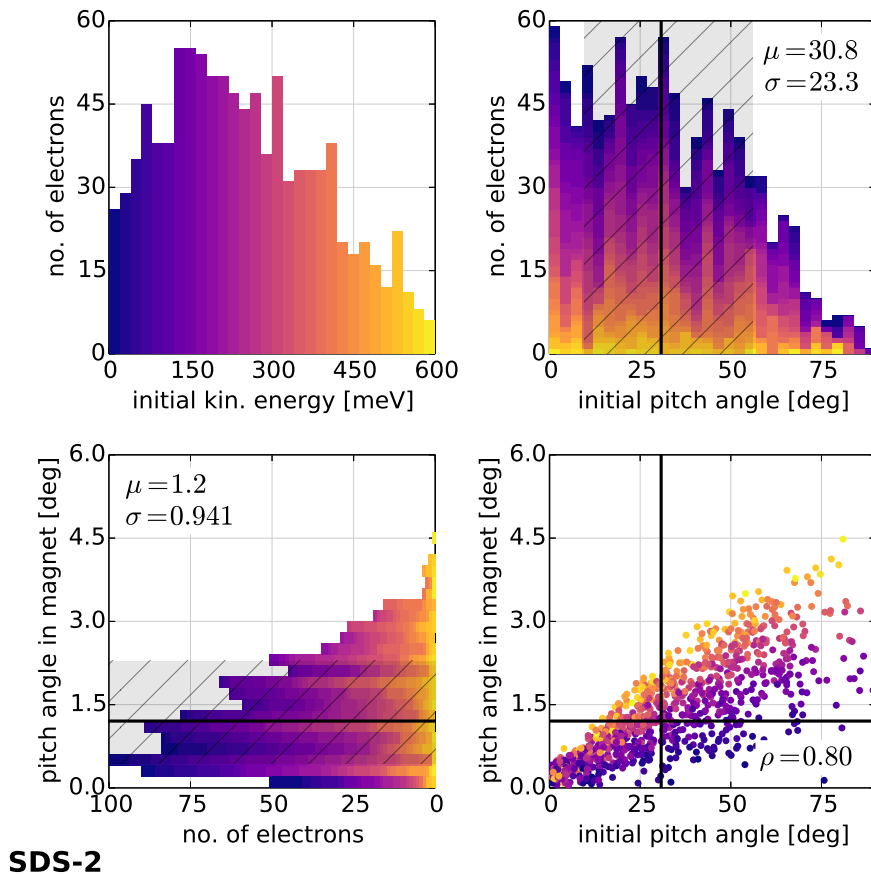


Figure 4.79.: Correlation of simulated energy distributions in the SDS-2 setup. The four plots show the initial energy distribution (top right) and the energy distribution in the spectrometer entry magnet (bottom left) together with their correlation (bottom right) at nominal high voltage ($U_{start} = -18.6\text{ kV}$, $U_{acc} = 5\text{ kV}$) with $\alpha_p = 0^\circ$. The distributions and data points in the correlation plot are colored by the initial pitch angle of the electrons (top left). The solid lines and hatched areas mark the median and 1σ -width of the angular distributions. The correlation plot shows that the initial energy distribution of the electrons is completely reproduced in the magnet (correlation coefficient $\rho = 1.0$). The produced energy distribution is also not affected by the angular distribution of the electrons in this setting.

Angular distributions

A different behavior can be observed for the angular distribution, which is investigated in figure 4.80. Similar to the figure above, the initial and final angular distributions are plotted against each other in a correlation plot, and the colors indicate different kinetic energies from the initial energy distribution. The simulation has been performed at zero-angle ($\alpha_p = 0^\circ$), resulting in the asymmetric distribution in the entry magnet that has been observed already in figure 4.76 above. The correlation plot indicates that the angular distributions are strongly correlated – higher initial pitch angles to produce higher pitch angles in the magnet – but in contrast to the energy distributions the correlation is not maximal ($\rho = 0.8$).



SDS-2

Figure 4.80.: Correlation of simulated angular distributions in the SDS-2 setup. The plot shows the initial angular distribution (top right) and the angular distribution in the spectrometer entry magnet (bottom left) with their correlation (bottom right) at nominal high voltage ($U_{start} = -18.6$ kV, $U_{acc} = 5$ kV) and $\alpha_p = 0^\circ$. The distributions and data points in the correlation plot are colored by the initial kinetic energy of the electrons (top left). The solid lines and hatched areas mark the median and 1σ -width of the angular distributions. At this plate angle, an asymmetric angular distribution is produced in the entry magnet due to the “wrap-around” effect of the pitch angle that was discussed earlier in this section. The median of the distribution is therefore shifted to a larger pitch angle of 1.2° . The correlation plot shows the interesting feature that electrons with higher kinetic energy also produce larger pitch angles in the magnet, as indicated by the colors. The observed angular spread is therefore also affected by the initial energy spread of the electrons.

What is interesting here is that there is a clear connection between the initial kinetic energy and the resulting pitch angle, as indicated by the colors. The correlation plot shows that higher initial energies (lighter colors) produce larger pitch angles in the entry magnet, and vice versa. The final angular distribution that is shown on the bottom left also indicates that electrons with higher energies also contribute more to the observed angular spread – the pitch angles above 3° are dominated by light colors, i. e. initial energies of more than 450 meV in this case. Hence if only low-energetic electrons were present, the observed angular spread would be considerably smaller.

This unexpected correlation can be explained by considering the non-adiabatic acceleration processes inside the source. The electrostatic acceleration field must work against the magnetic guiding field to

imprint a defined pitch angle on the electrons, which is represented in the Lorentz equation

$$\vec{F} = m_e \vec{a} = q \cdot (\vec{E} + \vec{v} \times \vec{B}) \quad \text{with} \quad E_{kin} = \frac{1}{2} m_e v^2, \quad (4.107)$$

where \vec{v} indicates the electron's velocity that is related to its kinetic energy. Therefore at higher energy, the acceleration becomes more dominated by the magnetic guiding field and the electrostatic acceleration is less effective. Given the initial $\cos \theta$ -distribution of the emitted electrons, the resulting pitch angle is typically larger for electrons at higher energies.

Conclusively, the achieved angular spread does not only depends on the acceleration voltage U_{acc} and the configuration of the magnetic fields at the electron source, but also on the energy distribution of the emitted electrons. This means that varying the wavelength of the incident UV light at the photocathode, which defines the energy spread according to $E_e = h\nu - \Phi$ (cmp. section 4.2.2) also influences the angular spread that can be observed in a transmission function measurement. It should be noted that this effect is overshadowed by the direct contribution of the energy distribution to the transmission function, which is typically more pronounced with the electron source that is discussed in this work⁶⁴. However, one should consider this effect if the angular distribution is investigated for measurements where the electron source was tuned to achieve a small energy spread, i. e. at UV wavelengths that match the photocathode work function.

Non-zero plate angles

Finally, the correlation between the angular distributions can be investigated for the case of non-zero plate angles. Figure 4.81 shows the correlation plot for $\alpha_p = 8^\circ$. The produced pitch angle in the magnet is much larger than at the zero-angle setting, and an symmetric angular distribution is observed. Similar to the above plot, electrons with larger kinetic energies lead to a broadening of the angular distribution, while low-energetic electrons contribute mainly to the sharp peak that is observed. In the angular distribution plot (bottom left in the figure), this is clearly visible since the darker colors (low energies) are only visible close to the peak, while the lighter colors (higher energies) span the full range of the produced pitch angles. The observed correlation between energy and angular distribution is therefore independent of the plate angle, and seems to be a general effect that influences the electron transport inside the electron source.

⁶⁴. An estimation of the net effect of the angular distribution on the observed transmission width was performed in section 4.6.5. For an angular distribution with $\hat{\theta} = \sigma_\theta = 2^\circ$ in the entry magnet, the effective energy spread in the analyzing plane of the spectrometer is less than 10 meV according to (4.88), which is extremely small w. r. t. the actual energy spread of up to 300 meV at small UV wavelengths.

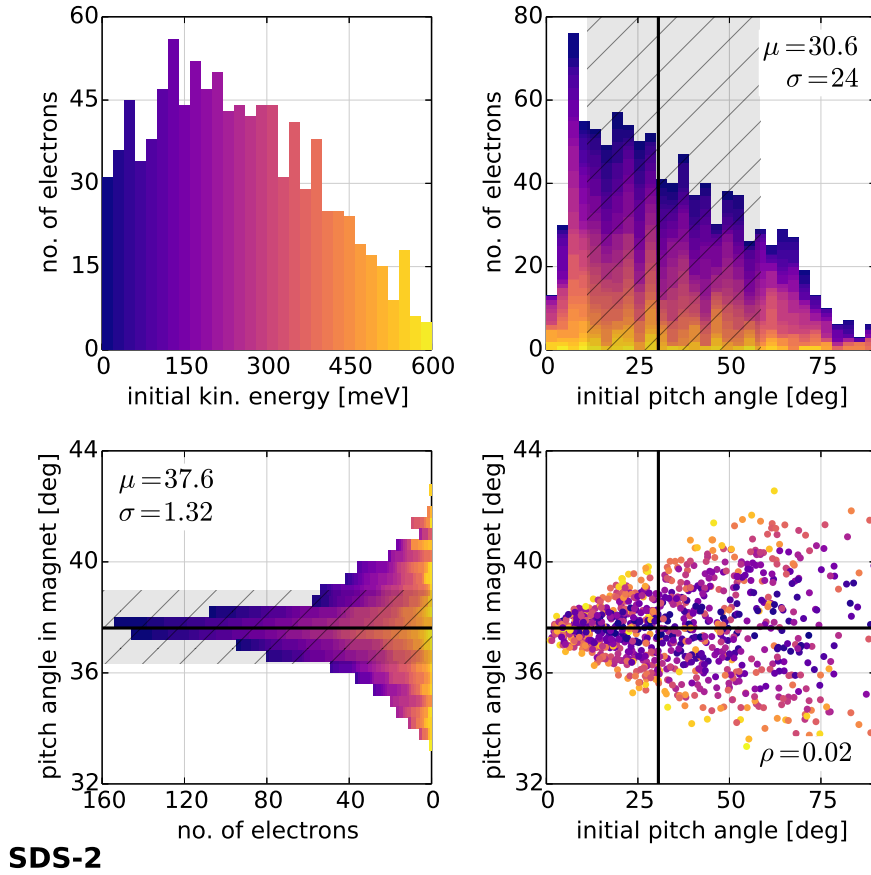


Figure 4.81.: Correlation of simulated angular distributions at increased plate angle in the SDS-2 setup. The plot is similar to figure 4.80 and uses the same settings, but now at a non-zero plate angle of $\alpha_p = 8^\circ$ where the resulting pitch angle in the entry magnet is larger. Since the “wrap-around” effect of the pitch angle only occurs at small values $\theta \rightarrow 0^\circ$, which is not the case here, the angular distribution in the magnet is now symmetric. The correlation plot confirms the observed behavior that the angular distribution is influenced by the electron energy. With the symmetric angular distribution, one observes that electrons with higher energies contribute more to the part of the angular distribution that has pitch angles far away from its median value. This is also indicated by the colors in the histogram on the bottom left, where darker colors are only seen near the median.

4.8.7 Zero-angle dependency on the dipole voltage

The commissioning measurements of the electron source indicated that the zero-angle is affected by changes to the dipole voltage U_{dip} . Experimentally, the zero-angle offset for a given tilt axis (horizontal or vertical) is determined by investigating the electron rate at different plate angles α_p while the source operates “on” the transmission edge, so that the rate is sensitive to the pitch angle of the electrons (see section 4.4). With particle-tracking simulations it is possible to investigate the produced pitch angle at different settings of α_p directly. The dependency on the plate angle can then be investigated to find the zero-angle offset; this method is equivalent to the one used in the measurement analysis. Because the zero-angle is an important parameter that affects the simulation results, the results discussed here were produced before running any other simulations and included in the simulation geometry. This ensures

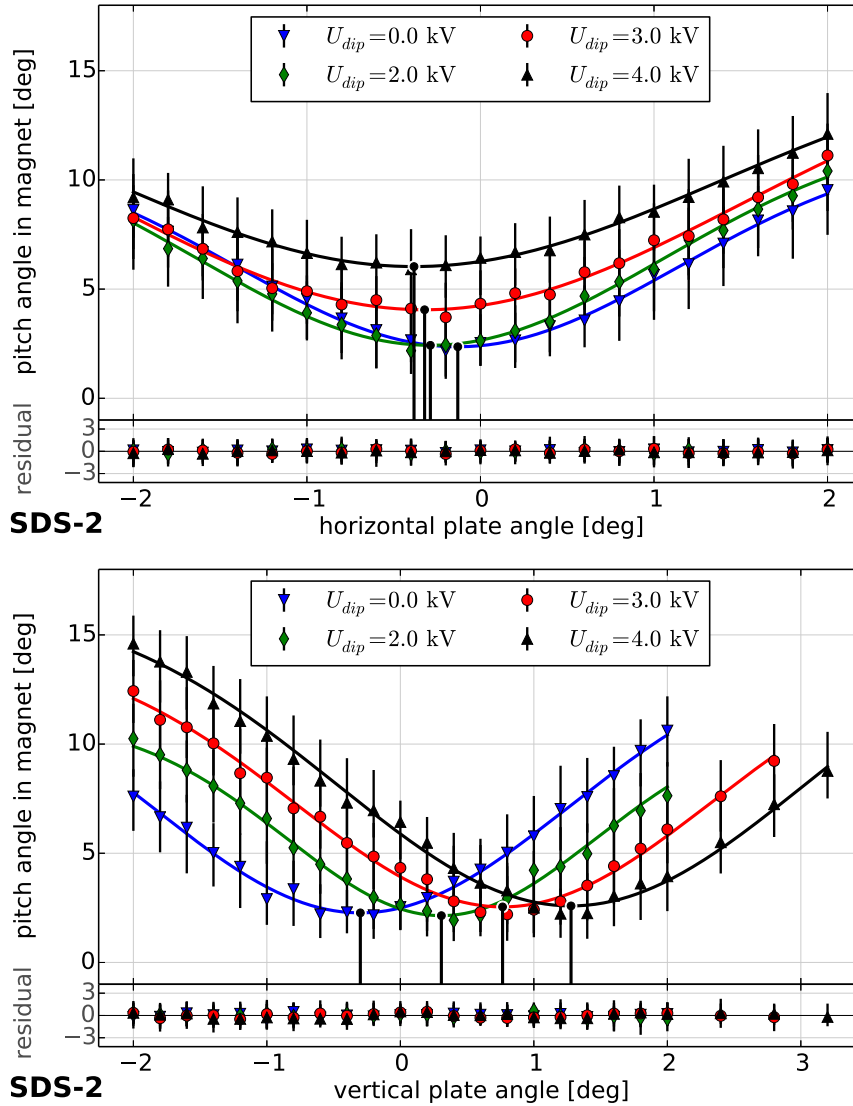


Figure 4.82.: Simulated zero angles in the SDS-2 setup. The plot shows simulated pitch angles in the spectrometer entry magnet for different horizontal and vertical plate angles around $\alpha_{h,v} = 0^\circ$. The simulation was performed at nominal conditions ($U_{start} = -18.6$ kV, $U_{acc} = 5$ kV) and at different dipole voltages $U_{dip} = 0$ kV to 4 kV. The observed behavior reflects the dependency of the electron rate on the plate angle that was seen in zero-angle measurements (cmp. figure 4.49). The resulting pitch angles can be described by a normal distribution, where the peak position corresponds to the zero-angle offset for the respective tilt axis. The results are used in the simulation geometry to perform a zero-angle correction that is equivalent to the approach used in measurements. The electric field of the dipole electrode has a considerable effect on the zero-angle in vertical direction, whereas the determined zero-angles for the horizontal axis do not show a strong dependency on U_{dip} . A similar effect was observed in the MoS measurements (figure 4.28). The dependency is partly explained by the stray electric field of the dipole electrode that affects the electron acceleration.

that a plate angle $\alpha_p = 0^\circ$ (zero-angle) always produces the minimal pitch angle in the spectrometer entry magnet.

Figure 4.82 shows the simulated zero-angle at the SDS-2 setup for both tilt axes. The results for different dipole voltages $U_{dip} = 0$ kV to 4 kV are compared to investigate a possible dependency on this parameter. In corresponding zero-angle measurements, it was found that the vertical zero-angle is shifted significantly by changing the dipole voltage, while the horizontal zero-angle remains nearly constant (section 4.6.3). Interestingly, this behavior was not seen in the MoS measurements, where instead a dependency on the magnetic field was observed⁶⁵. These measurement results indicate that the zero-angle can depend on certain operational parameters such as the dipole voltage, so that precise commissioning measurements are required to correctly determine the zero-angle offset in different conditions. The simulated zero-angles for both setups are listed in table 4.31.

The simulations (and corresponding investigations of the electromagnetic conditions at the photocathode) indicate that the dependency on the dipole voltage is caused by the stray electric field of the dipole electrode. Because the electrode is mounted close to the tiltable source cage, the highly asymmetric dipole field influences the conditions close to the photocathode. Hence, it affects the electron acceleration processes and modifies the resulting pitch angle in the spectrometer entry magnet. The electrons emitted from the photocathode are sensitive to field inhomogeneities and are strongly influenced by so-called *phase effects*. Because of the typically large cyclotron radii of the electrons in the low magnetic field at the emission spot and a low cyclotron frequency, electrons that are emitted with different azimuthal angles (phases) follow slightly different trajectories. If field inhomogeneities are present, the initial phase of the electron determines which region of the electromagnetic fields the electron will cross, which can result in a different outcome of the acceleration phase.

Note that the dipole field cannot be the only explanation for this behavior, as figure 4.82 shows a shifted zero-angle also for the case where $U_{dip} = 0$ V (where no dipole field is present). It is not entirely clear what effects cause the remaining dependency on the starting phase of the electrons. One possible explanation are inhomogeneities and asymmetries in the magnetic fields that are caused by the misalignment of the electron source w. r. t. the magnet system. Such misalignments have been included in the simulation geometry to produce results that match the measurement data (see section 4.8.1).

Phase effects have already been identified as a source for the observed asymmetries in the produced pitch angle in earlier measurements and simulations [Zac14]. These results are now confirmed by the detailed simulations with a 3D model of the electron source that features components like the asymmetric dipole electrode, which was not included before due to practical reasons.

65. The MoS setup uses two different magnetic field settings: nominal ($B_{start} = 21$ mT) and enhanced ($B_{start}^+ = 28$ mT).

Table 4.31.: Simulated zero angles at different dipole voltages.

setup	U_{acc}	U_{dip}	I_{coil}	$\alpha_{0,h}$	$\alpha_{0,v}$
SDS-2	5 kV	4 kV	—	$-0.38(16)^\circ$	$1.26(10)^\circ$
		3 kV	—	$-0.32(13)^\circ$	$0.77(10)^\circ$
		2 kV	—	$-0.28(10)^\circ$	$0.33(10)^\circ$
		10 V	—	$-0.12(10)^\circ$	$-0.31(10)^\circ$
	3 kV	2 kV	—	$0.12(22)^\circ$	$1.01(21)^\circ$
MoS	5 kV	2 kV	-35 A	$0.17(13)^\circ$	$-0.12(5)^\circ$
		2 kV	0 A	$-0.09(8)^\circ$	$-0.13(7)^\circ$
		1 kV	0 A	$-0.04(6)^\circ$	$-0.06(8)^\circ$

4.8.8 Influence of the acceleration voltage

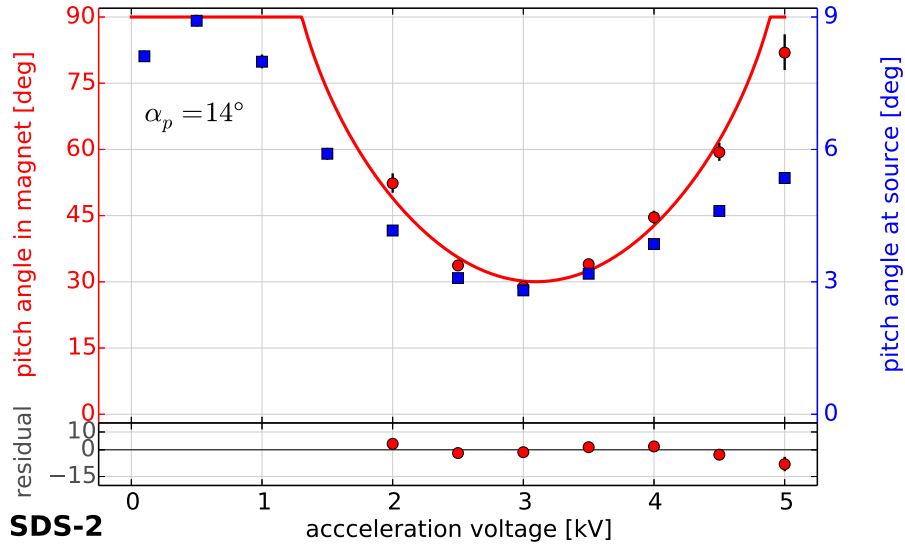


Figure 4.83.: Simulated pitch angles at different acceleration voltages in the SDS-2 setup. The plot shows the produced pitch angles in the spectrometer entry magnet (red, left axis) and at the end of the source cage (blue, right axis) in dependency of the acceleration voltage $U_{acc} = 0$ kV to 5 kV. The simulation was performed at a large plate angle $\alpha_p = 14^\circ$ (to increase the sensitivity on the produced pitch angle) and at nominal settings ($U_{start} = -18.6$ kV, $U_{dip} = 3$ kV). The produced pitch angle clearly depends on the acceleration voltage. When reducing the acceleration voltage to roughly 2 kV, the pitch angle decreases due to the changed electron acceleration. At lower acceleration voltages $U_{acc} \lesssim 2$ kV, the angular distribution of the emitted electrons is not collimated efficiently and the produced pitch angle increases accordingly. At this plate angle, the produced pitch angle can become large enough to be sensitive to magnetic reflection, which is observed for $U_{acc} \leq 1.5$ kV in this case. The dependency on U_{acc} in this simulation reflects a similar observation in corresponding measurements at the MoS (figure 4.38). The fit here uses the same model (4.70) and is in good agreement with the simulated data.

In addition to the dipole voltage, the acceleration voltage U_{acc} also has a prominent effect on the produced pitch angle. The design of the electron source is based on a strong acceleration field inside the plate-capacitor setup that is responsible for imprinting a defined pitch angle on the electrons. Without the acceleration voltage, the angular distribution of the emitted electrons cannot be collimated efficiently into a narrow distribution and the resulting angular spread in the spectrometer entry magnet is extremely large.

Figure 4.83 shows the simulated pitch angles at different acceleration voltages $U_{acc} = 0.5\text{ kV}$ at nominal conditions ($U_{start} = -18.6\text{ kV}$, $U_{dip} = 3\text{ kV}$). The simulations were performed at a non-zero plate angle $\alpha_p = 14^\circ$. At this setting, the acceleration voltage has a significant effect on the produced pitch angle as it directly affects the electron acceleration processes at the photocathode. The adiabatic transformation of the pitch angle increases the sensitivity of the simulation, as a small change in θ_{source} at the end of the source cage is increased to a much larger change in θ at the spectrometer magnet. Hence, the non-linear behavior of the adiabatic transformation emphasizes any differences in the produced pitch angle. Table 4.32 lists the pitch angle θ_{source} at the end of the source cage and θ_{mag} in the spectrometer entry magnet for different settings of U_{acc} under otherwise nominal conditions.

A reduction of U_{acc} from 5 kV to 3 kV results in an almost threefold reduction of the produced pitch angle, as seen in the figure. In contrast, a further reduction of the acceleration voltage increases the pitch angle again, until magnetic reflection is observed at $U_{acc} \leq 1.5\text{ kV}$ when the pitch angle becomes too large to reach the entry magnet. Note that in SDS-2 measurements where magnetic reflection occurs at the pinch magnet as well, the maximal pitch angle is limited to $\theta_{max} = 69.9^\circ$. The observed behavior is extremely similar to measurement results that were obtained at the MoS setup, where the influence of different acceleration voltages on the produced pitch angle was investigated (section 4.5.6). Especially the fact that a minimal pitch angle is produced at intermediate acceleration voltages around 3 kV is in good agreement with the measurement. Unfortunately, such a measurement was not performed at the SDS-2 setup.

The simulations confirm that there is an optimal setting for the acceleration voltage that produces the minimal pitch angle, which is lower than the nominal setting of $U_{acc} = 5\text{ kV}$. It should be noted that although a smaller pitch angle might be advantageous in some cases and would likely result in a smaller angular spread as well, the electron source would not be able to produce pitch angles up to 90° within the available range of plate angles $\alpha_p \leq 16^\circ$. However, this is a required feature to perform the spectrometer commissioning, where pitch angles over the complete possible range 0° to 90° must be produced to determine the spectrometer transmission function and its energy resolution.

Table 4.32.: Simulated pitch angles at different acceleration voltages in the SDS-2 setup.

α_p	U_{dip}	U_{acc}	θ_{source}	θ_{mag}
14°	3 kV	5.0 kV	5.4(1)°	81.9(40)°
		4.5 kV	4.6(1)°	59.4(20)°
		4.0 kV	3.9(1)°	44.6(14)°
		3.5 kV	3.2(1)°	34.0(11)°
		3.0 kV	2.8(1)°	28.8(11)°
		2.5 kV	3.1(1)°	33.7(13)°
		2.0 kV	4.2(1)°	52.3(22)°
		1.5 kV	5.9(1)°	—
		1.0 kV	8.0(2)°	—
		0.5 kV	8.9(1)°	—
		0.1 kV	8.1(1)°	—

4.8.9 Influence of the starting voltage

Section 4.8.5 discussed the effects of a reduced starting voltage U_{start} on the angular distribution that is achieved by the electron source. It was observed that reducing the starting voltage increases the pitch angle in the spectrometer entry magnet, which is explained by the influence of U_{start} on the electron acceleration processes. The reduced gain in longitudinal kinetic energy of the electrons in this case results in a larger pitch angle, which is defined by the ratio between transversal and longitudinal energy.

Figure 4.84 further investigates this effect and shows the produced pitch angle in dependency of the plate angle α_p for different values of U_{start} . The simulations were performed at otherwise nominal high voltage settings. The reduced starting voltages $U_{start} = -5.6$ kV to -8.6 kV were also used in corresponding SDS-2 measurements (section 4.6.4). A significant shift of the pitch angle that is produced at a given plate angle α_p towards larger values is observed when the starting voltage is reduced. Consequently, the reflection angle α_{max} where the produced electrons reach a pitch angle $\theta_{max} = 69.9^\circ$ in the entry magnet shifts to lower values as magnetic reflection is reached at smaller plate angles. The observed dependency on α_p is again described by the adiabatic transformation model (4.55). Table 4.33 lists the corresponding fit results with the reflection angles α_{max} for each setting.

As discussed earlier, the dependency of the produced pitch angle on U_{start} can be explained by assuming that the transversal energy E_\perp of the produced electrons is nearly independent of the starting voltage, as it is determined by the strong acceleration field at the photocathode (which is independent of the starting voltage, $U_{acc} = 5$ kV = const.; cmp. figure 4.25). The longitudinal energy E_\parallel , however, increases after the electrons leave the plate-capacitor setup and are accelerated towards ground potential at the spectrometer entrance. Here the reduced starting voltage comes into effect and decreases the achieved energy,

$$qU_{start} = E_{kin} = E_\perp + E_\parallel \quad \text{with } E_\perp \approx \text{const.} \quad (4.108)$$

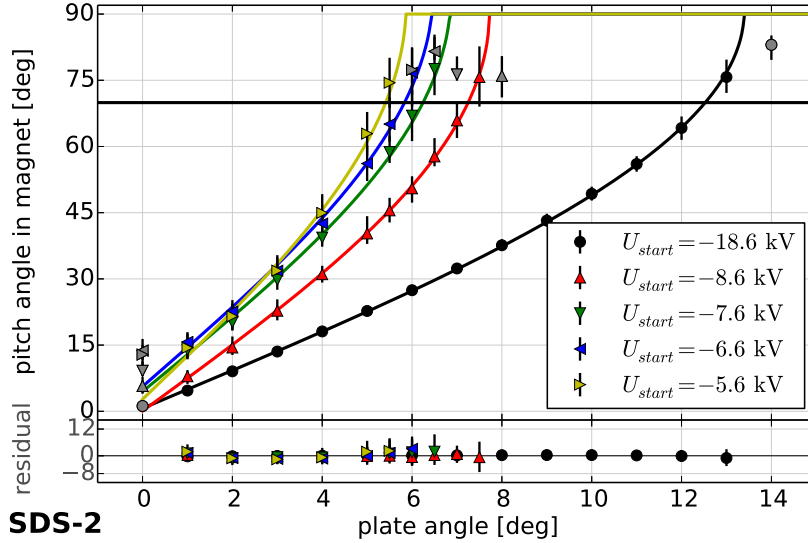


Figure 4.84.: Simulated pitch angles at different start voltages in the SDS-2 setup. The plot shows the pitch angle at the spectrometer entry magnet for different plate angles $\alpha_p = 0^\circ$ to 14° and $\alpha_{az} = 0^\circ$. The starting voltage was reduced to $U_{start} = -5.6$ kV to -8.6 kV; the nominal setting of -18.6 kV is shown for comparison. The simulation was performed at nominal settings ($U_{acc} = 5$ kV, $U_{dip} = 3$ kV). The horizontal black line indicates the cut-off angle $\theta_{max} = 69.9^\circ$ due to magnetic reflection at the pinch magnet. Due to the reduced starting voltage, the pitch angle that is produced at a given setting of α_p increases significantly. Magnetic reflection is observed at smaller values of α_p ; the reflection angle α_{max} shifts consistently with lower starting voltages. The pitch angle dependency on U_{start} is in agreement with corresponding measurements (see figure 4.51). Like in figure 4.74, the first and last data point in each setting are excluded from the fit due to the systematic shift of the median pitch angle and the deformation of the angular distribution due to magnetic reflection (gray symbols). One can also see that at reduced voltage, the zero-angle setting $\alpha_p = 0^\circ$ produces large pitch angles that deviate from the fit model.

The changed ratio between transversal and longitudinal energy corresponds to a changed pitch angle according to (2.1).

Another interesting observation is that the pitch angle that is produced at the zero-angle setting $\alpha_p = 0^\circ$ increases considerably as the starting voltage is reduced. Figure 4.84 shows that the simulated pitch angles at this setting are clearly in disagreement with the fit model (4.55). At the nominal high voltage setting, the angular distribution at $\alpha_p = 0^\circ$ becomes asymmetric (section 4.8.5) so that the determined pitch angle systematically shifts to larger values. At reduced voltage, however, the pitch angle reaches values of almost 15° at the zero-angle setting, which cannot be explained by this effect. Hence, the observed deviation shows that the zero-angle setting changes due to the reduced starting voltage, i. e. the plate angle $\alpha_p = 0^\circ$ does not produce the minimal possible pitch angle in this case. This is also indicated by the larger offset values in the fit functions for θ_{mag} that are listed in table 4.33, which are significantly larger than in the nominal setting with $U_{start} = -18.6$ kV.

The influence on the zero-angle has important consequences for measurements that are performed at reduced starting voltage (or spectrometer voltage, since $U_{start} \approx U_{spec}$ typically). The zero-angle offsets that were determined beforehand at the nominal high voltage setting become invalid in this case, and the zero-angle measurement must be repeated to produce comparable results. Unfortunately, this

influence was not considered in the SDS-2 measurements. The effect on the zero-angle is evaluated in more detail below.

Table 4.33.: Fit results of simulated pitch angles at reduced start voltage.

setup	U_{start}	θ_{mag}	α_{max}
SDS-2	-18.6 kV	$\arcsin(4.28 \cdot \alpha_p) + 0.7^\circ$	12.5(5) $^\circ$
	-8.6 kV	$\arcsin(7.44 \cdot \alpha_p) + 0.0^\circ$	7.2(5) $^\circ$
	-7.6 kV	$\arcsin(8.35 \cdot \alpha_p) + 4.5^\circ$	6.2(4) $^\circ$
	-6.6 kV	$\arcsin(8.85 \cdot \alpha_p) + 5.6^\circ$	5.8(4) $^\circ$
	-5.6 kV	$\arcsin(9.76 \cdot \alpha_p) + 2.73^\circ$	5.4(3) $^\circ$

Effect on the zero angle

Figure 4.85 shows zero-angle simulations, following the same approach that was discussed in section 4.82. A significant shift of the zero-angle offset is observed when the starting voltage U_{start} or the acceleration voltage U_{acc} is reduced from the nominal setting. Table 4.34 shows the resulting zero-angle offset on both tilt axes for the different settings. In contrast to the dipole voltage U_{dip} , which tends to only affect the zero-angle on one axis, the starting and acceleration voltages influence the zero-angle on both axis. This is explained by the greater effect on the electron acceleration processes in the source, which are largely defined by these two parameters. As explained above, the voltages effect the resulting transversal and longitudinal energy of the produced electrons, which is directly related to the achieved pitch angle.

Consequently, the zero-angle is modified by three voltage parameters of the electron source: the dipole voltage U_{dip} , the starting voltage U_{start} , and the acceleration voltage U_{acc} . Changes to any of these parameters therefore require a new measurement of the zero-angle offset to ensure that that a minimal pitch angle is produced at the zero-angle setting $\alpha_p = 0^\circ$. As this was not considered in the SDS-2 commissioning measurements at reduced starting voltage, the corresponding measurements are affected by a wrong zero-angle setting, which explains the observed effects (see section 4.6.4). The effect of an improper zero-angle setting on measurements is discussed in section 4.8.11 below, together with the possible influence from other effects such as misalignments of the photocathode w. r. t. the source geometry. Note that for zero-voltage measurements at $U_{start} = -200$ V and $U_{acc} = 100$ V, the changed zero-angle does not play a significant role since the spectrometer is typically operated at reduced voltage as well in this setting ($U_{spec} \approx U_{start}$) and thus achieves a higher energy resolution. The angular distribution of the produced electrons is not relevant to the measurement under these conditions.

Table 4.34.: Simulated zero angles at different voltage settings in the SDS-2 setup.

setup	U_{dip}	U_{start}	U_{acc}	$\alpha_{0,h}$	$\alpha_{0,v}$
SDS-2	2 kV	-18.6 kV	5 kV	-0.28(10) $^\circ$	0.33(10) $^\circ$
		-18.6 kV	3 kV	0.12(22) $^\circ$	1.01(21) $^\circ$
		-9.3 kV	5 kV	0.38(7) $^\circ$	-0.44(7) $^\circ$

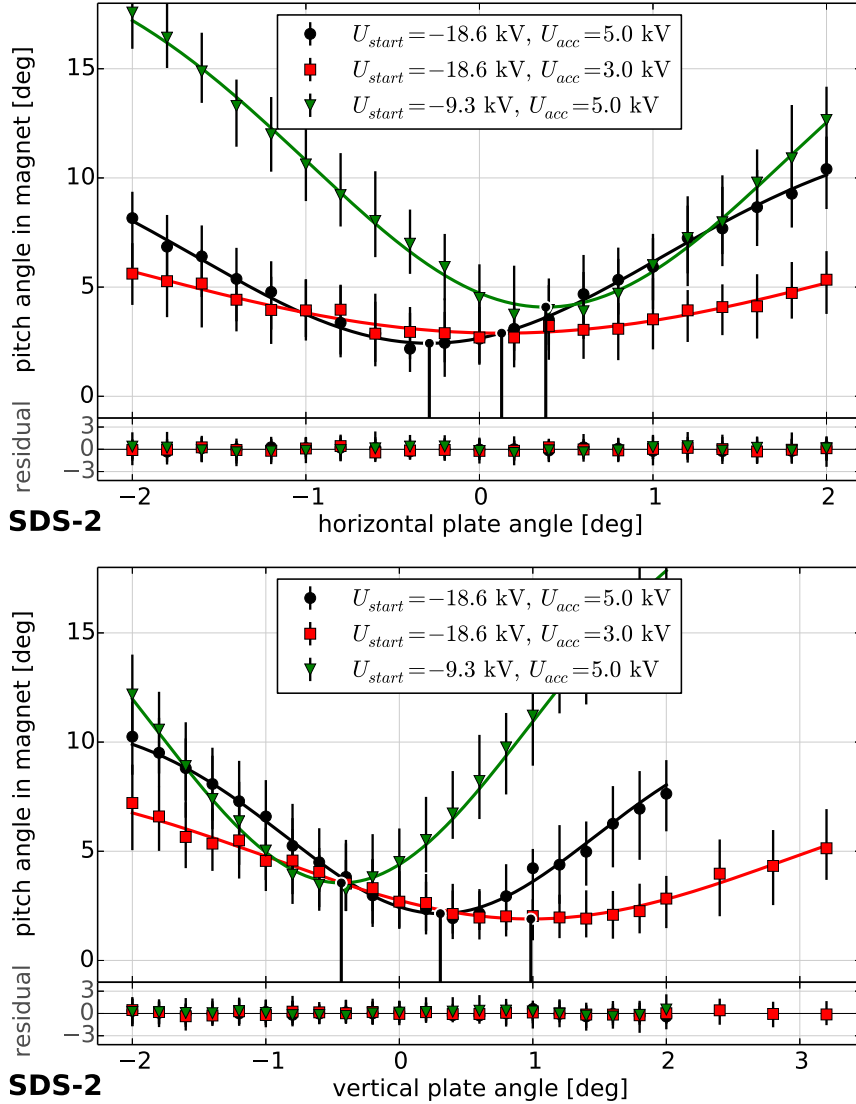


Figure 4.85.: Simulated zero angles with reduced voltage settings in the SDS-2 setup. The plot shows the simulated pitch angle in dependency of the horizontal and vertical plate angle around $\alpha_{h,v} = 0^\circ$. The observed behavior can be described by a normal distribution to determine the zero-angle offset (cmp. figure 4.82). The simulations were performed at nominal high voltage ($U_{start} = -18.6$ kV, $U_{acc} = 5$ kV) and at reduced voltage ($U_{start} = -9.3$ kV, $U_{acc} = 5$ kV). For comparison, the effect of a reduced acceleration voltage $U_{acc} = 3$ kV in the high voltage case is shown as well. The dipole voltage was set to $U_{dip} = 2$ kV here. For both tilt axes, the zero-angle offset is shifted by reducing either the starting voltage or the acceleration voltage. This clearly shows that both parameters have a considerable effect on the electron acceleration processes due to their influence on E_{\perp} and E_{\parallel} that determine the produced pitch angle θ .

4.8.10 Influence of photocathode misalignments

The MoS and SDS-2 measurements showed a considerable asymmetry in the produced pitch angle at different azimuthal tilt directions α_{az} . This was most prominently observed in magnetic reflection

measurements, where the reflection angle α_{max} that corresponds to magnetic reflection shifted to different values depending on the azimuthal plate angle. In a perfectly aligned system, one would not expect such an asymmetry. In one measurement at the SDS-2 setup, the deviation between $\alpha_{az} = 0^\circ, 180^\circ$ (horizontal tilt axis) was more than 3° for α_{max} , which is extremely large considering that $\alpha_{max} \approx 14^\circ$ in this setup (see section 4.6.4).

One possible explanation for these asymmetries is a misalignment of the photocathode (electron emission spot) against the geometry of the electron source. Normally the source design ensures that the photocathode is central to the back plate, and the plate-capacitor setup shares its central axis with the grounded source cage and the source vacuum chamber. Hence, the plate setup features complete axial symmetry and no misalignments should occur. However, even a small mechanical misalignment could severely affect the electron acceleration process due to the small distance between front and back plate ($d = 10$ mm), the small front plate aperture ($r_{ap} = 3$ mm) and the strong electric field at the photocathode ($E \approx 550$ kV/m). It is therefore expected that a misalignment of the photocathode w. r. t. the source setup modifies the produced pitch angle.

Figure 4.86 shows the result of zero-angle simulations that were performed at nominal settings ($U_{start} = -18.6$ kV, $U_{acc} = 5$ kV, $U_{dip} = 3$ kV) with an artificial misalignment of the photocathode. To implement this in the simulation geometry, the back plate with the photocathode was shifted away from the central axis of the plate setup and the grounded source cage. The simulations were performed with an offset of 2 mm in four different azimuthal direction that correspond to the two tilt axes (horizontal axis, Δx ; vertical axis; Δy). The results are compared with the aligned system where no offset is implemented. Note that due to practical reasons this implementation shifts the complete back plate against the front plate, which is mechanically impossible due to the source design. In reality, one would expect that only the emission spot is shifted on the back plate surface. However, given the size of the back plate (radius 30 mm) that is much larger than the photocathode (radius 100 μ m), this implementation is assumed to be equivalent to such a small shift.

The offset of 2 mm is significant considering the diameter of the front plate aperture (6 mm in SDS-2) at a distance of only 10 mm to the emission spot. It is therefore expected that the misalignment has a considerable effect on the electric field at the photocathode, which influences the electron acceleration accordingly. The figure confirms this expectation and shows that the produced pitch angle is shifted to larger values for tilt directions α_{az} in direction of the misalignment offset, and to smaller values for the opposite direction (e. g. larger pitch angles are produced for $\alpha_{az} = 0^\circ$ at an offset of $\Delta x = 2$ mm on the horizontal axis). The other axis is affected much less. Table 4.35 lists the simulated zero angles on both axes for the investigated offsets.

The simulations show that a photocathode misalignment of 2 mm shifts the zero-angle offset by 1.5° on the given tilt axis (e. g. the horizontal tilt axis if a horizontal offset Δx is applied). The resulting asymmetry between the magnetic reflection angles α_{max} is twice as large, $\Delta\alpha_{max} = 3^\circ$, since the pitch angle is shifted to larger values in one tilt direction and to smaller values in the opposite direction. This shift is similar to the effects that were observed for changed starting, acceleration and dipole voltages or different magnetic fields, which all affect the produced pitch angle and modify the zero-angle offset of the electron source. Hence, the changed pitch angle due to misalignments of the photocathode can be described by a changed zero-angle on the given tilt axis. It is therefore possible to correct any such misalignment by performing a zero-angle measurement, which is part of the regular commissioning procedure of the electron source.

Since the zero-angle measurements that were performed during source commissioning would include a misalignment correction, a photocathode misalignment cannot explain the asymmetries between different tilt axis that were observed in the measurement results (see table 4.15). In fact, a photocathode misalignment would only be relevant if it occurred *after* the zero-angle offsets have been determined. Given the technical design of the source, where the photocathode holder is mounted into an aperture at the back plate and fastened with several screws, this seems highly unlikely. Although these results do not exclude that an actual misalignment of the photocathode was present in the SDS-2 measurement phase, the observed pitch angle asymmetries must be explained by a different mechanism. The next section will discuss the effects of an improper determination of the zero-angle offset itself, which could result from a number of causes.

Table 4.35.: Simulated zero angles with misaligned photocathode in the SDS-2 setup.

Δx	Δy	$\alpha_{0,h}$	$\alpha_{0,v}$
0 mm	0 mm	$-0.07(7)^\circ$	$0.03(7)^\circ$
0 mm	2 mm	$-0.51(9)^\circ$	$1.49(9)^\circ$
0 mm	-2 mm	$0.37(9)^\circ$	$-1.44(8)^\circ$
2 mm	0 mm	$1.40(9)^\circ$	$0.48(9)^\circ$
-2 mm	0 mm	$-1.54(9)^\circ$	$-0.40(10)^\circ$

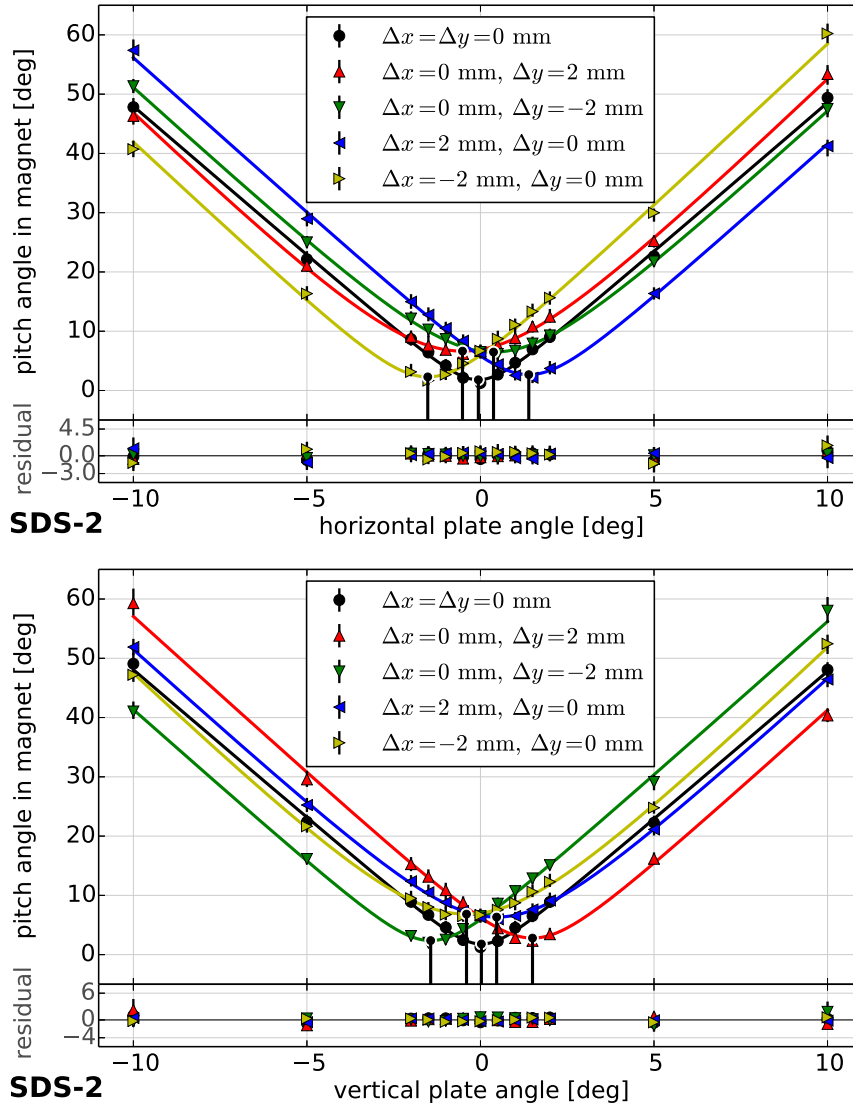


Figure 4.86.: Simulated pitch angles with misaligned photocathode in the SDS-2 setup. The plot shows simulated pitch angles for different horizontal and vertical plate angles around $\alpha_{h,v} = 0^\circ$, similar to the zero-angle simulations (figure 4.82). The simulations were performed at nominal setting ($U_{start} = -18.6$ kV, $U_{acc} = 5$ kV, $U_{dip} = 3$ kV). The photocathode (electron emission spot) was misaligned w. r. t. to the source chamber and the plate-capacitor setup in this case. This results in the given offset against the central axis of the source geometry; the simulations use an offset of 2 mm on each axis to investigate asymmetries of the observed effects. The misalignment results in a considerable shift of the produced pitch angle for the respective tilt axis on which the offset was implemented; the other axis is much less affected (note that both plots use the same colors for a given setting). The observed shift can be described by a changed zero-angle offset. These results show that the produced pitch angle is sensitive to photocathode misalignments, but the effect can be corrected by a zero-angle measurement.

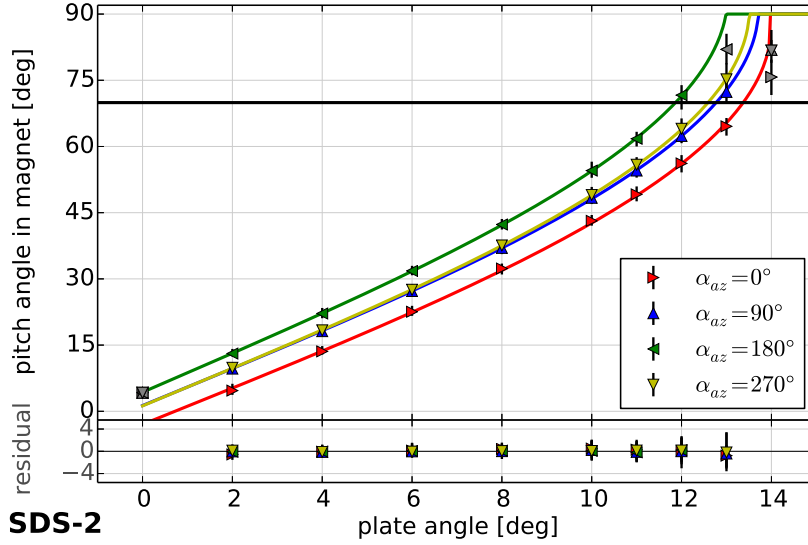


Figure 4.87.: Simulated pitch angles with zero-angle offset in the SDS-2 setup. The plot shows the produced pitch angle in dependency of the plate angle $\alpha_p = 0^\circ$ to 14° in different azimuthal directions $\alpha_{az} = 0^\circ, 180^\circ, 90^\circ, 270^\circ$. The simulations were performed at nominal conditions ($U_{start} = -18.6\text{ kV}$, $U_{acc} = 5\text{ kV}$, $U_{dip} = 3\text{ kV}$) and include an artificial zero-angle offset $\Delta\alpha_{0,h} = 1^\circ$ on the horizontal tilt axis. The added zero-angle offset is equivalent to an improperly determined zero-angle setting during measurements or simulations, which allows to investigate the influence from such effects. The observed behavior is comparable to the case where no artificial offset is present (figure 4.74), but now a significant asymmetry is seen between the azimuthal directions. This is especially visible in the point where the pitch angle reaches magnetic reflection at $\theta_{max} = 69.9^\circ$ (indicated by the horizontal black line); the reflection angle α_{max} where this occurs shows a clear dependency on α_{az} .

4.8.11 Influence of zero angle offsets

The previous sections 4.8.7 and 4.8.8 investigated the effects of different operational parameters on the zero-angle of the electron source. Any change of the dipole voltage U_{dip} , the acceleration voltage U_{acc} or the starting voltage U_{start} is reflected by a zero-angle shift that must be determined by corresponding measurements. Section 4.8.10 showed that the zero-angle is also affected by photocathode misalignments.

It is now interesting to investigate the effects of an improperly determined zero-angle on the produced pitch angle, since a wrong zero-angle offset would affect simulations as well as measurements. This is also extremely relevant for the SDS-2 commissioning, where measurements at reduced starting voltage ($U_{start} = -5.6\text{ kV}$ to -8.6 kV) have been carried out without re-measuring the zero-angle since its dependency of U_{start} was not considered when performing the measurement series. Furthermore, it cannot be ruled out that the zero-angle itself was determined incorrectly during measurements, e. g. due to an improper fit of measurement data, unknown systematic shifts like voltage or intensity fluctuations that affect the results, or human error when updating the zero-angle offset correction in the slow-control software⁶⁶. In both cases, a wrong zero-angle setting would affect all following

⁶⁶. The LabView-based control software for the electron source uses absolute offsets for the two tilt angle sensors on each axis, which are read out to control the tilt actuation of the source cage. The measured zero-angle offsets must be subtracted

measurements. This section investigates how a wrong zero-angle setting can affect the produced pitch angles.

Figure 4.87 shows the produced pitch angle in dependency of the plate angle α_p for different azimuthal directions at nominal conditions ($U_{start} = -18.6$ kV, $U_{acc} = 5$ kV, $U_{dip} = 3$ kV). Here an artificial zero-angle offset of $\Delta\alpha_{0,h} = 1^\circ$ on the horizontal axis was implemented into the simulation geometry, causing the observed deviation from figure 4.74 where the correct zero-angle was used. A clear asymmetry between the pitch angles produced at different azimuthal directions α_{az} is observed here, and the reflection angle α_{max} where magnetic reflection is observed at $\theta_{max} = 69.9^\circ$ in the entry magnet shifts accordingly. Note that the reflection angle is more sensitive to small changes in θ due to the non-linear behavior of the adiabatic transformation (4.55) at large values of α_p . Table 4.36 shows the resulting values for α_{max} in dependence of α_{az} and compares the result to the nominal conditions without zero-angle offset.

The deviation $\Delta\alpha_{max}$ corresponds to the difference between the nominal value for α_{max} without offset (table 4.29) and the simulation result discussed here. Interestingly, the artificial offset on the horizontal axis only affects the reflection angle in horizontal tilt direction ($\alpha_{az} = 0^\circ, 180^\circ$), while no deviation to the nominal values is seen for the vertical axis. Note that if an improperly determined zero-angle is used during measurements, one would expect an offset in both tilt axis so that the resulting pitch angles show a more complex dependency on α_{az} .

These investigations confirm the produced pitch angle is extremely sensitive to the zero-angle setting that is used. It can therefore be expected that an improper determination of the zero-angle would have a significant effect on measurements (or simulations, although here the zero-angle correction procedure is simpler and therefore less prone to error). It must be emphasized that for this reason, a correct measurement of the zero-angle is of crucial importance for precise measurements with the electron source. The observed influence of the zero-angle can likely explain the asymmetries that were observed in magnetic reflection measurements at the Mos (section 4.5.5) and SDS-2 setups (section 4.6.4).

Table 4.36.: Fit results of simulated pitch angles with zero-angle offset.

setup	α_{az}	θ_{mag}	α_{max}	$\Delta\alpha_{max}$
SDS-2	0°	$\arcsin(4.10 \cdot \alpha_p) - 3.0^\circ$	$13.4(4)^\circ$	$0.9(9)^\circ$
	180°	$\arcsin(4.40 \cdot \alpha_p) + 4.8^\circ$	$11.9(17)^\circ$	$-0.9(21)^\circ$
	90°	$\arcsin(4.18 \cdot \alpha_p) + 1.3^\circ$	$12.8(15)^\circ$	$0.0(19)^\circ$
	270°	$\arcsin(4.24 \cdot \alpha_p) + 1.2^\circ$	$12.6(17)^\circ$	$0.0(22)^\circ$

4.8.12 Comparison with SDS-1 design

In the first SDS commissioning phase (SDS-1, 2013), the electron source was already in operation to determine the transmission properties of the main spectrometer. As it turned out during the measurements and the following analysis, the source could not achieved angular selectivity in this setting and the produced pitch angle were considerably smaller than expected. This prevented to carry out

manually from the current values to implement a changed zero-angle. It is possible that the two offsets for both axes were mixed up in this process, or that the calculation was performed incorrectly with a wrong sign.

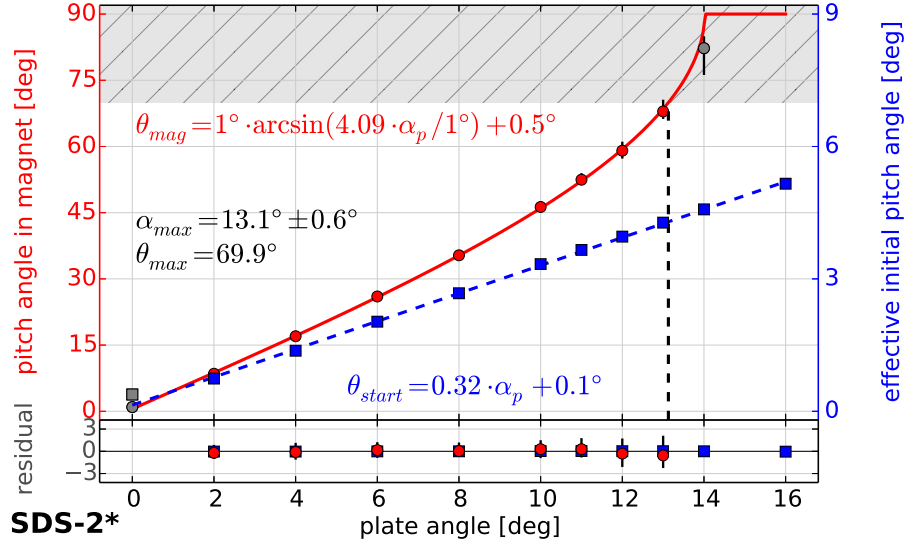


Figure 4.88.: Simulated pitch angles with larger front plate aperture in the SDS-2 setup. The plot shows the produced pitch angle in dependency of the plate angle $\alpha_p = 0^\circ$ to 14° for $\alpha_{az} = 0^\circ$. The electron setup was modified to feature the SDS-1 front plate design (with $\varnothing 24$ mm aperture) and uses otherwise nominal conditions ($U_{start} = -18.6$ kV, $U_{acc} = 5$ kV, $U_{dip} = 3$ kV, SDS-2 magnetic fields with $B_{start} = 29$ mT). The shaded area at the top indicates the cut-off due to magnetic reflection at the pitch magnet. Comparing the results with figure 4.74, the pitch angle in the spectrometer entry magnet (red, left axis) is only slightly larger than in the standard SDS-2 setup. Magnetic reflection occurs at $\alpha_{max} = 13.1^\circ$ in this case, which is compatible with the SDS-2 setup where reflection is reached at 12.5° . As before, the overall behavior is described by the fit model (4.55) that was derived earlier; the gray data points are again excluded from the fit. The pitch angle θ_{source} at the end of the source cage (blue, right axis) shows a linear dependency on α_p , which is expected from previous investigations. This result shows while the larger front plate aperture in the SDS-1 design clearly influences the produced pitch angle, the observed differences to the SDS-2 setup are too small to fully explain the results of the SDS-1 measurements.

the transmission function measurements as planned and was therefore a severe limitation of the setup. Hence, the transmission properties of the spectrometer could not be investigated in full detail [Gro15].

Apart from differences in the technical design of the electron source⁶⁷, the SDS-1 setup featured two major differences w. r. t. the SDS-2 case:

- The magnetic field at the electron source was considerably larger due to an improper alignment of the electron source during installation [Zac14], which shifted the source closer to the spectrometer entry magnet. Given the mechanical limit of the plate angle $\alpha_p \leq 10^\circ$ in the SDS-1 setup – the preliminary tilt actuation mechanism reduced the standard range of 16° – this limited the maximal pitch angle that can be produced in the magnet to roughly 30° instead of the 90° that were intended.
- The front plate of the electron source used a larger aperture of $\varnothing 24$ mm instead of the $\varnothing 6$ mm in the SDS-2 design. Simulations results from [Zac14] indicate that the larger aperture results

⁶⁷. For example, the tilt actuation of the plate setup had to be performed by a preliminary system using a movable pin in a vacuum feed-through, instead of the improved SDS-2 mechanism that relies on linear motors that can tilt both axis independently.

in a larger amount of stored electrons between the photocathode and the spectrometer if the source is operated out of transmission (i. e. negative surplus energy $qU_{start} < 0$), where electrons do not reach the detector. According to recent investigations in [Wie16], these stored electrons affect the observed transmission function (see also section 4.5.3). It is thus possible that the deviations from the expected transmission functions that were observed in [Gro15] were caused by this effect.

In addition to the different magnetic field and the effects from stored electrons, which will not be discussed here, the larger front plate aperture also affects the electrostatic acceleration field at the photocathode. It is expected that the decrease by a factor of 2 in aperture radius has a noticeable effect on the electric field since the distance between back and front plate is only 10 mm, i. e. of the same order of magnitude. Since the non-adiabatic acceleration defines the produced pitch angle, it is interesting to investigate this effect by comparing the SDS-1 plate design with the conditions at the SDS-2 setup.

Figure 4.88 shows the produced pitch angles in the spectrometer entry magnet and at the end of the source cage at plate angles $\alpha_p = 0^\circ$ to 14° for $\alpha_{az} = 0^\circ$. The simulations were performed at nominal SDS-2 conditions ($U_{start} = -18.6$ kV, $U_{acc} = 5$ kV, $U_{dip} = 3$ kV, $B_{start} = 29$ mT, $B_{PS2} = 4.5$ T), but feature the larger front plate aperture of $\varnothing 24$ mm that was used in the SDS-1 measurements. It is observed that the pitch angle that is produced for a given plate angle α_p is slightly larger than in the standard SDS-2 design (figure 4.74). This is also the case for the pitch angle θ_{source} at the end of the source chamber. This indicates that the larger aperture of the front plate only has little effect on the electron acceleration processes and the resulting pitch angle.

The observation is confirmed by the reflection angle, which shifts to a slightly smaller value of $\alpha_{max} = 13.1(6)^\circ$ in this modified setup. In the standard SDS-2 setup a reflection angle of $12.5(5)^\circ$ was determined (section 4.8.4); both results are in agreement within their given uncertainty. Additional investigations of the electromagnetic conditions in this modified setup show that the axial electric field reduces from 550 kV/m to about 500 kV/m due to the larger aperture. Similar differences are seen for the radial field, which is responsible for imprinting a pitch angle on the emitted electrons (cmp. section 4.8.2). This small difference is given by the fact that the photocathode is coaxial to the aperture, and the size of the aperture is comparable to the distance between the plates ($d = 10$ mm). The size of the aperture therefore does not cause large changes in the electric acceleration field, and the net effect on the produced pitch angle is small.

Conclusively, although the size of the front plate aperture has some influence on the pitch angle that is produced by the electron source, only a small difference in θ was observed here with the modified setup under otherwise nominal SDS-2 conditions. The changed front plate design therefore cannot explain the severe limitations of the electron source that were encountered in the SDS-1 setup if only the electron acceleration processes are considered. It is therefore more reasonable to attribute these limitations to differences in the magnetic fields that were caused by an improper axial alignment of the source, since the produced pitch angle is extremely sensitive to variations in the magnetic field between photocathode and spectrometer entry magnet. Other effects like a higher storage probability for electrons that do not reach the detector during measurements could play a significant role as well.

4.8.13 Summary

In addition to the detailed source commissioning measurement that were discussed earlier in this chapter, sophisticated particle-tracking simulations were carried out to gain a better understanding of the electron acceleration and transport processes in the electron source. These processes define the resulting energy and angular distribution of the produced electrons, which have a large impact on the transmission functions that are measured with the electron source. Since these processes depend on many parameters like applied voltages or the magnetic fields at the setup, simulations can provide important input to analyze measurement data.

The KASPER framework that was utilized for these simulations provided a mature version of the Kassiopeia simulation software with many useful features and improvements that were added after the SDS-1 measurement phase ended [Gro15, F⁺17]. One feature that was crucial to perform the simulations that were presented in this section is the improved navigation algorithm that allows an extremely flexible configuration with dynamically adjusted step sizes and changing parameters as the simulated electron propagates through the simulation geometry. This flexibility allowed to improve both speed and accuracy of the simulation by fine-tuning the simulation parameters. Another crucial component for the simulations is the KEMField package to compute the electromagnetic fields. By using its 3D field computation features, it was possible to implement the electron source nearly 1:1 into the simulation geometry, including the half-shell dipole electrode (which breaks axial symmetry), the tilting mechanisms of the source and the misalignments that were determined at the SDS-2 setup. The simulations also greatly benefited from the GPU-acceleration features that are available in KEMField, which allow to perform parts of the computation on a dedicated graphics card using the OpenCL framework.

The simulations therefore contain many important components of the electron source. Many source characteristics that were observed during the commissioning measurements could be reproduced in the simulation results, although not always with an exact quantitative agreement. Since the simulation results are generally consistent, the observed discrepancies between measurement and simulations are attributed to unknown misalignments of the systems and the limited knowledge of the electromagnetic conditions, and not to issues with the simulation configuration or the software.

Figure 4.89 shows a comparison of SDS-2 measurement results that confirm angular selectivity, and corresponding simulations that use an estimated initial energy distribution and a $\cos\theta$ angular distribution for the simulated electrons. The simulation geometry closely follows the actual setup and implements all crucial components such as the dipole electrode, as well as results from alignment measurements at the SDS-2 setup. It is seen that measurements and simulations are in good agreement and yield comparable results, which verifies that particle-tracking simulations can be used in combination with measurements to gain a more detailed understanding of the source characteristics.

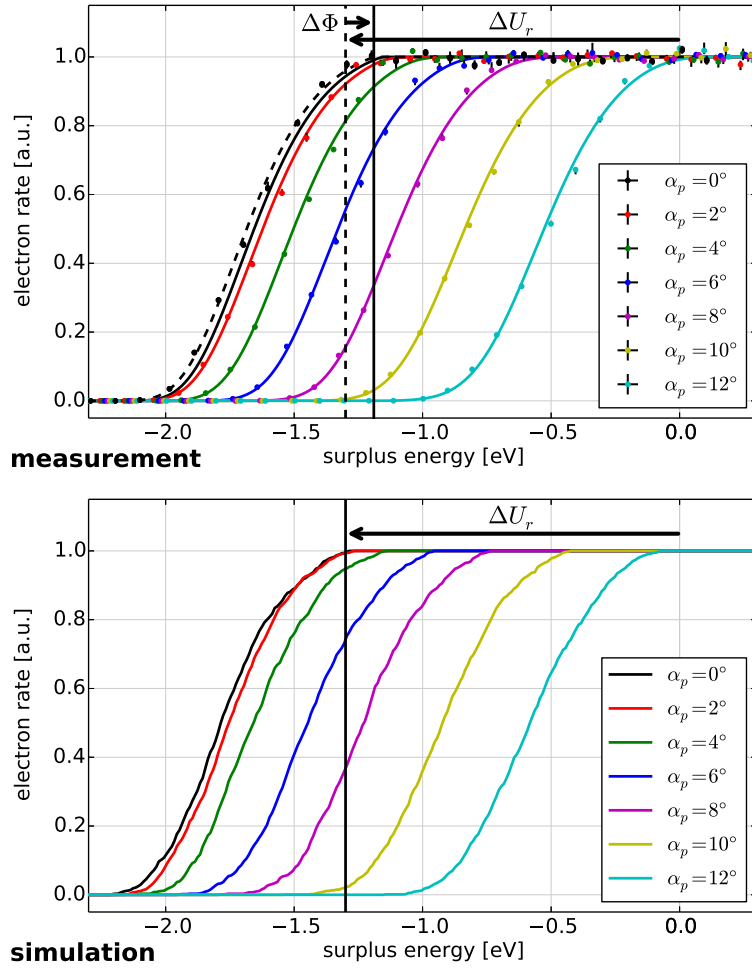


Figure 4.89.: Comparison between measured and simulated transmission functions at the SDS-2 setup. Transmission functions were measured and simulated at different plate angles $\alpha_p = 0^\circ$ to 12° and $\alpha_{az} = 0^\circ$ at nominal conditions ($U_{spec} = -18.6$ kV, $U_{acc} = 5$ kV, $U_{dip} = 3$ kV, $B_{start} = 29$ mT, $B_{min} = 0.38$ mT, $B_{max} = 5.1$ T). As expected, the transmission functions shift to larger surplus energies for increasing plate angles, corresponding to the energy resolution ΔE of the spectrometer under the current conditions. The simulations use an asymmetric initial energy distribution (4.39) that is comparable to the measured energy distribution at $\alpha_p = 0^\circ$ ($\hat{E} = 0.49$ eV, $\sigma'_E = 0.22$ eV, $\kappa = 0.3$) and a $\cos \theta$ initial angular distribution. The simulated transmission functions are in good agreement with the measurement data, which confirms that angular selectivity and the produced angular distribution in the spectrometer energy magnet is reproduced in simulations. The vertical lines mark the position of the transmission edge, which is mainly determined by the potential depression of the main spectrometer ($\Delta U_r = -1.30$ V according to simulations). In measurements, the edge position is additionally shifted by the work function difference between electron source photocathode and main spectrometer ($\Delta\Phi = \Phi_{src} - \Phi_{spec} = 0.11(1)$ eV). The transmission function measurements are thus sensitive to work function changes of the spectrometer.

4.9 Investigation of systematic uncertainties

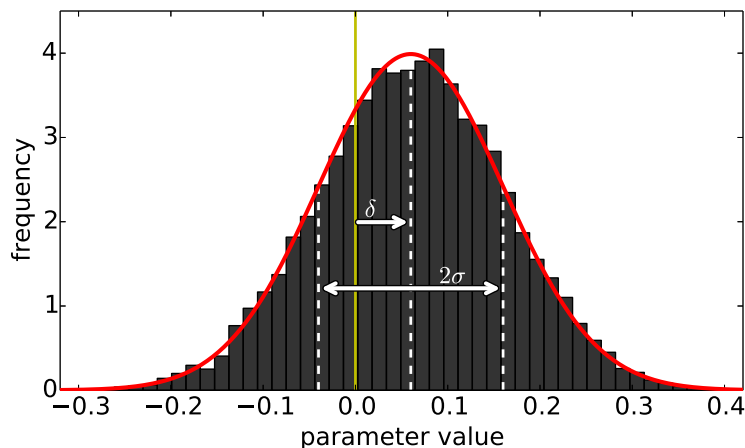


Figure 4.90.: Estimating systematic and statistical uncertainties from toy data samples. The data samples are analyzed (e. g. by a fit) and the resulting parameter values p_i are plotted in individual histograms where they can be compared with the known “true” values on which the toy data set is based upon. A possible systematic bias of the fit results is then visible as an offset δ between the median of the results (central dashed line) and the true value (yellow line). Similarly, the statistical uncertainty of the fit results can be estimated from the 1σ -width of the histogram (outer dashed lines). The example shows samples from a normal distribution to visualize the procedure. Typically, the investigated parameters are the results of fits on a given data set with several data samples.

The sections 4.5 and 4.6 presented measurement results where transmission functions were investigated with the analytical model that was implemented earlier (see section 4.1.1). An important question in this context is how precisely the original energy and angular distributions can be recovered from the analysis of measurement data. Especially with the complex fit model, which is based on integrating the distributions to obtain a transmission function, there could be an unknown systematic bias that contributes to the uncertainty of the fit results. This would directly affect any results derived from these measurements, e. g. the angular and energy spread or position of the transmission edge. Derived properties such as the effective analyzing potential and the magnetic field at the analyzing plane of the spectrometer also suffer from these systematic uncertainties, since their analysis relies on the same approach.

Fortunately, it is possible to investigate these systematic uncertainties through a Monte-Carlo model in a Bayesian context. The method that is utilized here is similar to the analysis of systematic uncertainties of the complete KATRIN experiment, which has been carried out in [Kle14]. The overall strategy is to generate a series of *toy data samples* from a given parameter set, which resembles actual measurement data (i. e. including statistical uncertainties). The toy data set is then analyzed by the same methods that are applied to measurement data. In the case that is investigated here, the analysis is based on fitting the analytical transmission model to each toy data sample to obtain its energy or angular distribution.

By comparing many of these *toy experiments*, a statement about the expected systematic and statistical uncertainty of the fit results can be made. The original parameters of the toy experiment – the *true values* – are known in this case, since they are used to generate toy data. The average parameter values

of the fit results of all toy data samples can then be compared to the corresponding true values, which yields an estimate of the systematic offset. Similarly, the spread of the fit results is an estimate for the actual statistical uncertainty.

This method is showcased in figure 4.90, where 10 000 toy data samples – in this example, the individual values are simply sampled from a normal distribution – are investigated to determine their systematic bias δ and their statistical uncertainty σ . Following the same approach, it is possible to determine these values for any set of toy data samples, such as results from a fit process.

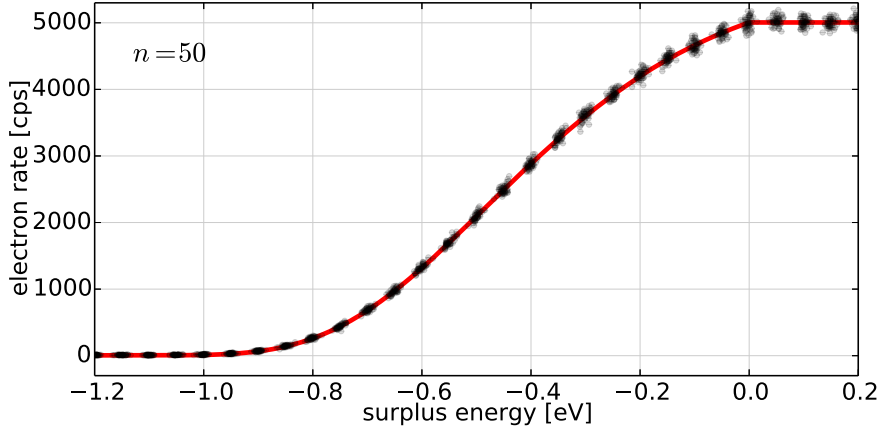


Figure 4.91.: Toy model for the investigation of systematic uncertainties. The plot shows 50 data sets (toy data samples) that were created by random sampling from the analytical transmission model (4.10), using typical parameter settings (amplitude 5 kcps, background 5 cps, “BroadZero/0V” setting (see table 4.37)). The underlying model is indicated by the red line. The randomized data samples are varied in surplus energy and electron rate, including Poisson fluctuations ($\sigma_N = \sqrt{N}$) and random Poisson-distributed background. Each toy data sample with several data points can then be fitted and analyzed by statistical method to investigate a possible systematic bias of the fit, as shown in figure 4.90).

The transmission function measurements with the electron source yield important results both for the commissioning of the device itself and for the investigation of the spectrometer transmission properties. The analysis method is examined in this section, using the following approach:

1. Generate a toy model $T(E)$ according to (4.10). A transmission function is computed from a given angular and energy distribution together with additional parameters, like the electromagnetic settings of the spectrometer and the operational parameters of the electron source.

The toy model that is used here has a total of 10 parameters that can be adjusted for different investigations:

- the nominal electron rate ($R = 5$ kcps);
- the background level ($R_b = 5$ cps);
- the position of the transmission edge (ΔU_0);
- the energy mean, spread and shape ($\hat{E}, \sigma_E, \kappa_E$);
- the angular mean and spread ($\hat{\theta}, \sigma_\theta$);
- the spectrometer retarding potential ($U_{ana} = -200$ kV, $-18\,600$ kV, see below);

- the magnetic fields at the analyzing plane ($B_{min} = 0.36$ mT); and
- the magnetic fields at the spectrometer entrance and exit ($B_{PS2} = 4.5$ T, $B_{max} = 5.1$ T).

While the parameters of the energy and angular distributions and the position of the transmission edge is typically varied to investigate different conditions, the remaining parameters use the given nominal values that are used in all toy experiments discussed in this section. The nominal values correspond to the typical settings at the SDS-2 setup.

2. Generate n samples of toy data. The toy data is sampled from the toy model that was defined beforehand, and includes random variations of the observable (the electron rate \dot{N}). Each sample therefore resembles one individual toy measurement.

A sample consists of a set of data points, where the electron rate at different surplus energies $\Delta E = q\Delta U = q(U_{start} - U_{spec})$ is observed. To generate a realistic data set, the surplus energy at each data point is randomly shifted according to a normal distribution; this models the uncertainty on the measured surplus energy which is caused e. g. by voltage fluctuations. In this case, an uncertainty $\delta E = 6$ meV is used, which corresponds to the estimated uncertainty of the surplus energy in the SDS-2 measurements. The toy model is then evaluated at each data point to determine the corresponding electron rate (with $0 \leq \dot{N} \leq R$). To implement rate fluctuations that are observed in reality, the determined rate is modified by a Poisson distribution with $\sigma_{\dot{N}} = \sqrt{\dot{N}}$. Finally, the electron rate is shifted by a Poisson-distributed background rate around R_b .

Conclusively, the electron rate \dot{N} at a data point with given surplus energy ΔE is described by

$$\dot{N}(\Delta E) = \text{poiss}(R \cdot T(\Delta E')) + \text{poiss}(R_b), \quad (4.109)$$

$$\Delta E' = \text{norm}(\Delta E, \delta E), \quad (4.110)$$

where $T(E)$ is the transmission probability given by the analytical model (4.10), $\text{poiss}(\lambda)$ refers to a random value from a Poisson distribution with expectation value λ , and $\text{norm}(\mu, \sigma)$ refers to a random value from a normal distribution with expectation value μ and width σ . Figure 4.91 shows a toy experiment with several toy data samples that were created by this method.

3. Analyze the n toy data samples. Each sample is fitted individually, using the same analysis methods that are applied to the measurement data (see section 4.4).

The analysis is implemented in *Peaberry* (section 3.8) and first applies a *parameter guess* to determine optimal initial parameters for the fit. The fit itself is performed here with MINUIT2+MINOS, and the fit results are collected for further analysis. Note that the analysis of measurement data uses MCMC fit methods instead of MINUIT2 to improve the fit stability and the estimation of parameter uncertainties⁶⁸. However, due to the long running time of MCMC fits (typically $\mathcal{O}(1$ h) per data set), it is not possible to use this method here where up to 10 000 samples are investigated in a single toy experiment.

The analysis is performed for different toy experiments, corresponding to the different measurements that were performed with the electron source. For example it is possible to use a fixed angular distribution in the model in order to determine the energy distribution from the given toy data sample, or vice versa. In all cases, the amplitude of the electron signal and the background level is included as a free parameter in the fit.

68. MCMC is typically less dependent on the initial parameter guess than complementary methods, and include all parameter correlations by design due to their sampling of the likelihood parameter space during the fit process.

The remainder of this section discusses three different approaches:

- **Energy distribution:** This toy experiment correspond to measurements where the energy distribution is investigated to determine the energy spread of the produced electrons. The fit uses 5 parameters (R , R_b , \hat{E} , σ_E , κ_E) with a fixed angular distribution and a pre-determined transmission edge position.
 - **Energy distribution with transmission edge:** This approach is equivalent to the 5-parameter fit, but additionally includes the position of the transmission edge ΔE_0 as a free parameter in the fit. This allows to investigate how much the correlations between the position edge and the energy distribution affects the fit results. This toy experiment therefore uses 6 parameters in the fit.
 - **Angular distribution:** This toy experiment corresponds to measurements where the angular distribution is investigated with a given energy distribution, in order to determine the pitch angle and angular spread of the electrons. The fit uses a fixed energy distribution and transmission edge, and has 4 parameters (R , R_b , $\hat{\theta}$, σ_θ).
4. Combine the analysis results. For each fit parameter, the values returned by the individual fits can be collected in a histogram for statistical analysis.

Ideally, the fit results are symmetrically distributed around the *true value* of the fit parameter⁶⁹ and follows a normal distribution, where its width corresponds to the uncertainty of the results that was estimated by the fit. The results from a toy experiment typically deviate from this ideal case. If a systematic bias is present, the median of the histogram – the *expected value* of the fit – is shifted away from the true value by a systematic error δ . Similarly, the width of the histogram – the *expected uncertainty* σ – can be different from the uncertainty that has been estimated by the fit (cmp. figure 4.90).

The different toy experiments that have been carried out use different parameter sets, depending on the corresponding measurement. While the energy distribution is determined from a measurement at reduced spectrometer voltage (“0V” setting, $U_{spec} = -200$ V) and at a source tilt angle of $\alpha_p = 0^\circ$ (“zero-angle”), the angular distribution is measured at high voltage (“HV” setting, $U_{spec} = -18.6$ kV) while varying the tilt angle to produce different pitch angles ($0^\circ \leq \alpha_p \leq 16^\circ$). Table 4.37 lists the different parameters sets that were used in order to investigate the influence of different energy and angular distributions on the fit results. These parameter set are referenced below, where the different toy experiments are discussed.

69. The true value is known from the toy model, from which the toy data set is sampled.

Table 4.37.: Parameter sets for the toy models used to evaluate systematic uncertainties.

setting	edge ΔU_0	— energy —			— angle —	
		mean \hat{E}	width σ'_E	shape κ	mean $\hat{\theta}$	width σ_θ
BroadZero	0 eV	0.4 eV	0.3 eV	0.3	2°	2°
BroadSmall	0 eV	0.4 eV	0.3 eV	0.3	25°	5°
BroadMedium	0 eV	0.4 eV	0.3 eV	0.3	50°	5°
BroadLarge	0 eV	0.4 eV	0.3 eV	0.3	75°	5°
NarrowZero	0 eV	0.25 eV	0.25 eV	0.15	2°	2°

4.9.1 Energy distribution and transmission edge

The analytical model (4.10) describes arbitrary transmission functions by contributions from an energy and angular distribution of the electrons, while also taking into account effects such as magnetic reflection at the MAC-E filter. By performing dedicated measurements at different settings, it is possible to disentangle both contributions and determine all parameters with good accuracy.

Additionally to these distributions, the observed transmission function is shifted on the energy axis – i. e. to a different range of surplus energies – due to the retarding potential in the analyzing plane⁷⁰. The position of the transmission edge – the surplus energy where the transmission function reaches its nominal amplitude – is therefore an additional parameter in the model ($\Delta E_0 = q\Delta U_0$, see above) that describes this shift.

One would expect that this edge position can be determined together with the energy distribution directly from a measurement, since the position of the transmission edge corresponds to an electron energy $E_e = 0$ eV at the photocathode. It is thus independent of other energy or angular parameters. A fit using the analytical model should therefore be able to determine the edge position correctly, together with the parameters of the energy distribution.

However, an investigation of the systematic uncertainties of such fits shows that the fit routine prefers slightly more positive edge positions, i. e. shifting the fitted transmission function towards higher surplus energies than expected from the measurement data. It is believed that this bias is caused by strong correlations between the parameters of the energy distribution and the edge position. In general, the fit process samples from a multi-dimensional parameter space to optimize the resulting χ^2 (or $\ln L$). Parameter correlations affect the convergence of the fit and can drive the resulting outcome (“best-fit result”) away from the actual values. Toy experiments allow to investigate such effects, because the actual values (“true” values) are known.

Figure 4.92 shows the corresponding fit results using one toy experiment with multiple data samples, as discussed above. The expected value for the transmission edge as a fit parameter (“edge”, parameter ΔU_0) shows a large discrepancy to the true value that was used to generate the toy data samples. Due to correlations between the parameters, the wrongly determined edge position also affects other fit

⁷⁰. The surplus energy of the electrons is measured as the difference between starting voltage and spectrometer voltage, $\Delta E = q\Delta U = q(U_{start} - U_{spec})$. Due to the potential depression at the spectrometer and additional effects like differences in the corresponding work functions, the transmission edge is typically shifted to $\Delta E \neq 0$.

parameters such as the energy spread (“ewidth”, σ_E) or the energy limit (“limit”, E_{max}) of the emitted electrons. Both parameters are extremely relevant in the analysis of measurement data. Table 4.38 shows similar results for other toy experiments that were investigated.

The investigation shows that correlations between the fit parameters result in a wrongly determined edge position that affects other fit parameters as well. To resolve this issue, the analysis method was modified so that the edge position is determined beforehand from the measurement data, so that the actual fit only determines the energy distribution and uses a fixed value of ΔU_0 . This alternative approach is discussed below.

Table 4.38.: Fit results of different toy data samples, using the 6-parameter fit model.

setting		edge ΔU_0		mean \hat{E}		width σ'_E		shape κ	
		true	fit	true	fit	true	fit	true	fit
HV	BroadZero	0	0.04(2)	0.4	0.46(3)	0.3	0.27(1)	0.3	0.24(4)
	BroadSmall	0	0.00(4)	0.4	0.41(6)	0.3	0.29(4)	0.3	0.28(8)
	NarrowZero	0	0.06(2)	0.25	0.35(4)	0.25	0.21(1)	0.15	0.06(4)
0V	BroadZero	0	0.03(2)	0.4	0.45(3)	0.3	0.28(1)	0.3	0.25(3)
	BroadSmall	0	0.01(2)	0.4	0.41(4)	0.3	0.29(2)	0.3	0.28(5)
	NarrowZero	0	0.06(1)	0.25	0.36(1)	0.25	0.21(1)	0.15	0.05(3)

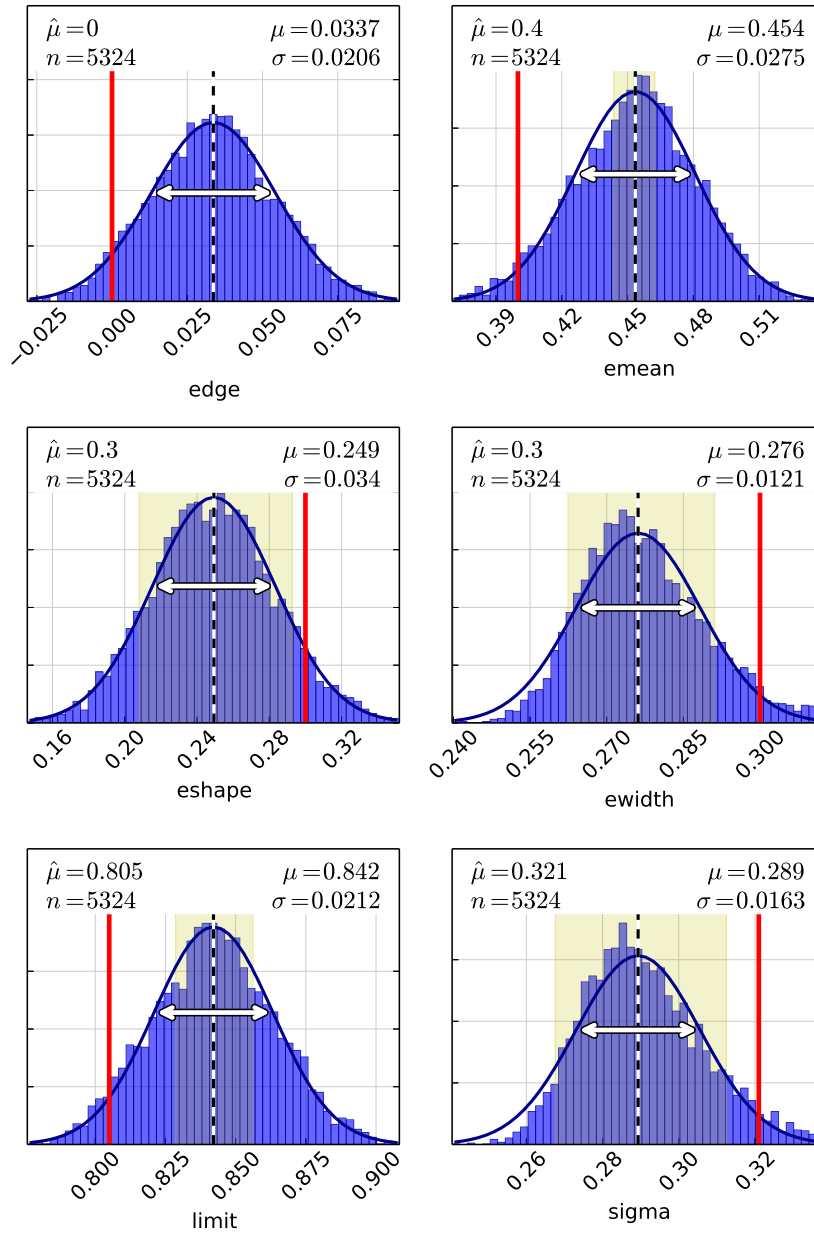


Figure 4.92.: Fit result of 10 000 toy data samples, using the 6-parameter fit model (energy distribution and transmission edge). The toy model uses the “BroadSmall/0V” parameter set (table 4.37), which corresponds to a typical energy distribution measurement with the electron source. The angular parameters are kept fixed in the fit to obtain the energy parameters mean energy \hat{E} (emean), width σ'_E (ewidth), shape κ (eshape); and the position of the transmission edge ΔU_0 (edge). The energy limit E_{max} (limit) and the energy spread σ_E (spread) are derived from the energy parameters according to (4.41). The plots show the distribution of the fit results for each parameter. In some cases the fit did not achieve a result due to numerical instabilities, which reduces the number of samples n . The vertical red line indicates the “true” parameter value which the fit should reproduce, the dashed line and the arrow indicate the median and 1σ -width of the histogram. The shaded yellow region indicates the average uncertainty that was estimated by the fit. All parameters show a considerable systematic bias, which limits the accuracy of the 6-parameter fit to obtain the energy distribution.

4.9.2 Energy distribution

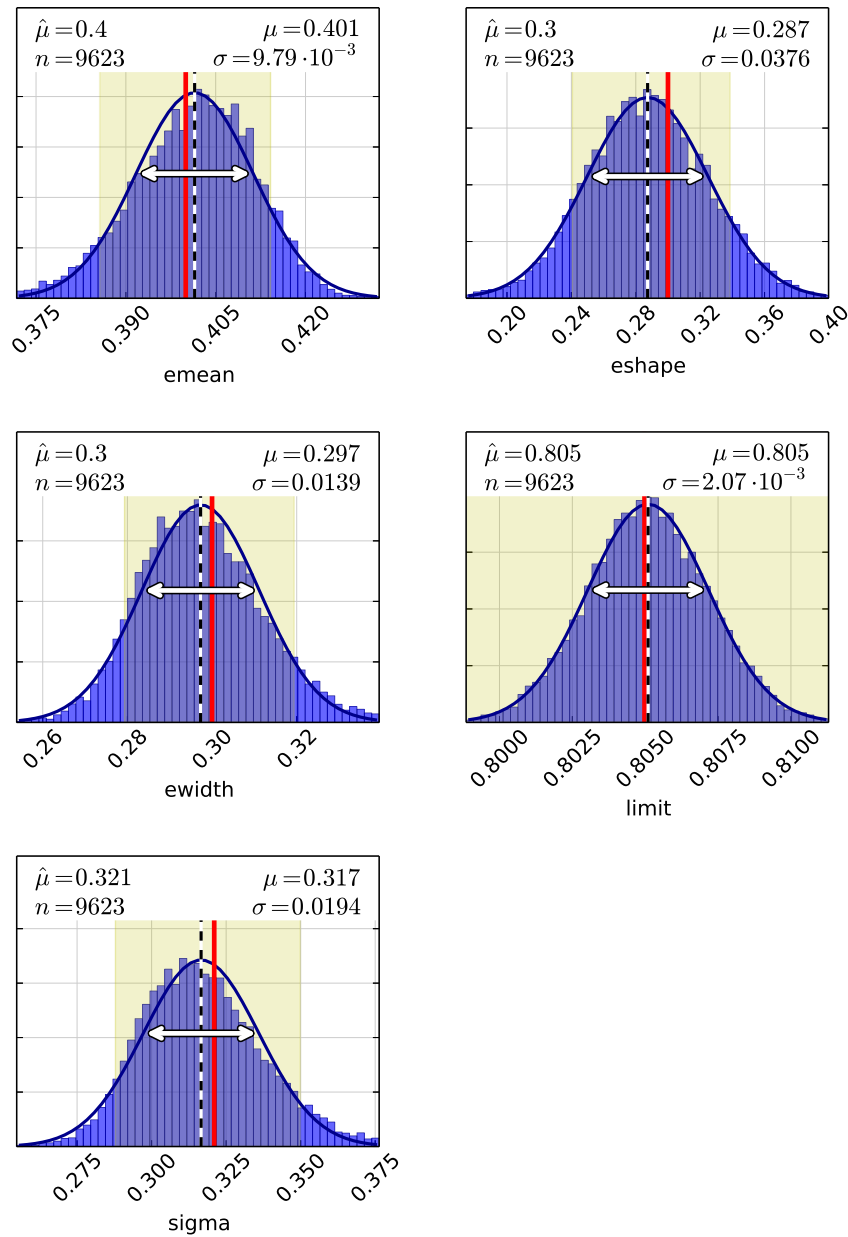


Figure 4.93.: Fit result of 10000 toy data samples, using the 5-parameter fit model (energy distribution). The toy model uses the “BroadSmall/0V” parameter set as in figure 4.92. In this case, the position of the transmission edge is kept fixed at a pre-determined value to reduce parameter correlations that affect the fit results. The number of fitted parameters is therefore reduced by one. In this setting, the fit accurately reproduces the true parameter values (red vertical lines), which is a significant improvement over figure 4.92 where several parameters showed a systematic bias.

As an alternative to the approach above, in this case the fit uses a fixed position of the transmission edge ($\Delta U_0 = \text{const.}$) to determine the energy distribution from an observed transmission function.

With this method, the correlations between the edge position and the energy parameters do not result in a systematic bias of the determined parameters. A downside of this method is that the edge position must be determined beforehand with sufficient accuracy.

This alternative approach was investigated by toy experiments as well. Figure 4.93 shows the results for the same data set as in figure 4.92, but with the edge position fixed at its “true” value $\Delta U_0 = 0$ eV. A comparison between the two figures clearly shows that the fit results are now in better agreement with the true parameter values. In fact, the expected values of the fit parameters reproduce the corresponding true values within the estimated uncertainties, as indicated in the figure. Table 4.39 shows the results for other toy experiments that use different parameter sets. The results can be compared with table 4.38 accordingly.

The new approach considerably improves the accuracy of the fit results (reduces the systematic bias) and is therefore preferred in the analysis of measurement data. To determine the position of the transmission edge, an iterative method is used here. By investigating several observed transmission functions, a first estimate of the edge position that is slightly “above” the transmission function is determined (i. e. at a more positive surplus energy than visible in the measurement data, where the nominal electron rate is observed). This estimated edge position must be in agreement with *all* transmission functions in the measurement series. It is now possible to shift the edge position towards smaller surplus energies, until it becomes impossible to describe all of the observed transmission functions with the analytical model and the given edge position. In the end, one finds a value ΔU_0 that has a minimal distance to the actual (“true”) transmission edge and is consistent with all measurements in a specific measurement series.

It would be possible to automate this process in a MCMC-based approach that re-runs the individual fits for every new edge position until the optimal value has been found⁷¹. This approach would thus run several MCMC fits on given measurement data at each step of the “global” fit that optimizes the edge position. However, because of the long running times of the individual fits and the limited time available, such an automated process has not been implemented here. Instead, the edge position was shifted manually at a reasonable step size of 0.01 eV to find the desired optimum. The accuracy of the edge position is therefore limited to 10 eV, and the next section discusses how this systematic uncertainty affects the outcome of the fit results.

Table 4.39.: Fit results of different toy data samples, using the 5-parameter fit model.

setting		mean \hat{E}		width σ'_E		shape κ	
		true	fit	true	fit	true	fit
HV	BroadZero	0.4	0.40(1)	0.3	0.30(1)	0.3	0.29(4)
	BroadSmall	0.4	0.40(1)	0.3	0.30(2)	0.3	0.29(5)
0V	BroadZero	0.4	0.40(1)	0.3	0.30(1)	0.3	0.29(4)
	BroadSmall	0.4	0.40(1)	0.3	0.30(1)	0.3	0.29(4)

⁷¹. A similar method has been used in [Erh16] to find a “best-match” result over several data sets in order to determine the magnetic field in the analyzing plane from a series of transmission measurements.

Influence of the transmission edge

The proposed analysis strategy requires to determine the position of the transmission edge beforehand and keep the value ΔU_0 fixed during the fit. It is therefore important to investigate how a systematic bias in this value affects the outcome of the fit. If, for example, the edge position has been wrongly determined, the fit could yield a wrong energy distribution that does not match the actual conditions. Due to the strong correlations between fit parameters, especially between the transmission edge ΔU_0 and the mean energy \hat{E} , this effect must be considered here.

Table 4.40 shows the results of different toy experiments that were carried out as discussed above. The table lists the parameters that are relevant to describe the effective energy spread of the electrons: the mean energy \hat{E} , the upper limit of the energy distribution E_{max} , and the energy spread σ_E (corresponding to the effective 1σ -width of the distribution⁷²). In contrast to the results discussed earlier, here the edge position was set to a “wrong” value on purpose, i. e. with an offset to its true value of 0 eV that is used to generate the toy data samples (cmp. table 4.37). This investigation used only 1000 toy data samples (instead of the 10 000 samples that were used before) to speed up computation time. The “0V/BroadZero” and “0V/NarrowZero” parameter sets corresponds to the setting that is typically used in a measurement to determine the energy distribution ($U_{spec} = -200$ V, $\alpha_p = 0^\circ$), using two different angular distributions to investigate how this affects the sensitivity to the edge position ΔU_0 .

The edge position was shifted in the range $\Delta U_{bias} = -50$ meV to 50 meV around the true value in 10 meV steps:

$$\Delta U_0 = 0 \text{ eV} + \Delta U_{bias}. \quad (4.111)$$

In the analysis of the measurements, and uncertainty of 10 meV is assumed for the edge position (see sections 4.5.6 and 4.6.5). As expected, the accuracy of the fit results worsens significantly when the edge offset is increased. The discrepancy for all three energy parameters show a strong dependency on the edge position. Especially for large offset values δU_0 , the observed discrepancy becomes larger than the estimated uncertainty of the fit results.

From the results shown here, the systematic uncertainties of the three fit parameters are estimated to a maximum of

$$\delta \hat{E} = \delta E_{max} = \delta \sigma_E \leq 0.02 \text{ eV}, \quad (4.112)$$

assuming a 10 meV bias in the edge position. The uncertainty increases if the energy distribution becomes narrower (second parameter set), since in this case a small absolute shift of the transmission edge has a larger influence on the correlated parameters. Conclusively, the additional systematic uncertainty of 20 meV must be considered when discussing the transmission functions that have been observed in a measurement.

72. Note that the Gaussian energy spread σ_E used here is different from the width parameter σ'_E . It can be computed from a given energy distribution via (4.41).

Table 4.40.: Fit results of different toy data samples with a transmission edge offset, using the 5-parameter fit model.

setting		bias ΔU_{bias}	mean \hat{E}		limit E_{max}		spread σ_E	
			true	fit	true	fit	true	fit
0V	BroadZero	-0.05 eV	0.4	0.30(2)	0.80	0.74(1)	0.32	0.39(4)
		-0.02 eV	0.4	0.37(1)	0.80	0.78(1)	0.32	0.34(3)
		-0.01 eV	0.4	0.38(1)	0.80	0.79(1)	0.32	0.32(2)
		0.00 eV	0.4	0.40(1)	0.80	0.81(1)	0.32	0.32(2)
		0.01 eV	0.4	0.42(1)	0.80	0.82(1)	0.32	0.31(2)
		0.02 eV	0.4	0.43(1)	0.80	0.83(1)	0.32	0.30(2)
		0.05 eV	0.4	0.30(2)	0.80	0.74(1)	0.32	0.39(4)
	NarrowZero	-0.05 eV	0.25	0.07(5)	0.62	0.52(2)	0.25	0.37(6)
		-0.02 eV	0.25	0.20(2)	0.62	0.59(1)	0.25	0.28(3)
		-0.01 eV	0.25	0.23(2)	0.62	0.61(1)	0.25	0.27(2)
		0.00 eV	0.25	0.25(1)	0.62	0.62(1)	0.25	0.25(2)
		0.01 eV	0.25	0.27(1)	0.62	0.64(1)	0.25	0.24(1)
		0.02 eV	0.25	0.29(1)	0.62	0.65(1)	0.25	0.23(1)
		0.05 eV	0.25	0.34(1)	0.62	0.68(1)	0.25	0.21(1)

4.9.3 Angular distribution

For measurements that are performed at non-zero plate angles, $\alpha_p > 0^\circ$, the angular distribution of the electrons must be considered in addition to the energy distribution. Typically, the analysis is based on a reference measurement at zero-angle where the energy distribution was determined beforehand. The parameters of the angular distribution can then be determined by a fit with the analytical model where the energy parameters are kept fixed at their pre-determined values ($\hat{E} = \text{const.}$ etc.). Because the energy distribution is not modified when the plate angle is varied (which is verified by simulations, see section 4.8.5), this approach allows to disentangle the two distributions.

The angular distribution is described by the mean angle (“amean”, $\hat{\theta}$) and the angular spread (“awidth”, σ_θ) of the electrons in the spectrometer entry magnet. Especially for extremely small ($\theta \rightarrow 0^\circ$) or extremely large pitch angles ($\theta \rightarrow 90^\circ$), the analytical model is not overly sensitive to changes in the angular distribution. In these cases, large regions in the parameter space produce nearly equivalent results (i. e. similar angular distributions and transmission functions). This allows the fit to converge to an outcome that does not correspond to the actual angular distribution, although a good χ^2 value has been achieved and the analytical model matches the measurement data.

Figure 4.94 shows the result of a toy experiment with 10 000 samples, where the angular distribution was fitted to toy data samples. The method is equivalent to the investigation of the energy distribution that was discussed earlier. For intermediate pitch angles ($\theta \approx 15^\circ$ to 75°) the fit achieves a good accuracy of the resulting parameters. In the case shown at the top of the figure with $\hat{\theta} = 25^\circ$, the mean angle and the angular spread both match the corresponding true values. The angular distribution can

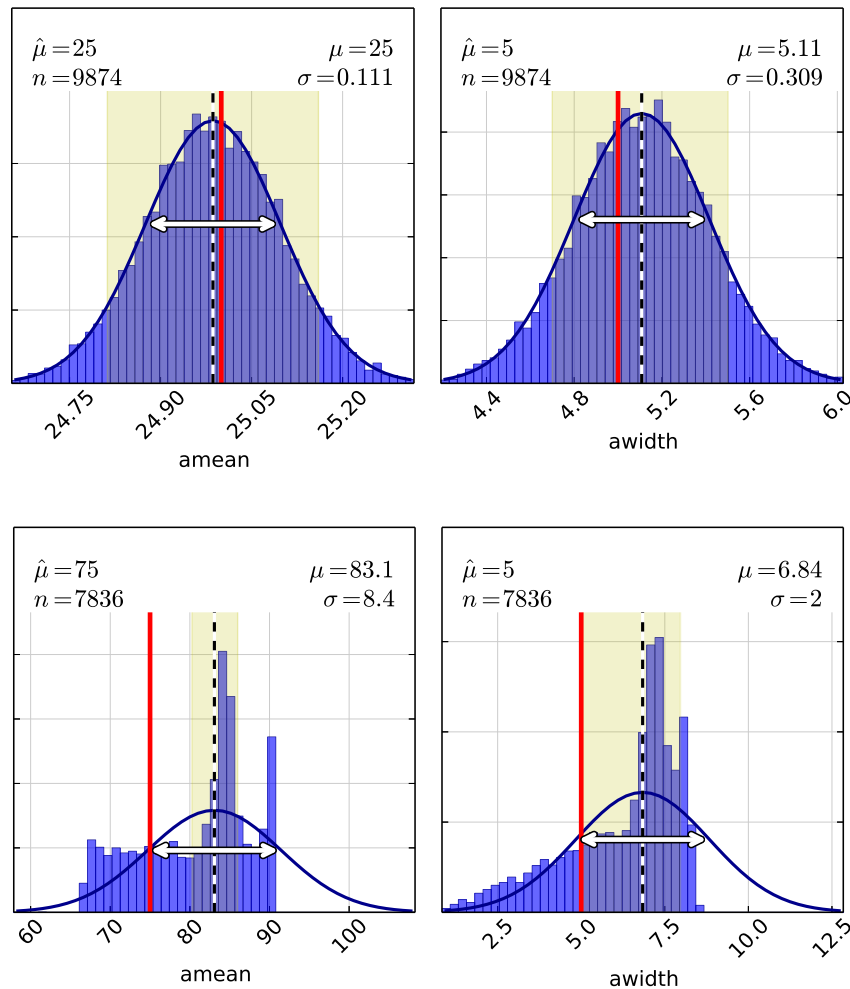


Figure 4.94.: Fit results of 10000 toy data samples, using the 4-parameter fit model (angular distribution). The figure shows results for two toy models using the “BroadSmall/HV” (top) and the “BroadLarge/HV” parameter set (bottom). The two parameter sets correspond to different pitch angles (see table 4.37). In this case, the transmission edge position and the energy parameters are kept fixed during the fit, so that the angular distribution can be determined. In the settings with small pitch angle (top), the fit accurately reproduces the true values for the mean pitch angle $\hat{\theta}$ (amean) and the angular spread σ_{θ} (awidth). The accuracy decreases if larger pitch angles are investigated (bottom), since the analytical model becomes increasingly insensitive to the actual angular parameters for pitch angles $\theta \rightarrow 0^{\circ}$ and $\theta \rightarrow 90^{\circ}$. This increases the systematic uncertainty for these cases.

therefore be determined accurately, provided that the correct energy distribution is known. On the other hand, the limited sensitivity of the fit for $\theta \rightarrow 0^{\circ}$, 90° is seen as a deviation of the fit results from their true values in the bottom part of the figure, where the fit yields $\hat{\theta} = 83.1^{\circ}$ in contrast to the true value of 75° . Table 4.41 shows results for different toy experiments, where different angular distributions have been investigated. The limitations of the analytical model for extreme cases of θ can be seen clearly: At a small pitch angle of 2° , the angular spread σ_{θ} that is determined by the fit is extremely small and deviates by one order of magnitude from its true value. At a large pitch angle of

75°, the mean angle $\hat{\theta}$ and the angular spread σ_θ are considerably overestimated, but are in agreement with their true values within the estimated uncertainty.

This investigation yields several conclusions that should be considered when discussing transmission function measurements:

- The analytical model is not sensitive to the angular distribution at extremely small or extremely large pitch angles. The fit results can therefore show large deviations to the true values in these cases.
- For small pitch angles, the angular spread tends to be underestimated on a large scale, yielding unrealistic values of less than 1°.
- For large pitch angles, the mean angle and angular spread tend to be slightly overestimated.

From the observed discrepancies between the true angular parameters and the fit results, the systematic uncertainty of the mean angle and the angular spread are estimated to

$$\delta\hat{\theta} = 1^\circ \text{ to } 10^\circ, \quad (4.113)$$

$$\delta\sigma_\theta = 2^\circ. \quad (4.114)$$

The uncertainty of the mean angle rises towards larger pitch angles (i. e. it scales with $\hat{\theta}$). Note that only three toy experiments have been considered here due to time constraints, which makes it difficult to obtain an accurate description of the systematic uncertainties for the angular distribution.

Table 4.41.: Fit results of different toy data samples, using the 4-parameter fit model.

setting		mean angle		angular spread	
		true	fit	true	fit
HV	BroadZero	2°	2.7(7)	2°	0.10(1)
	BroadSmall	25°	25.0(1)	5°	5.1(3)
	BroadMedium	50°	50.0(2)	5°	5.1(3)
	BroadLarge	75°	83.1(84)	5°	6.8(20)

4.10 Chapter summary

In this chapter, a pulsed angular-selective mono-energetic UV photoelectron source for commissioning measurements of the KATRIN main spectrometer was discussed. This electron source was developed over the recent years at WWU Münster [Zac14, Val09] and has already been used in the first SDS commissioning phase [Gro15]. Due to issues with the SDS-1 setup that limited the functionality of the source prevented to carry out all measurements as planned, the source design was reworked and improved before the second commissioning phase at the main spectrometer. The improvements include design changes of the plate-capacitor setup, an improved tilt actuation by linear motors, improved UV optics that allow automated measurements at variable wavelength, and a new slow-control interface that provides remote control during measurements.

The new setup was mounted at the monitor spectrometer for extended functionality tests and commissioning measurements of the source. This allowed to verify that the source meets all requirements at a MAC-E filter setup that provides comparable conditions as the main spectrometer. This additional measurement phase was deemed necessary to circumvent the issues in the SDS-1 phase, where the source had been shown to work in a laboratory setup at WWU Münster, but could not achieve full functionality at the KATRIN site. The monitor spectrometer measurements verified that the new design works well at a MAC-E filter setup, and the electron source is able to produce electrons with well-defined energy and pitch angle. Angular selectivity as a key feature of the source for the spectrometer commissioning was confirmed, and many source characteristics such as the energy and angular spread of the produced electrons at different operational parameters were determined. These test measurements also provided a nice opportunity to test the reworked slow-control system, and to develop measurement and analysis strategies that would prove to be extremely helpful during the following SDS-2 measurements.

The source was mounted at the main spectrometer after these successful test measurements, where a UHV manipulator allowed to move the source around the magnetic flux tube to study the spectrometer transmission function for individual detector pixels. Precise alignment measurements were carried out to reduce the misalignment of the source w. r. t. the magnet setup and other systems, and to include misalignments in the corresponding simulations. Unfortunately an extended maintenance break was required after first measurements during the SDS-2 phase, where the high voltage design of the source was reworked and the photocathode replaced. After re-installation at the main spectrometer it was possible to carry out the source commissioning as planned. The source characteristics were shown to be in general agreement with the results from the monitor spectrometer setup, and again the source was able to meet all its requirements. It was confirmed that transmission function measurements with the electron source are sensitive to changes of the effective work function of the spectrometer. Furthermore, a novel method to determine the work function of the source photocathode was developed that is complementary to the well-established approach by R.H. FOWLER, and does not require a dedicated measurement. After the successful commissioning of the source it was used in many important measurements, e. g. to determine the main spectrometer transmission properties.

The various measurements were backed by detailed particle-tracking simulations with the software Kassiopeia [F⁺17], which allowed to gain more insight into the electron acceleration and transport mechanisms in the source that are extremely relevant for the source characteristics, especially the angular and energy spread of the produced electrons. The simulations were performed in a 3D setup with components such as the half-shell dipole electrode that break axial symmetry. The KEMField package with its GPU-acceleration capabilities provided a great toolkit to perform these simulations in a

reasonable time frame. It was found that the energy distribution of the electrons in the spectrometer entry magnet is fully consistent with the initial distribution after their emission from the photocathode, which allows to investigate the initial energy spread in transmission function measurements. The angular spread, on the other hand, is not only affected by the electromagnetic conditions at the source and the plate tilt angle, which is a crucial feature to achieve angular selectivity, but also by the kinetic energy of the electrons due to the complex electron acceleration mechanisms. The simulations also investigated the influence of different operational parameters, such as the starting or acceleration voltage, on the source characteristics. It was found that all these parameters affect the produced pitch angle. Possible misalignments of the photocathode w. r. t. the symmetry axis of the electron source also affect the pitch angle and could explain some of the asymmetries observed during measurements. In general, the simulations are in agreement with measurement results and could reproduce many characteristics of the source, such as the dependency of the produced pitch angle on the plate angle. Differences between simulations and measurements are mainly attributed to unknown misalignments of the individual components.

The source commissioning measurements overall were a great success and showed that the electron source meets all its design requirements. The electron source was used in the SDS-2 measurement phase to study the transmission properties of the main spectrometer [Erh16] and to verify the integrity of the inner-electrode system [Bar16], among many other dedicated measurements. The source was also used in combination with the magnetic pulse (chapter 5) to investigate its timing characteristics. The measurement and analysis techniques learned during the commissioning measurements and the experience with 3D simulations of the source setup will be of great advantage for upcoming commissioning of the full KATRIN beamline, which utilize a different photoelectron source at the Rear Section. Although this source is based on a different design, its key features and major characteristics – e. g. angular selectivity or the energy spread of the produced electrons – are expected to show a similar behavior as discussed in this chapter.

Active background reduction by magnetic pulse

Great care has been taken at the KATRIN experiment to reduce the electron background observed at the main spectrometer. Background electrons that overlap energetically with signal electrons cannot be discriminated and thus have a significant impact on the neutrino mass sensitivity (section 2.3). Hence, it is crucial to reduce this background component as much as possible. A background level of better than 10^{-2} cps in the signal energy region is aimed for.

One major background process is the decay of radioactive isotopes in the inner volume of the main spectrometer. These nuclear decays can produce high-energetic electrons that are stored in the spectrometer for up to several hours, during which they produce large amounts of low-energetic secondary electrons via scattering processes with residual gas. Some of these electrons are accelerated by the electrostatic retarding potential when exiting the spectrometer, and thus arrive at the detector in the same energy region as the signal electrons. Especially the decay of the radon isotopes ^{219}Rn and ^{220}Rn can be problematic in this context, since both are abundant at the main spectrometer. The short half-life of these isotopes allows them to decay inside the inner spectrometer volume before being pumped out by the vacuum system, where they eventually produce large amounts of radon-induced background.

Passive countermeasures have been implemented to reduce the number of radon isotopes that enter the main spectrometer (section 2.1). However, it is difficult to completely prevent any nuclear decays in the large spectrometer volume. Furthermore, additional background sources could exist that have not yet been accounted for. This provides a strong motivation to extend the experimental setup by active background-reduction methods, which can be applied dynamically during regular measurements in case an increased background level is observed.

So far, two such methods have been implemented and were tested during the SDS commissioning phases. The *electric dipole* method applies a dipole field within the entire spectrometer volume in order to move stored electrons out of the magnetic flux tube [Hil16]. The *magnetic pulse* method reduces or inverts the magnetic field in the spectrometer in order to deform the magnetic guiding field, which forces stored electrons against the vessel walls where they are subsequently removed [Ott10a]. The latter method has been implemented over the course of this thesis and is discussed in this chapter. The technical design and the results of the commissioning measurements will also be published in [B⁺17b].

5.1 Background from nuclear decays

This section discusses the processes that can result in radon-induced background at the main spectrometer, and shows how passive and active methods can reduce this background component. The working principle of the magnetic pulse method is presented at the end of this section. The technical design of the magnetic pulse system that has been implemented at the main spectrometer will be discussed in section 5.2.

5.1.1 Background from stored particles

Background processes in the spectrometer section contribute to the overall background level and thus affect the statistical uncertainty of the experiment. An increased background level thus reduces the neutrino mass sensitivity, as shown in figure 5.1. Especially background that is created by nuclear decays in the spectrometer volume, e. g. induced by decays of radon isotopes, affects the sensitivity. This background component typically occurs in “clusters” of correlated events, i. e. short time periods where a significant rate increase that is related to a nuclear decay is observed [Har15, Wan13].

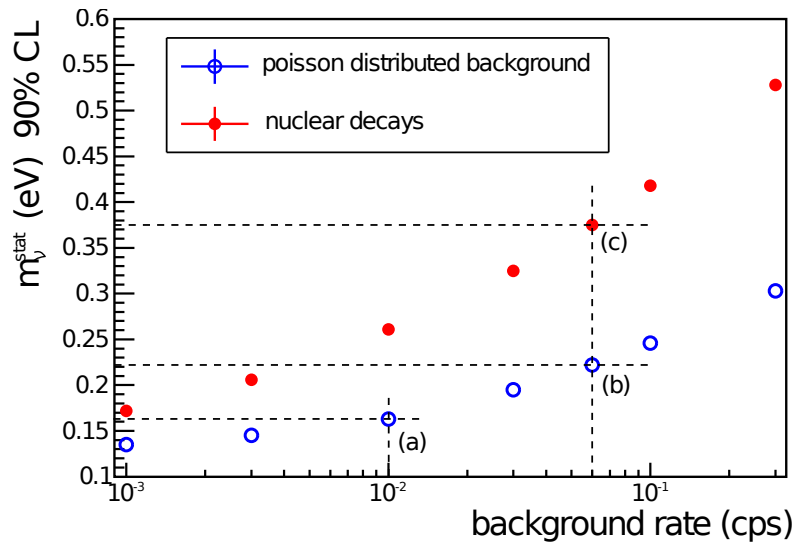


Figure 5.1.: Statistical uncertainty of the neutrino mass in dependency of the background level. The total uncertainty of the experiment depends on the statistical uncertainty and can be minimized by achieving a low background level. At the design goal of 10^{-2} cps, a statistical uncertainty of better than 0.17 meV is reached (a). A higher background level will increase the statistical uncertainty (b). Nuclear decays in the spectrometer are especially problematic because they create non-Poissonian background that typically occurs in correlated “event clusters”. This type of background has an increased impact on the statistical uncertainty (c). It is therefore crucial to reduce the background that is related to nuclear decays as much as possible to achieve the sensitivity goal. Figure from [Wan13].

Radon background

It is known from earlier investigations of the background at the pre- and main spectrometer that an important background-production process is the nuclear decay of the radon isotopes ^{219}Rn and ^{220}Rn [M⁺13, F⁺11]. Both decays are accompanied by the emission of high-energetic (primary) electrons, as seen in figure 5.2. The vacuum system at the main spectrometer features several turbo-molecular pumps (TMPs) that achieve a short turn-around time

$$t_{vac} = \frac{V_{MS}}{S_{TMP}} \approx 350 \text{ s}, \quad (5.1)$$

where $V_{MS} = 1240 \text{ m}^3$ is the spectrometer volume and $S_{TMP} = 3505 \text{ l/s}$ is the TMP pumping speed [M⁺13]. Hence, any long-lived isotopes are typically pumped out before they can decay. A well-known background source that is common in other experiments, the decay of ^{222}Rn with a half-life of $t_{1/2}(^{222}\text{Rn}) = 3.8 \text{ d} \gg t_{vac}$, is therefore not an issue at the KATRIN experiment. The isotopes ^{219}Rn and ^{220}Rn , however, have considerably shorter half-lives of $t_{1/2}(^{219}\text{Rn}) = 3.96 \text{ s}$ and $t_{1/2}(^{220}\text{Rn}) = 55.6 \text{ s}$, respectively. It is thus possible for these isotopes to decay inside the spectrometer volume before being pumped out, thereby initiating background-production processes [Mer12, Wan13].

One major source for ^{219}Rn molecules are the non-evaporable getter (NEG) pumps that are used at the main spectrometer to achieve the necessary ultra-high vacuum (UHV) conditions ($p \leq 10^{-11} \text{ mbar}$). With a total amount of 60 kg of NEG material that is installed at the pump ports, a total emanation rate of $0.12 \text{ }^{219}\text{Rn/s}$ is expected. Additionally, ^{219}Rn and ^{220}Rn is emitted from the weldings in the stainless steel material of the spectrometer vessel. Although the steel itself was selected specifically to achieve a low background level, it is difficult to completely avoid a contamination with radioactive isotopes in the welding processes during the construction of the vessel. Another source for these isotopes is auxiliary equipment installed at the main spectrometer, such as ceramic insulators that typically contain a small amount of natural radioactive isotopes. From these sources, an emanation rate of $0.03 \text{ }^{219}\text{Rn/s}$ and $0.08 \text{ }^{220}\text{Rn/s}$ is expected [M⁺13].

Both radon isotopes decay into an excited polonium atom. During the de-excitation process or the following decay into a daughter nucleus, which happens within a few ps, electrons covering a wide energy range are emitted [M⁺13, W⁺13]:

- *Conversion electrons* result directly from the de-excitation of the polonium state. They are released if the wave function of a shell electron is non-vanishing at the nucleus and if the γ -transition is suppressed, which is typically the case for heavy nuclei [Bro01, Wu07]. In the case of polonium de-excitation, these electrons can have energies up to 450 keV.
- *Shake-off electrons* are created if the emitted α -particle knocks out an electron from the atomic shells [R⁺75a, R⁺75b]. These electrons are emitted with energies up to 80 keV.
- *Shell reorganization electrons* are created if the emission of the α -particle results in a non-adiabatic change of the nuclear potential [Han74]. In the case that is considered here, this leads to the emission of mostly low-energetic electrons with a combined energy of roughly 230 eV.
- *Auger electrons* can be produced if earlier emission processes leave vacancies in the atomic shell. This often leads to a cascade of relaxation processes where multiple electrons are emitted [B⁺95]. These electrons reach energies up to 20 keV.

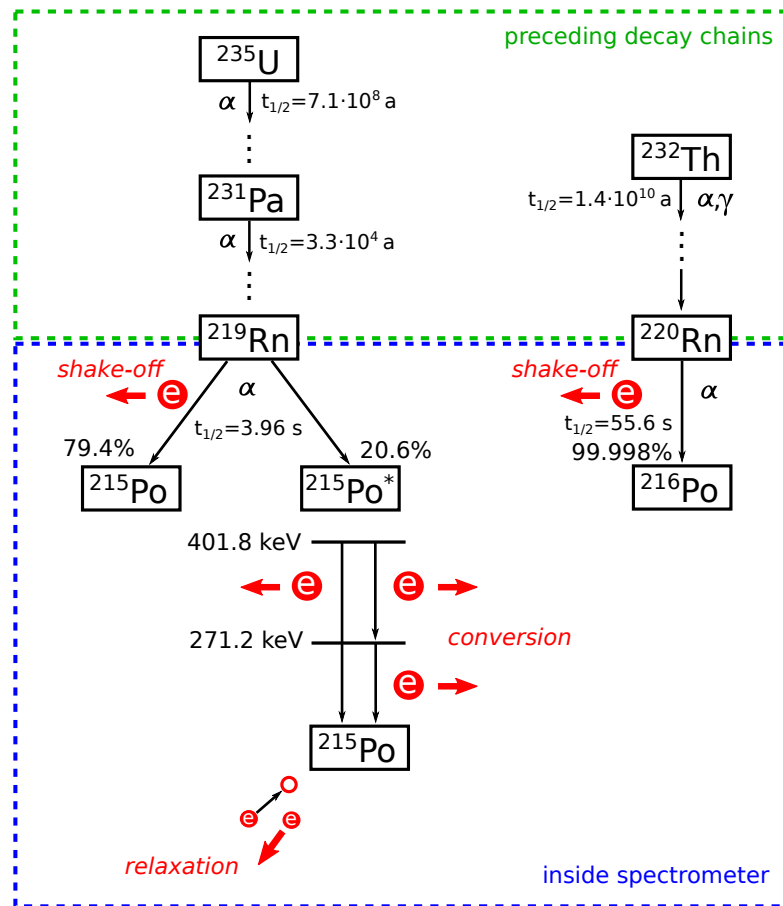


Figure 5.2.: Radon decay processes at the main spectrometer. *Top:* The presence of non-equilibrium decay chains in the used materials leads to the emanation of short-lived radon isotopes ^{219}Rn and ^{220}Rn . Typical sources are the NEG pumps of the vacuum system or the steel weldings of the spectrometer vessel. *Bottom:* α -decays in the spectrometer volume produce electrons that cover a wide energy range up to several 100 keV. These primary electrons can become stored inside the spectrometer. The electrons are created by a combination of shake-off, conversion, Auger and other relaxation processes in the daughter nucleus of the radon decay. ^{220}Rn decays into the ground state of the daughter nucleus, so that no conversion electrons are emitted in this case. Figure adapted from [Wan13].

Storage conditions

The MAC-E filter achieves a superior energy resolution with a large angular acceptance and is thus ideally suited for kinematic neutrino mass measurements (see section 2.2). However, it also creates excellent storage conditions for electrons of a wide energy range by the *magnetic bottle effect*. This effect is related to the adiabatic collimation, which is a key feature of the MAC-E filter principle, and is thus intrinsic to the setup. Electrons that are created inside the spectrometer volume e. g. by nuclear decays can become stored by the strong magnetic fields at the spectrometer entrance and exit. Stored electrons can participate in scattering processes with residual gas, which creates low-energetic secondary electrons that can reach the detector. This is visualized in figure 5.3.

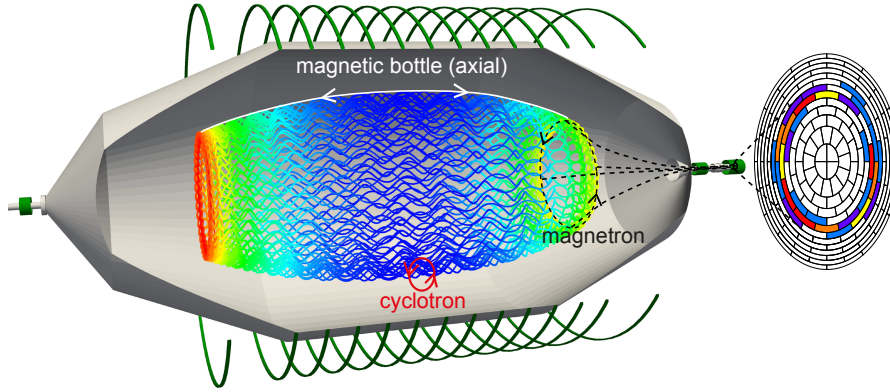


Figure 5.3.: Typical trajectory of a stored electron in the main spectrometer. Similarly to a classical *Penning trap*, stored electrons undergo an axial oscillation where they are continuously reflected at both ends of the spectrometer by the *magnetic bottle effect*. Additionally, a slow *magnetron drift* occurs in azimuthal direction, which results in a “tubular” shape of the electron trajectory that is typical for stored electrons. A *cyclotron motion* is superimposed on the whole electron trajectory. Low-energetic secondary electrons that are created by scattering processes of the stored electron with residual gas can often escape the spectrometer and are thus observed at the detector, where they contribute to the observed background level. Under certain experimental settings (enhanced vacuum pressure), the circular projection of the electron trajectory is visible on the pixelated detector. Figure from [Har15].

In the adiabatic motion of electrons in the spectrometer the magnetic moment (2.6) is conserved [Jac62],

$$\mu = \frac{E_{\perp}}{B} = \frac{E \cdot \sin^2 \theta}{B} = \text{const.} . \quad (5.2)$$

Due to the dependency on the magnetic field B , this results in the conversion of transversal and longitudinal kinetic energy, $E_{\perp} \leftrightarrow E_{\parallel}$, as the electron moves through the inhomogeneous magnetic field at the main spectrometer. Consequently, the pitch angle $\theta = \angle(\vec{p}, \vec{B})$ increases if the electron moves into a high-field region.

Electrons are *magnetically reflected* if their pitch angles reaches 90° on their trajectory. For electrons that are created in the spectrometer at a magnetic field B_0 and electric potential U_0 with an initial pitch angle θ_0 , one must consider that the magnetic field increases towards the spectrometer entrance and exit and the electron is accelerated by the electric potential. By defining a maximal transversal kinetic energy E_{\perp}^{\max} at which an electron can leave the spectrometer without reflection, one can derive a condition for the initial pitch angle from (2.1) and (2.6):

$$\sin^2 \theta_0 = \frac{E_{\perp}^{\text{start}}}{E_0} \quad \wedge \quad \frac{E_{\perp}^{\text{start}}}{E_{\perp}^{\max}} = \frac{B_0}{B_{\max}} \quad \wedge \quad E_{\perp}^{\max} < E_0 + qU_0 \quad (5.3)$$

$$\Rightarrow \theta_0 < \arcsin \left(\sqrt{\frac{E_0 + qU_0}{E_0} \cdot \frac{B_0}{B_{\max}}} \right), \quad (5.4)$$

where $B_{\max} > B_0$ is the magnetic field at the spectrometer entrance ($B_{PS2} = 4.5$ T) or the spectrometer exit ($B_{\max} = 6$ T), and E_0 is the initial kinetic energy of the electron. The value E_{\perp}^{\max} is determined by the local magnetic field and corresponds to the local width of the transmission function, i. e. $E_{\perp}^{\max} =$

0.93 eV for $B_0 = 0.3$ mT and $B_{max} = 6$ T in the standard KATRIN setup. If the electron starts at ground potential, $U_0 = 0$, or is extremely high-energetic, $E_0 \gg qU_0$, the above equation corresponds to the “classic” condition for magnetic reflection (2.21). Since electrons that are produced by nuclear decays typically follow an isotropic emission profile with $\bar{\theta} \approx 60^\circ$, they are efficiently stored by the magnetic bottle effect.

At nominal magnetic field, the storage condition for these electrons is only broken by one of the following possibilities:

- The transversal energy E_\perp decreases below a certain threshold where the acceleration by the electric fields at the main spectrometer overcomes the magnetic reflection condition. This circumvents magnetic reflection and only occurs at small energies, $E_\perp \leq 1$ eV. The transversal energy of stored electrons decreases over time through the emission of synchrotron radiation,

$$\Gamma = \frac{\dot{E}_\perp}{E_\perp} = \frac{e^4 B^4}{3\pi\epsilon_0 m_e^3 c^3}, \quad (5.5)$$

where B is the magnetic field at the electron trajectory. Since only transversal energy is radiated away in this process, this effect also slowly reduces the pitch angle. However, since the amount of radiated energy is rather small, the storage condition is typically satisfied for a long time.

- The transversal energy is large enough so that the electron’s cyclotron radius, $r_c \propto E_\perp/B$, becomes larger than the spectrometer radius. In this case, the electron will eventually hit the vessel walls or a part of the inner-electrode system, which removes the electron from the spectrometer volume. At the analyzing plane where the minimal magnetic field is encountered ($B_{min} \approx 0.3$ mT), the spectrometer radius is 4.9 m. The energy threshold for this process is therefore $E_\perp^{max} = 180$ keV, so that electrons with smaller energies that are created by nuclear decays are typically stored.
- The overall kinetic energy is too large to fulfill adiabaticity, which is only the case for extremely high-energetic electrons. Electrons that do not move adiabatically encounter rapid changes in E_\perp , which eventually results in one of the other two conditions to be fulfilled.

Since a considerable fraction of high-energetic electrons that is created by nuclear decays has transversal energies that fulfill the storage condition, they can be stored for up to several hours. During this time, they can create a large amount of low-energetic secondary electrons by scattering processes with the residual gas in the spectrometer. Although secondary electrons can become stored as well, some fraction can escape the spectrometer and reach the detector. These electrons are accelerated by the electrostatic retarding potential of the MAC-E filter and thus fall into the same region-of-interest (ROI) of the signal electrons, $E \approx E_0 = 18.6$ keV. This background is difficult to discriminate, and dedicated methods to reduce this background component are therefore required to reach the sensitivity goal.

5.1.2 Countermeasures against radon-induced background

Passive background reduction

The NEG pumps at the main spectrometer are responsible for the emission of large amounts of ^{219}Rn molecules that can reach the spectrometer volume. To reduce the amount of ^{219}Rn decays in the spectrometer, LN₂-cooled *baffles* have been installed in front of the three pump ports. The baffles consist of copper plates that are arranged in a triangular shape to block the line-of-sight between

the NEG material and the spectrometer volume. The heavy radon molecules are thus forced to hit the plate surface, which is operated at cryogenic temperature < 100 K, so that radon molecules are adsorbed. Lighter molecules that are abundant in the residual gas (e. g. hydrogen) can move around the copper plates and are pumped out. The baffles therefore do not significantly reduce the pump speed of the main spectrometer vacuum system [Har15, Gör14].

During the SDS-2 commissioning measurements, it was shown that the baffles efficiently block radon isotopes from entering the spectrometer volume and therefore can be used to reduce the background level. Figure 5.4 shows a clear temperature dependency of the observed background rate, indicating that the radon-induced background is considerably reduced when the baffles operate at cryogenic temperatures. The combined analysis of the SDS-2 measurements yields a reduction of the radon-induced background by 95%. The baffles reduce the emanation rate from the NEG pumps to $0.04(1)$ $^{219}\text{Rn/s}$ instead of the 0.12 $^{219}\text{Rn/s}$ that are emitted without baffles [Har15].

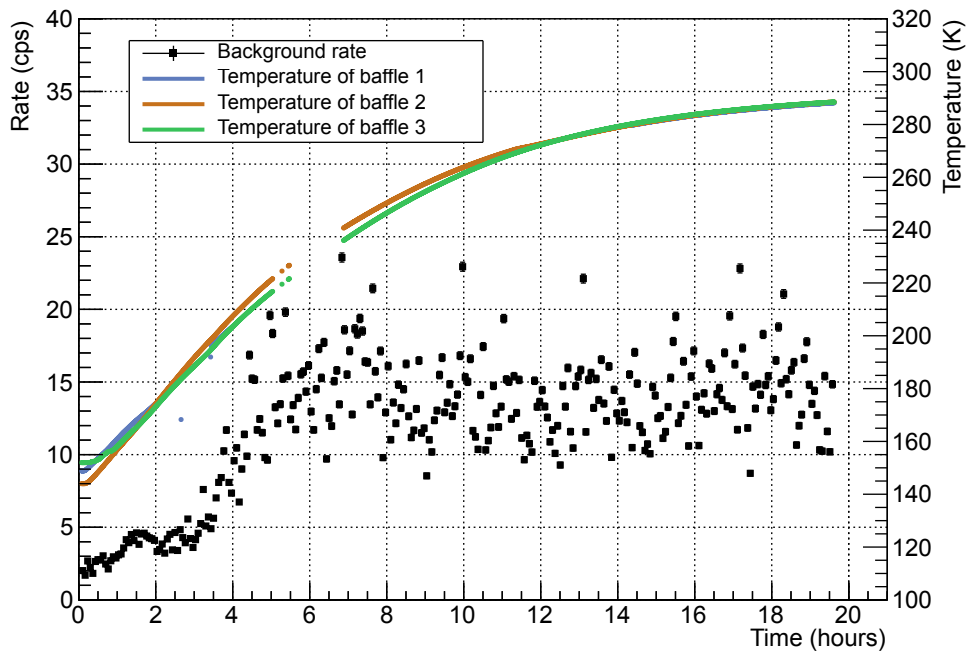


Figure 5.4.: Observed background with cold and warm baffles. The plot shows the observed rate over time while the 3 baffles are warmed up from 150 K to 290 K over 20 h. A special electromagnetic setting was used to artificially increase the radon-induced background [Gör14]. A rate increase of 500% is observed during the warm-up process as the temperature increases above $T_{thr} \approx 190$ K. Note that the temperatures are from sensors placed at the baffle exhaust lines, which have proven to give inaccurate readings. The actual baffle temperature is expected to be considerably lower. Figure from [Har15].

Active background reduction

In addition to this passive background reduction method, the main spectrometer also allows to implement active method that aim to remove stored electrons from the spectrometer volume. Two comple-

mentary methods have been conceived, which were implemented and tested during the SDS-1 and SDS-2 commissioning phases:

- **Electric dipole:** This method applies an electric dipole field throughout the complete spectrometer volume. The field is created by the inner-electrode (IE) system, which is mounted on the inside of the spectrometer vessel (see section 2.1) and was designed with this possibility in mind. Each wire electrode ring is divided into two half-ring segments, which splits the complete electrode system along the horizontal axis. A voltage difference up to 1 kV can be applied between the two segments. This “dipole mode” can be used in addition to the typical configuration of the system, where different voltages are applied to the individual electrode rings in order to optimize the transmission properties of the MAC-E filter.

Due to this design, the dipole field is oriented mainly in horizontal direction and achieves a field strength up to $E_{dip} \approx 100$ V/m. Together with the magnetic guiding field that is mainly oriented in axial direction inside the spectrometer, $\mathbf{B} \approx B_z$, the method induces a vertical $\mathbf{E} \times \mathbf{B}$ drift on the stored electrons,

$$\vec{v}_{drift} = \frac{\vec{E}_{dip} \times \vec{B}}{|\vec{B}|^2} \propto \frac{E_{dip}}{B_z} \approx 3 \cdot 10^5 \text{ m/s}, \quad (5.6)$$

where $B_z = B_{min} = 0.38$ mT is the magnetic field at the analyzing plane; the drift speed decreases for larger magnetic fields. The drift mostly affects stored electrons since they are exposed to the dipole field for a longer time than electrons that are transmitted towards the detector, which only pass through the dipole field once. The vertical movement eventually forces the stored electrons against the vessel walls, where they are removed if they hit an electrode surface.

This background reduction method is expected to be efficient for low-energetic electrons [Wan13]. Its implementation and the commissioning measurements are discussed in [Hil16].

- **Magnetic pulse:** This method reduces the magnetic field in the spectrometer for a short time (“pulse”) in order to break the magnetic guiding of stored electrons. The field reduction is performed through the existing air coil systems at the main spectrometer, which are typically used to fine-tune the magnetic field and thus optimize the transmission properties. By inverting the electric current in the air coils, the magnetic field $\mathbf{B} \approx B_{min} = 0.3$ mT in the spectrometer volume is significantly reduced (or even inverted, $\mathbf{B} < 0$) on a short timescale of roughly 1 s. The field reduction deforms the magnetic flux tube, increases the cyclotron radius of the electrons and induces radial drifts. All these effects can be used to force stored electrons against the vessel walls to remove them from the spectrometer volume.

This method is expected to be most efficient for high-energetic electrons [Wan13], for which the electric dipole method is less efficient. The method is based on an idea by E. OTTEN [Ott10a] and will be discussed in detail in the remainder of this section.

- Another method to actively remove stored electrons from the spectrometer is by electron-cyclotron resonance (ECR) heating. The basic principle is to apply a high-frequency electromagnetic field through the wire electrode system in order to increase the kinetic energy of the stored electrons. This method was not implemented at the main spectrometer and is therefore not further discussed. Dedicated test measurements have been performed before the spectrometer commissioning phases. A description of this method is given in [M⁺12].

Magnetic pulse

This chapter focuses on the magnetic pulse method, which is based on a rapid reduction of the magnetic guiding field in the spectrometer volume. This is supposed to break the storage conditions for both low- and high-energetic electrons if an inversion of the magnetic field is achieved, which removes primary and secondary electrons that were created by nuclear decays.

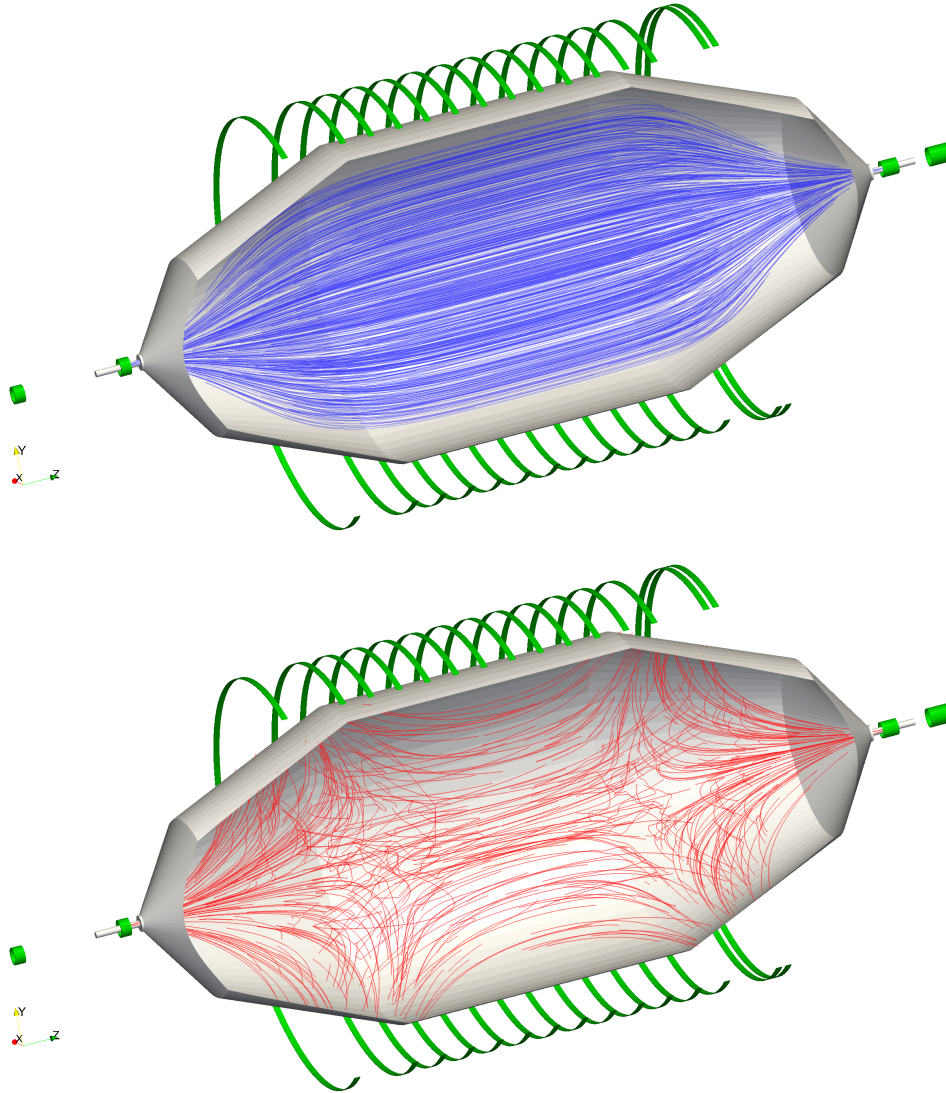


Figure 5.5.: Flux tube deformation during a magnetic pulse. *Top:* Under nominal conditions, the 191 T cm^2 flux tube is fully contained inside the spectrometer (gray). Electrons follow the magnetic field lines (blue) and can be transmitted through the spectrometer or become stored by the magnetic bottle effect. *Bottom:* The flux tube is deformed by inverting the magnetic field during a magnetic pulse. This is achieved by reverting the electric current in all air coils (large green circles) simultaneously. This changes the direction of the field lines (red), so that electrons are now guided against the vessel walls. Stored electrons following the field lines thus can be removed from the spectrometer. The whole field-inversion occurs on a timescale of roughly 1 s.

Under nominal conditions, the 191 T cm^2 flux tube that transports electrons from the source to the detector is fully contained inside the spectrometer volume. Electrons from the source are either transmitted to the FPD or reflected at the analyzing plane, according to the working principle of the MAC-E filter (see section 2.2). Electrons that are created inside the spectrometer volume e.g. by nuclear decays can become stored by the magnetic bottle effect.

Figure 5.5 visualizes the difference between the flux tube under nominal conditions and the conditions when the magnetic field is inverted by a magnetic pulse. The field reduction is typically applied by simultaneously inverting the currents in the LFCS air coils surrounding the spectrometer. The field reduction has several effects on electrons that move through the spectrometer volume, which can be used to remove stored electrons.

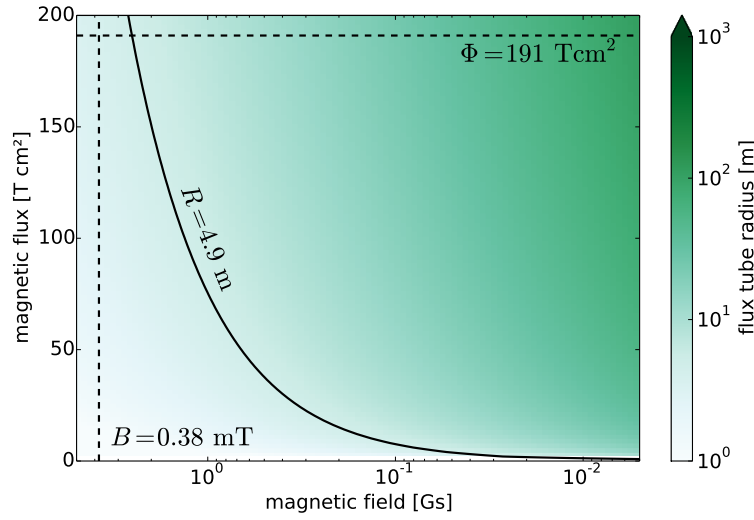


Figure 5.6.: Increase of the flux tube radius during a magnetic pulse. The plot shows the radius of the flux tube (5.7) against the conserved magnetic flux, Φ , and the strength of the magnetic field, $|\vec{B}|$. As before, the magnetic field decreases towards the right and the dashed vertical line marks the nominal magnetic field. The horizontal line indicates the 191 T cm^2 flux tube that is transported to the detector. The flux tube widens as the magnetic field is reduced. The solid line corresponds to the vessel radius of 4.9 m at the analyzing plane. The flux tube region that is above this line is not contained inside the spectrometer. Depending on the reduction of the magnetic field, the outer regions of the flux tube are moved against the vessel walls so that stored electrons are removed from the spectrometer.

- **Flux tube radius:** The magnetic guiding field in the main spectrometer conserves the magnetic flux $\Phi = 191 \text{ T cm}^2$, which creates a flux tube that transports electrons from the source to the detector (see section 2.2):

$$\Phi = \oint \vec{B} d\vec{A} \approx B_z \cdot \pi r_{max}^2 = \text{const.} \quad (5.7)$$

The value $A = \pi r_{max}^2$ corresponds to the cross-sectional area of the flux tube with radius r_{max} at the given magnetic field \vec{B} . The approximation $A \propto B$ is only correct in a homogeneous magnetic field; in an inhomogeneous field like the one at the main spectrometer an integration is required. Under nominal conditions, the flux tube is completely contained in the spectrometer vessel, $r_{max} < R = 4.9 \text{ m}$ in the analyzing plane (with $B \approx 0.3 \text{ mT}$).

Consequently, a reduction of the magnetic field results in a widening of the flux tube, i. e. an increase of r_{max} . At some point, the magnetic field lines of the flux tube will connect to the vessel walls. In this case the outer regions of the flux tube are not contained inside the spectrometer and electrons following the corresponding field lines will be guided against the vessel walls. A slight reduction of the magnetic field therefore allows to remove stored electrons from the outer region of the flux tube, while a stronger field reduction will also affect electrons in the flux tube region close to the spectrometer axis. This is shown in figure 5.6.

If the magnetic field is reduced to 0.01 mT, the flux tube radius at the analyzing plane increases from 4 m under nominal conditions to roughly 25 m, which is considerably larger than the spectrometer radius. A large fraction of electrons is guided against the vessel walls in this case. When the field in the spectrometer is completely inverted, $B < 0$, the direction of the guiding field at the spectrometer center changes. Consequently, all field lines of the flux tube connect to the vessel walls; this is shown at the bottom of figure 5.5. Electrons are therefore removed from the spectrometer independently of their kinetic energy.

The increase of the flux tube radius shows a high removal efficiency if the magnetic field is reduced sufficiently, i. e. decreased by several order of magnitude or even inverted. It is the dominant electron-removal process in the magnetic pulse method. However, the removal efficiency is limited since electrons can be magnetically reflected if $|B| > 0$, which prevents them from reaching the vessel walls. This results in some fraction of stored electrons not being removed from the flux tube. The effect is further investigated by particle-tracking simulations that are discussed in section 5.4.

- **Cyclotron radius:** Electrons that move adiabatically in a magnetic guiding field undergo a cyclotron motion (gyration) around a magnetic field line. The cyclotron radius is defined as

$$r_c = \frac{p_{\perp}}{|q||\vec{B}|} \propto \frac{\sqrt{E_{\perp}}}{B}, \quad (5.8)$$

where p_{\perp} , E_{\perp} and q are the transversal electron momentum, its transversal energy and its charge, and \vec{B} is the strength of the magnetic guiding field.

When the magnetic field is reduced, the cyclotron radius increases accordingly (figure 5.7). Electrons with given transversal kinetic energy are therefore removed from the spectrometer volume if their cyclotron radius exceeds the dimensions of the spectrometer vessel, $r_c \geq R$ with $R = 4.9$ m in the central spectrometer section. Note that electrons moving on outer field lines require a smaller increase of r_c and are therefore removed more efficiently by this effect.

Since r_c depends on the electron energy, this effect is more efficient for high-energetic electrons. One can estimate this effect by considering an electron in the analyzing plane at $B = B_{ana} = 0.38$ mT = const., where it has a cyclotron radius of 0.9 m at a large transversal energy of $E_{\perp} = 10$ keV. Its cyclotron radius becomes larger than the spectrometer radius at $B = 0.07$ mT, which removes the electron from the spectrometer volume. On the other hand, a low-energetic electron with $E_{\perp} = 10$ eV at the same conditions has a cyclotron radius of 3 cm at the analyzing plane and requires a field reduction to $B = 0.002$ mT to be removed by this effect.

It is important to consider that (5.8) contains the *magnitude* of the magnetic field $|\vec{B}|$. The cyclotron radius therefore increases again when the magnetic field is inverted ($B < 0$), so that the removal efficiency decreases after this point.

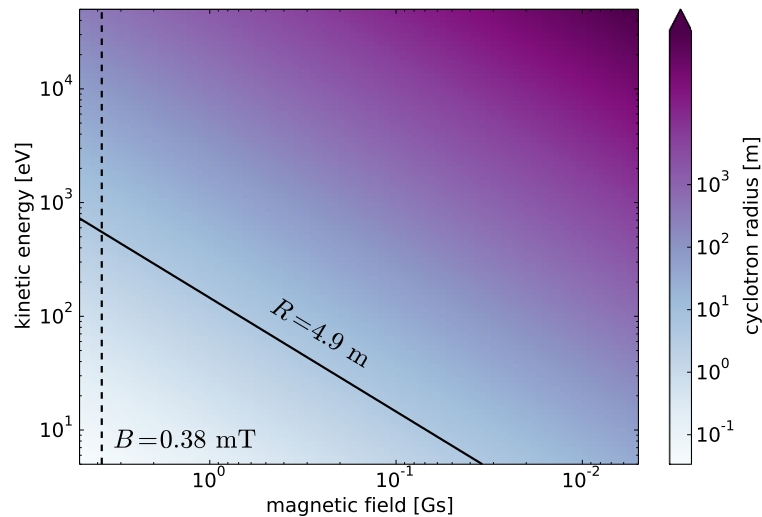


Figure 5.7.: Increase of the cyclotron radius during a magnetic pulse. The plot shows the cyclotron radius (5.8) against the transversal kinetic energy of the electron, E_{\perp} , and the strength of the magnetic guiding field, $|\vec{B}|$. The magnetic field decreases towards the right; the dashed vertical line marks the nominal magnetic field at the analyzing plane (SDS-2: $B_{ana} = 0.38$ mT). The cyclotron radius increases as the magnetic field is reduced. The solid line corresponds to the vessel radius ($R = 4.9$ m at the analyzing plane). Electrons with cyclotron radii above this line cannot be stored in the spectrometer, so that electrons are removed by a reduction of the magnetic field. Note that this plot assumes a constant magnetic field $B = B_{ana}$. Electrons that move inside the spectrometer undergo adiabatic transformation (2.7) with $\sqrt{E_{\perp}} \propto B$ and are thus expected to be removed at smaller kinetic energies for a given magnetic field at the analyzing plane.

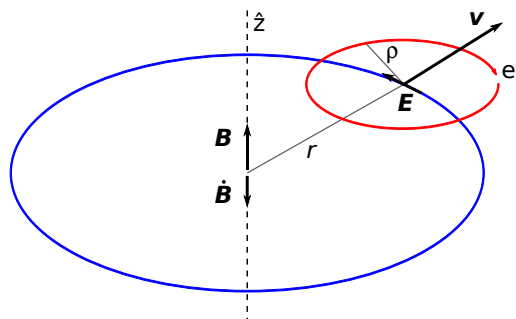


Figure 5.8.: Induced radial drift by a magnetic field change. An electron in the spectrometer is moving on a cyclotron trajectory with radius $\rho = r_c$ at a radial distance r from the central axis \hat{z} . A reduction of the magnetic field, $\dot{B} < 0$, will induce an electric field \vec{E}_{ind} in the spectrometer volume according to Maxwell's law (5.9). The electric field is oriented in azimuthal direction if $B = B_z$. The combination of the magnetic guiding field and the induced electric field then results in a radial $E \times B$ drift \vec{v} that is directed outwards, i. e. increases the radius r . The electron is thus moved towards the vessel walls as the magnetic field is reduced. Consequently, the drift direction changes if the magnetic field is increased again to its nominal level after a magnetic pulse was applied. Figure adapted from [Ott10a].

- **Radial drift:** According to the third Maxwell equation,

$$\nabla \times \vec{E}_{ind} = \frac{\partial \vec{B}}{\partial t} = \dot{\vec{B}}, \quad (5.9)$$

a change of the magnetic guiding field $\dot{\vec{B}}$ induces an electric field \vec{E}_{ind} inside the spectrometer. Because the magnetic field is oriented mainly in axial direction in the spectrometer volume, $\vec{B} \approx (0, 0, B_z)$, the induced field will be oriented in azimuthal direction. Depending on the sign of $\dot{\vec{B}}$ (field decrease or increase), the field will point in clockwise or counter-clockwise direction (figure 5.8).

The combination of the magnetic guiding field with the induced electric field results in an $E \times B$ drift,

$$\vec{v}_{drift} = \frac{\vec{E}_{ind} \times \vec{B}}{|\vec{B}|^2}. \quad (5.10)$$

Given the constraint that the electric field points in azimuthal direction, it can be easily derived from (5.9). This yields

$$E_{ind} = E_\phi = \frac{r}{2} \cdot \dot{B}_z, \quad (5.11)$$

where r is the radial distance of the electron's guiding center (i. e. the field line) to the spectrometer axis. The resulting $E \times B$ drift points in radial direction and is defined by the linear differential equation

$$v_{drift} = \dot{r} = \frac{E_\phi \cdot B_z}{B_z^2} = \frac{r}{2} \cdot \frac{\dot{B}_z}{B_z}. \quad (5.12)$$

Due to the factor $1/B_z$ in this term, the drift speed is maximal for $B_z \approx 0$. The dependency on r increases the drift as the magnetic field reduces and the electron moves to a larger field line radius.

The resulting drift will move stored electrons towards the vessel walls while the magnetic field is decreasing, and thus increases the removal efficiency of the magnetic pulse. The process does not depend on the kinetic energy of the electrons or on the magnitude of the magnetic field, but is more efficient for electrons on outer field lines with large r . The drift speed is strongly time-dependent due to the exponential behavior of $B(t)$ (and thus \dot{B}). One can safely assume such a behavior since the magnetic pulse is based on the current inversion in a magnetic coil, which typically yields an exponential time-dependency¹.

Since the field reduction is typically applied through magnetic coils, it is expected that the magnetic field follows an exponential behavior during a pulse cycle,

$$B(t) \propto \exp\left(-\frac{t}{\tau}\right), \quad (5.13)$$

where $\tau = \mathcal{O}(0.5 \text{ s})$ is the typical time constant of the field change. Under nominal conditions with $B = 0.38 \text{ mT}$ in the analyzing plane of the spectrometer, the *maximal* drift speed reaches values around 150 m/s. The average drift speed is substantially smaller due to the typically

1. This is confirmed by corresponding measurements, see section 5.3.2.

exponential behavior of the field change (5.13), and thus often not sufficient to move electrons towards the vessel walls within the typical pulse length of 1 s. Hence, the net drift that moves an electron towards the vessel walls during a full pulse cycle only plays a significant role for electrons that are stored in the outer flux tube region, $r_0 \geq 3.6$ m in the analyzing plane at nominal conditions. In comparison with other effects – the increase of the cyclotron radius and the widening of the flux tube that was discussed above – it is therefore believed that the radial drift only plays a minor role in the removal of stored electrons. A significant drift is only induced when a rapid change of the magnetic field occurs, which is prevented at the main spectrometer due to effects that slow down the field change (see section 5.3.3).

Furthermore, the direction of the drift changes after a magnetic pulse is applied and the magnetic field increased back to its nominal level. In this case it is possible that electrons from the vessel walls are moved into the inner spectrometer volume, as the drift now points inwards. This could result in more electrons becoming stored at the end of a magnetic pulse, which reduces the overall removal efficiency. To counteract this background-production process, a combination of the electric dipole with the magnetic pulse was suggested, where the electric dipole field is applied at the end of a magnetic pulse in order to remove the low-energetic stored electrons. It should be noted that no such effect has been observed in the corresponding measurements (see e. g. section 5.3), which indicates that the inwards drift has no significant impact on the removal efficiency of the magnetic pulse.

5.2 The magnetic pulse system

To apply a magnetic pulse in order to remove stored electrons from the spectrometer volume, a method to invert the magnetic field inside the main spectrometer needs to be implemented. This is only possible in the central spectrometer section where the magnetic field is small (lower mT range). At the entrance and exit regions of the spectrometer, the stray field of the strong superconducting solenoids does not allow rapid field changes. Fortunately, the air coil system – which is originally intended to fine-tune the magnetic field in the main spectrometer – provides an excellent possibility to apply magnetic pulses. The overall concept and the technical design of the system will be discussed in this section.

5.2.1 Using the air coil system to apply a magnetic pulse

The KATRIN experiment has two air coil systems implemented at the main spectrometer. Both are intended to fine-tune the magnetic field in the spectrometer, especially in vicinity of the analyzing plane where the energy analysis is performed (see sections 2.1 and 2.2). Another important aspect is the compensation of the earth's magnetic field in order to create a homogeneous magnetic field at the analyzing plane [E⁺16, G⁺13b, G⁺09].

The air coil system can be divided into two groups (figure 5.9):

- **LFCS:** The low field compensation system (LFCS) consists of 14 air coils that are equidistantly placed along the spectrometer axis. The coils have a diameter of roughly 6 m and enclose the spectrometer vessel. Each coil has multiple loops of aluminum wire and is operated at currents

up to 100 A by independent power supplies². The LFCS compensates the z-component of the earth's magnetic field (i. e. in axial direction of the spectrometer). The individual coil currents can be adjusted to optimize the magnetic field inside the spectrometer and to adjust the shape of the flux tube³.

- **EMCS:** The earth magnetic field compensation system (EMCS) consists of 2 sets of horizontal wire loops (“cosine coils”) that are wound multiple times around the spectrometer in axial direction. The loops are typically operated at currents up to 50 A by independent power supplies. The EMCS compensates the remaining two components of the Earth's magnetic field (i. e. in horizontal and vertical direction). By small current adjustments it is possible to move the flux tube within the spectrometer vessel.

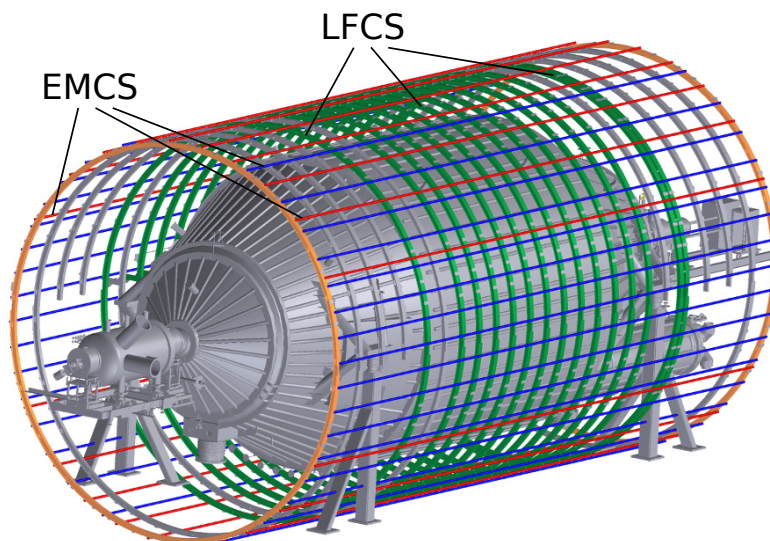


Figure 5.9.: The air coil system at the main spectrometer. The *low field compensation system* (LFCS) uses 14 air coils (green) that are placed along the spectrometer axis. It is intended to fine-tune the magnetic field close to the analyzing plane and optimize the transmission properties of the spectrometer. It also compensates the axial component of the earth's magnetic field. The *earth magnetic field compensation system* (EMCS) uses horizontal wire loops (“cosine coils”) (red/blue) that are wound around the spectrometer in axial direction. It compensates the remaining two components of the earth's magnetic field and can be used to move the magnetic flux tube within the spectrometer in horizontal/vertical direction. Each of the 16 air coils from both system is operated by an independent power supply that provides currents up to 100 A. The low inductance of the coils allows fast changes of the operating current, which can be utilized by a dedicated system to apply magnetic pulses. Figure from [G⁺13b].

The LFCS and EMCS support a flexible configuration of the magnetic field since all air coils are operated by independent power supplies. The power supplies are integrated with the existing slow-control system and allow a remote control of the output current. Due to weight restrictions of the air coil support structure, aluminum wires are used for both air coil systems. This increases the electrical resistance to roughly 0.4 mΩ/m, which is 50% larger than copper [G⁺09]. The LFCS air coils typically

2. Recently, a hardware upgrade was performed to allow currents up to 180 A in the upcoming SDS-3 commissioning phase.

3. The flux tube radius is directly correlated to the magnetic field, see (5.7).

have an inductance of 3 mH and an electrical resistance of 0.144 Ω , yielding a small time constant of $\tau = L/R \approx 21$ ms that allows fast current changes [E⁺16].

A magnetic pulse – i. e. a reduction or inversion of the magnetic field in the spectrometer – can be applied by reducing or reverting the air coil currents. One possibility would be to simply ramp down the power supplies to 0 A, so that the magnetic field is reduced. This method, however, has several disadvantages. The rather slow ramping speed of the devices prohibits a fast reduction of the magnetic field. Furthermore, the power supplies require some time to stabilize after changes of the output current. Both effects result in a longer time that is required to apply a single magnetic pulse and thus reduce the available time for regular measurements. This method also does not allow to revert the air coil currents, so that the pulse amplitude (i. e. the field reduction) is rather limited. Hence, a more advantageous method to perform fast current changes was investigated, which allows to revert the electric current in the air coils without adjusting the power supplies. In general, this approach is faster than ramping and thus reduces the required stabilization time, and achieved a smaller magnetic field in the spectrometer by doubling the pulse amplitude.

A device to perform such current inversions in a high-current load circuit has been designed in a joint effort by KIT Karlsruhe and WWU Münster. It can be placed between each air coil and the corresponding power supply and allows to invert the current in the load circuit without significantly affecting the current source. The current inversion can be applied either statically (for dedicated measurements where special magnetic field settings are used) or dynamically (to apply a magnetic pulse on a short timescale for background reduction). The term *FlipBox* has been coined for this device.

In the SDS-1 commissioning phase, a single FlipBox prototype was available for functionality tests and basic measurements. For the SDS-2 commissioning phase, all LFCS and EMCS air coils were equipped with FlipBox units to allow a synchronous current inversion and maximize the pulse amplitude. The magnetic pulse system also allows a more flexible configuration of the magnetic field (static inversion of currents) and has been utilized in various background measurements during the SDS-2 phase.

5.2.2 Working principle of the FlipBox units

The *H-bridge* is a well-known method to revert the electric current in a load circuit without any adjustments to the current source (figure 5.10). Essentially, it consists of four switches that are interconnected to form a H-shaped circuit design. The load circuit is connected to the source by two switches at any given time. The current direction can be inverted by changing all switches from conducting to isolating and vice versa. When the switches are realized e. g. through electro-mechanical relays or *metal-oxide-semiconductor field-effect transistors* (MOSFETs) that are remotely operated, the current direction can be controlled by an external signal. A major advantage of this design, besides its simplicity, is that the load circuit can be completely isolated from the control circuit that manages the individual switches. The maximal current and the operating voltage of the load circuit is only limited by the specifications of the relays or MOSFETs. Different implementations of the control circuit are easily possible, e. g. to manually switch the current direction or to allow remote operation.

This concept is ideal to implement a magnetic pulse system for the KATRIN experiment. It provides a reliable method to invert the individual air coil currents and can be controlled by an external trigger signal, which allows integration with the existing slow-control system. Since the air coil system was

already installed when the magnetic pulse system was developed, the FlipBox device is implemented as several individual modules that can be placed between each air coil and its power supply.

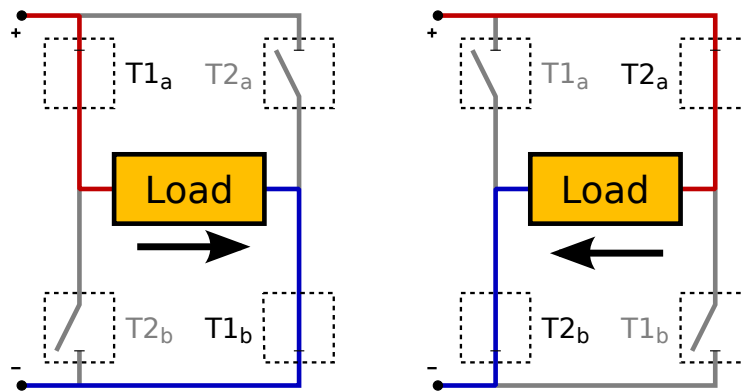


Figure 5.10.: Schematic drawing of the FlipBox operating scheme. The design of the system is based on the so-called “H-bridge” circuit, which uses four independent switches (e. g. MOSFETs) to invert the current direction in a load circuit without affecting the current source. *Left:* Only the switches $T1_{a,b}$ are conducting, so that the load circuit is connected to the source in “positive” current direction. *Right:* By cycling all four switches, $T2_{a,b}$ become conducting so that the current direction in the load circuit changes to “negative”. The current in the load circuit has been inverted without affecting the source.

Each FlipBox unit utilizes four high-current MOSFETs (International Rectifier IRFP4368PBF) that allow currents up to 195 A at 75 V. Electro-mechanical relays were also considered during early development, but this option was discarded due to possible influences from the magnetic fields at the experimental site. MOSFETs, on the other hand, are purely electronic devices that are not affected by magnetic fields. The MOSFETs are operated by a combination of DC-DC converters (Traco Power TME 1212S) and opto-couplers (Fairchild Semiconductors FOD3180). This design decouples the control circuit from the load circuit and provides a galvanic insulation. This is especially important since all air coils are connected to a common slow-control system, where any cross-talk between the individual air coils must be prevented. The design could be easily extended to use multiple MOSFETs in parallel to increase the maximal current. A schematic layout of the FlipBox control circuit is available in appendix A.

The timing of the internal processes is fully controlled by an 8-bit microprocessor (Microchip PIC16F876A-I/SP), which allows a flexible configuration of the system. To perform a current switch, the load circuit is first disconnected from the power source at a time t_0 . After a short delay $\Delta t < 10$ ms the load circuit is reconnected to the source with inverse polarity. This is shown schematically in figure 5.11. The additional delay is implemented to prevent shoot-through in the source circuit, which could severely affect the power supply⁴. The control circuit operates each MOSFET individually to perform the current-switch when an external trigger signal is received.

The inductance of the air coils results in a *voltage spike* U_{ind} that is induced in the load circuit when the polarity is reverted. The voltage spike typically exceeds the specifications of the used MOSFETs, $U_{max} = 75$ V. In order to protect the MOSFETs against this over-voltage, *transient voltage suppressor*

4. The delay time must be kept as short as possible to ensure a stable operation of the power supplies. The load-free time while the air coil is disconnected forces the power supply to regulate its output power. This requires some stabilization phase before measurements at nominal magnetic field can be continued after a magnetic pulse was applied.

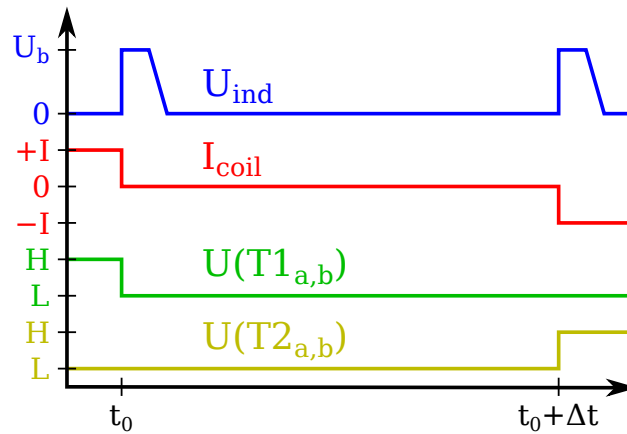


Figure 5.11.: Switching process of the FlipBox device. The load circuit (air coil) is operated at a current $I_{coil} \leq 100$ A. The state of each MOSFET is controlled by their gate voltage $U(T1_{a,b})$ and $U(T2_{a,b})$, which defines the current direction in the load circuit (see figure 5.10). The values H, L indicate the conducting or isolating state, respectively. By switching off $T1_{a,b}$ at t_0 , the load circuit is disconnected from the current source. This induces a voltage spike U_{ind} in the load circuit, which could result in the destruction of the MOSFETs. TVS diodes with a breakdown voltage $U_b = 40$ V are mounted in parallel to each MOSFET, which limit the voltage spike to $U_{ind} \leq U_b$. After some delay time $\Delta t < 10$ ms, the MOSFETs $T2_{a,b}$ are switched to conductive mode so that the load circuit is reconnected to the power source with inverse polarity. The delay is intended to prevent shoot-through in the source circuit and protects the power supply from accidental short-circuits.

(TVS) diodes (ST Microelectronics BZW50) are mounted in parallel to each MOSFET's source-drain terminals. The TVS diodes are normally insulating, but switch to fully conductive state when their breakdown voltage $U_b = 40$ V is exceeded. The diodes thus short-circuit the load circuit during a voltage spike and limit the voltage at the MOSFETs, $U_{ind} \leq U_b$. The excess power is dissipated through the internal electric resistance of the air coil. Measurement show that this is typically the case within 1 ms, which is considerably shorter than the 10 ms delay time. The voltage spikes therefore do not affect the current-switch process.

The maximal thermal power dissipation of each MOSFET is 520 W at 25 °C. Since only two MOSFETs are active at the same time, the maximal thermal power is about 1.2 kW per FlipBox. This maximum is typically not reached since the air coils are operated below the MOSFET specifications ($I_{coil} \leq 100$ A and $U_{coil} \leq 15$ V). The thermal power is distributed over heat sinks that are mounted on each MOSFET and actively cooled by four high-volume air fans (Sunon MB60251VX-000U-A99) that achieve a total air flow of 2×45.9 m³/h through the FlipBox casing. The FlipBox units are operated in the main spectrometer hall, where a stable temperature of 18 °C is achieved. Under nominal conditions, the temperature at the active MOSFETs is less than 40 °C. At the maximal current of 190 A (5 A safety margin), the MOSFETs reach temperatures of 70 °C, which is still completely within their specifications. To ensure safe long-term operation of the system, the temperature in each FlipBox unit is monitored by the slow-control system, using two temperature sensors that are placed on the MOSFET heat sinks. It is thus possible to shut down the power supplies if the temperature exceeds reasonable limits.

5.2.3 FlipBox integration and performance tests

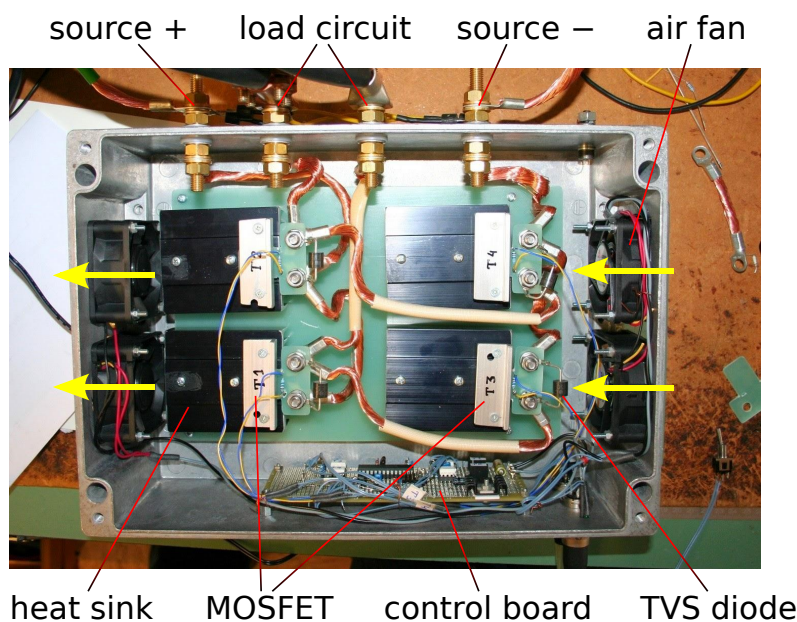


Figure 5.12.: FlipBox prototype for SDS-1 measurements. The technical design follows the H-bridge concept (figure 5.10), where four high-current MOSFETs are operated by a control circuit. The FlipBox connects the load circuit (air coil) to a current source (power supply) and allows to revert the polarity of the load circuit. TVS diodes protect the MOSFETs against voltage spikes that occur from switching the polarity due to the coil inductance. The thermal power of the MOSFETs is dissipated over heat sinks that are actively cooled by four air fans (air flow indicated by yellow arrows). The control board allows to change the polarity by a remote signal, which is used in the SDS-2 measurement phase to integrate the FlipBox units with the slow-control system.

A total of 17 FlipBox units have been manufactured at the electronics workshop at WWU Münster prior to the SDS-2 commissioning phase (14 LFCS, 2 EMCS, 1 backup unit). The units were transported to KIT Karlsruhe and integrated with the existing air coil and slow-control system for the SDS-2 measurements (figure 5.13). Their design is based on the prototype unit that was available during the SDS-1 measurement phase. This prototype is shown in figure 5.12.

The FlipBox units have been integrated with the existing air coil slow-control system. In the original design, the system allowed to adjust the output current of the individual air coils in order to adjust the magnetic field in the spectrometer. The FlipBox units extend the system to also change the current direction in the air coils. Both parameters can be controlled remotely e. g. by an ORCA run script (section 3.6), which allows automated measurements. Magnetic pulses can be applied at regular intervals (pulse cycle); this mode of operation is directly provided by the slow-control software that is implemented in LabView. Furthermore, the air coil currents can be statically inverted for dedicated measurements with special magnetic field settings (e. g. investigations of the main spectrometer background). In earlier measurement phases the air coils had to be rewired manually in order to change their polarity, then rewired again to continue measurements at nominal magnetic field.

A reference signal is provided by the FlipBox control board which indicates the polarity of the load circuit. This signal is fed into the DAQ system at the FPD to include the timestamp of each current-switch in the run data that is taken during a measurement. The analysis of the measurement data can

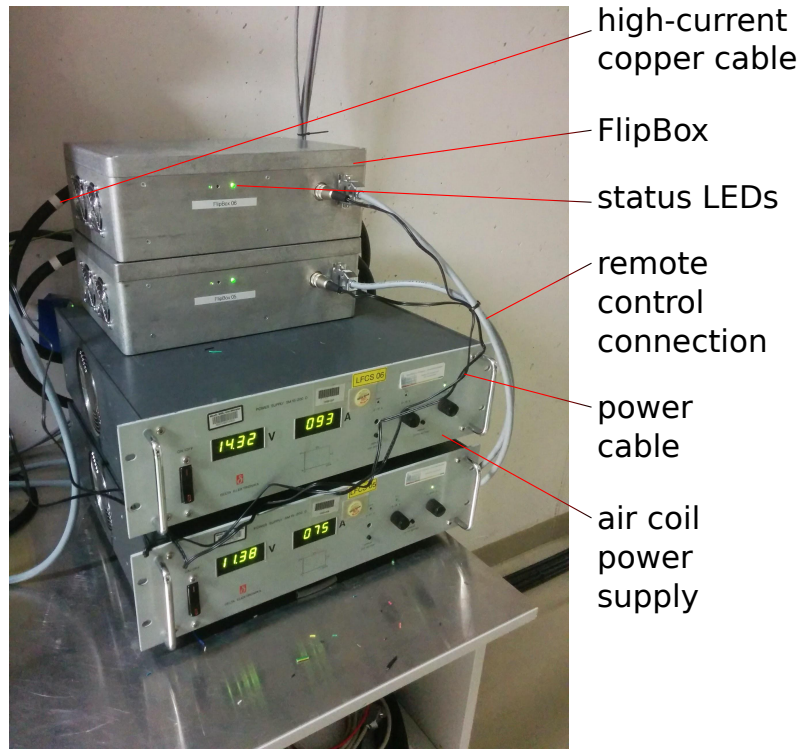


Figure 5.13.: Installed FlipBox units for the SDS-2 measurements. The FlipBox units are placed on top of the power supplies that correspond to the individual air coils. Flexible copper cables are used to connect each FlipBox to the power supply; the air coils are then connected directly to the FlipBox output terminals. LEDs indicate the operational status of the device (large green LED) and the polarity of the load circuit (small LEDs; green indicates “nominal” and yellow “inverse” polarity). The units are integrated with the slow-control system that also manages the power supplies. The SDS-2 system allows to remotely adjust the individual air coil currents (magnitude and polarity) and can be used to apply magnetic pulses through the air coil system.

therefore utilize this timing information, e. g. to distinguish individual pulse cycles. It is necessary to use the DAQ system here since the magnetic pulses are typically applied on a timescale of a few ms regarding their starting time, and use pulse lengths of 1 s to 5 s. This is too fast for the slow-control system, which is intended to monitor experimental parameters at intervals of 10 s. The integration with the DAQ system allows to monitor the magnetic pulse system on a per-event basis with accurate timestamps.

5.3 Measurements at the main spectrometer

The magnetic pulse method presented in this thesis has been tested successfully in the two commissioning phases of the KATRIN main spectrometer performed in 2013 (SDS-1) and 2014/2015 (SDS-2). The measurements allowed to verify the functionality of the magnetic pulse system and to determine its impact on the observed background. These measurements will be discussed in this section.

5.3.1 Experimental setup

In the SDS-1 phase, a single FlipBox prototype was available that allowed to pulse one LFCS air coil. In this phase, functionality test to verify the stability of the system and measurements with an radioactive $^{83\text{m}}\text{Kr}$ source were performed. The $^{83\text{m}}\text{Kr}$ measurements allowed to investigate the removal of low- and high-energetic stored electrons that result from nuclear decays inside the spectrometer volume. The system was upgraded for the SDS-2 phase, where all air coils were equipped with FlipBox units and the complete magnetic pulse setup was integrated with the existing slow-control system. In this phase, measurements were performed with a radioactive ^{220}Rn source and at nominal background to further investigate the removal efficiency of the system. Furthermore, the magnetic pulse was combined with the electron source discussed in chapter 4 to investigate the pulse timing inside the spectrometer. Figure 5.14 depicts the integration of the magnetic pulse system at the main spectrometer.

Operational parameters

The magnetic pulse is typically applied through the LFCS air coils, which achieves the maximal effect on the magnetic field near the analyzing plane of the spectrometer. The LFCS allows to deform the magnetic flux tube to a large extent, depending on the strength of the magnetic pulse (i. e. the achieved field reduction). This is shown schematically in figure 5.15. It would also be possible to use the EMCS, where a magnetic pulse would move the flux tube inside the spectrometer in horizontal or vertical direction so that it eventually touches the vessel walls. The two possibilities could also be combined in order to maximize the removal efficiency. However, the measurements discussed below were performed with the magnetic pulse being applied through the LFCS air coils and the EMCS operating at nominal settings. In all electron rate measurements, the spectrometer was operated at high voltage with $U_{ana} \approx U_{spec} = -18.6\text{ kV}$.

Table 5.1 lists the LFCS settings that were used in the two measurement phases. The nominal setting in both cases is the 3.8 G setting⁵ with $B_{ana} \approx 0.38\text{ mT}$ at the analyzing plane. Since only one FlipBox prototype was available in the SDS-1 phase, a special setting (“setting A”) was conceived to maximize the field reduction when only LFCS air coil #8 is pulsed [BEG⁺13]. In the SDS-2 phase, some measurements were performed at enhanced magnetic field (5.0 G setting with $B_{ana} \approx 0.50\text{ mT}$). Furthermore, functionality tests were performed with all LFCS coils set to the same current (with a maximum of 100 A). The strongest magnetic pulse is generally achieved when all air coils operate at maximal current. In this case the amplitude of the current inversion in all air coils is maximal. Such a setting, however, has considerable drawbacks regarding the transmission properties of the MAC-E

5. The standard settings are typically named “3.8 G”, “5 G” and so on, i. e. using non-SI units in their name. From here on, the standard settings will be referenced by their corresponding SI unit (1 G = 0.1 mT).

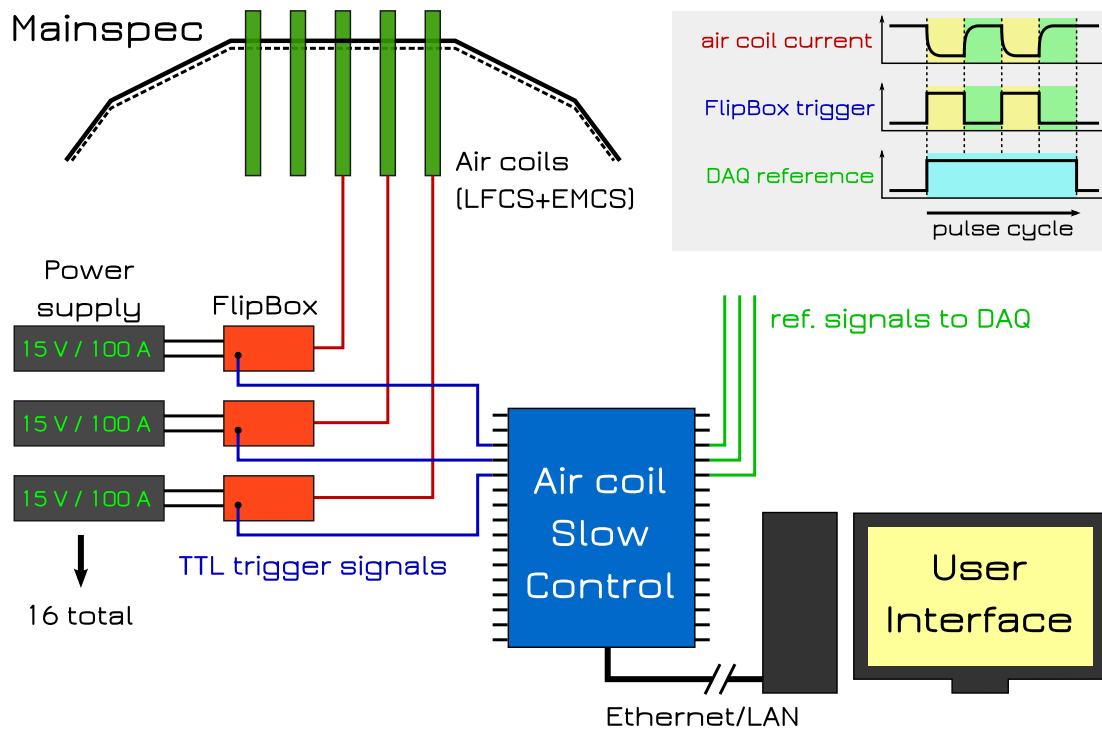


Figure 5.14.: Magnetic pulse system at the main spectrometer. Each of the 16 air coil power supplies has been equipped with a FlipBox device before the start of the SDS-2 measurement phase. The current polarity of the individual air coils is controlled by the air coil slow-control system to allow remote operation. It is possible to automatically change coil polarities and apply magnetic pulses during a measurement run through the ORCA scripting interface. Multi-pulse cycles can be performed where a single trigger signal initiates a series of pulses. A reference signal is fed into the DAQ system to determine the exact timestamp where a polarity switch occurred, which is necessary for data analysis and will be required later during neutrino mass measurements in order to exclude run data during a magnetic pulse from the analysis.

filter and the overall background level. It is therefore not used in typical measurements. Note that LFCS #14 is operated at inverse current direction under nominal conditions in order to counteract the stray field of the pinch magnet at the spectrometer exit. This air coil is therefore excluded from the magnetic pulse. Hence, the magnetic pulse is applied by inverting LFCS #1–13 in the SDS-2 measurements.

Achieved magnetic fields

The magnetic field B_{ana} at the analyzing plane depends on the used air coil setting. It defines the maximal flux tube radius according to (5.7). When the magnetic field is reduced sufficiently e. g. by a magnetic pulse, the radius increases above the dimensions of the spectrometer vessel. In this case, the magnetic field lines begin to connect to the vessel walls (figure 5.15). As explained in section 5.1.2, this allows stored electrons that follow the magnetic field lines to be removed. If the strength of the magnetic pulse is not sufficient to completely reduced the magnetic field, only electrons from the outer flux tube regions are guided towards the vessel walls. Electrons are thus not removed from the

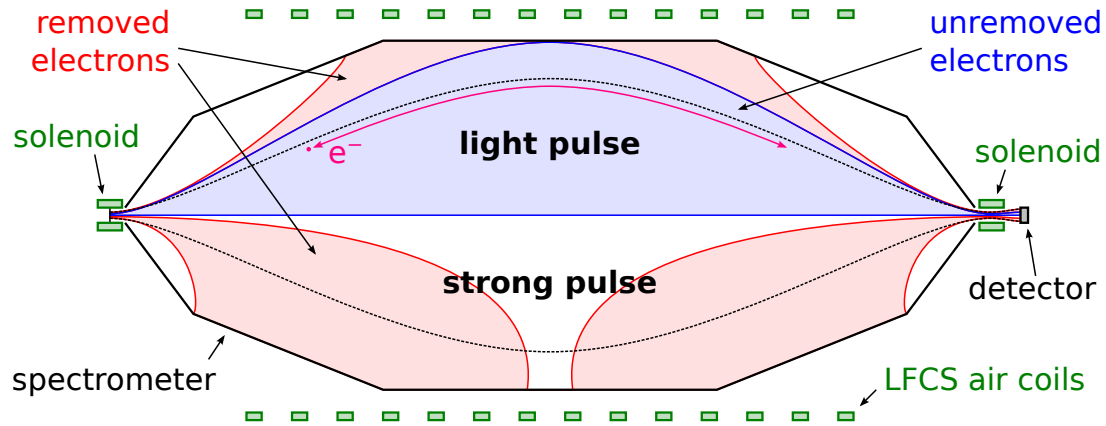


Figure 5.15.: Schematic view of a typical magnetic pulse measurement. Under nominal conditions, the 191 T cm^2 flux tube is fully contained inside the spectrometer (dashed black lines). Electrons can become stored by the *magnetic bottle effect* and create background due to scattering processes, which is partly transmitted to the detector and observed as increased electron rate. The magnetic pulse is typically applied via LFCS air coils in order to deform the flux tube so that the field lines connect to the vessel walls (shaded areas). *Upper half:* A light magnetic pulse that does not completely invert the magnetic field will only remove electrons from the outer flux tube region (red area). The inner region is still fully contained inside the spectrometer so that stored electrons are not removed (blue area). *Lower half:* A strong magnetic pulse that reaches $B \leq 0$ in the spectrometer forces the complete flux tube against the vessel walls. In this case, all stored electrons that reach the vessel walls are removed from the flux tube volume.

inner volume. Only a sufficient field reduction causes the flux tube to split up so that all field lines connect to the vessel walls.

Table 5.2 shows the magnetic field B_{ana} and the effective flux tube radius r_{ana} at the analyzing plane for the different settings from table 5.1. Under nominal conditions ($B_{ana} = 0.38 \text{ mT}$), the flux tube is contained inside the spectrometer with $r_{ana} < R = 4.9 \text{ m}$. At the enhanced magnetic field setting ($B_{ana} = 0.5 \text{ mT}$), the radius decreases due to the higher magnetic field. A magnetic pulse reduces the magnetic field and reaches a minimal level B_{ana}^* for $t \rightarrow \infty$ (typically $t \gtrsim 1 \text{ s}$, see below). The flux tube radius increases accordingly to r_{ana}^* . For the case where the magnetic field is inverted, $B_{ana} < 0$, the flux tube radius (5.7) is undefined. The table compares the nominal setting with a magnetic pulse where either LFCS air coil #8 or #1–13 are inverted.

For the SDS-1 setup, one can see that a magnetic pulse using LFCS #8 at the 0.38 mT setting is insufficient to increase the flux tube radius above the spectrometer dimensions, $r_{ana}^* = 4.76 \text{ m} < R$. The removal efficiency is therefore severely limited in this case. The special LFCS setting “A”, on the other hand, reduces the minimal field achieved by the magnetic pulse to $B_{ana}^* = 0.23 \text{ mT}$ and moves the outer flux tube region against the vessel walls, $r_{ana}^* = 6.11 \text{ m} > R$.

In the SDS-2 setup where all LFCS air coils can be pulsed, the magnetic field is inverted to $B_{ana}^* = -0.16 \text{ mT}$ in the 0.38 mT setting. In this case, the flux tube is fully inverted (so that r_{ana}^* is undefined) and the maximal efficiency is achieved. This is also the case for the enhanced magnetic field setting at 0.5 mT , where the inverted magnetic field is even smaller. The maximal pulse amplitude is achieved at the 100 A setting with $\Delta B = B_{ana} - B_{ana}^* = 1.73 \text{ mT}$.

Table 5.1.: LFCS settings used in magnetic pulse measurements.

LFCS coil	— SDS-1 —		— SDS-2 —		
	3.8 G	setting A	3.8 G	5.0 G	100 A
#1	28.6 A	0.0 A	21.1 A	52.9 A	100 A
#2	24.0 A	40.0 A	25.7 A	15.2 A	100 A
#3	17.3 A	30.0 A	20.3 A	33.7 A	100 A
#4	22.1 A	30.0 A	28.4 A	34.5 A	100 A
#5	33.5 A	30.0 A	38.8 A	61.8 A	100 A
#6	36.4 A	0.0 A	27.5 A	75.7 A	100 A
#7	35.8 A	20.0 A	34.4 A	27.1 A	100 A
#8	54.1 A	96.0 A	50.7 A	49.5 A	100 A
#9	10.2 A	30.0 A	10.4 A	64.4 A	100 A
#10	52.1 A	0.0 A	44.4 A	46.6 A	100 A
#11	32.0 A	30.0 A	37.2 A	52.5 A	100 A
#12	20.1 A	30.0 A	21.0 A	29.8 A	100 A
#13	29.8 A	40.0 A	43.3 A	52.2 A	100 A
* #14	-51.8 A	-50.0 A	-50.4 A	-47.8 A	-100 A

Table 5.2.: Magnetic field at different LFCS settings.

phase	setting	— nominal —		— LFCS #1–13 —		— LFCS #8 —	
		B_{ana}	r_{ana}	B_{ana}^*	r_{ana}^*	B_{ana}^*	r_{ana}^*
SDS-1	0.38 mT	0.38 mT	4.00 m	—	—	0.30 mT	4.76 m
	setting A	0.38 mT	4.02 m	—	—	0.23 mT	6.11 m
SDS-2	0.38 mT	0.38 mT	4.01 m	-0.16 mT	<i>inv.</i>	—	—
	0.5 mT	0.51 mT	3.45 m	-0.28 mT	<i>inv.</i>	—	—
	100 A	0.93 mT	2.54 m	-0.80 mT	<i>inv.</i>	—	—

5.3.2 Magnetic fields at the spectrometer

To verify the functionality of the magnetic pulse system and to determine the time constant of the magnetic field change, a measurement with a fast fluxgate sensor (Bartington Instruments Mag-03MSB1000, 1 ms sampling interval) was performed before the start of the SDS-2 measurement phase. At this point the main spectrometer was not in operation yet, which allowed to attach the sensor directly to the outer vessel wall inside the high-voltage area. The sensor was placed close the center of the spectrometer, i. e. the analyzing plane, where the field change due to a magnetic pulse is expected to be maximal.

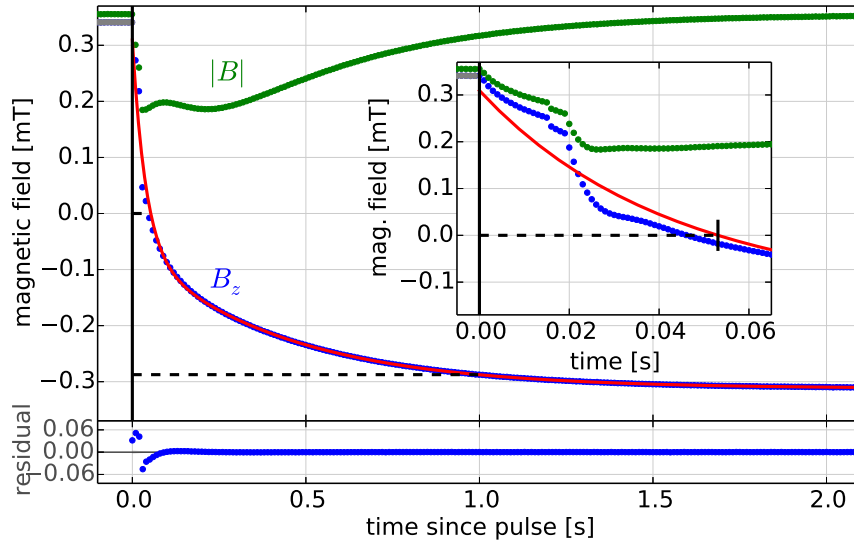


Figure 5.16.: Magnetic field at the main spectrometer during a magnetic pulse. A fluxgate sensor was mounted on the outer vessel wall close to the analyzing plane to measure the field $B_z(t)$. A magnetic pulse was initiated at $t = 0$ by inverting LFCS #1–13 in the 0.38 mT LFCS setting, with $B(t = 0) = 0.34$ mT at the sensor position. The plot shows the axial field (blue) and the total field (green), which includes radial components. The time dependency is described by a combination of two exponential curves (5.14) with time constants τ_{slow}, τ_{fast} . The field is inverted at $t \geq t_{inv} \approx 50$ ms and reaches a stable inverted level of $B_{inv} = -0.31$ mT within 1 s after the start of the pulse. At $t < t_{inv}$ the observed field deviates strongly from the exponential curve as shown in the inset (see running text). It is generally expected that the magnetic field *inside* the spectrometer shows a similar exponential behavior with comparable or longer time constants, depending on the additional slow-down due to eddy currents in the vessel hull.

Figure 5.16 shows the axial magnetic field B_z and the total field $|\vec{B}|$ during a magnetic pulse. The pulse is applied by inverting LFCS air coils #1–13 simultaneously. The air coils were operated at the 0.38 mT setting to determine the time dependency of the magnetic field under nominal conditions. The test measurement was also performed at air coil currents up to 100 A to maximize the pulse amplitude⁶. The 0.38 mT setting achieves $B_0 = B_z(t = 0) \approx 0.34$ mT at the sensor position. The field is smaller than the nominal value $B_{ana} = 0.38$ mT at the analyzing plane due to the radial distance from the spectrometer

6. The measurement also served as a safety test to investigate possible stability issues with the superconducting solenoids due to the rapid field change. No such effects have been observed, and it was concluded that the magnetic pulse has no safety implications for the operation of the four solenoids at the main spectrometer.

axis. The magnetic pulse inverts the magnetic field to $B_{inv} = B_z(r \rightarrow \infty) = -0.31$ mT. The inverted level is reached at about 1 s after the start of the magnetic pulse.

The time-dependent axial magnetic field can be described by a combination of two exponential curves. This model produces better fit results than a simple exponential curve. It uses two independent amplitudes and time constants,

$$B_z(t > 0) = a_{slow} \cdot \exp\left(\frac{-t}{\tau_{slow}}\right) + a_{fast} \cdot \exp\left(\frac{-t}{\tau_{fast}}\right) + b, \quad (5.14)$$

where $b = B_{inv}$ is the inverted field. The fit result is shown in figure 5.16 and the corresponding parameters are listed in table 5.3. The table also contains the results for measurements that were performed at different magnetic field settings⁷. These results are generally consistent with the nominal setting, indicating that there are no large systematic effects that depend on the achieved magnetic field.

The magnetic field is reduced to zero at $t_{inv} \approx 50$ ms and is inverted after this point. The two time constants in (5.14) describe the long-term behavior where the magnetic field slowly reaches the inverted level B_{inv} , and the short-term behavior that dominates the field change for small $t \lesssim t_{inv}$. The long-term behavior can be described by a *relaxation time* $t_{90} \approx 1$ s at which 90% of the inverted field is reached. The relaxation times listed in the table shows a slight dependency on the magnetic field setting, but is generally in agreement between the different measurements. One can therefore conclude that the used field setting has no significant impact on the timing parameters of the magnetic pulse. It essentially only affects the pulse amplitude and the minimal and maximal magnetic field that is achieved.

The axial magnetic field in figure 5.16 shows a strong deviation from the exponential model during the first few ms while the magnetic field is reduced rapidly, $t < t_{inv}$. Here the magnetic field is modified by the direct influence of the individual air coils. Although the closest air coil LFCS #8 is expected to dominate the observed field, adjacent air coils will also affect the field to some extent. The deviation cannot be explained by the air coils being operated at different currents (thereby resulting in different timing characteristics) since the deviation is also observed in the 100 A setting and others where all air coils are operated at the same current. Instead, the observed deviation is attributed to the mutual inductance of the air coils. Since any field change in one air coil is counteracted by the inductance of adjacent air coils, the mutual inductance effectively increases the time constant $\tau_{LFCS} \approx 21$ ms that is normally attributed to each air coil (see section 5.2.1). The strength of this effect depends on the distance between two air coils and their currents. The overall field change thus becomes a superposition of the contributions from the individual air coils. A full description of this effect would need to include *all* combinations of the 14 air coils and is thus difficult to calculate.

However, a detailed description of the short-term behavior is not necessary since the removal processes are dominated by the long-term behavior where the magnetic field is inverted. The slow component of the field change ($\tau_{slow} \approx 400$ ms) is roughly one order of magnitude larger than the fast component. This observation can be explained by *eddy currents* that are induced in the stainless steel hull of the spectrometer vessel. The hull has a thickness of 35 mm and thus provides a large amount of conductive material where currents can be induced by a magnetic field change. The eddy currents counteract the field change imposed by the LFCS air coils and thus slow down the observed field change. Hence, the long-term behavior of the magnetic pulse is dominated by eddy currents and consequently features a time constant that is larger than expected from a simple description of the air coil systems as a large *LR*-circuit.

7. At the “40 A–100 A” settings all LFCS air coils operate at the same current, cmp. table 5.1.

The measurement with a fluxgate sensor on the vessel wall can only determine the magnetic field change outside the spectrometer vessel. However, it is believed that the field *inside* the spectrometer shows a similar exponential behavior with comparable or longer time constants, depending on how much the field change inside the spectrometer is slowed down e. g. by eddy currents on the vessel hull (cmp. section 5.3.3). The sensor measurement therefore indicates that the magnetic pulse requires a minimal length of at least 1 s in order to fully invert the magnetic field inside the spectrometer.

Table 5.3.: Timing parameters of the LFCS pulse at different current settings.

setting	$B_z(t=0)$	χ^2/ndf	τ_{fast}	τ_{slow}	t_{90}	t_{inv}
0.38 mT	0.34 mT	1.47	38.3(1) ms	432.6(1) ms	996.2(2) ms	53.1(1) ms
40 A	0.37 mT	1.52	38.9(1) ms	430.1(1) ms	990.4(3) ms	69.4(1) ms
60 A	0.52 mT	1.60	39.3(1) ms	432.0(1) ms	994.8(2) ms	60.4(1) ms
80 A	0.69 mT	1.31	39.6(1) ms	436.6(1) ms	1005.3(2) ms	61.1(1) ms
100 A	0.85 mT	2.21	52.2(1) ms	439.7(1) ms	1012.5(2) ms	74.3(1) ms
weighted average:			41.3(1) ms	433.73(2) ms	1000.6(1) ms	64.5(1) ms

5.3.3 Measurements with an electron beam

The photoelectron source that was presented in chapter 4 was attached to the main spectrometer entrance during the SDS-2 measurement phase. A pulsed electron beam is produced by the photoelectric effect from UV light that is provided by a laser. The electrons are emitted with known energy and angular distribution and a small pulse width of 40 ns (see section 4.3.1). The source is intended to investigate the transmission properties of the MAC-E filter [Erh16, Gro15]. Since the electrons in the spectrometer are sensitive to the electromagnetic conditions, the electron beam allows to investigate the magnetic field in the spectrometer directly. This creates a complementary method to the sensor-based field measurement that was discussed above.

From the description of the magnetic pulse principle in section 5.1 it is clear that electrons cannot be transmitted through the spectrometer when the magnetic field is inverted and the field lines connect to the vessel walls. In this case, electrons entering the spectrometer will be simply guided against the vessel walls, instead of reaching the detector. The disappearance of the electron signal that is normally observed at the detector therefore allows to investigate the field change inside the spectrometer. It corresponds to the time when the magnetic field becomes inverted, so that the delay time w. r. t. the start of the magnetic pulse at $t = 0$ can be determined. The delay is expected to depend on the field line the electrons are following since outer field lines are affected earlier than field lines close to the spectrometer axis. The measurement approach is shown schematically in figure 5.17.

Table 5.4 shows the measured pulse delay t_{start} under nominal conditions (0.38 mT setting) that was measured with the electron beam. The magnetic pulse used a length of 2 s to ensure that the magnetic field is fully inverted before returning to the nominal field. The movable electron source was positioned to three positions on the pixelated detector wafer (figure 5.18) in order to investigate the radial dependency of the field change. As expected, the electron beam disappears earlier at the outer pixels (#52 and #100). This is explained by the smaller distance of the field lines to the vessel walls, so that a smaller field reduction is necessary (cmp. figure 5.17). In a similar approach the delay time

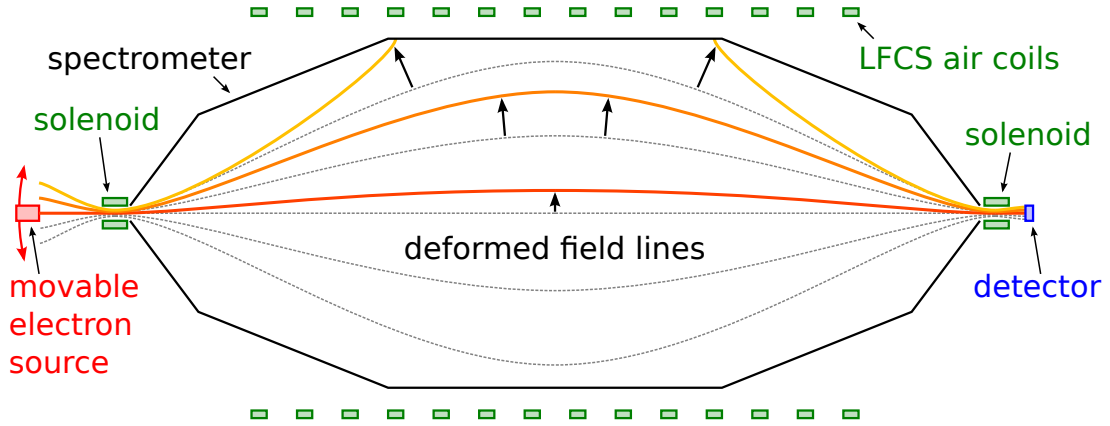


Figure 5.17.: Schematic view of the electron beam measurement. The electron source (red) emits an electron beam into the spectrometer (black). The source can be moved within the magnetic flux tube that is contained inside the spectrometer. Under nominal conditions, electrons follow the field lines (dashed lines) and are transmitted to the detector (blue). A magnetic pulse that is applied through the LFCs air coils (green) deforms the flux tube so that field lines move towards the vessel walls according to (5.7). Field lines that connect to the vessel walls do not allow electrons to be transmitted. The time when the disappearance of the electron signal on the detector is observed allows to investigate time-dependency of the magnetic field inside the spectrometer. It is thus possible to directly determine the timing characteristics of the magnetic pulse.

t_{stop} until the electron re-appears after the end of the magnetic pulse can be determined so that an effective pulse length $\Delta t = t_{stop} - t_{start}$ can be computed; these parameters are also listed in the table.

According to (5.7), the radius of the flux tube increases as the magnetic field is reduced. In order to force the electron beam against the vessel walls, the field must be reduced sufficiently so that the given field line reaches a radius $r > R = 4.9$ m in the analyzing plane (where R is the spectrometer radius). The required magnetic field B_{dis} for the electron beam to disappear can be estimated by

$$B_{dis} \approx \frac{\Phi(r_{ana})}{\pi R^2} = B_{ana} \cdot \frac{r_{ana}^2}{R^2}, \quad (5.15)$$

where r_{ana} is the field line radius in the analyzing plane at nominal magnetic field $B_{ana} = 0.38$ mT. The value $\Phi(r_{ana}) \approx B_0 \cdot \pi r_{ana}^2 \leq 191$ T cm² is the magnetic flux that is enclosed by the magnetic field lines. The maximal value corresponds to the flux tube that is transported to the detector under nominal conditions. The corresponding values for r_{ana} and B_{dis} for the three investigated detector pixels are given in table 5.4.

One can see that electrons on a central field line (pixel #2) require a considerably smaller magnetic field to be guided against the vessel walls. Due to the exponential behavior (5.14) of the magnetic field during a magnetic pulse, more time is required to reach this point. The observed delay time is therefore larger for inner detector pixels. The observed delay times $t_{start} = \mathcal{O}(300$ ms) are generally in agreement

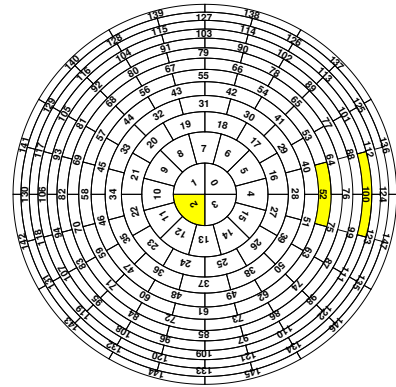


Figure 5.18.: FPD pixel mapping used in the pulse timing measurements.

with the timing characteristics that were determined by the sensor-based field measurement (see above). However, the direct measurement indicated that the field is already inverted at $t_{inv} \approx 50$ ms after the pulse. Therefore after this time, all field lines should connect to the vessel walls and no electron signal should be observed. Although it is expected that the delay time is increased for inner pixels from the discussion above, a discrepancy of at least 200 ms is observed for the outer pixel #100.

This result indicates that the field change inside the spectrometer is delayed w. r. t. to the magnetic field that was measured on the outside of the vessel walls. This is also confirmed by particle-tracking simulations that will be discussed in section 5.4.5. This observation further strengthens the assumption that eddy currents in the spectrometer vessel hull slow down the field change. From this measurement one can conclude that a minimal pulse length of about 0.5 s is required to fully invert the magnetic field inside the spectrometer, so stored electrons can be removed from the complete flux tube volume.

Table 5.4.: Timing of the magnetic pulse inside the main spectrometer.

pixel #	t_{start}	t_{stop}	Δt_{pulse}	r_{ana}	B_{dis}
2	409 ms	2275 ms	1866 ms	0.223 m	0.8 μ T
52	308 ms	2371 ms	2063 ms	2.564 m	99 μ T
100	251 ms	2455 ms	2455 ms	3.449 m	178 μ T

5.3.4 Measurements with a radioactive ^{83m}Kr source

Only one FlipBox prototype was available in the SDS-1 measurement phase. It was therefore possible to pulse one LFCS air coil in order to investigate the effect on stored electrons and to perform basic tests of the system. The maximal field reduction is achieved by using an air coil close to the analyzing plane, where the nominal magnetic field is small enough to be significantly reduced by inverting a single air coil. To further increase the pulse amplitude a special LFCS setting was used (setting “A”, see table 5.1), where LFCS air coil #8 is inverted in a magnetic pulse.

The measurement was performed with a radioactive source to investigate the electron removal processes and the rate reduction that can be achieved with the magnetic pulse. A ^{83}Rb emanator ($t_{1/2}(^{83}\text{Rb}) = 86$ d) was attached to one of the pump ports at the main spectrometer. In this setup, radioactive ^{83m}Kr can enter the spectrometer vessel where it decays with $t_{1/2}(^{83m}\text{Kr}) = 1.8$ h and produces low- and high-energetic electrons. These electrons can become stored inside the spectrometer and create low-energetic electron background (see section 5.1.1). The ^{83m}Kr isotope can decay into two excited states via γ -transitions to $E_1 = 32.15$ keV and $E_2 = 9.41$ keV. Conversion electrons are emitted from the K-shell after the 32 keV transition with $E_{K32} = 17.825$ keV and a naturally extremely sharp line width of only 2.7 eV. Electrons are also emitted at multiple conversion lines around 30 keV and 9 keV, but cannot be distinguished by the detector (which achieves an energy resolution of typically 1.4 keV, see section 2.1). Figure 5.20 shows the decay scheme of ^{83}Rb to ^{83}Kr ; the isomeric ^{83m}Kr state is emphasized at the bottom.

This isotope is also used in regular calibration measurements at the monitor spectrometer [S^+13a , Z^+13]. Note that the stored-electron background in the main spectrometer is typically caused by ^{220}Rn nuclei that are emanated from the NEG pumps. The measurement discussed here uses a differ-

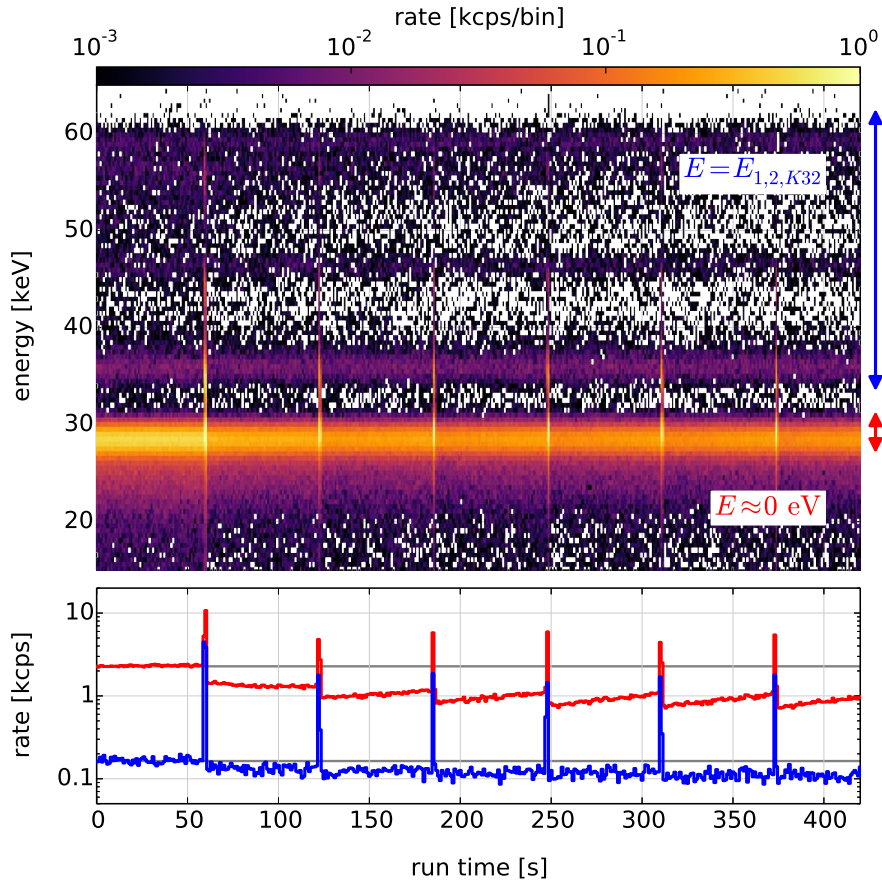


Figure 5.19.: Magnetic pulse with $^{83\text{m}}\text{Kr}$ source at the SDS-1 setup. A magnetic pulse was applied every 60 s by inverting LFCS air coil #8 in setting “A” (using the FlipBox prototype). *Top:* The energy spectrum at the detector shows three distinctive lines from high-energetic primary electrons that result from nuclear decays of $^{83\text{m}}\text{Kr}$ (blue; $E = \{E_1, E_2, E_{K32}\}$). Another prominent line results from low-energetic secondaries which are produced in scattering processes (red; $E \approx 0 \text{ eV}$). The electron energy is shifted by 28.6 keV due to the acceleration by the retarding potential and the post-acceleration electrode. *Bottom:* A rate reduction in both energy regimes is observed when a magnetic pulse is applied, which is attributed to the removal of stored electrons. The observed rate gradually increases afterwards due to continuous nuclear decays in the spectrometer that produce new stored electrons. A rapid rate increase (“rate spike”) is observed during a magnetic pulse, where electrons from the vessel walls can reach the detector directly. The gray line indicates the nominal background level at the beginning of the measurement. It is possible to reduce the average background level by repeated applications of a magnetic pulse. Runs: 8390

ent isotope, but allows to investigate the removal of stored electrons even better due to its distinguished electron energies.

A fraction of low- and high-energetic electrons is emitted towards the detector, where an increased rate is observed. The energy resolution of the FPD allows to distinguish between the different energy regimes, so that the effect of the magnetic pulse can be investigated independently. The kinetic energy of the electrons that reach the detector is elevated by 28.72 keV by the retarding potential of the spectrometer ($U_{ana} \approx -18.6 \text{ kV}$), the post-acceleration electrode (PAE) in front of the detector ($U_{PAE} = 10 \text{ kV}$) and the detector bias voltage ($U_{bias} = 120 \text{ V}$). Due to the deadlayer of the FPD wafer

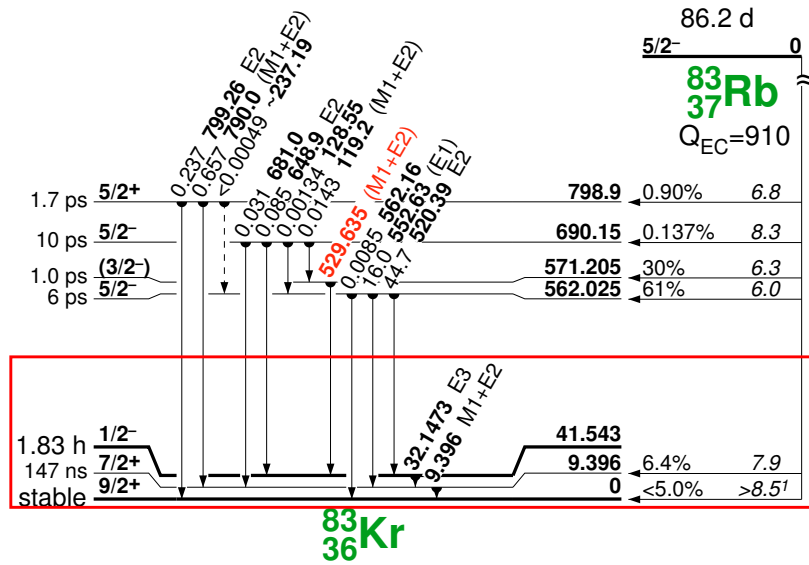


Figure 5.20.: The decay scheme of ^{83}Rb into ^{83}Kr . The ^{83}Rb isotope decays into $^{83\text{m}}\text{Kr}$ via an electron capture process (EC). The isomeric $^{83\text{m}}\text{Kr}$ state is reached with a branching ratio of 78% and decays into the ground state via two γ -transitions at 32.2 keV and 9.4 keV. Multiple conversion electrons are emitted from these transitions. Figure adapted from [Z⁺13].

(see section 2.1), electrons lose about 500 eV of their kinetic energy before detection. This results in two regions-of-interest (ROIs) for low- and high-energetic electrons at $E_L = 26.7$ keV to 31.7 keV and $E_H = 33.1$ keV to 62.9 keV, respectively⁸.

Figure 5.19 shows the observed electron rate while magnetic pulses are applied at an interval of 60 s. The plot shows the energy spectrum over time (top) and the electron rate in the low- and high-energy regimes (bottom). The energy spectrum shows several distinct lines that correspond to the primary and secondary electrons that are produced by nuclear decays of $^{83\text{m}}\text{Kr}$. The high-energy regime shows the three lines E_1 , E_2 , E_{K32} , while the low-energy regime corresponds to secondary electrons. The rate in the low-energy regime is considerably higher since a larger fraction of electrons can escape the spectrometer, as indicated by simulations (section 5.4.3).

The electron rate in both energy regimes is significantly reduced by applications of the magnetic pulse. After a magnetic pulse the observed rate gradually increases towards a nominal level. This increase is explained by the continuous $^{83\text{m}}\text{Kr}$ decays in the spectrometer, which create new electrons that can become stored again. Consequently, the average rate can be reduced by applying magnetic pulse in sufficiently short intervals before the rate has increased to the nominal level. This overall rate reduction is seen in the shown measurement. During a magnetic pulse, a prominent “rate spike” is observed where the observed rate suddenly increases. This effect is caused by deformation of the flux tube due to the field reduction, which allows electrons created at the vessel walls (e. g. due to cosmic muons) to reach the detector directly. Hence, the magnetic shielding effect (section 2.1) is suspended during a magnetic pulse and a strong rate increase is observed. The rate spikes are therefore an excellent indicator for the functionality of the magnetic pulse system.

⁸. The analysis of SDS measurements typically assumes ROIs with a lower/upper width of 2 keV/3 keV for signal and background electrons [Har15].

The observed rate reduction allows to determine an effective removal efficiency,

$$R = \frac{\dot{N}_{before} - \dot{N}_{after}}{\dot{N}_{before}}, \quad (5.16)$$

where \dot{N}_x corresponds to the observed electron rate directly before and directly after the magnetic pulse. The corresponding values over multiple pulse cycles are listed in table 5.5 for the low-energy regime⁹. The table also shows the removal efficiency R after each pulse cycle, which shows that electrons are removed with each application of the magnetic pulse. A stable removal efficiency of roughly 30% is reached after a few pulse cycles; this is due to new electrons that become stored in between two pulses as more radioactive $^{83\text{m}}\text{Kr}$ nuclei enter the spectrometer (cmp. figure 5.19). The amount of removable electrons is thus always larger than zero, and a rate reduction is observed.

Since the pulse interval of 60 s is shorter than the “relaxation time” required to reach the nominal electron rate of $\dot{N}_0 = 2.35(2)$ kcps at during one pulse cycle, the overall electron rate is reduced in this measurement. While the first three pulses reduce the observed rate to some extent, after four cycles the electron rate shows a repetitive pattern. This indicates that the maximal removal efficiency has been reached at this point. After seven cycles the total removal efficiency is $R_{max} = 0.69(2)$. The average rate has been reduced to $\dot{N}_{red} = 0.87(4)$ kcps, which is 64% lower than the nominal electron rate. Note that since only one pulse air coil was available during SDS-1 and the magnetic field in the spectrometer cannot be fully inverted in this setup, it is expected that the removal efficiency R is less than 100%.

The measurement therefore proves that the magnetic pulse method can remove stored electrons that result from nuclear decays in the spectrometer volume. A repeated application of magnetic pulses allows to maximize the overall removal efficiency. A reduction of the average background rate is achieved when the pulses are applied in a sufficiently short interval, which depends on the amount of radioactive nuclei that are emitted into the spectrometer. While for the $^{83\text{m}}\text{Kr}$ measurement discussed here an interval of about 60 s is necessary, it could be considerably longer when no radioactive source is used and less electrons decay inside the spectrometer volume.

Table 5.5.: Removal efficiency of the magnetic pulse with a $^{83\text{m}}\text{Kr}$ source.

n_{pulse}	t_{pulse}	\dot{N}_{before}	\dot{N}_{after}	R
1	60 s	2.35(2) kcps	1.44(2) kcps	0.39(1)
2	120 s	1.30(2) kcps	0.97(1) kcps	0.25(1)
3	180 s	1.15(2) kcps	0.84(1) kcps	0.27(2)
4	240 s	1.07(1) kcps	0.79(1) kcps	0.26(1)
5	300 s	1.06(1) kcps	0.75(1) kcps	0.29(1)
6	360 s	1.06(1) kcps	0.73(1) kcps	0.31(1)
7	420 s	1.04(1) kcps	0.71(1) kcps	0.31(1)
total:		2.35(2) kcps	0.72(1) kcps	0.69(2)

9. Note that only low-energetic electrons contribute to the background level that is relevant to the neutrino mass sensitivity of the experiment. High-energetic electrons are therefore not further discussed here.

5.3.5 Measurements with a radioactive ^{220}Rn source

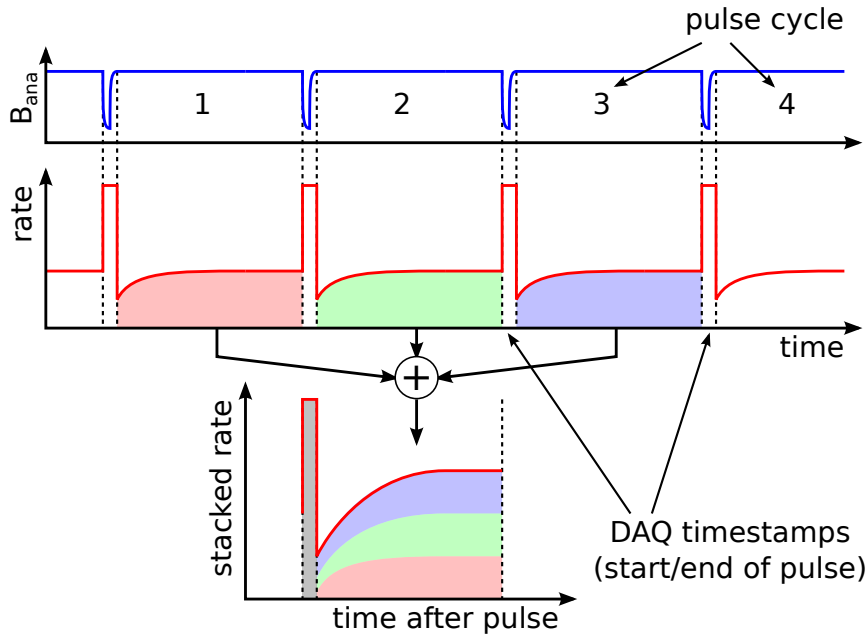


Figure 5.21.: Rate stacking of magnetic pulse measurements. The timestamp of the DAQ reference signal indicates the start and end of each magnetic pulse, where the magnetic field in the spectrometer is reduced (blue). The timestamps can be used to align multiple pulse cycles (red) into one “stacked” rate histogram that corresponds to the average electron rate. This method reduces the statistical uncertainty and thus improves the measurement result, which is especially important for the extremely low electron rates that are typical in background measurements.

In the SDS-2 measurement phase, all LFCS and EMCS air coils were equipped with FlipBox units. This allowed to perform magnetic pulse measurements at nominal magnetic field settings. A magnetic pulse is applied by inverting LFCS air coils #1–13 simultaneously to achieve the maximal field reduction.

Similar to the SDS-1 measurements, the magnetic pulse method was investigated with a radioactive source that was attached to the main spectrometer. In this case, a ^{220}Rn source¹⁰ was placed in a vacuum chamber at one of the pump ports. The radioactive nuclei enter the spectrometer and decay with $t_{1/2}(^{220}\text{Rn}) = 55.6\text{ s}$. Since the SDS-2 measurement phase featured LN_2 -cooled baffles at the pump ports to prevent radon nuclei from entering the spectrometer (section 5.1.2), it was necessary to increase the baffle temperature to about 110 K in order to decrease their blocking efficiency. In this setup, a nominal background rate of 5.2(2) cps in the low-energy regime was achieved under nominal conditions (0.38 mT setting with $B_{ana} \approx 0.38\text{ mT}$).

To improve the statistical uncertainty of the measurement at this low electron rate, magnetic pulses were applied in a regular interval to determine an average rate. This “rate stacking” is possible since the exact start and end time of each magnetic pulse is available through the DAQ reference signal (section 5.2), which can be used to align the individual pulse cycles with high precision. The method is shown schematically in figure 5.21.

10. The source is a so-called “Glühstrumpf” (gas mantle) that emanates ^{220}Rn nuclei from the thorium decay chain.

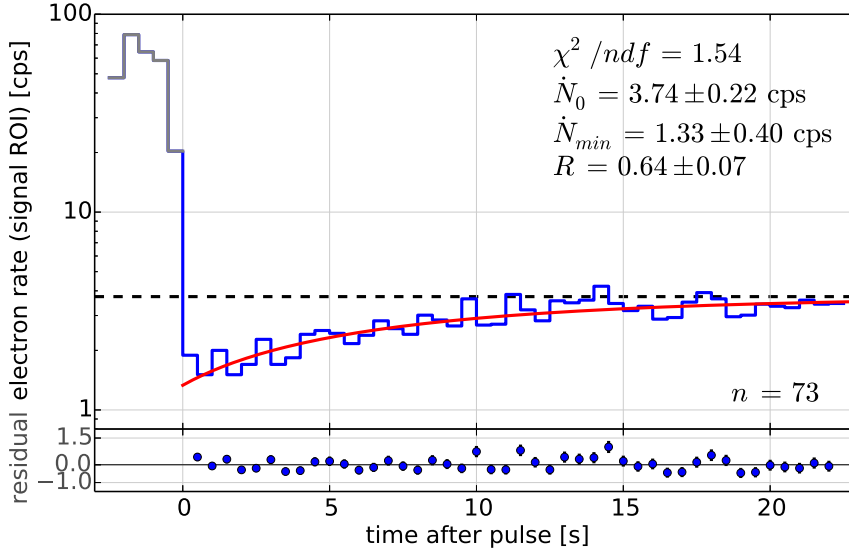


Figure 5.22.: Magnetic pulse with ^{220}Rn source at the SDS-2 setup (0.38 mT setting). In this measurement a magnetic pulse was applied every 30 s by inverting LFCS #1–13 with a pulse length of 1 s. The plot shows the “stacked” electron rate (0.5 s bins), which corresponds to the average rate over $n = 73$ pulse cycles. The individual cycles were aligned according to the timestamp of the reference DAQ signal that indicates the start of each pulse. The rate increase between the individual pulse is due to continuous nuclear decays in the spectrometer and can be described by an exponential model. The removal efficiency is determined by comparing the nominal electron before the pulse, \dot{N}_0 , to the electron rate directly after the pulse, \dot{N}_{min} . As before, a rate spike is visible during the magnetic pulse which indicates that the system is working as expected. Runs: 22889

The measurement was repeated at two different LFCS settings (0.38 mT and 0.5 mT) and different pulse lengths ($\Delta t_{pulse} = 1\text{ s}, 2\text{ s}, 5\text{ s}$) to investigate the effect on the observed background rate. Figure 5.22 shows the average electron rate at the nominal 0.38 mT setting at a pulse length of 1 s. The magnetic pulse was applied in 30 s intervals, resulting in a total number of 73 pulse cycles that were “stacked” as explained above. The electron rate shows a similar behavior as in the SDS-1 measurement where a $^{83\text{m}}\text{Kr}$ source was used. Between two magnetic pulse, the rate gradually increases due to continuous nuclear decays in the spectrometer. A rate spike is visible at the beginning of each pulse cycle, when the magnetic field is inverted during a magnetic pulse. The rate increase after the pulse can be described by an exponential model,

$$\dot{N}(t > 0) = -a \cdot \exp\left(\frac{-t}{\tau}\right) + b, \quad (5.17)$$

where τ is the corresponding time constant, $a = \Delta\dot{N} = \dot{N}_0 - \dot{N}_{min}$ is the rate reduction and $b = \dot{N}_0 = \dot{N}(t \rightarrow \infty)$ is the nominal rate. The time constant depends on the electron storage conditions and the amount of radioactive nuclei in the spectrometer. It is expected to be independent of the pulse settings if the maximal removal efficiency is achieved. A *removal efficiency* can be defined similarly to (5.16),

$$R = \frac{\Delta\dot{N}}{\dot{N}_0}. \quad (5.18)$$

Table 5.5 lists the results of the individual measurements that were performed with the ^{220}Rn source. Due to the low electron rate and the rather short measurement time of 1 hour per setting, the fit

results are affected by large uncertainties despite the rate-stacking technique that was explained above. This is especially the case for the time constant τ . However, several observations can be made from the measurements discussed here:

- The removal efficiency R does not depend on the pulse length, and comparable values are achieved for different pulse lengths of 1 s to 5 s. This is in agreement with the earlier observation that the magnetic field in the spectrometer is fully inverted for pulse lengths of at least 1 s. It is thus not possible to further increase the removal efficiency by extending the pulse length.
- The time constant τ and the nominal rate \dot{N}_0 depends on the LFCS setting that is used in the measurement. This is certainly expected since the storage conditions for electrons in the spectrometer change with the magnetic field.
- Due to the changed storage conditions and the different nominal rate, the removal efficiency also depends on the LFCS setting. The amplitude of the magnetic pulse is larger at the 0.5 mT setting since the air coils operate at higher currents in this case (cmp. table 5.2). However, the measurements indicate that the removal efficiency is actually 25% lower on average when the higher magnetic field setting is used ($R_{3.8} = 0.67(4)$ versus $R_{5.0} = 0.50(1)$). This indicates that a stronger magnetic pulse – which requires a air coil setting with higher currents – does not necessarily increase its removal efficiency.

Note that this observation cannot be explained by the smaller radius of the flux tube at the higher magnetic field. In this case a larger field reduction is necessary to force stored electrons against the vessel walls. However, following the discussion in section 5.3.3, this only affects the delay time after the start of the pulse at which the field is completely inverted. With a pulse length of 1 s or more, one can safely assume that full inversion is achieved regardless of the magnetic field setting. Hence, the maximal removal efficiency is achieved. The observed difference therefore must be explained by other effects, such as changed storage conditions.

This measurements discussed here could prove that the magnetic pulse is able to remove stored electrons from ^{220}Rn decays and reduce the observed background rate. This confirms the observations made in the SDS-1 measurement phase, where a $^{83\text{m}}\text{Kr}$ source was used. The SDS-2 measurements allowed to investigate the electron removal under more realistic conditions (^{220}Rn nuclei that enter the spectrometer through the baffle system, complete magnetic pulse system operating at standard LFCS settings) and thus provide a better evaluation of the magnetic pulse method.

Table 5.6.: Removal efficiency of the magnetic pulse with a ^{220}Rn source.

setting	pulse	χ^2/ndf	τ	\dot{N}_0	\dot{N}_{min}	$\Delta\dot{N}$	R
0.38 mT	1 s	1.55	9.4(22) s	3.7(2) cps	1.3(4) cps	2.4(2) cps	0.64(7)
	2 s	1.44	20.1(78) s	4.9(9) cps	1.2(17) cps	3.7(8) cps	0.76(26)
	5 s	0.77	12.1(31) s	4.2(3) cps	1.4(6) cps	2.8(3) cps	0.68(10)
	weighted average:		12.9(13) s	4.06(7) cps	1.32(3) cps	2.78(9) cps	0.67(4)
0.5 mT	1 s	1.19	19.5(106) s	6.0(11) cps	2.6(21) cps	3.4(10) cps	0.57(20)
	2 s	1.13	15.5(72) s	5.4(7) cps	2.7(12) cps	2.7(6) cps	0.50(12)
	5 s	1.17	14.3(65) s	4.8(5) cps	2.7(9) cps	2.2(4) cps	0.45(9)
	weighted average:		16.3(9) s	5.29(10) cps	2.68(2) cps	2.67(14) cps	0.50(1)

5.3.6 Measurements at nominal background

In addition to measurements with a radioactive source that were discussed above, the SDS-2 measurement phase allowed to investigate the removal efficiency for the remaining “nominal” background that is observed at the main spectrometer. A long-term “overnight” measurement was therefore performed at nominal conditions without any artificial increase of the background level. The LN_2 -cooled baffles were operated at their nominal temperature around 85 K to block radon from entering the spectrometer. Complementary measurements show that the baffle system efficiently prevents radon nuclei from entering the spectrometer [Gör14, Har15]. It is therefore expected that due to the low amount of stored electrons in the spectrometer, the rate reduction by the magnetic pulse is substantially smaller than with artificially enhanced background.

Figure 5.23 shows a measurement where a magnetic pulse was applied in regular intervals of 30 s over several hours at the 0.38 mT LFCS setting. The plot combines a total number of 1544 pulse cycles that are averaged by the stacking method (figure 5.21). As before, a prominent rate spike is visible at the start of the pulse cycles while the magnetic field is inverted. This clearly indicates that the magnetic pulse system is working as expected. However, no rate reduction is observed and the electron rate between the pulse cycles is constant at $\dot{N}_0 = 514(3)$ mcps. This is consistent with measurements of the baffle efficiency, which are discussed e. g. in [Har15]. Figure 5.24 shows that when all three baffles are operated at cryogenic temperature, the radon-induced background rate reduces by roughly 95%. The remaining background of 560 mcps is assumed to originate from other sources that are not correlated with nuclear decays in the spectrometer. Unfortunately, the magnetic pulse method (and neither the electric dipole [Hil16]) is able to remove this type of background. It is currently under investigation which processes are responsible for the remaining background and which countermeasures are available. A possible explanation that has been investigated are Rydberg atoms that originate from the vessel walls after decays of ^{210}Pb . These highly excited neutral states are neither hindered by the inner-electrode system nor by the shielding effect of the axial magnetic field, and thus enter the magnetic flux tube. Here they can become ionized by thermal radiation and thus produce low-energetic electron background. A detailed description of these processes is given in [Har15].

The measurement indicates that the magnetic pulse method is unable to further reduce the background level that was observed at the main spectrometer in the SDS-2 commissioning phase. This

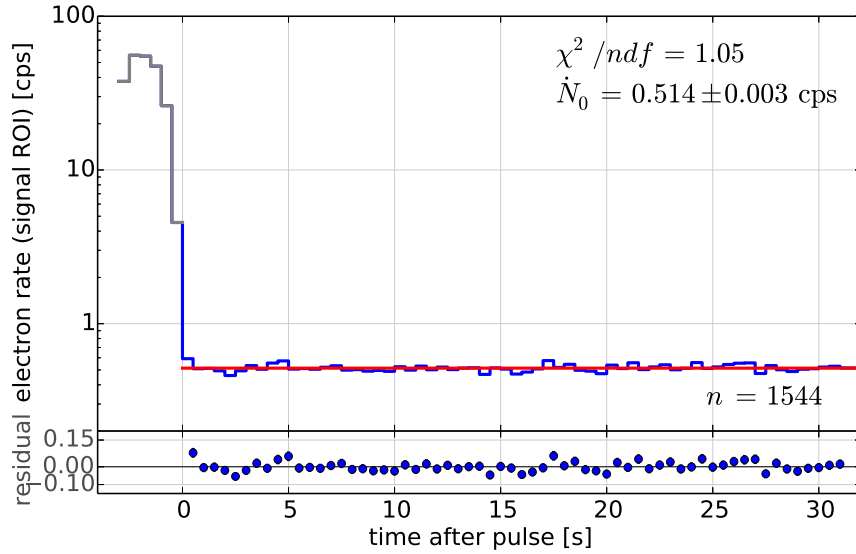


Figure 5.23.: Magnetic pulse with nominal background at the SDS-2 setup (0.38 mT setting). In this measurement a magnetic pulse was applied every 30 s by inverting LFCS #1–13 with a pulse length of 1 s. The plot shows the “stacked” electron rate (0.5 s bins) from $n = 1544$ pulse cycles. The cycles were aligned by the timestamp of the reference DAQ signal. The measurement was performed without radioactive sources and cold baffles ($T \approx 85$ K). In this case the magnetic pulse does not affect the electron rate, which is stable at 0.514(3) cps. This is different from the measurements with a radioactive source (figure 5.22, where a rate reduction was observed. The visible rate spike at the beginning of the pulse cycles indicates that the magnetic pulse is applied continuously; the inability to reduce the electron rate therefore cannot be attributed to a malfunctioning of the system.

Runs: 25065–25079

is of course disadvantageous for the experiment, which requires a low background level to reach its sensitivity goal. It should be noted that the sensitivity can be significantly improved by optimizing the measurement time distribution and other operational parameters [Kle14]. Furthermore, as discussed in section 5.1.1 a single nuclear decay in the spectrometer could increase the background level over several hours. This becomes more relevant if the overall rate is lower and a small background increase has a noticeable impact on the sensitivity. Therefore if it is possible to reduce the background level by other (passive or active) methods, the magnetic pulse system could become relevant to achieve a minimal background level. It can be triggered dynamically during regular neutrino mass measurements if a background increase is observed.

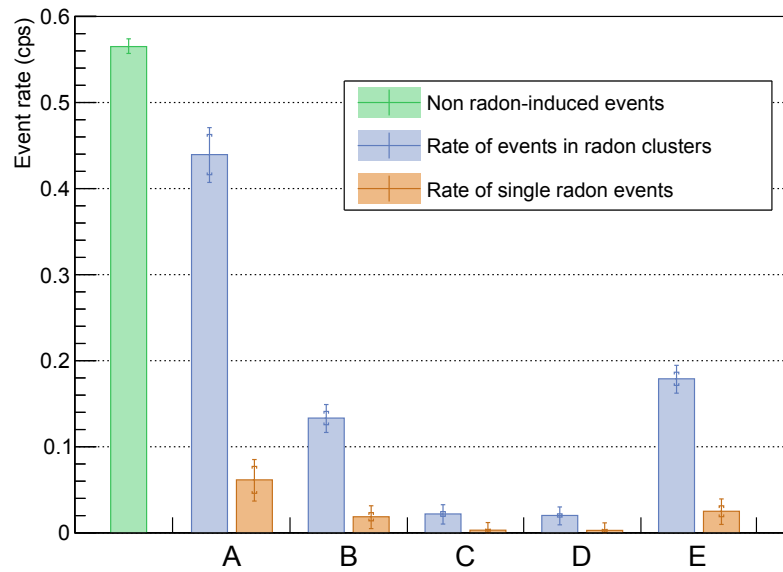


Figure 5.24.: Background reduction by LN₂-cooled baffles. The plot compares the background level that is attributed to radon decays in the spectrometer (red/blue) with other background that is assumed to originate from other sources (green). The majority of radon-induced background occurs in correlated events (“clusters”) due to the background production processes in the spectrometer. The letters A–E refer to different settings of the baffle system. Between setting “A” (warm baffles; no blocking of radon nuclei) and “C–D” (cold baffles, maximal blocking efficiency) the radon-induced background is considerably reduced by roughly 95%. One can therefore assume that with all baffles operating at cryogenic temperatures, the amount of radon that is emitted into the spectrometer is extremely small. The magnetic pulse method is thus unable to further reduce the background level. Figure from [Har15].

5.3.7 Summary

The magnetic pulse method was implemented with a prototype system for first functionality test during the SDS-1 commissioning phase, where measurements with a radioactive $^{83\text{m}}\text{Kr}$ source were carried out. These measurements allowed to study the effect of the magnetic pulse on stored electrons in different energy regimes, and to test the technical implementation at the KATRIN experimental site. It was shown that the field reduction by the magnetic pulse results in the removal of stored high-energetic electrons from the main spectrometer volume. The method was implemented with a “FlipBox” device that is designed as a H-bridge and performs a current-inversion in the attached air coil circuit, through which the magnetic field reduction in the spectrometer volume is implemented. The prototype design turned out to be reliable even at maximal air coil current.

After these successful measurements that acted as a proof-of-principle test, the prototype design was used as a basis to equip all LFCS and EMCS air coils at the main spectrometer with individual “FlipBox” devices. For the SDS-2 commissioning measurements, this system was implemented at the main spectrometer and integrated with the existing hardware and slow-control system. A connection to the DAQ system for each device allows to record the timestamp of each magnetic pulse during data-taking, which is an important feature for the analysis of measurement data. The magnetic pulse system operated continuously during the second half of the SDS-2 phase, and was also utilized to perform a static current-inversion of specific air coils for dedicated measurements at special magnetic field settings.

The SDS-2 commissioning measurements of the magnetic pulse method were able to confirm the SDS-1 results. Since the hardware system was now fully implemented, the removal efficiency for stored electrons could be determined under nominal conditions, where all LFCS air coils are inverted simultaneously in a nominal magnetic field setting. It was shown that if radon-induced background is present at the main spectrometer, the magnetic pulse can remove stored electrons and reduce the observed background rate. However, since passive background reduction methods like the LN_2 -cooled baffles turned out to be extremely efficient in suppressing radon-induced background, the magnetic pulse method could not achieve a background reduction at nominal conditions with cold baffles.

5.4 Particle-tracking simulations

The software *Kassiopeia* performs particle-tracking simulations which allow to further investigate the magnetic pulse method. *Kassiopeia* is part of the KASPER framework that was discussed in chapter 3. With *Kassiopeia* it is possible to track electrons inside the main spectrometer geometry at a given magnetic field. A new module that implements time-dependent magnetic fields was developed during the course of this thesis. The simulations provide a better insight into the time-dependent storage conditions and the electron removal processes that occur during a magnetic pulse.

5.4.1 Simulation setup

Electromagnetic fields

The magnetic pulse was implemented into *Kassiopeia* as a new field-computation module (section 3.5.1), which applies a time-dependent *scaling factor* to a static magnetic field that is defined by the simulation geometry. The KASPER framework already includes the main spectrometer geometry of the SDS-1 and SDS-2 measurement phase, including the magnet system with the LFCS air coils.

The approach using a scaling factor allows for great flexibility in the definition of the magnetic field and the ramping method: one can select individual magnets (e. g. air coils) that are varied in the simulation, and different representations of the field change are possible (such as linear or exponential models). The total magnetic field that is evaluated during particle-tracking is given by the contributions from the static field \vec{B}_{stat} and the dynamic field $\vec{B}_{dyn}(t)$, which gives

$$\vec{B}(\vec{x},t) = \vec{B}_{stat}(\vec{x}) + \vec{B}_{dyn}(\vec{x},t), \quad (5.19)$$

$$= \vec{B}_{stat}(\vec{x}) + f(t) \cdot \vec{B}_{dyn}(\vec{x},t=0), \quad (5.20)$$

where $f(t)$ is the time-dependent scaling factor that describes the field change and (\vec{x},t) are the position and time of the field evaluation, which are defined by the properties of the simulated particle.

In the magnetic pulse simulations, the static contributions typically correspond to the superconducting solenoids and the un-pulsed air coils (e. g. LFCS #14 which is already inverted) and the dynamic field is given by the pulsed air coils (e. g. LFCS #1–13). Here a double-exponential ramping model is used, which is based on the magnetic field measurement during a magnetic pulse (see section 5.3.2). The measurement indicated that the field change at the spectrometer vessel can be described by a combination of two exponential curves with independent time constants τ_{fast} and τ_{slow} , and this description is used for the simulated magnetic field as well. The scaling factor is then given by

$$f(t) = \left[\exp\left(-\frac{t-t_0}{\tau_{fast}}\right) + \exp\left(-\frac{t-t_0}{\tau_{slow}}\right) \right] - 1, \quad (5.21)$$

where t_0 is the starting time of the magnetic pulse (typically $t_0 = 0$).

The changing magnetic field $\dot{\vec{B}}$ results in an induced electric field E_{ind} according to Maxwell's law (cmp. section 5.1.2). In the main spectrometer, the magnetic field is mainly oriented in axial direction, $\vec{B} \approx (0, 0, B_z)$. The induced electric field is thus oriented in azimuthal direction, $E_{ind} \approx E_\phi$, and can be computed according to (5.9) and (5.12). Its implementation in *Kassiopeia* uses the derivative $\dot{f}(t)$

of the scaling factor (5.21),

$$E_\phi(\vec{x}, t) = -\frac{r}{2} \dot{f}(t) \cdot \vec{B}_{dyn}(\vec{x}, t = 0), \quad (5.22)$$

$$\dot{f}(t) = -\frac{1}{\tau_{fast}} \cdot \exp\left(-\frac{t-t_0}{\tau_{fast}}\right) - \frac{1}{\tau_{slow}} \cdot \exp\left(-\frac{t-t_0}{\tau_{slow}}\right), \quad (5.23)$$

where $r = \sqrt{x^2 + y^2}$ is the radial position of the simulated particle.

Storage and exit conditions

The simulations presented here use a quasi-static approach in order to reduce the computation time. A completely dynamic simulation would require to perform tracking for individual electrons over a time t that corresponds to the pulse length, $0 \leq t \leq t_{max} = 1$ s. Even with adiabatic tracking where a step size of roughly 1 cm is used (cmp. section 3.3.4), the large dimensions of the main spectrometer and the high oscillation frequency of stored electrons would result in an extremely large number of simulation steps. The axial oscillation period of a stored electron in the main spectrometer (figure 5.3) is typically $T_{osc} = \mathcal{O}(10 \text{ us})$ depending on its energy and pitch angle. With a spectrometer length of roughly 20 m, the given step size and the total simulation time of 1 s results in $\mathcal{O}(100 \cdot 10^6)$ steps for a single electron. Although this number could probably be reduced by optimizing the simulation, a full Monte Carlo simulation with thousands of electrons would require unfeasibly long computation times.

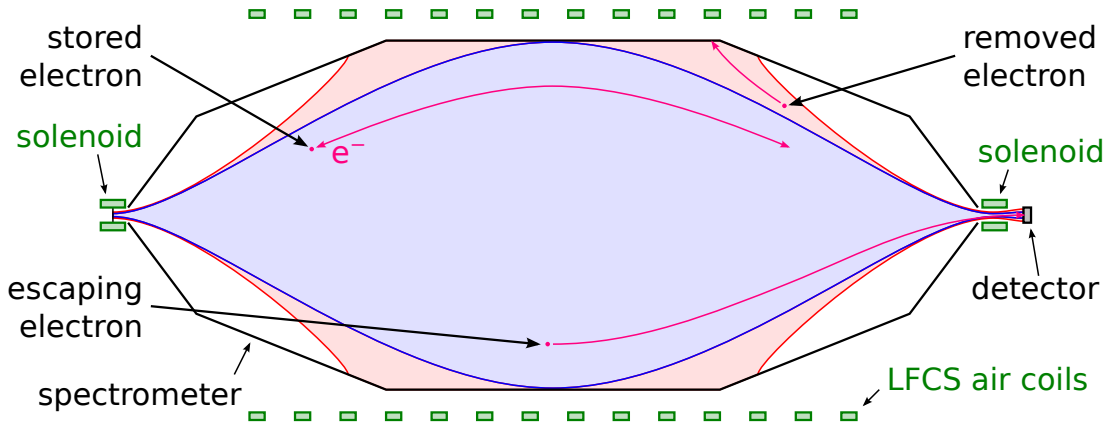


Figure 5.25.: Typical electron trajectories in a magnetic pulse simulation. The storage conditions for electrons at a given magnetic field setting can be examined by creating electrons randomly inside the spectrometer volume in a Monte Carlo approach. At fixed operational parameter (magnetic field), the storage conditions are static. This allows a comparison between different times $t = \{t_1, t_2, \dots\}$ during a magnetic pulse, where the magnetic field is varied according to (5.19). In the simulation, electron tracks are terminated when the electron is either *stored* in the flux tube, *removed* at the vessel walls or when it *escapes* towards the source or detector. When a large number of electrons is investigated, the amount of terminated tracks allows to determine the *storage probability* and the *removal efficiency*. Electrons that escape towards the detector are contributing to the observed background. In a measurement the observed electron rate can be used to estimate the amount of stored and removed electrons.

A significant improvement is possible due to the fact that the field change is substantially slower than the electron propagation: given the small oscillation period T_{osc} , the magnetic field during one

oscillation can be assumed to be static. Hence, the electron trajectory is not affected by the field change on this short timescale. One can therefore perform simulations at different *fixed* times $t = 0$ s to 1 s where particle-tracking is performed with a static magnetic field $\vec{B}(t = \text{const.})$. The magnetic pulse is applied at $t_0 = 0$ s. In this case one can examine the storage conditions and the amount of removed electrons without the need to perform time-intensive simulations.

The simulated electrons that are created at a given time t are accounted into three categories as depicted in figure 5.25. Note that the given storage probabilities and removal efficiencies depend on the (initial) kinetic energy of the electron due to (5.4) that describes the magnetic bottle effect.

- **Stored electrons:** These electrons do not reach the vessel walls or escape through the entrance and exit regions of the spectrometer. Instead they are stored inside the spectrometer volume by the *magnetic bottle effect*, where the electron is reflected as it moves into a region with higher magnetic field (see section 2.2). The storage probability depends on the initial pitch angle of the electron and the magnetic field at its point of creation according to (5.4). Under nominal conditions, electrons from nuclear decays that typically follow an isotropic angular distribution are efficiently stored due to the high magnetic fields at the entrance and exit regions ($B \gg 1$ T). This is an intrinsic effect of the MAC-E filter.

In the simulation, electrons that are reflected twice are considered to be stored. This is implemented by using the “trapped” terminator in the Kassiopeia configuration (section 3.3.7). At the main spectrometer, where an asymmetric magnetic field setup is used (4.3 T at the entrance and 5.1 T at the exit), it is possible for an electron to be reflected at the exit region with higher magnetic field before escaping through the entrance region where the magnetic field is lower. Hence, an electron can safely be considered “stored” after two reflections have occurred.

The *storage probability* for electrons created at a time t can be estimated by the ratio between the number of stored electrons, n_{sto} , and the number of created electrons, $n = \mathcal{O}(10\,000)$:

$$p_s(t) = \frac{n_{sto}(t)}{n}. \quad (5.24)$$

The value $p_s(t)$ can be determined for different energy regimes if the simulation is configured accordingly. In the simulations presented here, three energy regimes are considered (see below). To investigate how the storage conditions change during a magnetic pulse, the storage probability is compared for different times t where the magnetic field is different.

- **Escaping electrons:** Some fraction of created electrons are not stored by the magnetic bottle effect, which allows them to leave the spectrometer through the entrance and exit regions. This is typically the case for electrons with small pitch angles that can bypass the magnetic reflection. The electrons thus escape towards the source or the detector.

According to (5.4), the minimal pitch angle of an escaping electrons is defined by the highest magnetic field in the setup. In the simulations discussed here, this is the case at the superconducting solenoids placed at the entrance and exit of the spectrometer. Electrons are therefore considered to escape when they passed either one of the solenoids,

$$z \leq -12.2 \text{ m} \quad \vee \quad z \geq 12.2 \text{ m}, \quad (5.25)$$

where z is the axial position of the electron.

The electrons that arrive at the detector contribute to the observed background level. Since the storage conditions at a fixed magnetic field are not time-dependent, the number of observed

electrons n_{det} can be used to estimate the number of stored electrons n_{sto} inside the spectrometer. The two values are related by the *escape probability*, which is defined as

$$p_{e,det}(t) = \frac{n_{det}(t)}{n_{sto}(t)}. \quad (5.26)$$

An equivalent definition is used for the electrons escaping towards the source, $p_{e,src}(t)$, although these electrons cannot be detected. The total escape probability is then

$$p_e(t) = p_{e,det}(t) + p_{e,src}(t) = \frac{n_{det}(t) + n_{src}(t)}{n_{sto}(t)}. \quad (5.27)$$

- **Removed electrons:** Electrons are removed from the flux tube volume if they reach the vessel walls or a part of the inner-electrode system. To simplify the simulation geometry and to reduce the computation time, only the vessel walls are considered in the simulation¹¹. Under nominal conditions, electrons that are created in the flux tube volume are not removed since the flux tube is fully contained inside the spectrometer vessel. This changes only when a magnetic pulse is applied and the flux tube radius increases accordingly, or when extremely high-energetic electrons are considered. In the latter case, a fraction of created electrons hits the vessel walls already at nominal magnetic field.

In the simulation, electrons that reach a radial position r larger than the main spectrometer radius ($R_{max} = 4.9$ m) are considered to be removed,

$$r \geq R(z), \quad (5.28)$$

where $R(z) \leq R_{max}$ is the spectrometer radius at the axial position z of the electron.

The *removal probability* is defined equivalently to (5.24):

$$p_r(t) = \frac{n_{rem}(t)}{n}. \quad (5.29)$$

Similarly, the effective *removal efficiency* at a time t can be determined by comparing the number of removed and escaping electrons, n_{rem} and n_{esc} , with the number of electrons that are stored under nominal conditions, $n_{sto}(t = 0)$. The efficiency indicates the amount of originally stored electrons that are removed by the magnetic pulse,

$$\epsilon(t) = \frac{n_{rem}(t) + n_{esc}(t)}{n_{sto}(t = 0)} - \frac{n_{rem}(t = 0) + n_{esc}(t = 0)}{n_{sto}(t = 0)}. \quad (5.30)$$

The value $n_{rem}(t = 0) + n_{esc}(t = 0)$ accounts for electrons that reach the vessel walls or escape the spectrometer at nominal magnetic field. It thus ensures $\epsilon(t = 0) = 0$, so that the removal efficiency only considers electrons that are actually removed by the magnetic pulse.

11. Due to the small distance between the inner electrode and the vessel walls of roughly 5 cm, this simplification does not affect the accuracy of the simulation results.

5.4.2 Magnetic field reduction

Figure 5.26 compares the magnetic field in the main spectrometer under nominal conditions, $B = B_0$, with the magnetic field at the end of a magnetic pulse when the inverted level has been reached, $B = B_{inv}$. Here the standard SDS-2 parameters were used (3.8 G LFCS setting with inverted LFCS air coils #1–13 for the magnetic pulse). The colors and contour lines indicate the strength of the magnetic field strength $|\vec{B}|$, and the arrow symbols show the direction of the magnetic field vector \vec{B} . The magnetic field at the entrance and exit regions (red colors) is largely unaffected by the magnetic pulse since it is dominated by the strong stray field of the superconducting solenoids. Under nominal conditions, the magnetic field lines lead from the detector to the source¹² so that electrons can be transmitted through the spectrometer. The magnetic field reaches values around 0.4 mT at the spectrometer center (analyzing plane). The magnetic bottle effect, which results from the strong magnetic field at the entrance and exit regions, provides excellent storage conditions for electrons that are created inside the spectrometer (see section 5.1.1).

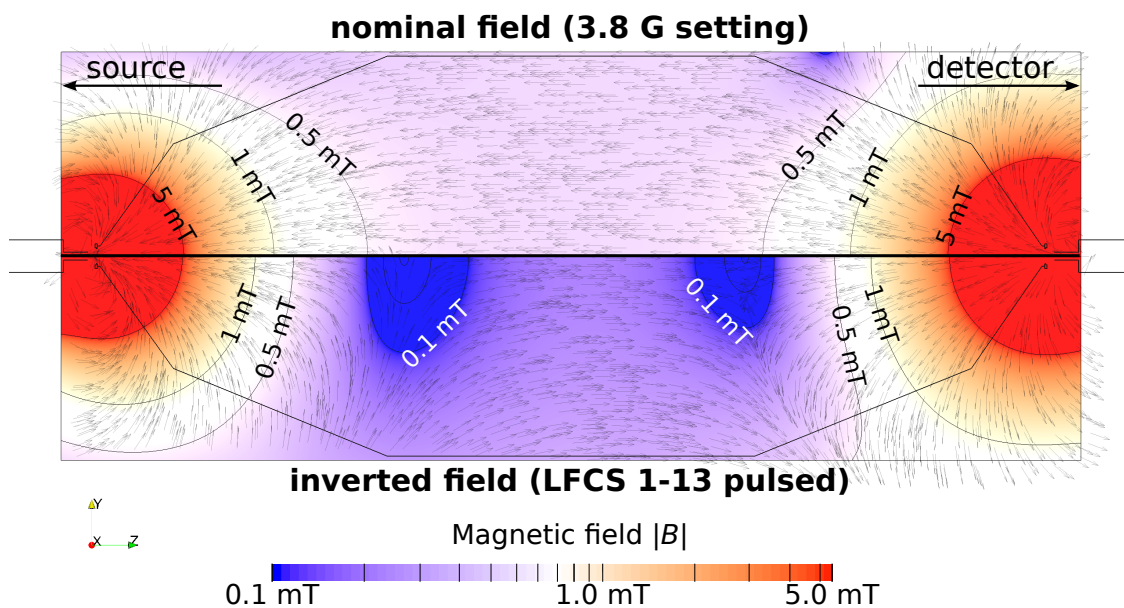


Figure 5.26.: Magnetic field under nominal conditions and during a magnetic pulse. The colors indicate the strength of the magnetic field limited to the range 0.1 mT to 5 mT. Contour lines are added to allow a better comparison. The small arrows indicate the direction of the magnetic field vector \vec{B} . *Top half:* Under nominal conditions (3.8G setting), the magnetic field leads from the detector to the source so that electrons can be transmitted. The magnetic field reaches a minimal value of roughly 0.4 mT at the center of the spectrometer. *Bottom half:* The magnetic field is inverted by a magnetic pulse that is applied through LFCS air coils #1–13. The field lines deform so that source and detector are now connected to the vessel walls. A new region where electrons can become stored forms at the center of the spectrometer, which is clearly indicated by the increasing density of the magnetic field lines towards the vessel walls.

When the magnetic field is inverted, the flux tube is deformed and the field lines connect the entrance and exit regions to the vessel walls. Electrons that were originally stored in these regions can now reach the vessel walls and are therefore removed. However, the field inversion also creates new regions

12. The shown field direction from the detector towards the source is by convention.

inside the spectrometer where electrons can become stored. The blue regions in the figure have a small magnetic field of $B_{min} \approx 0.1$ mT. These regions are surrounded by a higher magnetic field that reaches $B_{max} \gtrsim 0.2$ mT at the vessel walls. Electrons following the field lines through these low-field regions are therefore again exposed to the magnetic bottle effect.

The storage probability for an electron that starts at the center of the spectrometer (analyzing plane) at $U_0 = -18.6$ kV and $B_0 = B_{min} \approx 0.1$ mT can be estimated via (5.4). However, given the case shown in figure 5.26 where the field lines lead towards the vessel walls, one must consider that the electron only gains little kinetic energy as it moves away from the analyzing plane, $E_{gain} = q\Delta U \ll qU_0$. In this case an electron is magnetically reflected if it starts with a pitch angle

$$\theta_0 \geq \theta_{mir} = \arcsin \left(\sqrt{\frac{E_0 + q\Delta U}{E_0} \cdot \frac{0.1 \text{ mT}}{0.2 \text{ mT}}} \right) = 90^\circ \quad \text{for } E_0 < \Delta E, \quad (5.31)$$

where E_0 is the initial energy of the electron. For a voltage difference of $\Delta U = 1$ kV between analyzing plane and the end of the central spectrometer section that is determined from simulations, the reflection angle quickly reduces for initial energies $E_0 > 1$ keV. Hence, electrons that are created in the low-field region with energies of several keV are stored efficiently in the central spectrometer section, despite the magnetic field inversion.

From this observations it is expected that in the typical magnetic pulse configuration where the magnetic field is inverted through the LFCS air coils, the method is unable to remove electrons from the low-field regions at the spectrometer center. The removal efficiency of the magnetic pulse method is therefore intrinsically limited. The removal efficiency and the storage conditions will be further investigated in the remainder of this section.

5.4.3 Removal efficiency

The measurements at the main spectrometer showed a clear reduction of the electron background attributed to nuclear decays. A removal efficiency around 60% was achieved with a radioactive ^{220}Rn source (section 5.3.5). This value indicates that a fraction of stored electrons is not efficiently removed by the magnetic pulse, despite the magnetic field being fully inverted. Particle-tracking simulations allow to investigate the removal efficiency and its dependency on the magnetic field in detail.

Stored electrons are influenced by various effects when a magnetic pulse is applied, as discussed in section 5.1.2. The dominant effect is the widening of the flux tube at reduced magnetic field, which forces stored electrons against the vessel walls. This effect can be easily investigated in particle-tracking simulations: a large number of electrons ($n = 25\,000$) is started at random positions inside the nominal flux tube volume at the main spectrometer. The volume is defined by the magnetic field (3.8 G setting, cmp. table 5.2) and the magnetic flux (191 T cm^2), yielding a radius of 4.0 m at the analyzing plane. The electrons are created with random pitch angle $0^\circ \leq \theta_0 \leq 90$ and follow an isotropic distribution. The initial kinetic energy is split into a low-energy ($E_0 = 0.1 \text{ eV}$ to 10 eV), a high-energy ($E_0 = 10 \text{ eV}$ to 1000 eV) and an extremely high-energy regime ($E_0 = 1 \text{ keV}$ to 100 keV). The low-energy regime corresponds to secondary electrons that are typically created by scattering processes following a nuclear decay. The electrons are tracked until one of the three conditions discussed above is met.

Figure 5.27 shows the storage probability (5.24), removal probability (5.29) and escape probability (5.26) over time. Kassiopeia simulations were performed at fixed starting times $t = 0$ s to 1 s for the electrons in 10 ms steps to investigate the time-dependency of the storage conditions. A magnetic

pulse was initiated at $t_0 = 0$ s with time constants $\tau_{fast} = 30$ ms and $\tau_{slow} = 420$ ms, which loosely matches the measurement results (cmp. figure 5.16). The magnetic field thus follows an exponential behavior (5.19) and decreases gradually over time.

The storage probability shows a qualitatively similar behavior in all energy regimes. During the first few ms the probability does not change since the flux tube is still fully contained inside the spectrometer. As the field further reduces, the outer regions of the flux tube connect to the vessel walls. This is the case at $t \approx 20$ ms, when the storage probability begins to decrease significantly. Consequently, the removal probability as electrons start hitting the vessel walls. The escape probability is only slightly affected. This is explained by the simulations, which show that most of the escaping electrons are created near the entrance/exit regions where the magnetic field is larger. The magnetic bottle effect is thus less pronounced for these electrons and the escape probability does not depend significantly on the magnetic field in the spectrometer.

As a result of the increased removal probability, the removal efficiency (indicated by the dotted line) increases as well. At $t \approx 170$ ms the field is reduced sufficiently to connect all of the field lines to the vessel walls, so that the flux tube splits up and disconnects the entrance and exit regions of the spectrometer. At this point, the removal efficiency reaches a maximum of 75% to 85% in the three energy regimes. In the extremely high-energy regime, a large fraction of electrons escapes the spectrometer during a magnetic pulse, instead of reaching the vessel walls. This is due to the different storage conditions in this energy regimes. Conclusively, the maximal removal efficiency depends on the energy regime of the electrons although the simulation results indicate that the magnetic pulse affects both primary and secondary electrons that originate from nuclear decays. As the magnetic field further reduces, a decrease in the removal efficiency is observed. This is in agreement with the discussion above, from which it is expected that inverting the magnetic field creates new possibilities for electrons storage.

The limited removal efficiency is also in agreement with the SDS-2 measurement results, where a total efficiency around 70% was determined. The observed difference of roughly 10% is likely related to the simulation parameters, which do not completely match the experimental conditions. Especially the timing parameters of the field change inside the spectrometer are only known with little accuracy¹³. Furthermore, the distribution of low- and high-energetic electrons in the spectrometer volume is entirely unknown, and the simulations simply used a homogeneous electron distribution. The time-dependency of the storage conditions and their effect on the removal efficiency is further evaluated in section 5.4.6 below.

Under nominal conditions, the storage probability is between 75% AND 95% for low- and high-energetic electrons in the simulation. The remaining electrons are escaping from the spectrometer, and roughly half of them reaches the FPD (10.4% for the low-energy regime). This allows to estimate the amount of stored electrons in the spectrometer from the observed electron rate at the detector. However, it must be considered that the electrons that escape towards the detector are mostly created near the exit region of the spectrometer. In the simulations, only about 10% of the observed electrons are created inside the spectrometer volume at $|z| \leq 10$ m. A decrease of the electron rate that is observed in a measurement therefore indicates a removal of electrons from the spectrometer, but it is extremely difficult to determine the actual removal efficiency experimentally by comparing the electron rate at the detector.

13. The timing parameters have been determined by a magnetic field measurement with a sensor placed on the outside of the spectrometer vessel, which cannot determine the field *inside* the spectrometer accurately.

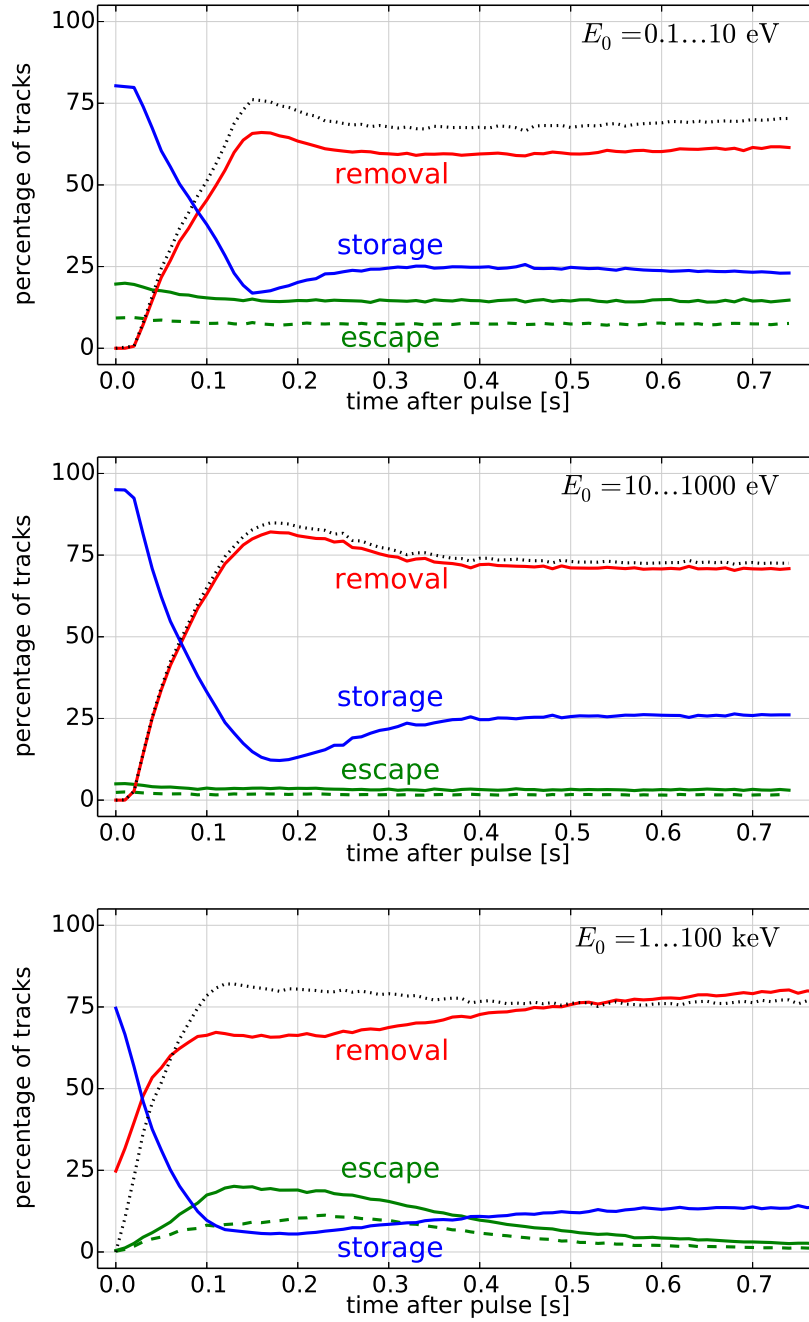


Figure 5.27.: Simulated removal efficiency of the magnetic pulse. The plots show the relative fraction of removed, stored and escaping electrons (solid lines) from a total number of 25 000 electrons that were created randomly in the nominal flux tube volume. The dashed lines at the bottom indicate electrons reaching the detector. The dotted line corresponds to the removal efficiency $\epsilon(t)$ (5.30). A magnetic pulse was applied at $t_0 = 0 \text{ s}$ by inverting LFCS air coils #1–13 in the 3.8 G setting. The individual figures correspond to the low-energy ($E_0 = 0.1 \text{ eV}$ to 10 eV ; top), high-energy ($E_0 = 10 \text{ eV}$ to 1000 eV ; middle) and extremely high-energy regime ($E_0 = 1 \text{ keV}$ to 100 keV ; bottom). The removal efficiency shows a similar behavior in all three cases and reaches a maximum at $t = 0.1 \text{ s}$ to 0.2 s , but is different in its absolute value.

This approach has been used in the analysis of the SDS-1 and SDS-2 measurements, where the observed electron rate before and after a magnetic pulse was compared to determine the removal efficiency (section 5.3). The discussion here strongly suggests that the measured removal efficiencies must be taken with care, as they likely give a false impression regarding the amount of actually removed electrons. They are thus not fully comparable to the simulation results. On the other hand, only electrons that arrive at the detector – and thus contribute to the background level – affect the sensitivity of the KATRIN experiment. The experimentally determined rate reduction is thus more relevant to the experiment than the simulated removal efficiency.

5.4.4 Trapping probability

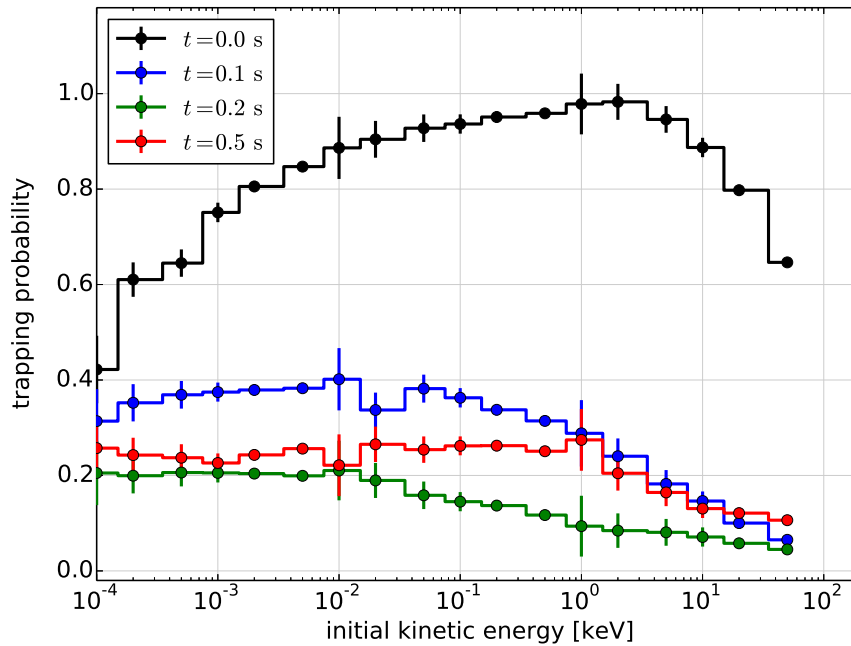


Figure 5.28.: Simulated trapping probability during a magnetic pulse. The plot shows the fraction of electrons that become stored in the main spectrometer for different energies ($E_0 = 0.1 \text{ eV}$ to $100 \cdot 10^3 \text{ eV}$) at different times during a magnetic pulse. While the overall trapping probability is high at nominal conditions ($t = 0 \text{ s}$), it is significantly reduced as the magnetic field is inverted. The minimal trapping probability is achieved at $t \approx 0.2 \text{ s}$ when the magnetic field is nearly zero. When the field is inverted ($t \gtrsim 0.5 \text{ s}$), the trapping probability rises again due to the changed storage conditions.

Another way to examine the storage conditions during a magnetic pulse is to compute the trapping probability over the full energy range from 0.1 eV to 100 keV that was investigated in the particle-tracking simulations. This allows to compare the effect of the magnetic pulse on the different energy regimes directly.

Figure 5.28 shows the trapping probability at different times after a magnetic pulse was initiated under nominal conditions (3.8 G settings, inverting LFCS #1–13). It is observed that the overall trapping probability is rather large especially for electron energies around $E_0 = 1 \text{ eV}$ to 1000 eV at nominal magnetic field, $B_0 \approx 0.38 \text{ mT}$ at $t = 0 \text{ s}$. The probability is considerably reduced already by a small

reduction of the magnetic field at $t = 0.1$ s. The magnetic pulse affects electrons of the full energy range, with a slightly larger efficiency for high-energetic electrons above 100 eV. At $t = 0.2$ s, where the magnetic field reaches nearly zero in the main spectrometer, the trapping probability reaches a minimum since the majority of electrons created in the spectrometer volume can now reach the vessel walls. The picture changes as the magnetic field is further inverted, and an increased trapping probability is observed at $t = 0.5$ s.

These observations are in agreement with the investigation of the removal efficiency that has been discussed above. It is clearly observed that the magnetic pulse can remove electrons of a wide energy range from less than 1 eV up to the 100 keV range. The maximal removal efficiency is achieved when the magnetic field is reduced to zero in the main spectrometer volume, and increases again as the inverted level is reached during the magnetic pulse. This increase is linked to the changing storage conditions as a result of the magnetic field reduction, which allows electrons to become stored again if the magnetic field is inverted below zero. This effect is further investigated in section 5.4.6 below.

5.4.5 Pulse timing

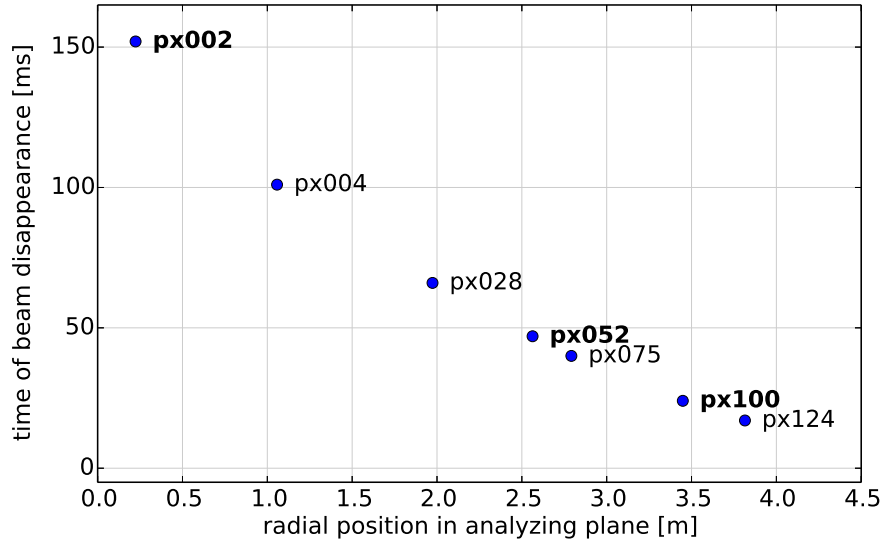


Figure 5.29.: Simulated pulse timing for different FPD pixels. The plot shows the time when a specific magnetic field line, which under nominal conditions (3.8 G LFCS setting) hits an FPD pixel, connects to the vessel walls. This corresponds to the disappearance of an electron beam that enters the spectrometer at the source side. A corresponding measurement was performed in the SDS-2 phase (section 5.3.3). The plot shows the simulated delay time against the radial position of the electron in the analyzing plane under nominal conditions. As expected, the delay increases for inner field lines (small radii in the analyzing plane), since a lower magnetic field is necessary to move the field lines towards the vessel walls. Due to the exponential behavior of the field change (5.19), this results in a later disappearance time.

It is also possible to examine the timing of the magnetic pulse inside the main spectrometer by particle-tracking simulations. In the SDS-2 measurement a pulsed electron beam was used to observe the time of beam disappearance at the detector in dependency of the radial position on the FPD wafer (section 5.3.3). Since the electrons are sensitive to the field inside the spectrometer, this allows to

investigate the delay between the start of a magnetic pulse and an observable field change inside the spectrometer. The observed delay corresponds to the time when the magnetic field line that guides an electron connects to the vessel walls due to the field reduction. At this point, electrons on the given field line are no longer transmitted. The measurement showed that inner field lines, where the electron has a smaller radius in the analyzing plane, require a stronger reduction of the magnetic field to move the field lines outwards. The observed delay thus decreases for outer detector pixels (cmp. figure 5.17). In the simulations it is possible to determine the time of disappearance precisely by tracking electrons from the source through the spectrometer.

Figure 5.29 shows the beam disappearance time (i. e. the delay to the start of the magnetic pulse) in dependency of the detector pixel. The investigated pixels are shown in figure 5.30. The pixels that are indicated in bold letters have been investigated in the SDS-2 measurement. The corresponding radial position in the analyzing plane under nominal conditions (3.8 G LFCS setting) is indicated by the ordinate axis in the figure.

As expected, the delay is maximal for the innermost pixel #2 and decreases for larger field line radii. This is in good agreement with the measurements, where a similar behavior was observed. The values for the radial position r_{ana} and the simulated delay time t_{start} are listed in table 5.7. The measured delay time t_{start}^* for the investigated pixels is added for comparison. Interestingly, a considerable deviation $\Delta t_{start} = t_{start}^* - t_{start} \gg 0$ is observed between simulation and measurement. For the three pixels where the delay time can be compared, the deviation is consistent with an average of $\Delta t_{start} \approx 247$ ms. The deviation is extremely large considering the magnitude of t_{start} , which is on the order of 100 ms. One could argue that the deviation is a result of inaccurately determined delay times which lead to a systematic error. However, the experimentally determined value is known with high accuracy (few ms) from the timestamp of the DAQ reference signal, while the simulated value is determined directly from the simulation results. It is therefore concluded that the deviation must be a physical effect that slows down the field change and results in an additional delay that is not considered in the simulations.

A likely explanation for this effect are *eddy currents* in the spectrometer vessel hull. These currents would counteract the magnetic field change and thus increase the time constants in \dot{B} . Eddy currents have already been suggested to explain the observed time constants in the magnetic field sensor measurement (section 5.3.2). It was assumed that the magnetic field inside the spectrometer follows the measured magnetic field on the outside with similar timing characteristics. However, the comparison between measurement and simulations discussed here suggests that the field change inside the spectrometer is further slowed down by about 250 ms w. r. t. to the sensor measurement (from which the time constants used in the simulation have been derived). Given that a magnetic pulse is typically applied with a length of 1 s or more, this additional delay has no significant impact on the removal efficiency. In any case, the magnetic field in the spectrometer is fully inverted so that the maximal removal efficiency is achieved. This is also confirmed by the measurements with an electron beam and with different radioactive source, which were discussed in section 5.3).

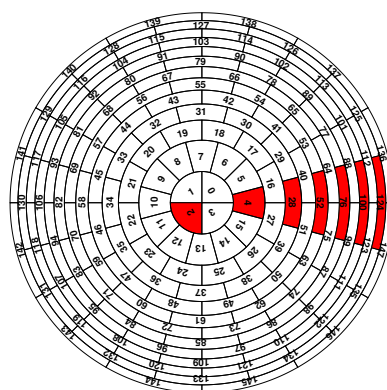


Figure 5.30.: FPD pixel mapping used in the pulse timing simulations.

Table 5.7.: Magnetic pulse delay times for different detector pixels.

pixel#	r_{ana}	t_{start}	t_{start}^*	Δt_{start}
2	0.22 m	153 ms	409 ms	256 ms
4	1.06 m	102 ms	—	—
28	1.97 m	67 ms	—	—
52	2.56 m	48 ms	308 ms	260 ms
75	2.79 m	41 ms	—	—
100	3.45 m	25 ms	251 ms	226 ms
124	3.82 m	18 ms	—	—

5.4.6 Storage conditions

A deeper understanding of the magnetic pulse method can be gained by examining the *electron density* in the main spectrometer during a pulse cycle. The changing storage conditions due to the magnetic field reduction affect the electron density, so that the electron removal processes can be investigated.

The axial symmetry of the electromagnetic fields in the main spectrometer allows to visualize the electron density in cylindric coordinates without loss of accuracy. Each (z, r) -bin therefore corresponds to a tube segment with length Δz and width Δr . The bin volume V is then calculated as

$$V = \Delta z \cdot \pi((r + \Delta r)^2 - r^2), \quad (5.32)$$

where r is the inner radius of the given bin.

The electron density can be computed directly from the simulation results. For the discussion here it is defined as the average time a single electron spends in one (z, r) -bin in the spectrometer, normalized to the corresponding bin volume. The electron density is thus given in units of s/m^3 and calculated as a two-dimensional histogram where each electron contributes a weight

$$w = \frac{1}{n} \cdot \frac{\Delta t}{V}, \quad (5.33)$$

where n is the total number of simulated electrons, Δt is the time the electron spends in the given bin, and V is the bin volume from (5.32).

The quasi-static simulation method that was explained in section 5.4.1 has been used here as well. A total number of 25 000 electrons were created randomly inside the nominal flux tube volume at each fixed time $t = 0$ s to 0.5 s. The resulting electron density can be compared between the different starting times and for different energy regimes.

Decreasing magnetic field

Figure 5.31 shows the electron density under nominal conditions (3.8 G setting at $t = 0$ ms) for the high-energy regime ($E_0 = 10\,1000eV$). The storage conditions change when a magnetic pulse is applied and the magnetic field is reduced. The electron density is affected accordingly as electrons are removed from the flux tube volume. The magnetic pulse uses the same settings as before (LFCS #1–13 with $\tau_{fast} = 30$ ms and $\tau_{slow} = 420$ ms) and is initiated at $t = 0$.

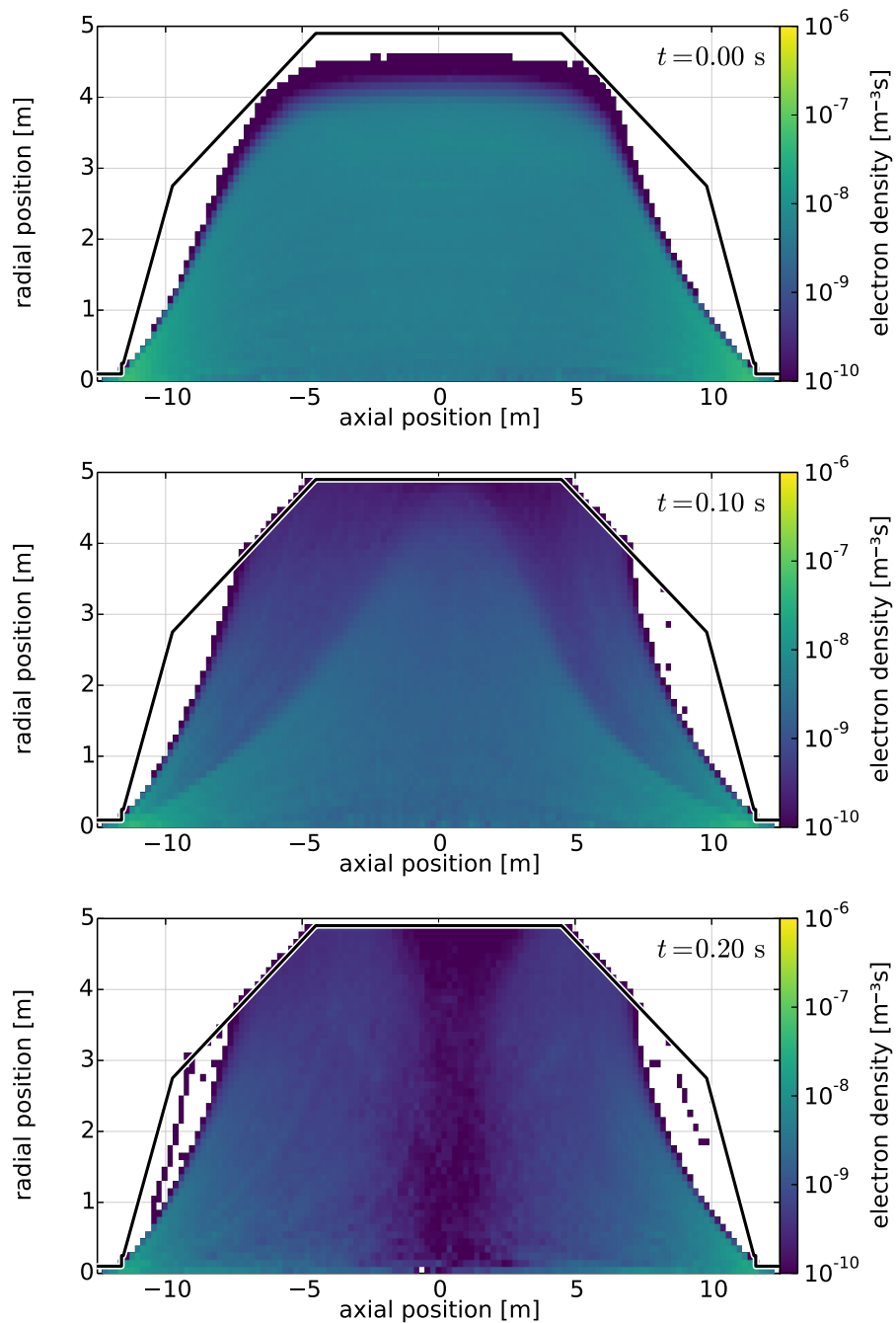


Figure 5.31.: Simulated electron density during a magnetic pulse (high-energy regime). The histogram was created according to (5.33) and shows the average time an electron spends in each (z, r) -bin normalized to the bin volume. A total number of 25 000 electrons were started randomly in the nominal flux tube volume at fixed starting times $t = 0.0$ s to 1.0 s. This plot shows electrons of the high-energy regime with $E_0 = 10$ eV to 1000 eV. The density changes as the magnetic pulse progresses and the magnetic field is reduced. Electrons are removed especially from the outer flux tube region. When the magnetic field is inverted at $t \geq 0.2$ s, the overall electron density is considerably reduced w. r. t. nominal conditions.

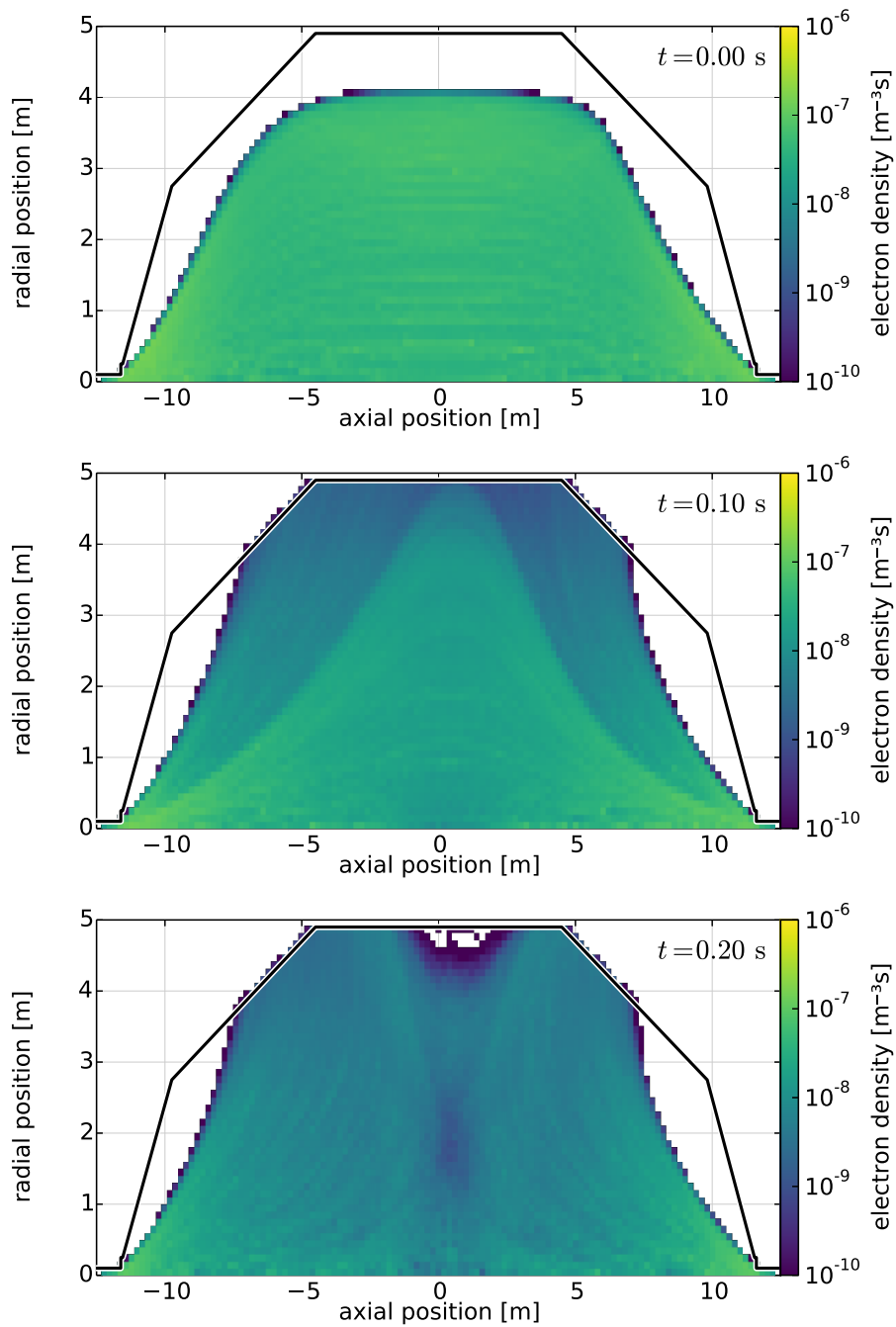


Figure 5.32.: Simulated electron density during a magnetic pulse (low-energy regime). The plot is similar to figure 5.31, but shows the conditions for low-energetic electrons with $E_0 = 0.1$ eV to 10 eV. Apart from the overall higher density in this energy regime, which is mainly caused by the smaller velocity of the electrons, the observed behavior is similar to the case of high-energetic electrons.

At $t = 0.1$ s, the flux tube radius is increased by the reduced magnetic field. This is clearly visible as the outer flux tube region has moved towards the vessel walls in the second plot in the figure. Electrons that in these regions are subsequently removed from the flux tube, which is observed as a decrease in

electron density by roughly one order of magnitude. The inner region of the flux tube is still contained inside the spectrometer, although it is deformed by the changed magnetic field. The electron density here is therefore comparable with nominal conditions. At $t = 0.2$ s, the magnetic field is reduced sufficiently so that the flux tube is now completely split up. The entrance and exit regions of the spectrometer are disconnected from each other, and all magnetic field lines connect to the vessel walls. At this point, also electrons from the inner flux tube region are removed as well. The overall electron density is significantly reduced because a large fraction of electrons is now guided against the vessel walls, which is especially visible in the central spectrometer region ($|z| \lesssim 1$ m).

Figure 5.32 shows the same plots for the low-energy regime ($E_0 = 0.1$ MeV), which is associated with secondary electrons that result from nuclear decays in the spectrometer. The electron density is generally higher due to the smaller velocity of these electrons, which consequently spend more time in each (z, r) -bin. Apart from this difference in magnitude, the density shows a similar behavior as in the high-energy case. Again, the density is reduced as the field lines begin to connect to the vessel walls. At $t = 0.2$ s, a considerable fraction of electrons is removed from the flux tube volume.

Inverted magnetic field

From the discussion earlier in this section it is expected that the removal efficiency of the magnetic pulse is intrinsically limited and not all of the stored electrons can be removed. So far, the investigation of the electron density showed that at $t \approx 0.2$ s the flux tube splits up and all magnetic field lines connect to the vessel walls. Hence, any electrons (including the ones that are stored under nominal conditions) that follow the magnetic field lines can reach the vessel walls and be removed. It is now interesting to examine the storage conditions at a later time during a magnetic pulse, where the magnetic field has been fully inverted.

Figure 5.33 shows the electron density for the low-energy, high-energy and extremely high-energy ($E_0 = 1$ keV to 100 keV) regimes. At $t = 0.5$ s, the magnetic field nearly reached its inverted level, $B = B_{inv} \approx -B_0$. The overall conditions for electrons inside the spectrometer are comparable to the nominal conditions in this case: the cyclotron radius and the magnetic bottle effect both depend on the *magnitude* of the magnetic field, so that similar conditions are created and electrons can be stored inside the spectrometer volume. There is also no radial drift affecting the electrons since the magnetic field reached a stable level at this point, $\dot{B} \approx 0$. Consequently, the storage probability for electrons created in the spectrometer is now increased w. r. t. to earlier times t where the magnetic field had a smaller magnitude. The electron density in the central section of the spectrometer ($|z| \lesssim 4$ m) is therefore increased in comparison with figure 5.31 and 5.32. The extremely high-energetic electrons show a similar behavior, and it can be concluded that electrons the magnetic pulse similarly affects electrons in the different energy regimes.

As discussed in section 5.4.2, the magnetic pulse achieves an inversion of the magnetic field in the central spectrometer region. However, it also creates regions where an extremely small magnetic field is surrounded by regions of higher magnetic field, so that electrons moving through these regions can become stored by the magnetic bottle effect. These electrons are reflected before they can reach the vessel walls, and are therefore not removed from the spectrometer volume by the magnetic pulse. This effect limits the removal efficiency of the magnetic pulse and is difficult to avoid.

Extending the pulse length will not improve the situation since the magnetic field has reached a stable level already at $t \approx 0.5$ s. The storage conditions are therefore not changed by this option. It could be

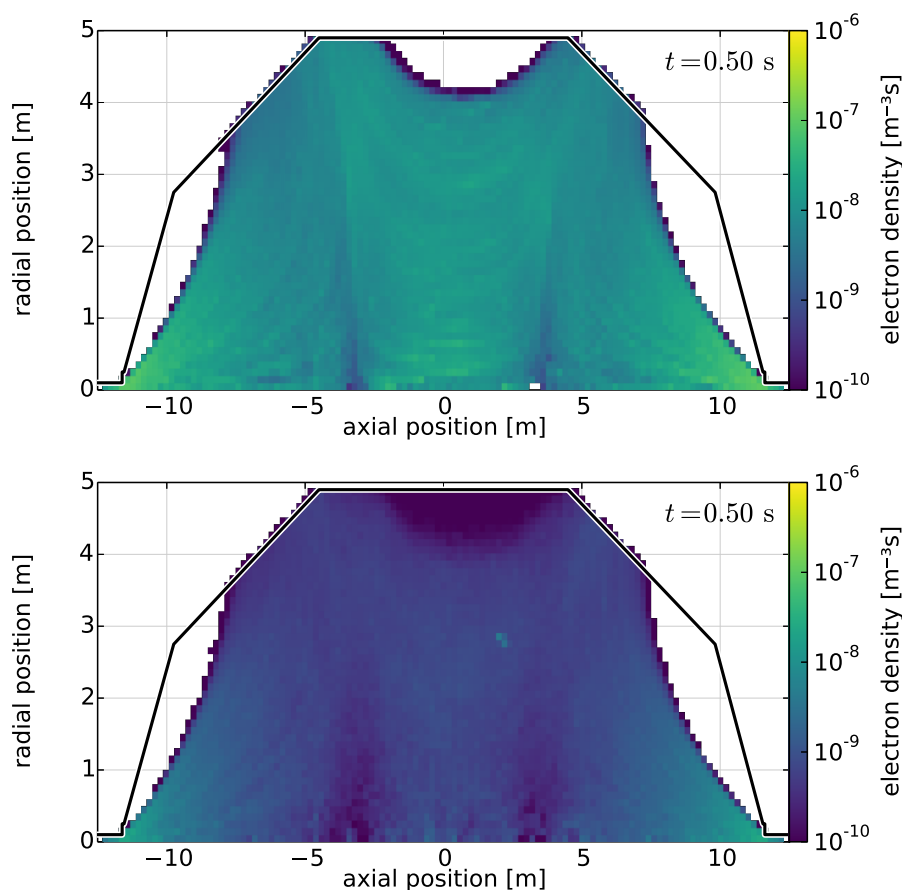


Figure 5.33.: Simulated electron density at inverted magnetic field. The plot shows the conditions for low- and high-energetic electrons after the magnetic field in the spectrometer is nearly completely inverted. The storage conditions are extremely different than at nominal conditions ($t = 0$). The magnetic field inversion creates a new flux tube region where electrons can become stored again. This is visible as an increase electron density in the central spectrometer region ($|z| \lesssim 4$ m). Electrons in these regions are affected by the *magnetic bottle effect*, so that a significant fraction of electrons cannot reach the vessel walls. The removal efficiency of the magnetic pulse is therefore limited if the magnetic field inside the spectrometer is inverted.

of interest, however, to investigate other possibilities to increase the removal efficiency. Although these ideas are purely speculative, they are listed here to be considered in possible future measurements:

- A fast sequence of magnetic pulses that are applied in a short time (e. g. 3 pulses within 10 s) could induce a “mixing” of stored electrons due to the induced radial drifts. This could lead to electrons being transferred from a “storage” region to a region where they are removed by a following magnetic pulse, thereby increasing the overall removal efficiency.

Measurements that investigated the intrinsic electron trap between the pre- and main spectrometer indicated that a magnetic pulse sequence with 3 or more pulse improves the removal efficiency w. r. t. to a single magnetic pulse [Hil11]. It should be noted, however, that the electromagnetic conditions in this setup are completely different from the main spectrometer, so the results cannot be compared directly.

- Another, similar option could be a “pulse sweep”, where the individual LFCS air coils are not pulsed simultaneously but in sequence. In principle, the existing slow-control interface allows to set arbitrary delays for the single FlipBox units w. r. t. the common trigger signal. This allows to implement different sweeping modes, e. g. by reverting the air coils next to the analyzing plane earlier than the ones at the entrance and exit regions of the spectrometer, or vice versa. Such a pulse sweep would drastically change the time-dependency of the magnetic field inside the spectrometer and could thus induce a mixing effect that allows more electrons to reach the vessel hull.
- In general, electrons can only be stored by the magnetic bottle effect when a guiding field exists, i. e. when the magnetic field in the spectrometer is non-zero. Without a magnetic field, the electrons completely lose their guiding and – neglecting the possible influence from electric fields that exist in the main spectrometer – move freely towards the vessel walls. Hence, the magnetic pulse method could be modified to not *invert* the magnetic field, but to reach a magnetic field close to zero instead.

The method could be implemented by switching off all LFCS air coils simultaneously or by ramping their power supplies to extremely small currents. Due to the slow change of the magnetic field inside the spectrometer that was discussed earlier, pulse lengths around 1 s would be required to reduce the magnetic field in this case as well. In both cases, the power supply would be affected by the change of output current; the magnetic pulse system, however, is based on a fast current inversion *without* affecting the power supply in order to ensure stable operation. Hence, it would be difficult to change the operation mode of the magnetic pulse without creating new disadvantages, and this is currently not intended.

5.4.7 Summary

Particle-tracking simulations with the software Kassiopeia were carried out to further investigate the magnetic pulse method after the successful commissioning of the complete system in the SDS-2 phase. Like with the investigation of the electron source by simulations (section 4.7), these simulations allowed to gain a better understanding of the electron removal processes due to the magnetic pulse.

By using a quasi-static approach in the Monte-Carlo simulations where the storage conditions are evaluated over time at different magnetic field settings, it was possible to study the energy dependency of the electron removal processes in a reasonable time frame. Earlier investigations of a similar setup in [Beh12] showed that a full simulation with dynamic magnetic fields is extremely time-intensive, since typically a larger number of simulation steps must be performed while the magnetic field is only reduced by a small amount due to the long time constants of the magnetic pulse.

It was found that by inverting the magnetic field inside the spectrometer volume, new storage conditions for electrons are created in the deformed magnetic flux tube. This effect occurs if $B_{min} < 0$, which is the case if the magnetic pulse is applied via the LFCS air coils. Due to the design of the magnetic pulse system, it is not easily possible to circumvent this issue, e. g. by achieving a magnetic field $B_{min} \approx 0$ in the spectrometer where the storage conditions are lifted. This would require a different design concept where the air coil currents are not fully inverted, which is difficult to implement given the requirement for a small timescale of roughly 1 s for the magnetic pulse and the hardware modifications that would be necessary.

Furthermore, the comparison between simulations and measurement with the electron source (which is discussed in chapter 4) showed that the magnetic field change inside the spectrometer vessel is slower than measured directly on the outside of the vessel walls. This confirms that eddy currents in the stainless steel vessel are induced during the magnetic pulse, and have a measurable effect on the time constant of the field inversion.

5.5 Chapter summary

In this chapter, the principles and the technical implementation of the magnetic pulse method for active removal of stored electrons from the main spectrometer was discussed. Following an approach conceived by E. OTTEN [Ott10a], the method was implemented in a joint effort between WWU Münster and KIT Karlsruhe and commissioned during the first and second SDS measurement phases at the KATRIN experiment.

The technical design of this method is based on a current inversion in the LFCS (and possibly, the EMCS) air coils at the main spectrometer within a short time frame of less than 1 s, which results in a fast reduction of the magnetic field inside the spectrometer vessel. The current inversion is achieved by a dedicated “FlipBox” system, which is designed a H-bridge circuit with an interface to the KATRIN slow-control system and can invert currents up to 190 A with adjustable timing characteristics. It was found that the dominant effect for electron removal is the deformation of the magnetic flux tube due to the reduced magnetic field according to $r_{max}^2 \propto B_{min}$, which forces stored electrons against the vessel walls. Other effects like the increase of the cyclotron radius or the induced $E \times B$ drift in radial directions play a minor role in this case.

Commissioning measurements with this method were performed during the SDS-1 and SDS-2 phases. The SDS-1 measurements could achieve a proof-of-principle with a prototype system and artificially enhanced background via a ^{83m}Kr source at the main spectrometer. It was found that the magnetic pulse method affects both low-energetic secondaries and high-energetic primary electrons from this nuclear decay, and achieves a considerable reduction of the observed background rate. The full system was implemented for the SDS-2 measurement phase, where all LFCS and EMCS air coils were equipped with FlipBox devices. The magnetic pulse method was investigated with the help of the electron source (chapter 4) to study the timing characteristics of the field reduction inside the spectrometer, which showed that a minimal pulse length of roughly 0.5 s is required to force electrons from the inner spectrometer volume onto the vessel walls. This is longer than expected from direct magnetic field measurements on the outside of the spectrometer vessel, which is attributed to eddy currents that are induced in the vessel hull. Measurements with a radioactive ^{222}Rn source at the main spectrometer confirmed the earlier results of the SDS-1 phase and showed a significant reduction of the radon-induced background rate. Under nominal conditions with $B_{min} = 0.38$ mT, a relative rate reduction (removal efficiency) of $R_{38} = 67(4)\%$ was found in this setting. Unfortunately, these results were not reproduced in a setup without artificial background, where no effect on the observed background rate was observed. This result is attributed to the high efficiency of passive background reduction methods, especially the LN_2 -baffles at the main spectrometer pump ports, which limit the amount of radioactive radon nuclei inside the spectrometer. Conclusively, the remaining background is cannot be caused by stored electrons in the spectrometer volume.

In addition to measurements, particle-tracking simulations were performed with the Kassiopia software [F⁺17]. These simulations followed a quasi-static approach where the magnetic field at the main spectrometer and the electron storage conditions are evaluated during a magnetic pulse at fixed time intervals. This is possible since dynamic effects do not play a significant role during electron removal. The simulations showed that the removal efficiency of the magnetic pulse is energy-dependent and larger for high-energetic stored electrons. This provides a strong motivation to use the magnetic pulse together with the complementary electric dipole method, which is more effective for low-energetic electrons. Furthermore, the simulations verified that the removal efficiency of the magnetic pulse is inherently limited to $R < 100\%$ in the current setup. Since the magnetic field inside the spectrometer

is inverted during a magnetic pulse, $B_{min} < 0$, a new storage region at the central spectrometer section is created. Electrons in this region cannot be removed by the magnetic pulse, since the magnetic bottle effect prevents them from reaching the vessel walls even if the magnetic flux tube is deformed due to the reduced magnetic field. Given the current technical design that inverts the air coil currents, it is difficult to circumvent this limitation.

The magnetic pulse method was developed, implemented and tested at the main spectrometer over the course of this thesis. It was shown that the method is able to remove a large fraction of stored electrons from the spectrometer volume and can significantly reduce the observed radon-induced background rate. At the SDS-2 setup, a considerable amount of background that originates from other non-radon source was present, which is not affected by the magnetic pulse. The existing passive background reduction methods efficiently reduce the amount of radon in the main spectrometer, rendering the magnetic pulse method unable to reduce the observed background at nominal SDS-2 conditions. Future measurements where a lower background is expected could again benefit from the magnetic pulse method if a radon-induced background component is found. In this case it would be interesting to test the combination of the two complementary active background removal techniques, magnetic pulse and electric dipole, as this is expected to increase their overall removal efficiency. Furthermore, it could be of interest to investigate the current limitations of the magnetic pulse method due to its technical implementation in order to improve its removal efficiency, e. g. by applying shorter magnetic pulses on purpose to limit the field reduction in the spectrometer vessel, which is expected to prevent the creation of new storage regions during the pulse.

Conclusions and outlook

The neutrino began its career as an elementary particle almost 90 years ago when it was postulated by W. PAULI as a ‘desperate remedy’ [Pau30] to bring the continuous energy spectrum of the β -decay in line with basic principles of physics, where energy and momentum is always conserved. Since then, we learned many details about the nature of the neutrino through a variety of experiments and theoretical investigations, but even today some of its characteristics remain unknown. One of the most important questions in current particle physics is the absolute mass scale of the neutrino. The neutrino mass as a key parameter is not only relevant to particle physics, but also to astrophysics and cosmology due to the neutrino influence on the development of the universe. Neutrino oscillations, whose discovery was awarded with a Nobel Prize to T. KAJITA and A.B. MACDONALD only recently, provide evidence for a small, but non-vanishing rest mass of the neutrino and require an extension of the established standard model of particle physics. However, no experiment has yet been able to determine the neutrino mass directly and provide a clear answer to the question of its absolute mass scale.

One method to access the absolute neutrino mass scale are purely kinematic measurements that are based on the MAC-E filtering technique, which combines a magnetic guiding field with an electrostatic retarding potential. Earlier experiments at Mainz and Troitsk were able to establish upper limits for the ‘average mass of the electron-antineutrino’ of $m_{\nu_e} < 2.1 \text{ eV}/c^2$ [OG14] by this approach. The KATRIN experiment aims to considerably improve the neutrino mass sensitivity to $0.2 \text{ eV}/c^2$ at 90% C. L. [A⁺05b] by implementing the MAC-E filter method in a large-scale setup. The experiment uses a windowless gaseous tritium source that generates up to 10^{10} β -decay electrons per second, which are magnetically guided through a beamline and into the main spectrometer. The spectrometer operates as a MAC-E filter and achieves an energy resolution of $\Delta E = 0.93 \text{ eV}$ at the tritium endpoint of $E_0 = 18.6 \text{ keV}$ with a large acceptance angle $\theta_0 \leq 51^\circ$ for β -decay electrons. The neutrino mass is determined from an integral measurement of the tritium β -spectrum by counting electrons that are transmitted at different retarding potentials. The sensitivity of the experiment is reduced by background processes in the main spectrometer, such as the decay of radon nuclei in the spectrometer volume and radon daughters implanted into the spectrometer walls. KATRIN aims to limit the overall background rate to $\dot{N}_b < 10 \text{ mcps}$ to achieve its target sensitivity.

The complex experimental setup of KATRIN provides a strong motivation for dedicated simulation and analysis software that is able to fulfill the requirements in accuracy and flexibility. The KASPER

framework has been developed in a joint effort by the international collaboration over the recent years, combining earlier software developments for particle-tracking, field computation and analysis tasks. The simulation software *Kassiopéia* [F⁺17] allows to investigate charged particles in complex electromagnetic fields. It utilizes the *KGeoBag* and *KEMField* libraries, which are part of the *KASPER* framework, to implement simulation geometries and compute 3D electromagnetic fields. The primary toolkit for the analysis of measurement data is *BEANS*, which allows to construct analysis workflows that perform tasks like energy calibration, data cuts and integration with slow-control data. Access to measurement and slow-control data is provided by *KaLi*. A new post-analysis framework *Peaberry* was developed over the course of this thesis to help with the analysis of measurement data and simulation results. It is written in the Python programming language and provides a common interface to data handling routines, statistical analysis and plotting capabilities.

The transmission properties of the *KATRIN* main spectrometer are extremely relevant to the outcome of the experiment, as they affect the energy resolution of the *MAC-E* filter. Inhomogeneities in its electromagnetic fields are expected due to the large size of the spectrometer vessel ($\varnothing 10$ m). To consider these inhomogeneities in the analysis of neutrino mass measurements, the electromagnetic conditions in the analyzing plane of the *MAC-E* filter need to be determined precisely for different detector pixels in dedicated commissioning measurements. Such measurements require an electron source that provides electrons with a sharp energy and angular distribution, which act as a probe for the electromagnetic fields in the *MAC-E* filter. An electron source design that is based on the emission of electrons from a photocathode via the photo-electric effect and the subsequent non-adiabatic acceleration in a strong electric field had been developed in earlier works [V⁺09, V⁺11, B⁺14a]. By mounting the photocathode in a plate-capacitor setup, which achieves an electrostatic acceleration field and can be tilted against the direction of the magnetic field, it is possible to emit electrons with well-defined pitch angles into the spectrometer. This feature is known as angular selectivity and a crucial requirement to use the source as a calibration device. The electron source was used during the first SDS commissioning phase (SDS-1) at the main spectrometer after detailed studies at WWU Münster [Zac14]. Although many characteristics of the main spectrometer could be investigated in this period, the source setup was not able to fulfill all requirements that are needed to fully determine the spectrometer transmission properties [Gro15].

For this reason, the electron source setup underwent various design improvements during preparation for the second SDS commissioning phase (SDS-2). To verify the functionality of the new design in a *MAC-E* filter setup, a dedicated electron source commissioning phase was carried out at the *KATRIN* monitor spectrometer, which provides similar electromagnetic conditions as the main spectrometer. It was found that the reworked electron source performs well in this *MAC-E* filter setup and meets all design requirements. The electron source provided full angular selectivity, covering a range of selectable pitch angles up to 90° in the spectrometer entry magnet with an angular spread of typically less than 6° . The energy spread of the emitted electrons depends on the wavelength of the incident UV light at the photocathode, which is expected from the principles of photo-emission. The gold photocathode that was used in these measurements achieved an energy spread of $0.09(7)$ eV to $0.31(5)$ eV for wavelengths of roughly 302 nm to 266 nm, which is completely sufficient for calibration measurements at the main spectrometer. A work function of 3.777 eV \pm 0.027 eV(sys) \pm 0.008 eV(stat) for the gold photocathode was measured *in-situ* by the method developed by R.H. FOWLER [Fow31]. The work function is substantially lower than reference values around 5 eV for a clean surface under ultra-high vacuum conditions, which is in full agreement with earlier measurements [Zac14] and attributed to surface effects (e. g. impurities) that reduce the observed work function. The maximal electron rate that can be achieved with the current source design was measured to 530 kcps, with the possibility

to reach $5 \cdot 10^7$ cps after minor modifications to the setup. This electron rate was determined using a novel analysis method that is largely unaffected by event pile-up at the detector that is common at high count rates.

The electron source was mounted at the main spectrometer after the successful test measurements at the monitor spectrometer. The source commissioning at the SDS-2 setup was able to confirm the earlier results. The energy spread of the produced electrons was determined to 0.067(7) eV to 0.284(15) eV for a new gold photocathode at UV wavelengths of approximately 316 nm to 266 nm. For a silver photocathode that was used in the beginning of the SDS-2 measurements, an energy spread of 0.065(15) eV to 0.210(17) eV was determined for wavelengths 314 nm to 264 nm. The considerably smaller energy spread is due to the higher work function of the silver photocathode, which was measured to $3.855 \text{ eV} \pm 0.026 \text{ eV}(\text{sys}) \pm 0.002 \text{ eV}(\text{stat})$. This value is also lower than the reference value of roughly 4 eV [Eas70], but the observed difference is significantly smaller than for the gold photocathode. It is believed that this is due to a silver oxide layer on the photocathode surface that builds up after exposure to ambient air and has an increasing effect on the work function, in addition to other surface effects that generally reduce the work function. The work function for the gold photocathode used during SDS-2 measurements was measured to $3.764 \text{ eV} \pm 0.024 \text{ eV}(\text{sys}) \pm 0.002 \text{ eV}(\text{stat})$, which is consistent with the monitor spectrometer results. The SDS-2 measurements showed that transmission functions that are measured with the electron source are sensitive to the effective work function of the main spectrometer electrode system, where the retarding potential is applied. If the work function of the source photocathode is known from independent measurements, the absolute work function of the spectrometer can be determined. This parameter is relevant to neutrino mass measurements, as any work function drift would affect the retarding potential in the analyzing plane where the energy analysis is performed. During the SDS-2 measurements it was found that the spectrometer work function reduced by 0.27(7) eV over a time frame of 3 months; however, it must be considered that the spectrometer was not baked out before this measurement phase and the improving vacuum conditions over time likely affected the surface conditions at the spectrometer electrodes.

In addition to the commissioning measurements, detailed particle-tracking simulations were carried out with Kassiopeia to gain a better understanding of the source characteristics. The simulation geometry was constructed after CAD drawings of the electron source and included data from alignment measurements at the SDS-2 setup to achieve the best possible match to the real setup. In general, the simulation results are in good agreement with the measurements performed at the monitor and main spectrometer. The simulated angular spread is comparable with measurement results and shows that the simulations can reproduce the experimental conditions. It was found that the angular spread of the produced electrons is influenced by their initial kinetic energy at the photocathode, and electrons with higher energy tend to increase the observed angular spread. The energy distribution of the electrons is not affected by the electron acceleration processes in the source, except for the overall energy gain due to electrostatic acceleration. The width (energy spread) and shape (asymmetry) of the energy distribution in the spectrometer entry magnet reproduces the initial distribution, which allows to determine these parameters directly in a transmission function measurement. Changes to the operational parameters, such as the starting, acceleration or dipole voltages, were found to have a large impact on the electron source performance and influence the electron acceleration processes. Calibration measurements to find the so-called zero-angle, which ensures that a minimal pitch angle is produced at a plate tilt angle of 0° , are essential to use the source in commissioning measurements and must be repeated if any operational parameters are changed. It was found that a magnetic reflection measurement could provide better accuracy in finding the zero-angle than the established measurement procedure, and should be used as a complementary method in future measurements.

Although the MAC-E filter setup achieves a superior energy resolution together with a large acceptance angle for signal electrons, it also features an intrinsic “magnetic bottle” effect with excellent storage conditions for electrons that are produced inside the spectrometer volume. Due to the negative impact of a high background rate on the neutrino mass sensitivity, it is crucial to efficiently suppress background from stored electrons in the KATRIN experiment. A major source for this type of background are decays of radioactive radon isotopes ^{219}Rn and ^{220}Rn that emanate from the vessel walls and NEG pumps at the main spectrometer. Their short half-lives allows them to enter the spectrometer volume and produce large amounts of low- and high-energetic electrons during their decay processes, which increases the observed background level before they are pumped out. Passive background reduction methods such as LN_2 -cooled baffles at the NEG pump ports have been implemented to prevent radon nuclei from entering the spectrometer and provide excellent suppression of radon-induced background [Har15]. In addition, active methods were developed and commissioned during the SDS-1 and SDS-2 measurement phases. These methods apply an electric dipole field in the main spectrometer [Hil16] or reduce the magnetic guiding field by a “magnetic pulse” on a short timescale. The magnetic pulse system was developed after an idea by E. OTTEN [Ott10a] in a joint effort between WWU Münster and KIT Karlsruhe. The removal method is applied by inverting the currents in the LFCS air coils that surround the main spectrometer vessel, thereby inverting the magnetic guiding field in a large part of the spectrometer volume. The current-inversion is performed by so-called “FlipBox” devices that are placed in between each air coil and its corresponding power supply. They are designed after the H-bridge principle and capable of inverting currents up to 190 A.

First functionality tests of this method were performed with a single prototype FlipBox in the SDS-1 commissioning phase. Measurements with artificially enhanced background from a $^{83\text{m}}\text{Kr}$ source allowed to study the impact of the magnetic field reduction on stored electrons with energies between a few eV and about 30 keV. It was found that the magnetic pulse can remove stored electrons from the spectrometer volume over a wide energy range and significantly reduce the observed background level. Commissioning measurements with the complete magnetic pulse system were performed during the SDS-2 phase. With all LFCS and EMCS air coils at the KATRIN main spectrometer equipped with FlipBox devices, it was possible to completely invert the magnetic field in the central spectrometer section and study this removal method in more detail. The timing characteristics of the magnetic pulse were examined by direct magnetic field measurements at the outside of the vessel walls, and by measurements with an electron beam that was provided by the UV photoelectron source that is presented in this thesis. It was found that eddy currents in the vessel hull of the main spectrometer considerably slow down the magnetic field change, and a pulse length of approximately 1 s is required until the inversion of the magnetic field inside the spectrometer is completed. Measurements were carried out with enhanced background from a ^{222}Rn source, which yielded an average removal efficiency of 67(4) % under nominal SDS-2 conditions. This value is comparable to the SDS-1 results and shows that the removal efficiency of the magnetic pulse method is inherently limited due to the inversion of the magnetic field, which was further investigated by simulations (see below). Finally, measurements at a nominal background level of 514 mcp/s in SDS-2 were carried out, i. e. with cold baffles and without artificial background enhancement. It was found that the magnetic pulse cannot reduce the observed background level in this setting, which is attributed to the high efficiency of the baffle system in suppressing radon-induced background, and the comparatively large amount of background that cannot be attributed to nuclear decays inside the spectrometer volume. The measurements showed that unfortunately, the magnetic pulse method does not provide an effective countermeasure against this type of background. Meanwhile it is known that the major fraction of background originates

from the decay of radon daughters implanted into the spectrometer walls, liberating excited neutral atoms (“Rydberg”) which are ionized by black-body radiation in the spectrometer volume.

The magnetic pulse method was further studied by Kassiopeia simulations. A quasi-static approach was implemented where the electron storage conditions are evaluated at fixed points in time during a magnetic pulse. This method is believed to yield accurate results since the field change is slow w. r. t. the electron velocity and dynamic effects such as drifts have been found to only play a minor role in the electron removal process. The dominant electron removal process during a magnetic pulse is the deformation of the magnetic flux tube due to the reduced magnetic field, which guides any stored electrons towards the vessel walls where they are subsequently removed. Since electrons follow the magnetic guiding field regardless of their kinematic properties, this effect is largely energy-independent. However, it was found that the inversion of the magnetic field, which is typically reached within a few 100 ms after a pulse was initiated, creates new storage conditions in the central spectrometer section. The inverted magnetic field features a global absolute minimum at the spectrometer center and increases towards the flat cone section of the main spectrometer, where the field lines connect to the vessel walls. This prevents a considerable fraction of electrons from being removed, as they are reflected by the magnetic bottle effect before reaching the vessel walls. This effect is the cause of the inherently limited removal efficiency of the magnetic pulse method, but difficult to circumvent in the current design that is based on a full current inversion in the air coil system. Different methods to improve this behavior and to avoid the residual trapping effects have been discussed at the end of chapter 5 and need to be tested experimentally and by simulations.

The experience gained during the commissioning measurements of the electron source, both in terms of experimental techniques and analysis methods, will be of advantage for the upcoming commissioning of the entire KATRIN beamline. These measurements will use a different electron source at the rear section, which shares many design principles with the electron source presented in this work. Additionally, the detailed simulations allowed to gain an excellent understanding of the electron acceleration and transport mechanisms inside the electron source, which are at least partly applicable to similar designs and can therefore provide vital input to these future measurements. The magnetic pulse system was fully implemented at the main spectrometer and allows to invert the air coil currents dynamically for the application of magnetic pulses, but also statically for measurements at special magnetic field settings. This possibility was often utilized for various measurements in the SDS-2 measurement phase, and is therefore considered a valuable enhancement of the experimental setup. The magnetic pulse method was proven to be effective in removing stored electrons from the main spectrometer volume, although no reduction of the nominal background level at the SDS-2 setup was observed. Since it is expected for future measurements at the KATRIN beamline to achieve a considerably lower spectrometer background, it is possible that the magnetic pulse method can eventually contribute to the overall background reduction by removing the remaining fraction of radon-induced background that is not suppressed by passive methods.

List of Figures

1.1.	Theoretical energy spectrum of the β -decay.	2
1.2.	Changing flavor composition of neutrinos due to neutrino oscillations.	5
1.3.	Fluxes of ^8B solar neutrinos.	7
1.4.	Limits on the neutrino mass for normal and inverted hierarchy.	9
1.5.	Differential energy spectrum of tritium β -decay.	14
2.1.	The KATRIN experiment.	17
2.2.	The windowless gaseous tritium source (WGTS).	18
2.3.	The differential and cryogenic pumping sections (DPS-2/CPS).	19
2.4.	The main spectrometer.	20
2.5.	The monitor spectrometer.	21
2.6.	The focal-plane detector system.	23
2.7.	Electromagnetic fields in the KATRIN setup.	24
2.8.	Electromagnetic shielding at the main spectrometer.	26
2.9.	Radon-induced background processes.	27
2.10.	Movement of a charged particle in a magnetic field.	29
2.11.	Schematic drawing of a MAC-E filter with its key components.	32
2.12.	Transmission function of a MAC-E filter.	33
2.13.	Effects of electromagnetic inhomogeneities on the transmission function.	36
2.14.	Response function for the KATRIN main spectrometer.	39
2.15.	Model parameters of the integral β -spectrum.	40
2.16.	Estimated sensitivity on m_{ν_e} for different measurement time distributions (MTD).	44
3.1.	The KASPER framework.	49
3.2.	The Kassiopeia logo.	50
3.3.	Schematic representation of a Kassiopeia run.	51
3.4.	Difference between exact and adiabatic tracking.	56
3.5.	Schematic representation of the KGeoBag geometry tree.	69
3.6.	Zonal harmonic approximation to evaluate a magnetic field.	73
3.7.	Comparison between three interpolation methods.	76
3.8.	The ORCA software at the FPD system.	81
3.9.	BEANS peripheral software.	83

3.10. Structure of the Peaberry framework.	92
3.11. Example output of a Peaberry analysis run.	95
3.12. Comparison of different Peaberry fit methods.	96
3.13. MCMC trace plot with affine-invariant sampling.	102
3.14. MCMC corner plot after affine-invariant sampling.	104
4.1. Transmission function for different calibration sources.	107
4.2. Analytical transmission functions at different pitch angles.	109
4.3. Analytical transmission functions at different pitch angles at reduced voltage.	110
4.4. Analytical transmission function with different energy distributions.	111
4.5. Electron surplus energy in the main spectrometer.	112
4.6. Schematic drawing of the electron source photocathode.	118
4.7. Density distribution in a free electron gas.	119
4.8. Schematic picture of the photoemission process.	120
4.9. Alternative models to describe the photo-electron energy spectrum.	125
4.10. Schematic drawing of the electron source setup.	127
4.11. Gaussian model to describe the photo-electron angular spectrum.	128
4.12. The electron source in the pre-SDS-2 setup.	130
4.13. The improved electron source setup in the SDS-2 phase.	131
4.14. Electric discharge caused by charge build-up on ceramic insulators.	132
4.15. The plate-capacitor setup and the photocathode.	133
4.16. The optical system.	136
4.17. The control software to operate the electron source.	138
4.18. The electron source control rack used in SDS-2 measurements.	139
4.19. Emission profiles for the LEDs used at the MoS and SDS-2 setups.	142
4.20. Typical electron energy spectrum at the SDS-2 setup.	143
4.21. Determining the electron rate by percentiles from a measured rate trend.	144
4.22. Measured electron yield before and after corrections.	151
4.23. Electron source setup at the monitor spectrometer (MoS).	153
4.24. Electron source chamber at the monitor spectrometer (MoS).	154
4.25. High voltage setup at the monitor spectrometer (MoS).	156
4.26. Electron rate stability at the MoS setup.	157
4.27. Transmission functions with different dipole voltages at the MoS setup.	159
4.28. Zero angle with nominal magnetic field at the MoS setup.	161
4.29. Magnetic reflection with nominal magnetic field at the MoS setup.	164
4.30. Magnetic reflection with enhanced magnetic field at the MoS setup.	167
4.31. Magnetic reflection measured by varying the acceleration voltage at the MoS setup.	170
4.32. Magnetic reflection with different magnetic field and dipole settings at the MoS setup.	171
4.33. Energy spread with different wavelengths at the MoS setup.	173
4.34. Energy spread with different starting voltages at the MoS setup.	176
4.35. Angular selectivity with $\alpha_{az} = 0^\circ$ at the MoS setup.	178
4.36. Angular selectivity with reduced acceleration voltage at the MoS setup.	181
4.37. Produced pitch angles with different plate angle at the MoS setup.	182
4.38. Produced pitch angles with different acceleration voltages at the MoS setup.	184
4.39. Azimuthal-dependent transmission measurements with $\alpha_p = 6^\circ$ at the MoS setup.	185
4.40. Azimuthal transmission-edge scan with $\alpha_p = 8^\circ$ at the MoS setup.	187
4.41. Work function measurement at the MoS setup.	189

4.42. Typical energy spectrum in high-rate measurements at the MoS setup.	192
4.43. Poisson fit model for high-rate measurements.	193
4.44. High-rate measurement at the MoS setup.	195
4.45. Electron source setup with manipulator at the main spectrometer (SDS-2).	198
4.46. Electron rate and photodiode stability at the SDS-2 setup.	200
4.47. Correlation between electron rate and photodiode voltage at the SDS-2 setup. . . .	201
4.48. Electron rate over multiple days at the SDS-2 setup.	203
4.49. Zero angle after the maintenance break at the SDS-2 setup.	204
4.50. Magnetic reflection under nominal conditions at the SDS-2 setup.	206
4.51. Magnetic reflection with reduced voltage at the SDS-2 setup.	209
4.52. Energy spread with different wavelengths at the SDS-2 setup (silver photocathode). .	210
4.53. Energy spread with different wavelengths at the SDS-2 setup (gold photocathode). .	213
4.54. Vacuum pressure during the SDS-2 measurement phase.	216
4.55. Energy spread with different wavelengths at the SDS-2 setup.	218
4.56. Angular spread with different wavelengths at the SDS-2 setup.	220
4.57. Angular distributions with different plate angles at the SDS-2 setup.	222
4.58. Produced pitch angles with different plate angle at the SDS-2 setup.	225
4.59. Work function measurement with Ag photocathode at the SDS-2 setup.	226
4.60. Work function measurement with Au photocathode at the SDS-2 setup.	228
4.61. Issues with Kapton-insulated high voltage wire at the electron source.	230
4.62. Simulation geometry of the SDS-2 setup.	236
4.63. Electrode geometry of the electron source.	237
4.64. Line-scan measurement and corresponding simulation in the SDS-2 setup.	244
4.65. Pixel mapping simulation for selected detector pixels in the SDS-2 setup.	246
4.66. Comparison of simulated and measured magnetic fields at the SDS-2 and MoS setups.	248
4.67. Electromagnetic conditions at the electron source in the SDS-2 and MoS setups. . .	250
4.68. Electron transport at the electron source in the SDS-2 setup.	252
4.69. Step size, energy violation and non-adiabaticity in the electron source simulations at the SDS-2 setup.	255
4.70. Simulated electron trajectories in the SDS-2 (top) and MoS (bottom) setups.	257
4.71. Simulated electron trajectories at zero voltage in the SDS-2 setup.	258
4.72. Simulated angular distributions for different plate angles in the SDS-2 and MoS setups.	260
4.73. Simulated pitch angles for different plate angles in the SDS-2 and MoS setups. . . .	263
4.74. Simulated pitch angles for different plate angles in the SDS-2 setup.	264
4.75. Simulated energy and angular distributions at zero voltage in the SDS-2 setup. . . .	265
4.76. Simulated energy and angular distributions at high voltage in the SDS-2 setup. . . .	267
4.77. Simulated energy and angular distributions at high voltage and increased plate angle in the SDS-2 setup.	268
4.78. Simulated energy and angular distributions at reduced voltage in the SDS-2 setup. .	270
4.79. Correlation of simulated energy distributions in the SDS-2 setup.	272
4.80. Correlation of simulated angular distributions in the SDS-2 setup.	273
4.81. Correlation of simulated angular distributions at increased plate angle in the SDS-2 setup.	275
4.82. Simulated zero angles in the SDS-2 setup.	276
4.83. Simulated pitch angles at different acceleration voltages in the SDS-2 setup.	278
4.84. Simulated pitch angles at different start voltages in the SDS-2 setup.	281
4.85. Simulated zero angles with reduced voltage settings in the SDS-2 setup.	283

4.86. Simulated pitch angles with misaligned photocathode in the SDS-2 setup.	286
4.87. Simulated pitch angles with zero-angle offset in the SDS-2 setup.	287
4.88. Simulated pitch angles with larger front plate aperture in the SDS-2 setup.	289
4.89. Comparison between measured and simulated transmission functions at the SDS-2 setup.	292
4.90. Estimating systematic and statistical uncertainties from toy data samples.	293
4.91. Toy model for the investigation of systematic uncertainties.	294
4.92. Fit result of 10 000 toy data samples, using the 6-parameter fit model (energy distribution and transmission edge).	299
4.93. Fit result of 10 000 toy data samples, using the 5-parameter fit model (energy distribution).	300
4.94. Fit results of 10 000 toy data samples, using the 4-parameter fit model (angular distribution).	304
5.1. Statistical uncertainty of the neutrino mass in dependency of the background level. .	310
5.2. Radon decay processes at the main spectrometer.	312
5.3. Typical trajectory of a stored electron in the main spectrometer.	313
5.4. Observed background with cold and warm baffles.	315
5.5. Flux tube deformation during a magnetic pulse.	317
5.6. Increase of the flux tube radius during a magnetic pulse.	318
5.7. Increase of the cyclotron radius during a magnetic pulse.	320
5.8. Induced radial drift by a magnetic field change.	320
5.9. The air coil system at the main spectrometer.	323
5.10. Schematic drawing of the FlipBox operating scheme.	325
5.11. Switching process of the FlipBox device.	326
5.12. FlipBox prototype for SDS-1 measurements.	327
5.13. Installed FlipBox units for the SDS-2 measurements.	328
5.14. Magnetic pulse system at the main spectrometer.	330
5.15. Schematic view of a typical magnetic pulse measurement.	331
5.16. Magnetic field at the main spectrometer during a magnetic pulse.	333
5.17. Schematic view of the electron beam measurement.	336
5.18. FPD pixel mapping used in the pulse timing measurements.	336
5.19. Magnetic pulse with ^{83m}Kr source at the SDS-1 setup.	338
5.20. The decay scheme of ^{83}Rb into ^{83}Kr	339
5.21. Rate stacking of magnetic pulse measurements.	341
5.22. Magnetic pulse with ^{220}Rn source at the SDS-2 setup (0.38 mT setting).	342
5.23. Magnetic pulse with nominal background at the SDS-2 setup (0.38 mT setting). . .	345
5.24. Background reduction by LN ₂ -cooled baffles.	346
5.25. Typical electron trajectories in a magnetic pulse simulation.	349
5.26. Magnetic field under nominal conditions and during a magnetic pulse.	352
5.27. Simulated removal efficiency of the magnetic pulse.	355
5.28. Simulated trapping probability during a magnetic pulse.	356
5.29. Simulated pulse timing for different FPD pixels.	357
5.30. FPD pixel mapping used in the pulse timing simulations.	358
5.31. Simulated electron density during a magnetic pulse (high-energy regime).	360
5.32. Simulated electron density during a magnetic pulse (low-energy regime).	361
5.33. Simulated electron density at inverted magnetic field.	363

List of Tables

1.1. Weak isospin doublets in the standard model.	3
3.1. Results from different Peaberry fit methods.	97
4.1. Observed hysteresis effect between transmission functions at different dipole voltages.	160
4.2. Measured zero angle offsets at different dipole voltages and magnetic field settings. .	163
4.3. Measured reflection angles at different magnetic field settings.	166
4.4. Observed asymmetries in the reflection angle measurements.	169
4.5. Measured magnetic reflection in dependency of acceleration voltage.	171
4.6. Measured reflection angles in dependency of the dipole voltage at different field settings.	172
4.7. Measured energy distributions at different wavelengths.	177
4.8. Measured angular distributions at different plate angles.	180
4.9. Measured angular distributions at acceleration voltages.	182
4.10. Measured angular distributions for different azimuthal angles.	186
4.11. Fit results for the azimuthal transmission-edge scan.	188
4.12. Comparison of the determined work functions for a gold photocathode.	191
4.13. Measured zero angle offsets before and after maintenance break.	205
4.14. Measured reflection angles.	208
4.15. Observed asymmetries in the reflection angle measurements.	208
4.16. Measured reflection angles at reduced voltage.	209
4.17. Measured energy distributions for Ag photocathode at different wavelengths.	212
4.18. Measured energy distributions for Au photocathode at different wavelengths.	214
4.19. Determined energy parameters for different setups and different wavelengths.	214
4.20. Observed work function change over the SDS-2 measurement phase.	217
4.21. Comparison of energy distributions for Au photocathode at different voltage settings.	219
4.22. Measured angular distributions for Au photocathode at different wavelengths.	221
4.23. Measured angular distributions for Au photocathode at different plate angles.	224
4.24. Comparison of the determined work functions for a silver photocathode.	229
4.25. Comparison of the determined work functions for a gold photocathode.	230
4.26. Important parameters of the electron source simulations and their default values. . .	240
4.27. Alignment parameters of the electron source and PS magnet system.	243
4.28. Simulated pitch angles at different plate angles for $\alpha_{az} = 0^\circ$	261

4.29. Fit results of simulated pitch angles at different azimuthal plate angles.	262
4.30. Simulated kinetic energies and pitch angles at different simulation setting in the SDS-2 setup.	271
4.31. Simulated zero angles at different dipole voltages.	278
4.32. Simulated pitch angles at different acceleration voltages in the SDS-2 setup.	280
4.33. Fit results of simulated pitch angles at reduced start voltage.	282
4.34. Simulated zero angles at different voltage settings in the SDS-2 setup.	282
4.35. Simulated zero angles with misaligned photocathode in the SDS-2 setup.	285
4.36. Fit results of simulated pitch angles with zero-angle offset.	288
4.37. Parameter sets for the toy models used to evaluate systematic uncertainties.	297
4.38. Fit results of different toy data samples, using the 6-parameter fit model.	298
4.39. Fit results of different toy data samples, using the 5-parameter fit model.	301
4.40. Fit results of different toy data samples with a transmission edge offset, using the 5-parameter fit model.	303
4.41. Fit results of different toy data samples, using the 4-parameter fit model.	305
5.1. LFCS settings used in magnetic pulse measurements.	332
5.2. Magnetic field at different LFCS settings.	332
5.3. Timing parameters of the LFCS pulse at different current settings.	335
5.4. Timing of the magnetic pulse inside the main spectrometer.	337
5.5. Removal efficiency of the magnetic pulse with a $^{83\text{m}}\text{Kr}$ source.	340
5.6. Removal efficiency of the magnetic pulse with a ^{220}Rn source.	344
5.7. Magnetic pulse delay times for different detector pixels.	359

List of Acronyms

AES	Auger electron spectroscopy	GSL	GNU Scientific Library
BEM	boundary element method	HV	high-voltage
CAD	computer-aided design	IE	Inner Electrode
CKrS	condensed krypton source	IH	inverted hierarchy
CMB	cosmic microwave background	KATRIN	Karlsruhe Tritium Neutrino experiment
CNB	cosmic neutrino background	KIT	Karlsruhe Institut für Technologie
CPS	Cryogenic Pumping Section	LFCS	Low Field Correction System
CSV	comma-separated values	MAC-E	magnetic adiabatic collimation with electrostatic filtering
DAQ	data-acquisition	MCMC	Markov Chain Monte-Carlo
DET	Detector magnet	MobSU	mobile sensor unit
DPS-2	Differential Pumping Section	MoS	Monitor Spectrometer
EBPVD	electron beam physical vapor deposition	MOSFET	metal–oxide–semiconductor field-effect transistor
EMCS	Earth Magnetic Field Compensation System	MS	Main Spectrometer
EMD	electromagnetic design	MSW	Mikheyev–Smirnov–Wolfenstein
FEM	finite element method	MTD	measurement time distribution
FFTM	fast Fourier-transform multipole	ND	neutral density
FPD	Focal Plane Detector		

NEG	non-evaporable getter	ROI	region of interest
NH	normal hierarchy	RS	Rear Section
NME	nuclear matrix element	SDS	spectrometer and detector section
ODE	ordinary differential equation	SNR	signal-to-noise ratio
PAE	Post-Acceleration Electrode	STS	source and transport section
PCH	Pinch magnet	TLK	Tritium Labor Karlsruhe
PDG	particle data group	TMPs	turbo-molecular pumps
PEEK	polyether ether ketone	ToF	time-of-flight
PS	Pre-Spectrometer	TVS	transient voltage suppressor
PS1	Pre-Spectrometer magnet 1	UHV	ultra-high vacuum
PS2	Pre-Spectrometer magnet 2	VTK	The Visualization Toolkit
PTB	Physikalisch-Technische Bundesanstalt	WGTS	Windowless Gaseous Tritium Source
RAID	redundant array of independent disks	XPS	X-ray photon spectroscopy
RH	Robin-Hood		

References

- [A⁺89] W. DAVID ARNETT, JOHN N. BAHCALL, ROBERT P. KIRSHNER ET AL. *Supernova 1987A*. *Annu. Rev. Astron. Astrophys.*, 27(1):629–700, 1989. URL: <http://www.annualreviews.org/doi/10.1146/annurev.aa.27.090189.003213>, doi:10.1146/annurev.aa.27.090189.003213.
- [A⁺00] V.N. ASEEV, A.I. BELESEV, A.I. BERLEV ET AL. *Energy loss of 18 keV electrons in gaseous T₂ and quench condensed D₂ films*. *EPJ D*, 10(1):39–52, 2000. URL: <http://dx.doi.org/10.1007/s100530050525>, doi:10.1007/s100530050525.
- [A⁺01] Q. R. AHMAD, R. C. ALLEN, T. C. ANDERSEN ET AL. *Measurement of the Rate of $\nu_e + d \rightarrow p + p + e^-$ Interactions Produced by ^8B Solar Neutrinos at the Sudbury Neutrino Observatory*. *Phys. Rev. Lett.*, 87:071301, Jul 2001. URL: <http://link.aps.org/doi/10.1103/PhysRevLett.87.071301>, doi:10.1103/PhysRevLett.87.071301.
- [A⁺02] Q. R. AHMAD, R. C. ALLEN, T. C. ANDERSEN ET AL. *Direct Evidence for Neutrino Flavor Transformation from Neutral-Current Interactions in the Sudbury Neutrino Observatory*. *Phys. Rev. Lett.*, 89:011301, Jun 2002. URL: <http://link.aps.org/doi/10.1103/PhysRevLett.89.011301>, doi:10.1103/PhysRevLett.89.011301.
- [A⁺05a] B. AHARMIM, S. N. AHMED, A. E. ANTHONY ET AL. *Electron energy spectra, fluxes, and day-night asymmetries of ^8B solar neutrinos from measurements with NaCl dissolved in the heavy-water detector at the Sudbury Neutrino Observatory*. *Phys. Rev. C*, 72:055502, Nov 2005. URL: <http://link.aps.org/doi/10.1103/PhysRevC.72.055502>, doi:10.1103/PhysRevC.72.055502.
- [A⁺05b] J. ANGRİK, T. ARMBRUST, A. BEGLARIAN ET AL. *KATRIN Design Report 2004, Wissenschaftliche Berichte FZKA 7090*. Technical report, Forschungszentrum Karlsruhe, 2005. URL: <http://bibliothek.fzk.de/zb/berichte/FZKA7090.pdf>.
- [A⁺06] M. H. AHN, E. ALIU, S. ANDRINGA ET AL. *Measurement of neutrino oscillation by the K2K experiment*. *Phys. Rev. D*, 74:072003, Oct 2006. URL: <http://link.aps.org/doi/10.1103/PhysRevD.74.072003>, doi:10.1103/PhysRevD.74.072003.
- [A⁺11a] K.N. ABAZJIAN, E. CALABRESE, A. COORAY ET AL. *Cosmological and astrophysical neutrino mass measurements*. *Astropart. Phys.*, 35(4):177 – 184, 2011. URL: <http://www.sciencedirect.com/science/article/pii/S0927650511001344>, doi:10.1016/j.astropartphys.2011.07.002.
- [A⁺11b] V. N. ASEEV, A. I. BELESEV, A. I. BERLEV ET AL. *Upper limit on the electron antineutrino mass from the Troitsk experiment*. *Phys. Rev. D*, 84:112003, Dec 2011. URL: <http://link.aps.org/doi/10.1103/PhysRevD.84.112003>, doi:10.1103/PhysRevD.84.112003.

- [A⁺12a] Y. ABE, C. ABERLE, J. C. DOS ANJOS ET AL. *Reactor $\bar{\nu}_e$ disappearance in the Double Chooz experiment*. Phys. Rev. D, 86:052008, Sep 2012. URL: <http://link.aps.org/doi/10.1103/PhysRevD.86.052008>, doi:10.1103/PhysRevD.86.052008.
- [A⁺12b] J. K. AHN, S. CHEBOTARYOV, J. H. CHOI ET AL. *Observation of Reactor Electron Antineutrinos Disappearance in the RENO Experiment*. Phys. Rev. Lett., 108:191802, May 2012. URL: <http://link.aps.org/doi/10.1103/PhysRevLett.108.191802>, doi:10.1103/PhysRevLett.108.191802.
- [A⁺12c] F. P. AN, J. Z. BAI, A. B. BALANTEKIN ET AL. *Observation of Electron-Antineutrino Disappearance at Daya Bay*. Phys. Rev. Lett., 108:171803, Apr 2012. URL: <http://link.aps.org/doi/10.1103/PhysRevLett.108.171803>, doi:10.1103/PhysRevLett.108.171803.
- [A⁺13] M. AGOSTINI, M. ALLARDT, E. ANDREOTTI ET AL. *Results on Neutrinoless Double- β Decay of ^{76}Ge from Phase I of the GERDA Experiment*. Phys. Rev. Lett., 111:122503, Sep 2013. URL: <http://link.aps.org/doi/10.1103/PhysRevLett.111.122503>, doi:10.1103/PhysRevLett.111.122503.
- [A⁺14] ADE, P. A. R., AGHANIM, N., ARMITAGE-CAPLAN, C. ET AL. *Planck 2013 results. XVI. Cosmological parameters*. Astron. Astrophys., 571:A16, 2014. URL: <http://dx.doi.org/10.1051/0004-6361/201321591>, doi:10.1051/0004-6361/201321591.
- [A⁺15a] J.F. AMSBAUGH, J. BARRETT, A. BEGLARIAN ET AL. *Focal-plane detector system for the KATRIN experiment*. Nucl. Instr. Meth. Phys. Res. A, 778:40 – 60, 2015. URL: <http://www.sciencedirect.com/science/article/pii/S0168900215000236>, doi:10.1016/j.nima.2014.12.116.
- [A⁺15b] D. M. ASNER, R. F. BRADLEY, L. DE VIVEIROS ET AL. *Single-Electron Detection and Spectroscopy via Relativistic Cyclotron Radiation*. Phys. Rev. Lett., 114:162501, Apr 2015. URL: <http://link.aps.org/doi/10.1103/PhysRevLett.114.162501>, doi:10.1103/PhysRevLett.114.162501.
- [A⁺16a] M. AGOSTINI, M. ALLARDT, A.M. BAKALYAROV ET AL. *Search of Neutrinoless Double Beta Decay with the GERDA Experiment*. Nuclear and Particle Physics Proceedings, 273:1876 – 1882, 2016. 37th International Conference on High Energy Physics (ICHEP). URL: <http://www.sciencedirect.com/science/article/pii/S2405601415007920>, doi:10.1016/j.nuclphysbps.2015.09.303.
- [A⁺16b] M. ARENZ, M. BABUTZKA, M. BAHR ET AL. *Commissioning of the vacuum system of the KATRIN Main Spectrometer*. J. Instrum., 11(04):P04011, 2016. URL: <http://stacks.iop.org/1748-0221/11/i=04/a=P04011>, doi:10.1088/1748-0221/11/04/P04011.
- [AR87] W. DAVID ARNETT, JONATHAN L. ROSNER. *Neutrino mass limits from SN1987A*. Phys. Rev. Lett., 58:1906–1909, May 1987. URL: <http://link.aps.org/doi/10.1103/PhysRevLett.58.1906>, doi:10.1103/PhysRevLett.58.1906.
- [Arl09] H. ARLINGHAUS. *Investigation of the muon-induced secondary electron background in the KATRIN Experiment*. PhD thesis, Westfälische Wilhelms-Universität Münster, 2009.
- [B⁺81] G. BEAMSON, H.Q. PORTER, D.W. TURNER. *The collimating and magnifying properties of a superconducting field photoelectron spectrometer*. J. Phys. A, 14(2):256, 1981. URL: <http://stacks.iop.org/0022-3735/14/i=2/a=526>, doi:10.1088/0022-3735/14/2/526.
- [B⁺95] J. BARÓ, J. SEMPÁU, J.M. FERNÁNDEZ-VAREA ET AL. *PENELOPE: An algorithm for Monte Carlo simulation of the penetration and energy loss of electrons and positrons in matter*. Nucl. Instrum. Meth. B, 100(1):31–46, 1995. URL: <http://www.sciencedirect.com/science/article/pii/0168583X95003495>, doi:10.1016/0168-583X(95)00349-5.
- [B⁺12] M BABUTZKA, M BAHR, J BONN ET AL. *Monitoring of the operating parameters of the KATRIN Windowless Gaseous Tritium Source*. New J. Phys., 14(10):103046, 2012. URL: <http://stacks.iop.org/1748-0221/14/i=10/a=103046>.

- iop.org/1367-2630/14/i=10/a=103046, doi:10.1088/1367-2630/14/10/103046.
- [B⁺13a] S. BAUER, B. GREES, D. SPITZER ET AL. *Ellipsometry with polarisation analysis at cryogenic temperatures inside a vacuum chamber*. Rev. Sci. Instrum., 84(12), 2013. URL: <http://scitation.aip.org/content/aip/journal/rsi/84/12/10.1063/1.4838555>, doi:10.1063/1.4838555.
- [B⁺13b] S. BAUER, R. BERENDES, F. HOCHSCHULZ ET AL. *Next generation KATRIN high precision voltage divider for voltages up to 65kV*. J. Instrum., 8(10):P10026, 2013. URL: <http://stacks.iop.org/1748-0221/8/i=10/a=P10026>, doi:10.1088/1748-0221/8/10/P10026.
- [B⁺13c] J. BEHRENS, T. CORONA, F. GLÜCK ET AL. *EMD consequences of electrical shorts at the inner electrode system*. Technical report, KIT Karlsruhe, 2013. internal report (BSCW). URL: <https://fuzzy.fzk.de/bscw/bscw.cgi/d875477/430-doc-3-9002-EMD%20consequences%20of%20electrical%20shorts%20at%20the%20inner%20electrode%20system.pdf>.
- [B⁺14a] M. BECK, K. BOKELOH, H. HEIN ET AL. *An angular-selective electron source for the KATRIN experiment*. J. Instrum., 9(11):P11020, 2014. URL: <http://stacks.iop.org/1748-0221/9/i=11/a=P11020>, doi:10.1088/1748-0221/9/11/P11020.
- [B⁺14b] J. BEHRENS, V. HANNEN, H.-W. ORTJOHANN ET AL. *Overview of e-gun measurements at the monitor spectrometer*. Technical report, Westfälische Wilhelms-Universität Münster, 2014. internal report (SVN). URL: https://nuserv.uni-muenster.de/svn/katrin/SDS_commissioning/ComponentDocumentation/Egun_MonSpec/Egun_MonSpec.pdf.
- [B⁺15] J. BARRETT, J. A. FORMAGGIO, T. J. CORONA. *A method to calculate the spherical multipole expansion of the electrostatic charge distribution on a triangular boundary element*. Prog. Electromagn. Res. B, 63:123–143, 2015. URL: <http://www.jpier.org/PIERB/pier.php?paper=15061904>, doi:10.2528/PIERB15061904.
- [B⁺17a] J. BEHRENS, P. C.-O. RANITZSCH, M. BECK ET AL. *A mono-energetic, angular-selective UV photo-electron source for commissioning of the KATRIN experiment*. Eur. Phys. J. C, 77(6):410, 2017. URL: <https://link.springer.com/article/10.1140%2Fepjc%2Fs10052-017-4972-9>, doi:10.1140/epjc/s10052-017-4972-9.
- [B⁺17b] J. BEHRENS ET AL. *Reduction of stored-particle background by magnetic pulse at the KATRIN experiment*. 2017. in preparation.
- [Bab14] M. BABUTZKA. *Design and development for the Rearsection of the KATRIN experiment*. PhD thesis, Karlsruhe Institut für Technologie, 2014.
- [Bar16] J. P. BARRETT. *A Spatially Resolved Study of the KATRIN Main Spectrometer Using a Novel Fast Multipole Method*. PhD thesis, University of North Carolina at Chapel Hill, 2016.
- [Bau13] S. BAUER. *Energy calibration and stability monitoring of the KATRIN experiment*. PhD thesis, Westfälische Wilhelms-Universität Münster, 2013.
- [BE14] J. BEHRENS, S. ENOMOTO. *e-gun pulser latency*, Nov 2014. electronic logbook (internal site). URL: <https://neutrino.ikp.kit.edu:8080/SDS-Measurements+Phase+2/26>.
- [BEG⁺13] J. BEHRENS, M. ERHARD, F. GLÜCK ET AL. *Active background removal methods with Krypton*, Sep 2013. electronic logbook (internal site). URL: <https://neutrino.ikp.kit.edu:8080/SDS-Measurements+Phase/293>.
- [Beh12] J. D. BEHRENS. *Simulations of stored electrons in the Penning trap between the KATRIN spectrometers*. Diploma thesis, Westfälische Wilhelms-Universität Münster, 2012.
- [Beh14] J. BEHRENS. *Report on the e-gun test measurements at the monitor spectrometer*. Technical report, Westfälische Wilhelms-Universität Münster, 2014. internal report (SVN). URL: https://nuserv.uni-muenster.de/svn/katrin/SDS_commissioning/CommissioningDocument/SDSphase2/MeasurementReports/Egun_MonSpec/Egun_MonSpec_report.pdf.

- [BEK⁺15] J. BEHRENS, M. ERHARD, M. KRAUS ET AL. *e-gun commissioning*, Feb 2015. electronic logbook (internal site). URL: <https://neutrino.ikp.kit.edu:8080/SDS-Measurements+Phase+2/88>.
- [BEW⁺15] J. BEHRENS, M. ERHARD, K. WIERMAN ET AL. *Continuing the tale of e-gun problems (+ measurements)*, Mar 2015. electronic logbook (internal site). URL: <https://neutrino.ikp.kit.edu:8080/SDS-Measurements+Phase+2/124>.
- [BHO⁺15] J. BEHRENS, V. HANNEN, H.-W. ORTJOHANN ET AL. *e-gun repair report*, Feb 2015. electronic logbook (internal site). URL: <https://neutrino.ikp.kit.edu:8080/main-spectrometer/944>.
- [BM14] R. A. BATTYE, A. MOSS. *Evidence for Massive Neutrinos from Cosmic Microwave Background and Lensing Observations*. Phys. Rev. Lett., 112:051303, Feb 2014. URL: <http://link.aps.org/doi/10.1103/PhysRevLett.112.051303>, doi:10.1103/PhysRevLett.112.051303.
- [Bro01] E. BROWNE. *Nuclear Data Sheets for A = 215,219,223,227,231*. Nucl. Data Sheets, 93(4):763 – 1061, 2001. URL: <http://www.sciencedirect.com/science/article/pii/S009037520190016X>, doi:10.1006/ndsh.2001.0016.
- [BS64a] C. N. BERGLUND, W. E. SPICER. *Photoemission Studies of Copper and Silver: Experiment*. Phys. Rev., 136:A1044–A1064, Nov 1964. URL: <http://link.aps.org/doi/10.1103/PhysRev.136.A1044>, doi:10.1103/PhysRev.136.A1044.
- [BS64b] C. N. BERGLUND, W. E. SPICER. *Photoemission Studies of Copper and Silver: Theory*. Phys. Rev., 136:A1030–A1044, Nov 1964. URL: <http://link.aps.org/doi/10.1103/PhysRev.136.A1030>, doi:10.1103/PhysRev.136.A1030.
- [Bus14] R. BUSSE. *Characterisation of a photocathode for a monoenergetic electron source for the KATRIN experiment*. Bachelor's thesis, Westfälische Wilhelms-Universität Münster, 2014.
- [BW14] J. BEHRENS, C. WEINHEIMER. *WGTS emulation with the Münster e-gun*. internal document, 2014.
- [C⁺56] C. L. COWAN, F. REINES, F. B. HARRISON ET AL. *Detection of the Free Neutrino: a Confirmation*. Science, 124(3212):103–104, 1956. URL: <http://science.sciencemag.org/content/124/3212/103>, doi:10.1126/science.124.3212.103.
- [C⁺98] BRUCE T. CLEVELAND, TIMOTHY DAILY, JR. RAYMOND DAVIS ET AL. *Measurement of the Solar Electron Neutrino Flux with the Homestake Chlorine Detector*. Astrophys. J., 496(1):505, 1998. URL: <http://stacks.iop.org/0004-637X/496/i=1/a=505>.
- [Car10] B.C. CARLON. *Elliptic integral*. In F. W. J. Olver, D. M. Lozier, R. F. Boisvert et al., editors, *NIST Handbook of Mathematical Functions*. Cambridge University Press, 2010.
- [Cha14] J. CHADWICK. *Intensitätsverteilung im magnetischen Spektren der β -Strahlen von Radium B + C*. Verhandlungen der Deutschen Physikalischen Gesellschaft, 16:383–391, 1914.
- [Col13] ICECUBE COLLABORATION. *Evidence for High-Energy Extraterrestrial Neutrinos at the IceCube Detector*. Science, 342(6161), 2013. URL: <http://science.sciencemag.org/content/342/6161/1242856>, doi:10.1126/science.1242856.
- [Cor14] T. J. CORONA. *Methodology and application of high performance electrostatic field simulation in the KATRIN experiment*. PhD thesis, University of North Carolina at Chapel Hill, 2014.
- [D⁺13a] P. S. BHUPAL DEV, SRUBABATI GOSWAMI, MANIMALA MITRA ET AL. *Constraining neutrino mass from neutrinoless double beta decay*. Phys. Rev. D, 88:091301, Nov 2013. URL: <http://journals.aps.org/prd/abstract/10.1103/PhysRevD.88.091301>, doi:10.1103/PhysRevD.88.091301.
- [D⁺13b] G. DREXLIN, V. HANNEN, S. MERTENS ET AL. *Current Direct Neutrino Mass Experiments*. Adv. High Energy Phys., 2013:293986, 2013. URL: <http://www.hindawi.com/journals/ahep/2013/293986/>, doi:10.1155/2013/293986.

- [Dir28] P. A. M. DIRAC. *The Quantum Theory of the Electron*. Proc. R. Soc. A, 117(778):610–624, 1928. URL: <http://rspa.royalsocietypublishing.org/content/117/778/610>, doi:10.1098/rspa.1928.0023.
- [DS73] R.J. D'ARCY, N.A. SURPLICE. *Electric charges on stainless steel surfaces: The effects of hydrogen, charged particles, illumination, and electric fields on the work function*. Surf. Sci., 34(2):193–211, 1973. URL: <http://www.sciencedirect.com/science/article/pii/0039602873901155>, doi:10.1016/0039-6028(73)90115-5.
- [DuB32] LEE A. DUBRIDGE. *A Further Experimental Test of Fowler's Theory of Photoelectric Emission*. Phys. Rev., 39:108–118, Jan 1932. URL: <http://link.aps.org/doi/10.1103/PhysRev.39.108>, doi:10.1103/PhysRev.39.108.
- [Dyb17] S. DYBA. *Field shaping with the Inner Wire electrode and setup of the condensed Krypton source at the KATRIN Experiment*. PhD thesis, Westfälische Wilhelms-Universität Münster, 2017. in preparation.
- [E⁺14] M ERHARD, S BAUER, A BEGLARIAN ET AL. *High-voltage monitoring with a solenoid retarding spectrometer at the KATRIN experiment*. J. Instrum., 9(06):P06022, 2014. URL: <http://stacks.iop.org/1748-0221/9/i=06/a=P06022>, doi:10.1088/1748-0221/9/06/P06022.
- [E⁺16] M. ERHARD, S. BAUER, A. BEGLARIAN ET AL. *Technical Design and Commissioning of the KATRIN Large Volume Air Coil System*. J. Instrum., 2016. submitted.
- [Eas70] D. E. EASTMAN. *Photoelectric Work Functions of Transition, Rare-Earth, and Noble Metals*. Phys. Rev. B, 2:1–2, Jul 1970. URL: <http://link.aps.org/doi/10.1103/PhysRevB.2.1>, doi:10.1103/PhysRevB.2.1.
- [EBO15] M. ERHARD, J. BEHRENS, H.-W. ORTJOHANN. *eGun Alignment*, Jul 2015. electronic logbook (internal site). URL: <https://neutrino.ikp.kit.edu:8080/main-spectrometer/1564>.
- [Ein05] A. EINSTEIN. *Über einen die Erzeugung und Verwandlung des Lichtes betreffenden heuristischen Gesichtspunkt*. Ann. Phys. (Berlin), 322(6):132–148, 1905. URL: <http://onlinelibrary.wiley.com/doi/10.1002/andp.19053220607>, doi:10.1002/andp.19053220607.
- [Eno13] S ENOMOTO. *Status of BEANS: KATRIN Analysis Platform for Real Physicists*. Talk at 30. KATRIN Collaboration Meeting, Karlsruhe, 29 Oct 2013, 2013.
- [Eno15] S ENOMOTO. *BEANS Applications for KATRIN (extensions for SDS+STS)*. Talk at 25. KATRIN Collaboration Meeting, Karlsruhe, 2 Mar 2015, 2015.
- [Erh16] M. G. ERHARD. *Influence of the magnetic field on the transmission characteristics and neutrino mass systematic of the KATRIN experiment*. PhD thesis, Karlsruhe Institut für Technologie, 2016.
- [F⁺98] Y. FUKUDA, T. HAYAKAWA, E. ICHIHARA ET AL. *Evidence for Oscillation of Atmospheric Neutrinos*. Phys. Rev. Lett., 81:1562–1567, Aug 1998. URL: <http://link.aps.org/doi/10.1103/PhysRevLett.81.1562>, doi:10.1103/PhysRevLett.81.1562.
- [F⁺11] F. M. FRÄNKLE, L. BORNSCHEIN, G. DREXLIN ET AL. *Radon induced background processes in the KATRIN pre-spectrometer*. Astropart. Phys., 35(3):128 – 134, 2011. URL: <http://www.sciencedirect.com/science/article/pii/S0927650511001290>, doi:10.1016/j.astropartphys.2011.06.009.
- [F⁺12] J. A. FORMAGGIO, P. LAZIC, T. J. CORONA ET AL. *Solving for micro- and macro-scale electrostatic configurations using the robin hood algorithm*. Prog. Electromagn. Res. B, 39:1–37, 2012. URL: <http://www.jpier.org/PIERB/pier.php?paper=11112106>, doi:10.2528/PIERB11112106.
- [F⁺17] D. FURSE, S. GROH, N. TROST ET AL. *Kassiopeia: A Modern, Extensible C++ Particle Tracking Package*. NJP, 19(5):053012, 2017. URL: <http://iopscience.iop.org/article/10.1088/1367-2630/aa6950>, doi:10.1088/1367-2630/aa6950.

- [Fer34] E. FERMI. *Versuch einer Theorie der β -Strahlen. I.* Z. Phys., 88(3):161–177, Mar 1934. URL: <http://link.springer.com/article/10.1007/BF01351864>, doi:10.1007/BF01351864.
- [Fis14] S. FISCHER. *Commissioning of the KATRIN Raman system and durability studies of optical coatings in glove box and tritium atmospheres.* PhD thesis, Karlsruhe Institut für Technologie, 2014.
- [FM⁺13] D. FOREMAN-MACKEY, D. W. HOGG, D. LANG ET AL. *emcee: The MCMC Hammer.* Publ. Astron. Soc. Pac., 125(925):306, 2013. URL: <http://stacks.iop.org/1538-3873/125/i=925/a=306>, doi:10.1086/670067.
- [Fow31] R. H. FOWLER. *The Analysis of Photoelectric Sensitivity Curves for Clean Metals at Various Temperatures.* Phys. Rev., 38:45–56, Jul 1931. URL: <http://link.aps.org/doi/10.1103/PhysRev.38.45>, doi:10.1103/PhysRev.38.45.
- [Frä10] F. M. FRÄNKLE. *Background Investigations of the KATRIN Pre-Spectrometer.* PhD thesis, Karlsruhe Institut für Technologie, 2010.
- [Ful16] A. FULST. *Investigations of Time-of-Flight Methods for the KATRIN Experiment.* Master's thesis, Westfälische Wilhelms-Universität Münster, 2016.
- [Fur15] D. L. FURSE. *Techniques for Direct Neutrino Mass Measurement Utilizing Tritium β -Decay.* PhD thesis, Massachusetts Institute of Technology, 2015.
- [G⁺09] F. GLÜCK, S. MERTENS, A. OSIPOWICZ ET AL. *Air Coil System & Magnetic Field Sensor System.* Technical report, KIT Karlsruhe, 2009. internal report (BSCW). URL: <https://fuzzy.fzk.de/bscw/bscw.cgi/d530439/Air%20Coil%20System%20and%20Magnetic%20Field%20Sensor%20System.pdf>.
- [G⁺10] W. GIL, J. BONN, B. BORNSCHEIN ET AL. *The Cryogenic Pumping Section of the KATRIN Experiment.* IEEE Trans. Appl. Supercond., 20(3):316–319, June 2010. URL: <http://ieeexplore.ieee.org/xpl/articleDetails.jsp?arnumber=5371979>, doi:10.1109/TASC.2009.2038581.
- [G⁺11] A. GANDO, Y. GANDO, K. ICHIMURA ET AL. *Constraints on θ_{13} from a three-flavor oscillation analysis of reactor antineutrinos at KamLAND.* Phys. Rev. D, 83:052002, Mar 2011. URL: <http://link.aps.org/doi/10.1103/PhysRevD.83.052002>, doi:10.1103/PhysRevD.83.052002.
- [G⁺12] W. GIL, J. BONN, O. DORMICCHI ET AL. *Status of the Magnets of the Two Tritium Pumping Sections for KATRIN.* IEEE Trans. Appl. Supercond., 22(3):4500604–4500604, June 2012. URL: <http://ieeexplore.ieee.org/xpl/articleDetails.jsp?arnumber=6072243>, doi:10.1109/TASC.2011.2175353.
- [G⁺13a] A. GANDO, Y. GANDO, H. HANAKAGO ET AL. *Limit on Neutrinoless $\beta\beta$ Decay of ^{136}Xe from the First Phase of KamLAND-Zen and Comparison with the Positive Claim in ^{76}Ge .* Phys. Rev. Lett., 110:062502, Feb 2013. URL: <http://link.aps.org/doi/10.1103/PhysRevLett.110.062502>, doi:10.1103/PhysRevLett.110.062502.
- [G⁺13b] FERENC GLÜCK, GUIDO DREXLIN, BENJAMIN LEIBER ET AL. *Electromagnetic design of the large-volume air coil system of the KATRIN experiment.* New J. Phys., 15(8):083025, 2013. URL: <http://stacks.iop.org/1367-2630/15/i=8/a=083025>, doi:10.1088/1367-2630/15/8/083025.
- [G⁺14] L. GASTALDO, K. BLAUM, A. DOERR ET AL. *The Electron Capture ^{163}Ho Experiment ECHo.* J. Low Temp. Phys., 176(5):876–884, 2014. URL: <http://link.springer.com/article/10.1007/s10909-014-1187-4>, doi:10.1007/s10909-014-1187-4.
- [GB76] M.L. GLASSER, A. BAGCHI. *Theories of photoemission from metal surfaces.* Prog. Surf. Sci., 7(3):113 – 148, 1976. URL: <http://www.sciencedirect.com/science/article/pii/0079681676900034>, doi:10.1016/0079-6816(76)90003-4.
- [GC⁺12] J. J. GOMEZ-CADENAS, J. MARTIN-ALBO, M. MEZZETTO ET AL. *The search for neutrinoless dou-*

- ble beta decay*. Riv. Nuovo Cimento, 02(0), 2012. URL: <http://www.sif.it/riviste/ncr/econtents/2012/035/02/article/0>, doi:10.1393/ncr/i2012-10074-9.
- [Glu11a] F. GLUCK. *Axisymmetric electric field calculation with zonal harmonic expansion*. Prog. Electromagn. Res. B, 32:319–350, 2011. URL: <http://www.jpier.org/PIERB/pier.php?paper=11042106>, doi:10.2528/PIERB11042106.
- [Glu11b] F. GLUCK. *Axisymmetric magnetic field calculation with zonal harmonic expansion*. Prog. Electromagn. Res. B, 32:351–388, 2011. URL: <http://www.jpier.org/PIERB/pier.php?paper=11042108>, doi:10.2528/PIERB11042108.
- [Gör14] S. GÖRHARDT. *Background Reduction Methods and Vacuum Technology at the KATRIN Spectrometer*. PhD thesis, Karlsruhe Institut für Technologie, 2014.
- [Gro15] S. GROH. *Modeling of the response function and measurement of transmission properties of the KATRIN experiment*. PhD thesis, Karlsruhe Institut für Technologie, 2015.
- [GW10] J. GOODMAN, J. WEARE. *Ensemble samplers with affine invariance*. Comm. App. Math. Comp. Sci., 5(1):65–80, 2010. URL: <http://msp.org/camcos/2010/5-1/p04.xhtml>, doi:10.2140/camcos.2010.5.65.
- [H⁺13] V. HANNEN, H.-W. ORTJOHANN, M. ZACHER ET AL. *Electrical short circuits in the main spectrometer wire electrode*. Technical report, Westfälische Wilhelms-Universität Münster, 2013. internal report (BSCW). URL: https://fuzzy.fzk.de/bscw/bscw.cgi/d875473/430-doc-3-9001-shortcircuit_report.pdf.
- [H⁺17] V. HANNEN, I. HEESE, C. WEINHEIMER ET AL. *Deconvolution of the energy loss function of the KATRIN experiment*. Astropart. Phys., 89:30–38, 2017. URL: <http://www.sciencedirect.com/science/article/pii/S0927650517300348>, doi:10.1016/j.astropartphys.2017.01.010.
- [Han74] J. S. HANSEN. *Internal ionization during alpha decay: A new theoretical approach*. Phys. Rev. A, 9:40–43, Jan 1974. URL: <http://link.aps.org/doi/10.1103/PhysRevA.9.40>, doi:10.1103/PhysRevA.9.40.
- [Har15] F. HARMS. *Characterization and Minimization of Background Processes in the KATRIN Main Spectrometer*. PhD thesis, Karlsruhe Institut für Technologie, 2015.
- [Has70] W. K. HASTINGS. *Monte Carlo sampling methods using Markov chains and their applications*. Biometrika, 57(1):97–109, 1970. URL: <http://biomet.oxfordjournals.org/content/57/1/97.abstract>, doi:10.1093/biomet/57.1.97.
- [Her87] H. HERTZ. *Ueber einen Einfluss des ultravioletten Lichtes auf die elektrische Entladung*. Ann. Phys. (Berlin), 267(8):983–1000, 1887. URL: <http://onlinelibrary.wiley.com/doi/10.1002/andp.18872670827>, doi:10.1002/andp.18872670827.
- [Hil11] B. HILLEN. *Untersuchung von Methoden zur Unterdrückung des Spektrometeruntergrunds beim KATRIN-Experiment*. PhD thesis, Westfälische Wilhelms-Universität Münster, 2011.
- [Hil16] D. HILK. *Electric field simulations and electric dipole investigations at the KATRIN main spectrometer*. PhD thesis, Karlsruhe Institut für Technologie, 2016.
- [HW97] J. R. M. HOSKING, J. R. WALLIS. *Regional frequency analysis: an approach based on L-moments*, chapter A.8. Cambridge University Press, 1997.
- [Jac62] J. D. JACKSON. *Classical Electrodynamics*, chapter 12. Wiley & Sons Ltd., 1962. URL: <https://archive.org/details/ClassicalElectrodynamics>.
- [Jan15] A. JANSEN. *The cryogenic pumping section of the KATRIN experiment – Design studies and experiments for the commissioning*. PhD thesis, Karlsruhe Institut für Technologie, 2015.

- [Jos13] L. JOSTEN. *Readout and control of a UHV manipulator for calibration measurements at the KATRIN main spectrometer*. Bachelor's thesis, Westfälische Wilhelms-Universität Münster, 2013.
- [JR75] F. JAMES, M. ROOS. *Minuit - a system for function minimization and analysis of the parameter errors and correlations*. *Comput. Phys. Commun.*, 10(6):343 – 367, 1975. URL: <http://www.sciencedirect.com/science/article/pii/0010465575900399>, doi: 10.1016/0010-4655(75)90039-9.
- [K⁺05] CH. KRAUS, B. BORNSCHEIN, L. BORNSCHEIN ET AL. *Final results from phase II of the Mainz neutrino mass search in tritium β decay*. *Eur. Phys. J. C*, 40(4):447–468, Apr 2005. URL: <http://link.springer.com/article/10.1140/epjc/s2005-02139-7>, doi: 10.1140/epjc/s2005-02139-7.
- [Kit88] C. KITTEL. *Einführung in die Festkörperphysik*, chapter 6, pages 159–169. R. Oldenbourg Verlag, München, 7 edition, 1988.
- [KKK06] H. V. KLAPDOR-KLEINGROTHAUS, I. V. KRIVOSHEINA. *The evidence for the observation of $0\nu\beta\beta$ decay: The identification of $0\nu\beta\beta$ events from the full spectra*. *Mod. Phys. Lett. A*, 21(20):1547–1566, 2006. URL: <http://www.worldscientific.com/doi/abs/10.1142/S0217732306020937>, doi:10.1142/S0217732306020937.
- [Kle14] M. KLEESIEK. *A Data-Analysis and Sensitivity-Optimization Framework for the KATRIN Experiment*. PhD thesis, Karlsruhe Institut für Technologie, 2014.
- [Kos12] A. KOSMIEDER. *Tritium Retention Techniques in the KATRIN Transport Section and Commissioning of its DPS2-F Cryostat*. PhD thesis, Karlsruhe Institut für Technologie, 2012.
- [Kra16] M. KRAUS. *Energy-scale systematics at the KATRIN main spectrometer*. PhD thesis, Karlsruhe Institut für Technologie, 2016.
- [L⁺06] X. LUO, CHR. DAY, V. HAUER ET AL. *Monte Carlo simulation of gas flow through the KATRIN DPS2-F differential pumping system*. *Vacuum*, 80(8):864 – 869, 2006. URL: <http://www.sciencedirect.com/science/article/pii/S0042207X05003891>, doi:10.1016/j.vacuum.2005.11.044.
- [L⁺12] S. LUKIĆ, B. BORNSCHEIN, L. BORNSCHEIN ET AL. *Measurement of the gas-flow reduction factor of the KATRIN DPS2-F differential pumping section*. *Vacuum*, 86(8):1126 – 1133, 2012. URL: <http://www.sciencedirect.com/science/article/pii/S0042207X11003800>, doi: 10.1016/j.vacuum.2011.10.017.
- [LL05] W. LI, D. Y. LI. *On the correlation between surface roughness and work function in copper*. *J. Chem. Phys.*, 122(6), 2005. URL: <http://scitation.aip.org/content/aip/journal/jcp/122/6/10.1063/1.1849135>, doi:10.1063/1.1849135.
- [LP06] J. LESGOURGUES, S. PASTOR. *Massive neutrinos and cosmology*. *Phys. Rep.*, 429(6):307 – 379, 2006. URL: <http://www.sciencedirect.com/science/article/pii/S0370157306001359>, doi: 10.1016/j.physrep.2006.04.001.
- [LS85] V. M. LOBASHEV, P. E. SPIVAK. *A method for measuring the electron antineutrino rest mass*. *Nucl. Instr. Meth. Phys. Res. A*, 240(2):305 – 310, 1985. URL: <http://www.sciencedirect.com/science/article/pii/0168900285906400>, doi:10.1016/0168-9002(85)90640-0.
- [M⁺53] N. METROPOLIS, A. W. ROSENBLUTH, M. N. ROSENBLUTH ET AL. *Equation of State Calculations by Fast Computing Machines*. *J. Chem. Phys.*, 21(6):1087–1092, 1953. URL: <http://scitation.aip.org/content/aip/journal/jcp/21/6/10.1063/1.1699114>, doi: 10.1063/1.1699114.
- [M⁺62] ZIRO MAKI ET AL. *Remarks on the Unified Model of Elementary Particles*. *Progress of Theoretical Physics*, 28(5):870–880, 1962. URL: <http://ptp.oxfordjournals.org/content/28/5/870.abstract>, doi:10.1143/PTP.28.870.

- [M⁺12] S. MERTENS, A. BEGLARIAN, L. BORNSCHEIN ET AL. *Stochastic heating by ECR as a novel means of background reduction in the KATRIN spectrometers*. Journ. Instr., 7(08):P08025, 2012. URL: <http://stacks.iop.org/1748-0221/7/i=08/a=P08025>, doi:10.1088/1748-0221/7/08/P08025.
- [M⁺13] S. MERTENS, G. DREXLIN, F.M. FRÄNKLE ET AL. *Background due to stored electrons following nuclear decays in the KATRIN spectrometers and its impact on the neutrino mass sensitivity*. Astropart. Phys., 41:52 – 62, 2013. URL: <http://www.sciencedirect.com/science/article/pii/S0927650512001892>, doi:10.1016/j.astropartphys.2012.10.005.
- [Mac14] C. MACOLINO. *Results on Neutrinoless Double-Beta Decay from GERDA Phase I*. Mod. Phys. Lett. A, 29:1430001, 2014. URL: <http://www.worldscientific.com/doi/abs/10.1142/S0217732314300018>, doi:10.1142/S0217732314300018.
- [Mer12] S. MERTENS. *Study of Background Processes in the Electrostatic Spectrometers of the KATRIN experiment*. PhD thesis, Karlsruhe Institut für Technologie, 2012.
- [MS86] S. P. MIKHEYEV, A. YU. SMIRNOV. *Resonant amplification of ν oscillations in matter and solar-neutrino spectroscopy*. Nuovo Cimento C, 9(1):17–26, 1986. URL: <http://dx.doi.org/10.1007/BF02508049>, doi:10.1007/BF02508049.
- [NIS12] NIST/SEMATECH. *e-Handbook of Statistical Methods*, chapter Percentiles. 2012. URL: <http://www.itl.nist.gov/div898/handbook/prc/section2/prc262.htm>.
- [Nob95] *The Nobel Prize in Physics 1995 – Press Release*, 1995. Nobelprize.org. URL: http://www.nobelprize.org/nobel_prizes/physics/laureates/1995/press.html?
- [Nob02] *The Nobel Prize in Physics 2002 – Press Release*, 2002. Nobelprize.org. URL: http://www.nobelprize.org/nobel_prizes/physics/laureates/2002/press.html?
- [Nob08] *The Nobel Prize in Physics 2008 – Press Release*, 2008. Nobelprize.org. URL: http://www.nobelprize.org/nobel_prizes/physics/laureates/2008/press.html?
- [Nob15] *The Nobel Prize in Physics 2015 – Press Release*, 2015. Nobelprize.org. URL: http://www.nobelprize.org/nobel_prizes/physics/laureates/2015/press.html?
- [NS⁺16] M. NEWVILLE, T. STENSITZKI ET AL. *Non-Linear Least-Squares Minimization and Curve-Fitting for Python*, 2016. URL: <http://cars9.uchicago.edu/software/python/lmfit/lmfit.pdf>.
- [Nuc08] A. NUCCIOTTI. *The MARE Project*. J. Low Temp. Phys., 151(3):597–602, 2008. URL: <http://dx.doi.org/10.1007/s10909-008-9718-5>, doi:10.1007/s10909-008-9718-5.
- [O⁺12] A OSIPOWICZ, W SELLER, J LETNEV ET AL. *A mobile magnetic sensor unit for the KATRIN main spectrometer*. J. Instrum., 7(06):T06002, 2012. URL: <http://stacks.iop.org/1748-0221/7/i=06/a=T06002>, doi:10.1088/1748-0221/7/06/T06002.
- [OG14] K.A. OLIVE, PARTICLE DATA GROUP. *Review of Particle Physics*. Chin. Phys. C, 38(9):090001, 2014. 2015 update. URL: <http://stacks.iop.org/1674-1137/38/i=9/a=090001>, doi:10.1088/1674-1137/38/9/090001.
- [Ott10a] E. OTTEN. *Removal of stored particles in MAC-E filters*. internal document, 2010.
- [Ott10b] E. OTTEN. *Searching the absolute neutrino mass in tritium β -decay—interplay between nuclear, atomic and molecular physics*. Hyperfine Interact., 196(1):3–23, 2010. URL: <http://link.springer.com/article/10.1007/s10751-009-0150-2>, doi:10.1007/s10751-009-0150-2.
- [OW08] E. W. OTTEN, C. WEINHEIMER. *Neutrino mass limit from tritium β decay*. Rep. Prog. Phys., 71(8):086201, 2008. URL: <http://stacks.iop.org/0034-4885/71/i=8/a=086201>, doi:10.1088/0034-4885/71/8/086201.
- [P⁺92] A. PICARD, H. BACKE, H. BARTH ET AL. *A solenoid retarding spectrometer with high resolu-*

- tion and transmission for keV electrons.* Nucl. Instr. Meth. Phys. Res. B, 63(3):345 – 358, 1992. URL: <http://www.sciencedirect.com/science/article/pii/0168583X9295119C>, doi:10.1016/0168-583X(92)95119-C.
- [P⁺10] G. PAGLIAROLI, F. ROSSI-TORRES, F. VISSANI. *Neutrino mass bound in the standard scenario for supernova electronic antineutrino emission.* Astropart. Phys., 33(5–6):287 – 291, 2010. URL: <http://www.sciencedirect.com/science/article/pii/S0927650510000484>, doi:10.1016/j.astropartphys.2010.02.007.
- [P⁺15] FLORIAN PRIESTER, MICHAEL STURM, BEATE BORNSCHEIN. *Commissioning and detailed results of KATRIN inner loop tritium processing system at Tritium Laboratory Karlsruhe.* Vacuum, 116:42 – 47, 2015. URL: <http://www.sciencedirect.com/science/article/pii/S0042207X15000846>, doi:10.1016/j.vacuum.2015.02.030.
- [Pau30] W. PAULI. *Offener Brief an die Gruppe der Radioaktiven bei der Gauvereins-Tagung zu Tübingen, Dez 1930.* URL: <https://cds.cern.ch/record/83282?ln=fr>.
- [PB02] Z. PEI, C. N. BERGLUND. *Angular Distribution of Photoemission from Gold Thin Films.* Jpn. J. Appl. Phys., 41(1A):L52, 2002. URL: <http://stacks.iop.org/1347-4065/41/i=1A/a=L52>, doi:10.1143/JJAP.41.L52.
- [PD⁺15] NATHALIE PALANQUE-DELABROUILLE, CHRISTOPHE YÈCHE, JULIEN BAUR ET AL. *Neutrino masses and cosmology with Lyman-alpha forest power spectrum.* J. Cosmol. Astropart. Phys., 2015(11):011, 2015. URL: <http://stacks.iop.org/1475-7516/2015/i=11/a=011>, doi:10.1088/1475-7516/2015/11/011.
- [Pon57] B. PONTECORVO. *Mesonium and anti-mesonium.* Sov. Phys. JETP, 6:429, 1957. [Zh. Eksp. Teor. Fiz. 33, 549 (1957)].
- [Pot13] A. POTTHOFF. *Aufbau einer durchstimmbaren UV-Lichtquelle für das KATRIN-Experiment.* Bachelor's thesis, Westfälische Wilhelms-Universität Münster, 2013.
- [Pri13] F. PRIESTER. *Tritiumtechnologie für die fensterlose Quelle WGTS von KATRIN.* PhD thesis, Karlsruhe Institut für Technologie, 2013.
- [R⁺75a] M. S. RAPAPORT, F. ASARO, I. PERLMAN. *K-shell electron shake-off accompanying alpha decay.* Phys. Rev. C, 11:1740–1745, May 1975. URL: <http://link.aps.org/doi/10.1103/PhysRevC.11.1740>, doi:10.1103/PhysRevC.11.1740.
- [R⁺75b] M. S. RAPAPORT, F. ASARO, I. PERLMAN. *L- and M-shell electron shake-off accompanying alpha decay.* Phys. Rev. C, 11:1746–1754, May 1975. URL: <http://link.aps.org/doi/10.1103/PhysRevC.11.1746>, doi:10.1103/PhysRevC.11.1746.
- [Ran14] P. RANITZSCH. *e-gun status*, Nov 2014. electronic logbook (internal site). URL: <https://neutrino.ikp.kit.edu:8080/main-spectrometer/760>.
- [Res17] O. REST. *Precision high voltage at the KATRIN experiment and a new method for an absolute calibration at ppm level for the KATRIN high voltage dividers.* PhD thesis, Westfälische Wilhelms-Universität Münster, 2017. in preparation.
- [S⁺95] G. F. SAVILLE, P. M. PLATZMAN, G. BRANDES ET AL. *Feasibility study of photocathode electron projection lithography.* J. Vac. Sci. Technol. B, 13(6):2184–2188, 1995. URL: <http://scitation.aip.org/content/avs/journal/jvstb/13/6/10.1116/1.588101>, doi:10.1116/1.588101.
- [S⁺13a] M. SLEZÁK, S. BAUER, O. DRAGON ET AL. *Electron line shape of the KATRIN monitor spectrometer.* J. Instrum., 8(12):T12002, 2013. URL: <http://stacks.iop.org/1748-0221/8/i=12/a=T12002>, doi:10.1088/1748-0221/8/12/T12002.
- [S⁺13b] NICHOLAS STEINBRINK, VOLKER HANNEN, ERIC L MARTIN ET AL. *Neutrino mass sensitivity by MAC-E-Filter based time-of-flight spectroscopy with the example of KATRIN.* New J. Phys.,

- 15(11):113020, 2013. URL: <http://stacks.iop.org/1367-2630/15/i=11/a=113020>, doi: 10.1088/1367-2630/15/11/113020.
- [Sch13] S. SCHAMS. *Data Analysis Tools and Sterile Neutrino Investigations for the KATRIN Experiment*. Diploma thesis, Karlsruhe Institut für Technologie, 2013.
- [Sch14] J. SCHWARZ. *The Detector System of the KATRIN Experiment – Implementation and First Measurements with the Spectrometer*. PhD thesis, Karlsruhe Institut für Technologie, 2014.
- [She92] C. S. SHERN. *Changes in Work Function of Hydrogen and Oxygen Adsorption on Pt(110) Surface Measured by Mirror Electron Microscope-LEED*. CJP, 30(6):841–850, 1992. URL: <http://psroc.org.tw/cjp/issues.php?vol=30&num=6>.
- [Sle15] M. SLEZAK. *Monitoring of the energy scale in the KATRIN neutrino experiment*. PhD thesis, NPI/Czech Academy of Sciences, 2015.
- [SV05] A. STRUMIA, F. VISSANI. *Implications of neutrino data circa 2005*. Nucl. Phys., B726:294–316, 2005. arXiv:hep-ph/0503246, doi:10.1016/j.nuclphysb.2005.07.031.
- [T⁺09] TH THÜMMLER, R MARX, CH WEINHEIMER. *Precision high voltage divider for the KATRIN experiment*. New J. Phys., 11(10):103007, 2009. URL: <http://stacks.iop.org/1367-2630/11/i=10/a=103007>, doi:10.1088/1367-2630/11/10/103007.
- [Tro17] N. TROST. *Modeling and measuring of Rydberg state related background at the KATRIN main spectrometer*. PhD thesis, Karlsruhe Institut für Technologie, 2017. in preparation.
- [V⁺09] K VALERIUS, M BECK, H ARLINGHAUS ET AL. *A UV LED-based fast-pulsed photoelectron source for time-of-flight studies*. New J. Phys., 11(6):063018, 2009. URL: <http://stacks.iop.org/1367-2630/11/i=6/a=063018>, doi:10.1088/1367-2630/11/6/063018.
- [V⁺11] K VALERIUS, H HEIN, H BAUMEISTER ET AL. *Prototype of an angular-selective photoelectron calibration source for the KATRIN experiment*. J. Instrum., 6(01):P01002, 2011. URL: <http://stacks.iop.org/1748-0221/6/i=01/a=P01002>, doi:10.1088/1748-0221/6/01/P01002.
- [V⁺15] P. VOGEL, L.J. WEN, C. ZHANG. *Neutrino oscillation studies with reactors*. Nat. Commun., 6(6935), Apr 2015. URL: <http://www.nature.com/articles/ncomms7935>, doi:10.1038/ncomms7935.
- [Val09] K. VALERIUS. *Spectrometer-related background processes and their suppression in the KATRIN experiment*. PhD thesis, Westfälische Wilhelms-Universität Münster, 2009.
- [Van14] J. VANDENPLAS. *Frequentism and Bayesianism: A Python-driven primer*. arXiv, Nov 2014. URL: <http://arxiv.org/abs/1411.5018>, arXiv:1411.5018.
- [W⁺99] CH. WEINHEIMER, B. DEGENDDAG, A. BLEILE ET AL. *High precision measurement of the tritium β spectrum near its endpoint and upper limit on the neutrino mass*. Phys. Lett. B, 460(1–2):219 – 226, 1999. URL: <http://www.sciencedirect.com/science/article/pii/S0370269399007807>, doi:10.1016/S0370-2693(99)00780-7.
- [W⁺13] N. WANDKOWSKY, G. DREXLIN, F. M. FRÄNKLE ET AL. *Validation of a model for radon-induced background processes in electrostatic spectrometers*. J. Phys. G, 40(8):085102, 2013. URL: <http://stacks.iop.org/0954-3899/40/i=8/a=085102>, doi:10.1088/0954-3899/40/8/085102.
- [W⁺14] B.L. WALL, J.F. AMSBAUGH, A. BEGLARIAN ET AL. *Dead layer on silicon p–i–n diode charged-particle detectors*. Nucl. Instr. Meth. Phys. Res. A, 744:73 – 79, 2014. URL: <http://www.sciencedirect.com/science/article/pii/S016890021301752X>, doi:10.1016/j.nima.2013.12.048.
- [Wan13] N. WANDKOWSKY. *Study of background and transmission properties of the KATRIN spectrometers*. PhD thesis, Karlsruhe Institut für Technologie, 2013.

- [Wie16] K. WIERMAN. *Charge Accumulation in the KATRIN Main Spectrometer*. PhD thesis, University of North Carolina at Chapel Hill, 2016.
- [Wil66] R. G. WILSON. *Vacuum Thermionic Work Functions of Polycrystalline Be, Ti, Cr, Fe, Ni, Cu, Pt, and Type 304 Stainless Steel*. *J. Appl. Phys.*, 37(6):2261–2267, 1966. URL: <http://scitation.aip.org/content/aip/journal/jap/37/6/10.1063/1.1708797>, doi:10.1063/1.1708797.
- [Win14] D. WINZEN. *Development of an angular selective electron gun for the KATRIN main spectrometer*. Diploma thesis, Westfälische Wilhelms-Universität Münster, 2014.
- [Wol78] L. WOLFENSTEIN. *Neutrino oscillations in matter*. *Phys. Rev. D*, 17:2369–2374, May 1978. URL: <http://link.aps.org/doi/10.1103/PhysRevD.17.2369>, doi:10.1103/PhysRevD.17.2369.
- [Wol15] J. WOLF. *KATRIN-3D-drawings / Components 2015 / beamline*, 2015. BSCW (internal site). URL: <https://fuzzy.fzk.de/bscw/bscw.cgi/964292>.
- [Wu07] S.-C. WU. *Nuclear Data Sheets for A = 216*. *Nucl. Data Sheets*, 108(5):1057 – 1092, 2007. URL: <http://www.sciencedirect.com/science/article/pii/S0090375207000415>, doi:10.1016/j.nds.2007.04.001.
- [Z⁺13] M ZBOŘIL, S BAUER, M BECK ET AL. *Ultra-stable implanted ⁸³Rb/^{83m}Kr electron sources for the energy scale monitoring in the KATRIN experiment*. *J. Instrum.*, 8(03):P03009, 2013. URL: <http://stacks.iop.org/1748-0221/8/i=03/a=P03009>, doi:10.1088/1748-0221/8/03/P03009.
- [Zac14] M. ZACHER. *High-field electrodes design and an angular-selective photoelectron source for the KATRIN spectrometers*. PhD thesis, Westfälische Wilhelms-Universität Münster, 2014.

Danksagung

Ich möchte mich an dieser Stelle bei all denen bedanken, die Ihren Teil zu dieser Dissertation beigetragen haben. Es ist nicht einfach, nach all den Jahren eine Liste aller Personen zusammenzutragen, die mich bei diesem Projekt unterstützt haben. Daher entschuldige ich mich hier im Voraus bei allen, die ich hier vergesse.

Herrn Prof. Dr. Christian Weinheimer danke ich für zwei spannende Dissertationsprojekte, bei denen ich viele neue Erfahrungen sammeln konnte. Dankbar bin ich ihm auch für die immerwährende Unterstützung bereits seit meiner Diplomandenzeit und die Möglichkeit, an so vielen verschiedenen Konferenzen, Tagungen und Workshops teilzunehmen. Meinem Zweitgutachter Herrn Prof. Dr. Dieter Frekers danke ich ebenfalls für die Betreuung und vor allem dafür, dass er sich so kurzfristig als Gutachter bereit erklärt hat.

Hervorheben möchte ich die angenehme Arbeitsatmosphäre im IKP und die wahnsinnig tolle Zusammenarbeit. Stellvertretend für die jeweiligen Arbeitsgruppen danke ich hier Prof. Dr. Dieter Frekers, Prof. Dr. Alexander Kappes, Prof. Dr. Alfons Khoukaz und Prof. Dr. Johannes Wessels. Diese Arbeit wäre ohne die technische und organisatorische Unterstützung seitens der IKP-Mitarbeiter nicht möglich gewesen. Vor allem Hans-Werner Ortjohann hatte für jede technische Herausforderung eine Lösung parat und hat wesentlich zum Gelingen dieser Arbeit beigetragen. Auch danken möchte ich der Elektronik-Werkstatt, vor allem Roland Berendes und Wladimir Buglak für die Entwicklung der FlipBox, sowie der feinmechanischen Werkstatt, die beide immer großartige Arbeit geleistet haben. Durch Michaela Erdmann, Uta Mayer, Wolfgang Grundschöttl und später Andreas Boonk war zudem immer für alle organisatorischen und praktischen Belange gesorgt. Volker Hannen und Philipp Ranitzsch sind nicht nur Ihren zahlreichen Verpflichtungen als Postdocs stets souverän nachgekommen, sondern haben auch bei vielen Gelegenheiten dafür gesorgt, dass die Arbeit am KATRIN-Experiment allen Herausforderungen zum Trotz viel Spaß gemacht hat. Für das Korrekturlesen meiner Arbeit, viele anregende Diskussionen und die tolle Unterstützung danke ich Stephan Dyba, Oliver Rest und Daniel Winzen. Die Betreuung der IT-Infrastruktur am IKP war ein sehr spannendes Langzeitprojekt und wäre ohne Tom Dietel, Martin Kohn, Volker Hannen und später Tobias Böwing sicherlich nicht möglich gewesen. Dem Organisations-team für unser Astroseminar danke ich für die erfolgreiche Zusammenarbeit und die schöne gemeinsame Zeit. Außerdem bedanke ich mich bei den vielen Personen, die ich während meiner Zeit an der Uni kennengelernt habe – ganz besonders Raffi, sowie Alex, Andy, Axel, Christian, Daniel, Freya, Julia, Jonas, Maik, Manne, Maren, Matthias, Michael, Nicho, Christoph, Florian, Oliver, Simon, Stephan, Thomas, Tobi, Umut und ganz vielen anderen – für die zahlreichen lustigen Aktionen und Erlebnisse an und neben der Universität.

Auch meinen Kollegen am KIT, wo ich neben zwei Messphasen auch viel Zeit bei diversen Meetings und Workshops verbracht habe, möchte ich danken. Prof. Guido Drexlin, Kathrin Valerius und Thomas Thümmler danke ich für eine tolle Organisation und Hilfe bei allen möglichen Angelegenheiten. Armen Beglarian, Holger Frenzel, Joachim Wolf, Sascha Wüstling und viele andere haben durch ihre Expertise und ihre hervorragende Arbeit sehr viel zu dieser Arbeit beigetragen. Für anregende Gespräche und eine tolle Zeit in Karlsruhe danke ich außerdem unter anderem Daniel, Fabian, Johannes, Marco, Nancy, Nikolaus und Susanne. Das „e-Gauner“-Team mit Philipp, Moritz, Stefan, Marcel, John und Kevin hat die Messungen mit der Elektronenquelle und vor allem die Analyse der Daten überhaupt erst ermöglicht. Auch hier bedanke ich mich sehr für die gute Zusammenarbeit und für die tolle Arbeitsatmosphäre. Für die Mitentwicklung der Software, die ein ganz wesentlicher Teil dieser Arbeit ist, sowie für Unterstützung bei allen möglichen Programmier- und sonstigen Aufgaben danke neben ich neben bereits genannten Personen Dan, TJ und ganz Besonders Sanshiro.

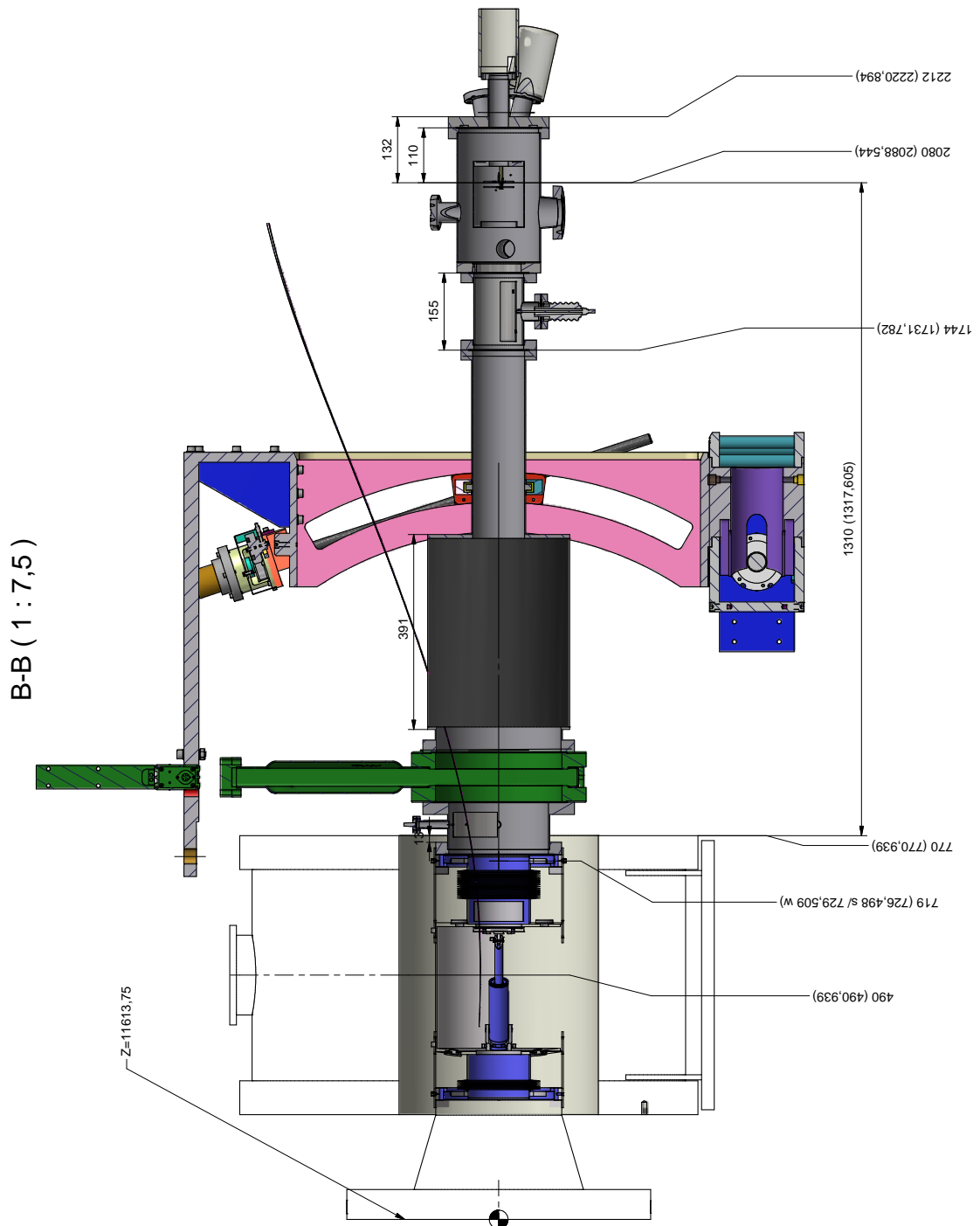
Bedanken möchte ich mich auch bei meiner Familie und den Leuten, die schon fast mit dazu gehören. Bastian und Fred haben mich über viele Jahre hinweg begleitet und hatten dabei immer ein offenes Ohr für allerlei Probleme. Außerdem danke ich meinen Großeltern und anderen Verwandten, die mich immer unterstützt haben. Marita, Kira, Michelle und Marcel danke ich für die schöne gemeinsame Zeit während Schule und Studium. Ich danke meiner Mutter Sabine mit Micha und Selina und ganz besonders meinem Vater Hans-Gerd, der mich seit mehr als 30 Jahren immerzu unterstützt hat und bei dem ich froh bin, ihn an meiner Seite zu wissen.

Zu guter Letzt aber noch ein Wort an alle, die mich in den vergangenen 10 Jahren in Münster von der Einschreibung zum Diplom bis hin zur Promotion begleitet haben: Es war eine tolle Zeit, und ich darf mich glücklich schätzen, so viele tolle Leute kennengelernt zu haben. Bleibt, wie ihr seid!

Technical design drawings

Electron source setup and alignment measurement results

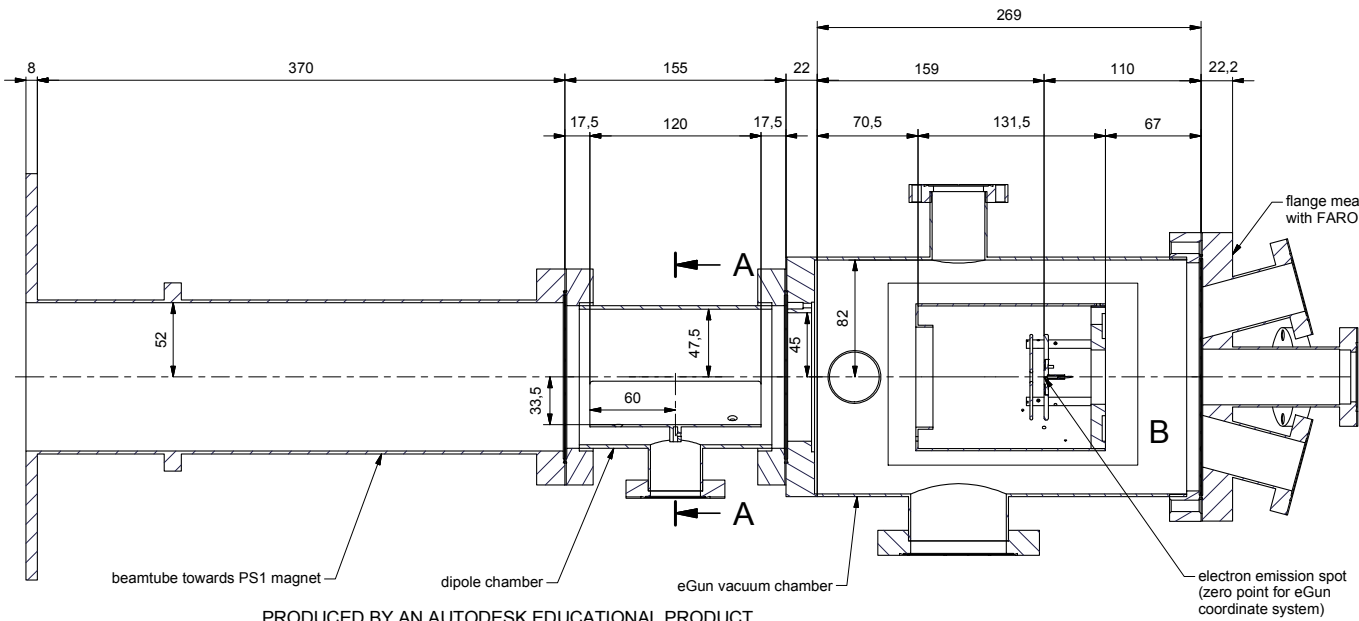
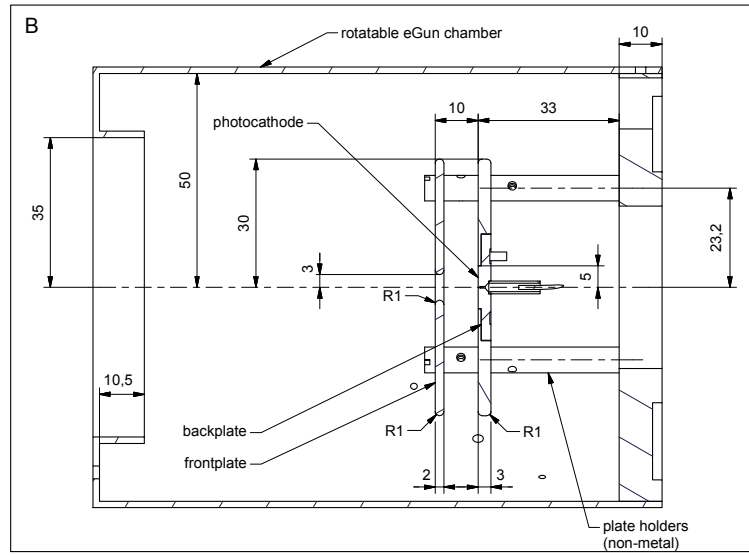
The drawing shows the complete setup for the SDS-2 measurements with the electron source vacuum chamber (right), the large UHV manipulator (center) and the PS2 magnet (left). The indicated distances are measured against the reference point (far left). The numbers show the design value; numbers in brackets refer to the results of the alignment measurements.



Electron source vacuum chamber

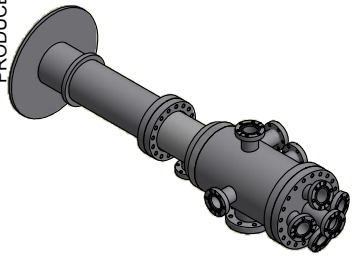
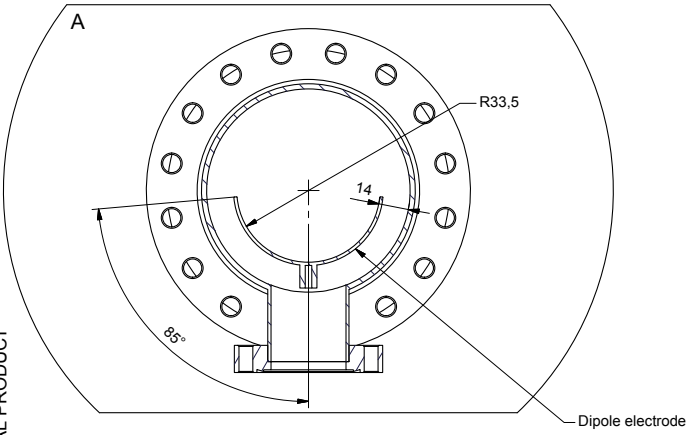
The drawing shows the source vacuum chamber up to the large flange where the manipulator bellow is attached. The simulation geometry of the electron source is based on this design drawing; the relevant dimensions are indicated.

PRODUCED BY AN AUTODESK EDUCATIONAL PRODUCT



PRODUCED BY AN AUTODESK EDUCATIONAL PRODUCT

PRODUCED BY AN AUTODESK EDUCATIONAL PRODUCT



eGun geometry for simulation

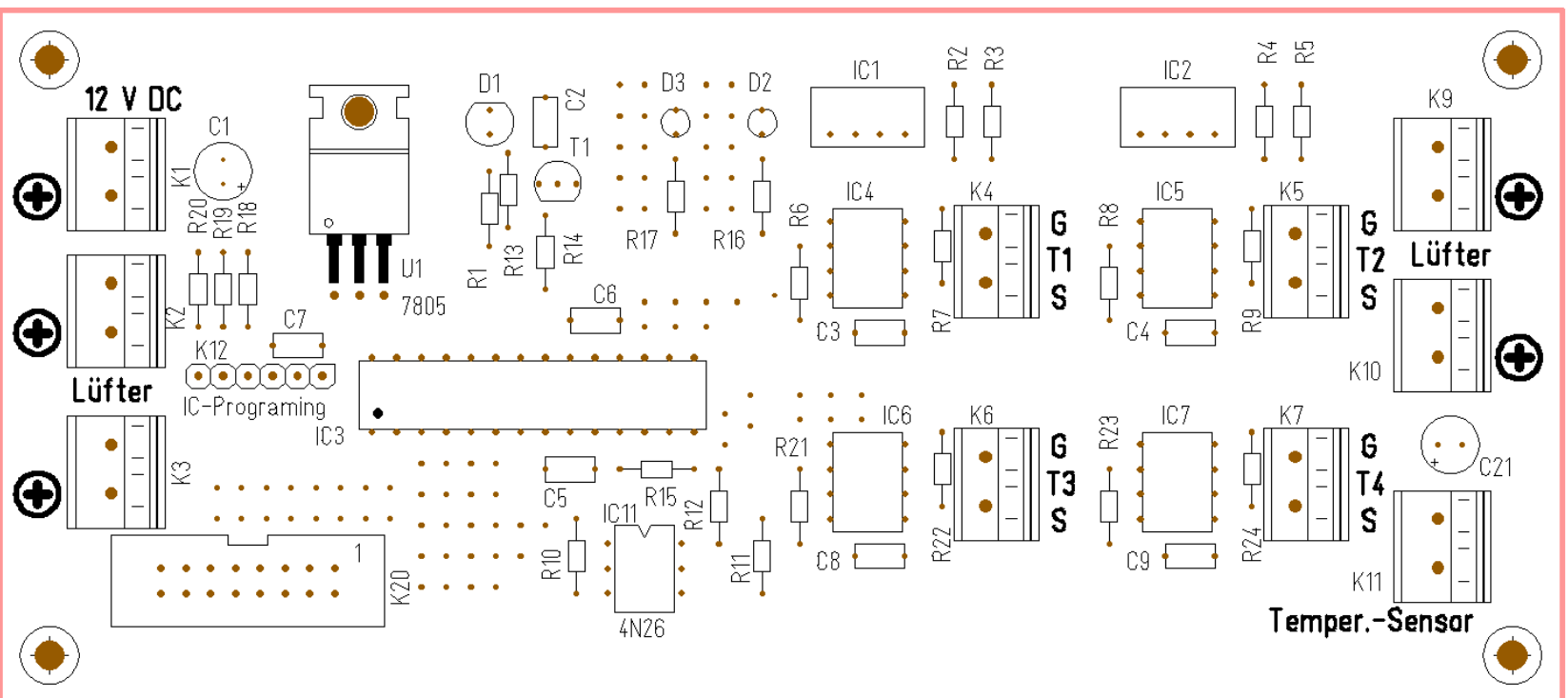
SDS-2 // 2014-09-15

J. Behrens / WWU Münster

PRODUCED BY AN AUTODESK EDUCATIONAL PRODUCT

Board layout of the FlipBox control circuit.

The drawing shows the component layout of the FlipBox control board. The control board is mounted inside each FlipBox device and connects the individual components.



Lebenslauf / Curriculum Vitae

Lebenslauf

Name: Jan David Behrens
Geburtsdatum: 25.03.1986
Geburtsort: Crailsheim
Staatsangehörigkeit: deutsch
Eltern: Johannes-Gerhard Behrens
Sabine Behrens-Marks, geb. Korffmann

Schulbildung

1992 – 1996 Grundschole, 26892 Lehe
1996 – 1998 Orientierungsstufe, 26892 Dörpen
1998 – 2005 Gymnasium, 26871 Papenburg
9.5.2005 Allgemeine Hochschulreife

Zivildienst

7/2005 – 3/2006 Zivildienst im Bereich Naturschutz bei
Landkreis Emsland, FB Naturschutz, 49716 Meppen

Studium

10/2006 – 8/2012 Studium der Physik an der
Westfälischen Wilhelms-Universität, 48149 Münster
10/2011 – 7/2012 Diplomarbeit in Kern- & Teilchenphysik
*Simulations of stored electrons in the Penning trap
between the KATRIN spectrometers*
13.8.2012 Diplomprüfung

Promotionsstudium

1.9.2012 Beginn der Dissertation am Institut für Kernphysik
unter der Betreuung von Herrn Prof. Dr. Christian Weinheimer

Berufstätigkeit

3/2006 – 5/2006 Aushilfskraft bei
Gartenbau F. Schulz, 26871 Papenburg
2/2011 – 8/2012 Studentische Hilfskraft am Institut für Kernphysik der
Westfälischen Wilhelms-Universität Münster
9/2012 – 12/2016 Wissenschaftlicher Mitarbeiter am Institut für Kernphysik der
Westfälischen Wilhelms-Universität Münster

Münster, den _____
